MASS TRANSFER AND CHEMICAL INTERACTIONS IN SUBDUCTION ZONES

By

Emmanuel Avila Codillo
B.S., University of the Philippines, Diliman (2015)

Submitted to the Department of Earth, Atmospheric, and Planetary Sciences in partial fulfillment of the requirements for the degree of

Doctor of Philosophy

at the

MASSACHUSETTS INSTITUTE OF TECHNOLOGY

and the

WOODS HOLE OCEANOGRAPHIC INSTITUTION

February 2023

Signature of Author

_____

Joint Program in Oceanography/Applied Ocean Science and Engineering
Massachusetts Institute of Technology and
Woods Hole Oceanographic Institution
January 10, 2023

Certified by

_____

Dr. Véronique Le Roux
Thesis Co-supervisor

_____

Dr. Frieder Klein
Thesis Co-supervisor

Accepted by

_____

Dr. Véronique Le Roux
Chair, Joint Committee for Marine Geology and Geophysics
Massachusetts Institute of Technology/
Woods Hole Oceanographic Institution

Mass Transfer and Chemical Interactions in Subduction Zones

By

Emmanuel A. Codillo

THESIS ABSTRACT

Subduction zones are important sites of material recycling on Earth, with volatiles playing key roles in mass transfer processes and magma formation. This thesis investigates outstanding questions associated with a continuum of interrelated processes that occur as oceanic plates descend in subduction zones by integrating petrological and geochemical constraints from exhumed high-pressure rocks and erupted arc magmas, high pressure-temperature laboratory experiments, and thermodynamic calculations. Chapters 2 and 3 investigate the fluid-mediated reactions between mafic and ultramafic rocks at conditions relevant to the slab-mantle interface and show that Mg-metasomatism of mafic rocks to form chlorite-rich assemblages is favored and is likely more pervasive in subduction zones than in oceanic settings. Contrary to common belief, talc is unlikely to form in high abundance in ultramafic rocks metasomatized by Si-rich slab-derived fluids. This means that talc-rich assemblages formed via Si-metasomatism along the slab-mantle interface are less likely to be playing prominent roles in volatile transport, in facilitating slow-slip events, and in controlling the decoupling-coupling transition of the plate interface. Chapter 4 experimentally investigates the phase equilibria, melting, and density evolution of mélange rocks that formed by mixing and fluid-rock interactions. Results show that melting of mélanges is unlikely to occur along slab-tops at pressures ≤ 2.5 GPa. Accordingly, diapirism into the hotter mantle wedge would be required to initiate melting. The density contrast between mélanges and the overlying mantle would allow for buoyancy-driven diapirism at relatively low pressures and melting could subsequently occur in the hotter mantle wedge during ascent. However, diapir buoyancy may be limited at higher pressures due to the formation of abundant garnet especially in mélange rocks with peraluminous composition. Chapter 5 experimentally investigates the compositions of melts and mineral residues from melting of a mantle wedge hybridized with small amounts of mélange rocks to simulate an end-member scenario where solid mélange diapirs dynamically interact with the mantle wedge. Results from laboratory experiments show that melting of a mélange-hybridized mantle wedge can produce melts that display compositional characteristics similar to arc magmas. Finally, Chapter 6 presents new interpretations on the evolution of slab-to-mantle transfer mechanisms from subduction initiation to arc maturity. Analyses of published magma compositions from global arcs reveal that melting of mélange plays an increasingly important role in magma formation as slab-tops cool and arcs

mature over time. This trend is attributed to the deepening of the decoupled plate interface during subduction where mélange zones can form more extensively and contribute to the melting process more significantly. Taken together, this thesis highlights (i) the dynamic connection between mechanical mixing of different lithologies and fluid-rock interactions along the slab-mantle interface, (ii) how these processes modify the petrophysical and geochemical properties of subducted materials, and (iii) how these processes collectively influence the mechanisms of slab-to-mantle transfer, elemental cycles, and the formation of arc magmas worldwide.

Thesis Co-supervisor: Dr. Véronique Le Roux
Title: Associate Scientist with Tenure
Department of Geology and Geophysics
Woods Hole Oceanographic Institution

Thesis Co-supervisor: Dr. Frieder Klein
Title: Associate Scientist with Tenure
Department of Marine Chemistry and Geochemistry
Woods Hole Oceanographic Institution

Acknowledgment

This thesis will not be possible without the support of many people within and beyond the walls of the MIT-WHOI Joint Program.

First off, I am forever grateful to my advisors Veronique Le Roux and Frieder Klein for taking a chance on me. I don't know how to thank them enough for all the time, knowledge, and support that they have given me. They have afforded me the freedom to explore scientifically but at the same time made sure that I wasn't going on a crazy detour. I don't remember how many times I have walked into their offices just to talk about random ideas I made up. Despite their busy schedules, they have always given their full attention. They have helped me in every step, especially in gaining my style and confidence as a scientist and as a person.

Vero, I don't know if any of these would happen if you never responded to a lowly undergraduate student from the Philippines asking for a copy of your research paper on December 27, 2014. That single action set off a chain reaction that brought me to this point. You're the catalyst and I will strive to be a catalyst for other students as well in the future. Frieder, it is an honor to be a dude working with you! I will strive to spread the teachings of "Dudeism" and fluid-rock interactions in the world. Thanks for the many morning coffee and chats about rocks and life in Mclean 200. Frieder and Vero, I feel so lucky and privileged to be your student. I'm looking forward to doing more amazing science with you.

My committee has been an invaluable source of knowledge and patience, particularly during the last 6 months of writing. Peter Barry, as the chair of defense, has provided guidance throughout. As a committee and as individuals, Horst R. Marschall, Jessica Warren and Oli Jagoutz have always made themselves available to answer questions, provide ideas and necessary constructive criticisms, all to strengthen my understanding of subduction zones and fluid-rock interaction processes. In addition to my thesis committee, many people have helped along the way. Nobu Shimizu is sincerely thanked for his dedication to teaching, especially when he stood up and volunteered to teach me anything and everything about subduction zones. I will never forget your willingness to drive for 2 hours (one-way) to Woods Hole during COVID times when people have not gotten vaccinated yet just to chat with me about trace elements and isotopes of arc magmas. His wisdom and kindness are unreal. Henry Dick welcomed me in his lab (and home) and gave me access to his collection of oceanic rocks. He gave me a solid foundation on the petrology and tectonics of the ocean floor from his never-ending litany about the compositional/lithological heterogeneity and temperature variations in the oceanic upper mantle. I hope that I contributed new knowledge in this thesis that is something you have not seen from the Josephine ophiolite before :) Glenn Gaetani is thanked for all the great discussions about experiments and of life. I value his insights on how to be an experimental petrologist and the vastness of questions that can be tackled using carefully thought out experiments. Glenn gladly chaired my generals exam in my 2nd year and has been a supporter ever since. Mark Kurz has sailed and brought me to ~3500 mbsl in the Mid-Atlantic Ridge via the submersible Alvin. That experience is arguably one of my best experiences ever. I am grateful for always checking up on my research and my well-being, albeit his constant attempt, and failure, in luring me to the world of noble gas geochemistry. Tim Grove

is thanked for teaching some of the best classes I have ever taken. I have enjoyed his Advanced Petrology and Thermodynamics classes, and the beauty of G-X plots in understanding fundamental Earth processes. I also thank Mark Behn for his insights on anything geodynamics, and for emphasizing the importance of my experimental data in improving the current geodynamic models of subduction zones. Forrest Horton and Andy Cross are great additions to the department and I enjoyed every bit of our discussions about olivine, talc, and garnet over cold beer. Brian Monteleone and Neel Chatterjee are thanked for their invaluable help and expertise in enabling me to obtain high-quality measurements of my rocks.

A significant chunk of research stems from my involvement in PIRE: ExTerra Field Institute and Research Endeavor (EFIRE) to examine rocks exhumed from paleo-subduction zones. I have met and spent two amazing summers in Western Europe with some of the best metamorphic petrologists in the world. Thanks to Sarah Penniston-Dorland, Maureen Feineman, Matthew Kohn, Philippe Agard, Othmar Muntener, Jay Ague, Samuel Angiboust, Ethan Baxter, Marco Scambelluri, Grace Beaudoin, Kirkland Broadwell, Gabe Epstein, Will Hoover, Buchanan Kerswell, Ryan Stoner, Paul Starr, Besim Dragovic, Guillaume Bonnet, Joshua Garber, Jaime Barnes, Gray E. Bebout, Andrew Smye, Brad Hacker, Mark Caddick, and all the undergraduate students involved. This experience has expanded the breadth and depth of my research and forged new collaborations that I am positive to last for a long time.

I have also been fortunate to be a part of several oceanographic cruises aboard the R/V Neil Armstrong (SCARF), R/V Atlantis (Popping rocks), and FS Sonne (SWIR-Marion). I have interacted with many fantastic colleagues such as Dan Brunelli, Jurgen Koepke, Maurice Tivey, Adam Soule, and Mike Cheadle during those expeditions.

The MIT-WHOI Joint Program provides unparalleled support for its graduate students in the form of the Academic Programs Office. Julia Westwater, Dean Margaret Tivey, Lea Fraser, Christine Charette, Kama Thieler, Meredith Bittrich, Ann Tarrant, Tatiana Resende, Kris Kipp, Tricia Nesti, and the people who have come before them are sincerely thanked for their support throughout the 5.5 years. I also thank Geology and Geophysics administrative staff, namely Sally Houghton and Kelly Servant for always cheering me up. Outside APO and G&G, I am grateful to people in the facilities who keep WHOI labs running smoothly. In particular, I'd like to thank Dan Mullen and Ross for bringing me to work every day, and to Rose for taking good care of all of us. These many people constitute an important leg to which WHOI firmly stands on.

The students and friends who have been with me in graduate school have been a continual source of knowledge, ideas, support, and inspiration. I believe that their friendship is a big part of what kept me going and endured the pain of research during COVID-19 pandemic. I am extremely grateful to James Andrew Leong and Paolo Andre Benavides for the gift of friendship. I look forward to more food trips with you in the US and abroad. To Dr. Carlo Arcilla, you've enabled this friendship and this PhD possible. Thank you! To the Sunfish for keeping my sanity in check: Adrian Garcia, Alia Hidayat, Ben Granzow, Becca Chmiel, Drew Hirzel, Ellen Lalk, Fiona Clerc, Jing He, Jingxuan Li, Kalina Grabb, Kevin Doherty, Lauren Dykman, Nastasia Simetra, Riss Kellogg, Tyler Tamasi, Victoria Preston. Shout out to Fiona for the music (symphony orchestra

and jazz) and drinks, and Alia, Lauren, and Drew for random walks. I am grateful to Chloe Smith and Jonas Kaare-Rasmusen for their friendship. Thanks to Ben Urann, Billy Shinevar, Hannah Mark, Jianhua Gong, Emily Cooperdock, and Ayla Pamukcu for being my 'senpai' at WHOI. You have been such great role models and mentors.

I thank my housemates and pseudo-housemates: Kelsey Chenoweth, Eve Cinquino, Jenny Cramer, Kaitlyn Fouke, Dennis Giaya, Lina Taenzer, Lukas Lobert, Alexander Okamoto, Ranny Passos, Ethan Jezek, Kayla Arjabi, Elena Ceballos Romero, Peter Crockford, Ichiko Sugiyama, Alexandra Padilla, Marisa Launay, Luis Ga Rodriguez, Suzy Richards, and Vinny Amaral. I especially thank Jean and Dan Johnston for welcoming me to their lovely home at 9 Fern Lane for 5 years. Special mention to Seth Cones and Youenn Jezequel. Thanks to Youenn for teaching me the best French words and that butter is life. To Seth, I don't know how I could have survived life and work during the pandemic without your friendship. Thank you. I promise to give you a ride to wherever you want someday. With whisky, I will remember you and merde (i.e. Youenn), and all our Happy Fridays with friends. Thanks to Coffee Obsession for enabling my work. Coffee O has kept me well-caffeinated with a daily dose of large iced coffee house blend with cream.

To my family - mama, papa, and ate - I dedicate the entirety of this thesis to you. You're the only reason why I could go this far. I have always felt your presence, love, and support even though we are so far apart. Your prayers have always sustained me. I cannot possibly thank you enough for everything. I always carry you in my dreams; together we fly.

Whoever is reading this thesis, thank you. I am grateful.

Funding Support

This work has been supported financially by the National Science Foundation-Office of International Science & Engineering, Petrology & Geochemistry (NSF-OISE) PIRE, Award# 1545903 to F.K. and the Geoprisms program Collaborative Research Award# 1852610 to V.L.R. Research support through the WHOI Ocean Ventures Fund, US Science Support Program E-FIRE European Training Fund, WHOI Conference Fund are awarded to E.A.C.

Table of contents

List of Figures

Chapter 1

Chapter 2

Chapter 3

Figure S3. Predicted mineral assemblages of reaction-path models that simulated metasomatism at 400°C and 1.5 GPa as a function of fluid-to-rock ratio.
Figure S4. Predicted mineral assemblages of reaction-path models that simulated metasomatism at 500°C and 1.5 GPa) as a function of fluid-to-rock ratio.
Figure S5. Predicted mineral assemblages of reaction-path models that simulated metasomatism at 600°C and 1.5 GPa as a function of fluid-to-rock ratio.
Figure S6. (a) MgO/SiO_2 vs. Al_2O_3 plot of the starting ultramafic compositions. (b) Predicted Mg/Si of fluids in equilibrium with a metabasalt and a metapelite from 300–600 °C, 1–2.5 GPa.

Chapter 4

Figure 1. Geochemical characteristics and discrimination using (a) immobile element Cr/Al vs Al_2O_3 systematics and (b) N-MORB normalized trace element compositions.
Figure 2. Experimental conditions, phase equilibria and melting relations of (a) SY325, (b) SY400B, and (c) C647 mélanges.
Figure 3. Representative backscattered electron (BSE) images of SY325 experiments from subsolidus to suprasolidus conditions.
Figure 4. Representative electron backscatter (BSE) images of SY400B experiments from subsolidus to suprasolidus conditions.
Figure 5. Representative backscattered electron (BSE) images of C647 experiments from subsolidus to suprasolidus conditions.
Figure 6. Total alkali versus SiO_2 variation in wt. % of experimental melts from this study.
Figure 7. Major element variations (a) SiO_2, (b) MgO, (c) Al_2O_3, (d) FeO* (as total FeO),(e) CaO, (f) $Na_2O + K_2O$ of experimental mélange melts from this study vs. temperature.
Figure 8. Variations in the compositions of main residual mineral phases in the experiments as functions of temperature and pressure.
Figure 9. Experimentally-constrained solidus of different starting mélange rocks between 1.5 and 2.5 GPa.
Figure 10. Comparison of the density evolution of mélange rocks constrained by mélange melting experiments (points; this study) and thermodynamic models.
Figure 11. Comparison of the mineralogy and phase proportions constrained by mélange melting experiments (colored points; this study) and thermodynamic models.
Figure 12. Schematic cartoon that portrays the possible fates of mélange rocks along the slab-mantle interface in warm (Cascadia) and cold (Tonga) subduction zones based on this study.

Figure S1. Concentration (log)-concentration (log) plot of all the major elements measured in experimental melts and residual minerals.

Chapter 5

Chapter 6

Figure S8. Extent of trace-element fractionations in (a) Ba/Th, (b) Nd/Sr, (c) Ce/Pb, (d) Th/Nb, and (e) Cs/Rb, produced during hydrous melting of sediment, during mélange melting, and during melting of mélange-hybridized mantle.

List of Tables

Chapter 2

Chapter 3

Chapter 4

Table 10. Summary of major phase proportions in SY400B experiments constrained using LIME and their respective bulk and solid densities.
Table S11. Summary of major phase proportions in SY325 experiments constrained using LIME and their respective bulk and solid densities.
Table S12. Summary of major phase proportions in C647 experiments constrained using LIME and their respective bulk and solid densities.

Chapter 5

Table S1. Major and trace element compositions of starting materials.
Table S2. Major and trace element compositions of experimental peridotite-mélange melts.
Table S3. Summary of experimental set-up.
Table S4. Compiled major and trace element compositions of experimental melts from other studies on mantle wedge hybridization.
Table S5. Major element composition of mineral phases analyzed by EPMA.

Chapter 6

Table S1. Compilation of geochemical data from the Izu-Bonin arc.
Table S2. Summary of elemental and isotopic compositions of subducted materials and ambient mantle, and relevant partition coefficients used in melting and dehydration models.
Table S3. Compilation of geochemical data from the Philippine, Ryukyu, Cascadia, Kurile, Kamchatka, and Mariana arc

Chapter 1

Introduction

1.1 Background and motivation

Subduction zones are important sites of material and volatile recycling on Earth. The return of the oceanic lithosphere into the deep mantle along >55000 km of ocean trenches is a fundamental geodynamic process that connects many Earth-scale processes (Figure 1; Canfield, 2004; Dickinson, 1970; Stolper and Bucholz, 2019). This process leads to some of the most catastrophic events known, from explosive volcanic eruptions to large magnitude earthquakes and associated tsunamis, all of which have influenced human civilizations over the past millennia (Robock, 2015; Rymer, 2015; Sheets, 2015; Wallace, 2005; Williams-Jones and Rymer, 2015). This importance has made the understanding of fundamental processes that operate in subduction zones a focus of intensive research campaigns over the last few decades. As new geophysical, petrological and geochemical data have become available since the dawn of the modern plate

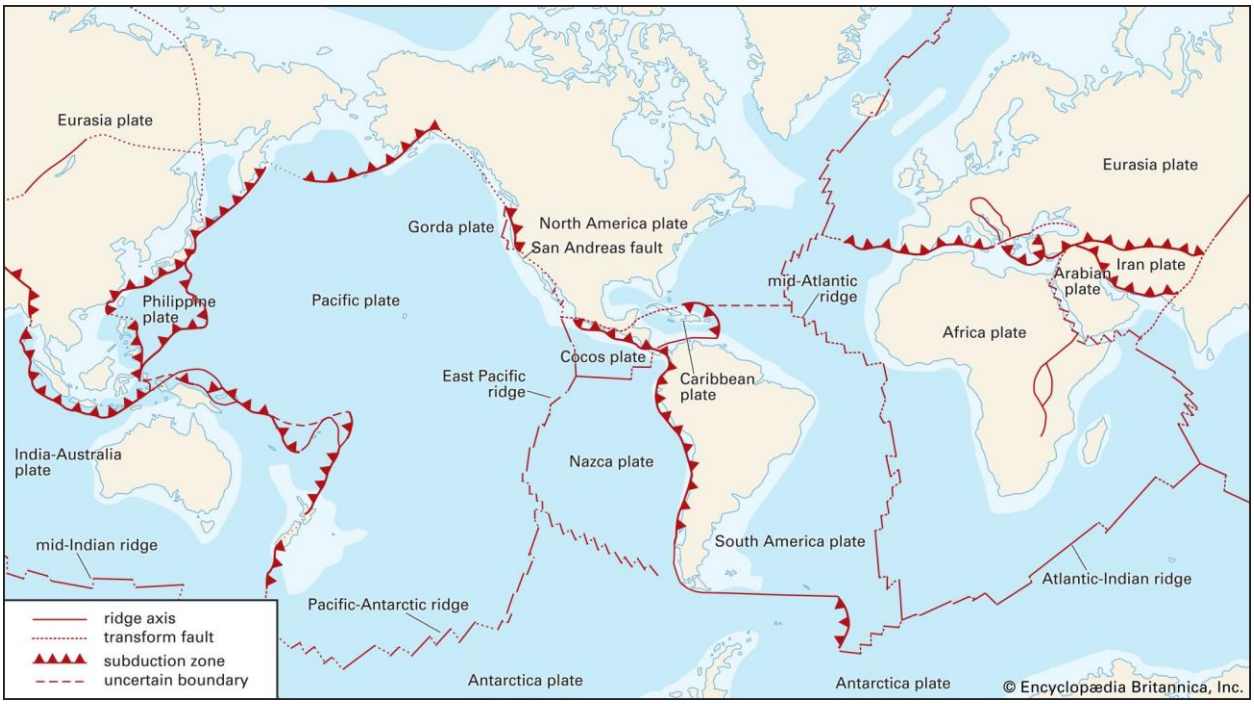

Figure 1. A map of the major tectonic boundaries on Earth, namely ocean ridges, transform faults, and subduction zones. (https://www.britannica.com/science/subduction-zone#/media/1/570643/151217)

tectonics theory in the late 1960s (Dickinson, 1970), significant progress has been made in our understanding of the physics of plate subduction and magma generation, and the chemistry of pre-subducting oceanic materials and erupted arc magmas (Alt, 1995; Alt et al., 1986; Gill, 1981; Spandler and Pirard, 2013).

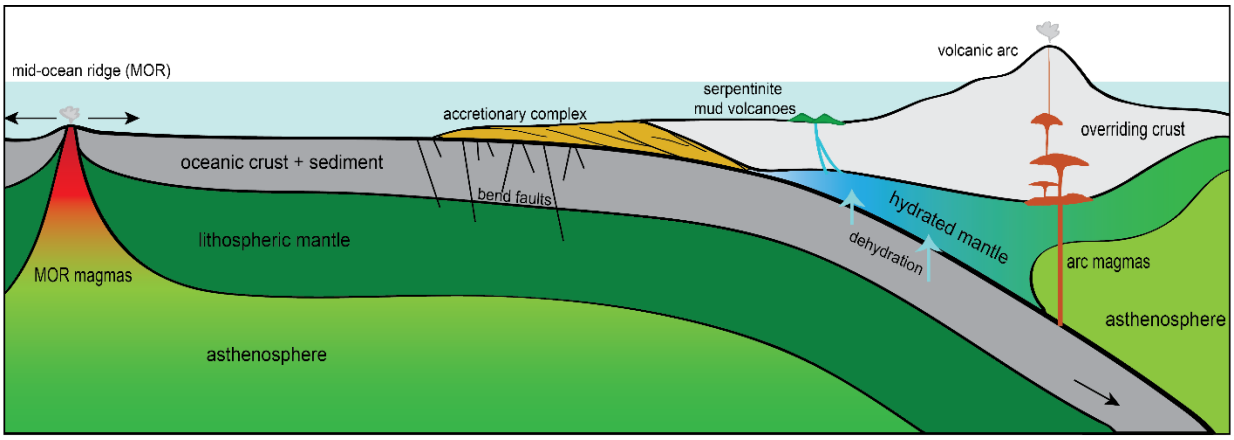

Figure 2. Schematic cross section of divergent and convergent plate boundaries. New oceanic lithosphere is formed by decompression melting of mantle in a mid-ocean ridge. As soon as it is formed, it moves away from ridge, cools down and densify while being altered by seawater or hydrothermal fluid. This old, cold, and dense oceanic lithosphere eventually subducts underneath a more buoyant plate in subduction zones. This process leads to the hydration (serpentinization) and/or melting of mantle wedge to form arc magmas. Figure not to scale.

Plate tectonic theory serves as a unifying framework that describes many fundamental Earth-scale processes that occur over geologic time, such as the formation of lithospheric plates at oceanic spreading centers, as well as their destruction in subduction zones (Figure 2). In this framework, new oceanic lithosphere is formed along mid-ocean ridge and backarc spreading centers where two tectonic plates are moving away from each other. As soon as it is formed at a ridge, oceanic lithosphere cools down by a combination of conductive heat loss and through the convection of seawater or hydrothermal fluids as it moves away from the ridge axis. Far from spreading centers, this cool and variably altered oceanic lithosphere is denser than when it was at the ridge axis. Continued cooling and densification of the oceanic lithosphere as it ages eventually causes it to sink and subduct underneath a more buoyant plate in a convergent margin. The return of this old, cold, and dense slab of oceanic lithosphere to deeper and warmer asthenosphere causes perturbations in the thermal structure, especially at the interface between the subducted slab and the overlying mantle. This characteristically low geothermal gradient is unique to subduction zones

and plays a central role in all the fundamental subduction zone processes such as dehydration, melting, explosive arc volcanism, and seismicity.

In subduction settings, oceanic plate materials including sediments, variably altered igneous crust, and hydrothermally-altered lithospheric mantle (serpentinite) are delivered to deeper depths where they are exposed to increasing pressure (*P*) and temperature (*T*) conditions (Gill, 1981; Pearce, 1982; Ringwood, 1974; Tera et al., 1986; Wyllie, 1973). The subducting slab delivers water and other volatile components (*e.g.*, CO_2, SO_2) which can influence the rheology and transport properties of the Earth's deep interior. Fluids that contain fluid-mobile elements (*e.g.*, Ba, Pb, Sr, K) and redox-sensitive elements (*e.g.*, Fe, S) are released from the subducting slab, migrate to the overlying mantle, and participate in formation of arc magmas, continental crust, and some of the world's most economically important ore deposits (Bebout, 1991; Grove et al., 2002; Kelley and Cottrell, 2009; Kushiro, 1973; Mungall, 2002; Schmidt and Poli, 2014, 1998). Subducted oceanic materials may also generate mineralogical, chemical, and isotopic heterogeneities in the deep mantle which are later sampled during ocean island magmatism (Bebout, 2007; Rampone and Hofmann, 2012). However, even more than half a century later since this paradigm was established, outstanding questions such as how deformation, mixing of different lithologies, and fluid-rock interactions along the plate interface modify the petrophysical, geochemical, and redox properties of subducted materials, and how these processes collectively influence the mechanisms of slab-to-mantle transfer, cycling of elements and volatiles, and the formation of arc magmas worldwide, remain poorly understood.

Relative to the composition of mid-ocean ridge basalt (MORB), arc magmas are geochemically enriched in large-ion lithophile elements (LILE; *e.g.* Rb, K, Cs) and light rare Earth elements (LREE; La, Ce, Nd), but are depleted in high field strength elements (HFSE; Nb, Ta, Zr, Hf) (Gill, 1981; McCulloch and Gamble, 1991; Pearce, 1982). The distinct geochemical characteristics of erupted arc magmas in subduction zones record the transfer process and contribution of subducted oceanic materials into the source region of magmas. The recycling of elements from the subducting lithosphere back to the overlying crust, atmosphere and oceans is one of the most important of geochemical cycles on Earth. Therefore, subduction zones play a pivotal role in maintaining the balance in material exchange between the surface and deep Earth reservoirs over geologic time. To understand this complex material exchange and the efficiency of

recycling processes, it is necessary to understand the reactions that occur during subduction that allow for the transfer of material from the subducting slab to the overlying mantle wedge.

Experimental studies over the past decade have focused on establishing the phase relations of individual subducted lithologies (*e.g.*, basalt, sediment, peridotite) over a range of *P* and *T* conditions (Carter et al., 2015; Hermann and Rubatto, 2009; Hermann and Spandler, 2008; Klimm et al., 2008; Schmidt and Poli, 2014; Till et al., 2012; Ulmer and Trommsdorff, 1995). This approach assumes a closed-system wherein each precursor oceanic rock retains its geochemical characteristics during subduction. The closed-system assumption is inherent in mass-balance calculations commonly performed to constrain the efficiency of the recycling process by comparing the fluxes between slab inputs entering trenches and arc outputs measured in arc volcanoes. For instance, this mass-balance approach has been applied to evaluate the fluxes of volatiles (*e.g.*, carbon, nitrogen) and noble gases (*e.g.*, helium) in individual subduction zones (de Leeuw et al., 2007; Elkins et al., 2006; Mitchell et al., 2010; Plank and Langmuir, 1993; Plank and Manning, 2019). Here, it is an implicit assumption that the mass transfer processes and chemical interactions within subduction zones do not affect the fate of subducted elements and volatiles at depth. Nonetheless, when integrated with thermal models of the slab and the overlying mantle, these experimental data on individual subducted lithologies help to identify important hydrous minerals (*e.g.*, chlorite, amphibole) and devolatilization reactions that release water and other volatiles at forearc and subarc depths (Davies and Stevenson, 1992; Furukawa, 1993; Peacock, 2009; Ringwood, 1974; Syracuse et al., 2010).

The most poorly understood processes at convergent plate margins are the metamorphic, metasomatic, and structural modifications that oceanic lithosphere experiences as it gets subducted to deeper depths. Field, petrological, and geochemical evidence suggest that subducted materials are subjected to combined, and sometimes coeval, deformation processes and fluid-rock interactions that can significantly modify their petrophysical (*e.g.*, density, magnetic susceptibility), geochemical (*e.g.*, trace elements, water and other volatiles) and redox (e.g., bulk-rock Fe^{3+}/Fe_{total}) characteristics (Agard et al., 2018; Angiboust et al., 2014, 2012; Bebout, 2013, 2007, 1991; Bebout and Penniston-Dorland, 2016; Codillo et al., 2022; Gyomlai et al., 2021; King et al., 2006; Miller et al., 2009; Penniston-Dorland et al., 2014; Pogge von Strandmann et al., 2015). The intense shearing and deformation juxtapose lithologies with different chemical compositions sometimes in block-in-matrix fabrics commonly referred to as a mélange (Figure 3).

Previous studies on exhumed high-pressure mélange zones indicate that these zones record fluid-mediated metasomatism of juxtaposed lithologies through a combination of fluid infiltration and diffusional mass transfer processes (Bebout and Barton, 2002; Bebout, 1991; Breeding et al., 2004; Codillo et al., 2022; King et al., 2006; Miller et al., 2009; Sorensen and Grossman, 1989). Mélange rocks display compositional and petrophysical characteristics that are distinct from their protoliths (Bebout and Barton, 2002; Codillo et al., 2022; Gyomlai et al., 2021; King et al., 2007, 2006; Miller et al., 2009). Therefore, the formation of mélange zones can influence the rheology of the plate interface (Agard et al., 2018; Hirauchi et al., 2020, 2013) and the nature of slab-to-mantle transfer processes in subduction zones (Codillo et al., 2022, 2018, 2018; Cruz-Uribe et al., 2018; Marschall and Schumacher, 2012; Nielsen and Marschall, 2017).

Understanding the processes that operate in subduction zones clearly requires a multidisciplinary approach that integrates constraints from studies of natural rocks, laboratory experiments, and theoretical constraints. This is necessary because these approaches often have complementary strengths. For instance, exhumed high-pressure terranes may offer the most direct way to constrain the mass transfer and chemical interactions within subduction zones (Bebout, 2013; Bebout and Barton, 2002; Bebout and Penniston-Dorland, 2016). However, the accurate interpretation of such complex terranes requires distinguishing between signatures of high-pressure metasomatic processes in subduction zones, reworking and incomplete preservation during exhumation, and inherited oceanic alteration prior to subduction. Equilibrium thermodynamics are often used in conjunction with petrological studies of exhumed high-pressure rocks. Thermodynamic phase equilibrium and reaction-path models enable the ability to constrain the *P-T* conditions experienced by these rocks as well as simulate fluid-rock interactions over a range conditions (Connolly, 2009; Holland and Powell, 2011; Sverjensky, 2019). Application of equilibrium thermodynamics requires the selection of appropriate equilibrium mineral compositions which assumes that reaction did approach equilibrium. However, this task is difficult in high-pressure metasomatic rocks because they typically preserve disequilibrium features, such as complex mineral zoning, produced by one or a combination of changes in pressure, temperature, or bulk composition due to fluid-rock interactions (Beinlich et al., 2010; Goncalves et al., 2013). In addition, the robustness and applicability of equilibrium thermodynamics are also limited by the quality of thermodynamic data and solution models of minerals, aqueous fluids, and silicate melts. This limitation can be circumvented by performing laboratory experiments under controlled

conditions. Experimental petrology enables the determination of phase equilibria, melting reactions and their respective rates, and melt compositions over a range of *P*-*T* conditions, oxygen fugacity (fO_2), and bulk compositions (Holloway and Wood, 2012). It can also be used to evaluate reaction overstepping (i.e. a reaction occurs at higher temperatures than thermodynamically predicted). However, the changing pressures and temperatures experienced by slab materials during subduction over geological timescales are difficult to replicate in laboratory experiments, and the conditions and rates for these reactions remain debated. This thesis leverages the combined strengths of all these approaches to circumvent the limitations intrinsic to each of them.

1.2 Thesis Outline

This thesis aims to brush some colors on a commonly assumed black box that is the slab-mantle interface region. My thesis highlights the dynamic connections between deformation, mechanical mixing of different lithologies, and fluid-rock interactions processes along the slab-mantle interface. In particular, my contributions have improved our understanding of how these processes modify the petrophysical, geochemical, and redox properties of subducted materials, and

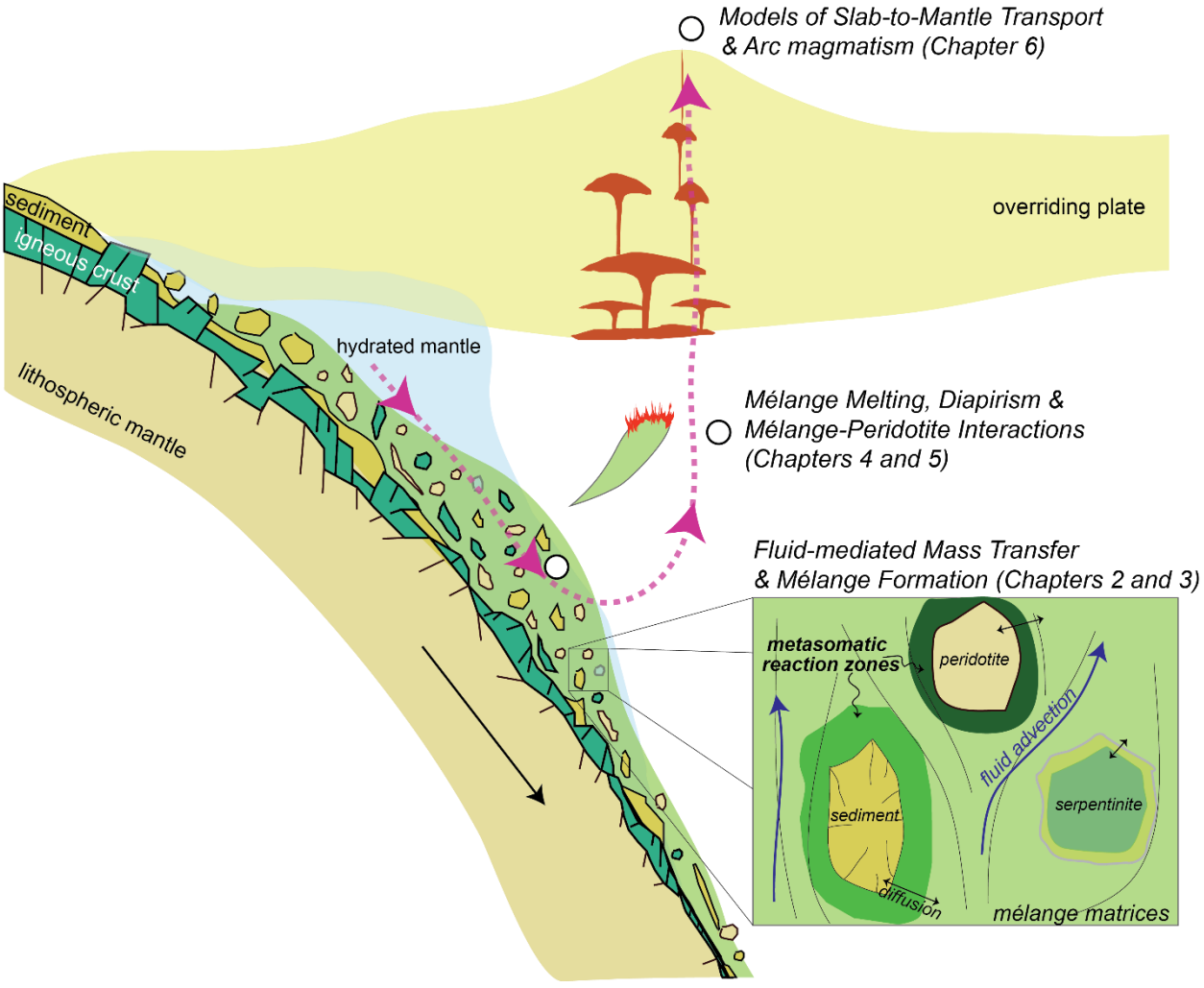

Figure 3. Schematic representation of a subduction zone with emphasis on the mechanical and metasomatic interactions in the subducting slab and the overriding lithosphere. This proposal outlines a continuum of processes and interactions (pink dashed arrow) within a subduction zone, encompassing (i) the formation of mélanges via aqueous fluid-rock interactions in Chapters 2 and 3, (iii) the physical and geochemical consequences of mélange melting and diapirism in Chapters 4 and 5, and (iv) slab-to-mantle transfer mechanism in global arcs in Chapter 6.

how these processes collectively influence the mechanisms of slab-to-mantle transfer, cycling of elements and volatiles, and the formation of arc magmas worldwide.

This thesis stands on three legs that integrate constraints from (1) petrology and geochemistry of exhumed high-pressure rocks and erupted arc magmas, (2) high *P-T* laboratory experiments, and (3) theoretical thermodynamic constraints to investigate a continuum of interrelated mass-transfer and chemical interactions – *aqueous fluid-rock reactions, melting and melt-rock reactions, arc volcanism* – in subduction zones. This thesis is divided into seven chapters as outlined below and depicted in Figure 3.

Chapter 2 paints a different picture of the nature and style of metasomatism at high *P-T* conditions, such as in subduction zones, as compared to low *P-T* oceanic settings. As a consequence of the subduction process, subducted materials are often subjected to combined, and sometimes coeval, deformation processes and fluid-rock interactions that modify their petrophysical, geochemical, and redox characteristics. However, accurate interpretations of exhumed high-pressure rock records require an understanding of how, where, and when metasomatism occurred. Chapter 2 investigates the formation of a metasomatic reaction zone in between eclogitic metagabbro and serpentinite in the exhumed high-pressure Voltri Massif (Ligurian Alps, Italy) to gain insights on the fluid-mediated mass transfer between mafic ultramafic rocks in subduction zones. In this chapter, I integrated results from field work, petrology, and element and isotope geochemistry of exhumed high-pressure rocks, coupled with thermodynamic phase equilibrium and reaction-path models to demonstrate that fluid-mediated mass transfer was dominated by Mg transfer from serpentinite to metagabbro that started during prograde metamorphism and likely continued through peak and retrograde conditions. The fluid-mediated mass transfer led to significant mineralogical, chemical, and petrophysical changes of the reacted metagabbro. In contrast to oceanic settings, our thermodynamic models predict the predominance of aqueous Mg species in fluids that equilibrate with serpentinite under high-pressure subduction zone conditions. This result implies that Mg-metasomatism of mafic rocks to form chlorite-rich assemblages is favored and likely pervasive in subduction zones than in oceanic settings. As documented in Chapter 3, Mg-metasomatism of mafic rocks led to the dissolution of trace-element-rich phases such as rutile and zircon that resulted in trace-element fractionations (*e.g.*, Th/Nb, Zr/Sm, Hf/Nd) otherwise commonly attributed to metamorphic dehydration and melting processes. Because of the widespread occurrence of juxtaposed mafic and ultramafic rocks

along the slab-mantle interface, metasomatism between juxtaposed rocks may result in enhanced trace-element fractionation.

Results from Chapter 2 imply that the formation of talc by Si-metasomatism of ultramafic rocks (i.e. steatitization), a process common in oceanic settings, is less prevalent in subduction zones. This result is surprising because talc formation and distribution in subduction zones are believed to play important roles in volatile cycling, rheological properties, and control the down-dip limit of the decoupling of the slab-mantle interface (e.g., French and Condit, 2019; Peacock and Hyndman, 1999; Peacock and Wang, 2021). Illuminating the conditions that facilitate talc formation at high *P-T* conditions is necessary in assessing its role in fundamental subduction zone processes. Building on the results of Chapter 2, in Chapter 3, I investigate the conditions that promote - or limit- the formation of talc by Si-metasomatism of ultramafic rocks by slab-derived fluids using thermodynamic reaction-path models. I show that the metasomatic formation of talc at the slab-mantle interface is restricted to a limited set of environmental conditions, because its formation is highly sensitive to the compositions of the mantle rocks and reactant fluids. These results mean that talc is unlikely to form in high abundance in ultramafic rocks metasomatized by Si-rich slab-derived fluids and calls into question the importance of talc formed by Si-metasomatism of ultramafic rocks in subduction zones. In contrast to talc, my reaction-path models predict the ubiquitous formation of chlorite along with other silicate minerals and implies that chlorite may be playing the more predominant role in processes that were previously and tentatively attributed to talc.

Results of Chapters 2 and 3 call into question the assumption that subducted materials can be regarded as a closed-system throughout subduction. This assumption is central to traditional models (hereafter referred to as model 1 to represent the family of traditional models) of slab-to-mantle transfer and arc magma formation. This model envisions that the addition of different slab components to the source region of arc magmas is facilitated by fluids and/or melts derived from the dehydration and/or melting of individual subducted materials (*e.g.*, sediment, igneous crust, serpentinized slab mantle) depending on the *P-T* condition. However, as shown in Chapters 2 and 3, metasomatic rocks are compositionally distinct from their precursor materials. The role of metasomatic rocks is central to the mélange-melting model (model 2). This model envisions the addition of different slab components through fluids and/or melts sourced from the dehydration and/or melting of mélange rocks either along the slab-mantle interface or during ascent as buoyant

diapirs. These mélange diapirs can transport subducted slab components and subject them to *P-T* conditions that are not accounted for in the traditional models (model 1) of dehydration reactions and melting along the slab-top. However, whether diapirs can form is tightly linked to their respective phase equilibria, melting and density evolution of the slab-top mélange, all of which are poorly understood.

Chapter 4 experimentally investigates the phase equilibria, melting, and density evolution of mélange rocks along representative slab-top *P-T* conditions to assess their likelihood to melt along the slab-top or detach and rise as diapirs into the overlying mantle. I conducted a series of high *P-T* laboratory experiments using a piston-cylinder apparatus on mélange rocks from exhumed high-pressure terranes of Syros (Greece) and Santa Catalina Island (USA) over a wide range of *P-T* conditions. Experimental results show that melting of the mélange rocks is unlikely to occur, even along a warm slab-top at pressures $\leq$ 2.5 GPa. Under experimental conditions, subsolidus mélanges are dominated by hydrous minerals such as chlorite, talc, and amphibole, which are sufficiently buoyant compared to the overlying peridotite mantle and thus favoring diapirism and ascent. Because of the inverted thermal gradient of the mantle wedge, melting of mélange rocks is expected during ascent. However, instantaneous melt extraction of low-viscosity hydrous mélange melts would densify the solid residue and arrest further ascent. In addition, diapir buoyancy may be limited at higher pressures due to the formation of garnet, especially in mélange rocks with peraluminous compositions.

The compositions of experimental mélange melts display major element characteristics that are broadly similar to the hydrous partial melts of individual subducted materials (e.g., sediment, amphibolite, basalt). Trace-element rich phases such phengite, phlogopite, epidote, ilmenite, and titanite minerals are found to stably coexist with hydrous mélange melts. Consequently, this would result in trace-element fractionation in the melts that could resemble the compositions of natural arc magmas. These findings imply that previous geochemical studies of erupted arc magmas that invoked hydrous partial melts of discrete subducted materials (model 1) during slab-to-mantle transfer may be equally compatible with models that invoke hydrous mélange melts as transport agents (model 2) (Elliott et al., 1997; Kelemen et al., 2003; Li et al., 2022; Prouteau et al., 2001; Rapp, R et al., 1999; Schiano et al., 1995).

Geodynamic models predicted the formation and rise of diapirs that transport mélange rocks away from the slab-mantle interface into the hot zones of the mantle wedge (Gerya and

Yuen, 2003; Hall and Kincaid, 2001; Zhu et al., 2009). However, the geochemical consequence of mélange-peridotite interactions in the mantle wedge on arc magma formation is unknown. Chapter 5 experimentally investigates the melting of a mantle wedge hybridized by small volume proportions of mélange components and determines the composition of the melts and mineral residues. Results show that the compositions of the experimental melts produced by melting of mélange-hybridized mantle display major, trace, and the fractionated trace-element ratios that are characteristic of erupted arc magmas worldwide. This underlines the potentially important role of mélange diapirs as a mechanism of delivering subducted slab signatures into the source of arc magmas.

Results of Chapters 2, 3, 4, and 5 have illuminated the importance of fluid-rock interactions in the formation of mélange rocks along the slab-mantle interface, as well as the physical and geochemical consequences of mélange melting and diapirism. How this continuum of processes manifests in the compositions of erupted arc magmas remains unknown. In fact, whether slab-to-mantle transfer primarily occurs through the release of individual slab components as advocated by traditional models (model 1; *e.g.*, fluids, altered oceanic crust melts, sediment melts) or by physical mixing at the slab-mantle interface through the formation of km-thick zones of mélanges (model 2) remains highly debated (Li Huijuan et al., 2022; Marschall and Schumacher, 2012; Nielsen and Marschall, 2017; Turner and Langmuir, 2022).

In Chapter 6, I use published volcanic rock compositions from the Izu-Bonin arc and presents new interpretations on the evolution of slab-to-mantle transfer mechanisms from subduction initiation to arc maturity. My results show that while traditional models of slab-to-mantle transfer mechanisms should account for arc magma variability in the early (warm) stages of subduction, mélange formation is required to explain arc magma geochemistry in the cold and mature stage. Building on the results from the Izu-Bonin data, I used a global arc magma compilation from other cold and warm subduction zones to show that arc magmas generated in convergent margins with warmer slab-top temperatures record the transfer of hydrous melts from discrete subducted slab components (sediments, altered oceanic crust). In contrast, arc magmas generated in convergent margins with colder slab-top temperatures record a process whereby hydrous melts originate from mélange zones (the mantle is physically mixed with slab components before melting occurs). This dichotomy between warm and cold arcs reflects the wider decoupled

zone expected in cold slabs, where mélange zones can form more extensively and contribute to the melting process more significantly.

In summary, this thesis utilized a multi-pronged approach that integrated constraints from detailed investigations of natural rocks, high *P-T* laboratory experiments, and theoretical thermodynamic models to elucidate some of the complex and hidden, yet important processes that operate within subduction zones. The chapters in this thesis are intended to be five separate manuscripts, which are published (**Chapter 2, 3, 5**), submitted (**Chapter 6**), and in preparation (**Chapter 4**). I have also included collaborative research manuscripts that build on the findings of my research works. The corresponding publication references are listed below.

Published:

Codillo, E. A., Klein, F., & Marschall, H. R. 2022. Preferential Formation of Chlorite over Talc during Si-metasomatism of Ultramafic Rocks in Subduction Zones. Geophysical Research Letters, 49, e2022GL100218. https://doi.org/10.1029/2022GL100218

Codillo, E. A., Klein, F., Dragovic, B., Marschall, H. R., Baxter, E., Scambelluri, M., & Schwarzenbach, E. 2022. Fluid-mediated mass transfer between mafic and ultramafic rocks in subduction zones. Geochemistry, Geophysics, Geosystems, 23, e2021GC010206. https:// doi.org/10.1029/2021GC010206

Codillo, E.A., Le Roux, V., Marschall, H.R., 2018. Arc-like magmas generated by mélange-peridotite interaction in the mantle wedge. Nature Communications 9, 2864. https://doi.org/10.1038/s41467-018-05313-2

Submitted

Codillo, E.A., Le Roux, V. Mélange melting predominant in cold and mature arc (*submitted*)

In preparation:

Codillo E.A., Le Roux V., Klein B., Behn M., Marschall H., & Bebout G. The rising of mélanges: experimental constraints on mélange rock densities and solidus temperatures in subduction zones (*in preparation for EPSL*)

Codillo E.A., Klein B. Thermodynamic and experimental constraints on the pressure and temperature limits of serpentinization in subduction zones (*in preparation for Geology*)

Collaborative manuscripts:

Schwarzenbach E., Streicher L., Dragovic B., **Codillo E.A.**, Scicchitano M.R., Wiechert U., Klein F., Marschall H.R., Scambelluri M. Mobilization of isotopically heavy sulfur during serpentinite subduction (*to be submitted for Science Advances; This research builds on the findings of my previous work in Voltri Massif in Chapter 3*)

Brown A., Dragovic B., **Codillo E.A.**, Rojas Kolomiets E., Bizimis M., Marschall H. R., Scambelluri M. The behavior of Mo isotopes during high-pressure metamorphism and metasomatism: a case study from the Ligurian Alps and northern. (*This research builds on the findings of my previous work in Voltri Massif in Chapter 3*)

References

Agard, P., Plunder, A., Angiboust, S., Bonnet, G., Ruh, J., 2018. The subduction plate interface: rock record and mechanical coupling (from long to short timescales). Lithos 320–321, 537–566. https://doi.org/10.1016/j.lithos.2018.09.029

Alt, J.C., 1995. Subseafloor Processes in Mid-Ocean Ridge Hydrothennal Systems, in: Seafloor Hydrothermal Systems: Physical, Chemical, Biological, and Geological Interactions, Geophysical Monograph Series. pp. 85–114. https://doi.org/10.1029/GM091p0085

Alt, J.C., Honnorez, J., Laverne, C., Emmermann, R., 1986. Hydrothermal alteration of a 1 km section through the upper oceanic crust, Deep Sea Drilling Project Hole 504B: Mineralogy, chemistry and evolution of seawater-basalt interactions. Journal of Geophysical Research: Solid Earth 91, 10309–10335. https://doi.org/10.1029/JB091iB10p10309

Angiboust, S., Agard, P., Yamato, P., Raimbourg, H., 2012. Eclogite breccias in a subducted ophiolite: A record of intermediate-depth earthquakes? Geology 40, 707–710. https://doi.org/10.1130/G32925.1

Angiboust, S., Glodny, J., Oncken, O., Chopin, C., 2014. In search of transient subduction interfaces in the Dent Blanche–Sesia Tectonic System (W. Alps). Lithos 205, 298–321. https://doi.org/10.1016/j.lithos.2014.07.001

Bebout, G., 2013. Metasomatism in Subduction Zones of Subducted Oceanic Slabs, Mantle Wedges, and the Slab-Mantle Interface, in: Metasomatism and the Chemical Transformation of Rock. pp. 289–349. https://doi.org/10.1007/978-3-642-28394-9_9

Bebout, G., Barton, M., 2002. Tectonic and metasomatic mixing in a high-T, subduction-zone m??lange - Insights into the geochemical evolution of the slab-mantle interface. https://doi.org/10.1016/S0009-2541(02)00019-0

Bebout, G.E., 2007. Metamorphic chemical geodynamics of subduction zones. Earth and Planetary Science Letters 260, 373–393. https://doi.org/10.1016/j.epsl.2007.05.050

Bebout, G.E., 1991. Field-Based Evidence for Devolatilization in Subduction Zones: Implications for Arc Magmatism. Science 251, 413. https://doi.org/10.1126/science.251.4992.413

Bebout, G.E., Penniston-Dorland, S.C., 2016. Fluid and mass transfer at subduction interfaces—The field metamorphic record. Lithos 240–243, 228–258. https://doi.org/10.1016/j.lithos.2015.10.007

Beinlich, A., Klemd, R., John, T., Gao, J., 2010. Trace-element mobilization during Ca-metasomatism along a major fluid conduit: Eclogitization of blueschist as a consequence of fluid–rock interaction. Geochimica et Cosmochimica Acta 74, 1892–1922. https://doi.org/10.1016/j.gca.2009.12.011

Breeding, C.M., Ague, J.J., Bröcker, M., 2004. Fluid–metasedimentary rock interactions in subduction-zone mélange: Implications for the chemical composition of arc magmas. Geology 32, 1041–1044. https://doi.org/10.1130/G20877.1

Canfield, D.E., 2004. The evolution of the Earth surface sulfur reservoir. Am J Sci 304, 839. https://doi.org/10.2475/ajs.304.10.839

Carter, L.B., Skora, S., Blundy, J.D., De Hoog, J.C.M., Elliott, T., 2015. An Experimental Study of Trace Element Fluxes from Subducted Oceanic Crust. Journal of Petrology 56, 1585–1606. https://doi.org/10.1093/petrology/egv046

Codillo, E.A., Klein, F., Dragovic, B., Marschall, H.R., Baxter, E., Scambelluri, M., Schwarzenbach, E., 2022. Fluid-mediated Mass Transfer between Mafic and Ultramafic rocks in Subduction Zones. Geochemistry, Geophysics, Geosystems.

Codillo, E.A., Le Roux, V., Marschall, H.R., 2018. Arc-like magmas generated by mélange-peridotite interaction in the mantle wedge. Nature Communications 9, 2864. https://doi.org/10.1038/s41467-018-05313-2

Connolly, J.A.D., 2009. The geodynamic equation of state: What and how. Geochemistry, Geophysics, Geosystems 10. https://doi.org/10.1029/2009GC002540

Cruz-Uribe, A.M., Marschall, H.R., Gaetani, G.A., Le Roux, V., 2018. Generation of alkaline magmas in subduction zones by partial melting of mélange diapirs—An experimental study. Geology 46, 343–346. https://doi.org/10.1130/G39956.1

Davies, J.H., Stevenson, D.J., 1992. Physical model of source region of subduction zone volcanics. Journal of Geophysical Research: Solid Earth 97, 2037–2070. https://doi.org/10.1029/91JB02571

de Leeuw, G.A.M., Hilton, D.R., Fischer, T.P., Walker, J.A., 2007. The He–CO2 isotope and relative abundance characteristics of geothermal fluids in El Salvador and Honduras: New constraints on volatile mass balance of the Central American Volcanic Arc. Earth and Planetary Science Letters 258, 132–146. https://doi.org/10.1016/j.epsl.2007.03.028

Dickinson, W.R., 1970. Global Tectonics. Science 168, 1250–1259. https://doi.org/10.1126/science.168.3936.1250

Elkins, L.J., Fischer, T.P., Hilton, D.R., Sharp, Z.D., McKnight, S., Walker, J., 2006. Tracing nitrogen in volcanic and geothermal volatiles from the Nicaraguan volcanic front. Geochimica et Cosmochimica Acta 70, 5215–5235. https://doi.org/10.1016/j.gca.2006.07.024

Elliott, T., Plank, T., Zindler, A., White, W., Bourdon, B., 1997. Element transport from slab to volcanic front at the Mariana arc. Journal of Geophysical Research: Solid Earth 102, 14991–15019. https://doi.org/10.1029/97JB00788

French, M.E., Condit, C.B., 2019. Slip partitioning along an idealized subduction plate boundary at deep slow slip conditions. Earth and Planetary Science Letters 528, 115828. https://doi.org/10.1016/j.epsl.2019.115828

Furukawa, Y., 1993. Depth of the decoupling plate interface and thermal structure under arcs. Journal of Geophysical Research: Solid Earth 98, 20005–20013. https://doi.org/10.1029/93JB02020

Gerya, T.V., Yuen, D.A., 2003. Rayleigh–Taylor instabilities from hydration and melting propel 'cold plumes' at subduction zones. Earth and Planetary Science Letters 212, 47–62. https://doi.org/10.1016/S0012-821X(03)00265-6

Gill, J., 1981. Orogenic Andesites and Plate Tectonics, 1st ed. Springer Berlin, Heidelberg.

Goncalves, P., Marquer, D., Oliot, E., Durand, C., 2013. Thermodynamic Modeling and Thermobarometry of Metasomatized Rocks, in: Metasomatism and the Chemical Transformation of Rock: The Role of Fluids in Terrestrial and Extraterrestrial Processes. Springer Berlin Heidelberg, Berlin, Heidelberg, pp. 53–91. https://doi.org/10.1007/978-3-642-28394-9_3

Grove, T., Parman, S., Bowring, S., Price, R., Baker, M., 2002. The role of an H2O-rich fluid component in the generation of primitive basaltic andesites and andesites from the Mt. Shasta region, N California. Contributions to Mineralogy and Petrology 142, 375–396. https://doi.org/10.1007/s004100100299

Gyomlai, T., Agard, P., Marschall, H.R., Jolivet, L., Gerdes, A., 2021. Metasomatism and deformation of block-in-matrix structures in Syros: The role of inheritance and fluid-rock

interactions along the subduction interface. Lithos 386–387, 105996. https://doi.org/10.1016/j.lithos.2021.105996

Hall, P.S., Kincaid, C., 2001. Diapiric Flow at Subduction Zones: A Recipe for Rapid Transport. Science 292, 2472. https://doi.org/10.1126/science.1060488

Hermann, J., Rubatto, D., 2009. Accessory phase control on the trace element signature of sediment melts in subduction zones. Chemical Geology 265, 512–526. https://doi.org/10.1016/j.chemgeo.2009.05.018

Hermann, J., Spandler, C.J., 2008. Sediment Melts at Sub-arc Depths: an Experimental Study. Journal of Petrology 49, 717–740. https://doi.org/10.1093/petrology/egm073

Hirauchi, K., den Hartog, S.A.M., Spiers, C.J., 2013. Weakening of the slab–mantle wedge interface induced by metasomatic growth of talc. Geology 41, 75–78. https://doi.org/10.1130/G33552.1

Hirauchi, K., Yamamoto, Y., den Hartog, S.A.M., Niemeijer, A.R., 2020. The role of metasomatic alteration on frictional properties of subduction thrusts: An example from a serpentinite body in the Franciscan Complex, California. Earth and Planetary Science Letters 531, 115967. https://doi.org/10.1016/j.epsl.2019.115967

Holland, T.J.B., Powell, R., 2011. An improved and extended internally consistent thermodynamic dataset for phases of petrological interest, involving a new equation of state for solids. Journal of Metamorphic Geology 29, 333–383. https://doi.org/10.1111/j.1525-1314.2010.00923.x

Holloway, J.R., Wood, B.J., 2012. Simulating the Earth: Experimental Geochemistry. Springer Netherlands.

Kelemen, P., Yogodzinski, G., Scholl, D., 2003. Along-strike variation in the Aleutian Island Arc: Genesis of high Mg# andesite and implications for continental crust. Geophysical Monograph Series 138, 223–276. https://doi.org/10.1029/138GM11

Kelley, K.A., Cottrell, E., 2009. Water and the Oxidation State of Subduction Zone Magmas. Science 325, 605–607. https://doi.org/10.1126/science.1174156

King, R.L., Bebout, G.E., Grove, M., Moriguti, T., Nakamura, E., 2007. Boron and lead isotope signatures of subduction-zone mélange formation: Hybridization and fractionation along the slab–mantle interface beneath volcanic arcs. Chemical Geology 239, 305–322. https://doi.org/10.1016/j.chemgeo.2007.01.009

King, R.L., Bebout, G.E., Moriguti, T., Nakamura, E., 2006. Elemental mixing systematics and Sr–Nd isotope geochemistry of mélange formation: Obstacles to identification of fluid sources to arc volcanics. Earth and Planetary Science Letters 246, 288–304. https://doi.org/10.1016/j.epsl.2006.03.053

Klimm, K., Blundy, J.D., Green, T.H., 2008. Trace Element Partitioning and Accessory Phase Saturation during H2O-Saturated Melting of Basalt with Implications for Subduction Zone Chemical Fluxes. Journal of Petrology 49, 523–553. https://doi.org/10.1093/petrology/egn001

Kushiro, I., 1973. Origin of some magmas in oceanic and circum-oceanic regions. Tectonophysics 17, 211–222. https://doi.org/10.1016/0040-1951(73)90003-6

Li Huijuan, Hermann Joerg, Zhang Lifei, 2022. Melting of subducted slab dictates trace element recycling in global arcs. Science Advances 8, eabh2166. https://doi.org/10.1126/sciadv.abh2166

Li, S.-M., Wang, Q., Zhu, D.-C., Cawood, P.A., Stern, R.J., Zhao, Z., 2022. Formation of Continental Crust by Diapiric Melting of Recycled Crustal Materials in the Mantle Wedge. Geophysical Research Letters 49, e2021GL097515. https://doi.org/10.1029/2021GL097515

Marschall, H.R., Schumacher, J.C., 2012. Arc magmas sourced from mélange diapirs in subduction zones. Nature Geosci 5, 862–867. https://doi.org/10.1038/ngeo1634

McCulloch, M.T., Gamble, J.A., 1991. Geochemical and geodynamical constraints on subduction zone magmatism. Earth and Planetary Science Letters 102, 358–374. https://doi.org/10.1016/0012-821X(91)90029-H

Miller, D.P., Marschall, H.R., Schumacher, J.C., 2009. Metasomatic formation and petrology of blueschist-facies hybrid rocks from Syros (Greece): Implications for reactions at the slab–mantle interface. Lithos 107, 53–67. https://doi.org/10.1016/j.lithos.2008.07.015

Mitchell, E.C., Fischer, T.P., Hilton, D.R., Hauri, E.H., Shaw, A.M., de Moor, J.M., Sharp, Z.D., Kazahaya, K., 2010. Nitrogen sources and recycling at subduction zones: Insights from the Izu-Bonin-Mariana arc. Geochemistry, Geophysics, Geosystems 11. https://doi.org/10.1029/2009GC002783

Mungall, J.E., 2002. Roasting the mantle: Slab melting and the genesis of major Au and Au-rich Cu deposits. Geology 30, 915–918. https://doi.org/10.1130/0091-7613(2002)030<0915:RTMSMA>2.0.CO;2

Nielsen, S.G., Marschall, H.R., 2017. Geochemical evidence for mélange melting in global arcs. Sci Adv 3. https://doi.org/10.1126/sciadv.1602402

Peacock, S.M., 2009. Thermal and metamorphic environment of subduction zone episodic tremor and slip. Journal of Geophysical Research: Solid Earth 114. https://doi.org/10.1029/2008JB005978

Peacock, S.M., Hyndman, R.D., 1999. Hydrous minerals in the mantle wedge and the maximum depth of subduction thrust earthquakes. Geophysical Research Letters 26, 2517–2520. https://doi.org/10.1029/1999GL900558

Peacock, S.M., Wang, K., 2021. On the Stability of Talc in Subduction Zones: A Possible Control on the Maximum Depth of Decoupling Between the Subducting Plate and Mantle Wedge. Geophysical Research Letters 48, e2021GL094889. https://doi.org/10.1029/2021GL094889

Pearce, J., 1982. Trace Element Characteristics of Lavas from Destructive Plate Boundaries, in: Andesites: Orogenic Andesites and Related Rocks. John Wiley and Sons.

Penniston-Dorland, S.C., Gorman, J.K., Bebout, G.E., Piccoli, P.M., Walker, R.J., 2014. Reaction rind formation in the Catalina Schist: Deciphering a history of mechanical mixing and metasomatic alteration. Chemical Geology 384, 47–61. https://doi.org/10.1016/j.chemgeo.2014.06.024

Plank, T., Langmuir, C.H., 1993. Tracing trace elements from sediment input to volcanic output at subduction zones. Nature 362, 739.

Plank, T., Manning, C.E., 2019. Subducting carbon. Nature 574, 343–352. https://doi.org/10.1038/s41586-019-1643-z

Pogge von Strandmann, P.A.E., Dohmen, R., Marschall, H.R., Schumacher, J.C., Elliott, T., 2015. Extreme Magnesium Isotope Fractionation at Outcrop Scale Records the Mechanism and Rate at which Reaction Fronts Advance. Journal of Petrology 56, 33–58. https://doi.org/10.1093/petrology/egu070

Prouteau, G., Scaillet, B., Pichavant, M., Maury, R., 2001. Evidence for mantle metasomatism by hydrous silicic melts derived from subducted oceanic crust. Nature 410, 197–200. https://doi.org/10.1038/35065583

Rampone, E., Hofmann, A., 2012. A global overview of isotopic heterogeneities in the oceanic mantle. Lithos 148, 247–261. https://doi.org/10.1016/j.lithos.2012.06.018

Rapp, R, Shimizu, N, Norman, M.D, Applegate, G.S, 1999. Reaction between slab-derived melts and peridotite in the mantle wedge: experimental constraints at 3.8 GPa. Chemical Geology 160, 335–356. https://doi.org/10.1016/S0009-2541(99)00106-0

Ringwood, A.E., 1974. The petrological evolution of island arc systems: Twenty-seventh William Smith Lecture. Journal of the Geological Society 130, 183–204. https://doi.org/10.1144/gsjgs.130.3.0183

Robock, A., 2015. Chapter 53 - Climatic Impacts of Volcanic Eruptions, in: Sigurdsson, H. (Ed.), The Encyclopedia of Volcanoes (Second Edition). Academic Press, Amsterdam, pp. 935–942. https://doi.org/10.1016/B978-0-12-385938-9.00053-5

Rymer, H., 2015. Part VII Volcanic Hazards, in: Sigurdsson, H. (Ed.), The Encyclopedia of Volcanoes (Second Edition). Academic Press, Amsterdam, pp. 895–896. https://doi.org/10.1016/B978-0-12-385938-9.02009-5

Schiano, P., Clocchiatti, R., Shimizu, N., Maury, R.C., Jochum, K.P., Hofmann, A.W., 1995. Hydrous, silica-rich melts in the sub-arc mantle and their relationship with erupted arc lavas. Nature 377, 595–600. https://doi.org/10.1038/377595a0

Schmidt, M.W., Poli, S., 2014. 4.19 - Devolatilization During Subduction, in: Treatise on Geochemistry: Second Edition. pp. 669–701. https://doi.org/10.1016/B978-0-08-095975-7.00321-1

Schmidt, M.W., Poli, S., 1998. Experimentally based water budgets for dehydrating slabs and consequences for arc magma generation. Earth and Planetary Science Letters 163, 361–379. https://doi.org/10.1016/S0012-821X(98)00142-3

Sheets, P., 2015. Chapter 76 - Volcanoes, Ancient People, and Their Societies, in: Sigurdsson, H. (Ed.), The Encyclopedia of Volcanoes (Second Edition). Academic Press, Amsterdam, pp. 1313–1319. https://doi.org/10.1016/B978-0-12-385938-9.00076-6

Sorensen, S.S., Grossman, J.N., 1989. Enrichment of trace elements in garnet amphibolites from a paleo-subduction zone: Catalina Schist, southern California. Geochimica et Cosmochimica Acta 53, 3155–3177. https://doi.org/10.1016/0016-7037(89)90096-3

Spandler, C., Pirard, C., 2013. Element recycling from subducting slabs to arc crust: A review. Lithos 170–171, 208. https://doi.org/10.1016/j.lithos.2013.02.016

Stolper, D.A., Bucholz, C.E., 2019. Neoproterozoic to early Phanerozoic rise in island arc redox state due to deep ocean oxygenation and increased marine sulfate levels. Proc Natl Acad Sci USA 116, 8746. https://doi.org/10.1073/pnas.1821847116

Sverjensky, D.A., 2019. Thermodynamic modelling of fluids from surficial to mantle conditions. Journal of the Geological Society 176, 348. https://doi.org/10.1144/jgs2018-105

Syracuse, E.M., van Keken, P.E., Abers, G.A., 2010. The global range of subduction zone thermal models. Physics of the Earth and Planetary Interiors 183, 73–90. https://doi.org/10.1016/j.pepi.2010.02.004

Tera, F., Brown, L., Morris, J., Sacks, I.S., Klein, J., Middleton, R., 1986. Sediment incorporation in island-arc magmas: Inferences from 10Be. Geochimica et Cosmochimica Acta 50, 535–550. https://doi.org/10.1016/0016-7037(86)90103-1

Till, C.B., Grove, T.L., Withers, A.C., 2012. The beginnings of hydrous mantle wedge melting. Contributions to Mineralogy and Petrology 163, 669–688. https://doi.org/10.1007/s00410-011-0692-6

Turner, S.J., Langmuir, C.H., 2022. An Evaluation of Five Models of Arc Volcanism. Journal of Petrology 63, egac010. https://doi.org/10.1093/petrology/egac010

Ulmer, P., Trommsdorff, V., 1995. Serpentine Stability to Mantle Depths and Subduction-Related Magmatism. Science 268, 858. https://doi.org/10.1126/science.268.5212.858

Wallace, P.J., 2005. Volatiles in subduction zone magmas: concentrations and fluxes based on melt inclusion and volcanic gas data. Journal of Volcanology and Geothermal Research 140, 217–240. https://doi.org/10.1016/j.jvolgeores.2004.07.023

Williams-Jones, G., Rymer, H., 2015. Chapter 57 - Hazards of Volcanic Gases, in: Sigurdsson, H. (Ed.), The Encyclopedia of Volcanoes (Second Edition). Academic Press, Amsterdam, pp. 985–992. https://doi.org/10.1016/B978-0-12-385938-9.00057-2

Wyllie, P.J., 1973. Experimental petrology and global tectonics —A preview. Tectonophysics 17, 189–209. https://doi.org/10.1016/0040-1951(73)90002-4

Zhu, G., Gerya, T.V., Yuen, D.A., Honda, S., Yoshida, T., Connolly, J.A.D., 2009. Three-dimensional dynamics of hydrous thermal-chemical plumes in oceanic subduction zones. Geochemistry, Geophysics, Geosystems 10. https://doi.org/10.1029/2009GC002625

Chapter 2

Fluid-mediated Mass Transfer between Mafic and Ultramafic rocks in Subduction Zones

This chapter was originally published as:

Codillo, E. A., Klein, F., Dragovic, B., Marschall, H. R., Baxter, E., Scambelluri, M., & Schwarzenbach, E. 2022. Fluid-mediated mass transfer between mafic and ultramafic rocks in subduction zones. Geochemistry, Geophysics, Geosystems, 23, e2021GC010206. https://doi.org/10.1029/2021GC010206. Used with permission as granted in the original copyright agreement.

Abstract

Metasomatic reaction zones between mafic and ultramafic rocks exhumed from subduction zones provide a window into mass-transfer processes at high pressure. However, accurate interpretation of the rock record requires distinguishing high-pressure metasomatic processes from inherited oceanic signatures prior to subduction. We integrated constraints from bulk-rock geochemical compositions and petrophysical properties, mineral chemistry, and thermodynamic modeling to understand the formation of reaction zones between juxtaposed metagabbro and serpentinite as exemplified by the Voltri Massif (Ligurian Alps, Italy). Distinct zones of variably metasomatized metagabbro are dominated by chlorite, amphibole, clinopyroxene, epidote, rutile, ilmenite, and titanite between serpentinite and eclogitic metagabbro. Whereas the precursor serpentinite and oxide gabbro formed and were likely already in contact in an oceanic setting, the reaction zones formed by diffusional Mg-metasomatism between the two rocks from prograde to peak, to retrograde conditions in a subduction zone. Metasomatism of mafic rocks by Mg-rich fluids that previously equilibrated with serpentinite could be widespread along the subduction interface, within the subducted slab, and the mantle wedge. Furthermore, the models predict that talc

formation by Si-metasomatism of serpentinite in subduction zones is limited by pressure-dependent increase in the silica activity buffered by the serpentine-talc equilibrium. Elevated activities of aqueous Ca and Al species would also favor the formation of chlorite and garnet. Accordingly, unusual conditions or processes would be required to stabilize abundant talc at high *P-T* conditions. Alternatively, a different set of mineral assemblages, such as serpentine- or chlorite-rich rocks, may be controlling the coupling-decoupling transition of the plate interface.

1 Introduction

The release of aqueous fluids from subducted sediments, altered oceanic crust, and serpentinized mantle is a fundamental process that drives arc volcanism, and facilitates the recycling of volatile and redox components from the solid Earth back to the ocean and atmosphere. Key to this understanding lies on the processes that set or modify the bulk compositions of subducted materials from oceanic settings up to subduction zones. Oceanic rocks and sediments are often subjected to combined, and sometimes coeval, deformation processes and fluid-rock interactions that can significantly modify their petrophysical (*e.g.,* density, magnetic susceptibility), geochemical (*e.g.,* trace elements, water and other volatiles), and redox properties prior to subduction. Important examples of these processes include serpentinization, carbonation, and talc-alteration of mantle rocks, as well as rodingitization, chloritization, and epidotization of mafic rocks (Bach et al., 2004; Bach and Klein, 2009; Honnorez and Kirst, 1975; Humphris and Thompson, 1978; Klein et al., 2009; Schwarzenbach et al., 2021). During subduction and exhumation, fluid-rock interactions at higher pressure and temperature conditions can further modify their geochemical, petrophysical, and redox characteristics. This is supported by field-based observations from exhumed high-pressure rocks in subduction zones worldwide (Bebout and Barton, 2002; Bebout and Penniston-Dorland, 2016; Breeding et al., 2004; Fryer, 2012; Gorman et al., 2019; Gyomlai et al., 2021; Harlow et al., 2016; Marschall et al., 2009; Pogge von Strandmann et al., 2015; Sorensen and Grossman, 1989).

Exhumed high-pressure terranes offer critical insights into the chemical interactions between disparate lithologies in subduction zones (notably serpentinites, eclogites, and metasedimentary rocks) that can produce complex reaction zones. However, accurate interpretation of such complex terranes requires distinguishing the signatures of high-pressure metasomatic processes in subduction zones from reworking and incomplete preservation during exhumation, and from inherited oceanic alteration prior to subduction (Bebout, 2007). This task is often challenging as some of the same mineral assemblages can form in low-

pressure oceanic and high-pressure subduction zone settings. For instance, hydrous mineral assemblages containing chlorite ± amphibole ± serpentine ± talc, which dominate the exhumed high-pressure metasomatic rocks in Syros (Greece), Santa Catalina Island (USA), New Caledonia, and many other high-pressure localities, also exist in low-pressure oceanic environments (Bach et al., 2004; Bebout and Barton, 2002; Boschi et al., 2006; Miller et al., 2009; Paulick et al., 2006; Spandler et al., 2008). This makes it difficult to determine the conditions and tectonic setting of mass transfer recorded by exhumed high-pressure terranes and adds uncertainty to the quantification of mass transfer in subduction zones. Importantly, as metasomatic interactions can occur at forearc to subarc depths, they are believed to profoundly influence arc magmatism and seismicity of the subducted slabs (Abers et al., 2006; Angiboust et al., 2012; Kirby et al., 2013; Marschall and Schumacher, 2012). Such metasomatic processes, though hidden from sight, are likely to be operational and pervasive at depth.

This study employs a multi-pronged approach to assess mass transfer between mafic and ultramafic rocks in subduction zones, using the high-pressure Voltri Massif (Ligurian Alps, Italy) as a natural laboratory. To that end, we integrate petrography, bulk-rock and mineral chemistry, radiogenic Sr isotopes, and petrophysical properties, with thermodynamic phase equilibria and reaction-path modeling to constrain how, where, and when metasomatism occurred. We demonstrate that fluid-mediated mass transfer was dominated by Mg from serpentinite to metagabbro at high-pressure, which lead to substantial mineralogical, chemical, and petrophysical changes. We discuss the geological implications of metasomatism for subduction environments where mafic and ultramafic rocks are juxtaposed, such as the slab-mantle interface, the mantle wedge, and within the subducting slab.

1.1 Geological background

Located in the Ligurian Alps of Italy, the Voltri Massif is composed of distinct tectonic slices of meta-ophiolitic rocks, oceanic metasediments, continent-derived plutonic rocks and metasediments, and oceanic mantle of subcontinental lithospheric origin. The whole massif records a complex tectonic history. The metamorphosed materials represent slivers of ocean floor formed during seafloor spreading in the former Liguro-Piedmont ocean in the Late Jurassic. This ocean floor was later subducted during the convergence of Europe and Adria in the Early Cretaceous about 25 Ma after cessation of the oceanic spreading (Hunziker, 1974) to reach peak eclogite-facies conditions, and locally these lithologies experienced subsequent minor greenschist-facies overprint during exhumation (Federico et al., 2007, 2005; Malatesta et al., 2012a; Messiga and Scambelluri, 1991; Rampone and Hofmann, 2012; Vignaroli et al., 2005). However, diverging views of the tectonic origins of rocks exposed in the Voltri Massif prevail in the literature. The presence of rodingites embedded within serpentines was interpreted to indicate pre-

subduction metasomatism of mafic oceanic crust (Piccardo, 2013; Scambelluri and Rampone, 1999). Accordingly, the structural, stratigraphic, and compositional relationships observed in the Voltri Massif were, to some extent, inherited signatures on the seafloor prior to subduction. However, additional alteration and mass transfer at high-pressure conditions were noted for some of the tectonic units in the Western Alps (*e.g.*, Monviso Unit, the Cascine Parasi mélange of the Voltri Massif) on the basis of petrologic, field structural, and thermobarometric evidence (Federico et al., 2015; Guillot et al., 2009; Malatesta et al., 2012a). For instance, structural aspects (i.e. block-in-matrix facies of metacrustal blocks within serpentinite domains) and heterogeneous peak metamorphic conditions recorded by different meta-crustal blocks within the massif led Malatesta et al. (2012) to suggest that the Voltri could be an exhumed sliver of a "fossil" serpentinite subduction channel mélange at the slab-mantle interface (Gerya and Stöckhert, 2006; Gerya and Yuen, 2003). The hydrous mineral assemblages (*e.g.*, chlorite, Ca-amphibole, epidote) sandwiched in between eclogites and serpentinites were proposed to have formed during the blueschist- to greenschist-facies retrograde exhumation (Federico et al., 2007; Malatesta et al., 2012a). A recent study investigated the *P*-*T*-time evolution and bulk Sm-Nd garnet ages of different high-pressure (HP) mafic rocks in the Voltri Massif to determine whether these mafic rocks were indeed exhumed as blocks within a chaotic mélange or as coherent sections of oceanic lithosphere (Starr et al., 2020). Different from previous studies (*e.g.*, Federico et al., 2007; Malatesta et al., 2012), it was suggested that a significant portion of the Voltri Massif was exhumed as large kilometric-scale coherent sections of ultramafic and mafic slab material (Cannaò et al., 2016; Smye et al., 2021; Starr et al., 2020). A more detailed assessment of the structural aspects of the entire Voltri Massif is discussed elsewhere (Federico et al., 2015, 2007; Malatesta et al., 2012a).

Our study focuses on the Voltri Massif, which is mainly composed of eclogite-facies metagabbro, metabasalt and metasediment enclosed in highly schistose serpentinites. The Voltri metagabbro crops out as meter-scale blocks mostly derived from precursor Fe-Ti gabbros surrounded by highly schistose serpentinites and chlorite schists. Metagabbro derived from Fe-Ti gabbros show higher garnet modal abundance compared with Mg-Al gabbro derivatives. A late stage retrograde greenschist facies assemblage (chlorite + actinolite + albite + quartz) partially replaced the eclogite-facies assemblage (Malatesta et al., 2012a; Vignaroli et al., 2005). Previous studies of high-pressure serpentinite at Voltri have documented a foliation in serpentinite that is generally parallel to the garnet-pyroxene foliation observed in adjacent eclogitic blocks (Cannaò et al., 2016; Federico et al., 2007; Haws et al., 2021; Malatesta et al., 2012a). Furthermore, a range of prograde to peak metamorphic conditions from 1.8–2.4 GPa and 500–600 °C occurring at ~50–33 Ma, followed by partial retrogression through blueschist- (~1.2 GPa and 550 °C) and greenschist-facies conditions (~0.8 GPa and 480 °C) occurring at ~34–24 Ma have been proposed for the

Voltri Massif metagabbros (Messiga et al., 1983; Messiga and Scambelluri, 1991; Smye et al., 2021, 2021; Starr et al., 2020; Vignaroli et al., 2005).

2 Materials and Methods

We sampled a transect across metasomatic reaction zones between juxtaposed serpentinite and eclogite-facies metagabbro (Figure 1a). This transect represents a traverse across a single, continuous metagabbro block into the surrounding serpentinite (N 44.478, E 8.599, 630 m above sea level; Figure. S1). There is no field evidence for multiple dismembered metacrustal blocks in the sampled transect. The timing of peak metamorphism of the eclogitic metagabbro block sampled in this study was previously constrained at ~40 Ma using Sm-Nd garnet geochronology (metagabbro block 3; Starr et al., 2020). A total of 22 discrete samples were collected using a diamond-tipped rock drill, covering > 3 m on the serpentinite side and ~1 m on the eclogitic metagabbro side relative to the original lithologic contact. Serpentinite and eclogitic metagabbro samples farthest away from the contact were chosen to represent rocks that are presumably the least affected by mass transfer processes. Caution was implemented during the selection of rocks to avoid weathered surfaces. Samples were classified into five zones based largely on mineralogy as follows: Zone I (samples V17-X808B14 to B22), Zone II (samples V17-X808B12 and V17-X808B13), Zone III (samples V17-X808B01 to B03), Zone IV (samples V17-X808B04 to V17-X808B08) and Zone V (samples V17-X808B09 and V17-X808B10). Henceforth, these samples will be referred to as *e.g.,* 'B01' for sample V17-X808B01, etc. In the field, serpentinite (Zone I) is separated from metagabbro (Zones II-V) by a sharp lithologic contact that can be traced laterally along the stretch of the outcrop. Zone II is distinguished in the field by its flaky appearance and is mainly composed of amphibole and chlorite with a foliation that is more apparent than in Zones III to V. The transitions between metasomatic reaction zones in the metagabbro are gradational, and distinguished primarily based on mineralogy (Figure 1a). Samples were inspected in transmitted and reflected light using a Zeiss AxioImager 2 microscope, with mineral identification and abundance estimates complemented by scanning electron microscopy (SEM), confocal Raman spectroscopy, electron microprobe analysis (EPMA), and thermogravimetric analysis (TGA). Loss on ignition of bulk rock samples were also determined using TGA (see supplementary material).

We performed equilibrium thermodynamic modeling of representative bulk compositions coupled with garnet isopleth modelling to provide constraints on the pressure and temperature conditions of mass transfer. Pseudosections were computed using the program Perple_X (version 6.9.0; Connolly, 2009) and the internally consistent dataset (version 5.5) of Holland and Powell (1998) in the MnO-Na_2O-CaO-FeO-MgO-Al_2O_3-SiO_2-H_2O-TiO_2-O_2 (MnNCFMASHTO) chemical system. Thermodynamic reaction-path models were developed using the EQ3/6 software package (Wolery, 1992) and the Deep Earth Water

(DEW) Model (Huang and Sverjensky, 2019; Sverjensky, 2019; Sverjensky et al., 2014) database to aid in the interpretation of fluid-rock interactions. In particular, we used reaction-path modelling to further assess the alteration history and concomitant mineralogical changes during a fluid-mediated reaction between hydrated ultramafic (serpentinites) and metamorphosed crustal rocks (metagabbro) at subduction-zone conditions guided by *P-T* constraints from equilibrium pseudosection and garnet isopleth models. Results of reaction-path models were compared to the sequence of mineral assemblages from petrographic observations. Detailed descriptions of the analytical techniques and the setup for thermodynamic phase equilibria and reaction-path modelling are provided in the supplementary material (Codillo, 2022).

3 Results

The mineral modal abundances, spatial distributions, and bulk petrophysical properties of the metasomatic reaction zones between the serpentinite and eclogitic metagabbro are shown in Figure 1 and reported along with bulk-rock major and trace-element concentrations, $^{87}Sr/^{86}Sr$ isotope ratios, and bulk-rock Fe(III) /Fe_T in the supplementary table. Note that the full extent of the reaction zone highlighted was not immediately apparent in the field. Based on petrographic and spectroscopic characterization, coupled with mineral chemical data and TGA-DSC measurements, we distinguish Zone I (antigorite + magnetite serpentinite), Zone II (chlorite + Ca-amphibole-rich metagabbro), Zone III (chlorite-rich metagabbro), Zone IV (epidote + Na-Ca amphibole-rich metagabbro), and Zone V (eclogitic metagabbro). The sharp lithologic-tectonic contact that separates the serpentinites and metagabbro is located in between Zones I and II. Zones II to IV consist of variably altered metagabbro with distinct mineralogical assemblages, sandwiched in between serpentinite (Zone I) and distal eclogitic metagabbro (Zone V). Consistent with previous findings (Cannaò et al., 2016; Haws et al., 2021; Malatesta et al., 2012a), the foliation in serpentinite is generally parallel to the foliation in the adjacent metagabbro block. A detailed assessment of the foliation and deformation processes in this transect is beyond the scope of this study.

3.1 Petrography

Zone I consists of highly deformed and foliated serpentinite that is similar to the mylonitic serpentinite that was studied by Cannaò et al. (2016). Samples of Zone I were collected from both the proximal and distal ends to the contact. Thin section petrography, Raman, SEM, and TGA-DSC analyses revealed nearly monomineralic serpentine (antigorite), in addition to traces of talc, magnetite, and relict chromite (Figure 2a; Figure S3). These minerals chiefly occur in non-pseudomorphic textures, whereas pseudomorphic mesh and bastite textures after olivine and pyroxene are rare and limited to undeformed

serpentinite domains (see Cannaò et al., 2016). Olivine and pyroxene are completely altered to serpentine with minor talc localized near the magnetite. Some accessory magnetite grains show alteration to iron oxy-hydroxide as identified by EPMA. We did not observe any systematic increase in the modal proportions of talc and magnetite towards the contact. Brucite was not detected in any sample using TGA-DSC or Raman spectroscopy (Klein et al., 2020). A subset of serpentinite samples that were collected farthest from the field contact reveal pseudomorphic textures, suggestive of serpentinization under static conditions. Antigorite was identified as the sole serpentine phase based on its characteristic Raman spectrum (Groppo et al., 2006; Petriglieri et al., 2015). Neither chrysotile nor lizardite were found in the samples (Figure S4).

Zone II is dominated by Ca-amphibole with subordinate chlorite intergrown with euhedral ilmenite. Calcic amphibole occurs as long prismatic grains embedded within a chlorite-rich matrix. Ilmenite is mantled by titanite. Rutile and magnetite are accessory phases in this zone (Figure 2b; Figures S2,4)

Zone III is mainly composed of chlorite, prismatic Ca-amphibole, clinopyroxene, and opaque minerals. Clinopyroxene cores are omphacitic and show an exsolution texture as well as variable replacement by chlorite whereas rims are diopsidic in composition. Rare garnet occurs as anhedral grains within a chlorite matrix and as inclusions in epidote and Ca-amphibole (close to the Zone IV contact, *e.g.*, samples B03 and B04). As in Zone II, ilmenite is mantled by titanite. Rutile is an accessory phase in this zone (Figure 2c-e; Figures S1,3).

Zone IV is characterized by a range of mineral assemblages that change in composition with distance from the contact. Samples closest to Zone V are characterized by garnet, omphacitic and diopsidic clinopyroxene, Na-Ca amphibole, ilmenite, rutile and titanite, minor albite, white mica, and quartz (Figure 2f-h). The modal abundances of diopsidic clinopyroxene, epidote, and Ca-amphibole in Zone IV increase towards the contact. Subdomains consist of 1) epidote + diopsidic clinopyroxene, albite, quartz, minor garnet, and localized veinlets of Na-Ca amphibole or 2) abundant garnet, along with minor epidote and Na-amphibole. Samples that are more proximal to the contact are dominated by epidote, diopsidic clinopyroxene, Ca-amphibole, and garnet with minor replacement by chlorite. Garnet contains Na-amphibole, clinopyroxene, white mica, ilmenite and rutile inclusions that were identified either petrographically or using confocal Raman spectroscopy (Figures S2,4). Interlocking grains of ilmenite and rutile that are mantled by titanite are present throughout Zone IV.

Zone V, collected farthest from the field contact, represents the least altered metagabbro and is dominated by garnet, omphacitic clinopyroxene, Na-Ca amphibole, Ti-rich phases (i.e. ilmenite, rutile, titanite), minor diopsidic clinopyroxene, epidote, albite, and accessory sulfide (pyrite) (Figure 2i-k; Figures S2,4). Similar to Zone IV, the opaque assemblage also shows interlocking grains of ilmenite and rutile that are mantled by titanite (Figure 2l). Garnet contains Na-Ca amphibole, clinopyroxene, epidote and paragonite (inferred to be pseudomorphic after lawsonite; Figure S5) and rutile inclusions that were

identified using confocal Raman spectroscopy. In comparison with Zones III and IV, garnet in samples in Zone V showed the least extensive replacement by chlorite.

3.2 Mineral chemistry variations

Average major element compositions of the major minerals in each zone are summarized in the supplementary table. Clinopyroxene is found in Zones II to V, and its composition varies systematically, especially in Zones II to IV. The major element compositions of the primary omphacitic clinopyroxene in Zones II-IV are variable, with Mg# [=molar Mg/(Mg+Fe)] ranging from ~0.5–0.7, while the secondary diopsidic clinopyroxene mantling the omphacitic clinopyroxene in Zones II and III shows a systematic increase in Mg# (0.72–0.81), along with CaO, MgO, and a decrease in Al_2O_3 contents, towards the contact (Figure 3b). Omphacitic clinopyroxene cores across the different zones are variably altered to diopsidic compositions (i.e. higher Ca and lower Na contents) and show patchy, μm-scale chlorite alteration (Figure 2i).

Garnet across the different zones displays systematic changes in core-to-rim compositions with distance to the lithologic contact (Figure 4, Figure S6). Euhedral to subhedral garnet (~1 mm average diameter in B09 and B10) in Zone V displays systematic decrease in MnO contents from core (> 5 wt. %) to rim (< 0.5 wt. %) at relatively constant and low CaO contents (≤ 8 wt. %). Garnet in sample B08 (~0.5 mm average diameter, Zone IV) shows compositional characteristics similar to garnet in Zone V with concentric Mn-growth zoning (i.e. decreasing Mn from core to rim) and low and constant CaO contents (Figure 4e,f). Garnet in sample B07 (~0.5 mm average diameter, Zone IV) also displays the same Mn-growth zoning and fairly low CaO contents. However, the garnet rims in sample B07 display slight enrichment in CaO contents (> 8 wt. %) relative to more distal samples (Figure 4g,h). The more proximal garnet in B06 (~0.4 mm average diameter, Zone IV) displays similar core-to-rim MnO zoning to the more distal samples but with distinctly opposite core-to-rim CaO trends. In particular, the cores of garnet in B06 have CaO contents similar to the garnet from more distal samples (~8 wt. %) but their rims systematically increase to up to ~12 wt. % CaO. Garnet in Zones IV and V has decreasing almandine contents and increasing pyrope contents from core (average of $Alm_{72}Prp_3Sps_{10}Grs_{16}$) to rim (average of $Alm_{74}Prp_{10}Sps_1Grs_{15}$). Samples in Zone IV that are more proximal to the contact have garnet that, on average, have lower almandine and higher grossular contents than more distal ones (Figure 3a). In addition, the core-to-rim variations in these proximal garnets show increasing grossular and decreasing spessartine contents from core ($Alm_{64}Prp_2Sps_{12}Grs_{22}$) to rim ($Alm_{63}Prp_3Sps_3Grs_{32}$). Garnet in samples more proximal to the contact, i.e. Zone III, are anhedral and pervasively resorbed and replaced by chlorite. This makes it difficult to determine whether the measured grain represents the core or rim. For this purpose, we assumed

that the rim would have the highest CaO content following the observed systematic trend from the closest garnets in Zone IV (B06 and B07). Garnets in Zone III are grossular-rich ($Alm_{62}Prp_8Sps_4Grs_{26}$ core to $Alm_{49}Prp_3Sps_3Grs_{45}$ rim), with CaO content exceeding the core-to-rim range of garnets from the more distal Zones IV and V. For instance, the compositions of anhedral garnet included within euhedral epidote ($Alm_{49}Prp_4Sps_4Grs_{43}$) and calcic amphibole ($Alm_{50}Prp_4Sps_4Grs_{42}$) are grossular-rich. The MnO contents of Zone III garnets remain within range of garnet compositions from Zones IV and V, with MnO contents plotting closer to the rim compositions of garnets from Zones IV and V (Figure 4i,j).

Amphiboles show a wide range of compositions, ranging from sodic to calcic. The MgO and CaO contents of amphiboles generally increase towards the contact. Following the classification of Hawthorne et al. (2012), Zones V and IV contain a wide variety of amphiboles belonging to the Na-Ca group (*e.g.*, winchite, ferri-winchite, barroisite, and katophorite) and the calcic group (*e.g.*, pargasite, actinolite, magnesio-ferri-hornblende, and magnesio-hornblende). Representative core-to-rim compositions of a subset show Na-Ca amphibole (winchite, katophorite) mantled by Ca-rich amphibole (mainly pargasite) in these zones. Zones II and III, which are the closest to the field contact, show less variability in composition compared to Zones IV and V. These zones contain dominantly Ca-rich amphibole, such as hastingsite, actinolite, and tremolite (Figure 3c).

The composition of chlorite (clinochlore) in Zones II and III shows a systematic increase in Mg and Si contents towards the contact (Figure 3b). The Mg# varies from 0.60 to 0.86, with higher values towards the contact. Such compositional variations reflect the combined Fe–Mg exchange between the Mg-endmember clinochlore and the Fe-endmember daphnite, and Tschermak's substitution between daphnite, clinochlore and amesite

Epidote comprises a dominant fraction of the mineral assemblage in Zone IV. Its composition varies within Zone IV, with generally higher Si (2.98–3.01 atoms per formula unit or a.p.f.u.) for samples farther from the contact to lower Si (2.91–2.95 a.p.f.u.) in samples closer to the contact. The calculated Fe(III) contents show a systematic increase towards the contact, from 0.20 to 0.89 a.p.f.u.

Antigorite is chemically homogenous in Zone I (34.1 wt. % MgO, 41.5 wt. % SiO_2, 8.6–8.8 wt. % FeO*, ~2.0 wt. % Al_2O_3), with a Mg# of 0.87 and has ~13 wt. % of structurally-bound water. Talc in Zone I also shows a homogenous composition (28.8 wt. % MgO, ~62.0 wt. % SiO_2, 2.5–2.7 wt. % FeO), with Mg# of 0.95 and has ~6 wt. % of structurally bound water.

Albite of near endmember composition is a minor phase and is generally found with epidote and diopsidic clinopyroxene in Zone IV. Ilmenite in Zones II and III shows variations in composition (49–51 wt. % TiO_2, 41.5–47.5 wt. % FeO, 0.4–1.7 wt. % MgO), with notable increases in Mg and decreases in Mn contents from Zone III to II. Titanite in Zones II and III shows a homogenous and near-stoichiometric

composition (37–39 wt. % TiO_2, ~30 wt. % SiO_2, and ~ 28 wt. % CaO). Accessory phases such as apatite and pyrite are observed in different zones but their compositions are not examined in this study.

3.3 Bulk-rock major element compositional variation

Systematic chemical changes are observed across the serpentinite-metagabbro transect (Figure 5). On a volatile-free basis, the MgO concentration is highest in serpentinite (Zone I) and gradually decreases towards Zone V. The CaO concentration is lowest in the serpentinite and highest in the metagabbro of Zone IV, but decreases towards Zone V. The concentration of SiO_2 shows limited variation in Zones I, IV and V but is lower in III, except for one sample in Zone II. The concentration of Al_2O_3 is mainly elevated in Zone III relative to the adjacent zones. The loss on ignition (LOI; taken as bulk H_2O) and MgO/SiO_2 show similar enrichment and depletion trends, which reflects the relative abundance of Ca-amphibole and chlorite in Zones II and III. The bulk-rock $Fe(III)/Fe_T$ display elevated ratios in Zone II-IV relative to V, with highest values in IV (Figure 5d). The modal mineralogy and major element compositions (and associated modal mineralogy) of the two samples in Zone V are generally similar, except for differences in Al_2O_3.

3.4 Bulk-rock trace element compositional and Sr isotopic variation

The rare earth element (REE) concentrations show systematic across-transect trends and a decoupling between light (L-) and heavy (H-) REE (Figure 6a). The LREE concentrations are lowest in serpentinite and are generally elevated in metagabbro in Zones II to V, reaching their highest concentrations in Zone IV. Enrichments in fluid-mobile elements (*e.g.*, Cs, Sr, Pb, Rb, Ba) are also observed in the samples with the highest LREE enrichments in Zone IV (Figure 6c). On the other hand, HREE concentrations are lowest in Zone I, but only gradually increase to roughly steady concentrations from Zones II to V. The peak enrichments in HREE are observed in Zone III, adjacent to the LREE-enriched Zone IV samples. Nickel and Cr show a gradual decrease from high concentrations in Zone I to Zones IV and V while Sc shows a step-wise function separating Zone I from Zones II-V (Figure 6b).

Primitive Mantle-normalized REE patterns of serpentinite vary little among the analyzed samples, and display a slight increase from La to Lu. In comparison, metagabbro in Zone II show similar primitive mantle-normalized abundances for LREE and Th, but with higher Sr and HREE relative to serpentinite. Metagabbro of Zone III is more enriched in REE, but is slightly depleted in fluid-mobile elements compared to Zone II. The metagabbros of Zone IV display the highest concentrations in LREE, Sr, and Pb among the measured samples. Metagabbros of Zone V have similar flat HREE patterns as in Zone IV, but are strongly depleted in LREE (relative to HREE), Sr, and Pb (Figure 7). The $(La/Sm)_N$ ratio (N, normalized to Primitive

Mantle) of serpentinite systematically increases towards the contact. Similarly, the $(La/Sm)_N$ increases towards the contact from Zone V to Zone II within the metagabbro side. Both metagabbro samples in Zone II have lower values of $(La/Sm)_N$ than the adjacent zones (Figure S7). The two samples from Zone V display similar primitive mantle-normalized trace element patterns expect for Zr, Hf, Nb, and Ta.

The age-corrected (40 Ma from Starr et al., 2020) bulk-rock $^{87}Sr/^{86}Sr$ isotope ratio of serpentinite is 0.7083 ± 0.0004 (average ± 1 SD). Metagabbro in Zones II to V displays a constant $^{87}Sr/^{86}Sr$ isotope ratio of 0.7037 ± 0.0001. This distribution reflects a step-function from the more radiogenic Sr in the serpentinite of Zone I to the less radiogenic Sr in Zones II to V (Figure 6d). The bulk-rock Sr concentration mirrors the bulk-rock CaO trend, with the highest values in Zone IV, the lowest in Zone I, and intermediate and roughly similar values across Zones II, III, and V.

3.5 Density and magnetic susceptibility

Variations in the mineralogy and bulk-rock chemistry are reflected in their bulk density and magnetic susceptibility. Across-transect variations between the serpentinite and metagabbro (Figure 1c) show that the density systematically decreases from the distal eclogite (ρ = 3.6 g/cm^3 in Zone V) towards the distal serpentinite (ρ = 2.6 g/cm^3 in Zone I) through the reaction zones II, III and IV, with values intermediate between Zones I and V. Zone IV has an average bulk density of ~3.5 g/cm^3 while Zones II and III have densities of 3.0 g/cm^3. The magnetic susceptibilities are low and near-constant for metagabbro of Zones IV and V (15.3–42.8 SI x10^{-5}) relative to high values in Zone III (238–375 SI x10^{-5}). Serpentinite of Zone I and metagabbro of Zone II have low and near-constant magnetic susceptibility values (11.0–134 x10^{-5} SI) comparable to Zones IV and V. For comparison, the bulk magnetic susceptibility reported for oceanic serpentinites can reach up to 12 x10^{-2} SI (Klein et al., 2014).

3.6 Pressure-temperature constraints

Thermodynamic phase equilibria were calculated in order to constrain the metamorphic *P-T* evolution of the Voltri metagabbro and the relative timing of mass transfer. Pseudosection modeling of the whole rock composition, coupled with garnet crystal core chemical isopleths, allows for the calculation of the *P-T* conditions of garnet growth initiation while pseudosection modeling of the matrix (fractionated whole rock) compositions, coupled with garnet crystal rim chemical isopleths, allows for the calculation of the peak to post-peak *P-T* conditions. Moreover, pseudosection modeling of the stable mineral assemblage using the whole rock compositions of the most reacted samples allows for calculation of the *P-T* conditions during the final stages of element mass transfer along the sample transect. In these samples, there are no

porphyroblastic phases, like garnet, that would significantly fractionate elements, thereby changing the effective whole rock compositions. For all pseudosection results presented below, uncertainties in pressure and temperature estimates are regarded to be on the order of □□0.1 GPa and □ 40 □C (Palin et al., 2016).

The results of the phase equilibria modeling for sample B10 (Zone V) are shown in Figure 8 and the results of modeling for representative bulk compositions of Zones II-IV are shown in Figure 9. Garnet crystal core growth is calculated to have occurred in the mineral assemblage field garnet + omphacite + chlorite + lawsonite + rutile (□ quartz). This calculated assemblage is broadly consistent with the petrographic observations of garnet cores containing inclusions of omphacite, lawsonite pseudomorphs and rutile. Garnet crystal rim growth is calculated to have occurred in the mineral assemblage field garnet + omphacite + amphibole + chlorite + rutile (□ talc). This is consistent with the observations of Na-amphibole inclusions within garnet and Na-Ca amphibole and chlorite in the matrix. While talc is calculated to have been stable during the growth of garnet rims, it is neither found as inclusions in garnet nor as a matrix phase. However, the calculated abundance of talc is < 0.1 vol. %, and is thus deemed negligible. Calculated *P-T* conditions for initial growth of garnet in sample B10, constrained by garnet core isopleth intersections and agreement between observed inclusion assemblages and calculated assemblages, are ~2.2 GPa and 430 □C. Calculated *P-T* conditions for garnet rim growth are ~2.5 GPa and ~520 □C (Figure 8). This is further defined as the peak *P-T* condition for the samples of interest.

Garnet core growth for sample B06 (Zone IV) is calculated to have occurred in the mineral field assemblage garnet + omphacite + chlorite + lawsonite + ilmenite + rutile (□ talc). This is broadly consistent with the observed garnet core inclusions, including omphacite, epidote + paragonite (inferred to be pseudomorphic after lawsonite), ilmenite and rutile. As above, the calculated abundance of talc was deemed negligible. Garnet rim growth in sample B06 is calculated to have occurred in the mineral field assemblage garnet + omphacite + chlorite + lawsonite + epidote + ilmenite + rutile (□ amphibole). This is consistent with observed garnet inclusions of omphacite, Na-amphibole, lawsonite pseudomorphs (epidote + white mica), ilmenite and rutile. Calculated *P-T* conditions for initial growth of garnet in sample B06 are ~2.4 GPa and 470 □C. Calculated *P-T* conditions for garnet rim growth are ~1.8 GPa and ~500 □C (Figure 9d). Modeling of the stable mineral assemblage using the matrix composition for sample B06 highlights partial re-equilibration at lower pressure. This is consistent with the presence of titanite rims around ilmenite and rutile, with a calculated maximum pressure (for the mineral assemblage omphacite + amphibole + chlorite + epidote + ilmenite + titanite) of ~0.8–0.9 GPa at ~475 □C (Figure 9e). With this estimate, we assume relatively isothermal decompression after attainment of peak *P-T* conditions, consistent with previous constraints (Malatesta et al., 2012a). In this portion of the phase diagram, the titanite-in reaction line has a negative dP/dT, and thus any early cooling upon decompression would result in traversing the reaction line at higher pressure. It should be noted, however, that the bulk rock $Fe(III)/Fe_T$ exerts a significant control

on the stability of Ti-bearing phases (Diener and Powell, 2010), and thus the maximum pressure at which titanite is stable may vary. For both samples B10 (Zone V) and B06 (Zone IV), a) the intersections of the garnet core compositional isopleths are situated up to 100 °C and from 0.4–1.0 GPa above the initial stability of garnet (see Figures 8 and 9d), and b) the estimated volume abundance of garnet at these points is ~2 vol. % and ~5 vol. %, respectively. The implications of these calculations will be discussed below (see section 4.4). However, it should be noted that model observations such as these have been attributed to either kinetic limitations to mineral growth (Carlson et al., 2015) or inaccuracies in bulk rock composition.

Phase equilibria modeling of sample B01 (Zone III), combined with a comparison of observed and calculated mineral assemblages, allows for the calculation of the *P-T* conditions during the final stages of metamorphism. This is motivated by the clear textural relationship of garnet replacement by chlorite which suggest that B01 last equilibrated at *P-T* conditions post eclogite-facies metamorphism. At the peak *P-T* conditions of ~2.5 GPa and ~520 □C, the calculated stable mineral assemblage is clinopyroxene + chlorite + talc + ilmenite + rutile. Comparisons between petrographic observations and calculated phase equilibria are suggestive of partial re-equilibration during decompression. These include a) the absence of talc in the observed stable mineral assemblage, b) blueschist-facies overprinting represented by the growth of Na-Ca amphibole at the expense of clinopyroxene at pressures below ~2.3 GPa (note the appearance of cpx grains in Figure 2f,g,i), and c) the presence of titanite mantling ilmenite throughout sample B01 (Figure 2c). The observed mineral assemblage clinopyroxene + amphibole + chlorite + ilmenite + titanite is calculated to occur at a maximum pressure of ~1.6 GPa at 500 □C. The appearance of magnetite, observed petrographically to be a late-stage phase, is calculated to be stable at pressures below ~0.7 GPa at 450–475 □C (Figure 8b). This is interpreted to record final equilibration associated with the early stages of exhumation and thus may help further constrain the retrograde metamorphic pressure-temperature history.

Sample B13 in Zone II represents one of the most strongly metasomatized bulk compositions along the transect. The calculated stable mineral assemblage at the peak *P-T* conditions is clinopyroxene + chlorite + talc + ilmenite (□ antigorite). Similar to sample B01 in Zone III, Ca-amphibole is calculated to be stable and form at the expense of clinopyroxene at pressures below ~2.3 GPa. Few other constraints on *P-T* conditions can be made from these lithologies. As mentioned earlier, the presence of magnetite as an accessory phase is calculated to be stable at pressures below ~0.6 GPa and temperatures below ~500 □C (Figure 9a).

In an attempt to calculate the *P-T* conditions of garnet growth in Zone III that experienced significant Ca enrichment and to identify the relative timing of this enrichment, the bulk composition for sample B03 was modeled (Figure 9c). Calculated garnet chemical isopleths were compared to measured garnet core and rim compositions. The calculated stable mineral assemblage at the peak *P-T* conditions is

garnet + clinopyroxene + chlorite + ilmenite + rutile. The calculated garnet composition at the peak *P-T* condition is $Alm_{32}Prp_{05}Sps_{07}Grs_{56}$. As noted earlier the observed compositions for garnet crystal core and rim in sample B03 are $Alm_{62}Prp_{8}Sps_{4}Grs_{26}$ and $Alm_{49}Prp_{3}Sps_{3}Grs_{45}$, respectively. The calculated garnet composition at the peak *P-T* condition provides a composition that is significantly more grossular-rich (and almandine-poor) than observed. The significance of this discrepancy for the timing of mass transfer will be discussed in section 4.4.

To summarize the results from phase equilibria modeling, Zones IV and V are inferred to record the prograde to peak to post-peak *P-T* conditions for the metagabbro-serpentinite contact studied here. The inferred peak *P-T* condition for this locality is ~2.5 GPa and 520 □C (Figure 9f). The similarity in the *P-T* path recorded in Zones IV and V suggests that the bulk compositions for these zones were established prior to peak metamorphic conditions. This is further supported by textural equilibrium in Zones IV and V (Figures 2g,j; Figure S2). The peak *P-T* constraints are also taken as a maximum *P-T* constraint for the formation of Zones II and III because of the clear petrographic relation of garnet being replaced by chlorite in these zones. Pervasive, although minor, blueschist- and greenschist-facies overprinting has already been inferred for lithologies across the Voltri Ophiolite (Starr et al., 2020). This is also evident in the studied metagabbro-serpentinite contact by localized partial re-equilibration of Zones II, III and IV. All samples from zones II to V contain Ti-bearing phases (i.e. rutile and ilmenite) that are mantled by titanite. Therefore, the *P-T* condition of formation of these titanite rims serve as a lower limit for the formation of Zones II and III (Figure 2l). Based on these and previous constraints, we infer a clockwise *P-T* path, that exhibits a phase of relatively isothermal decompression at ~500–520 □C from the peak pressure of ~2.5 GPa down to ~1.0 GPa (Figure 9f). Lastly, these results are consistent with previous regional thermobarometric constraints for the Voltri Massif (Malatesta et al., 2012a; Smye et al., 2021; Starr et al., 2020).

3.7 Reaction-path modeling

Reaction-path models were calculated to further constrain metasomatic reactions between serpentinite and metagabbro. In our models, we first calculated the aqueous fluid composition and equilibrium speciation controlled by a serpentinite assemblage composed of antigorite + clinopyroxene (diopside) + magnetite ± brucite, and tracked their activities as a function of temperature and pressure. We did not model serpentinization of mantle peridotite at subduction zone conditions. Rather, we calculated the composition of an aqueous fluid coexisting with, and buffered by a serpentinite assemblage. We present the speciation of Mg, Si, and Ca, and their activities from 300–550 °C and 1.0–2.5 GPa (Figure 10). Note that for the sake of clarity, we only report the two most abundant species of each of these elements. However, we do not report the predicted activities for Fe and Al species which are all below 10^{-5}. Over the

range of *P-T* conditions determined for the studied samples, $Mg(OH)_{2(aq)}$ is predicted to be the dominant species followed by $H_4SiO_{4(aq)}$ (i.e. $SiO_{2(aq)}$)and $H_3SiO_4^-$ in the fluid. The predicted activity of $Mg(OH)_{2(aq)}$ increases with increasing temperature but generally decreases with increasing pressure. Conversely, the activities of all Si species increase with increasing pressure while Ca species remain broadly unchanged. The activities of Ca species are predicted to remain fairly constant as temperature increases and are three orders of magnitude lower than the activity of $Mg(OH)_{2(aq)}$. Notably, the activities of Mg species are higher while the activities of Si species are lower in fluids coexisting with a brucite-bearing serpentinite compared to a brucite-free serpentinite at the same *P-T* conditions.

We then modeled the isobaric and isothermal metasomatism of gabbro by allowing it to react with a fluid that was in equilibrium with serpentinite (Figure 11). We used the *P-T* constraints derived from the pseudosection modeling (section 3.6) and predicted the fluid composition in equilibrium with a brucite-free serpentinite consistent with petrographic observations. The model procedure was to titrate gabbro in small increments into the fluid that previously equilibrated with serpentinite. The reaction path therefore portrays a system that is initially fluid-dominated but that becomes increasingly rock-dominated as more metagabbro is added. One could envision that this model represents local fluid–rock equilibria as fluid travels from serpentinite into gabbro (Figure 11). The possibly large porosity and permeability contrasts between serpentinite and metagabbro are likely to promote spatial variations in fluid fluxes and fluid-to-rock ratios between metagabbro block interior and surrounding serpentinite, as suggested by numerical models (Ague, 2007). This modelling approach circumvents some potential complexities in investigating subduction zone processes. For instance, our approach can simulate the reaction between a serpentinite-buffered fluid and adjacent metagabbro regardless of whether the release of fluids during subduction is episodic or continuous and whether the fluids are derived locally (i.e. from the breakdown of brucite in serpentinite) or externally (i.e. other subducted hydrated lithologies) as long as the fluids are last equilibrated with serpentinite before reacting with the metagabbro. In this study, we calculated two model series, one with gabbro and another one with eclogite as reactants. The gabbro-fluid model explores the possibility that fluid-mediated mass transfer occurred during prograde to peak metamorphism, modifying the bulk composition of each zone, before reaching peak eclogite-facies metamorphism and post-peak retrograde conditions. In comparison, the eclogite-fluid model explores the possibility that the fluid-mediated mass transfer only occurred at post-peak eclogite-facies and retrograde conditions. Importantly, only the model that used gabbro predicts mineral assemblages that are observed in the reaction zones (Figure 11). The model results for reaction with eclogite are presented in the supplement. The serpentinite-equilibrated fluid, before reaction with gabbro (indicated at the lowest ξ value, i.e. maximum f/r ratio), is predicted to be dominated by dissolved Mg in all models, with subordinate dissolved Si, Ca, Al, and Fe. The models generally show similar mineral assemblages between 450–550 °C. With decreasing f/r ratios over this temperature range, the predicted

sequence of minerals formed is antigorite + clinopyroxene → serpentine + clinopyroxene + chlorite → chlorite + clinopyroxene ± tremolite → garnet + chlorite + clinopyroxene → epidote + chlorite + clinopyroxene ± garnet → chlorite + clinopyroxene + epidote + paragonite ± plagioclase ± quartz. Magnetite is predicted to form in all simulations. The composition and oxygen fugacity (fO_2) of the coexisting fluid vary with increasing f/r. Over a range of modeled *P-T* conditions, the concentration of dissolved Mg decreases, while dissolved Si increases with decreasing f/r ratio. The dissolved Al concentration is most elevated at intermediate f/r ratios and is mirrored by depletions in Ca and Fe. The predicted fO_2 at intermediate f/r ratios is decreased relative to that of the most rock-buffered system (f/r = 10) (Figure S8). Under these conditions, the predicted mineral assemblage is dominated by tremolite, garnet, epidote, and paragonite.

The same general sequence of minerals is predicted with decreasing f/r ratio at higher pressures (1.5–2.5 GPa) with some notable differences. With increasing pressure, tremolite becomes unstable whereas epidote, paragonite, lawsonite, and talc become stable. These reaction-path model predictions are consistent with our petrographic observation of epidote + paragonite found as inclusions within garnet. Importantly, while we did not find lawsonite, paragonite and epidote could be retrograde replacement products after lawsonite. Taken together, the reaction path models are consistent with metasomatism that could have occurred over a range of *P-T* conditions from 450 to 550 °C and from 1.0 to 2.5 GPa.

The model results for the reaction of serpentinite-equilibrated fluid with eclogite are presented in the supplement (Figure S9). Before reaction with eclogite, the composition of the fluid in equilibrium with serpentinite is predicted to be dominated by dissolved Mg in all models, with subordinate dissolved Si, Ca, Al, and Fe. With decreasing f/r ratios at 2.0 GPa and 450 °C during reaction, the predicted sequence of minerals formed is antigorite + clinopyroxene → serpentine + clinopyroxene + chlorite → chlorite + clinopyroxene ± talc ± orthopyroxene ± quartz. At higher temperatures and similar pressure, garnet is predicted instead of talc. Magnetite is present in all model results. Note that the predicted minerals talc and orthopyroxene are not observed in Zones II to V.

4 Discussion

4.1 Constraints on the origins of serpentinite

Variably serpentinized ultramafic rocks are widespread along slow- and ultraslow-spreading mid-ocean ridges, passive margins, and subduction zones (Deschamps et al., 2013; Kodolányi et al., 2012). To assess whether the Voltri serpentinites originally formed in an oceanic setting or in a subduction zone, we compare the measured trace element compositions and the $^{87}Sr/^{86}Sr$ isotope ratios with those of serpentinites

from different tectonic settings, along with representative compositions of seafloor hydrothermal fluids and seawater. The generally smooth and flat chondrite-normalized REE patterns of the Voltri serpentinites are similar to those of mantle rocks that experienced limited degrees of melting (Figure 12a). The elevated LREE/HREE ratios (*e.g.,* La/Yb = 0.52–1.02) relative to the depleted MORB mantle (DMM = 0.53; Workman and Hart, 2005) are comparable to refertilized mantle impregnated by MORB melts in oceanic or in extensional settings (Deschamps et al., 2013; Kodolányi et al., 2012; Paulick et al., 2006; Rampone and Hofmann, 2012; Scambelluri et al., 2019). However, aqueous alteration of ultramafic rocks can impart significant changes in REE compositions (Klein et al., 2017; Paulick et al., 2006). Ocean-floor peridotites from passive margins and mid-ocean ridge settings are typically extensively to completely altered by seawater-derived hydrothermal fluids. While seawater shows fairly low REE abundances and a characteristic depletion in Ce relative to La (Elderfield and Greaves, 1982) (Figure 12a), high-temperature hydrothermal fluids are enriched in Eu and can impart a positive Eu anomaly on serpentinized peridotites (Douville et al., 2002; Paulick et al., 2006). The Voltri serpentinites lack strong positive Eu and negative Ce anomalies that would otherwise suggest reaction and equilibration with either black-smoker-type hydrothermal fluids or seawater, respectively (Cooperdock et al., 2018; Deschamps et al., 2013; Spandler et al., 2008), which also coincides with the low fluid-mobile element contents in the studied serpentinites. It is possible that such anomalies were obliterated or modified by subsequent metasomatism during subduction and exhumation; however, the absence of negative Ce anomalies and the presence of slightly negative Eu anomalies observed in most Voltri serpentinites calls for an open-system interaction of mantle rocks with relatively reducing aqueous fluids (German and Elderfield, 1990; Tostevin et al., 2016; Vitale Brovarone et al., 2020).

The radiogenic $^{87}Sr/^{86}Sr$ composition of the Voltri serpentinite (0.7083) cannot be explained by serpentinization of peridotite by less radiogenic Jurassic seawater ($^{87}Sr/^{86}Sr$ = 0.707) (Jones et al., 1994) (Figure 6d). Rather, it requires subsequent modification by another fluid that carried more radiogenic, crustal-derived Sr before or during subduction. Cannaò et al. (2016) examined the geochemistry of subducted, undeformed (static) and mylonitic serpentinites in the Voltri Massif. The more radiogenic Sr-isotope characteristics of mylonitic serpentinite were attributed to interaction with fluids derived from a sedimentary or crustal reservoir during the early stages of burial along the subduction interface. The chondrite-normalized REE compositions of our studied serpentinite resemble the mylonitic serpentinite but are distinct from the undeformed serpentinite domains in terms of LREE (Cannaò et al., 2016). Even though un-subducted oceanic serpentinites in the neighboring Northern Apennine Ophiolite (Italy) were reported to show similarly radiogenic Sr-isotope ratios ($^{87}Sr/^{86}Sr$ = 0.70337 to 0.7086; Schwarzenbach et al., 2021), we favor the interpretation where the Sr isotope composition of our studied serpentinite was obtained during

subduction in lieu of the textural and geochemical similarities with the mylonitic serpentinite studied by Cannaò et al. (2016).

The magnetic susceptibilities of Voltri serpentinite is fairly low, and comparable to serpentinite formed at low temperatures (< 200 °C) at the Iberian Margin (Klein et al., 2017, 2014). However, the bulk-rock Fe(III)/Fe_T values of the Voltri serpentinite (Fe(III)/Fe_T ~0.3; Figure 5d) are significantly lower than in completely serpentinized oceanic peridotites (Fe(III)/Fe_T > 0.84; Klein et al., 2014, 2009). Similar trends in Alpine serpentinites have been attributed to the reduction of ferric to ferrous iron during prograde metamorphism of lizardite and chrysotile to antigorite and the destabilization of magnetite (Debret et al., 2016, 2014). In Alpine serpentinites, it has been suggested that ferric iron can be reduced to ferrous iron while magnetite is destabilized during prograde metamorphism (Debret et al., 2016, 2014); however, recent studies call this inference into question as Alpine serpentinites have experienced distinctly different metamorphic conditions and their protolith compositions remain incompletely understood (Evans and Frost, 2021). It remains unclear whether the serpentinite studied here originally contained magnetite that destabilized during metamorphism or if oceanic serpentinization did not produce significant magnetite to begin with. If the REE patterns were not significantly modified during subduction, the lack of an Eu anomaly associated with high-temperature ridge crest hydrothermal fluids (Douville et al., 2002) is consistent with serpentinization at moderate temperatures, which would point to limited magnetite formation during serpentinization. The lower MgO/SiO_2 of serpentinites relative to the terrestrial melting array of peridotites would be consistent with MgO loss from brucite breakdown during subduction or possibly during weathering prior to subduction (Klein et al., 2020; Peters et al., 2020). The low Fe(III)/Fe_T values would be consistent with reduction of Fe(III) to Fe(II) during metamorphism (Debret et al., 2016, 2014). If no magnetite was initially formed during serpentinization (and considering that the studied Voltri serpentinites do not contain brucite), this could have been accommodated by reduction of Fe(III) to Fe(II) in serpentine. Overall, the results presented in this study are consistent with partial serpentinization in an oceanic setting with subsequent modifications of its chemical and mineralogical characteristics during high-pressure metamorphism and deformation.

4.2 Constraints on the formation of distal eclogitic metagabbro

The REE patterns of the most distal LREE-depleted metagabbros provide clues on the origin of their mafic protolith. The metagabbro from Zone V displays the most depleted LREE concentrations among the mafic rocks studied here. Previous studies have suggested that oceanic (Fe, Ti-rich) oxide gabbros were likely the protolith of the metagabbro in the study area (Malatesta et al., 2012a; Tribuzio et al., 1996). The abundance of the Ti-rich phases rutile and ilmenite, as well as the elevated bulk-rock FeO* (= total Fe as

FeO) and TiO_2 contents closely resemble those of oxide gabbro from the International Ocean Drilling Program (IODP) Site U1309 (Atlantis Massif), but are distinctly different from other gabbroic lithologies from the same IODP site (Godard et al., 2009) (Figure 13a). The chondrite-normalized trace element concentrations of the LREE-depleted metagabbro are plotted along with oceanic oxide gabbros from IODP Site U1309 (Figure 12b). Oceanic oxide gabbros show a wide range in chondrite-normalized compositions and Eu anomalies. Samples with elevated REE abundances show more pronounced negative Eu anomalies. Conversely, samples that are depleted in REE, especially in LREE, show weak positive Eu anomalies, which resemble the LREE-depleted (Zone V) metagabbro in this study. Alternatively, LREE depletion has been suggested to also occur at the gabbro-to-eclogite transition during prograde subduction (Becker et al., 2000; John et al., 2004; Tribuzio et al., 1996). For example, Tribuzio et al. (1996) investigated LREE-depleted oxide gabbro-derived lithologies equilibrated at blueschist and eclogite-facies conditions in Voltri and attributed the LREE depletion to the absence or destruction of LREE-compatible epidote minerals during prograde metamorphism. These observations imply that LREE depletion can occur at different stages over a wide range of *P-T* conditions and in distinct tectonic settings, from oceanic environments to subduction zones. Without additional constraints it remains challenging to differentiate a possible inherited LREE-depletion prior to subduction from LREE-depletion during high-pressure metamorphism. However, considering the very short length-scales, we infer that the lower chondrite-normalized LREE concentrations of Zone V relative to adjacent zones suggest that LREE depletion may have occurred during prograde subduction and contributed to the LREE budget of the adjacent metasomatic reaction zones.

4.3 Controls on the compositions of the studied metasomatic reaction zones

The overall distribution of major and trace elements in zones (II-IV) between serpentinite and eclogitic metagabbro may result from the interplay of three processes: (1) mass transfer by mechanical mixing of rocks, (2) mass transfer by diffusion across a chemical gradient, and/or by advection of external fluids. We discuss the potential contributions of each process below.

4.3.1 Mechanical mixing

Mechanical mixing of two or more chemically distinct rocks will result in a new rock with a composition that lies on a mixing line in between the endmembers (Bebout and Barton, 2002; Gorman et al., 2019). However, the bulk compositions of the metasomatic rocks in Zones II-IV do not lie along the bulk mixing trend between the most distal samples of Zone I and V (Figure 13b). Accordingly, the amphibole- and chlorite-rich assemblage (Zone II) along the field contact was not a simple binary mixture

of components from serpentinite and distal metagabbro. This is supported by the lack of correlation between Ni and Cr, which would otherwise be expected if the metasomatic rocks were formed by mechanical mixing of two endmember compositions (Gorman et al., 2019; Penniston-Dorland et al., 2014). Rather, Ni and Cr show large variations with trends similar to that of bulk-rock MgO concentration, which resemble sigmoidal profiles that are suggestive of diffusive transport from serpentine to metagabbro (Figure 6b). In addition, we used the ratios of two fluid-immobile elements (Figure 13b) and the bulk-rock $^{87}Sr/^{86}Sr$ isotope ratio as they are highly sensitive to protolith chemistry but are largely insensitive to fluid metasomatism. The clear step-wise pattern in $^{87}Sr/^{86}Sr$ isotope ratios separating Zones II to V from Zone I at the lithologic boundary does not support a mechanical mixing process as a key contributor to the compositional variability observed in the transect (Figure 6d). Likewise, the Sc concentration shows a step-function similar to the trace element ratios and Sr isotopes, reflecting its limited fluid mobility (Figure 6b). Hence, in contrast to the Catalina Schist (USA), where mechanical mixing of ultramafic and mafic blocks has been documented (Gorman et al., 2019; Penniston-Dorland et al., 2014), we found no evidence for mechanical mixing along the serpentinite-metagabbro contact studied here. It is also possible that shearing and deformation may have transposed and even stripped off metasomatic reaction zones along lithologic margins (Ague, 2007). However, this possibility can be ruled out in our studied transect based on the lack of geochemical evidence for mechanical mixing, as well as the contact-perpendicular sampling strategy in both the serpentinite and metagabbro, which would have captured any transposed reaction zones along the contact.

4.3.2 Mass transfer via advective and/or diffusive transport

The juxtaposition of different and chemically disparate rock-types favors fluid-mediated diffusive mass transfer (Bickle and McKenzie, 1987; Ferry and Dipple, 1991; Korzhinskii, 1965; Thompson, 1975). In a setting that is similar to the one examined here, Pogge von Strandmann et al. (2015) investigated metasomatism in an asymmetrical reaction zone between serpentinite and metatuffite in Syros (Greece) and observed strong Mg-isotope fractionations in the metatuffite proximal to the contact in a chlorite-rich zone. They showed that fluid-mediated diffusive transport across the transect involved multiple components, where the diffusive fluxes of components were driven by distinct chemical potentials. The extent of mass transfer was primarily controlled by the activities, solubility, and relative mobilities of the components across the contact. At Voltri, chemical and mineralogical changes along the transect can provide additional constraints on the mode of mass transfer between serpentinite and metagabbro. For instance, the sigmoidal patterns in bulk-rock MgO, H_2O, and Ni already suggest diffusive transport across the serpentinite-metagabbro transect.

In a purely diffusive regime without advective fluid flow, we would expect mineralogical reaction zones on both sides of the serpentinite-metagabbro contact via bi-directional metasomatism (Bach et al., 2013; Bach and Klein, 2009; Korzhinskii, 1968, 1965; Miller et al., 2009; Pogge von Strandmann et al., 2015; Thompson, 1975), which would result in Si-metasomatism of serpentinite and Mg-metasomatism of metagabbro. Yet, talc-alteration of serpentinite by Si-rich fluids is limited and there is no systematic increase in the modal proportion of talc in serpentinite towards the contact that would be expected in the absence of unidirectional advective fluid flow. The limited amount of talc in the studied serpentinite is similar to that of unsubducted serpentinite in the neighboring Northern Apennine Ophiolite (Italy), which suggest that the amount of talc in Voltri serpentinite was likely set in an oceanic setting, i.e. prior to subduction (Schwarzenbach et al., 2021). Accordingly, the asymmetry of the reaction zones could have resulted from unidirectional advective fluid flow that transported Mg from the serpentinite into the gabbro. To explain the asymmetry of the Syros transect, Pogge von Strandmann et al. (2015) suggested that the lack of talc-alteration on the serpentinite side can be attributed to congruent dissolution of serpentinite and Si export by contact-parallel fluid flow. However, advective mass transport was ruled out because the velocity of advection would have outpaced the mass transfer via diffusion (or the rate at which equilibrium partitioning can be attained) and would have destroyed the prominent negative δ^{26}Mg isotope fractionation that can only be achieved via diffusion.

Alternatively, the lack of talc alteration in serpentinite from Voltri and Syros may reflect the lack of chemical affinity for such a reaction to proceed at subduction zone *P-T* conditions. Even though talc would be thermodynamically stable at such *P-T* conditions, the formation of talc at the expense of serpentine (i.e. antigorite + $30SiO_{2(aq)}$ = 16talc + $15H_2O_{(l)}$) may not be favored. To test this, we evaluated the $a SiO_{2(aq)}$ in a fluid buffered by metagabbro and also modeled the reaction of such a fluid with serpentinite over a range of *P-T* conditions. Our thermodynamic calculations predict that the $a SiO_{2(aq)}$ of the fluid buffered by gabbro exceeds the $a SiO_{2(aq)}$ of the serpentine-talc equilibrium, despite the pressure-dependent increase in $a SiO_{2(aq)}$ buffered by the serpentine-talc equilibrium (Figure 14e,f). Accordingly, simple univariant phase equilibria would suggest that conditions were favorable to form talc at the expense of serpentine. However, the chemical affinity depends on the Gibbs free energy of the reaction at the temperature and pressure, which is affected by the equilibrium speciation of dissolved species. The reaction-path models at 400–500 °C predicted a talc-free alteration assemblage that is dominated by garnet + chlorite + serpentine (Figure 14a-d). The elevated activities of Al and Ca in the fluid may have inhibited the saturation of talc by promoting the formation of garnet and chlorite. In particular, the solubility of Al in aqueous fluids has been shown to increase significantly at high *P-T* conditions due to the formation of aluminosilicate complexes (Manning, 2007). This favors the saturation of Al-bearing phases, which likely explains the occurrence and abundance of chlorite-rich assemblages in reaction zones found in Volti and

possibly in other settings, where similar exhumed high-pressure rocks are found. Our findings are consistent with previous studies on talc schist in Santa Catalina Island (USA) which suggest that the Si/Al ratio of rocks and fluids plays a key role in stabilizing chlorite over talc (Bebout and Barton, 2002). However, the formation of talc in subduction zones can be facilitated where excess Si is available, such as in mélanges of Si-rich sediments and serpentinite, possibly at higher temperatures (Breeding et al., 2004; Miller et al., 2009). Another process that can yield sizeable talc deposits in both subduction zones and orogenic belts is mineral carbonation of serpentinite, facilitated by decarbonation of metamorphosed carbonate-rich sediments (Spandler et al., 2008).

Importantly, our thermodynamic calculations suggest that an external fluid is not required to explain the absence of talc and the observed asymmetry of reaction zones between serpentinite and metagabbro simply because the formation of talc is not favored. This would also imply that the asymmetrical reaction zones may not be taken as evidence against bidirectional diffusive transfer as changes may manifest differently on either side of a lithologic contact depending on thermodynamic controls. These findings are further supported by the sigmoidal concentration profiles of Mg, Ni, and H_2O that point to diffusive transfer from serpentinite to metagabbro (Figures 3a,f and 5b). The diffusive influx of Mg, Ni, and H_2O from serpentinite into the metagabbro led to the formation of hydrous minerals in Zones II and III and roughly similar bulk-rock MgO concentrations in these two zones. If the mass transfer between serpentinite and metagabbro is driven by the differences in the activity of Mg species, the minerals that are forming under this activity gradient are expected to record systematic variations in their mineral compositions (Korzhinskii, 1968; Miller et al., 2009; Pogge von Strandmann et al., 2015; Thompson, 1970). Evidence for that is provided by the increasing Mg contents of chlorite and amphibole towards the contact (Figure 3b,c).

Mass-balance constraints suggest that the formation of chlorite-rich schist at the expense of metagabbro in Zone III, not only requires the addition of Mg (~84 kg/m^2) and H_2O (~40 kg/m^2) but the removal of Ca (~10 kg/m^2) as well (Figure 13c; Figure S10). Note that the low concentrations of CaO in Zone III (Figure 5b) cannot be explained with simple dilution due to the addition of Mg. Indeed, mass balance calculations suggest that Ca was likely redistributed into the adjacent Zones II and IV, which led to the stabilization of Ca-amphibole and epidote. Zone IV experienced a significant enrichment in Ca (~104 kg/m^2) whereas Zone II displays a more muted Ca enrichment. Zone II and III likely experienced significant Ca losses during the formation of chlorite schist but later Ca redistribution into Zone II balanced out the initial Ca loss. We note that the bulk-rock CaO concentration correlates positively with the bulk-rock REE and fluid-mobile element patterns. Therefore, the bulk-rock distribution of these trace-elements may be intimately linked to the distribution of Ca. In particular, the dominant transport of Ca into the more interior

parts of the metagabbro explains the bulk-rock REE and fluid-mobile element concentration profiles (Figures 4b and 12e).

The maximum enrichment of LREE and fluid-mobile elements occurs within Zone IV, which also shows the highest CaO concentration, whereas the maximum enrichment of HREE is in Zone III (Figures 5a,c). The concentration profiles of Eu and Gd (MREE), which are geochemically intermediate between LREE and HREE, show peak enrichments coinciding with LREE and HREE enrichments. This trend is interpreted to indicate diffusion of trace elements within the metagabbro from Zones II-III into the more interior Zone IV. We infer that the observed lag in the position of peak enrichments between LREE and HREE reflects the difference in their bulk diffusivities, with LREE diffusing faster than HREE (with MREE having an intermediate bulk diffusivity). Assessment on bulk diffusion in natural polymineralic rocks requires constraints on the diffusivities of each constituent mineral, grain sizes, variations in interconnectivity of fast pathways (*e.g.*, pore fluids), and differences in the concentration of the diffusing element (diffusant) within each mineral phase or fluid (Watson and Baxter, 2007). All of these factors are difficult to constrain. Considering that the dominant mass transfer mechanism in our studied transect is diffusion mediated by interconnected pore fluids, transport through interconnected porosity becomes efficient if a significant amount of the REE is dissolved in the pore fluid. This in turn is a function of REE solubility in aqueous fluids. Fluid-rock partitioning studies display higher concentrations in LREE than HREE in aqueous fluids over a range of high *P-T* conditions (Kessel et al., 2005). The generally higher solubility of LREE relative to HREE would amount to their higher bulk diffusivity, if other factors mentioned above are set constant. Our interpretation of higher LREE diffusivities in pore fluids is further supported by the coinciding positions of LREE and fluid-mobile element peak enrichment. We infer that these trace elements are mainly hosted by epidote in Zone IV that is formed due to Ca addition (Figure 13e). While we did not measure the trace element composition of epidote in situ, previous studies have shown that LREE are compatible in epidote-bearing rocks from subduction zones (Ague, 2017; Carter et al., 2015). The strong correlations between bulk-rock CaO and LREE as well as the similarity in the position of peak enrichment (Fig. 5a, yellow bar) suggest that their mobilization and redistribution occurred simultaneously. In particular, the transport of Ca into Zone IV led to the formation of epidote minerals which have high affinity for LREE. The decreasing concentrations in CaO and LREE from Zones IV to V are also consistent with diffusion of these elements from Zone III into the metagabbro. The co-diffusion of Ca and LREE leads to the formation of Ca-rich minerals (*e.g.*, epidote) nearby that then become important hosts for these trace elements, preventing their further mobilization. The lack of a mineral host for the REE in Zones II and III is consistent with the lack of an REE enrichment in these zones. The diffusion of components towards the metagabbro may have contributed to the asymmetrical geometry of the reaction zone between the serpentinite and metagabbro, with enhanced alteration on the metagabbro side. On the

other hand, trace element changes in the serpentinite are less pronounced. This is exemplified by the enrichment in $(La/Sm)_N$ in the serpentinite that is most proximal to the contact (Figure S7).

4.4 Metamorphic and mass transfer history

In this section we further constrain the relative timing of metasomatism by integrating the *P-T* estimates derived from pseudosection and garnet isopleth models with Sr-isotope systematics and reaction path modeling. Consistent with Cannaò et al. (2016), serpentinization of peridotite in the Voltri Massif occurred at least partly in an oceanic setting whereas the Sr-isotope composition of serpentinite was likely set during the early stages of subduction. Field evidence suggests that the serpentinite and oxide gabbro were likely in contact while in an oceanic setting prior to subduction (Manatschal and Müntener, 2009; Piccardo, 2013; Scambelluri et al., 1995a). This is supported by field exposures of juxtaposed serpentinite and gabbroic bodies similar to our studied transect that are found in neighboring localities, such as the Northern Apennines that had never been subducted (Lagabrielle and Lemoine, 1997). However, our petrographic and geochemical evidence suggest that the mass transfer process that formed the metasomatic reaction zones likely occurred in a subduction zone setting.

Pseudosection and garnet isopleth modeling allows us to determine whether mass transfer between serpentinite and metagabbro occurred during prograde, peak, or retrograde metamorphism. Results from pseudosection models yielded *P-T* estimates for the onset of eclogitization (~430–470°C, 2.2–2.5 GPa) up to peak eclogite-facies metamorphism (~520°C, ~2.5 GPa) for Zones IV and V (Figure 9f). While the bulk composition during the earliest stages of garnet growth in sample B03 was possibly different from measured, our calculations likely represent a close approximation. However, it remains unclear whether the mineralogical and chemical differences between Zones IV and V developed during prograde-to-peak evolution or slightly post-peak (i.e. during near-isothermal decompression). The most prominent chemical and mineralogical changes can be attributed to the addition of Mg to the metagabbro that caused the formation of chlorite and the redistribution of Ca. Here we determine the timing of chlorite formation in Zones II and III and the enrichment of Ca in metagabbro of Zone IV relative to that in Zone V. We rely on garnet core-to-rim element variations in these zones to resolve the relative timing of Ca enrichment (Figures 3a and 4). Garnet cores in Zone IV and V have similar Ca contents, which suggests that bulk-rock Ca composition are similar at the initiation of garnet growth along the prograde path. The Ca contents of garnet in Zone IV (B06 and B07) increases systematically from core to rim, which is the opposite trend for garnet in Zone V. In addition, anhedral garnet in Zone III has higher Ca contents than garnet in Zones V but overlaps with garnet from Zone IV. These results imply that Ca becomes more available during the growth of garnet in Zones III and IV. Since garnet from the more distal sample B07 in Zone IV displays less pronounced core-to-rim Ca enrichment than in sample B06, this suggests that Ca availability diminishes

towards the metagabbro interior. We suggest that the bulk Ca-enrichment in Zone IV occurred or at least started during prograde eclogite-facies conditions. While garnet from exhumed (ultra) high-P metamorphic rocks in subduction zones have substantial Ca contents (8–9 wt. % CaO) *e.g.*, in Sifnos, Greece and Lago di Cignana, Italy (Dragovic et al., 2012; Groppo et al., 2009), these CaO concentrations are below those measured in garnet rims in Zone IV (up to ~12 wt. % CaO). If the Ca-enrichment in Zone IV would have occurred prior to subduction or even prior to the onset of garnet growth, subsequent eclogite-facies metamorphism would have formed garnets that would be significantly more grossular-rich (i.e. almandine-poorer) than the garnet analyzed in our samples (Figure 9c). Therefore, pre-subduction and pre-peak Ca-enrichment in Zone IV seem unlikely, which provides additional support for Ca enrichment occurring during prograde subduction up to peak depths.

The simultaneous addition of Mg and H_2O, and removal of Ca from the precursor metagabbro are necessary to form chlorite-rich schists in Zone III (Figures 12c,d). We have shown that Ca along with trace elements released from this process are redistributed into adjacent Zones II and IV. Therefore, the chlorite-rich schists in Zone III must have formed before or at the same time as Zones II and IV during prograde subduction. Fluid-rock interactions likely continued during peak and post-peak eclogite-facies metamorphism based on petrographic evidence of garnet replacement by chlorite (Figure 15). Evidence for subsequent retrograde overprinting and local re-equilibration during a near-isothermal decompression to ~1.0 GPa includes the presence of albite in Zone IV and V, titanite rims around rutile and ilmenite in Zones II-V, as well as calcic rims on sodic-calcic amphiboles (Malatesta et al., 2012b; Starr et al., 2020; this study).

Additional support is provided by the reaction-path models. One of our simplest reaction-path models, which explores the possibility that a single fluid-mediated mass transfer event occurred during prograde to peak eclogite-facies metamorphism predicts a succession of mineral assemblages that closely matches the ones observed in the transect. This implies that a single fluid-mediated mass transfer event may have occurred and set the bulk compositions of the metasomatic zones during prograde to peak eclogite-facies metamorphism. However, the duration of this event remains undetermined. We have shown that only reaction-path models that used a gabbroic mineral assemblage successfully predict a succession of mineral assemblages that closely matches the one observed in our studied transect whereas those with eclogitic mineral assemblage do not. This is consistent with pseudosection models that suggest the completion of that mass transfer prior to retrogression. The difference in the pressures estimated by pseudosection and garnet isopleth models (~2.2 GPa for garnet nucleation) and reaction-path models that successfully reproduced the mineral sequence may reflect either a reaction overstepping where garnet nucleation occurred at *P-T* conditions greater than initial garnet stability or inaccuracies in the effective bulk composition used for the pseudosection modeling. We speculate that garnet nucleation may have been

limited by the availability of fluid that promotes faster nucleation and growth. Additionally, we suspect that the effective bulk composition is changing as garnet grows. This could explain the discrepancy in the estimated garnet modal abundances (i.e. 2 and 5 vol. % for samples B10 and B06, respectively) at *P-T* conditions constrained by garnet crystal core chemistry.

Finally, while our reaction path models successfully reproduce the observed mineral sequence at pressures as low as 1 GPa, this is a minimum estimate, and indeed, mass transfer may have initiated at greater depths. Nonetheless, both models suggest that mass transferred occurred or at least initiated during prograde subduction. This is followed by a near-isothermal decompression with limited mass transfer, where metasomatic zones primarily underwent local re-equilibration and recrystallization (Figure 15).

4.5 Mg-metasomatism is favored in subduction zones

The strong positive correlations between bulk-rock concentrations of MgO and Ni, and bulk-rock MgO and LOI in all the samples, as well as the continuously decreasing concentration profiles of these elements (Figures 12d), suggest that the fluids equilibrated with serpentinite prior to metasomatism of metagabbro (Miller et al., 2009; Pogge von Strandmann et al., 2015). Phase equilibrium and thermodynamic studies have suggested that subducting oceanic crust can produce a continuous flux, and sometimes, episodic pulses of aqueous fluids through a series of mineral dehydration reactions up to eclogite-facies metamorphic conditions (Hacker, 2008; Schmidt and Poli, 2014, 1998; van Keken et al., 2011). This assures the availability of aqueous fluids at least along the slab-mantle interface. Of particular importance is the breakdown reaction of antigorite and brucite to form olivine and water, as this reaction is well-documented in the Vara serpentinite locality, which is in close proximity to our studied serpentinite (Cannaò et al., 2016; Scambelluri and Rampone, 1999), as well as in the neighboring Erro-Tobbio locality (Scambelluri et al., 1995b, 1991).

Recognizing possible regional sources of fluids in our study area, our thermodynamic calculations suggest that $Mg(OH)_{2(aq)}$ could have been a dominant species in the fluid that equilibrated at high concentrations with serpentinite at high *P-T* in a subduction zone. This suggests that the propensity for Mg-metasomatism by fluids that equilibrated with serpentinite is enhanced in subduction zone settings when compared with oceanic settings where the concentrations of dissolved Mg in hydrothermal fluids are low (cf. Bach et al., 2013). However, the differences in the predicted speciation and activities between low and high (1.0–2.5 GPa) pressure conditions may also in part reflect the limited availability of thermodynamic data for dissolved species at such high-pressure. The few available experimental studies and reports of fluid inclusions from high-pressure rocks in the Western Alps strongly suggest elevated dissolved Mg and elevated salinity in aqueous fluids (Iacovino et al., 2020; Scambelluri et al., 1997), lending credence to the thermodynamic predictions presented here. If these predictions are correct, the abundance of serpentinite

in subducted oceanic lithosphere, the overlying mantle wedge, and the slab-mantle interface would represent possible sites of where fluids can obtain high concentrations of dissolved Mg regardless of sources and compositions of the infiltrating fluid. In this scenario, the composition of a fluid that originates elsewhere (*e.g.*, breakdown of hydrous minerals from subducted, hydrothermally-altered igneous rocks and sediments) is modified as it infiltrates the serpentinite already present along the subduction interface. The resulting composition of the pore fluid buffered by serpentinite likely resembles the characteristic fluid composition (i.e. Mg-rich and Al, Fe, Ca-poor) even though the starting fluid had a different composition before it infiltrated and equilibrated with serpentinite. As these fluids infiltrate through and re-equilibrate with serpentinites, the intrinsic porosity of serpentinites (Tutolo et al., 2016) can store large amounts of pore fluids that may promote fluid-mediated diffusion and Mg-boundary metasomatism in juxtaposed crustal rocks.

4.6 The need for solid solutions in reaction path models to infer redox conditions in subduction zones

The present study may also provide clues about prevailing redox conditions during Mg-metasomatism of gabbros. The $Fe(III)/Fe_T$ of altered metagabbro in Zones II to IV is generally elevated when compared with metagabbro in Zone V. This could either reflect the pre-existing heterogeneity of the oxide gabbro precursor, or a result of oxidation during metasomatism (Figure S8). We attempted to use the reaction path models to constrain fO_2 as the fluid that previously equilibrated with serpentinite reacts with gabbro. Even though the models successfully reproduced the observed succession of mineral assemblages, they failed to reproduce the complexity of the natural system. One shortcoming of the models is attributed to the lack of solid solutions of Mg-Fe minerals in the thermodynamic database, most notably greenalite or cronstedtite in serpentine, the $Fe(OH)_2$ component of brucite, and the andradite component of garnet. Because the $Fe(III)/Fe_T$ of the modeled serpentinite was dictated by magnetite as the only Fe-bearing phase, the modeled fO_2 of the fluid in equilibrium with the serpentinite likely differed from that of the natural system. The lack of Fe(III)-components in the minerals predicted to form during metasomatism of gabbro introduce errors in the calculation of fO_2.

4.7 Geochemical and petrophysical implications of fluid-rock interactions in subduction zones

Fluid-mediated mass transfer between juxtaposed chemically disparate rock types can lead to the formation of a variety of metasomatic rocks with geochemical and petrophysical properties that are distinct from their precursors (Ague and Nicolescu, 2014; Angiboust et al., 2014, 2011; Bloch and Hofmann, 1978; Breeding et al., 2004; King et al., 2006; Miller et al., 2009; Mori et al., 2014; Penniston-Dorland et al., 2014; Pogge von Strandmann et al., 2015; Sanford, 1982). We have shown that serpentinite in subduction zones could produce fluids that are poor in Al, Fe, and Ca (< 0.001 molal at 1.0–2.5 GPa) but may contain substantial amounts of dissolved Mg (*e.g.,* 1.0–2.4 molal at 1.0 GPa; 0.6–1.1 molal at 2.5 GPa) through fluid-rock equilibration. This process is different from in-situ and active serpentinization of the shallow forearc mantle, which produces Mg-poor, Ca-rich fluids (*e.g.,* Mottl et al., 2004). These serpentinite-buffered fluids lead to Mg-metasomatism of mafic rocks and favor the ubiquitous formation of chlorite. Mg-chlorite is a rheologically weak metasomatic mineral that can contain up to ~13 wt. % water and be stable up to 800 °C at subarc depths (Okamoto et al., 2019; Pawley, 2003).

Thermodynamic predictions suggest that the distinct chemical potentials of dissolved species in equilibrium with serpentinite and gabbroic mineral assemblages can drive diffusive mass transfer. The asymmetrical geometry of the metasomatic reaction zone in gabbro and the lack of talc alteration of serpentinite in the studied transect underlines the lack of sufficient thermodynamic drive to form talc at the expense of serpentine at high *P-T* conditions in subduction zones (Figure 14). This is in contrast to the ubiquitous occurrence of talc-altered serpentinites that are juxtaposed to gabbro in oceanic settings (Bach et al., 2013, 2004; Paulick et al., 2006). A lack of extensively talc-altered serpentinite in subduction zones (Deschamps et al., 2013; Peters et al., 2017a) would likely affect the strength of the plate interface and the physical mechanisms controlling the coupling-decoupling depth in subduction zones. Owing to its high-pressure stability and rheological properties, the breakdown of talc has been suggested to reflect the downdip transition from a decoupled shear zone to a fully coupled plate interface (Peacock and Wang, 2021). Our thermodynamic calculations suggest that the formation of talc at the expense of serpentine by Si-metasomatism (via the reaction: antigorite + $30SiO_{2(aq)}$ = 16talc + $15H_2O_{(l)}$) may be more limited during subduction when compared with low pressure Si-metasomatism such as in oceanic settings where lower $SiO_{2(aq)}$ activities suffice to drive talc alteration. In subduction zones, talc-alteration of serpentinite is likely limited to settings where serpentinite and silica- or carbonate-rich sediments are juxtaposed, whereas juxtaposition of gabbro (mafic crustal) and serpentinite would favor chlorite over talc. If the coupling-decoupling transition between the subducting plate and overriding mantle is related to the presence of talc,

the juxtaposition of ultramafic rocks with sediment may be crucial (Abers et al., 2020; Marschall and Schumacher, 2012; Wada and Wang, 2009).

In this study, we show that the formation of different metasomatic rocks is associated with fractionation of certain trace-element ratios that otherwise would behave similarly during mantle melting processes. The N-MORB-normalized trace-element ratios of the metasomatic rocks are plotted in Figure 16a. We note that some ratios in the precursor rocks differ from N-MORB, likely reflecting the protolith (pre-subduction) compositions. Moreover, the metasomatic rocks are elevated in Cs/Rb, Cs/Yb, U/Nb, Th/Nb, Sr/Y, La/Sm, and Lu/Hf relative to the precursor. The opposite trend is observed in Hf/Nd, Pb/Ce, Zr/Sm, Sm/Nd, Sr/Nd, and Rb/Sr, where the metasomatic rocks record lower values compared to the precursor. Lastly, the ratios U/Th, Zr/Hf, Dy/Yb, Nb/Ta, Ba/Rb, and U/Pb of the metasomatic rocks are similar to both the precursor and to N-MORB. The Ba/Th ratio is similarly low in metasomatic and precursor rocks, relative to N-MORB. These imply that diffusive metasomatism can induce bulk-rock trace-element fractionations that are typically attributed to both melting and dehydration processes in subduction zones.

One notable observation is the lower Zr/Sm, Hf/Nd, and Th/Nb ratios in chlorite-amphibole schists (Zone II) and chlorite schists (Zone III) relative to the Zones IV and V metagabbro. This marked decrease in these ratios involves the localized mobilization of commonly assumed 'fluid-immobile' elements Zr, Hf, and Nb into the adjacent zones (Brenan et al., 1994; Kessel et al., 2005; Stalder et al., 1998). This localized mobilization is due to the destabilization of rutile (hosting Nb) and zircon (hosting Zr and Hf) in these metasomatic rocks. The destabilization of zircon is consistent with previous observation in the Franciscan Complex (USA) where zircon was inferred to be less stable in ultramafic compositions (King et al., 2003). The destabilization of rutile is supported by our thermodynamic models that predict rutile stability over a wide range of *P*-*T* conditions for bulk compositions similar to an oceanic oxide gabbro. We emphasize that the breakdown of these phases, notably rutile and zircon, in these metasomatic rocks resulted from the changes in bulk compositions and not from changes in pressure and temperature conditions. These fractionations are further enhanced by the diffusion and redistribution of REE from Zones II and III into Zone IV.

Another important observation is the lower Pb/Ce and Sr/Nd ratios in metasomatic rocks, particularly in chlorite-rich schists (Zone III) (Figure 16a). The depletions in Pb and Sr in chlorite schists are likely due to the crystal-chemical control of chlorite, lacking crystallographic sites for Ca^{2+}, which is typically substituted for by Sr^{2+} and Pb^{2+} (Spandler et al., 2014). Whereas Sr and Pb from Zones II and III may have back-diffused into Zone IV, this process did not significantly fractionate the bulk-rock Sr/Nd and Pb/Ce ratios of Zone IV relative to the most distal metagabbro. Thus, the formation of chlorite schists in between serpentinites and crustal rocks may preferentially liberate certain trace elements, such as Sr and

Pb. As noted earlier, the co-diffusion of Ca, LREE, Sr and Pb led to the formation of Ca-rich minerals (*e.g.*, epidote) nearby that then became important hosts for these trace elements and prevented their further mobilization. The fractionations in parent-daughter elements Rb/Sr, Sm/Nd and Lu/Hf are important as their Sr, Nd, and Hf isotope compositions will change over time due to radiogenic ingrowth. These isotopically distinct reservoirs can reside in the mantle and may even be sampled and recorded in the erupted mantle-derived magmas. Accordingly, the decrease in Sm/Nd and Rb/Sr ratios, and the increase in Lu/Hf ratio in metasomatic rocks relative to their precursor may lead to their time-integrated evolution to less radiogenic Nd and Sr isotopes, and more radiogenic Hf isotope compositions in the mantle.

In contrast, the lack of substantial modal, chemical, and Sr isotope changes in serpentinite domains suggest a pinned geochemical boundary condition in which the fluids buffered by serpentinite represent a large reservoir that is minimally affected by mass transfer from the juxtaposed metagabbro block. This scenario is possible if there is enough advective flow in the serpentinite matrix to keep fluid compositions relatively constant within the serpentinite domain. Another possibility is if diffusion through the serpentinite occurs relatively fast, which would transport solutes over larger length scales in the serpentinite than the length scales we observed for the metacrustal block (Ague, 2007; Ague and Rye, 1999). The spatially limited enrichment in $(La/Sm)_N$ in the most proximal serpentinite argues against fast diffusion rates of solutes through serpentinite for these elements. It is more likely that overall constancy in serpentinite composition in this study reflects a limited interconnected pore fluid in serpentinite that, in turn, limited diffusive transport across large length scales. The lack of significant enrichment in fluid-mobile elements in serpentinite argues against pervasive advective fluid flow within the serpentinite domain.

Physical mixing of different subducted materials and mantle rocks along the slab-mantle interface has been proposed as a key process in the formation of arc magmas (King et al., 2006; Marschall and Schumacher, 2012; Nielsen and Marschall, 2017). Geodynamic models have predicted the transport of intimately mixed materials (i.e. mélange) by buoyant diapirs into the mantle wedge, feeding the source of arc magmas (Gerya and Yuen, 2003; Zhu et al., 2009). The metasomatic reaction zone studied here records a decrease in bulk density associated with the transformation of a dry and dense metacrustal rock into a hydrous and less dense metasomatic rock. These results can be used to infer what could happen to subducted crustal rocks along the slab-mantle interface during subduction because the *P-T* conditions recorded by these rocks are relevant to cold and intermediate slab-top geotherms (Syracuse et al., 2010). The decrease in bulk densities during mass transfer would allow for dense subducted rocks to become positively buoyant relative to the overlying peridotite wedge (Figure 16b,c). The metasomatic reaction zone studied here records a decrease in bulk density associated with the transformation of a dry and dense metacrustal rock into a hydrous and less dense metasomatic rock, albeit over limited spatial scales. If this process were more

extensive, the decrease in bulk densities during mass transfer would allow for dense subducted rocks to become positively buoyant relative to the overlying peridotite wedge (Figure 16b,c). For instance, ~50% of a crustal precursor has to be converted into chlorite schists to make the entire block positively buoyant relative to the overlying mantle with a density of 3300 kg/m^3. Chlorite schist occupies a small volume in the studied transect, similar to other settings where serpentinite and metacrustal rock are juxtaposed (Angiboust et al., 2014; Bebout and Barton, 2002; Breeding et al., 2004; Gyomlai et al., 2021; Miller et al., 2009; Penniston-Dorland et al., 2014; Spandler et al., 2008). This may be due to an arrested reaction, *e.g.*, as the reactant fluid was completely consumed, or by cooling during exhumation (Pogge von Strandmann et al., 2015; Starr et al., 2020). The mechanical weakening of the reacted metacrustal rocks could localize both strain and fluid flow, further enhancing metasomatic reactions (Ague, 2007; Angiboust et al., 2011). If Mg-metasomatism of gabbro is more extensive than in the outcrop that we studied, buoyant metasomatic rocks could result in their detachment and rise as mélange diapirs from the slab-top to the overlying mantle, effectively delivering the compositional signatures of these rocks to the source of arc magmas (Codillo et al., 2018; Cruz-Uribe et al., 2018; Marschall and Schumacher, 2012). Fluids that are released during the high-temperature breakdown of Mg-chlorite (> 800 °C) can promote the partial melting of adjacent mafic crustal rocks within the mélange. Melting of rising mélange diapirs would further enhance the fractionated trace-element characteristics of the resulting partial melts (Cruz-Uribe et al., 2018).

5 Conclusions

Within the context of a serpentinite-metagabbro contact from the Voltri Massif (Italy), we evaluated the fluid-mediated mass transfer processes between mafic and ultramafic rocks in subducted oceanic lithosphere. In oceanic settings, diffusional metasomatism is particularly important at mid-ocean ridge settings of slow-spreading oceanic lithosphere where large chemical potential gradients of chemical species exist in juxtaposed mafic and ultramafic rocks resulting in significant mass transfer such as rodingitization, blackwall alteration, and steatitization. Metasomatic processes between mafic and ultramafic rocks can also occur in subduction zones; however, as this study documents, the elevated pressure and temperature conditions in subduction zones can modulate the speciation of fluids and saturation state of key minerals such as chlorite and talc. One of the main metasomatic processes documented in this study was mass transfer of Mg from serpentinite into gabbro that started during prograde metamorphism and likely continued through peak and retrograde conditions. In contrast to oceanic settings, our thermodynamic models predict the predominance of aqueous Mg species in fluids that equilibrate with serpentinite under high-pressure subduction zone conditions. Consistent with the observed Mg-metasomatism, our reaction-path models predict that fluids in equilibrium with serpentinite at high-pressure

conditions are more strongly enriched in dissolved Mg compared to low-pressure conditions. Therefore, Mg-metasomatism of crustal rocks to form chlorite-rich assemblages is favored in subduction zones. In contrast, Si-metasomatism of serpentinites to form talc-rich rocks (steatitization) is commonly found in oceanic settings, but is predicted to be less prevalent in subduction zones. This illustrates a different picture on the nature and styles of boundary metasomatism at high *P-T* conditions, such as in subduction zones, as compared to low *P-T* oceanic settings.

Metasomatism can lead to destabilization of trace element-rich phases. Collectively, the dissolution of phases such as rutile and zircon during metasomatism in subduction zones can result in trace-element fractionations (*e.g.*, Th/Nb, Zr/Sm, Hf/Nd) that are otherwise attributed to metamorphic dehydration and melting reactions. Because of the widespread occurrence of juxtaposed mafic and ultramafic rocks in subducting slabs, the slab-mantle interface, and the mantle wedge, metasomatism between these rocks may further enhance trace-element fractionation.

Acknowledgment

The authors would like to thank Dr. Jim Eckert (Yale) and Dr. Neel Chatterjee (MIT) for EPMA assistance, and Caitlin Brown (BC) for assistance in the Sr isotope measurements. E.A. Codillo would like to thank Dr. James Andrew Leong (LDEO) for discussion on the DEW model. M. Scambelluri acknowledges the Italian Ministry of Research MUR for granting the PRIN project n. 2017ZE49E7. This research was funded by NSF-OISE (Office of International Science & Engineering, Petrology & Geochemistry) PIRE, Award #1545903, and the WHOI Ocean Ventures Fund.

Data Availability Statement

The data and models that support the findings of this study are freely available in the data repository (DOI 10.5281/zenodo.6611548).

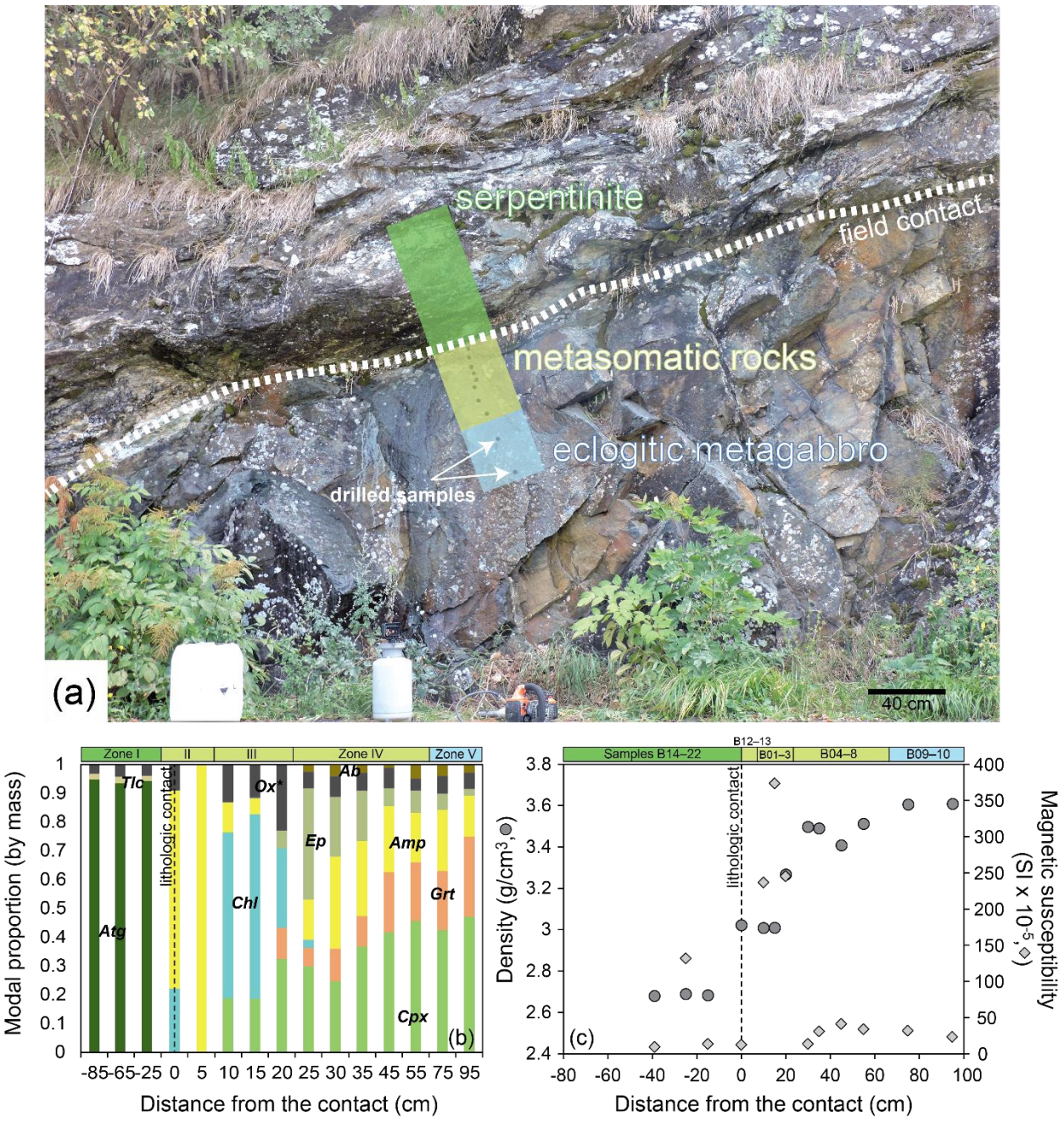
serpentinite
field contact
metasomatic rocks
eclogitic metagabbro
drilled samples
(a)
40 cm
Zone I
II
III
Zone IV
Zone V
Tlc
Atg
lithologic contact
Chl
Ox*
Ab
Ep
Amp
Grt
Cpx
(b)
Modal proportion (by mass)
Distance from the contact (cm)
B12–13
Samples B14–22
B01–3
B04–8
B09–10
lithologic contact
(c)
Density (g/cm3, ●)
Magnetic susceptibility (SI x 10-5, ◇)
Distance from the contact (cm)

Figure 1. Outcrop examined in this study a) Photograph of the sampled transect between serpentinite and metagabbro in the Voltri Massif. Circles indicate the locations where samples for this study were drilled out of the eclogite. The two lithologies were separated by a sharp lithologic contact that can be traced laterally along the stretch of the outcrop. Samples from serpentinite side were taken either by hand or by drilling in a region that is offset ~4 m to the left of the eclogite transect (not visible in this photo) which extends to ~2.25 m from the field contact between eclogite and serpentinite (white dashed line). The subdivision into eclogitic metagabbro, metasomatic rocks (reaction zones), and serpentinite is indicated by different colored regions. Zone II is distinguished in the field by its relatively weak and flaky consistence with foliation more pronounced than in Zones III-V. The mineralogical transitions from Zones III to V in the metagabbro block are diffuse and gradational. (b) Modal mineralogy, (c) bulk density and magnetic susceptibility across the serpentinite-metagabbro transect. Mineral proportions are given in fraction by mass, as calculated from thin-section chemical maps, coupled with modal estimates from mass-balance calculations using mineral and whole-rock compositions. Modal proportions of ilmenite, rutile, as well as their common replacement mineral titanite, were grouped and represented by Ox*. Note that the modal estimate at the contact (zero distance) was based on field observations, bulk composition, and TGA-DSC analysis.

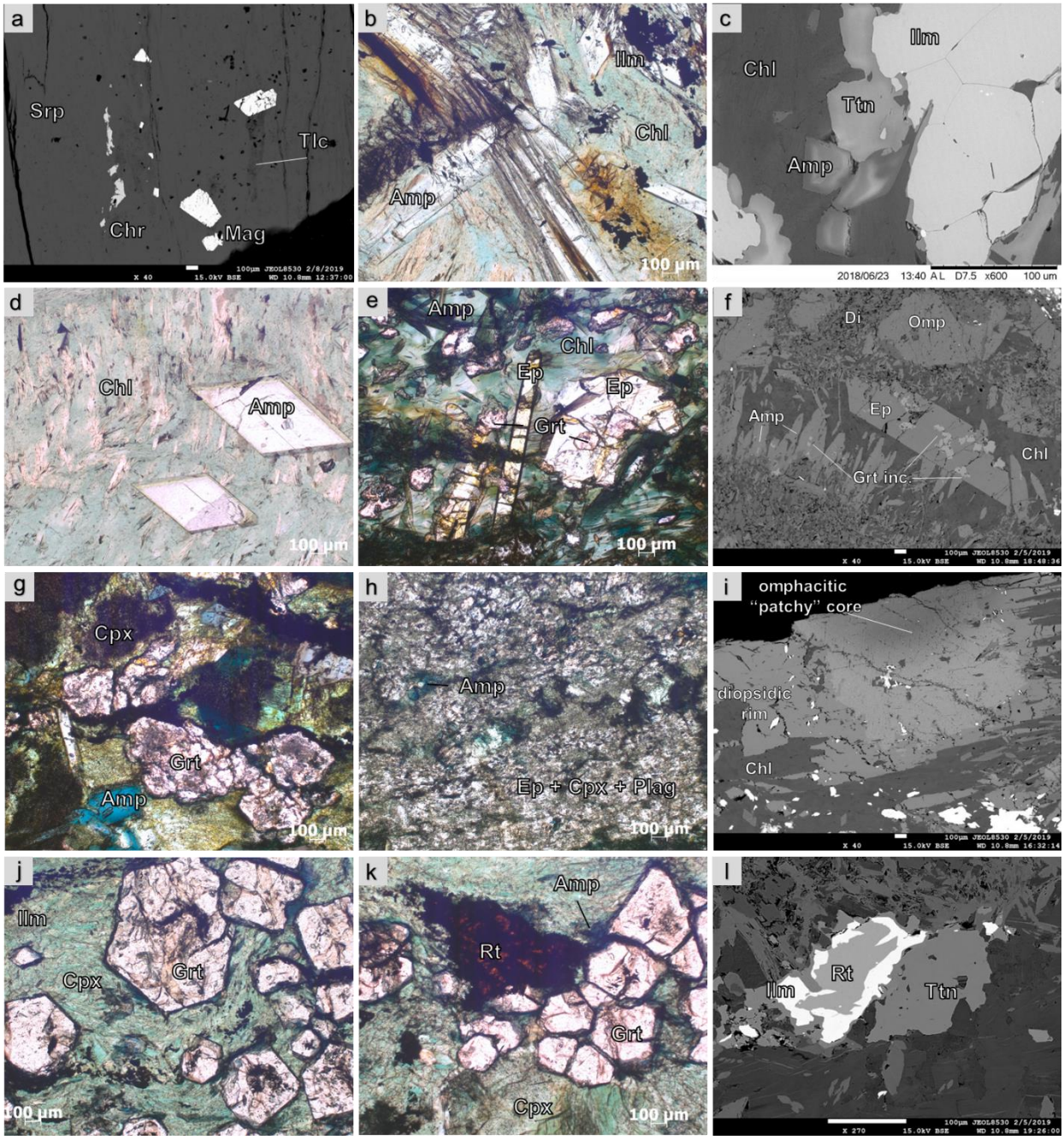

Figure 2. Representative photomicrographs and back-scatter electron (BSE) images of the serpentinite-metagabbro transect. (a) antigorite serpentinite with minor talc, magnetite, and chromite grains in Zone I, (b) euhedral, prismatic amphibole schist with chlorite and ilmenite in Zone II, (c) BSE image of ilmenite mantled by titanite coexisting with Ca-amphibole and chlorite typical for Zones II and III, (d) near-monomineralic chlorite schist with Ca-amphibole in Zone III,

(e) assemblage of chlorite + Ca amphibole + epidote (with anhedral garnet inclusion) in Zone IV, (f) BSE image of anhedral garnet included within euhedral epidote and Ca amphibole. This feature is common in samples of Zones III and IV. (g) Assemblage of subhedral to euhedral garnet, brown omphacitic clinopyroxene, and bluish Na-Ca amphibole in Zone IV, (h) aggregates of dominantly diopsidic clinopyroxene + epidote + plagioclase with minor Na-Ca amphibole, (i) omphacitic clinopyroxene core showing "patchy" exsolution texture, mantled by diposidic rim, (j-k) eclogitic metagabbro with euhedral garnet and omphacitic clinopyroxene, rutile, with minor amphibole in Zone V, and (l) BSE image of the assemblage of rutile and ilmenite mantled by titanite in Zone IV and V.

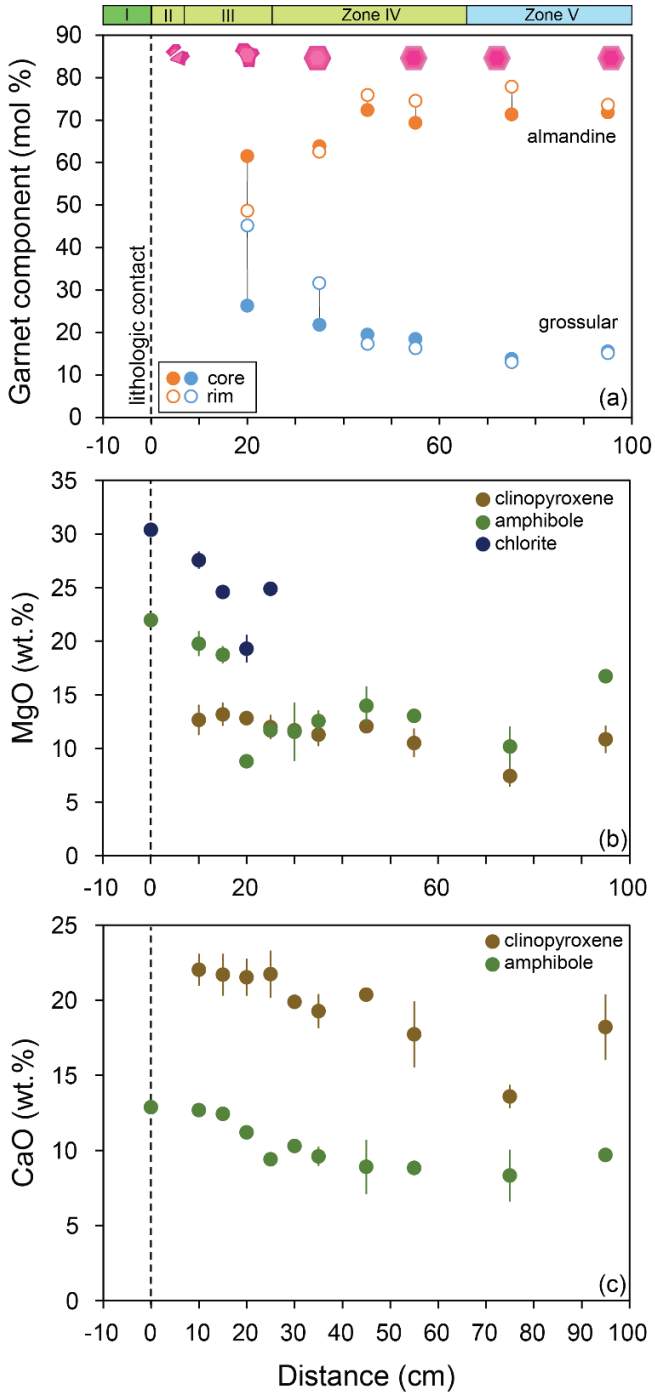

Figure 3. Compositional variations of major minerals across the serpentinite-metagabbro transect. (a) core-to-rim variations in almandine and grossular components in garnet (with schematics of

their morphology), (b) MgO contents variations (average + 1 SD) in clinopyroxene, amphibole, and chlorite, (c) CaO contents variations (average + 1 SD) in clinopyroxene and amphibole.

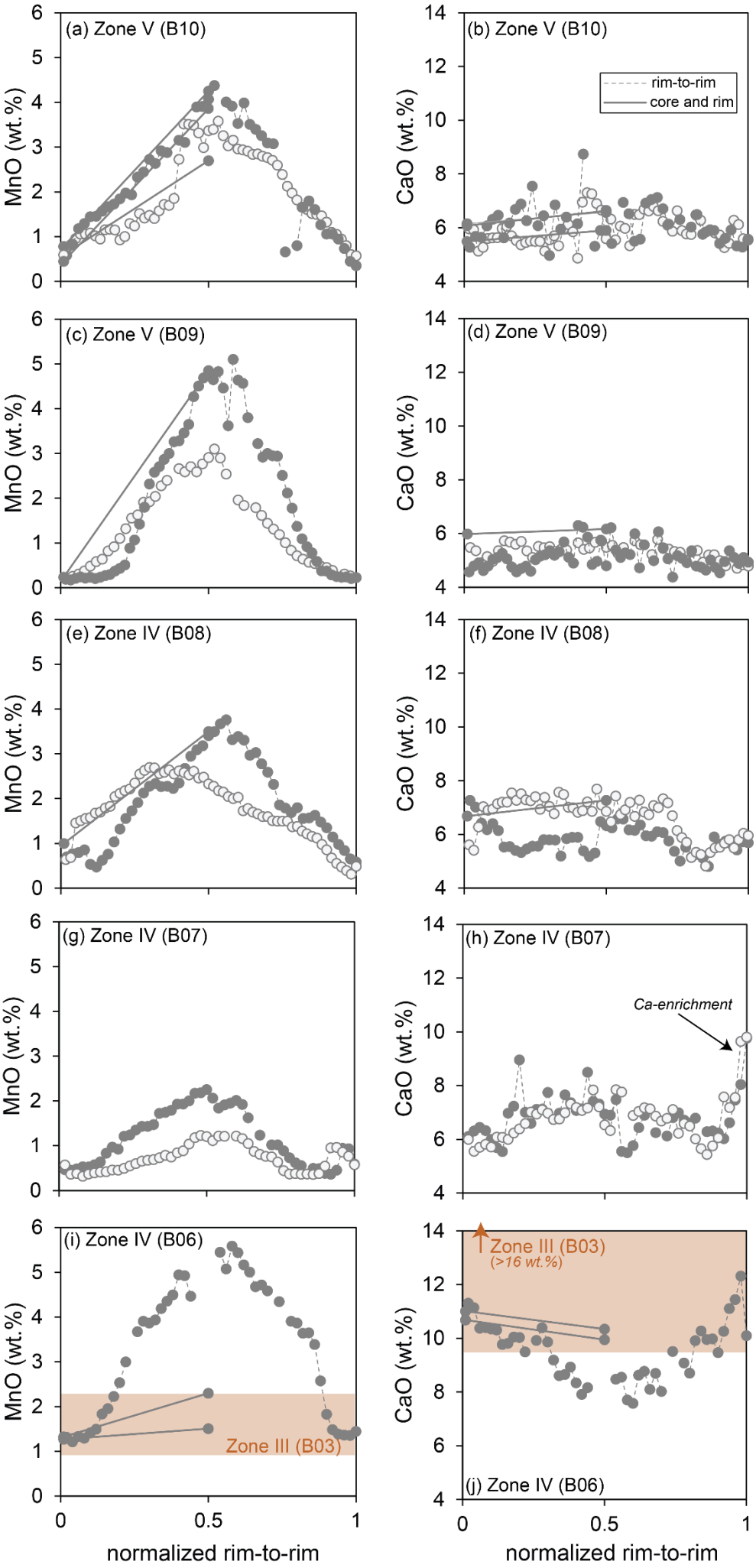
(a) Zone V (B10)
(b) Zone V (B10)
rim-to-rim
core and rim
(c) Zone V (B09)
(d) Zone V (B09)
(e) Zone IV (B08)
(f) Zone IV (B08)
(g) Zone IV (B07)
(h) Zone IV (B07)
Ca-enrichment
(i) Zone IV (B06)
Zone III (B03)
(>16 wt.%)
(j) Zone IV (B06)
MnO (wt.%)
CaO (wt.%)
normalized rim-to-rim

Figure 4. Representative rim-to-rim compositional variations of garnet from different zones. Variations in (a) MnO and (b) CaO contents (wt. %) are measured by EPMA. Different symbols represent different analyzed garnet grains for each zone. The rim-to-rim distance of garnet are normalized for comparison. Representative photomicrographs of measured grains are provided in the supplementary. Due to the difficulty in determining the core and rim of anhedral garnets in Zone III, we plotted the full range of measured composition instead.

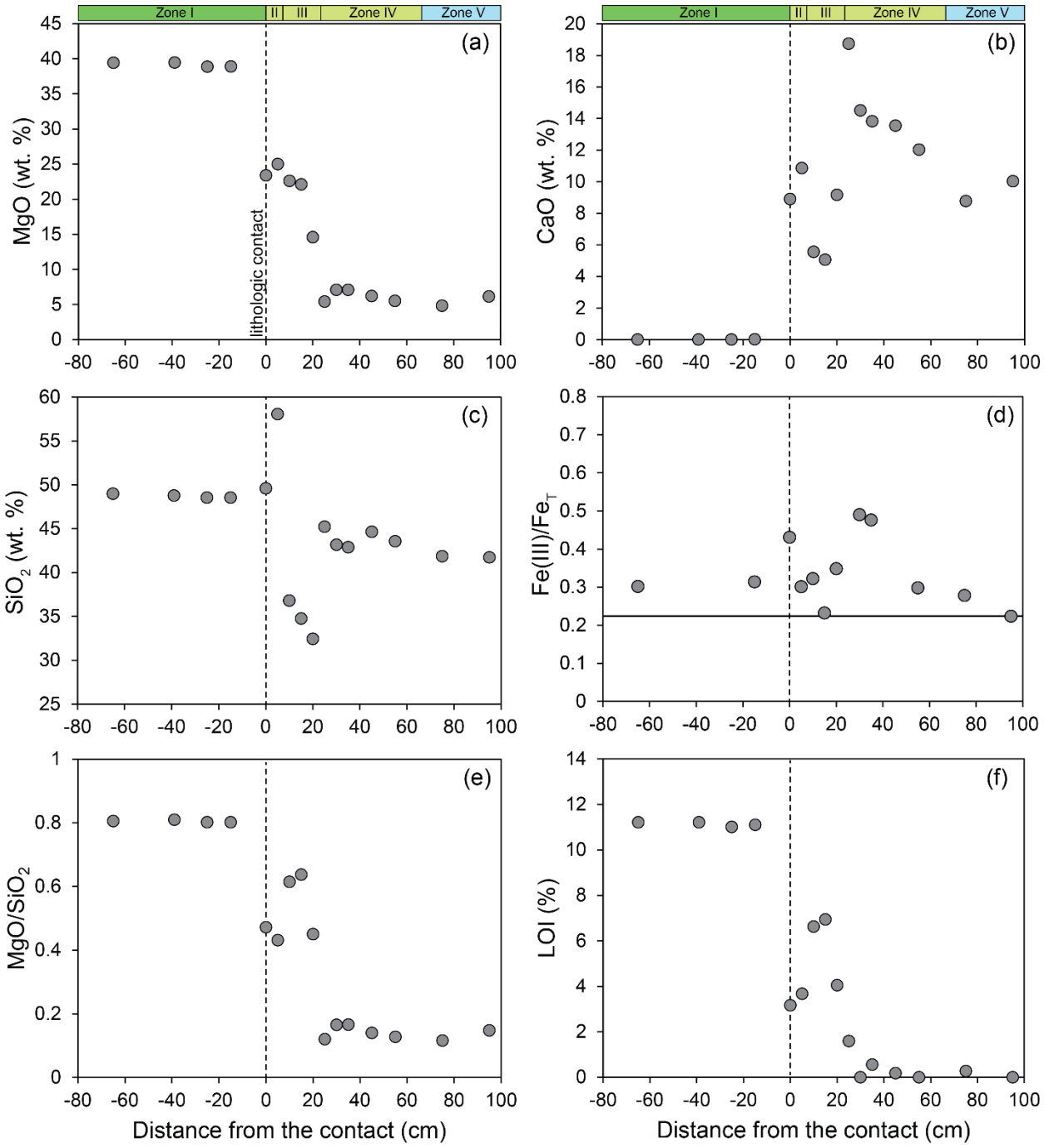

Figure 5. Bulk-rock major element concentrations (on a volatile-free basis), (a) MgO, (b) CaO, (c) SiO_2, (d) $Fe(III)/Fe_T$, (e) MgO/SiO_2, and (f) LOI across the serpentinite-metagabbro transect.

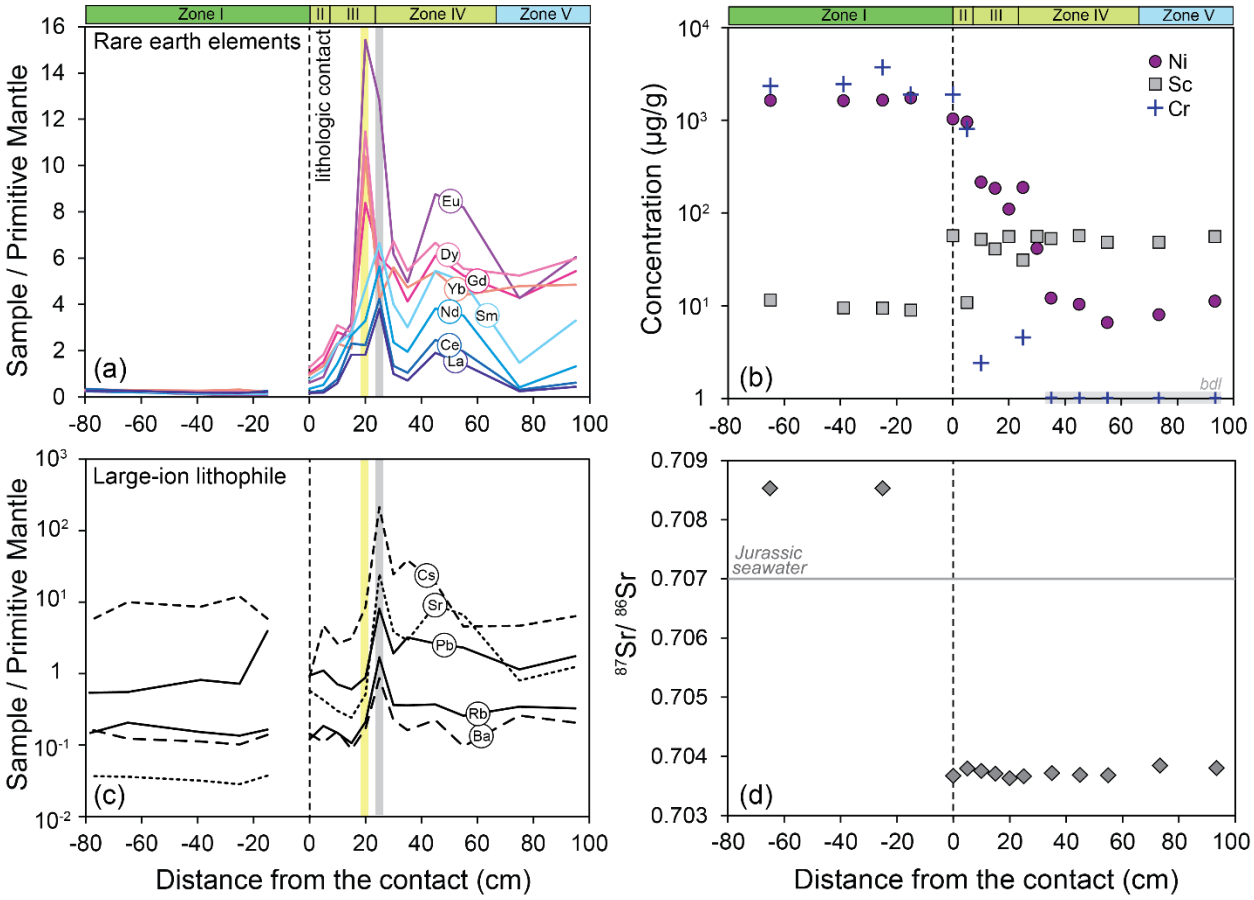

Figure 6. Bulk-rock trace-element concentrations normalized to primitive mantle (McDonough and Sun, 1995) and $^{87}Sr/^{86}Sr$ ratios across the serpentinite-metagabbro transect. (a) rare earth element (REE), (b) transition element (Ni,Cr, and Sc), and (c) large-ion lithophile element (LILE; Cs, Rb, Ba, Sr, Pb) , and (d) bulk-rock $^{87}Sr/^{86}Sr$ isotope ratios of the studied samples and Jurassic seawater from Jones et al. (1994). In (a) and (c), the yellow bar marks the location of peak enrichment for LREE and fluid-mobile LIL elements while the gray bar marks the location of peak enrichment for HREE.

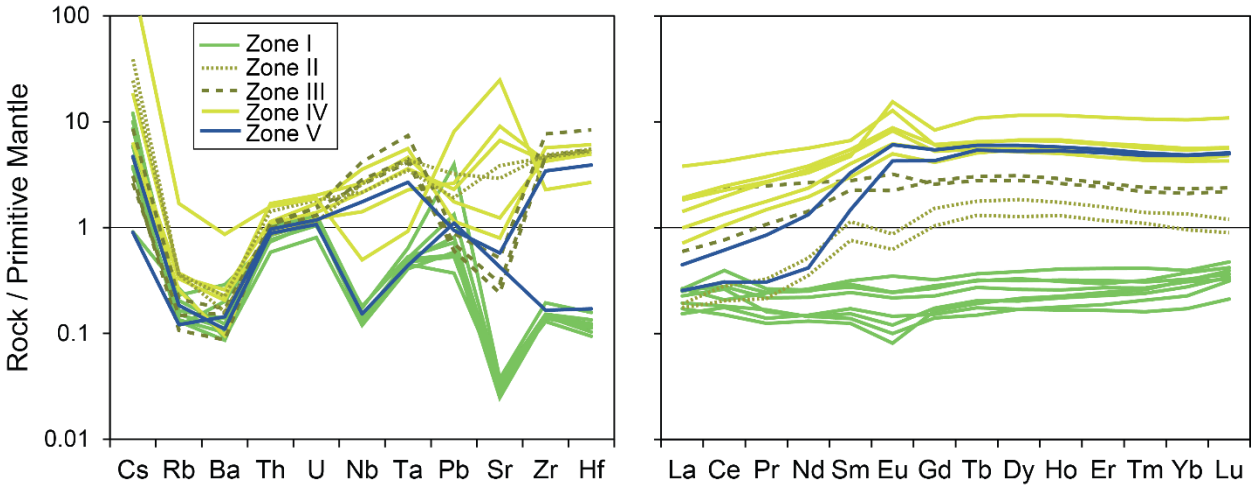

Figure 7. Primitive Mantle-normalized trace-element systematics of the Voltri serpentinite-metagabbro transect. Primitive mantle values are taken from McDonough and Sun (1995).

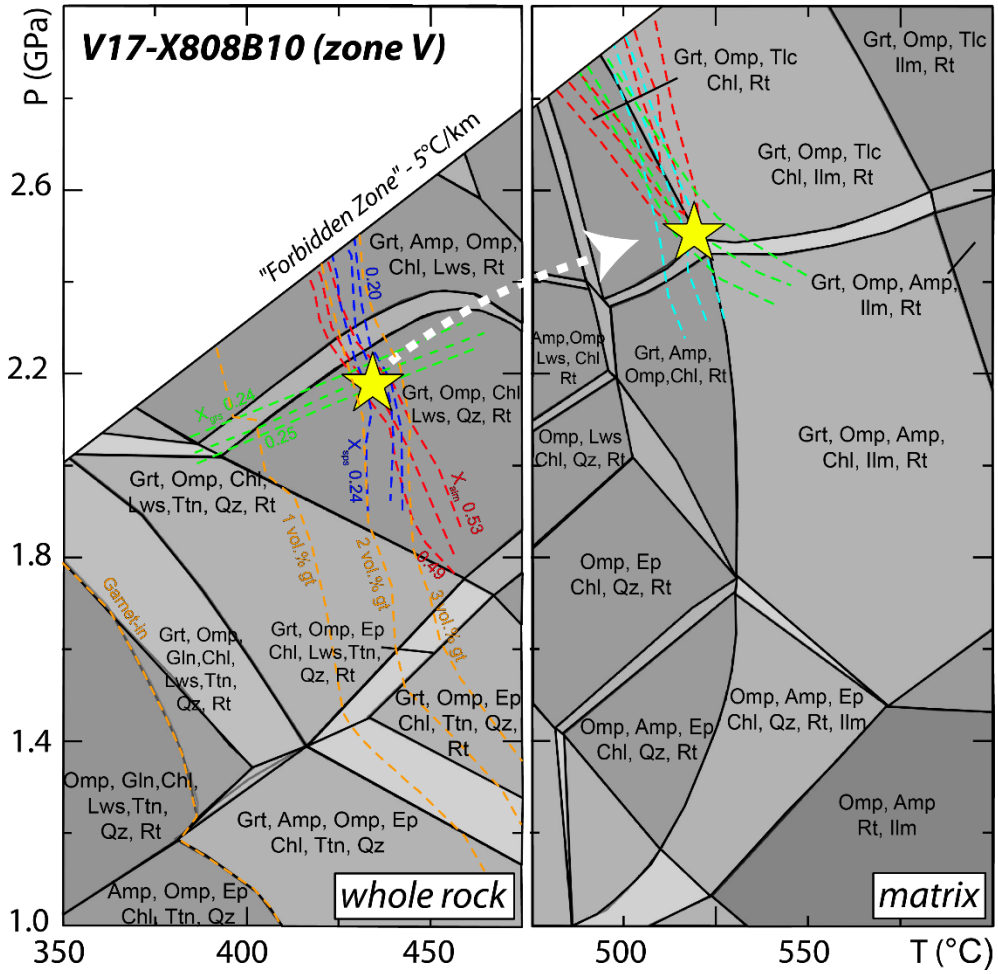

Figure 8. Pressure and temperature constraints on the initiation and termination of garnet growth determined for the MnNCFMASHTO chemical system. Pseudosection modelling for the whole rock composition (left panel) and matrix compositions (excluding garnet; right panel) are performed for the most distal eclogitic metagabbro (Zone V). Garnet chemical isopleths corresponding to observed core and rim garnet chemistry are plotted on whole-rock and matrix pseudosections, respectively (almandine=red, grossular=green, spessartine=blue). Garnet-in conditions and garnet modal abundances (vol. %; orange dashed lines) are also included. The intersection of the garnet core chemical isopleths constrains the *P-T* range for the initiation of garnet growth while the intersection of the garnet rim chemical isopleths constrains the *P-T* range at the termination of garnet growth

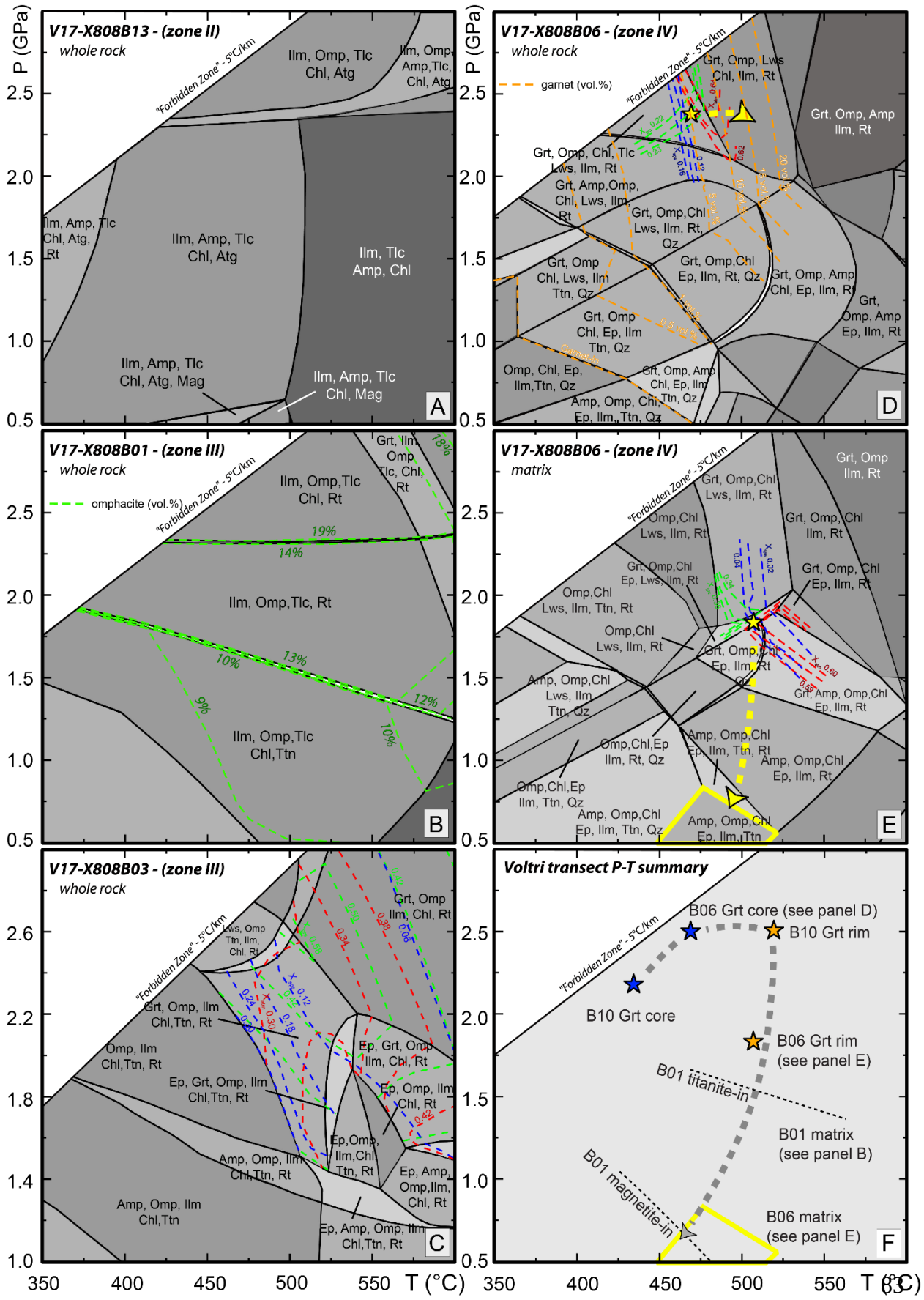
V17-X808B13 - (zone II)
whole rock
"Forbidden Zone" - 5°C/km
Ilm, Omp, Tlc
Chl, Atg
Ilm, Omp, Amp,Tlc, Chl, Atg
Ilm, Amp, Tlc Chl, Atg, Rt
Ilm, Amp, Tlc Chl, Atg
Ilm, Tlc Amp, Chl
Ilm, Amp, Tlc Chl, Atg, Mag
Ilm, Amp, Tlc Chl, Mag
A
V17-X808B06 - (zone IV)
whole rock
garnet (vol.%)
Grt, Omp, Lws Chl, Ilm, Rt
Grt, Omp, Amp Ilm, Rt
Grt, Omp, Chl, Tlc Lws, Ilm, Rt
Grt, Amp,Omp, Chl, Lws, Ilm, Rt
Grt, Omp,Chl Lws, Ilm, Rt, Qz
Grt, Omp Chl, Lws, Ilm Ttn, Qz
Grt, Omp,Chl Ep, Ilm, Rt, Qz
Grt, Omp, Amp Chl, Ep, Ilm, Rt
Grt, Omp, Amp Ep, Ilm, Rt
Grt, Omp Chl, Ep, Ilm Ttn, Qz
Omp, Chl, Ep, Ilm,Ttn, Qz
Grt, Omp, Amp Chl, Ep, Ilm Ttn, Qz
Amp, Omp, Chl, Ep, Ilm,,Ttn, Qz
D
V17-X808B01 - (zone III)
whole rock
omphacite (vol.%)
Grt, Ilm, Omp Tlc, Chl, Rt
Ilm, Omp,Tlc Chl, Rt
19%
14%
Ilm, Omp,Tlc, Rt
10%
13%
12%
9%
10%
Ilm, Omp,Tlc Chl,Ttn
B
V17-X808B06 - (zone IV)
matrix
Grt, Omp Ilm, Rt
Grt, Omp,Chl Lws, Ilm, Rt
Omp,Chl Lws, Ilm, Rt
Grt, Omp, Chl Ilm, Rt
Grt, Omp,Chl Ep, Lws, Ilm, Rt
Grt, Omp, Chl Ep, Ilm, Rt
Omp,Chl Lws, Ilm, Ttn, Rt
Omp,Chl Lws, Ilm, Rt
Grt, Omp,Chl Ep, Ilm, Rt Qz
Amp, Omp,Chl Lws, Ilm Ttn, Qz
Grt, Amp, Omp,Chl Ep, Ilm, Rt
Omp,Chl,Ep Ilm, Rt, Qz
Amp, Omp,Chl Ep, Ilm, Ttn, Rt
Amp, Omp,Chl Ep, Ilm, Rt
Omp,Chl,Ep Ilm, Ttn, Qz
Amp, Omp,Chl Ep, Ilm, Ttn, Qz
Amp, Omp,Chl Ep, Ilm,,Ttn
E
V17-X808B03 - (zone III)
whole rock
Grt, Omp Ilm, Chl, Rt
Lws, Omp Ttn, Ilm, Chl, Rt
Grt, Omp, Ilm Chl,Ttn, Rt
Omp, Ilm Chl,Ttn, Rt
Ep, Grt, Omp Ilm, Chl, Rt
Ep, Grt, Omp, Ilm Chl,Ttn, Rt
Ep, Omp, Ilm Chl, Rt
Ep,Omp, Ilm,Chl Ttn, Rt
Amp, Omp, Ilm Chl,Ttn, Rt
Ep, Amp, Omp,Ilm, Chl, Rt
Amp, Omp, Ilm Chl,Ttn
Ep, Amp, Omp, Ilm Chl,Ttn, Rt
C
Voltri transect P-T summary
"Forbidden Zone" - 5°C/km
B06 Grt core (see panel D)
B10 Grt rim
B10 Grt core
B06 Grt rim (see panel E)
B01 titanite-in
B01 matrix (see panel B)
B01 magnetite-in
B06 matrix (see panel E)
F
P (GPa)
T (°C)

Figure 9. Pseudosection modelling for representative samples in each metasomatic reaction zone in the MnNCFMASHTO chemical system. (a) whole-rock Zone II, (b) whole-rock Zone III, (c) whole-rock Zone III with predicted garnet chemical isopleths (almandine=red, grossular=green, spessartine=blue) calculated at peak *P-T* conditions as constrained by Zone V, (d-e) whole-rock and matrix, Zone IV, and (f) *P-T* summary for the entire metasomatic reaction zones. Garnet-in conditions and garnet modal abundances (vol. %; orange dashed lines) are also included in (d) while omphacite modal abundances (vol. %; green dashed lines) are included in (b). See text for details. Mineral abbreviations are from Whitney and Evans (2010).

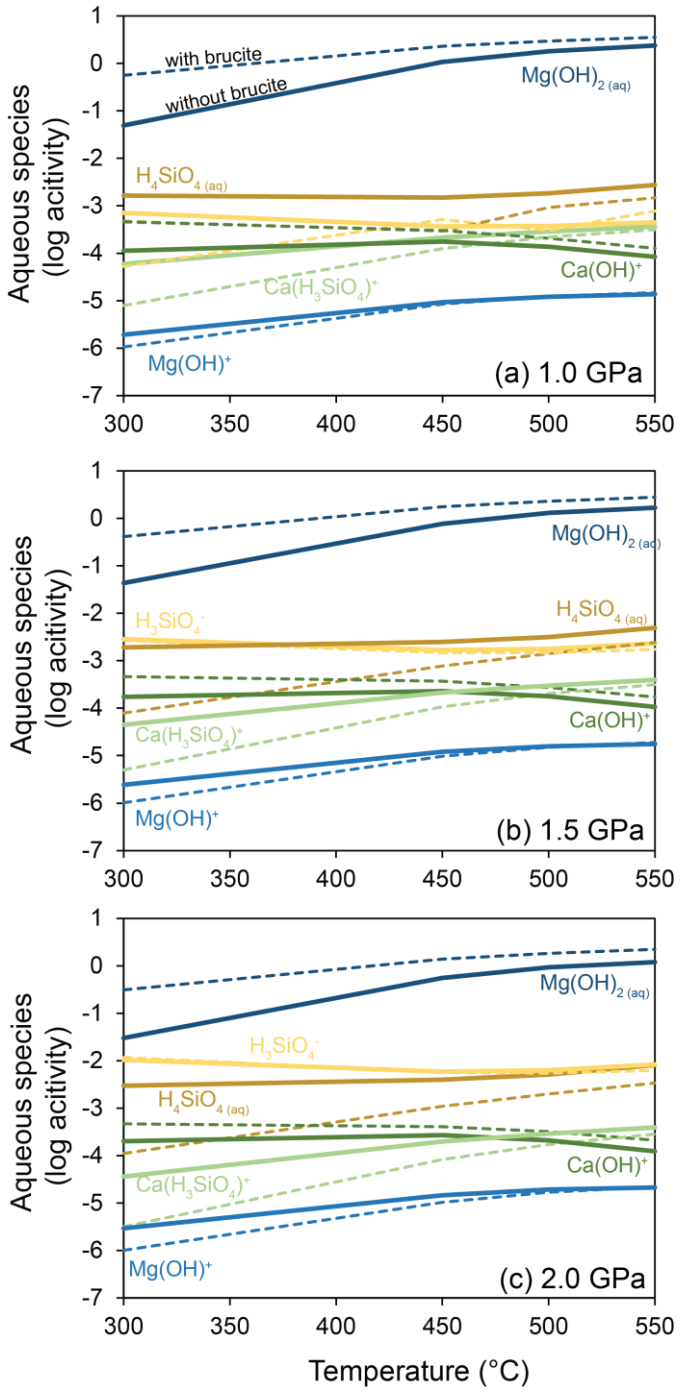

Figure 10. Predicted speciation and activities of Mg, Si, and Ca in equilibrium with serpentinite (i.e., antigorite + clinopyroxene + magnetite ± brucite), and their evolution with temperature (300–550 °C) and pressure (1.0–2.0 GPa) (panels a to c).

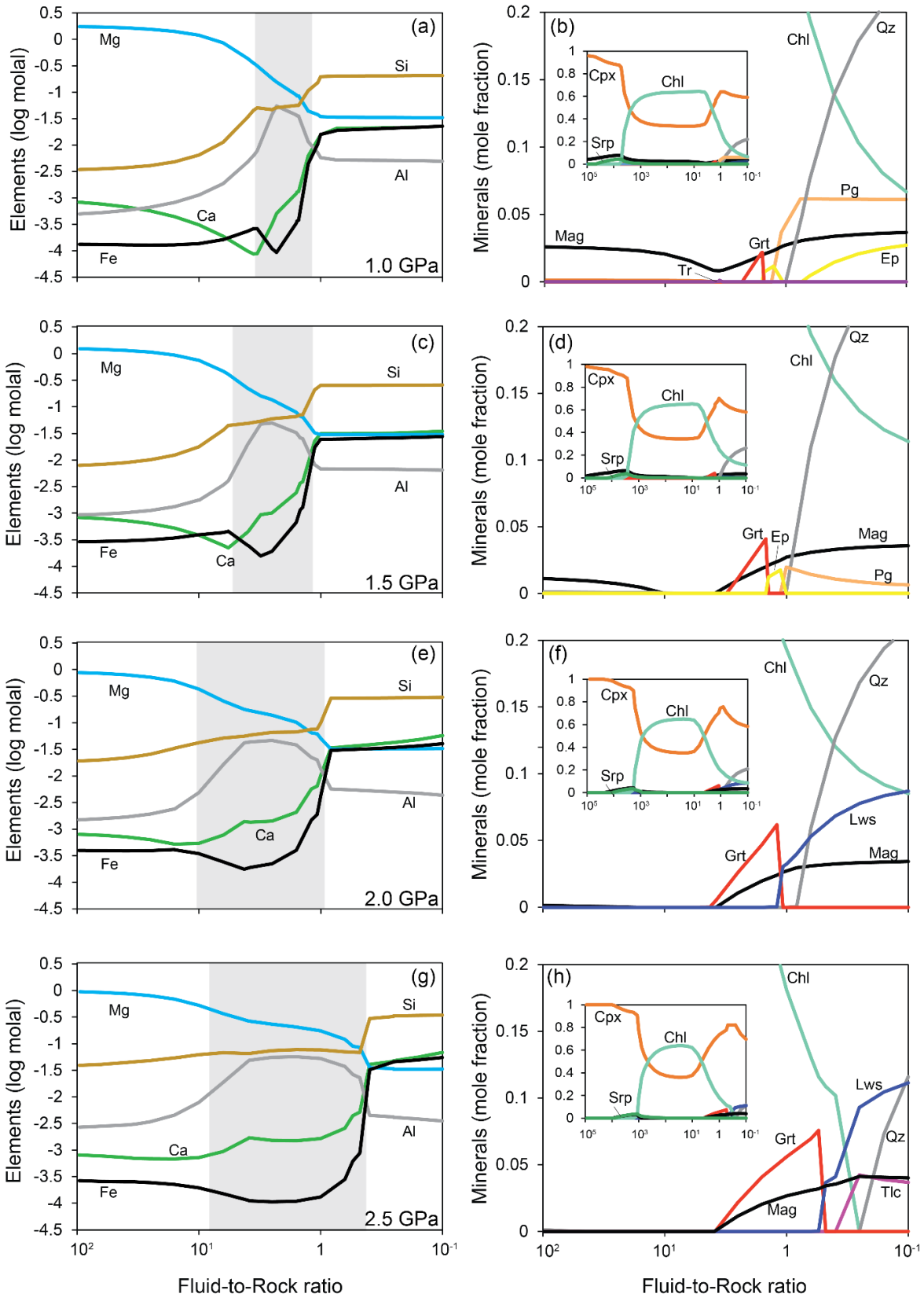
(a)
(b)
(c)
(d)
(e)
(f)
(g)
(h)
Elements (log molal)
Minerals (mole fraction)
Mg
Si
Al
Ca
Fe
Cpx
Chl
Srp
Qz
Pg
Mag
Grt
Tr
Ep
Lws
Tlc
1.0 GPa
1.5 GPa
2.0 GPa
2.5 GPa
Fluid-to-Rock ratio

Figure 11. Predicted alteration mineralogy and fluid composition during high *P*-*T* metasomatism as a function of fluid-to-rock mass ratio. A fluid equilibrated with serpentinite (at f/r ~100) is subsequently allowed to react with oxide gabbro at 500 °C, 1.0–2.5 GPa (a–h). The f/r ratio decreases as gabbro is titrated into the fluid. Mineral abbreviations are from Whitney and Evans (2010). Zones highlighted in gray indicate elevated Al contents in the equilibrium pore fluids.

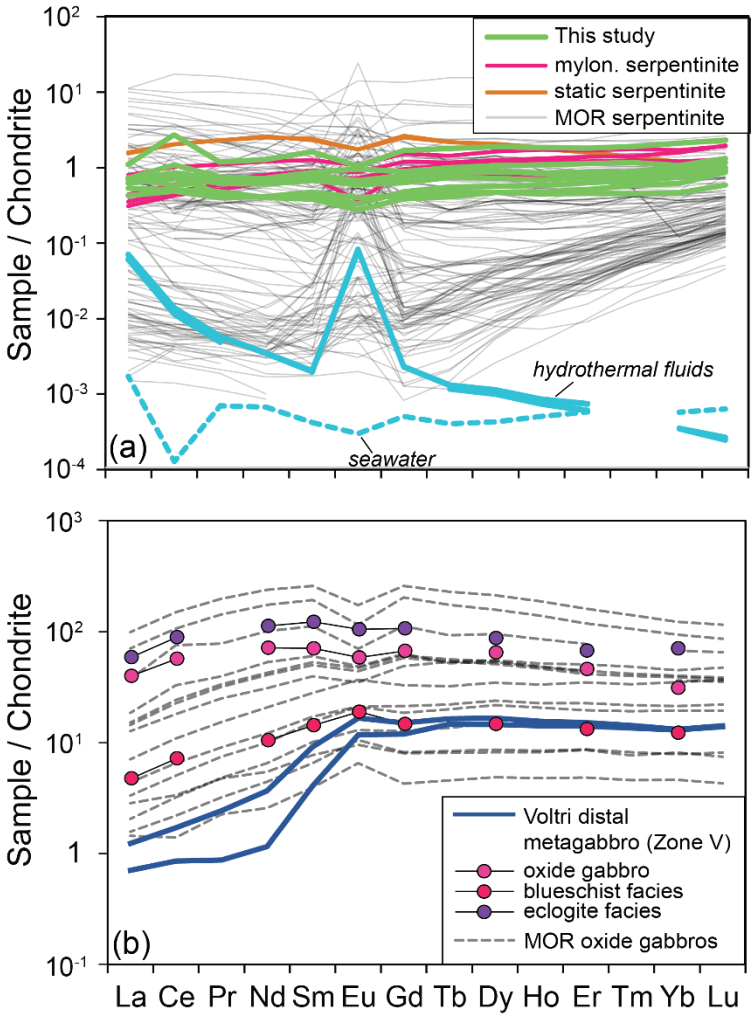

Figure 12. (a) Rare earth element systematics of Voltri serpentinites compared to the literature data of mylonic and static serpentinites from Voltri Massif (Cannao et al., 2016), compilation of serpentinites from mid-ocean ridges (Deschamps et al., 2013), hydrothermal fluids, and seawater (Douville et al., 2002). Concentrations of fluids are multiplied by 100 for scaling purposes. (b) Rare earth element systematics of the most distal LREE depleted eclogitic metagabbro of Zone V, compared to variably metamorphosed crustal rocks in the Votri region (Tribuzio et al., 1996) and a literature compilation of oxide gabbros from the Atlantis Massif (Godard et al., 2009). This comparison shows that LREE depletion in subducted crustal rocks may occur at different stages

over a wide range of *P*-*T* conditions and in distinct tectonic settings, from oceanic environments to subduction zones. CI chondrite values are taken from McDonough and Sun (1995).

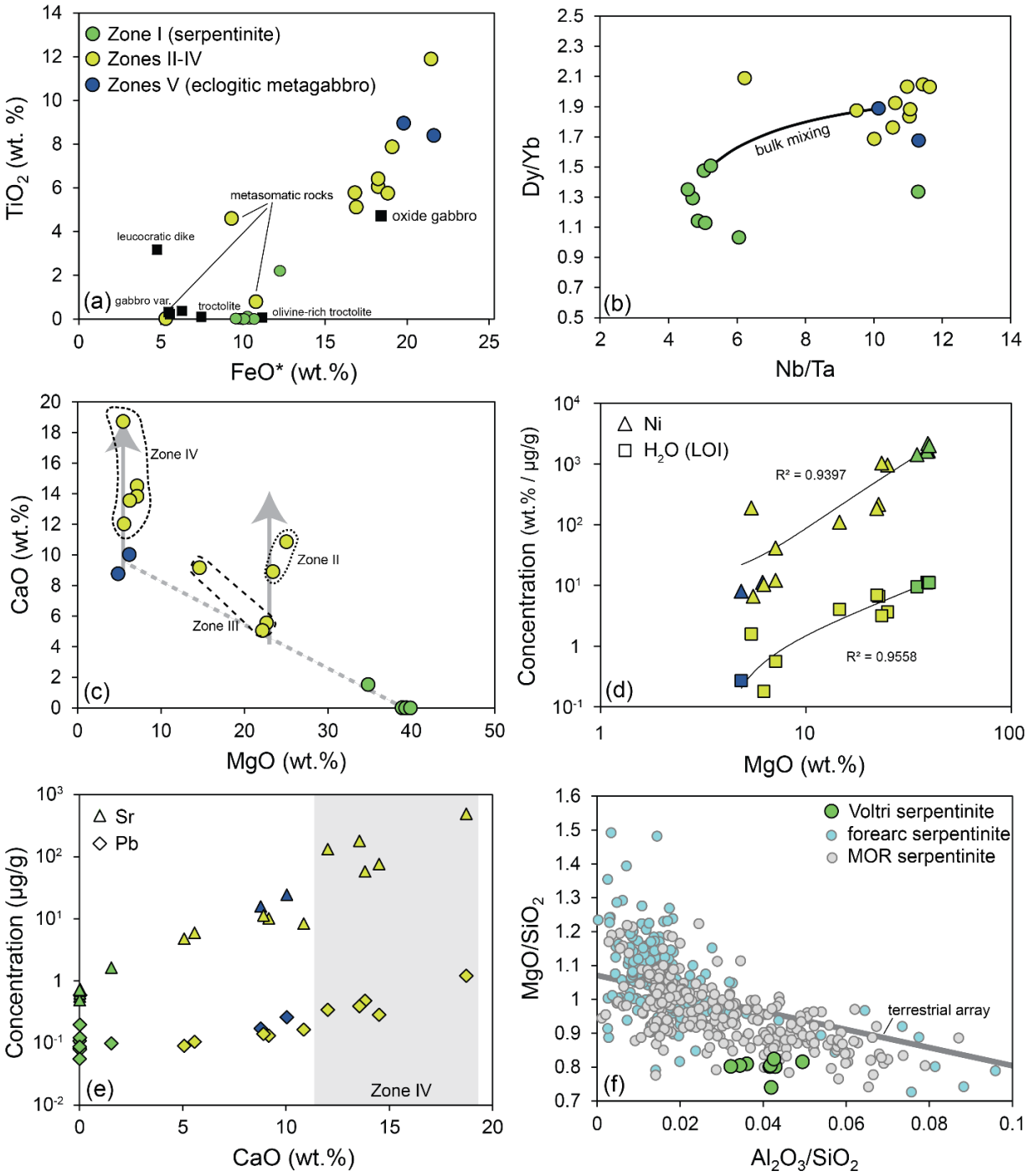

Figure 13. Variations among major and trace elements, and water. (a) TiO_2 vs FeO*, (b) Dy/Yb vs Nb/Ta, (c) CaO vs MgO, (d) Ni and H_2O (represented by LOI) vs MgO, (e) Pb and Sr vs CaO, and (f) $MgO/SiO_2/Al_2O_3/SiO_2$ of studied serpentinite along with literature data (Peters et al., 2017b) of mid-ocean ridge and forearc serpentinites. Data from Godard et al. (2009) in (a) are shown as black squares. The bulk mixing line between serpentinite and metagabbro in (b) was

calculated using the composition of distal eclogitic metagabbro and serpentinite assuming that their compositions were least affected by the mass transfer between the two lithologies. In (c), the dashed line connecting Zone I and V shows that Zones II, III, and IV require addition of CaO as depicted in gray arrows. In (d), the lines display the correlations among samples in terms of Ni vs. MgO (R^2 = 0.9397) and H_2O vs. MgO (R^2 = 0.9558). The gray zone in (e) marks samples from Zone IV.

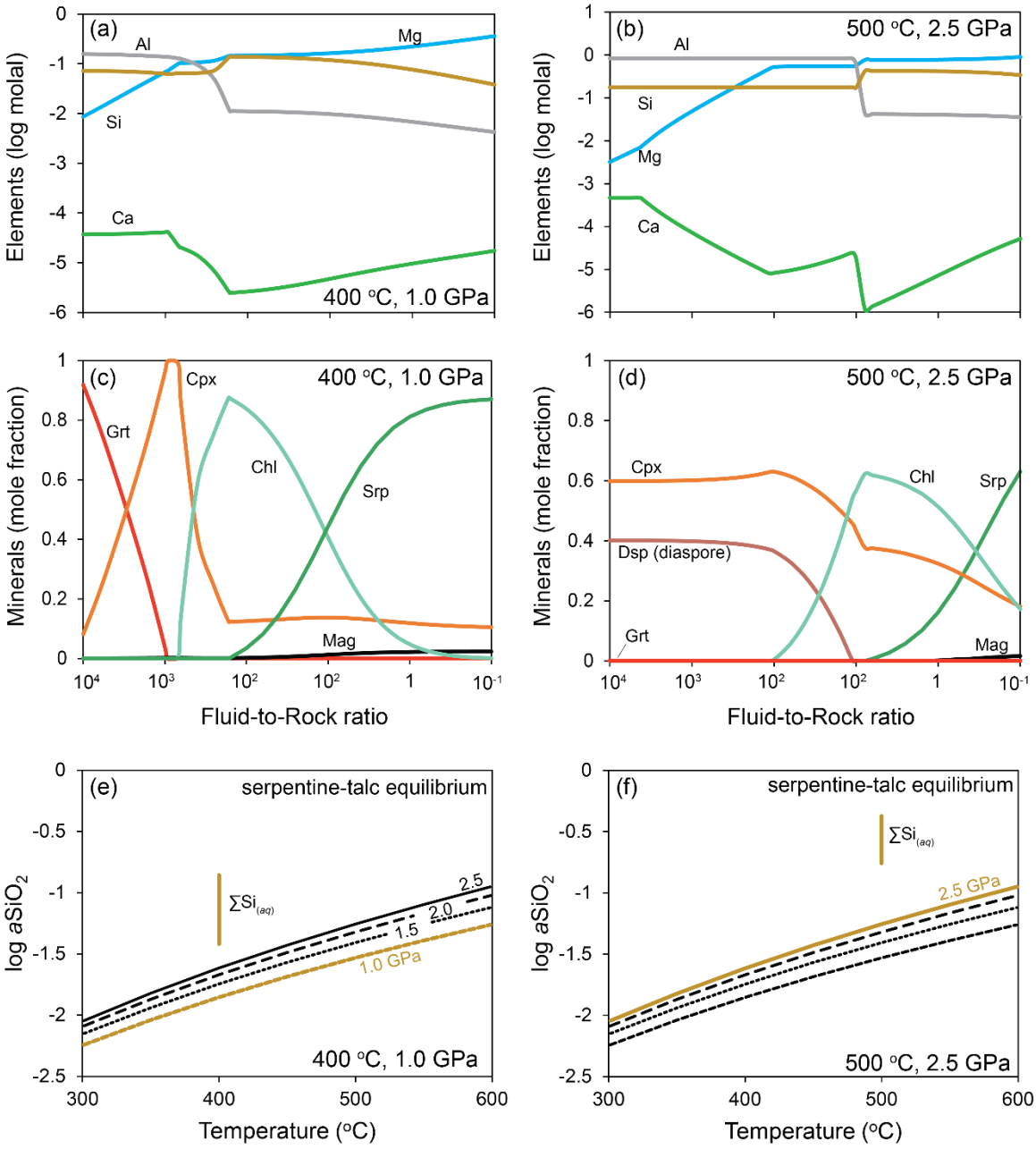

Figure 14. Predicted alteration mineralogy and fluid composition during high *P*-*T* metasomatism as a function of fluid-to-rock mass ratio. A fluid equilibrated with gabbro (Di + An, at f/r > 1000) is subsequently allowed to react with serpentinite at 400–500 °C, 1.0–2.5 GPa (a–d). The f/r decreases as serpentinite is titrated into the fluid. Mineral abbreviations are from Whitney and Evans (2010). Lower panels: Activity of silica buffered by serpentine-talc equilibrium from 1.0–2.5 GPa. The composition of dissolved Si from the reaction-path models plotted above the univariant line in the stability field of talc (e–f).

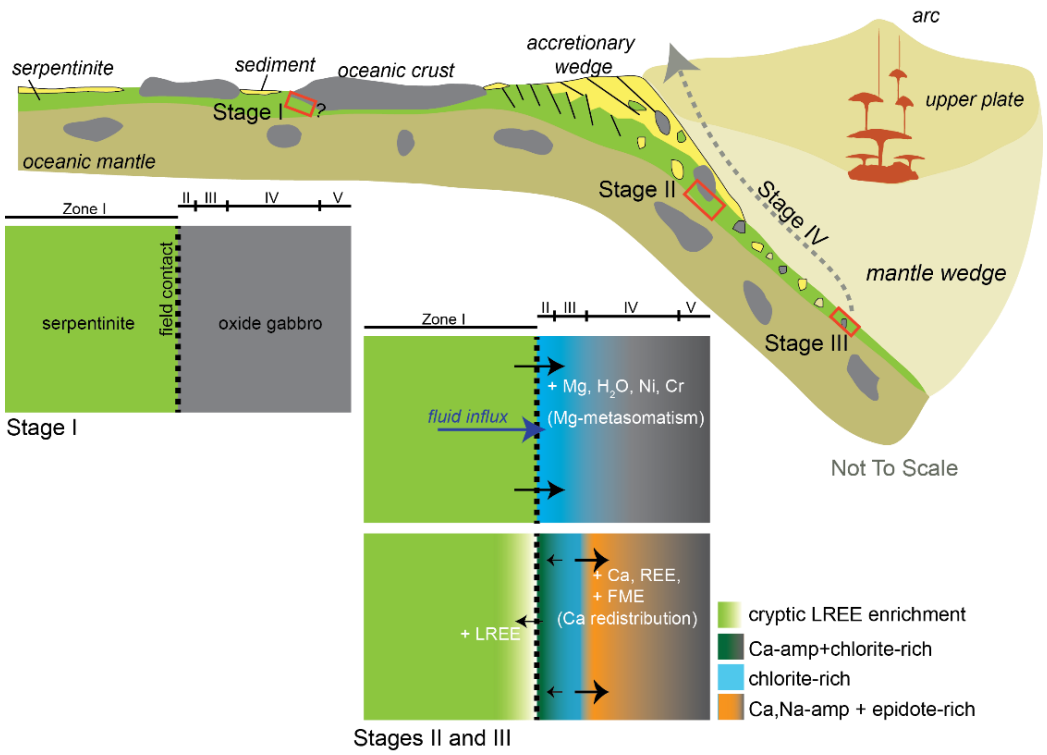

Figure 15. Summary of possible tectonic settings of mass transfer recorded by the studied serpentinite-metagabbro transect. Juxtaposition between serpentinite and metagabbro may have occurred in an oceanic setting prior to subduction in Stage I. Fluid-mediated mass transfer led to the development of metasomatic reaction zones that record significant Mg metasomatism and Ca redistribution in subducted metagabbro during prograde to peak eclogite-facies metamorphism in Stages II and III. Subsequent exhumation accompanied by limited mass transfer and local re-equilibration are displayed in Stage IV.

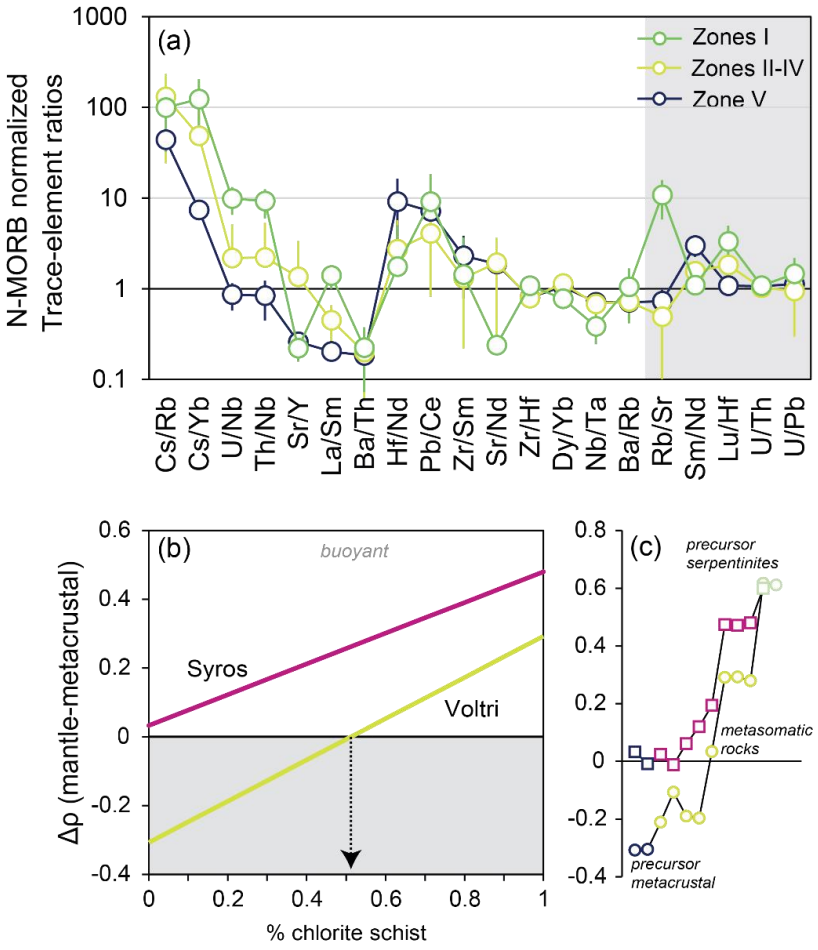

Figure 16. (a) N-MORB normalized trace element ratios of the entire serpentinite-metagabbro transect. Gray shaded ratios are radiogenic parent-daughter isotope pairs (b) Bulk density changes of precursor mafic crustal rock relative to mantle peridotite (DMM) as a function of chlorite content. (c) Bulk densities of serpentinite, metacrustal, and metasomatic rocks relative to mantle peridotite in Voltri Massif (this study) and Syros (Miller et al., 2009). N-MORB values are from Gale et al. (2013).

References

Abers, G.A., Keken, P.E. van, Kneller, E.A., Ferris, A., Stachnik, J.C., 2006. The thermal structure of subduction zones constrained by seismic imaging: Implications for slab dehydration and wedge flow. Earth and Planetary Science Letters 241, 387–397. https://doi.org/10.1016/j.epsl.2005.11.055

Abers, G.A., van Keken, P.E., Wilson, C.R., 2020. Deep decoupling in subduction zones: Observations and temperature limits. Geosphere 16, 1408–1424. https://doi.org/10.1130/GES02278.1

Ague, J., van Haren, J., 1996. Assessing metasomatic mass and volume changes using the bootstrap, with application to deep crustal hydrothermal alteration of marble. Economic Geology 91, 1169–1182. https://doi.org/10.2113/gsecongeo.91.7.1169

Ague, J.J., 2017. Element mobility during regional metamorphism in crustal and subduction zone environments with a focus on the rare earth elements (REE). American Mineralogist 102, 1796–1821. https://doi.org/10.2138/am-2017-6130

Ague, J.J., 2007. Models of permeability contrasts in subduction zone mélange: Implications for gradients in fluid fluxes, Syros and Tinos Islands, Greece. Chemical Geology 239, 217–227. https://doi.org/10.1016/j.chemgeo.2006.08.012

Ague, J.J., Nicolescu, S., 2014. Carbon dioxide released from subduction zones by fluid-mediated reactions. Nature Geoscience 7, 355.

Ague, J.J., Rye, D.M., 1999. Simple Models of CO2 Release from Metacarbonates with Implications for Interpretation of Directions and Magnitudes of Fluid Flow in the Deep Crust. Journal of Petrology 40, 1443–1462. https://doi.org/10.1093/petroj/40.9.1443

Angiboust, S., Agard, P., Raimbourg, H., Yamato, P., Huet, B., 2011. Subduction interface processes recorded by eclogite-facies shear zones (Monviso, W. Alps). Lithos 127, 222–238. https://doi.org/10.1016/j.lithos.2011.09.004

Angiboust, S., Agard, P., Yamato, P., Raimbourg, H., 2012. Eclogite breccias in a subducted ophiolite: A record of intermediate-depth earthquakes? Geology 40, 707–710. https://doi.org/10.1130/G32925.1

Angiboust, S., Pettke, T., Hoog, J.C.M.D., Caron, B., Oncken, O., 2014. Channelized Fluid Flow and Eclogite-facies Metasomatism along the Subduction Shear Zone. J. Petrology 55, 883–916. https://doi.org/10.1093/petrology/egu010

Bach, W., Garrido, C.J., Paulick, H., Harvey, J., Rosner, M., 2004. Seawater-peridotite interactions: First insights from ODP Leg 209, MAR 15°N. Geochemistry, Geophysics, Geosystems 5. https://doi.org/10.1029/2004GC000744

Bach, W., Jöns, N., Klein, F., 2013. Metasomatism Within the Ocean Crust, in: Harlov, D.E., Austrheim, H. (Eds.), Metasomatism and the Chemical Transformation of Rock: The Role of Fluids in Terrestrial and Extraterrestrial Processes. Springer Berlin Heidelberg, Berlin, Heidelberg, pp. 253–288. https://doi.org/10.1007/978-3-642-28394-9_8

Bach, W., Klein, F., 2009. The petrology of seafloor rodingites: Insights from geochemical reaction path modeling. Lithos 112, 103–117. https://doi.org/10.1016/j.lithos.2008.10.022

Baxter, E.F., DePaolo, D.J., 2002. Field measurement of high temperature bulk reaction rates II: Interpretation of results from a field site near Simplon Pass, Switzerland. American Journal of Science 302, 465–516. https://doi.org/10.2475/ajs.302.6.465

Bebout, G., Barton, M., 2002. Tectonic and metasomatic mixing in a high-T, subduction-zone m??lange - Insights into the geochemical evolution of the slab-mantle interface. https://doi.org/10.1016/S0009-2541(02)00019-0

Bebout, G.E., 2007. Metamorphic chemical geodynamics of subduction zones. Earth and Planetary Science Letters 260, 373–393. https://doi.org/10.1016/j.epsl.2007.05.050

Bebout, G.E., Penniston-Dorland, S.C., 2016. Fluid and mass transfer at subduction interfaces—The field metamorphic record. Lithos 240–243, 228–258. https://doi.org/10.1016/j.lithos.2015.10.007

Becker, H., Jochum, K.P., Carlson, R.W., 2000. Trace element fractionation during dehydration of eclogites from high-pressure terranes and the implications for element fluxes in subduction zones. Chemical Geology 163, 65–99. https://doi.org/10.1016/S0009-2541(99)00071-6

Bickle, M.J., McKenzie, D., 1987. The transport of heat and matter by fluids during metamorphism. Contributions to Mineralogy and Petrology 95, 384–392. https://doi.org/10.1007/BF00371852

Bloch, S., Hofmann, A.W., 1978. Magnesium metasomatism during hydrothermal alteration of new oceanic crust. Geology 6, 275–277. https://doi.org/10.1130/0091-7613(1978)6<275:MMDHAO>2.0.CO;2

Boschi, C., Früh-Green, G.L., Delacour, A., Karson, J.A., Kelley, D.S., 2006. Mass transfer and fluid flow during detachment faulting and development of an oceanic core complex, Atlantis Massif (MAR 30°N). Geochemistry, Geophysics, Geosystems 7. https://doi.org/10.1029/2005GC001074

Breeding, C.M., Ague, J.J., Bröcker, M., 2004. Fluid–metasedimentary rock interactions in subduction-zone mélange: Implications for the chemical composition of arc magmas. Geology 32, 1041–1044. https://doi.org/10.1130/G20877.1

Brenan, J.M., Shaw, H.F., Phinney, D.L., Ryerson, F.J., 1994. Rutile-aqueous fluid partitioning of Nb, Ta, Hf, Zr, U and Th: implications for high field strength element depletions in island-arc basalts. Earth and Planetary Science Letters 128, 327–339. https://doi.org/10.1016/0012-821X(94)90154-6

Cannaò, E., Scambelluri, M., Agostini, S., Tonarini, S., Godard, M., 2016. Linking serpentinite geochemistry with tectonic evolution at the subduction plate-interface: The Voltri Massif case study (Ligurian Western Alps, Italy). Geochimica et Cosmochimica Acta 190, 115–133. https://doi.org/10.1016/j.gca.2016.06.034

Carlson, W.D., Pattison, D.R.M., Caddick, M.J., 2015. Beyond the equilibrium paradigm: How consideration of kinetics enhances metamorphic interpretation. American Mineralogist 100, 1659–1667. https://doi.org/10.2138/am-2015-5097

Carter, L.B., Skora, S., Blundy, J.D., De Hoog, J.C.M., Elliott, T., 2015. An Experimental Study of Trace Element Fluxes from Subducted Oceanic Crust. Journal of Petrology 56, 1585–1606. https://doi.org/10.1093/petrology/egv046

Codillo, E., 2022. Fluid-mediated interactions between serpentinite and gabbro: fluid speciation and reaction-path models. https://doi.org/10.5281/zenodo.6611549

Codillo, E.A., Le Roux, V., Marschall, H.R., 2018. Arc-like magmas generated by mélange-peridotite interaction in the mantle wedge. Nature Communications 9, 2864. https://doi.org/10.1038/s41467-018-05313-2

Coggon, R., Holland, T.J.B., 2002. Mixing properties of phengitic micas and revised garnet-phengite thermobarometers. Journal of Metamorphic Geology 20, 683–696. https://doi.org/10.1046/j.1525-1314.2002.00395.x

Connolly, J.A.D., 2009. The geodynamic equation of state: What and how. Geochemistry, Geophysics, Geosystems 10. https://doi.org/10.1029/2009GC002540

Cooperdock, E.H.G., Raia, N.H., Barnes, J.D., Stockli, D.F., Schwarzenbach, E.M., 2018. Tectonic origin of serpentinites on Syros, Greece: Geochemical signatures of abyssal origin preserved in a HP/LT subduction complex. Lithos 296–299, 352–364. https://doi.org/10.1016/j.lithos.2017.10.020

Cruz-Uribe, A.M., Marschall, H.R., Gaetani, G.A., Le Roux, V., 2018. Generation of alkaline magmas in subduction zones by partial melting of mélange diapirs—An experimental study. Geology 46, 343–346. https://doi.org/10.1130/G39956.1

Debret, B., Andreani, M., Muñoz, M., Bolfan-Casanova, N., Carlut, J., Nicollet, C., Schwartz, S., Trcera, N., 2014. Evolution of Fe redox state in serpentine during subduction. Earth and Planetary Science Letters 400, 206–218. https://doi.org/10.1016/j.epsl.2014.05.038

Debret, B., Millet, M.-A., Pons, M.-L., Bouilhol, P., Inglis, E., Williams, H., 2016. Isotopic evidence for iron mobility during subduction. Geology 44, 215–218. https://doi.org/10.1130/G37565.1

Deschamps, F., Godard, M., Guillot, S., Hattori, K., 2013. Geochemistry of subduction zone serpentinites: A review. Lithos 178, 96–127. https://doi.org/10.1016/j.lithos.2013.05.019

Diener, J.F.A., Powell, R., 2012. Revised activity–composition models for clinopyroxene and amphibole. Journal of Metamorphic Geology 30, 131–142. https://doi.org/10.1111/j.1525-1314.2011.00959.x

Diener, J.F.A., Powell, R., 2010. Influence of ferric iron on the stability of mineral assemblages. Journal of Metamorphic Geology 28, 599–613. https://doi.org/10.1111/j.1525-1314.2010.00880.x

Douville, E., Charlou, J.L., Oelkers, E.H., Bienvenu, P., Colon, C.F.J., Donval, J.P., Fouquet, Y., Prieur, D., Appriou, P., 2002. The rainbow vent fluids (36°14′N, MAR): the influence of ultramafic rocks and phase separation on trace metal content in Mid-Atlantic Ridge hydrothermal fluids. Chemical Geology 184, 37–48. https://doi.org/10.1016/S0009-2541(01)00351-5

Downs, R.T., 2006. The RRUFF Project: an integrated study of the chemistry, crystallography, Raman and infrared spectroscopy of minerals. Program and Abstracts of the 19th General Meeting of the International Mineralogical Association in Kobe, Japan. https://doi.org/O03-13

Dragovic, B., Samanta, L.M., Baxter, E.F., Selverstone, J., 2012. Using garnet to constrain the duration and rate of water-releasing metamorphic reactions during subduction: An example from Sifnos, Greece. Chemical Geology 314–317, 9–22. https://doi.org/10.1016/j.chemgeo.2012.04.016

Elderfield, H., Greaves, M.J., 1982. The rare earth elements in seawater. Nature 296, 214–219. https://doi.org/10.1038/296214a0

Evans, K.A., Frost, B.R., 2021. Deserpentinization in Subduction Zones as a Source of Oxidation in Arcs: a Reality Check. Journal of Petrology 62. https://doi.org/10.1093/petrology/egab016

Federico, L., Capponi, G., Crispini, L., Scambelluri, M., Villa, I., 2005. 39Ar/40Ar dating of high-pressure rocks from the Ligurian Alps: Evidence for a continuous subduction?exhumation cycle. Earth and Planetary Science Letters 240, 668–680. https://doi.org/10.1016/j.epsl.2005.09.062

Federico, L., Crispini, L., Malatesta, C., Torchio, S., Capponi, G., 2015. Geology of the Pontinvrea area (Ligurian Alps, Italy): structural setting of the contact between Montenotte and Voltri units. Journal of Maps 11, 101–113. https://doi.org/10.1080/17445647.2014.945749

Federico, L., Crispini, L., Scambelluri, M., Capponi, G., 2007. Ophiolite mélange zone records exhumation in a fossil subduction channel. Geology 35, 499–502. https://doi.org/10.1130/G23190A.1

Ferry, J.M., Dipple, G.M., 1991. Fluid flow, mineral reactions, and metasomatism. Geology 19, 211–214. https://doi.org/10.1130/0091-7613(1991)019<0211:FFMRAM>2.3.CO;2

Fryer, P., 2012. Serpentinite mud volcanism: observations, processes, and implications. Annual Review of Marine Science 4, 345–373.

Gale, A., Dalton, C.A., Langmuir, C.H., Su, Y., Schilling, J.-G., 2013. The mean composition of ocean ridge basalts. Geochemistry, Geophysics, Geosystems 14, 489–518. https://doi.org/10.1029/2012GC004334

German, C.R., Elderfield, H., 1990. Application of the Ce anomaly as a paleoredox indicator: The ground rules. Paleoceanography 5, 823–833. https://doi.org/10.1029/PA005i005p00823

Gerya, T., Stöckhert, B., 2006. Two-dimensional numerical modeling of tectonic and metamorphic histories at active continental margins. International Journal of Earth Sciences 95, 250–274. https://doi.org/10.1007/s00531-005-0035-9

Gerya, T.V., Yuen, D.A., 2003. Rayleigh–Taylor instabilities from hydration and melting propel 'cold plumes' at subduction zones. Earth and Planetary Science Letters 212, 47–62. https://doi.org/10.1016/S0012-821X(03)00265-6

Godard, M., Awaji, S., Hansen, H., Hellebrand, E., Brunelli, D., Johnson, K., Yamasaki, T., Maeda, J., Abratis, M., Christie, D., Kato, Y., Mariet, C., Rosner, M., 2009. Geochemistry of a long in-situ section of intrusive slow-spread oceanic lithosphere: Results from IODP Site U1309 (Atlantis Massif, 30°N Mid-Atlantic-Ridge). Earth and Planetary Science Letters 279, 110–122. https://doi.org/10.1016/j.epsl.2008.12.034

Gorman, J.K., Penniston-Dorland, S.C., Marschall, H.R., Walker, R.J., 2019. The roles of mechanical mixing and fluid transport in the formation of reaction zones in subduction-related mélange: Evidence from highly siderophile elements. Chemical Geology 525, 96–111. https://doi.org/10.1016/j.chemgeo.2019.07.004

Grant, J.A., 1986. The isocon diagram; a simple solution to Gresens' equation for metasomatic alteration. Economic Geology 81, 1976–1982. https://doi.org/10.2113/gsecongeo.81.8.1976

Green, E., Holland, T., Powell, R., 2007. An order-disorder model for omphacitic pyroxenes in the system jadeite-diopside-hedenbergite-acmite, with applications to eclogitic rocks. American Mineralogist 92, 1181–1189. https://doi.org/10.2138/am.2007.2401

Gresens, R.L., 1967. Composition-volume relationships of metasomatism. Chemical Geology 2, 47–65. https://doi.org/10.1016/0009-2541(67)90004-6

Groppo, C., Beltrando, M., Compagnoni, R., 2009. The P–T path of the ultra-high pressure Lago Di Cignana and adjoining high-pressure meta-ophiolitic units: insights into the evolution of the subducting Tethyan slab. Journal of Metamorphic Geology 27, 207–231. https://doi.org/10.1111/j.1525-1314.2009.00814.x

Groppo, C., Rinaudo, C., Cairo, S., Gastaldi, D., Compagnoni, R., 2006. Micro-Raman spectroscopy for a quick and reliable identification of serpentine minerals from ultramafics. European Journal of Mineralogy 18, 319–329. https://doi.org/10.1127/0935-1221/2006/0018-0319

Guillot, S., Hattori, K., Agard, P., Schwartz, S., Vidal, O., 2009. Exhumation Processes in Oceanic and Continental Subduction Contexts: A Review, in: Lallemand, S., Funiciello, F. (Eds.), Subduction Zone Geodynamics. Springer Berlin Heidelberg, pp. 175–205.

Gyomlai, T., Agard, P., Marschall, H.R., Jolivet, L., Gerdes, A., 2021. Metasomatism and deformation of block-in-matrix structures in Syros: The role of inheritance and fluid-rock interactions along the subduction interface. Lithos 386–387, 105996. https://doi.org/10.1016/j.lithos.2021.105996

Hacker, B.R., 2008. H2O subduction beyond arcs. Geochemistry, Geophysics, Geosystems 9. https://doi.org/10.1029/2007GC001707

Harlow, G.E., Flores, K.E., Marschall, H.R., 2016. Fluid-mediated mass transfer from a paleosubduction channel to its mantle wedge: Evidence from jadeitite and related rocks from the Guatemala Suture Zone. Lithos 258–259, 15–36. https://doi.org/10.1016/j.lithos.2016.04.010

Haws, A.A., Starr, P.G., Dragovic, B., Scambelluri, M., Belmonte, D., Caddick, M.J., Broadwell, K.S., Ague, J.J., Baxter, E.F., 2021. Meta-rodingite dikes as recorders of subduction zone metamorphism and serpentinite dehydration: Voltri Ophiolite, Italy. Chemical Geology 565, 120077. https://doi.org/10.1016/j.chemgeo.2021.120077

Hawthorne, F.C., Oberti, R., Harlow, G.E., Maresch, W.V., Martin, R.F., Schumacher, J.C., Welch, M.D., 2012. Nomenclature of the amphibole supergroup. American Mineralogist 97, 2031–2048. https://doi.org/10.2138/am.2012.4276

Helgeson, H.C., 1969. Thermodynamics of hydrothermal systems at elevated temperatures and pressures. Am J Sci 267, 729. https://doi.org/10.2475/ajs.267.7.729

Holland, T., Powell, R., 2003. Activity–composition relations for phases in petrological calculations: an asymmetric multicomponent formulation. Contributions to Mineralogy and Petrology 145, 492–501. https://doi.org/10.1007/s00410-003-0464-z

Holland, T.J.B., Powell, R., 1998. An internally consistent thermodynamic data set for phases of petrological interest. Journal of Metamorphic Geology 16, 309–343. https://doi.org/10.1111/j.1525-1314.1998.00140.x

Honnorez, J., Kirst, P., 1975. Petrology of rodingites from the equatorial Mid-Atlantic fracture zones and their geotectonic significance. Contributions to Mineralogy and Petrology 49, 233–257.

Huang, F., Sverjensky, D.A., 2019. Extended Deep Earth Water Model for predicting major element mantle metasomatism. Geochimica et Cosmochimica Acta 254, 192–230. https://doi.org/10.1016/j.gca.2019.03.027

Humphris, S.E., Thompson, G., 1978. Hydrothermal alteration of oceanic basalts by seawater. Geochimica et Cosmochimica Acta 42, 107–125.

Hunziker, J.C., 1974. Rb-Sr and K-Ar age determination and the Alpine tectonic history of the Western Alps.

Iacovino, K., Guild, M.R., Till, C.B., 2020. Aqueous fluids are effective oxidizing agents of the mantle in subduction zones. Contributions to Mineralogy and Petrology 175, 36. https://doi.org/10.1007/s00410-020-1673-4

John, T., Scherer, E.E., Haase, K., Schenk, V., 2004. Trace element fractionation during fluid-induced eclogitization in a subducting slab: trace element and Lu–Hf–Sm–Nd isotope systematics. Earth and Planetary Science Letters 227, 441–456. https://doi.org/10.1016/j.epsl.2004.09.009

Jones, C.E., Jenkyns, H.C., Coe, A.L., Stephen, H.P., 1994. Strontium isotopic variations in Jurassic and Cretaceous seawater. Geochimica et Cosmochimica Acta 58, 3061–3074. https://doi.org/10.1016/0016-7037(94)90179-1

Kessel, R., Schmidt, M.W., Ulmer, P., Pettke, T., 2005. Trace element signature of subduction-zone fluids, melts and supercritical liquids at 120–180 km depth. Nature 437, 724–727. https://doi.org/10.1038/nature03971

King, R.L., Bebout, G.E., Moriguti, T., Nakamura, E., 2006. Elemental mixing systematics and Sr–Nd isotope geochemistry of mélange formation: Obstacles to identification of fluid sources to arc volcanics. Earth and Planetary Science Letters 246, 288–304. https://doi.org/10.1016/j.epsl.2006.03.053

King, R.L., Kohn, M.J., Eiler, J.M., 2003. Constraints on the petrologic structure of the subduction zone slab-mantle interface from Franciscan Complex exotic ultramafic blocks. GSA Bulletin 115, 1097–1109. https://doi.org/10.1130/B25255.1

Kirby, S., Engdahl, R.E., Denlinger, R., 2013. Intermediate-Depth Intraslab Earthquakes and Arc Volcanism as Physical Expressions of Crustal and Uppermost Mantle Metamorphism in Subducting Slabs, in: Subduction. American Geophysical Union (AGU), pp. 195–214. https://doi.org/10.1029/GM096p0195

Klein, F., Bach, W., Humphris, S.E., Kahl, W.-A., Jöns, N., Moskowitz, B., Berquó, T.S., 2014. Magnetite in seafloor serpentinite—Some like it hot. Geology 42, 135–138. https://doi.org/10.1130/G35068.1

Klein, F., Bach, W., Jöns, N., McCollom, T., Moskowitz, B., Berquó, T., 2009. Iron partitioning and hydrogen generation during serpentinization of abyssal peridotites from 15°N on the Mid-Atlantic Ridge. Geochimica et Cosmochimica Acta 73, 6868–6893. https://doi.org/10.1016/j.gca.2009.08.021

Klein, F., Humphris, S., Bach, W., 2020. Brucite formation and dissolution in oceanic serpentinite. Geochemical Perspectives Letters 16, 1–5. https://doi.org/10.7185/geochemlet.2035

Klein, F., Marschall, H.R., Bowring, S.A., Humphris, S.E., Horning, G., 2017. Mid-ocean Ridge Serpentinite in the Puerto Rico Trench: from Seafloor Spreading to Subduction. Journal of Petrology 58, 1729–1754. https://doi.org/10.1093/petrology/egx071

Kodolányi, J., Pettke, T., Spandler, C., Kamber, B.S., Gméling, K., 2012. Geochemistry of Ocean Floor and Fore-arc Serpentinites: Constraints on the Ultramafic Input to Subduction Zones. Journal of Petrology 53, 235–270. https://doi.org/10.1093/petrology/egr058

Korzhinskii, D.S., 1968. The theory of metasomatic zoning. Mineralium Deposita 3, 222–231. https://doi.org/10.1007/BF00207435

Korzhinskii, D.S., 1965. The theory of systems with perfectly mobile components and processes of mineral formation. American Journal of Science 263, 193–205. https://doi.org/10.2475/ajs.263.3.193

Lafuente, B., Downs, R.T., Yang, H., Stone, N., 2015. Highlights in Mineralogical Crystallography, in: Armbruster, T., Danisi, R.M. (Eds.), . De Gruyter (O), pp. 1–30. https://doi.org/10.1515/9783110417104-003

Lagabrielle, Y., Lemoine, M., 1997. Alpine, Corsican and Apennine ophiolites: the slow-spreading ridge model. Comptes Rendus de l'Académie des Sciences - Series IIA - Earth and Planetary Science 325, 909–920. https://doi.org/10.1016/S1251-8050(97)82369-5

Lanari, P., Engi, M., 2017. Local Bulk Composition Effects on Metamorphic Mineral Assemblages. Reviews in Mineralogy and Geochemistry 83, 55–102. https://doi.org/10.2138/rmg.2017.83.3

Malatesta, C., Crispini, L., Federico, L., Capponi, G., Scambelluri, M., 2012a. The exhumation of high pressure ophiolites (Voltri Massif, Western Alps): Insights from structural and petrologic data on metagabbro bodies. Tectonophysics 568–569, 102–123. https://doi.org/10.1016/j.tecto.2011.08.024

Malatesta, C., Crispini, L., Federico, L., Capponi, G., Scambelluri, M., 2012b. The exhumation of high pressure ophiolites (Voltri Massif, Western Alps): Insights from structural and petrologic data on metagabbro bodies. Tectonophysics 568–569, 102–123. https://doi.org/10.1016/j.tecto.2011.08.024

Manatschal, G., Müntener, O., 2009. A type sequence across an ancient magma-poor ocean–continent transition: the example of the western Alpine Tethys ophiolites. Tectonophysics 473, 4–19. https://doi.org/10.1016/j.tecto.2008.07.021

Manning, C., 2007. Solubility of corundum + kyanite in H2O at 700 C and 10 kbar: evidence for Al_Si complexing at high pressure and temperature. Geofluids 7, 258–269.

Marschall, H., Altherr, R., Gméling, K., Kasztovszky, Z., 2009. Lithium, boron and chlorine as tracers for metasomatism in high-pressure metamorphic rocks: A case study from Syros (Greece). MINERALOGY AND PETROLOGY 95, 291–302. https://doi.org/10.1007/s00710-008-0032-3

Marschall, H.R., Schumacher, J.C., 2012. Arc magmas sourced from mélange diapirs in subduction zones. Nature Geosci 5, 862–867. https://doi.org/10.1038/ngeo1634

McDonough, W.F., Sun, S. -s., 1995. The composition of the Earth. Chemical Geology 120, 223–253. https://doi.org/10.1016/0009-2541(94)00140-4

Messiga, B., Piccardo, G.B., Ernst, W.G., 1983. High-pressure Eo-Alpine parageneses developed in magnesian metagabbros, Gruppo di Voltri, Western Liguria, Italy. Contributions to Mineralogy and Petrology 83, 1–15. https://doi.org/10.1007/BF00373074

Messiga, B., Scambelluri, M., 1991. Retrograde P-T-t path for the Voltri Massif eclogites (Ligurian Alps, Italy): some tectonic implications. Journal of Metamorphic Geology 9, 93–109. https://doi.org/10.1111/j.1525-1314.1991.tb00506.x

Miller, D.P., Marschall, H.R., Schumacher, J.C., 2009. Metasomatic formation and petrology of blueschist-facies hybrid rocks from Syros (Greece): Implications for reactions at the slab–mantle interface. Lithos 107, 53–67. https://doi.org/10.1016/j.lithos.2008.07.015

Mori, Y., Shigeno, M., Nishiyama, T., 2014. Fluid-metapelite interaction in an ultramafic mélange: implications for mass transfer along the slab-mantle interface in subduction zones. Earth, Planets and Space 66, 47. https://doi.org/10.1186/1880-5981-66-47

Mottl, M.J., Wheat, C.G., Fryer, P., Gharib, J., Martin, J.B., 2004. Chemistry of springs across the Mariana forearc shows progressive devolatilization of the subducting plate. Geochimica et Cosmochimica Acta 68, 4915–4933. https://doi.org/10.1016/j.gca.2004.05.037

Nielsen, S.G., Marschall, H.R., 2017. Geochemical evidence for mélange melting in global arcs. Sci Adv 3. https://doi.org/10.1126/sciadv.1602402

Okamoto, A.S., Verberne, B.A., Niemeijer, A.R., Takahashi, M., Shimizu, I., Ueda, T., Spiers, C.J., 2019. Frictional Properties of Simulated Chlorite Gouge at Hydrothermal Conditions: Implications for Subduction Megathrusts. Journal of Geophysical Research: Solid Earth 124, 4545–4565. https://doi.org/10.1029/2018JB017205

Palin, R.M., Weller, O.M., Waters, D.J., Dyck, B., 2016. Quantifying geological uncertainty in metamorphic phase equilibria modelling; a Monte Carlo assessment and implications for tectonic interpretations. Geoscience Frontiers 7, 591–607. https://doi.org/10.1016/j.gsf.2015.08.005

Paulick, H., Bach, W., Godard, M., De Hoog, J.C.M., Suhr, G., Harvey, J., 2006. Geochemistry of abyssal peridotites (Mid-Atlantic Ridge, 15°20′N, ODP Leg 209): Implications for fluid/rock interaction in slow spreading environments. Chemical Geology 234, 179–210. https://doi.org/10.1016/j.chemgeo.2006.04.011

Pawley, A., 2003. Chlorite stability in mantle peridotite: the reaction clinochlore+enstatite=forsterite+pyrope+H2O. Contributions to Mineralogy and Petrology 144, 449–456. https://doi.org/10.1007/s00410-002-0409-y

Peacock, S.M., Wang, K., 2021. On the Stability of Talc in Subduction Zones: A Possible Control on the Maximum Depth of Decoupling Between the Subducting Plate and Mantle Wedge. Geophysical Research Letters 48, e2021GL094889. https://doi.org/10.1029/2021GL094889

Penniston-Dorland, S.C., Ferry, J.M., 2008. Element mobility and scale of mass transport in the formation of quartz veins during regional metamorphism of the Waits River Formation, east-central Vermont. American Mineralogist 93, 7–21. https://doi.org/10.2138/am.2008.2461

Penniston-Dorland, S.C., Gorman, J.K., Bebout, G.E., Piccoli, P.M., Walker, R.J., 2014. Reaction rind formation in the Catalina Schist: Deciphering a history of mechanical mixing and

metasomatic alteration. Chemical Geology 384, 47–61. https://doi.org/10.1016/j.chemgeo.2014.06.024

Peters, D., Bretscher, A., John, T., Scambelluri, M., Pettke, T., 2017a. Fluid-mobile elements in serpentinites: Constraints on serpentinisation environments and element cycling in subduction zones. Chemical Geology 466, 654–666. https://doi.org/10.1016/j.chemgeo.2017.07.017

Peters, D., Bretscher, A., John, T., Scambelluri, M., Pettke, T., 2017b. Fluid-mobile elements in serpentinites: Constraints on serpentinisation environments and element cycling in subduction zones. Chemical Geology 466, 654–666. https://doi.org/10.1016/j.chemgeo.2017.07.017

Peters, D., Pettke, T., John, T., Scambelluri, M., 2020. The role of brucite in water and element cycling during serpentinite subduction – Insights from Erro Tobbio (Liguria, Italy). Lithos 360–361, 105431. https://doi.org/10.1016/j.lithos.2020.105431

Petriglieri, J.R., Salvioli-Mariani, E., Mantovani, L., Tribaudino, M., Lottici, P.P., Laporte-Magoni, C., Bersani, D., 2015. Micro-Raman mapping of the polymorphs of serpentine. Journal of Raman Spectroscopy 46, 953–958. https://doi.org/10.1002/jrs.4695

Piccardo, G.B., 2013. Subduction of a fossil slow–ultraslow spreading ocean: a petrology-constrained geodynamic model based on the Voltri Massif, Ligurian Alps, Northwest Italy. International Geology Review 55, 787–803. https://doi.org/10.1080/00206814.2012.746806

Pogge von Strandmann, P.A.E., Dohmen, R., Marschall, H.R., Schumacher, J.C., Elliott, T., 2015. Extreme Magnesium Isotope Fractionation at Outcrop Scale Records the Mechanism and Rate at which Reaction Fronts Advance. Journal of Petrology 56, 33–58. https://doi.org/10.1093/petrology/egu070

Rampone, E., Hofmann, A., 2012. A global overview of isotopic heterogeneities in the oceanic mantle. Lithos 148, 247–261. https://doi.org/10.1016/j.lithos.2012.06.018

Sanford, R.F., 1982. Growth of ultramafic reaction zones in greenschist to amphibolite facies metamorphism. American Journal of Science 282, 543–616. https://doi.org/10.2475/ajs.282.5.543

Scambelluri, M., Cannaò, E., Gilio, M., 2019. The water and fluid-mobile element cycles during serpentinite subduction. A review. European Journal of Mineralogy 31, 405–428. https://doi.org/10.1127/ejm/2019/0031-2842

Scambelluri, M., Müntener, O., Hermann, J., Piccardo, G.B., Trommsdorff, V., 1995a. Subduction of water into the mantle: History of an Alpine peridotite. Geology 23, 459–462. https://doi.org/10.1130/0091-7613(1995)023<0459:SOWITM>2.3.CO;2

Scambelluri, M., Müntener, O., Hermann, J., Piccardo, G.B., Trommsdorff, V., 1995b. Subduction of water into the mantle: history of an Alpine peridotite. Geology 23, 459–462.

Scambelluri, M., Piccardo, G.B., Philippot, P., Robbiano, A., Negretti, L., 1997. High salinity fluid inclusions formed from recycled seawater in deeply subducted alpine serpentinite. Earth and Planetary Science Letters 148, 485–499. https://doi.org/10.1016/S0012-821X(97)00043-5

Scambelluri, M., Rampone, E., 1999. Mg-metasomatism of oceanic gabbros and its control on Ti-clinohumite formation during eclogitization. Contributions to Mineralogy and Petrology 135, 1–17. https://doi.org/10.1007/s004100050494

Scambelluri, M., Strating, E.H.H., Piccardo, G.B., Vissers, R.L.M., Rampone, E., 1991. Alpine olivine- and titanian clinohumite-bearing assemblages in the Erro-Tobbio peridotite (Voltri Massif, NW Italy). Journal of Metamorphic Geology 9, 79–91. https://doi.org/10.1111/j.1525-1314.1991.tb00505.x

Schmidt, M.W., Poli, S., 2014. 4.19 - Devolatilization During Subduction, in: Treatise on Geochemistry: Second Edition. pp. 669–701. https://doi.org/10.1016/B978-0-08-095975-7.00321-1

Schmidt, M.W., Poli, S., 1998. Experimentally based water budgets for dehydrating slabs and consequences for arc magma generation. Earth and Planetary Science Letters 163, 361–379. https://doi.org/10.1016/S0012-821X(98)00142-3

Schwarzenbach, E.M., Vogel, M., Früh-Green, G.L., Boschi, C., 2021. Serpentinization, Carbonation, and Metasomatism of Ultramafic Sequences in the Northern Apennine Ophiolite (NW Italy). Journal of Geophysical Research: Solid Earth 126, e2020JB020619. https://doi.org/10.1029/2020JB020619

Smye, A.J., Seman, S.M., Scambelluri, M., Starr, P.G., Federico, L., 2021. Exhumation dynamics of high-pressure metamorphic rocks from the Voltri Unit, Western Alps: constraints from

phengite Rb–Sr geochronology. Contributions to Mineralogy and Petrology 176, 14. https://doi.org/10.1007/s00410-020-01767-0

Sorensen, S.S., Grossman, J.N., 1989. Enrichment of trace elements in garnet amphibolites from a paleo-subduction zone: Catalina Schist, southern California. Geochimica et Cosmochimica Acta 53, 3155–3177. https://doi.org/10.1016/0016-7037(89)90096-3

Spandler, C., Hermann, J., Faure, K., Mavrogenes, J.A., Arculus, R.J., 2008. The importance of talc and chlorite "hybrid" rocks for volatile recycling through subduction zones; evidence from the high-pressure subduction mélange of New Caledonia. Contributions to Mineralogy and Petrology 155, 181–198. https://doi.org/10.1007/s00410-007-0236-2

Spandler, C., Pettke, T., Hermann, J., 2014. Experimental study of trace element release during ultrahigh-pressure serpentinite dehydration. Earth and Planetary Science Letters 391, 296–306. https://doi.org/10.1016/j.epsl.2014.02.010

Stalder, R., Foley, S.F., Brey, G.P., Horn, I., 1998. Mineral-aqueous fluid partitioning of trace elements at 900–1200°C and 3.0–5.7 GPa: new experimental data for garnet, clinopyroxene, and rutile, and implications for mantle metasomatism. Geochimica et Cosmochimica Acta 62, 1781–1801. https://doi.org/10.1016/S0016-7037(98)00101-X

Starr, P.G., Broadwell, K.S., Dragovic, B., Scambelluri, M., Haws, A.A., Caddick, M.J., Smye, A.J., Baxter, E.F., 2020. The subduction and exhumation history of the Voltri Ophiolite, Italy: Evaluating exhumation mechanisms for high-pressure metamorphic massifs. Lithos 376–377, 105767. https://doi.org/10.1016/j.lithos.2020.105767

Sverjensky, D.A., 2019. Thermodynamic modelling of fluids from surficial to mantle conditions. Journal of the Geological Society 176, 348. https://doi.org/10.1144/jgs2018-105

Sverjensky, D.A., Harrison, B., Azzolini, D., 2014. Water in the deep Earth: The dielectric constant and the solubilities of quartz and corundum to 60kb and 1200°C. Geochimica et Cosmochimica Acta 129, 125–145. https://doi.org/10.1016/j.gca.2013.12.019

Syracuse, E.M., Keken, P.E. van, Abers, G.A., 2010. The global range of subduction zone thermal models. Physics of the Earth and Planetary Interiors 183, 73–90. https://doi.org/10.1016/j.pepi.2010.02.004

Thompson, A.B., 1975. Calc-Silicate Diffusion Zones between Marble and Pelitic Schist. Journal of Petrology 16, 314–346. https://doi.org/10.1093/petrology/16.1.314

Thompson, J.B., 1970. Geochemical reaction and open systems. Geochimica et Cosmochimica Acta 34, 529–551. https://doi.org/10.1016/0016-7037(70)90015-3

Tostevin, R., Shields, G.A., Tarbuck, G.M., He, T., Clarkson, M.O., Wood, R.A., 2016. Effective use of cerium anomalies as a redox proxy in carbonate-dominated marine settings. Chemical Geology 438, 146–162. https://doi.org/10.1016/j.chemgeo.2016.06.027

Tribuzio, R., Messiga, B., Vannucci, R., Bottazzi, P., 1996. Rare earth element redistribution during high-pressure–low-temperature metamorphism in ophiolitic Fe-gabbros (Liguria, northwestern Italy): Implications for light REE mobility in subduction zones. Geology 24, 711–714. https://doi.org/10.1130/0091-7613(1996)024<0711:REERDH>2.3.CO;2

Tutolo, B.M., Mildner, D.F.R., Gagnon, C.V.L., Saar, M.O., Seyfried, W.E., Jr., 2016. Nanoscale constraints on porosity generation and fluid flow during serpentinization. Geology 44, 103–106. https://doi.org/10.1130/G37349.1

van Keken, P.E., Hacker, B.R., Syracuse, E.M., Abers, G.A., 2011. Subduction factory: 4. Depth-dependent flux of H2O from subducting slabs worldwide. Journal of Geophysical Research: Solid Earth 116. https://doi.org/10.1029/2010JB007922

Vignaroli, G., Rossetti, F., Bouybaouene, M., Massonne, H.-J., Theye, T., Fsaccenna, C., Funiciello, R., 2005. A counter-clockwise P–T path for the Voltri Massif eclogites (Ligurian Alps, Italy). Journal of Metamorphic Geology 23, 533–555. https://doi.org/10.1111/j.1525-1314.2005.00592.x

Vitale Brovarone, A., Sverjensky, D.A., Piccoli, F., Ressico, F., Giovannelli, D., Daniel, I., 2020. Subduction hides high-pressure sources of energy that may feed the deep subsurface biosphere. Nature Communications 11, 3880. https://doi.org/10.1038/s41467-020-17342-x

Wada, I., Wang, K., 2009. Common depth of slab-mantle decoupling: Reconciling diversity and uniformity of subduction zones. Geochemistry, Geophysics, Geosystems 10. https://doi.org/10.1029/2009GC002570

Watson, E.B., Baxter, E.F., 2007. Diffusion in solid-Earth systems. Earth and Planetary Science Letters 253, 307–327. https://doi.org/10.1016/j.epsl.2006.11.015

White, R.W., Powell, R., Clarke, G.L., 2002. The interpretation of reaction textures in Fe-rich metapelitic granulites of the Musgrave Block, central Australia: constraints from mineral equilibria calculations in the system K2O–FeO–MgO–Al2O3–SiO2–H2O–TiO2–Fe2O3.

Journal of Metamorphic Geology 20, 41–55. https://doi.org/10.1046/j.0263-4929.2001.00349.x

Whitney, D.L., Evans, B.W., 2010. Abbreviations for names of rock-forming minerals. American Mineralogist 95, 185–187. https://doi.org/10.2138/am.2010.3371

Wolery, T.J., 1992. EQ3/6, a software package for geochemical modeling of aqueous systems: Package overview and installation guide (Version 7.0). United States. https://doi.org/10.2172/138894

Workman, R.K., Hart, S.R., 2005. Major and trace element composition of the depleted MORB mantle (DMM). Earth and Planetary Science Letters 231, 53–72. https://doi.org/10.1016/j.epsl.2004.12.005

Zhang, Z., Duan, Z., 2005. Prediction of the PVT properties of water over wide range of temperatures and pressures from molecular dynamics simulation. Physics of the Earth and Planetary Interiors 149, 335–354. https://doi.org/10.1016/j.pepi.2004.11.003

Zhu, G., Gerya, T.V., Yuen, D.A., Honda, S., Yoshida, T., Connolly, J.A.D., 2009. Three-dimensional dynamics of hydrous thermal-chemical plumes in oceanic subduction zones. Geochemistry, Geophysics, Geosystems 10. https://doi.org/10.1029/2009GC002625

Chapter 3

Preferential Formation of Chlorite over Talc during Si-metasomatism of Ultramafic Rocks in Subduction Zones

This chapter was originally published as:

Codillo, E. A., Klein, F., & Marschall, H. R. 2022. Preferential Formation of Chlorite over Talc during Si-metasomatism of Ultramafic Rocks in Subduction Zones. Geophysical Research Letters, 49, e2022GL100218. https://doi.org/10.1029/2022GL100218. Used with permission as granted in the original copyright agreement.

Abstract

Talc formation via silica-metasomatism of ultramafic rocks is believed to play key roles in subduction zone processes. Yet, the conditions of talc formation remain poorly constrained. We used thermodynamic reaction-path models to assess the formation of talc at the slab-mantle interface and show that it is restricted to a limited set of pressure–temperature conditions, protolith, and fluid compositions. In contrast, our models predict that chlorite formation is ubiquitous at conditions relevant to the slab-mantle interface of subduction zones. The scarcity of talc and abundance of chlorite is evident in the rock record of exhumed subduction zone terranes. Talc formation during Si-metasomatism may thus play a more limited role in volatile cycling, strain localization, and in controlling the decoupling-coupling transition of the plate interface. Conversely, the observed and predicted ubiquity of chlorite corroborates its prominent role in slab-mantle interface processes that previous studies attributed to talc.

Plain Language Summary

In subduction zones, talc can form during chemical reactions of mantle rocks with silica-enriched fluids at the interface between descending oceanic plates and the overriding mantle. Its formation and distribution in subduction zones are believed to affect the volatile budget, rheological properties, and the down-dip limit of the decoupling of the slab-mantle interface. Therefore, illuminating the conditions that facilitate talc formation at high pressure-temperature conditions is key in assessing its roles in fundamental subduction zone processes. Using thermodynamic reaction-path models, we show that the formation of talc at the slab-mantle interface is restricted to a limited set of environmental conditions, because its formation is highly sensitive to the compositions of the mantle rocks and reactant fluids. Contrary to common belief, talc is unlikely to form in high abundance in ultramafic rocks metasomatized by Si-rich slab-derived fluids. Rather, our models predict the ubiquitous formation of chlorite along with other silicate minerals during Si-metasomatism due to the competing effects from other dissolved components that favor their formation over talc. This study calls into question the importance of talc during Si-metasomatism in subduction zones but highlights the more predominant role of chlorite.

1 Introduction

Talc [$(Mg,Fe)_3Si_4O_{10}(OH)_2$] is a hydrous phyllosilicate, which forms at the expense of ultramafic rocks in the oceanic crust, orogenic belts, and subduction zones (Boschi et al., 2006; Peacock and Hyndman, 1999). It contains ~5 wt.% water and can be stable to high temperatures (*T*) and pressures (*P*), suggesting that it is a potentially important mineral in the global water cycle (Bebout, 1991; Bose and Ganguly, 1995; Peacock, 1990). In wet conditions, talc is mechanically weak and can localize shear stress, thus affecting the rheological and seismogenic properties of faults and plate boundaries (Chen et al., 2017; Hirauchi et al., 2020, 2013; Moore and Lockner, 2007).

In subduction zones, pervasive mechanical mixing of sediments, mafic, and ultramafic rocks (Bebout, 2013; Bebout and Barton, 2002; Bebout and Penniston-Dorland, 2016) facilitates metasomatism which can favor talc formation (Manning, 1995; Peacock and Hyndman, 1999). Talc can form in high-pressure ultramafic rocks that have been enriched in SiO_2 through the reaction with silica-bearing aqueous fluids (Manning, 1997, 1995). Based on geophysical data, a ~4 km thick layer of altered ultramafic rock enriched in talc was inferred to be present at the slab-mantle interface in the central Mexican subduction zone (Kim et al., 2013).

Rheological contrasts between juxtaposed lithologies lead to strain partitioning and fluid flow along lithological boundaries further promoting metasomatic reactions (Ague, 2007). Previous laboratory friction experiments have shown that wet talc can be substantially weaker than antigorite, chlorite, and other hydrous minerals (Chen et al., 2017; Hirauchi et al., 2020, 2013; Moore and Lockner, 2007), which would promote mechanical weakening and decoupling of the slab-mantle interface (Abers et al., 2020; Marschall and Schumacher, 2012; Wada et al., 2008). The changes in the rheological properties and stress states of materials along the plate interface may manifest themselves as seismicity, such as slow slip events (Beroza and Ide, 2011; Rubin, 2008). The pressure-sensitive breakdown of talc into secondary mineral assemblage has recently been suggested to control the extent of mechanical coupling along the plate interface (Peacock and Wang, 2021). Therefore, illuminating the conditions that facilitate talc formation at high *P*-*T* conditions is important in assessing its importance in plate interface processes.

Metamorphosed siliceous and pelitic sediments, as well as basaltic crustal rocks commonly contain quartz, and fluids in equilibrium with these rocks are quartz saturated or even super-

saturated (Hacker et al., 2003; Manning, 1995). While fluids in equilibrium with subducted metabasalt and metapelite likely exhibit elevated silica activity, the presence of other silicate minerals (e.g., kyanite, garnet, paragonite, chlorite, epidote minerals) coexisting with quartz would also affect the speciation of other dissolved major elements (e.g., Al, Mg, Ca, Fe). The elevated *P-T* conditions in subduction zones are also expected to enhance the solubilities of dissolved elements through the formation of aqueous complexes (Manning, 2007, 2004; Sverjensky et al., 2014), which can directly affect metasomatic processes. However, such effects have remained understudied as the dielectric constant of water at pressures higher than 0.5 GPa was poorly constrained (Helgeson et al., 1981; Shock et al., 1992). The recent development of the Deep Earth Water (DEW) model allows for the prediction of the equilibrium constants of reactions to model fluid-rock interactions at high *P-T* conditions relevant to subduction zones (Huang and Sverjensky, 2019; Sverjensky, 2019; Sverjensky et al., 2014).

We used thermodynamic reaction path models to evaluate the successions of metasomatic reactions between ultramafic rocks and fluids previously equilibrated with metapelite or metabasalt over a range of *P-T* conditions relevant to slab-top geotherms of subduction zones. We compare our predictions with exhumed metamorphic rock record with known *P-T* histories. We discuss the petrological controls on talc and chlorite formation and highlight the implications of slab-derived fluid metasomatism of ultramafic rocks in subduction zones.

2 Methods

Thermodynamic reaction path models were set up to assess changes in mineralogy and fluid composition during Si-metasomatism of ultramafic rocks. Fluids equilibrated with metamorphosed mid-ocean ridge basalt (MORB) or a metapelite were subsequently allowed to react with ultramafic rocks at subduction zone conditions. To evaluate the effects of ultramafic protolith compositions on reaction pathways, we used monomineralic antigorite [$Mg_{48}Si_{34}O_{85}(OH)_{62}$], lherzolite (depleted MORB mantle, DMM), harzburgite (HZ1), and a more refractory harzburgite (HZ2) (Table S1). Models were calculated over a range of *P-T* conditions (1–2.5 GPa, 300–600 °C), and a range of fluid-to-rock (f/r) mass ratios, using the EQ3/6 software package version 6 (Wolery, 1992) and DEW database (Huang and Sverjensky, 2019; Sverjensky et al., 2014). The reaction-path portrays a system that is initially fluid-dominated, such as in a

fracture or vein, but then becomes increasingly rock-dominated as more ultramafic rock is added, such as in the rock matrix adjacent to a fracture or vein. We explored a range of f/r (i.e. f/r >> 1) to simulate conditions likely relevant to high permeability zones, such as along lithologic contacts and shear zones (Codillo, 2022). We also calculated reaction-path models to investigate the metasomatism of ultramafic rocks by fluids that previously equilibrated with quartz only (i.e. compositions of other dissolved elements are set to trace concentrations). Details on the reaction-path model setup are provided in the Supplementary Information.

3 Results

3.1. Predicted compositions of fluids in equilibrium with metabasalt, metapelite, or quartz

The Si concentration of a quartz-saturated fluid is predicted to increase steadily with increasing temperature and pressure. However, pressure appears to have a limited effect on the fluid composition when compared with changes in temperature. The concentrations of dissolved Mg, Si, and Al in equilibrium with metabasalt are predicted to increase steadily with increasing temperature while the concentration of dissolved Ca shows no systematic trends in response to changes in temperature (Fig. S1, Table S2). The concentrations of dissolved Al and Si in equilibrium with metapelite are predicted to increase with increasing temperature. The concentration of dissolved Mg is predicted to decrease with increasing temperature from 300 to 400 °C, and then slightly increase between 500 and 600 °C.

3.2. Modeled metasomatism of ultramafic rocks

To illustrate the effects of *P*, *T*, rock and fluid compositions on the metasomatic formation of talc, representative model results at 300 °C and 1.5 GPa are presented in Figs. 1, 2, and S2. In addition, the predicted mineral assemblages of reaction-path models that simulated Si-metasomatism at higher temperatures (400–600 °C) at 1.5 GPa are shown in Figs. S3-S5. All model results, including those for higher pressures, are available in the data repository. Models simulating the reaction of quartz-saturated fluid with antigorite predicted the formation of talc coexisting with quartz at all modeled *P-T* conditions (Table S3). At 300 °C and 1.5 GPa, metasomatism of DMM lherzolite is predicted to result in the formation of talc, clinopyroxene, and chlorite. At similar *P-T* condition, our models suggests the formation of talc together with

clinopyroxene + orthopyroxene + chlorite in the reaction between quartz-saturated fluid and a harzburgite (HZ1). Over the modeled conditions, metasomatism of DMM lherzolite by a quartz-saturated fluid predicted talc formation from 1.5 to 2.5 GPa, from 300 to up to 600 °C (Table S3). Metasomatism of HZ1 by a quartz-saturated fluid also predicted talc formation but at lower temperature (≤400 °C) compared with reaction with DMM. In contrast, talc is not predicted to form during metasomatism of the more refractory harzburgite (HZ2) in any of the modeled conditions (Table S3). In general, the predicted concentrations of dissolved Mg and Al increase, dissolved Si concentrations decrease, while dissolved Ca concentrations initially decrease then increase with decreasing f/r (Fig. 1).

Metasomatism of antigorite by fluids previously in equilibrium with a metabasalt is predicted to form talc coexisting with chlorite + clinopyroxene (diopside) + olivine at 300 °C and 1.5 GPa (Fig. S2). However, under the same *P-T* condition, talc is not predicted to form during metasomatism of DMM, HZ1, and HZ2. Instead, the models suggest the formation of Ca and Al-bearing minerals such as clinopyroxene, chlorite, garnet, pumpellyite, wollastonite, and diaspore (Fig. 2d-f). Our models predict that metasomatism of DMM, HZ1, and HZ2 by fluids that previously equilibrated with metabasalt yields talc over a narrow range of *P-T* condition, between 300 and 400 °C at 2 GPa (Table S3). With decreasing f/r, the concentrations of dissolved Mg and Al are predicted to increase while concentrations of dissolved Si are predicted to decrease during reaction with DMM and HZ1. During metasomatism of HZ2, concentrations of dissolved Al and Ca are predicted to initially increase and then decrease, while concentrations of dissolved Mg and Si initially decrease then increase with decreasing f/r (Fig. 1).

Metasomatism of antigorite by fluids that were previously in equilibrium with a metapelite is predicted to form talc coexisting with chlorite + quartz + diaspore at 300 °C and 1.5 GPa (Fig. S2). Metasomatism of HZ2 by a metapelite-equilibrated fluid is predicted to yield talc coexisting with chlorite + quartz + antigorite + tremolite at 300 °C and 1.5 GPa. Our models suggest that metasomatism of DMM and HZ1 yields chlorite, quartz, clinopyroxene, lawsonite, and diaspore under similar *P-T* condition. If the fluid previously equilibrated with metapelite, the models predict that talc formation is favored during metasomatism of more refractory ultramafic compositions (Table S3). With decreasing f/r, the concentrations of dissolved Si, Ca, and Al are predicted to increase while dissolved Mg decreases (Fig. 1).

4 Discussion

4.1. Effects of fluid and rock compositions on talc formation

Talc can form during serpentinization, closed-system metamorphism of serpentinite, and metasomatism of ultramafic rocks. Talc formation is favored during low-pressure serpentinization of pyroxene at temperatures of 400 °C or higher where olivine is stable in the presence of water (Evans, 1977; Frost and Beard, 2007; Klein et al., 2009). Prograde metamorphism of antigorite can yield olivine, talc, and water whereas retrograde metamorphism of antigorite can form chrysotile and talc (Schwartz et al., 2013). The volume of talc formation during serpentinization or closed-system metamorphism is small when compared with other reaction products. In contrast, the formation of sizeable talc deposits, such as those in the exhumed high-pressure terrane on Santa Catalina Island (USA), would require an open-system reaction involving the external addition of silica-bearing fluids into serpentinite (Bebout and Barton, 2002). The formation of talc at the expense of ultramafic rocks can be assessed using the simplified MgO-SiO_2-H_2O (MSH) system (Bowen and Tuttle, 1949; Evans, 1977).

Serpentinization

(R1) $90\ MgSiO_3 + 45\ H_2O = Mg_{48}Si_{34}O_{85}(OH)_{62} + 14\ Mg_3Si_4O_{10}(OH)_2$

(orthopyroxene) (antigorite) (talc)

Metamorphism

(R2) $5\ Mg_7Si_8O_{22}(OH)_2 + 2\ H_2O = 9\ Mg_3Si_4O_{10}(OH)_2 + 4\ Mg_2SiO_4$

(anthophyllite) (talc) (olivine)

(R3) $Mg_{48}Si_{34}O_{85}(OH)_6 = 18\ Mg_2SiO_4 + 4\ Mg_3Si_4O_{10}(OH)_2 + 27\ H_2O$

(antigorite) (olivine) (talc)

Si-metasomatism

(R4) $3\ Mg_2SiO_4 + 5\ SiO_{2\,(aq)} + 2\ H_2O = 2\ Mg_3Si_4O_{10}(OH)_2$

(olivine) (talc)

(R5) $3\ MgSiO_3 + SiO_{2\,(aq)} + H_2O = Mg_3Si_4O_{10}(OH)_2$

(orthopyroxene) (talc)

(R6) $Mg_{48}Si_{34}O_{85}(OH)_{62} + 30\ SiO_{2\ (aq)} = 16\ Mg_3Si_4O_{10}(OH)_2 + 15\ H_2O$

(antigorite) (talc)

While serpentinization and metamorphism of serpentinite can proceed without the addition or removal of components, except for water (e.g., R1–R3), the formation of talc may also be favored via the addition of SiO_2 to – or the removal of MgO from – an ultramafic rock. However, factors other than SiO_2 addition and MgO removal need to be considered when assessing the stability of talc, notably the compositions of the reactant rock and fluid, f/r, and temperature (Klein et al., 2013).

Our model predictions at 300 °C and 1.5 GPa suggest that the reaction of a quartz-saturated fluid with DMM, HZ1, or HZ2 can yield minerals such as chlorite, garnet, clinopyroxene, orthopyroxene, pumpellyite, in addition to talc. The formation of talc is predicted to be more favorable during Si-metasomatism of DMM and HZ1 when compared with HZ2 which we attribute to the higher bulk-rock Al contents and lower Mg/Si ratios in less melt-depleted mantle rocks (Fig. S6). The lower bulk-rock Al contents and higher Mg/Si of more melt-depleted mantle rocks (here HZ2) favor the formation of Al-bearing phases such as chlorite, paragonite, and garnet rather than talc (Fig. 2). Si-metasomatism of fertile mantle rocks is predicted to favor the formation of Ca-bearing phases such as clinopyroxene, lawsonite, and grossular-rich garnet due to their elevated bulk-rock Ca contents relative to refractory harzburgite.

Our models predict that metasomatism of antigorite by fluids that previously equilibrated with metabasalt can favor the formation of chlorite and clinopyroxene, in addition to talc (Fig. S2; Table S3). However, if the fluid equilibrates with metabasalt before reacting with peridotite (DMM, HZ1, and HZ2), talc formation is predicted to occur only between 300–400 °C at 2 GPa (Table S3). A possible explanation is the relatively high Si concentrations and low Mg/Si ratios of the fluid at these conditions when compared with similar temperatures at different pressures. We attribute talc formation during metasomatism of refractory HZ2 peridotite by fluids that previously equilibrated with metapelite with the relatively low bulk-rock Al contents and high Mg/Si ratios, as well as the low dissolved Al content and low Al/Si ratio of the reactant fluid (Table S3; Fig. S1, S6).

The reaction-path models suggest that the compositions of reacting fluids and whole-rocks at a given *P*-*T* condition are pivotal in controlling the chemical affinity to form talc. This implies that the formation of talc may be restricted to specific domains where rock and fluid compositions, as well as pressure and temperature are favorable, e.g., where sediments and refractory harzburgite are juxtaposed at 300–400 °C and 1–2 GPa. However, juxtaposition of mafic and ultramafic rocks is predicted to favor the formation of Ca- and Al-bearing phases such as chlorite, clinopyroxene, lawsonite, garnet, epidote, and paragonite over talc. A fluid that is Si-rich but Ca- and Al-poor could produce talc upon reaction with fertile ultramafic compositions; however, such fluid compositions seem unlikely considering the abundance of Ca- and Al-bearing phases in subducting slabs that become unstable during metamorphism.

4.2. Limited talc formation along the subduction interface

The thermal structure of subducting slabs is of central importance regarding the *P*-*T* stability of hydrous minerals. In addition to *P* and *T*, our calculations suggest that rock and fluid compositions should not be ignored when the stability of hydrous minerals in subduction zones is evaluated (Fig. 3a). Fig. 3b summarizes the conditions where talc formation is predicted relative to distinct slab-top geotherms (Syracuse et al., 2010). As talc formation during Si-metasomatism is favored at relatively low temperatures and pressures, we expect to find more talc in cold subduction zones, such as Izu-Bonin-Mariana and Tonga, than in warm subduction zones such as in Cascadia and Mexico. If this is correct, more extensive talc formation via Si-metasomatism of ultramafic rocks along the slab-mantle interface at subarc depths may be limited to cold subduction zones. We also infer that talc formation at the slab-mantle interface may be limited in subduction zones where sediments are scraped off before subduction or if the sediment layer of the subducting oceanic plate is thin.

Talc-bearing metamorphic rocks from the Arosa Zone (Switzerland) and on Santa Catalina Island (USA) can be used to further evaluate our model predictions. The Arosa Zone exhibits an exhumed plate interface that includes calcareous and pelitic schists, metabasite, marble, serpentinite, and chlorite and talc schists (Condit et al., 2022). Talc schist forms a 2–4 m thick layer between ultramafic and mafic rocks. While the *P*-*T* conditions of talc and chlorite formation at Arosa are unknown, it is estimated that the latest stage of subduction-related deformation of the region may have occurred at 300–350 °C and pressures above 0.7 GPa (Bachmann et al., 2009). If

we consider this estimate as a minimum bound for talc (and chlorite) formation due to its deformation texture, this would be comparable and consistent with our model prediction where talc can form at temperature ≤400 °C at 1 GPa.

On Santa Catalina Island (USA), a talc-bearing metasomatic reaction zone developed between serpentinite and metasediments. The heterogeneous mixture of metamorphosed rocks at Catalina recorded a wide range of *P-T* conditions of between ~200 ºC and ~700 °C and between 0.6 GPa and 1.2 GPa. The talc-bearing metamorphosed rocks in this locality record amphibolite-facies conditions (600–700 °C). This temperature range is significantly higher than the anticipated temperature range for talc formation based on our model predictions for pressures of less than 2 GPa. However, previous petrologic studies on Catalina have suggested that talc must have formed during or after the exhumation-related, chrysotile-bearing deformation observed in the serpentinite domains (Hirauchi et al., 2020; Hirauchi and Yamaguchi, 2007).

Talc can also form during mineral carbonation of ultramafic rocks (Okamoto et al., 2021). This process can transform a Si-undersaturated peridotite or serpentinite into soapstone (mainly talc and magnesite) or even listvenite (quartz and magnesite) without adding Si, as CO_2 reacts with Mg, Fe, and Ca to form carbonate, allowing Si to react with serpentine to form talc (Grozeva et al., 2017; Klein and Garrido, 2011). While a more detailed account of mineral carbonation is beyond the scope of this study, talc formation through this process may be most effective in subduction zones where the incoming plates carry large volumes of carbonate rocks, such as in the Aegean arc (Clift and Vannucchi, 2004).

4.3. Formation of chlorite along the subduction interface

Chlorite is predicted to form in almost all of our reaction path models (Fig. 3c). The elevated activity of Al species in fluids in equilibrium with metabasalt or metapelite with increasing temperature promotes the formation of chlorite upon reaction with ultramafic rocks. The increased solubility of Al in fluids with increasing temperature is facilitated by the formation of Al-complexes, such as $Al(OH)Si(OH)^-$ (Huang and Sverjensky, 2019; Manning, 2018). The predicted formation of chlorite is corroborated by the common occurrence of chlorite at the interface between juxtaposed mafic, pelitic, and ultramafic rocks in metamorphic terranes that record a wide range of *P-T* conditions (Bebout, 1991; Bebout and Penniston-Dorland, 2016;

Marschall and Schumacher, 2012). Here, Si-metasomatism of ultramafic rocks or Mg-metasomatism of mafic (or pelitic) rocks can yield chlorite-rich assemblages.

Examples of exhumed chlorite-bearing high-pressure rocks with well-constrained *P-T* histories support our model predictions (Fig. 2c). The exhumed high-pressure mélange in Syros (Greece), metamorphosed at 1.3–2.0 GPa and 470–520 °C (Breeding et al., 2004; Marschall et al., 2006), displays chlorite-rich reaction zone between mafic blocks and serpentinite matrix where serpentinite is altered to chlorite ± talc ± tremolite (Gyomlai et al., 2021). Similarly, the ultramafic mélange from the Nishisonogi (Japan), metamorphosed at ~1.3–1.4 GPa and ~440–520 °C (Mori et al., 2019; Moribe, 2013), consists of a matrix of chlorite-actinolite schists and serpentinite juxtaposed to metapelite (Mori et al., 2014). In addition, chlorite and amphibole-rich reaction rinds around mafic blocks on Santa Catalina Island (USA) display elevated MgO, Ni, Cr, Os, Ir and Ru, reflecting ultramafic protoliths (Bebout and Barton, 2002; Penniston-Dorland et al., 2014). Other examples of exhumed mantle wedge peridotite metasomatized by slab-derived fluids include the Higashi-Akaishi peridotite (Japan) and chlorite harzburgites in Cima di Gagnone (Switzerland). These exhumed metaperidotites record peak *P-T* conditions of ~700–800 °C and <3 GPa (Guild et al., 2020; Scambelluri et al., 2014). Metasomatism of these metaperidotites by slab-derived fluids may have occurred at or before the rocks had reached peak-metamorphic temperatures. In the Higashi-Akaishi peridotite, high-Mg chlorite and amphibole included within garnet and orthopyroxene were interpreted as a stable prograde assemblage (Enami et al., 2004; Hattori et al., 2010). At Cima di Gagnone, chlorite harzburgite lenses are embedded within metamorphosed pelite. These chlorite harzburgite lenses record enrichments in radiogenic Sr and Pb from the interactions with fluids derived from the enclosing metapelite (Cannaò et al., 2015; Scambelluri et al., 2014). Evidence for chlorite formation and stabilization in mantle rocks by slab-derived fluids is also found in multiphase inclusions in exhumed metaperidotite (Campione et al., 2017). For instance, primary mineral inclusions in mantle garnet from exhumed ultra-high-pressure peridotite (e.g., Maowu Ultramafic Complex in Eastern China, Bardane, Ugelvik and Svartberget in the Western Gneiss Region) include spinel + chlorite which were interpreted as crystallization products of dilute slab-derived aqueous fluids that percolated through mantle peridotites (Campione et al., 2017; Carswell and van Roermund, 2005; Malaspina et al., 2006; Van Roermund and Drury, 1998; Vrijmoed et al., 2008).

4.4. Implications for the rheology, slow slip, and coupling-decoupling transition of the slab-mantle interface

The structurally complex shear zones in subduction interface exposures preserve a mixture of rock types that vary strongly in their rheological properties (Agard et al., 2018). Previous studies have suggested that episodic slip occurs downdip of the seismogenic zone along the plate interface, where the brittle-ductile transition occurs (Audet and Kim, 2016; Bürgmann, 2018). Slow slip occurs over longer timescales and at lower slip rates than seismic ruptures but are episodic and faster than continuous aseismic creep (Beroza and Ide, 2011; Rogers and Dragert, 2003). Slow slip events are typically observed in warm subduction zones at conditions of very low shear stresses (<1 MPa) (Beroza and Ide, 2011; Hawthorne and Rubin, 2010). Their distributions vary between subduction zones, but the majority are found at an inferred depth range of 30 to 50 km and temperatures between 325 to 500 °C (Brown et al., 2009; Condit et al., 2020). However, the exact mechanisms and conditions controlling their occurrence remain debated (Behr and Bürgmann, 2021). Proposed mechanisms include high pore fluid pressure that may promote dilatant hardening (Segall et al., 2006) or by changing strain partitioning among different rock units (French and Condit, 2019). These fluids are believed to be generated by in-situ dehydration of subducting slab or updip flow of fluids sourced from portions of the subducted slabs that dehydrate at greater depths (Condit et al., 2020; Fagereng et al., 2017; Kodaira et al., 2004; Taetz et al., 2018). The latter mechanism, proposed in conjunction with high pore-fluid pressures, invokes the presence of weak minerals such as chlorite and talc (Condit et al., 2022; French and Condit, 2019; Hirauchi et al., 2020; Tarling et al., 2019). For instance, French and Condit (2019) suggested that the very low shear stresses determined for during slow slip events can be accommodated by frictional deformation of chlorite or talc at near-lithostatic pore-fluid pressures. This is particularly important as near-lithostatic fluid pressures have been inferred for the plate interface (Behr and Bürgmann, 2021; Condit and French, 2022; Furukawa, 1993).

This study provides additional constraints on strain localization and the potential link to slow slip events by illuminating the formation potential of talc and chlorite along the plate interface. Talc formation via Si-metasomatism may not be as pervasive as previously thought, because it is predicted to form at a restrictive set of conditions only. When fluid in equilibrium with metapelite reacts with an ultramafic rock, talc formation is predicted to be less favorable at temperatures above 400 °C at pressures below 2 GPa. If slow slip events depend on the presence

and rheological properties of talc at near-lithostatic fluid pressures, then these events would be more favored in subduction zones with cold slab-top geotherms and where the incoming plates contain abundant sediments. However, this is inconsistent with the common occurrence of slow slip events in warm subduction zones such as in Cascadia and Mexico where the incoming plates are sediment-poor (Clift and Vannucchi, 2004). The absence of large volumes of talc in exhumed high-pressure rocks that record peak pressures above 1 GPa, in conjunction with our model predictions (that cover *P*-*T* conditions that are not represented by the exhumed metamorphic rock record), tentatively suggest that talc formation via Si-metasomatism is less favorable in warm subduction zones than in cold ones. Therefore, talc formed during Si-metasomatism may be less important in promoting of slow slip events in warm subduction zones than previously thought (French and Condit, 2019).

The pressure-dependent breakdown of talc via the reaction with forsterite to form antigorite and enstatite has been suggested as a mechanism to explain the coupling of the slab and overlying mantle at ~80 km depth (Peacock and Wang, 2021). If our predictions are correct, the common decoupling-coupling transition along the plate interface in warm subduction zones would be difficult to explain with the breakdown of talc, since its formation via Si-metasomatism seems to be limited to a restricted set of environmental conditions. Alternatively, much of the talc may form via mineral carbonation rather than Si-metasomatism (Okamoto et al., 2021).

Since chlorite also displays low frictional strength (Fagereng and Ikari, 2020), its formation along the plate interface largely independent of the slab thermal structure may be more likely to facilitate strain localization and facilitate slow slip events when the pore fluid pressure approaches lithostatic condition. However, other processes or mechanisms are required for chlorite to host slow slips at depths where they are generated.

Downdip of the brittle-ductile transition, increasing temperature in the presence of fluids may further promote the metasomatic growth of chlorite at the expense of precursor rocks. This would promote decoupling and possibly the deepening of the decoupling-coupling transition of the plate interface over time (cf. Abers et al., 2020; Marschall and Schumacher, 2012).

Acknowledgment

This work was support by National Science Foundation Award # 1545903 (PIRE: ExTerra Field Institute and Research Endeavour), and the WHOI Ocean Ventures Fund.

Open Research

The data that support the findings of this study are freely available at https://doi.org/10.5281/zenodo.6760195. The Deep Earth Water (DEW) database and EQ3/6 thermodynamic codes are available online (http://www.dewcommunity.org/resources.html).

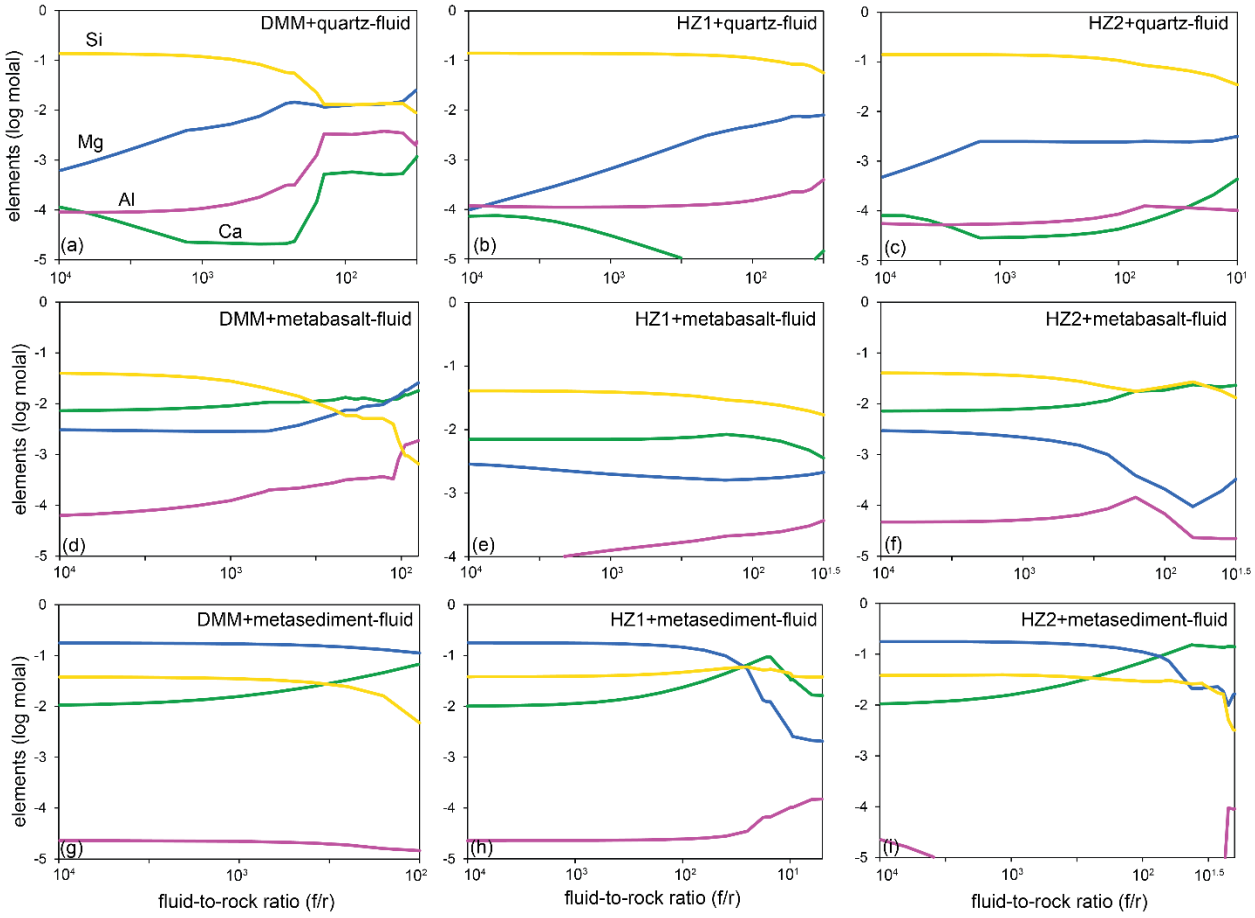

Fig. 1. Predicted pore fluid composition during high *P-T* (300°C, 1.5 GPa) Si-metasomatism of ultramafic rocks as a function of fluid-to-rock ratio. A fluid equilibrated with quartz (a-c), metabasalt (d-f), or metasediments (g-i) is subsequently allowed to react with ultramafic compositions (DMM, HZ1, and HZ2). The f/r decreases as ultramafic rock is titrated into the fluid.

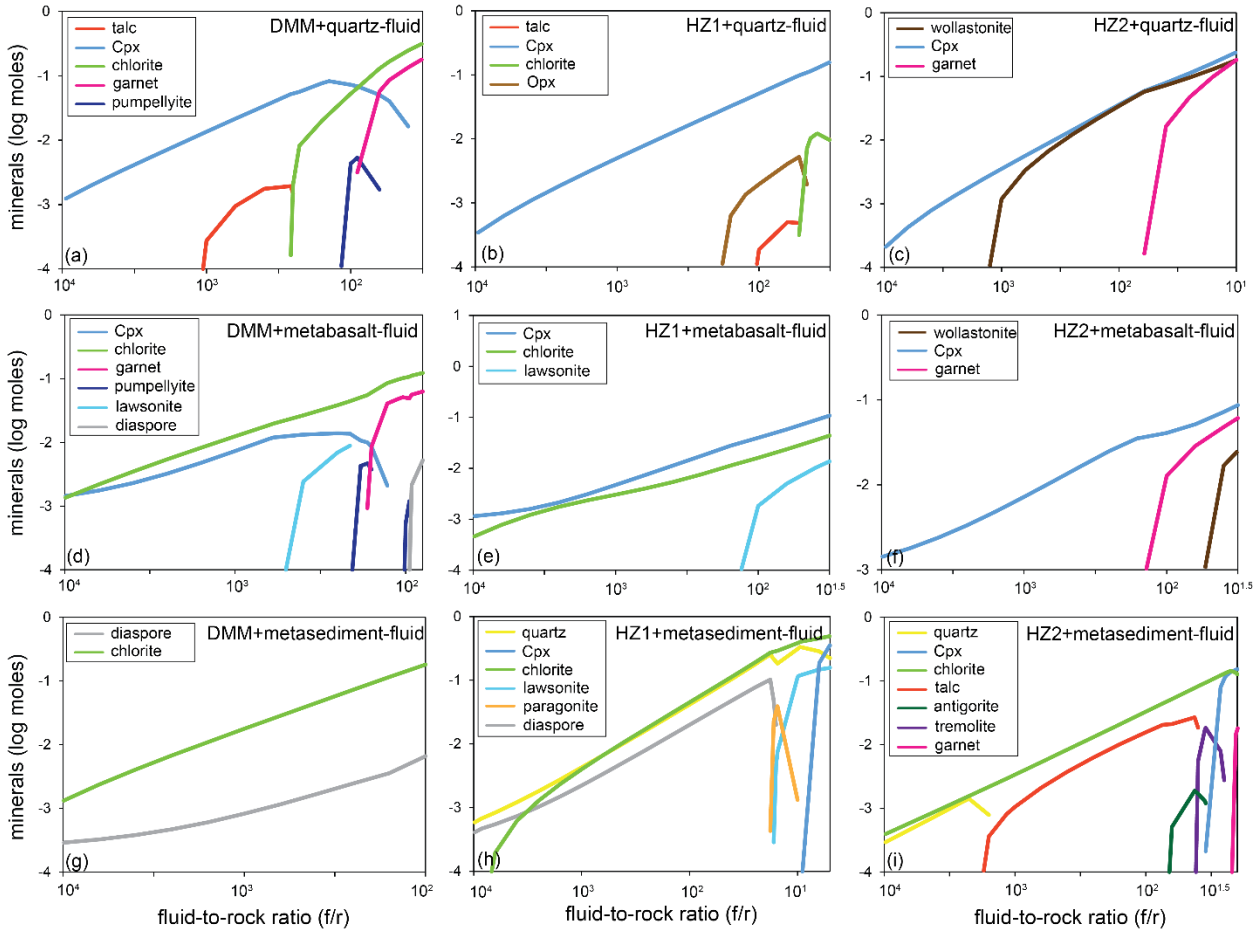

Fig. 2. Predicted mineral assemblages of reaction-path models that simulated high *P*-*T* (300°C, 1.5 GPa) metasomatism as a function of fluid-to-rock ratio. A fluid equilibrated with quartz (a-c), metabasalt (d-f), or metasediments (g-i) is subsequently allowed to react with ultramafic compositions (DMM, HZ1, and HZ2). The f/r decreases as ultramafic rock is titrated into the fluid. Mineral abbreviations are from Whitney and Evans (2010).

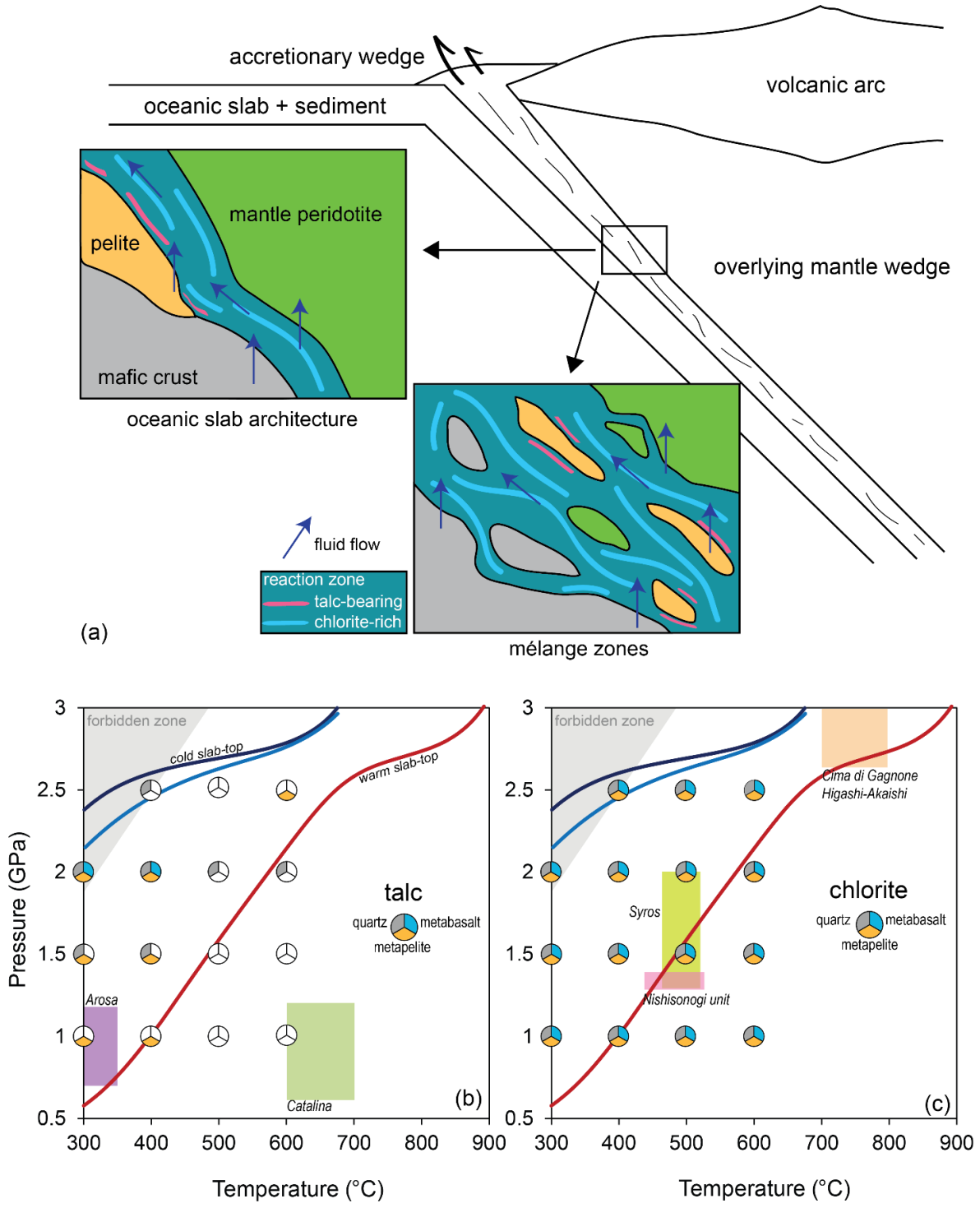

Fig. 3. (a) Illustration of the slab-mantle interface in subduction zones where talc and chlorite may be favored to form. Summary of the conditions that are predicted to favor the formation of talc (b) and chlorite (c) via Si-metasomatism of ultramafic rocks by slab-derived fluids. The predicted presence or lack of talc and chlorite is indicated by the color-coded pie charts which refer to distinct fluid compositions used in the reaction path models. The *P-T* conditions of field sites mentioned in the text are shown for comparison. Slab-top geotherms are taken from Syracuse et al. (2010).

References

Abers, G.A., van Keken, P.E., Wilson, C.R., 2020. Deep decoupling in subduction zones: Observations and temperature limits. Geosphere 16, 1408–1424. https://doi.org/10.1130/GES02278.1

Agard, P., Plunder, A., Angiboust, S., Bonnet, G., Ruh, J., 2018. The subduction plate interface: rock record and mechanical coupling (from long to short timescales). Lithos 320–321, 537–566. https://doi.org/10.1016/j.lithos.2018.09.029

Ague, J.J., 2007. Models of permeability contrasts in subduction zone mélange: Implications for gradients in fluid fluxes, Syros and Tinos Islands, Greece. Chemical Geology 239, 217–227. https://doi.org/10.1016/j.chemgeo.2006.08.012

Audet, P., Kim, Y., 2016. Teleseismic constraints on the geological environment of deep episodic slow earthquakes in subduction zone forearcs: A review. Tectonophysics 670, 1–15. https://doi.org/10.1016/j.tecto.2016.01.005

Bachmann, R., Oncken, O., Glodny, J., Seifert, W., Georgieva, V., Sudo, M., 2009. Exposed plate interface in the European Alps reveals fabric styles and gradients related to an ancient seismogenic coupling zone. Journal of Geophysical Research: Solid Earth 114. https://doi.org/10.1029/2008JB005927

Bebout, G., 2013. Metasomatism in Subduction Zones of Subducted Oceanic Slabs, Mantle Wedges, and the Slab-Mantle Interface, in: Metasomatism and the Chemical Transformation of Rock. pp. 289–349. https://doi.org/10.1007/978-3-642-28394-9_9

Bebout, G.E., 1991. Field-Based Evidence for Devolatilization in Subduction Zones: Implications for Arc Magmatism. Science 251, 413. https://doi.org/10.1126/science.251.4992.413

Bebout, G.E., Barton, M.D., 2002. Tectonic and metasomatic mixing in a high-T, subduction-zone mélange—insights into the geochemical evolution of the slab–mantle interface. Chemical Geology 187, 79–106. https://doi.org/10.1016/S0009-2541(02)00019-0

Bebout, G.E., Penniston-Dorland, S.C., 2016. Fluid and mass transfer at subduction interfaces—The field metamorphic record. Lithos 240–243, 228–258. https://doi.org/10.1016/j.lithos.2015.10.007

Behr, W.M., Bürgmann, R., 2021. What's down there? The structures, materials and environment of deep-seated slow slip and tremor. Philosophical Transactions of the Royal Society A: Mathematical, Physical and Engineering Sciences 379, 20200218. https://doi.org/10.1098/rsta.2020.0218

Beroza, G.C., Ide, S., 2011. Slow Earthquakes and Nonvolcanic Tremor. Annu. Rev. Earth Planet. Sci. 39, 271–296. https://doi.org/10.1146/annurev-earth-040809-152531

Boschi, C., Fruh-Green, G., Escartin, J., 2006. 31 - Occurrence and significance of serpentinite-hosted, talc-rich fault rocks in modern oceanic settings and ophiolite complexes. Ofioliti 31, 141–150.

Bose, K., Ganguly, J., 1995. Experimental and theoretical studies of the stabilities of talc, antigorite and phase A at high pressures with applications to subduction processes. Earth and Planetary Science Letters 136, 109–121. https://doi.org/10.1016/0012-821X(95)00188-I

Bowen, N.L., Tuttle, O.F., 1949. The System MgO—SiO2—H2O. GSA Bulletin 60, 439–460. https://doi.org/10.1130/0016-7606(1949)60[439:TSM]2.0.CO;2

Breeding, C.M., Ague, J.J., Bröcker, M., 2004. Fluid–metasedimentary rock interactions in subduction-zone mélange: Implications for the chemical composition of arc magmas. Geology 32, 1041–1044. https://doi.org/10.1130/G20877.1

Brown, J.R., Beroza, G.C., Ide, S., Ohta, K., Shelly, D.R., Schwartz, S.Y., Rabbel, W., Thorwart, M., Kao, H., 2009. Deep low-frequency earthquakes in tremor localize to the plate interface in multiple subduction zones. Geophysical Research Letters 36. https://doi.org/10.1029/2009GL040027

Bürgmann, R., 2018. The geophysics, geology and mechanics of slow fault slip. Earth and Planetary Science Letters 495, 112–134. https://doi.org/10.1016/j.epsl.2018.04.062

Campione, M., Tumiati, S., Malaspina, N., 2017. Primary spinel + chlorite inclusions in mantle garnet formed at ultrahigh-pressure. Geochemical Perspectives Letters 4, 19–23. https://doi.org/10.7185/geochemlet.1730

Cannaò, E., Agostini, S., Scambelluri, M., Tonarini, S., Godard, M., 2015. B, Sr and Pb isotope geochemistry of high-pressure Alpine metaperidotites monitors fluid-mediated element recycling during serpentinite dehydration in subduction mélange (Cima di Gagnone, Swiss Central Alps). Geochimica et Cosmochimica Acta 163, 80–100. https://doi.org/10.1016/j.gca.2015.04.024

Carswell, D.A., van Roermund, H.L.M., 2005. On multi-phase mineral inclusions associated with microdiamond formation in mantle-derived peridotite lens at Bardane on Fjørtoft, west Norway. European Journal of Mineralogy 17, 31–42. https://doi.org/10.1127/0935-1221/2005/0017-0031

Chen, X., Elwood Madden, A., Reches, Z., 2017. The frictional strength of talc gouge in high-velocity shear experiments: frictional strength of talc gouge. Journal of Geophysical Research: Solid Earth 122. https://doi.org/10.1002/2016JB013676

Clift, P., Vannucchi, P., 2004. Controls on tectonic accretion versus erosion in subduction zones: Implications for the origin and recycling of the continental crust. Reviews of Geophysics 42. https://doi.org/10.1029/2003RG000127

Codillo, E., 2022. Thermodynamic constraints on Si-metasomatism of ultramafic rocks in subduction zones. https://doi.org/doi.org/10.5281/zenodo.6760195

Condit, C.B., French, M.E., 2022. Geologic Evidence of Lithostatic Pore Fluid Pressures the Base of the Subduction Seismogenic Zone. Geophysical Research Letters 49, e2022GL098862. https://doi.org/10.1029/2022GL098862

Condit, C.B., French, M.E., Hayles, J.A., Yeung, L.Y., Chin, E.J., Lee, C.-T.A., 2022. Rheology of Metasedimentary Rocks at the Base of the Subduction Seismogenic Zone. Geochemistry, Geophysics, Geosystems 23, e2021GC010194. https://doi.org/10.1029/2021GC010194

Condit, C.B., Guevara, V.E., Delph, J.R., French, M.E., 2020. Slab dehydration in warm subduction zones at depths of episodic slip and tremor. Earth and Planetary Science Letters 552, 116601. https://doi.org/10.1016/j.epsl.2020.116601

Enami, M., Mizukami, T., Yokoyama, K., 2004. Metamorphic evolution of garnet-bearing ultramafic rocks from the Gongen area, Sanbagawa belt, Japan. Journal of Metamorphic Geology 22, 1–15. https://doi.org/10.1111/j.1525-1314.2003.00492.x

Evans, B.W., 1977. Metamorphism of Alpine Peridotite and Serpentinite. Annu. Rev. Earth Planet. Sci. 5, 397–447. https://doi.org/10.1146/annurev.ea.05.050177.002145

Fagereng, Å., Diener, J.F.A., Meneghini, F., Harris, C., Kvadsheim, A., 2017. Quartz vein formation by local dehydration embrittlement along the deep, tremorgenic subduction thrust interface. Geology 46, 67–70. https://doi.org/10.1130/G39649.1

Fagereng, Å., Ikari, M.J., 2020. Low-Temperature Frictional Characteristics of Chlorite-Epidote-Amphibole Assemblages: Implications for Strength and Seismic Style of Retrograde Fault Zones. Journal of Geophysical Research: Solid Earth 125, e2020JB019487. https://doi.org/10.1029/2020JB019487

French, M.E., Condit, C.B., 2019. Slip partitioning along an idealized subduction plate boundary at deep slow slip conditions. Earth and Planetary Science Letters 528, 115828. https://doi.org/10.1016/j.epsl.2019.115828

Frost, B.R., Beard, J.S., 2007. On Silica Activity and Serpentinization. Journal of Petrology 48, 1351–1368. https://doi.org/10.1093/petrology/egm021

Furukawa, Y., 1993. Depth of the decoupling plate interface and thermal structure under arcs. Journal of Geophysical Research: Solid Earth 98, 20005–20013. https://doi.org/10.1029/93JB02020

Grozeva, N.G., Klein, F., Seewald, J.S., Sylva, S.P., 2017. Experimental study of carbonate formation in oceanic peridotite. Geochimica et Cosmochimica Acta 199, 264–286. https://doi.org/10.1016/j.gca.2016.10.052

Guild, M.R., Till, C.B., Mizukami, T., Wallis, S., 2020. Petrogenesis of the Higashi-Akaishi Ultramafic Body: Implications for Lower Crustal Foundering and Mantle Wedge Processes. Journal of Petrology 61, egaa089. https://doi.org/10.1093/petrology/egaa089

Gyomlai, T., Agard, P., Marschall, H.R., Jolivet, L., Gerdes, A., 2021. Metasomatism and deformation of block-in-matrix structures in Syros: The role of inheritance and fluid-rock interactions along the subduction interface. Lithos 386–387, 105996. https://doi.org/10.1016/j.lithos.2021.105996

Hacker, B.R., Abers, G.A., Peacock, S.M., 2003. Subduction factory 1. Theoretical mineralogy, densities, seismic wave speeds, and H2O contents. Journal of Geophysical Research: Solid Earth 108. https://doi.org/10.1029/2001JB001127

Hattori, K., Wallis, S., Enami, M., Mizukami, T., 2010. Subduction of mantle wedge peridotites: Evidence from the Higashi-akaishi ultramafic body in the Sanbagawa metamorphic belt. Island Arc 19, 192–207. https://doi.org/10.1111/j.1440-1738.2009.00696.x

Hawthorne, J.C., Rubin, A.M., 2010. Tidal modulation of slow slip in Cascadia. Journal of Geophysical Research: Solid Earth 115. https://doi.org/10.1029/2010JB007502

Helgeson, H.C., Kirkham, D.H., Flowers, G.C., 1981. Theoretical prediction of the thermodynamic behavior of aqueous electrolytes by high pressures and temperatures; IV, Calculation of activity coefficients, osmotic coefficients, and apparent molal and standard and relative partial molal properties to 600 degrees C and 5kb. Am J Sci 281, 1249. https://doi.org/10.2475/ajs.281.10.1249

Hirauchi, K., den Hartog, S.A.M., Spiers, C.J., 2013. Weakening of the slab–mantle wedge interface induced by metasomatic growth of talc. Geology 41, 75–78. https://doi.org/10.1130/G33552.1

Hirauchi, K., Yamaguchi, H., 2007. Unique deformation processes involving the recrystallization of chrysotile within serpentinite: Implications for aseismic slip events within subduction zones. Terra Nova 19, 454–461. https://doi.org/10.1111/j.1365-3121.2007.00771.x

Hirauchi, K., Yamamoto, Y., den Hartog, S.A.M., Niemeijer, A.R., 2020. The role of metasomatic alteration on frictional properties of subduction thrusts: An example from a serpentinite body in the Franciscan Complex, California. Earth and Planetary Science Letters 531, 115967. https://doi.org/10.1016/j.epsl.2019.115967

Huang, F., Sverjensky, D.A., 2019. Extended Deep Earth Water Model for predicting major element mantle metasomatism. Geochimica et Cosmochimica Acta 254, 192–230. https://doi.org/10.1016/j.gca.2019.03.027

Kim, Y., Clayton, R.W., Asimow, P.D., Jackson, J.M., 2013. Generation of talc in the mantle wedge and its role in subduction dynamics in central Mexico. Earth and Planetary Science Letters 384, 81–87. https://doi.org/10.1016/j.epsl.2013.10.006

Klein, F., Bach, W., Jöns, N., McCollom, T., Moskowitz, B., Berquó, T., 2009. Iron partitioning and hydrogen generation during serpentinization of abyssal peridotites from 15°N on the Mid-Atlantic Ridge. Geochimica et Cosmochimica Acta 73, 6868–6893. https://doi.org/10.1016/j.gca.2009.08.021

Klein, F., Bach, W., McCollom, T.M., 2013. Compositional controls on hydrogen generation during serpentinization of ultramafic rocks. Lithos 178, 55–69. https://doi.org/10.1016/j.lithos.2013.03.008

Klein, F., Garrido, C.J., 2011. Thermodynamic constraints on mineral carbonation of serpentinized peridotite. Lithos 126, 147–160. https://doi.org/10.1016/j.lithos.2011.07.020

Kodaira, S., Iidaka, T., Kato, A., Park, J.-O., Iwasaki, T., Kaneda, Y., 2004. High Pore Fluid Pressure May Cause Silent Slip in the Nankai Trough. Science 304, 1295–1298. https://doi.org/10.1126/science.1096535

Malaspina, N., Hermann, J., Scambelluri, M., Compagnoni, R., 2006. Polyphase inclusions in garnet–orthopyroxenite (Dabie Shan, China) as monitors for metasomatism and fluid-related trace element transfer in subduction zone peridotite. Earth and Planetary Science Letters 249, 173–187. https://doi.org/10.1016/j.epsl.2006.07.017

Manning, C., 2007. Solubility of corundum + kyanite in H2O at 700°C and 10 kbar: evidence for Al_Si complexing at high pressure and temperature. Geofluids 7, 258–269.

Manning, C.E., 2018. Fluids of the Lower Crust: Deep Is Different. Annu. Rev. Earth Planet. Sci. 46, 67–97. https://doi.org/10.1146/annurev-earth-060614-105224

Manning, C.E., 2004. The chemistry of subduction-zone fluids. Earth and Planetary Science Letters 223, 1–16. https://doi.org/10.1016/j.epsl.2004.04.030

Manning, C.E., 1997. Coupled Reaction and Flow in Subduction Zones: Silica Metasomatism in the Mantle Wedge, in: Jamtveit, B., Yardley, B.W.D. (Eds.), Fluid Flow and Transport in Rocks: Mechanisms and Effects. Springer Netherlands, Dordrecht, pp. 139–148. https://doi.org/10.1007/978-94-009-1533-6_8

Manning, C.E., 1995. Phase-Equilibrium Controls on SiO2 Metasomatism by Aqueous Fluid in Subduction Zones: Reaction at Constant Pressure and Temperature. null 37, 1074–1093. https://doi.org/10.1080/00206819509465440

Marschall, H.R., Ludwid, T., Altherr, R., Kalt, A., Tonarini, S., 2006. Syros Metasomatic Tourmaline: Evidence for Very High-δ11B Fluids in Subduction Zones. Journal of Petrology 47, 1915–1942. https://doi.org/10.1093/petrology/egl031

Marschall, H.R., Schumacher, J.C., 2012. Arc magmas sourced from mélange diapirs in subduction zones. Nature Geosci 5, 862–867. https://doi.org/10.1038/ngeo1634

Moore, D.E., Lockner, D.A., 2007. Comparative Deformation Behavior of Minerals in Serpentinized Ultramafic Rock: Application to the Slab-Mantle Interface in Subduction Zones. null 49, 401–415. https://doi.org/10.2747/0020-6814.49.5.401

Mori, Y., Shigeno, M., Miyazaki, K., Nishiyama, T., 2019. Peak metamorphic temperature of the Nishisonogi unit of the Nagasaki Metamorphic Rocks, western Kyushu, Japan. Journal of Mineralogical and Petrological Sciences 114, 170–177. https://doi.org/10.2465/jmps.190423

Mori, Y., Shigeno, M., Nishiyama, T., 2014. Fluid-metapelite interaction in an ultramafic mélange: implications for mass transfer along the slab-mantle interface in subduction zones. Earth, Planets and Space 66, 47. https://doi.org/10.1186/1880-5981-66-47

Moribe, Y., 2013. Petrological study of the Nagasaki Metamorphic Rocks in the Nishisonogi Peninsula, western Kyusyu. Master's thesis, Kumamoto University, Kumamoto, Japan.

Okamoto, A., Oyanagi, R., Yoshida, K., Uno, M., Shimizu, H., Satish-Kumar, M., 2021. Rupture of wet mantle wedge by self-promoting carbonation. Communications Earth & Environment 2, 151. https://doi.org/10.1038/s43247-021-00224-5

Peacock, S., 1990. Fluid Processes in Subduction Zones. Science 248, 329–337. https://doi.org/10.1126/science.248.4953.329

Peacock, S.M., Hyndman, R.D., 1999. Hydrous minerals in the mantle wedge and the maximum depth of subduction thrust earthquakes. Geophysical Research Letters 26, 2517–2520. https://doi.org/10.1029/1999GL900558

Peacock, S.M., Wang, K., 2021. On the Stability of Talc in Subduction Zones: A Possible Control on the Maximum Depth of Decoupling Between the Subducting Plate and Mantle Wedge. Geophysical Research Letters 48, e2021GL094889. https://doi.org/10.1029/2021GL094889

Penniston-Dorland, S.C., Gorman, J.K., Bebout, G.E., Piccoli, P.M., Walker, R.J., 2014. Reaction rind formation in the Catalina Schist: Deciphering a history of mechanical mixing and metasomatic alteration. Chemical Geology 384, 47–61. https://doi.org/10.1016/j.chemgeo.2014.06.024

Rogers, G., Dragert, H., 2003. Episodic Tremor and Slip on the Cascadia Subduction Zone: The Chatter of Silent Slip. Science 300, 1942–1943. https://doi.org/10.1126/science.1084783

Rubin, A.M., 2008. Episodic slow slip events and rate-and-state friction. Journal of Geophysical Research: Solid Earth 113. https://doi.org/10.1029/2008JB005642

Scambelluri, M., Pettke, T., Rampone, E., Godard, M., Reusser, E., 2014. Petrology and Trace Element Budgets of High-pressure Peridotites Indicate Subduction Dehydration of Serpentinized Mantle (Cima di Gagnone, Central Alps, Switzerland). Journal of Petrology 55, 459–498. https://doi.org/10.1093/petrology/egt068

Schwartz, S., Guillot, S., Reynard, B., Lafay, R., Debret, B., Nicollet, C., Lanari, P., Auzende, A.L., 2013. Pressure–temperature estimates of the lizardite/antigorite transition in high pressure serpentinites. Lithos 178, 197–210. https://doi.org/10.1016/j.lithos.2012.11.023

Segall, P., Desmarais, E.K., Shelly, D., Miklius, A., Cervelli, P., 2006. Earthquakes triggered by silent slip events on Kīlauea volcano, Hawaii. Nature 442, 71–74. https://doi.org/10.1038/nature04938

Shock, E.L., Oelkers, E.H., Johnson, J.W., Sverjensky, D.A., Helgeson, H.C., 1992. Calculation of the thermodynamic properties of aqueous species at high pressures and temperatures. Effective electrostatic radii, dissociation constants and standard partial molal properties to 1000 °C and 5 kbar. Journal of the Chemical Society. 88, 803–826.

Sverjensky, D.A., 2019. Thermodynamic modelling of fluids from surficial to mantle conditions. Journal of the Geological Society 176, 348. https://doi.org/10.1144/jgs2018-105

Sverjensky, D.A., Harrison, B., Azzolini, D., 2014. Water in the deep Earth: The dielectric constant and the solubilities of quartz and corundum to 60kb and 1200°C. Geochimica et Cosmochimica Acta 129, 125–145. https://doi.org/10.1016/j.gca.2013.12.019

Syracuse, E.M., van Keken, P.E., Abers, G.A., 2010. The global range of subduction zone thermal models. Physics of the Earth and Planetary Interiors 183, 73–90. https://doi.org/10.1016/j.pepi.2010.02.004

Taetz, S., John, T., Bröcker, M., Spandler, C., Stracke, A., 2018. Fast intraslab fluid-flow events linked to pulses of high pore fluid pressure at the subducted plate interface. Earth and Planetary Science Letters 482, 33–43. https://doi.org/10.1016/j.epsl.2017.10.044

Tarling, M.S., Smith, S.A.F., Scott, J.M., 2019. Fluid overpressure from chemical reactions in serpentinite within the source region of deep episodic tremor. Nature Geoscience. https://doi.org/10.1038/s41561-019-0470-z

Van Roermund, Drury, 1998. Ultra-high pressure (P > 6 GPa) garnet peridotites in Western Norway: exhumation of mantle rocks from > 185 km depth. Terra Nova 10, 295–301. https://doi.org/10.1046/j.1365-3121.1998.00213.x

Vrijmoed, J.C., Smith, D.C., Van Roermund, H.L.M., 2008. Raman confirmation of microdiamond in the Svartberget Fe-Ti type garnet peridotite, Western Gneiss Region, Western Norway. Terra Nova 20, 295–301. https://doi.org/10.1111/j.1365-3121.2008.00820.x

Wada, I., Wang, K., He, J., Hyndman, R.D., 2008. Weakening of the subduction interface and its effects on surface heat flow, slab dehydration, and mantle wedge serpentinization. Journal of Geophysical Research: Solid Earth 113. https://doi.org/10.1029/2007JB005190

Whitney, D.L., Evans, B.W., 2010. Abbreviations for names of rock-forming minerals. American Mineralogist 95, 185–187. https://doi.org/10.2138/am.2010.3371

Wolery, T.J., 1992. EQ3/6, a software package for geochemical modeling of aqueous systems: Package overview and installation guide (Version 7.0). United States. https://doi.org/10.2172/138894

Chapter 4

The ascent of mélanges: experimental constraints on mélange rock densities and solidus temperatures in subduction zones

Abstract

Mélange rocks are mixtures of subducted materials and serpentinized mantle rocks that form along the slab-mantle interface in subduction zones. It has been suggested that mélange rocks may be able to ascend from the slab-top into the overlying mantle, as solid or partially molten buoyant diapirs, and transfer their compositional signatures to the source region of arc magmas. However, their ability to rise by buoyancy is in part tied to their phase equilibria during melting and residual densities after melt extraction, all of which are poorly constrained. Here, we report a series of piston-cylinder experiments on three natural mélange rocks that cover a range of mélange compositions at 1.5–2.5 GPa and 500–1050°C. We show that melting of mélanges is unlikely to occur along the slab-top at pressures ≤ 2.5 GPa, so that diapirism into the hotter mantle wedge would be required to initiate melting. For the two metaluminous mélange compositions, the bulk of residual phases is more buoyant than the overlying mantle at all *P*-*T* conditions investigated, opening the possibility of diapir formation. For peraluminous mélanges, diapir buoyancy is possible at 1.5 GPa but limited at 2.5 GPa due to the formation of abundant garnet primarily at the expense of chlorite. We also evaluate if thermodynamic modeling (Perple_X) can accurately reproduce the phase equilibria, solidus temperatures, and density evolution of mélange compositions. Our analysis shows some agreement between models and experiments in mélange rocks with low initial water contents and low-pressure (≤ 1.5 GPa) conditions. However, the discrepancy between models and experiments becomes larger at higher pressure and high-water contents. Results from this study provide experimental constraints on mélange buoyancy that can inform numerical models of mélange diapirism and influence the interpretations of both geophysical signals and geochemical characteristics of magmas in subduction zones.

1 Introduction

Subduction zones are highly dynamic regions on Earth where igneous oceanic crust, serpentinized peridotites, and sediments are brought back into the Earth's interior and variably influence the compositions of arc magmas worldwide (Hawkesworth et al., 1993; McCulloch and Gamble, 1991; Plank and Langmuir, 1993; Tera et al., 1986). The intense shearing, fluid metasomatism, and deformation processes occurring along the slab-mantle interface result in the development of mélange zones. Field observations of exhumed high-pressure mélange rocks often display blocks of crustal rocks embedded in mafic to ultramafic matrices (Bebout and Barton, 2002; Bebout, 1991; Codillo et al., 2022a; Harlow et al., 2015; Marschall and Schumacher, 2012; Miller et al., 2009). These mélange matrices may include monomineralic chlorite schist, talc schist, and jadeitite with variable amounts of amphibole, clinopyroxene, phengite, epidote, and accessory minerals, such as titanite, rutile, ilmenite, and zircon. These hybrid rocks display a wide range of elemental and isotopic signatures reflecting distinct input lithologies and fluids, but have phase equilibria different from any of the subducted inputs (Bebout and Barton, 2002; Bebout, 1991; Breeding et al., 2004; Codillo et al., 2022a; King et al., 2006; Marschall and Schumacher, 2012; Miller et al., 2009; Penniston-Dorland et al., 2014; Pogge von Strandmann et al., 2015; Sorensen and Grossman, 1989). It has been suggested that mélanges, in the form of melts or solid diapirs, may play an important role in controlling arc magma chemistry (Codillo et al., 2018; Cruz-Uribe et al., 2018; Marschall and Schumacher, 2012; Nielsen and Marschall, 2017; Parolari et al., 2021). Whether partial melting of mélange rocks occurs along the slab-top and/or in buoyant diapirs has implications for the timing and location of elemental fractionation associated with arc magmas (Cooper et al., 2012; Elliott et al., 1997; Hawkesworth et al., 1997; Li Huijuan et al., 2022; Plank et al., 2009; Schmidt, 2015; Turner et al., 2001). For instance, chemical thermometers (*e.g.*, light rare earth elements/Ti, K_2O/H_2O, H_2O/Ce), which are widely used to infer the slab-top temperatures assume that the phases (*e.g.*, phengite, epidote) responsible for elemental fractionations reside near the slab-top (Cooper et al., 2012; Hermann and Spandler, 2008; Klimm et al., 2008; Plank et al., 2009). However, if those minerals can be entrained by buoyant mélange diapirs, calculated temperatures would not indicate slab-top pressure conditions.

Geodynamic models predict that hydrated slab-top materials may become gravitationally unstable and form buoyant diapirs along a diagonal path away from the slab-top into the overlying

mantle (Behn et al., 2011; Castro et al., 2010; Castro and Gerya, 2008; Currie et al., 2007; Ducea et al., 2022; Gerya and Stöckhert, 2006; Gerya and Yuen, 2003; Klein and Behn, 2021; Miller and Behn, 2012; Zhu et al., 2009). These buoyant diapirs can transport slab components (*e.g.*, igneous crust, sediment, serpentinite, mélange rocks, and fluids) and subject them to *P-T* conditions that are otherwise unattainable in the conventional view of dehydration reactions and melting along the slab-top (c.f. Behn et al., 2011). Most of these geodynamic models have evaluated the potential for subducting sediments to rise buoyantly into the overlying mantle wedge (*e.g.*, Behn et al., 2011; Currie et al., 2007; Ducea et al., 2022; Gorczyk et al., 2006; Klein and Behn, 2021; Miller and Behn, 2012). These previous studies have identified parameters such as layer thickness and composition, and slab-top geotherm to be particularly important on diapir formation and their behavior in the mantle wedge. Additional lines of petrologic and geophysical evidence support diapiric transport of slab-derived materials into the overlying mantle. The presence of old xenocrystic zircons included within chromitite or entrained in erupted arc lavas were suggested to have been derived from subducted sediments that were transported via diapiric plumes that relaminated at the base of the overlying crust (Gómez-Tuena et al., 2018; Proenza et al., 2017). Similarly, geochemical and petrochronological data indicate contamination of ultramafic rocks by relaminated felsic granulite from the Náměšť Granulite Massif (Kusbach et al., 2015). Evidence from field relations, geochronologic, and geochemical data support the genetic relationship between alkaline arc rocks and exhumed mélange rocks found in the same locality in Western Tianshan (Wang et al., 2022). In addition, the *P-T* conditions recorded by high and ultra-high pressure subducted rocks (*e.g.*, Tso-Morari in Himalayas, North Qaidam UHP metamorphic belt in Northwest China, D'Entrecasteaux Islands in Papua New Guinea) are consistent with heating within the mantle wedge overlying the subducting slab (Chatterjee and Jagoutz, 2015; Little et al., 2011; Sharp et al., 1992; Yin et al., 2007). Lastly, analysis of P-wave scattering in the mantle wedge indicates the presence of seismic obstructions that were interpreted as buoyant materials rising away from the slab-top, consistent with previous observations (Gerya et al., 2006; Gorczyk et al., 2006; Lin et al., 2019, 2021)

However, the ability of mélange rocks to ascend by buoyancy from the slab top to the overlying mantle is tied to their phase equilibria, melting behavior, and densities, which are poorly constrained. In particular, we need to understand whether these mélange rocks melt along the slab top and how the melting process affects the density evolution of their melting residues. Mélange

rocks could either form buoyant diapirs that dehydrate and melt as they rise through the mantle wedge, or remain at the slab-top to dehydrate and melt when entrained to deeper depths.

Here we report the phase equilibria and residual densities during melting of three natural mélange rocks collected from several exhumed high-pressure localities. We performed a series of 30 high *P-T* melting experiments using piston cylinder apparatus at conditions relevant to subduction zone slab-top thermal structures (i.e. 500–1050 °C, 1.5–2.5 GPa) to estimate the *P-T* conditions at which mélange melting starts (solidus) and constrain the density evolution of mélange residues. Lastly, we compare how well phase equilibrium models (Perple_X; Connolly, 1990) reproduce the phase equilibria and melting behavior of these novel bulk compositions and discuss the implications for mélange diapirism in subduction zones.

2 Materials and methods

2.1 Starting material preparation

There exists a wide range in chemical and mineralogical compositions of exhumed mélange rocks worldwide. To account for their compositional variability, we selected three natural mélange rocks as starting materials based of their mineralogical assemblages, fluid-immobile element (i.e. Cr/Al vs Al_2O_3) chemistry, and trace element chemistry (Figure 1). Two mélange rocks from Syros, Greece (i.e. SY400B and SY325, see Miller et al., 2009) and one mélange rock from Santa Catalina, USA (i.e. C647, labeled 6-4-7 in King et al., 2006) were selected. These mélange rocks represent the matrices that formed by fluid-mediated mass transfer between juxtaposed mafic and ultramafic rocks in a subduction zone. The use of mélange matrix material in this study is supported by both field and geochemical evidence that they form at the expense of, and reflect contributions from their protoliths, making them representative of the composition of the mélange as a whole. Previous studies have constrained the peak metamorphic conditions of ~ 500–550 °C, 1.8–2.0 GPa for the exhumed high-pressure rocks in Syros (Breeding et al., 2004; Gyomlai et al., 2021; Miller et al., 2009) and ~600–700 °C, 0.9–1.3 GPa for Santa Catalina (King et al., 2006). These conditions are consistent with slab-top thermal models (Holt and Condit, 2021; Syracuse et al., 2010). The petrogenesis of the mélange matrix rocks used in this study are discussed in detail in previous studies (Gyomlai et al., 2021; King et al., 2006; Miller et al., 2009; Pogge von Strandmann et al., 2015).

SY325 mélange is Si-Mg rich (55 wt.%, 22 wt.%, respectively) and Al-poor (2 wt.%) while SY400B mélange is Si-Al rich (50 wt.%, 17 wt.%, respectively), Mg-poor (8 wt.%), both of which have water contents of ~3 wt. %. C647 mélange is Mg-Al rich (24 wt.%, 12 wt.%, respectively) and Si-poor (38 wt.%) with water content of ~8.5 wt. %. SY400B mélange displays the highest Cr/Al and lowest Al_2O_3 content, plotting closest to the mafic compositions represented by MORB (mid-ocean ridge basalt) and GLOSS (global subducting sediment) while SY325 mélange displays the lowest Cr/Al and highest Al_2O_3 content, plotting closest to the ultramafic compositions represented by DMM (depleted MORB mantle) and serpentinites. The composition of C647 mélange is intermediate between SY325 and SY400B in terms of Cr/Al and Al_2O_3 content (Figure 1a). The normalized trace-element composition of SY400B mélange displays elevated trace-element abundances that resemble GLOSS composition, whereas SY325 mélange displays the lowest trace-element abundances that plot close to DMM and serpentinite compositions. The normalized trace-element composition of C647 mélange plots in between SY325 and SY400B compositions (Figure 1b). Our starting material SY400B is compositionally similar to the starting material used in the experimental study of Cruz-Uribe et al. (2018) performed at higher temperature conditions. Homogeneous powders of each mélange rock were stored in a dry box until use. The mineralogical assemblages and whole-rock compositions (major and trace elements) of SY325, SY400B and C647 mélanges are reported in Table S1.

2.2 Experimental setup

Partial melting experiments were performed in a 0.5″ end-loaded solid medium piston-cylinder device at the Woods Hole Oceanographic Institution (USA). The starting materials were packed in Au capsules to minimize water and Fe losses. Approximately 35–45 mg of the starting material was packed in the Au capsule, triple-crimped and then welded shut. The sealed Au capsule was fitted inside a pre-dried and hollowed MgO spacer. All the experiments were performed in a CaF_2 pressure assembly with pre-dried crushable MgO spacers and straight-walled graphite furnace. Lubricated Pb foils were used to contain the friable CaF_2 assembly and to provide lubrication between the assembly and the bore of the pressure vessel.

The experiments were performed at 500–1050 °C and 1.5–2.5 GPa, a range of conditions where significant increase in the slab-top geotherms are predicted (Syracuse et al., 2010). Run duration was set at 96 hr or longer after comparing approach to chemical equilibrium from a 96 hr

to 144-hr time-series (see discussion below). Pressure was applied using the cold piston-in technique where the experiments were first raised to the desired pressure before heating them at desired temperature at the rate of 60 °C/min. The friction correction was determined from the Ca-Tschermakite breakdown reaction to the assemblage anorthite, gehlenite, and corundum at 12–14 kbar and 1300 °C and is within the pressure uncertainty (± 50 MPa). Thus, no correction was applied on the pressure in this study. Temperature was monitored and controlled in the experiments using $W_{97}Re_3/W_{75}Re_{25}$ thermocouple with no correction for the effect of pressure on thermocouple electromotive force. Temperatures were estimated to be accurate to ±10 °C and pressures to ±500 bars, and the thermal gradient over the capsule was <5 °C. The experiments were quenched by terminating power supply and the run products were recovered. The capsules were longitudinally cut in half before mounted in epoxy. All the mounted capsules were polished successively on 400- to 1200-grit SiC paper before the final polishing on nylon or velvet microcloth with polycrystalline diamond suspensions (3–0.25 μm) and 0.02 μm colloidal silica. Vacuum re-impregnation of capsules with epoxy was performed to reduce plucking-out of materials during polishing. The experimental conditions and run durations are summarized in Table S2.

2.3 Analytical techniques

The mineralogical and textural characterization of each experimental run products was performed using a Zeiss AxioImager 2 microscope complemented by scanning electron microscopy (SEM) using a Hitachi TM3000 equipped with a Bruker Quantax 70 energy-dispersive X-ray spectrometer at the Woods Hole Oceanographic Institution. The major element compositions of the quenched melts (when present) and coexisting silicate and oxide minerals from all experimental run products were analyzed by electron microprobe analysis (EPMA) using a JEOL JXA-8200 Superprobe at the Massachusetts Institute of Technology. Analyses were performed using a 15 kV accelerating potential and a 10 nA beam current. The beam diameter varied depending on the target point. For quenched glassy melt pools, beam diameters varied between 2 μm to 5 μm (mostly 5 μm) depending on the size of the melt pools. For silicate and oxide minerals, a focused beam (1 μm) was used. If a mineral phase showed significant compositional zoning from core to rim, spots were chosen along the rims of those phases as such analytical volumes are expected to be closer to equilibrium with the adjacent phases. If sector zoning is evident, such as in epidote mineral, multiple spots are analyzed on a single grain to

provide the compositional range as reflected by the standard deviation from the average. Data reduction was done using the CITZAF package. Counting times for most elements were 40 s on peak, and 20 s on background. In order to prevent alkali diffusion in glass, Na was analyzed first for 10 s on peak and 5 s on background. All phases (experimental melts and coexisting minerals) were quantified using silicate and oxide standards. Major element compositions of melts and minerals are reported in Tables S3–S5.

3 Results

3.1 Approach to equilibrium

We assessed the approach to equilibrium by performing time-series experiments at the lowest temperature condition where we could identify and measure the compositions of both minerals and glassy melt pools. We conducted experiments using SY325 starting material at 1000 °C, 1.5 GPa using two run durations (96 h and 144 h) and found no significant difference (within 1 σ) in the compositions of glassy melt and mineral phases for both experiments performed at different run durations (Figure S1). Based on the likelihood of approach to equilibrium in both experiments, we selected 96 h as a minimum run duration and applied this duration to other experiments. The maintenance of a closed system during all experiments and approach to equilibrium were further demonstrated by the following observations: (1) low values for the sum of residual squares ($\sum r^2$, most experiments have < 1), indicating reasonable mass balances (Tables S3–S5), (2) homogeneous distribution of minerals and melts throughout the capsule (slightly larger melt pools at the edges) and no systematic grain size variation that would suggest significant thermal gradient across the length of the capsule, (3) constancy of major element compositions in minerals and melt throughout the capsule in most experiments. An exception to this is the limited compositional zoning observed in some silicate minerals (*e.g.*, epidote and clinopyroxene in SY400B) in lowest temperature subsolidus experiments, likely due to slower rates of reactions under these low temperatures conditions (*e.g.*, Lakey and Hermann, 2022). Mass balances calculations in the subsolidus C647 mélange experiments at 1.5 and 2.5 GPa yielded high $\sum r^2$ (> 8), unless a free fluid phase was artificially added to the calculation. We did not measure compositions of the coexisting fluids but observed significant porosity (Figure 5). The addition of

a synthetic fluid in equilibrium with ultramafic composition of Dvir et al. (2011) in our mass-balance calculation yielded a better $\sum r^2$ (0.4–3.8) and accurately predicted mineral proportions. The near-solidus and suprasolidus experiments conducted at higher temperatures did not show any significant chemical zoning. The oxygen fugacity was not controlled in our experiments.

Modal proportions of minerals and melts for each experiment were estimated using two independent mass-balance approaches using the mineral and whole-rock compositions. We performed mass-balance calculations using the conventional Excel program Solver as well as the LIME program (Krawczynski and Olive, 2011). The LIME program is based on the isometric log-ratio transform that considers information and uncertainties on endmember and bulk compositions as well as phase-proportions. The LIME program outputs phase proportions with associated uncertainties (Tables S10–S12). Comparison of the predicted proportions of main mineral phases from two mass balance approaches showed good agreement, and provided a robust assessment of the phase proportions in the experimental run products (Figures S2–S4). The phase proportions calculated by both Solver and LIME are checked for consistency and verified by extensive petrographic observations performed in each experiment. Petrographic observations are also used to resolve if a discrepancy in the phase proportion estimates between Solver and LIME is observed. For instance, Solver and LIME estimated different relative proportions of Ca-bearing phases, clinopyroxene and amphibole, in an experiment (ECSY400B-10). Independent petrographic assessment on this experiment indicated that Solver estimates are more consistent with petrographic observations. The phase proportions (in wt. %) constrained by Solver are used in the succeeding sections after showing the good agreement with LIME estimates and that the phase proportions estimated by Solver are more consistent with petrographic observations in few experiments where estimates between LIME and Solver differed. Attainment of chemical equilibrium as reflected in good mass balances also indicated that Fe-loss was insignificant in the experiments. Accessory phases, such as zircon, apatite, and tourmaline, are reported when present, but their modal abundances were not quantified.

3.2 Mineral phase relations and textures

The experimental conditions and mineral phase assemblages and phase proportions constrained by Solver are reported in Tables 3–5 and displayed in Figure 2. Experiments performed

on SY325 mélange (~3 wt. % H_2O bulk) below the solidus are dominated by hydrous phases such as amphibole, chlorite, and talc occurring as euhedral and elongated grains (Figure 3a, b). Increased porosity in the experiments is coincident with the breakdown of chlorite and talc at temperature below 800 °C, indicating the presence of H_2O-rich fluid phase at experimental conditions (Figure 3c). Anthophylite is formed as a breakdown product of talc at 2.5 GPa. At near-solidus, small and elongated orthopyroxene laths are observed throughout the capsule surrounding larger grains of amphibole and clinopyroxene while interstitial melts are found locally around these orthopyroxene grains (Figure 3d) for both 1.5 and 2.5 GPa experiments. The solidus is constrained between 800–850 °C between 1.5 and 2.5 GPa. This is based on petrographic observation of the presence of glassy melt surrounding residual minerals. At temperatures above the solidus, the proportion of amphibole decreases until exhaustion between 900–1000 °C, while the proportion of orthopyroxene + clinopyroxene + melt increases and remains the stable assemblage at higher temperatures. Equant orthopyroxene and clinopyroxene grains are homogenously distributed across the length of the capsule and are surrounded by melts.

Experiments performed on SY400B mélange (~3 wt. % H_2O bulk) below the solidus are dominated by omphacitic clinopyroxene and minor amounts of phengite and chlorite. Small grains of titanite and epidote are interspersed throughout the capsule without any discernible mineral segregation textures. Accessory phases such as tourmaline, zircon, and apatite are also observed at 1.5 and 2.5 GPa (Figures 4 and 6). Omphacitic clinopyroxene and epidote minerals display some chemical zonation at these low-temperature subsolidus conditions (Figure 4a, b). For instance, at 600 °C (1.5 and 2.5 GPa), clinopyroxene grains display patchy appearance in BSE images wherein the limited 'light' cores have higher FeO and lower SiO_2 and Na_2O contents than the more dominant 'dark' mantle and rims (Figure S5). The major element compositions of euhedral and chemically homogenous clinopyroxene grains in these experiments are similar to the composition of the more dominant 'dark' mantle and rims. In addition, sector zoning is observed in epidote at low-temperature subsolidus conditions. The K-rich phase is dominated by phengite at low temperature whereas phlogopite replaces phengite at higher temperatures (≥ 800 °C). The solidus is constrained between 600–700 °C at 1.5 and 700–800 °C at 2.5 GPa based on petrographic observation of the presence of glassy melt. In experiments above the solidus, hydrous melt occurs in equilibrium with diopsidic clinopyroxene + amphibole + phlogopite + titanite + epidote, and minor amounts of tourmaline, oxide, and apatite. Phlogopite and amphibole display prismatic and

elongated habits surrounding larger clinopyroxene grains (Figure 4c, d). Albitic plagioclase is the Al-rich phase at 1.5 GPa and is replaced by garnet at 2.5 GPa. Plagioclase displays prismatic habit whereas garnet is generally equant (Figure 4c, e, f). Rutile is commonly found in high-temperature suprasolidus experiments. Melts occur as mostly dendrite-free homogenous glasses on the edges of the capsule and distributed in between mineral grains throughout the experimental run product (Figure 4e, f).

Experiments performed on C647 (8.5 wt. % H_2O bulk) below the solidus are dominated by sub equal proportion of chlorite and amphibole with euhedral and elongated grains distributed across the capsule. Small grains of ilmenite are also found (Figure 5a). The proportions of garnet + orthopyroxene + olivine increase whereas the proportions of chlorite and amphibole decrease with increasing temperatures at 1.5 GPa. We observed large porosity increase in the experiment at 900 °C and 1.5 GPa which is indicative of the presence of H_2O-rich fluid phase at experimental conditions (Figure 5b, c). The large amount of H_2O-rich fluid is produced by the breakdown of chlorite to form fine aggregates of olivine and minor orthopyroxene at temperatures above 900 °C. The subsolidus assemblage at 2.5 GPa is dominantly composed of garnet + olivine + amphibole ± clinopyroxene. Clinopyroxene is absent in 1.5 GPa experiments but is present at 2.5 GPa. Olivine grains are euhedral to subhedral whereas orthopyroxene and clinopyroxene are generally equant. Garnet grains commonly occur poikilitically enclosing other minerals (Figure 5c, d). The solidus is constrained below 950 °C at 1.5 GPa whereas the solidus is not found at 2.5 GPa and therefore should be located above 1000 °C. Above the solidus, melt forms in equilibrium with olivine + orthopyroxene + amphibole ± garnet ± Al-rich phase (likely an oxide). Ilmenite is the dominant oxide phase in the experiments along with minor amounts of rutile.

3.3 Compositions of experimental melts

The average melt compositions and 1 σ obtained using electron microprobe analysis are reported in Tables 3–5 and displayed in Figures 6 and 7. All experimental melts in this study are hydrous silicate melts and their compositions were measured on quenched dendrite-free glassy pools. For experiments above solidus, low-degree (< 5 wt. %) melts occurred mainly along mineral grain boundaries, while high-degree melts were distributed along grain boundaries and on the capsule edges (Figure 3). Interstitial melts found in between mineral grains are compositionally

similar (within analytical uncertainty) to the larger melt pools found on capsule edges. The H_2O content of experimental melts, estimated from the difference between 100 % and electron probe totals, range from ~7 to 15 wt. %. The H_2O contents of melts from SY325 mélange are broadly similar at ~9 wt. %, whereas the H_2O contents of melts from SY400B mélange decrease from ~15 to 6 wt. %, with increasing temperature, likely due to dilution. The H_2O content of melt from C647 mélange is estimated to be ~11 wt. %. On a volatile-free basis, the melt compositions range from a rhyolitic for SY325, mostly dacitic for SY400B, and a melt composition that straddles between basalt and basaltic for C647 mélange (Figure 6). The Mg# [= molar $Mg/(Mg + Fe^{2+})$] of all experimental melts range between 0.29–0.81.

The experimental melt compositions vary with increasing temperature at constant pressure (Figure 7). In particular, SiO_2 content decreases while Al_2O_3, FeO, MgO, and alkali contents increase with increasing temperatures in SY400B mélange experiments. The CaO content remains constant with increasing temperature, and is slightly higher at higher pressure. The compositions of SY400B mélange melts did not change substantially with pressure, except for a slightly higher Al_2O_3 content in melts at lower pressure. Experimental melts of SY325 mélange display limited variations in SiO_2, Al_2O_3, MgO, and CaO contents with increasing temperature. Compared to SY400B mélange experiments, the melt compositions of SY325 mélange display significant change with pressure. At 2.5 GPa, SY325 mélange melts display systematically lower FeO and CaO contents, and higher alkali contents, while SiO_2, Al_2O_3, and MgO are similar, compared to melts at 1.5 GPa and similar temperatures. The alkali content increases with increasing temperature for both SY400B and SY325 mélanges.

Experimental hydrous melts display systematic trends relative to one another, despite differences in the starting bulk compositions. C647 mélange melt displays the highest Al_2O_3 and lowest CaO contents, while SY325 melts display the lowest Al_2O_3 and highest SiO_2 contents. The SiO_2 content of SY400B mélange melts varies in between. The ranges in FeO and MgO contents for all the melts are limited (i.e. < 4 wt. % for both major element oxides). The CaO contents of melts from SY400B and SY325 mélanges (0.4–1.9 wt. % Al_2O_3) are significantly lower than the melt from C647 (11.3 wt. % Al_2O_3). The alkali content of C647 mélange melt is significantly lower than that of SY400B and SY325 mélange melts.

3.4 Compositions of experimental minerals

The mineral compositions determined using electron microprobe analysis are reported in Tables 6–8 and are displayed in Figure 8. In SY325 experiments, the major element compositions of amphibole, identified as actinolite (Hawthorne et al., 2012), display limited variations over the range of experimental temperatures and pressures. The Mg# of amphibole is slightly higher at 1.5 GPa (82.8–83.7) than at 2.5 GPa (82.5–82.8) at similar temperatures, with an average SiO_2 and CaO contents of 56.2 wt. % and 9.3 wt. %, respectively. The composition of orthopyroxene is rich in enstatite (En) components ranging from ~85 to 90 mol. % En. The orthopyroxene Mg# initially increases from 88.9 to 90.8 then decreases to 86.7, while the average Al_2O_3 content decreases from ~3 wt. % to ~0.3 wt. % with increasing temperature at constant pressure. The composition of clinopyroxene is diopsidic, with Mg# varying from 80.2 to 88.8. The major element compositions of clinopyroxene display limited variation between 900 and 1000 °C at both pressures. The average clinopyroxene SiO_2 content is slightly higher whereas clinopyroxene Na_2O content is lower at 1.5 than at 2.5 GPa. The compositions of chlorite and talc are both Mg-rich, with average Mg# of 83 and 93, respectively.

In SY400B experiments, the major element compositions of experimental minerals vary systematically with increasing temperature. The amphibole, which belongs to the Ca-Na group (dominantly pargasitic and taramitic) (Hawthorne et al., 2012), displays a steady decrease in the average SiO_2 content with increasing temperature (Figure 8a). The CaO content of amphibole increases with increasing temperature with amphibole displaying higher CaO contents at 1.5 GPa than at 2.5 GPa for similar experimental temperatures (Figure 8b). The clinopyroxene composition varies from omphacitic to diopsidic with increasing temperature, with Mg# varying from ~69 to 81. The clinopyroxene displays near-constant SiO_2 content (~56 wt. %) followed by a drop in SiO_2 content to around 52 wt. %. The observed drop in SiO_2 content occurs at a temperature interval between 700 and 800 °C at 1.5 GPa and between 900 and 1000 °C at 2.5 GPa (Figure 8c). The variation in jadeite (Jd) component is clinopyroxene varies from high (~46 mol. % Jd) to low (~12 mol. % Jd) and mirrors the SiO_2 trend. The average clinopyroxene CaO content increases with increasing temperature, wherein the CaO content is higher at 1.5 GPa than at 2.5 GPa for similar temperature (Figure 8d). The K-rich mineral in the SY400B experiment changes from phengite to phlogopite with increasing temperature (Figure 8e, f). Phengite displays limited variations in major element compositions at temperatures up to 800 °C, above which the average K_2O content

increases from ~6 to 9 wt. %. Phlogopite coexists with phengite at 800 and 900 °C, but becomes the sole K-rich phase above 900 °C. Phlogopite displays generally lower SiO_2 and higher K_2O contents than phengite. The main Al-rich mineral changes from plagioclase at 1.5 GPa to garnet at 2.5 GPa. The composition of plagioclase varies systematically from albitic Ab_{100} to $Ab_{66}An_{30}Or_4$, while the composition of garnet becomes more grossular-rich and almandine-poor from $Alm_{36}Prp_{48}Sps_2Grs_{14}$ to $Alm_{30}Prp_{47}Sps_1Grs_{22}$ with increasing temperature (Figure 8g). Epidote displays sector zoning wherein sectors show inverse correlation in CaO and FeO contents. The Mg# of Mg-chlorite is ~80.

In C647 experiments, the amphibole displays variable composition from magnesio-ferri-hornblende, actinolite, and pargasite (Hawthorne et al., 2012). The average SiO_2 and CaO contents initially increase at 700 °C then decrease with increasing temperature. The composition of garnet at 1.5 GPa becomes slightly more grossular-rich and almandine-poor from $Alm_{35}Prp_{50}Sps_2Grs_{14}$ to $Alm_{24}Prp_{53}Sps_1Grs_{22}$, whereas garnet at 2.5 GPa display limited compositional variation ($Alm_{22}Prp_{59}Sps_0Grs_{18}$ to $Alm_{21}Prp_{62}Sps_0Grs_{17}$), with increasing temperature. The average orthopyroxene Al_2O_3 content decreases with increasing temperature (Figure 8h). The average MgO and TiO_2 contents of ilmenite increase with increasing temperature. The Mg# varies between 86 and 89 in clinopyroxene, and between 78 and 87 in olivine. Limited variation in Mg# is observed in Mg-chlorite and orthopyroxene with values of approximately 85 and 84, respectively.

4 Discussion

4.1 Applicability of Syros and Santa Catalina mélange matrix rocks as starting materials

A necessary precaution implemented in this study is assuring that the mineralogy and geochemical characteristics of starting mélange materials are representative of mélange compositions that could form in-situ at the slab-mantle interface conditions, and not dominantly by retrograde re-equilibration at low *P-T* conditions. Our results indicate that the subsolidus assemblages at 1.5 GPa for SY325, SY400B, and C647 mélanges closely reproduced the reported thin section assemblages and modal proportions that were suggested to be represent equilibrium high *P-T* assemblages by previous petrogenetic studies on these mélange rocks (Figure S6; King et al., 2006; Miller et al., 2009). These findings support the applicability of these natural starting

materials as representative mélange compositions that can be found along the slab-mantle interface. These imply that the compositions of our experimental melts and solid residues, as well as their densities can be used to gain insight on subduction zone processes.

4.2 Solidi of mélange rocks

The experimentally-constrained solidi of the different mélange starting materials are shown in Figure 9, plotted along the solidi of other bulk compositions (*e.g.*, sediment, basaltic igneous crust, peridotite) relevant to subduction zone melting and the range of slab-top thermal structures. Experimental studies on fluid-saturated melting of subducting materials resulted in wet solidi between 600–700 °C at 1.5–2.5 GPa for both sediment and basaltic igneous crust compositions (Hermann and Spandler, 2008; Lambert and Wyllie, 1970; Liu et al., 1996; Nichols et al., 1994; Skora and Blundy, 2010; Till et al., 2012). We also plotted a field of wet sediment melting to account for the large compositional variability in subducting sediments. The solidus of SY400B mélange lies between 600–800 °C at 1.5–2.5 GPa. This solidus is comparable to wet solidi of sediment and basalt but is lower than the wet peridotite solidus at these pressures. The solidus of SY325 mélange lies between 800–900 °C at 1.5–2.5 GPa. This solidus is higher than SY400B mélange, subducted basalt and sediments. The solidus of SY325 mélange is lower than the wet peridotite solidus at 1.5 GPa, but is higher at 2.5 GPa. Lastly, the solidus of C647 mélange lies above 900 °C at 1.5–2.5 GPa and is significantly higher than the solidi of SY400B and SY325 mélanges, as well as the wet solidi of subducted materials and peridotite at similar pressures.

Assuming that the SY325 and C647 mélanges remain along the slab-mantle interface and are dragged down to deeper depths, the breakdown of hydrous minerals in these mélanges can provide the necessary fluid phase to initiate wet peridotite melting. Projecting our experimentally derived solidi back to representative slab-top geotherms, melting of SY325 and C647 mélanges are unlikely to occur along cold slab-tops at pressures less than 3 GPa, such as in Tonga and Mariana arcs. On the other hand, melting of SY400B and SY325 mélanges may be possible only along warm slab-tops at pressures of 2.5–3 GPa, such as in the Cascadia arc. Alternatively, the high-temperature conditions needed to melt these mélange rocks may be achieved in rising diapirs into the hotter mantle wedge. The latter mechanism was suggested as an efficient mechanism necessary to extract the elemental components (*e.g.*, Th, Pb) that form the sediment melt signature

in erupted arc lavas at high-temperature conditions (> 1000 °C) (Behn et al., 2011; Syracuse et al., 2010). Therefore, for pressures at or below 2.5 GPa, melting of mélange rocks along the slab-mantle interface is unlikely. Alternatively, buoyant instabilities may form diapirs that could deliver solid or partially molten mélange rocks into the hotter mantle wedge.

4.3 Slab mélange: To rise or not to rise?

The formation of buoyant diapirs from the slab-top is influenced by the density contrast between the materials along the slab-top and the overlying mantle, which remains poorly constrained for mélange compositions. In this study we evaluated the density contrast between mélange rocks relative to the overlying mantle peridotites over a range of *P-T* conditions (Figures 10). The bulk (mineral + melt) and solid (mineral-only) densities of each experimental run product are calculated from the mineral compositions and phase proportions using the approach of Abers and Hacker (2016). To minimize the uncertainty involved in using end-member mineral density in calculating for the bulk density, we calculated the bulk density accounting for the measured compositions of experimental minerals with solid-solutions and assumed a linear mixing between mineral end-member compositions available in the database. For example, the density of orthopyroxene at a *P-T* condition was calculated using the densities of end-member minerals, enstatite, ferrosilite, and wollastonite at that *P-T* condition, and their molar proportions for optimal accuracy. In addition, the melt density was calculated using the DensityX program (Iacovino and Till, 2018) while the melt viscosity was calculated using the parametrization of Giordano et al. (2008). The viscosities of hydrous mélange melts range from $10^{1.3}$–$10^{2.4}$ Pa·s for SY400B mélange, $10^{1.6}$–$10^{3.1}$ Pa·s for SY325 mélange, and $10^{1.1}$ Pa·s for C647 mélange (Table S9), well within the range of viscosities constrained for experimental anhydrous basaltic melts and hydrous sediment melts ($10^{2.5}$–$10^{-1.5}$ Pa·s) (Hack and Thompson, 2010; Schmidt, 2015). The low wetting angles (12–18°) determined for similar types of hydrous rhyolitic melts would allow for a near-instantaneous extraction of low-degree melts (Laporte, 1994). Accordingly, rapid escape of mélange partial melts upon crossing the solidus is permissible.

The calculated bulk and solid densities from the phase proportions constrained by Solver and LIME showed very good agreement with one another (Figure S7). The calculated bulk densities (from Solver) of subsolidus assemblages of SY400B, SY325, and C647 at 1.5–2.5 GPa

are roughly constant with increasing temperature, except for C647 mélange. At the lowest experimental temperature in 1.5 GPa, SY400B mélange displays the highest bulk density of 3180 kg/m^3, followed by SY325 and C647 mélanges with comparable bulk densities of 3000 kg/m^3 (Figure 10). The subsolidus bulk density increases with pressure. At 2.5 GPa, the bulk density of C647 mélange shows an increase to ~3500 kg/m^3 due to the stabilization of garnet in the subsolidus, a feature that is absent in the subsolidus assemblages of SY325 and SY400B mélanges with subsolidus bulk densities of 3050 and 3200 kg/m^3, respectively.

Melting leads to a decrease in bulk densities of SY400B and C647 mélanges whereas the opposite trend is observed for SY325 mélange. The decrease in bulk density upon melting of SY400B mélange reflects the decreased abundance of clinopyroxene and the formation of hydrous melt in equilibrium with low-density minerals such as phlogopite, plagioclase and amphibole. The decrease in bulk density in C647 mélange reflects the breakdown of garnet. In contrast, the slight increase in bulk density in SY325 mélange reflects the breakdown of dominantly amphibole to produce hydrous melt and anhydrous minerals olivine and orthopyroxene. For all the bulk compositions, the solid residue after melt extraction becomes denser, indicating that instantaneous melt extraction counteracts buoyancy.

Relative to the density of the overlying mantle peridotite (3300–3400 kg/m^3 at 500–1100 °C and 1.5–2.5 GPa), SY325 mélange can rise by buoyancy under our experimental temperatures and pressures, and melting may occur later during ascent through the mantle wedge. In comparison, SY400B mélange can also rise by buoyancy under experimental temperatures and pressures, and melting may occur near warm slab-top conditions and during diapir ascent through the mantle wedge. Due to the stabilization of large amounts of garnet, C647 mélange can rise but only at the lowest experimental temperature conditions (< 800 °C and 1.5 GPa), and melting is expected to be delayed during ascent, occurring only in the hotter portions of the mantle wedge. Since the subsolidus assemblage of C647 mélange is significantly denser than mantle peridotite at similar temperatures at 2.5 GPa, buoyancy and diapirism of C647 mélange is unlikely under these conditions. In this scenario, C647 mélange would remain along the slab-top and be dragged to deeper depths by corner flow until it melts at temperatures above 1000 °C.

Lakey and Hermann (2022) investigated the phase equilibria of two natural chlorite-rich lithologies (i.e. an epidote-omphacite-chlorite mélange and a monomineralic chlorite mélange) over a range of temperatures at pressures higher than investigated in this study. The results showed

that these mélange compositions display large jumps in bulk densities due to large amounts of subsolidus garnet that formed at the expense of chlorite, similar to our observations in C647 mélange. They argued that this process could lead to the densification of mélange rocks relative to the overlying mantle and inhibit diapirism. We report similar results for C647 at 2.5 GPa. However, our experimental study shows that SY325, SY400B, and C647 mélanges will remain buoyant over a wide range of *P-T* conditions during subduction. This study, along with the study of Lakey and Hermann (2022), highlights the importance of bulk composition in controlling the density evolution of natural mélanges and the likelihood of diapirism, especially those that favor garnet formation during prograde subduction.

Garnet is a common aluminous phase in high-pressure metamorphic rocks (*e.g.*, eclogite, garnetite, metasediment). Pseudosection modeling performed on bulk compositions relevant to individual slab materials supports the more favorable garnet formation in peraluminous (pelitic) than metaluminous (basaltic) compositions with increasing *P-T* conditions during subduction (Hacker et al., 2011; Wei and Powell, 2004). Using the Alumina Saturation Index (ASI = [molar Al_2O_3 / ($CaO + K_2O + Na_2O$)] (Nesbitt and Young, 1984)), the bulk composition of C647 is the most peraluminous (i.e. ASI > 1), followed by SY400B, and then SY325. Therefore, C647 mélange has the highest propensity to stabilize garnet early on during prograde subduction, consistent with our experimental observations. Similarly, the bulk mélange compositions used by Lakey and Hermann (2022) have ASI close to or above 1. This provides an explanation for the large amounts of subsolidus garnet in C467 mélange, as well as in the experiments of Lakey and Hermann (2022) conducted at higher pressure. On the other hand, SY400B mélange stabilized subsolidus garnet only at 2.5 GPa whereas SY325 mélange did not stabilize garnet at both pressures. This implies that the compositional variability in mélanges along the slab-mantle interface and their varying response to increasing *P-T* conditions during subduction would result in density sorting that preferentially allow metaluminous bulk compositions to form diapirs.

4.4 Comparison with thermodynamic phase equilibrium models

We independently assessed the phase equilibria, modal proportions, and density evolution of the three starting compositions using Perple_X 6.9.0 (Connolly, 1990) and the thermodynamic database of Holland et al. (2018) modified by Klein and Behn (2021) (Figures 10 and 11). Details

of the modeling procedure are found in the supplementary material. We calculated the phase equilibria for the same experimental bulk compositions and simulated two model set-ups. Model 1 simulates a water-saturated condition wherein a free fluid phase is always present at all *P-T* conditions. Model 2 simulates a scenario wherein the H_2O content is fixed at a value similar to the bulk starting composition. In model 2, a free fluid phase may or may not be present at a *P-T* condition depending on phase stability. The thermodynamically predicted solidi of the three mélange compositions all display negative slopes between 1.5 and 2.5 GPa, occurring at 750 and 690 °C for SY325, 640 and 600 °C for SY400B, and 860 and 600 °C for C647 mélange. The predicted solidi are similar between model 1 and model 2 but the predicted melt productivities are significantly higher in the water-saturated model 1 (Figure S8), and less consistent with experimental observations. Consequently, we favor model 2 for comparison with the experimental results.

Comparison in the phase proportions and calculated densities between thermodynamic models (i.e. model 2) and experiments showed reasonable agreement for SY325, SY400B, and C647 mélanges at 1.5 GPa. However, the models predict phase boundaries and onset of melting at lower temperatures at both 1.5 and 2.5 GPa. Differences between models and experiments are more apparent at higher pressure, especially in SY325 and C647 mélanges. For instance, the modal proportion and thermal stability limit of amphibole in SY325 mélange were severely under-predicted by models at 2.5 GPa. In addition, models also predicted an unrealistically low temperature of 600 °C for the onset of melting of C647 mélange at 2.5 GPa whereas our experiments at 900 and 1000 °C both indicate subsolidus regime. These results are consistent with values for the solidus of chlorite-rich ultramafic compositions found to be between 1100 and 1150 °C at 3 GPa (Lakey and Hermann, 2022). The models also reproduce the main mineralogy of SY400B mélange but under-predict the abundance and thermal stability of phlogopite and plagioclase, while the models over-predict garnet abundance. The models underestimate the phase stabilities of minerals such as epidote and titanite at both pressures. This can be attributed to the difference in bulk Fe^{3+}/Fe_{total} of our starting materials (not determined in this study) and the value assumed in the model calculations.

Accordingly, the observed differences in the phase equilibria between models and experiments translate to differences in calculated densities. Models predict density change associated with mineral reactions or phase transformations at lower temperatures than indicated

by experiments. Despite this offset, the models and experiments generally agree on whether mélange rocks would be buoyant relative to the overlying mantle, especially at low pressure. Models predicted higher solid density of SY400B mélange at > 3400 kg/m^3 than the overlying mantle due to the predicted garnet abundance at 2.5 GPa, at temperatures as low as 800 °C. Because the models predict extensive melting (up to 40 %) of C647 mélange at temperatures below 800 °C, the resulting bulk and solid densities are significantly different than our subsolidus experiments at similar experimental *P-T* conditions.

The differences between models and experiments are unlikely to have resulted from kinetic limitation in nucleation and growth in experiments because the offset remains similar in high-temperature, suprasolidus conditions. Instead, the differences in predicted solidus temperatures and Clapeyron slopes likely reflect a limited thermodynamic database that struggles to accurately predict the phase equilibria and melting of hybrid mélange compositions, especially at higher pressures. These findings imply that the use of phase equilibrium models (pseudosection) to assess the density evolution of mélange rocks may be a reasonable approximation at low-temperature and low-pressure subsolidus (metamorphic) conditions for water- 'poor' mélanges (< 3 wt. % H_2O, pressures ≤ 1.5 GPa). However, we caution on the use of these models at conditions above the solidus. In this case, a better understanding of the solubility of H_2O in mélange melts becomes crucial. For example, it is possible that the combination of large amounts of H_2O in the starting material C647 and the lack of activity-composition models that would allow for forward modeling of mélange melting may have contributed to the observed large discrepancy between model predictions and experiments.

4.6 Potential for mélange diapirism in subduction zones

The thickness and viscosity of the mélange layer along the slab-mantle interface would affect its overall buoyancy (Behn et al., 2011; Klein and Behn, 2021; Miller and Behn, 2012). While the layer thicknesses in individual subduction zones are poorly constrained, conservative estimates based on field mapping of exhumed high-pressure mélange terranes are in the order of hundreds of meters to kilometer-scale (Agard et al., 2018; Angiboust et al., 2014, 2013; Bebout and Penniston-Dorland, 2016). However, evaluating the viscosity contrast between the mélange layer and the overlying mantle is more difficult. This is primarily because of the lack of rheologic

flow laws for hydrous minerals, such as for chlorite, amphibole, serpentine, and mica which comprise the bulk of mélange at low-temperature conditions. In addition to density contrast, the influences of viscosity and layer thickness on the overall buoyancy (V) of mélange (as a diapir) relative to the overlying mantle is shown in the modified Stokes velocity (Burov et al., 2003; modified after Weinberg and Podladchikov, 1994),

$$V = C\frac{\frac{1}{3}(\Delta\rho g r^2)}{\eta}$$

where $\Delta\rho$ is the density difference between the overlying mantle and the mélange diapir, g is the gravitational acceleration, r is the diapir radius, and η is set to be the effective viscosity of the surrounding mantle. C is a function of the viscosity contrast between the diapir and the surrounding mantle, and has a value of 1 when η_{mantle} is significantly greater than the $\eta_{mélange}$. A value of 1 for C is warranted because the viscosities of hydrous minerals (*e.g.*, mica, serpentine; Hilairet et al., 2007; Kronenberg et al., 1990; Tullis and Wenk, 1994) at low temperature conditions are generally lower than of wet olivine (i.e. representing the overlying mantle; Hirth and Kohlstedt, 2004) under the same temperature conditions. The value of r effectively translates to the thickness of the mélange layer assuming that a diapir nucleates following a Rayleigh-Taylor instability with wavelength (λ) equal to $2\pi h/k$, where h is the layer thickness and k is the non-dimensional wave number (Jull and Kelemen, 2001; Klein and Behn, 2021; Zhang et al., 2020). Accordingly, the value of V is highest when the density difference between a thick mélange layer and the overlying mantle is largest, and when the viscosity difference between them is minimized (i.e. low viscosity overlying mantle).

The density of mélanges based on our experiments indicate that the abundance of low-density hydrous minerals such as chlorite, amphibole, talc, and mica promote larger density contrast with the overlying mantle at low *P*-*T* conditions. Even though exhumed high-pressure mélange terranes display significant lithologic heterogeneity, hydrous minerals such as chlorite and amphibole are found ubiquitously and in large abundance in these terranes. These observations are supported by petrologic and thermodynamic modeling studies that suggested formation of chlorite and other hydrous minerals by fluid-mediated metasomatism of ultramafic and mafic rocks are likely pervasive along the plate interface (Bebout and Barton, 2002; Bebout, 1991; Bebout and Penniston-Dorland, 2016; Codillo et al., 2022a, 2022b; Miller et al., 2009; Mori et al., 2014). This

implies that buoyancy and diapirism are possible within the thermal stability limit of chlorite at ~850 °C (Lakey and Hermann, 2022; Pawley, 2003). Since this temperature limit is not achieved along cold and intermediate slab-tops, and only at ~3 GPa in warm slab-tops, buoyancy and diapirism of chlorite-rich mélanges below 3 GPa would be possible for most subduction zones worldwide (Syracuse et al., 2010). However, our experimental data show that densification is likely to occur upon the formation of nominally-anhydrous minerals (*e.g.*, garnet and olivine) upon the breakdown of chlorite-rich assemblages (Figure 12). Because garnet is denser and likely more viscous than wet olivine over the range of our experimental temperatures (*e.g.*, Hirth and Kohlstedt, 2004; Ji and Martignole, 1994; Jull and Kelemen, 2001), its formation and abundance would likely arrest further ascent and result in the stagnation of mélange residue in the mantle (Lakey and Hermann, 2022).

5 Conclusion

This study provides an experimental basis to assess the phase equilibria, melting systematics, and density evolution of mélange rocks at *P-T* conditions relevant to subduction zones. We show that melting of mélange rocks is unlikely to occur along warm or cold subducting slabs at pressures ≤ 2.5 GPa. Instead, our calculations suggest that the density contrast between subsolidus mélange rocks and overlying mantle peridotite is sufficient to promote buoyancy and potential diapirism at least up to 2.5 GPa in metaluminous compositions. The formation of garnet at 2.5 GPa in peraluminous mélange rocks likely prevents significant diapirism. We also show that thermodynamic modeling approach can generally reproduce the subsolidus mineralogy and bulk density of the mélange rocks with low initial water contents (i.e. SY325 and SY400B) and at low-pressure conditions. However, discrepancies between models and experiments are larger at higher pressure (2.5 GPa) and for experiments with higher initial water contents, highlighting the need for an improved thermodynamic database that includes novel bulk compositions beyond the compositions of canonical subducting lithologies. This highlights the need for additional experimental constraints that span a wider range of *P-T* conditions and bulk compositions to better assess the likelihood of mélange diapirism in subduction zones. Results of this study suggest that buoyancy-driven ascent of mélanges into the overlying mantle may be an important and efficient process of slab-to-mantle transport of slab-derived components in subduction zones.

Figures

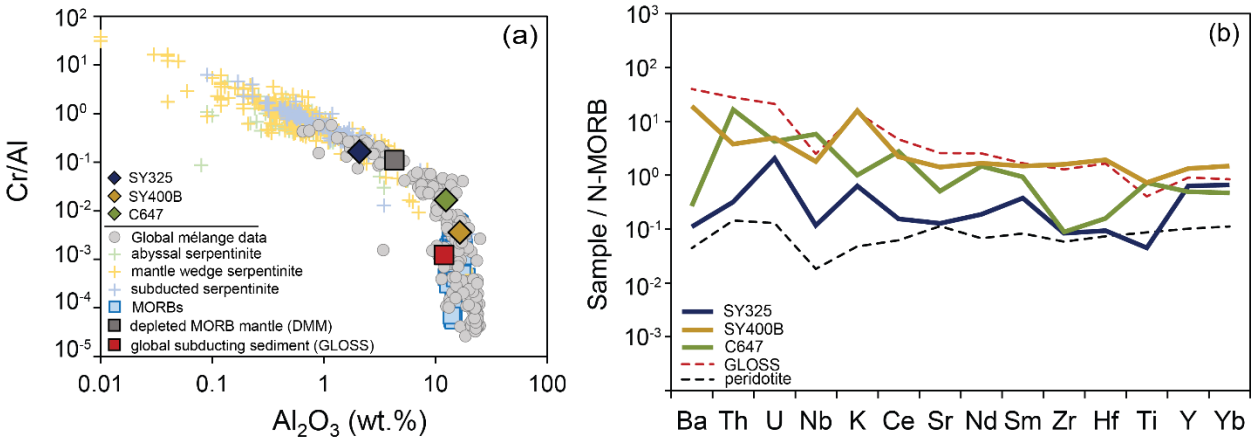

Figure 1. Geochemical characteristics and discrimination using (a) immobile element Cr/Al vs Al_2O_3 systematics and (b) N-MORB normalized trace element compositions. The three starting mélange compositions used in this study cover a large range of the natural variability of mélanges. The N-MORB (Gale et al., 2013), normalized trace element abundances of SY325, SY400B, and C647 mélanges are plotted along with DMM-like peridotite, and GLOSS. Literature data sources: Global mélange compilation (Marschall and Schumacher, 2012), abyssal, mantle wedge and subducted serpentinite compilation (Deschamps et al., 2013), MORB compilation (Gale et al., 2013), DMM composition (Workman and Hart, 2005), and GLOSS (Plank and Langmuir, 1998).

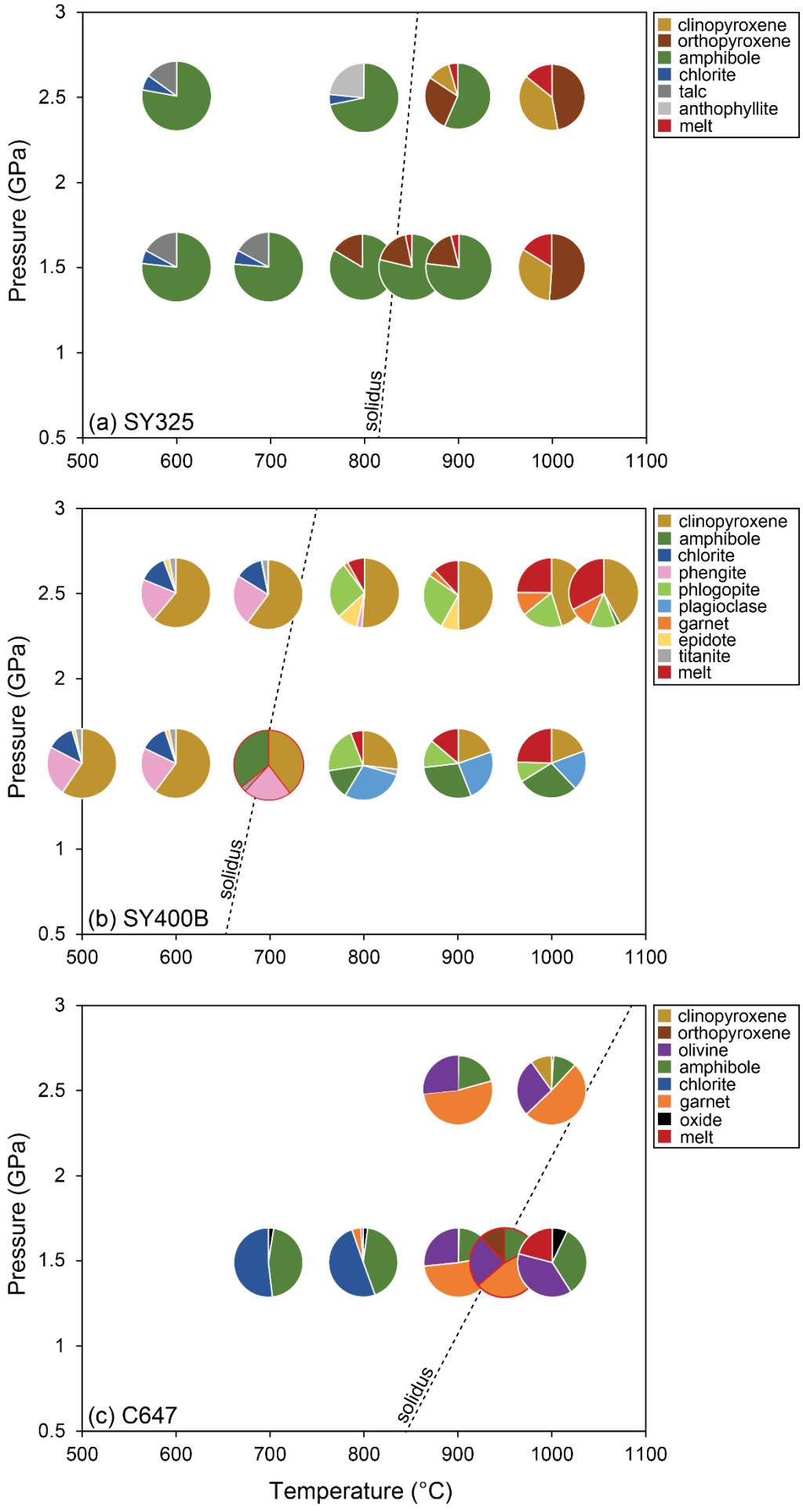
clinopyroxene
orthopyroxene
amphibole
chlorite
talc
anthophyllite
melt
Pressure (GPa)
3
2.5
2
1.5
1
0.5
solidus
(a) SY325
500
600
700
800
900
1000
1100
clinopyroxene
amphibole
chlorite
phengite
phlogopite
plagioclase
garnet
epidote
titanite
melt
Pressure (GPa)
solidus
(b) SY400B
clinopyroxene
orthopyroxene
olivine
amphibole
chlorite
garnet
oxide
melt
Pressure (GPa)
solidus
(c) C647
Temperature (°C)

Figure 2. Experimental conditions, phase equilibria and melting relations of (a) SY325, (b) SY400B, and (c) C647 mélanges. The solidus for each composition is constrained in dashed black line. The mineralogy and relative proportions (in wt. %) are depicted in colored pie charts. The red margin of pie chart indicates the presence of small amounts of melts but their compositions could not be determined accurately. The phase proportions are constrained using Solver. Mineral abbreviations are from Whitney and Evans (2010).

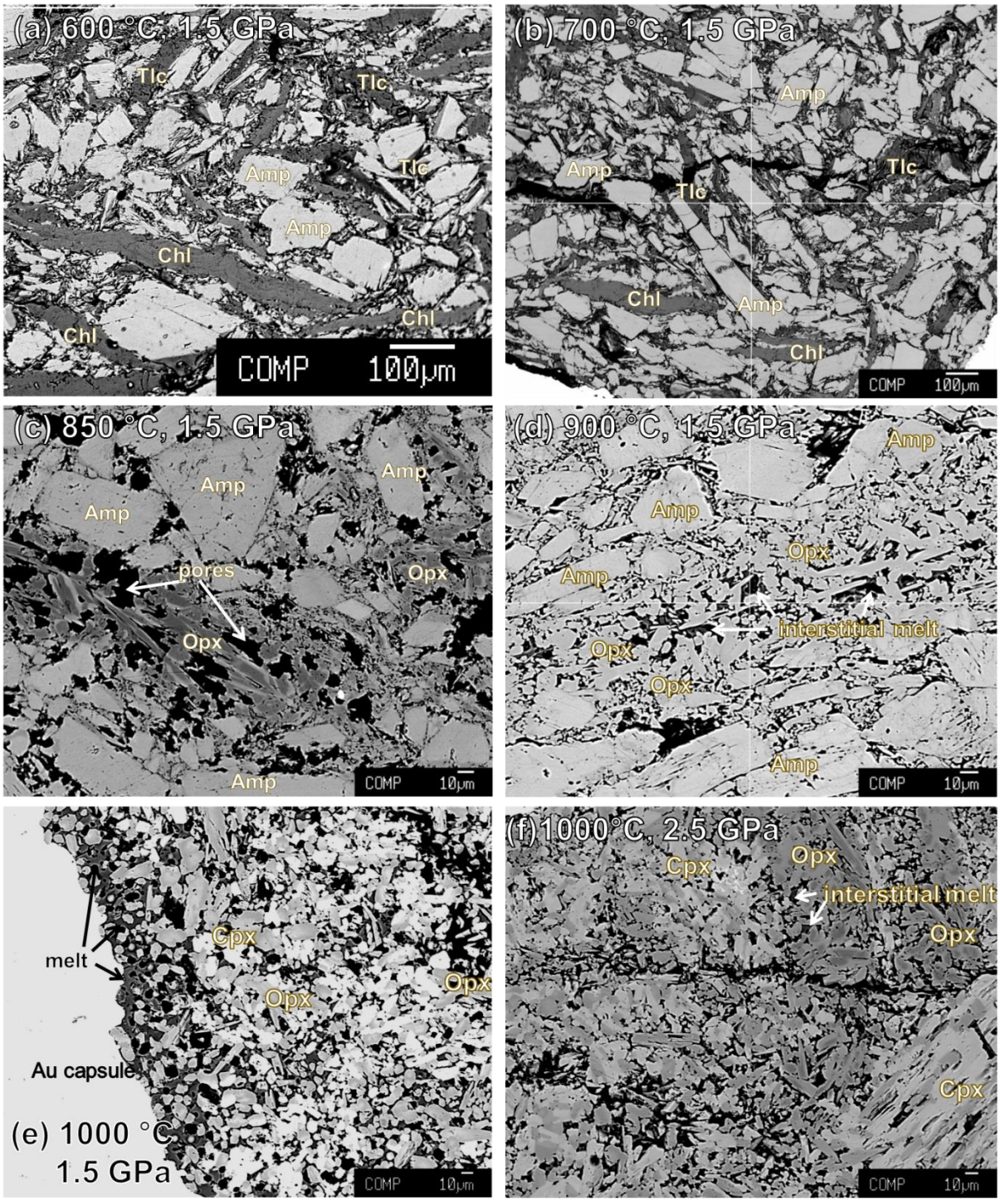

Figure 3. Representative backscattered electron (BSE) images of SY325 experiments from subsolidus to suprasolidus conditions. (a-b) Experiments conducted below the solidus are dominated by hydrous minerals such as amphibole, chlorite and talc that display homogenous distribution in the capsule. (c-d) Breakdown of chlorite and talc leads to porosity increase with

small amounts of interstitial melt. (e-f) Experiments above the solidus are dominated by anhydrous minerals orthopyroxene and clinopyroxene that are homogenously distributed in the capsule. (e) Relatively large melts pools along the capsule sides. Mineral abbreviations are from Whitney and Evans (2010).

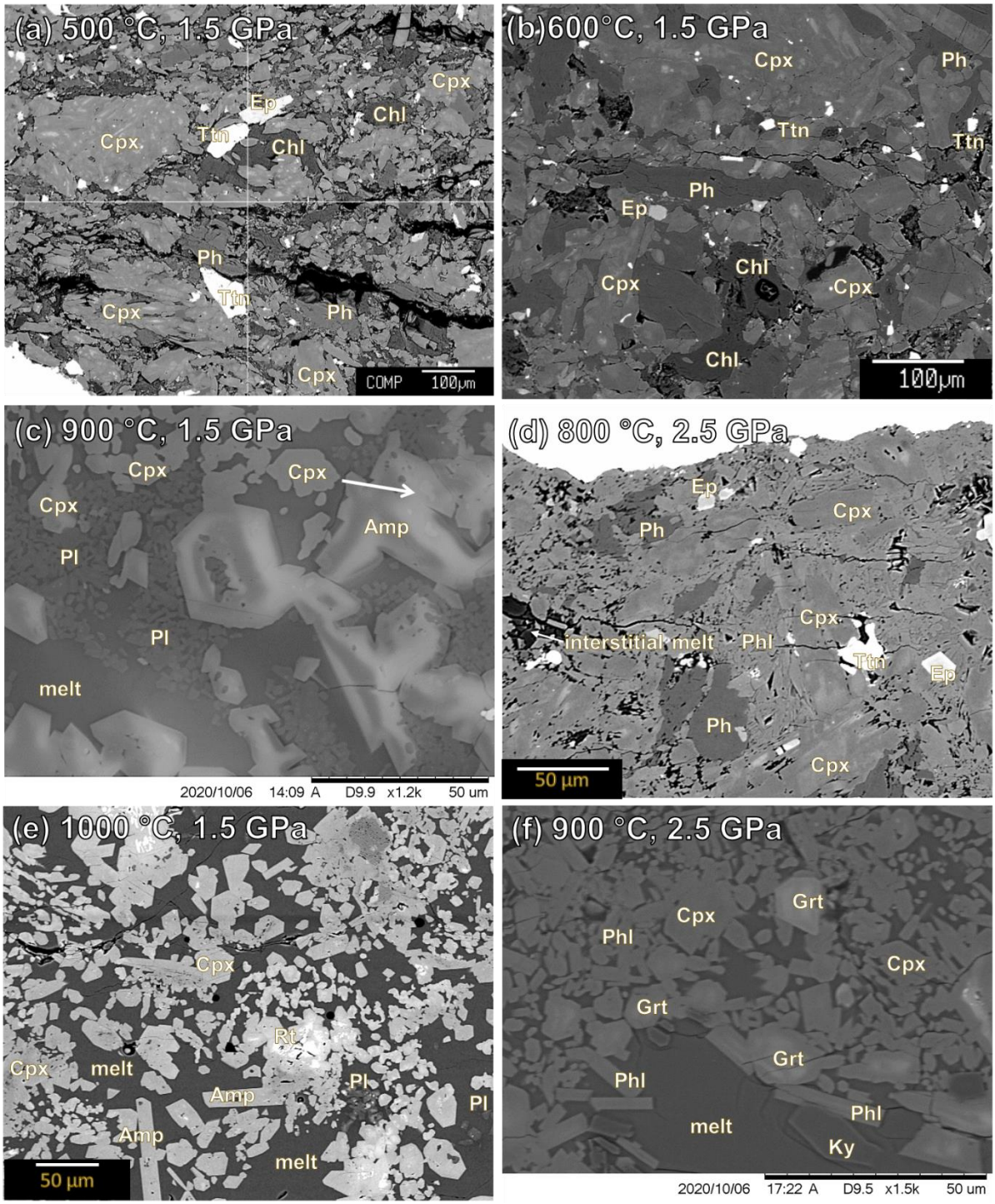

Figure 4. Representative electron backscatter (BSE) images of SY400B experiments from subsolidus to suprasolidus conditions. (a-b) Experiments conducted below the solidus are dominated by omphacitic clinopyroxene with minor amounts of phengite and chlorite, and traces of titanite and epidote that are homogenously distributed in the capsule. Clinopyroxene and epidote minerals display chemical zonations (see Figure S3 from magnified BSE images). (c-f) Experiments above the solidus display homogenous, dendrite-free melt in equilibrium with

diopsidic clinopyroxene, amphibole, phlogopite and an Al-rich phase (plagioclase at 1.5 GPa and garnet at 2.5 GPa). Traces of rutile, kyanite, and corundum are sometimes found along with melt. Mineral abbreviations are from Whitney and Evans (2010).

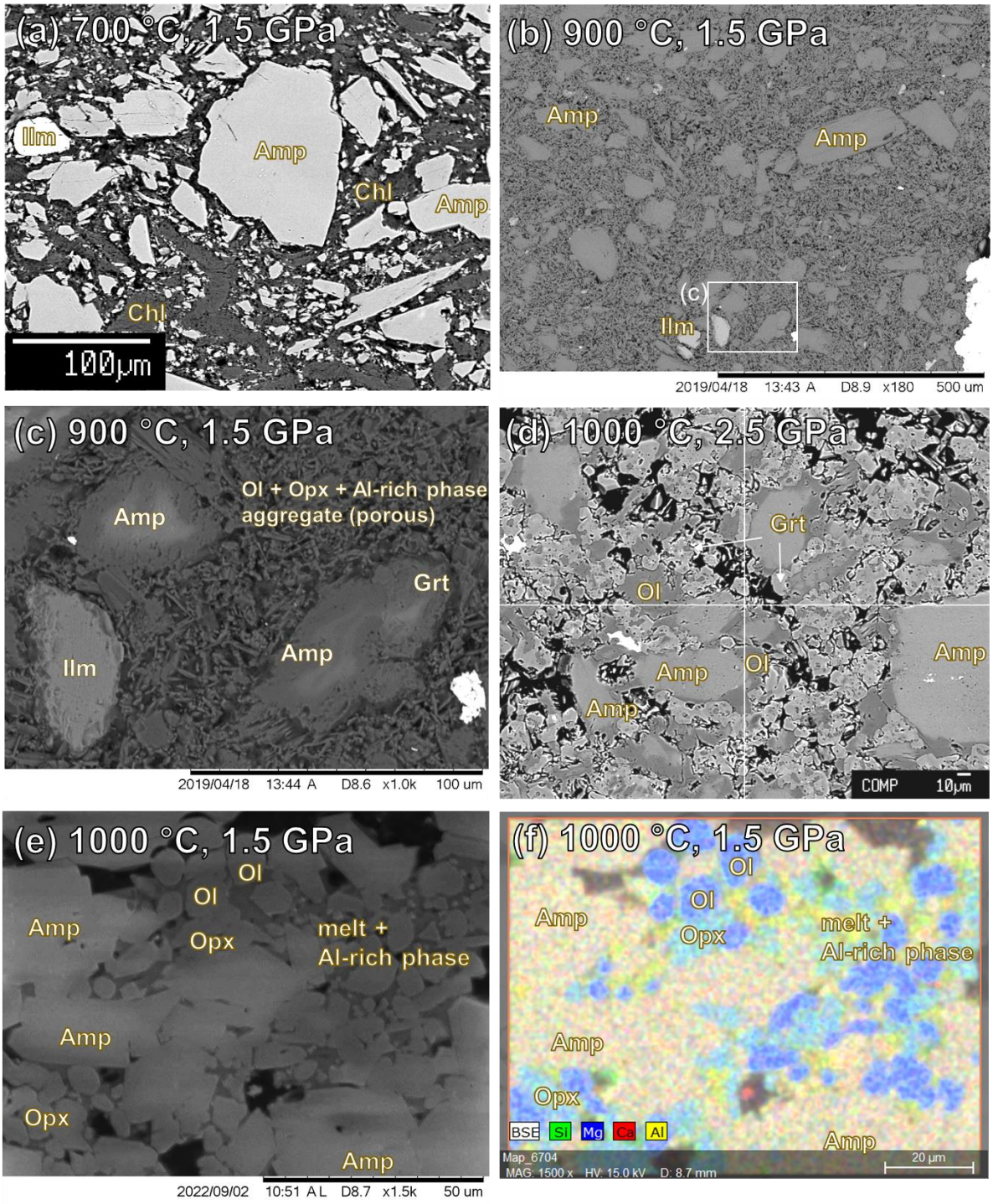

Figure 5. Representative backscattered electron (BSE) images of C647 experiments from subsolidus to suprasolidus conditions. (a) Experiment conducted below the solidus is dominated by sub-equal proportion of amphibole and chlorite with minor ilmenite. (b-d) Subsolidus breakdown of chlorite leads to garnet formation and porosity increase partially filled with fine aggregates of olivine and minor orthopyroxene. The large porosity indicates the former presence

of a H_2O-rich phase during the experiment. (e) Experiment above the solidus displays melt in equilibrium with amphibole, olivine, orthopyroxene, and minor fine-grained Al-rich phase. (f) Chemical map that display the relative concentrations of Si, Mg, Ca, and Al rastered over (e) to help identify the phases. Mineral abbreviations are from Whitney and Evans (2010).

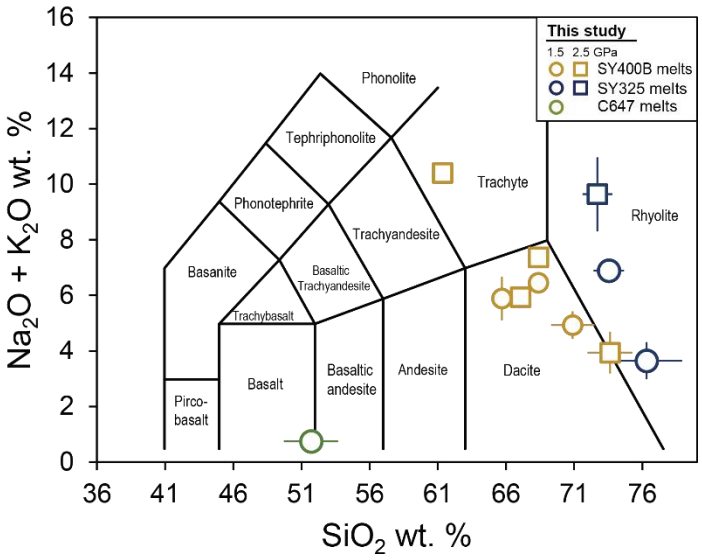

Figure 6. Total alkali versus SiO_2 variation in wt. % of experimental melts from this study. The data are plotted as averages (on volatile-free basis) with error bars representing 1 σ.

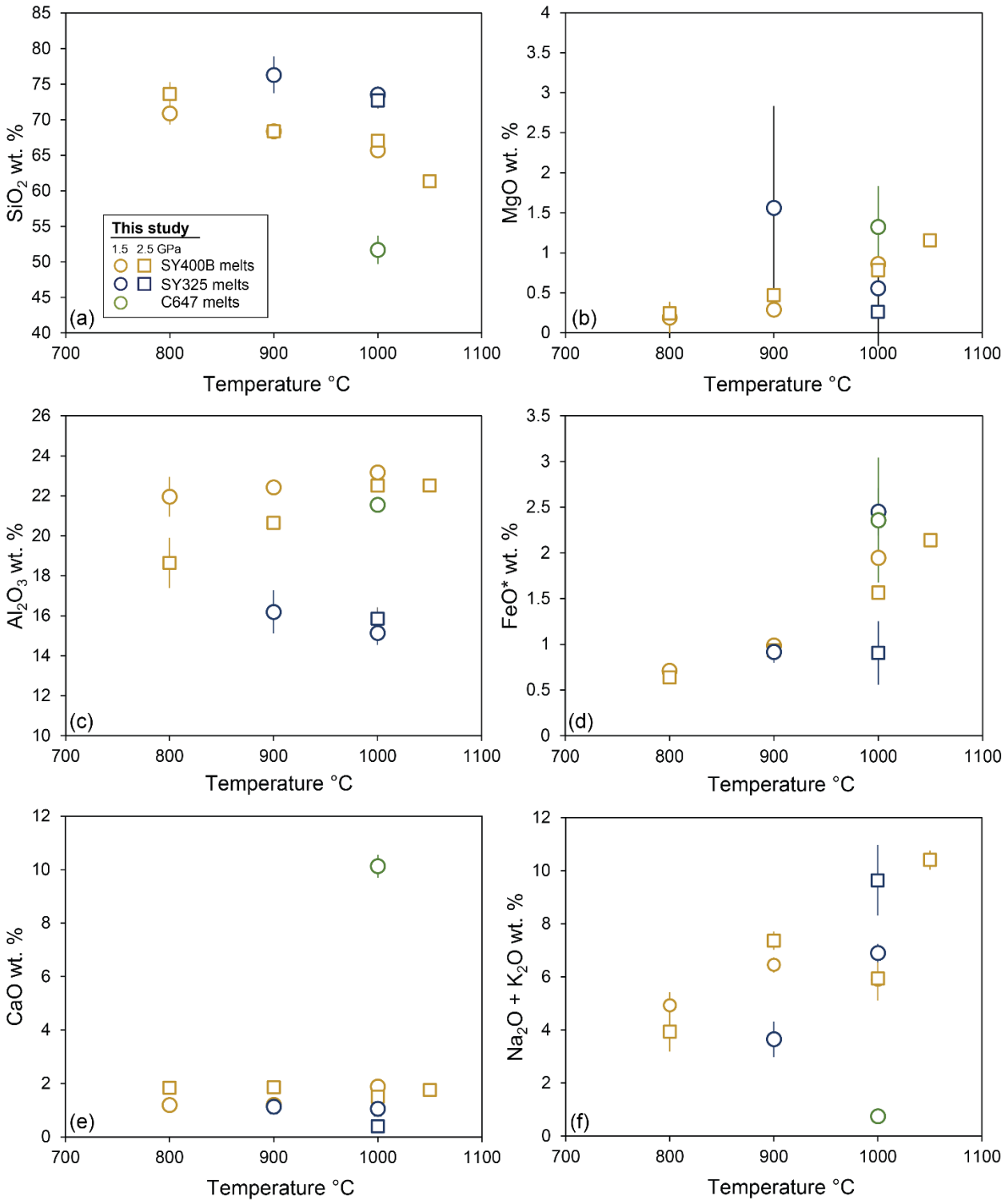

Figure 7. Major element variations (a) SiO_2, (b) MgO, (c) Al_2O_3, (d) FeO* (as total FeO),(e) CaO, (f) $Na_2O + K_2O$ of experimental mélange melts from this study vs. temperature. Symbols: Circles are experimental melts at 1.5 GPa while squares are from 2.5 GPa. The data are plotted as averages

(on volatile-free basis) with error bars representing 1 σ. When no error bars, error bars are smaller than symbols.

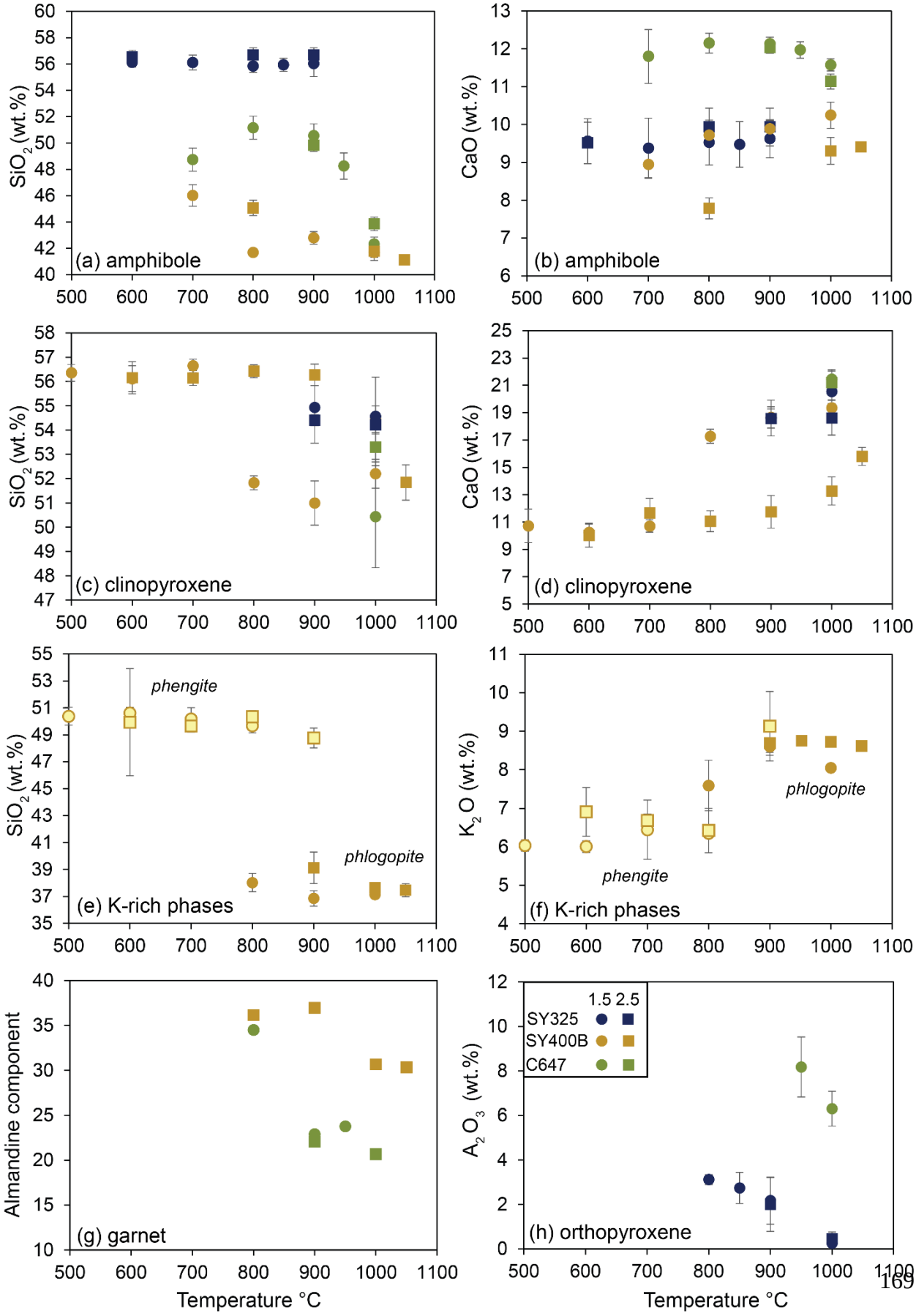
(a) amphibole
(b) amphibole
(c) clinopyroxene
(d) clinopyroxene
(e) K-rich phases
(f) K-rich phases
(g) garnet
(h) orthopyroxene
phengite
phlogopite
SiO2 (wt.%)
CaO (wt.%)
K2O (wt.%)
A2O3 (wt.%)
Almandine component
Temperature °C
1.5 2.5
SY325
SY400B
C647

Figure 8. Variations in the compositions of main residual mineral phases in the experiments as functions of temperature and pressure. Blue, yellow (including light yellow for phengite), and green symbols are used for SY325, SY400B, and C647 mélange experiments, respectively. Colored circle and square symbols indicate minerals from 1.5 and 2.5 GPa experiments, respectively. The data are plotted as averages with error bars representing 1 σ. When no error bars, error bars are smaller than symbols.

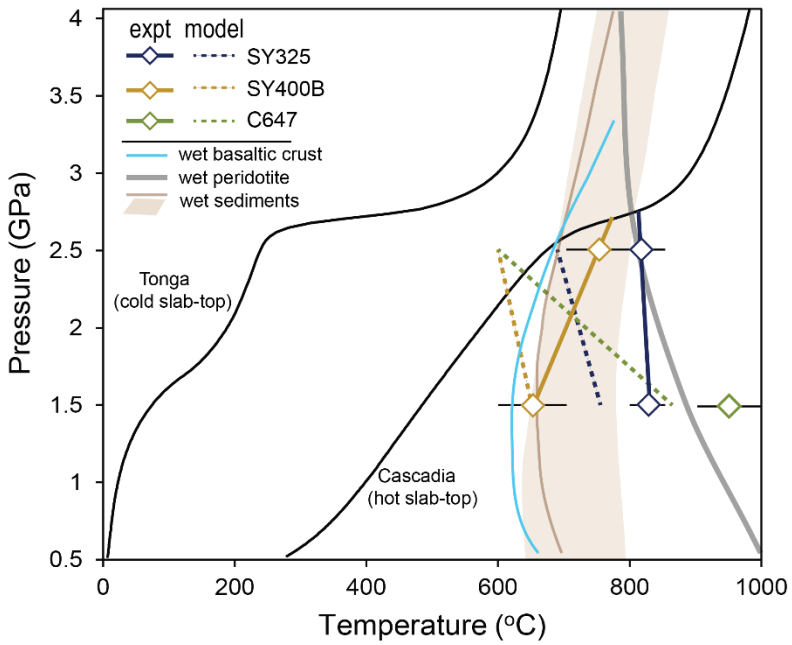

Figure 9. Experimentally-constrained solidus of different starting mélange rocks between 1.5 and 2.5 GPa. The solidi of SY400B and SY325 at pressure higher than 2.5 GPa are extrapolated by extending the traces of the solidi at 1.5 and 2.5 GPa until they intersect the warm slab-top geotherm. The solidus of C647 mélange should be located at temperature above 1000 °C at 2.5 GPa. The wet solidus of sediment, basaltic igneous crust, and peridotite, as well as the predicted solidi of mélange rocks by Perple_X model are plotted for comparison, along with slab-top geotherms representing a cold (Tonga) and a warm (Cascadia) subducting slab (D80 model of Syracuse et al., 2010). (Data references: Lambert and Wyllie, 1970; Liu et al., 1996; Mann and Schmidt, 2015; Nichols et al., 1994; Skora and Blundy, 2010; Till et al., 2012).

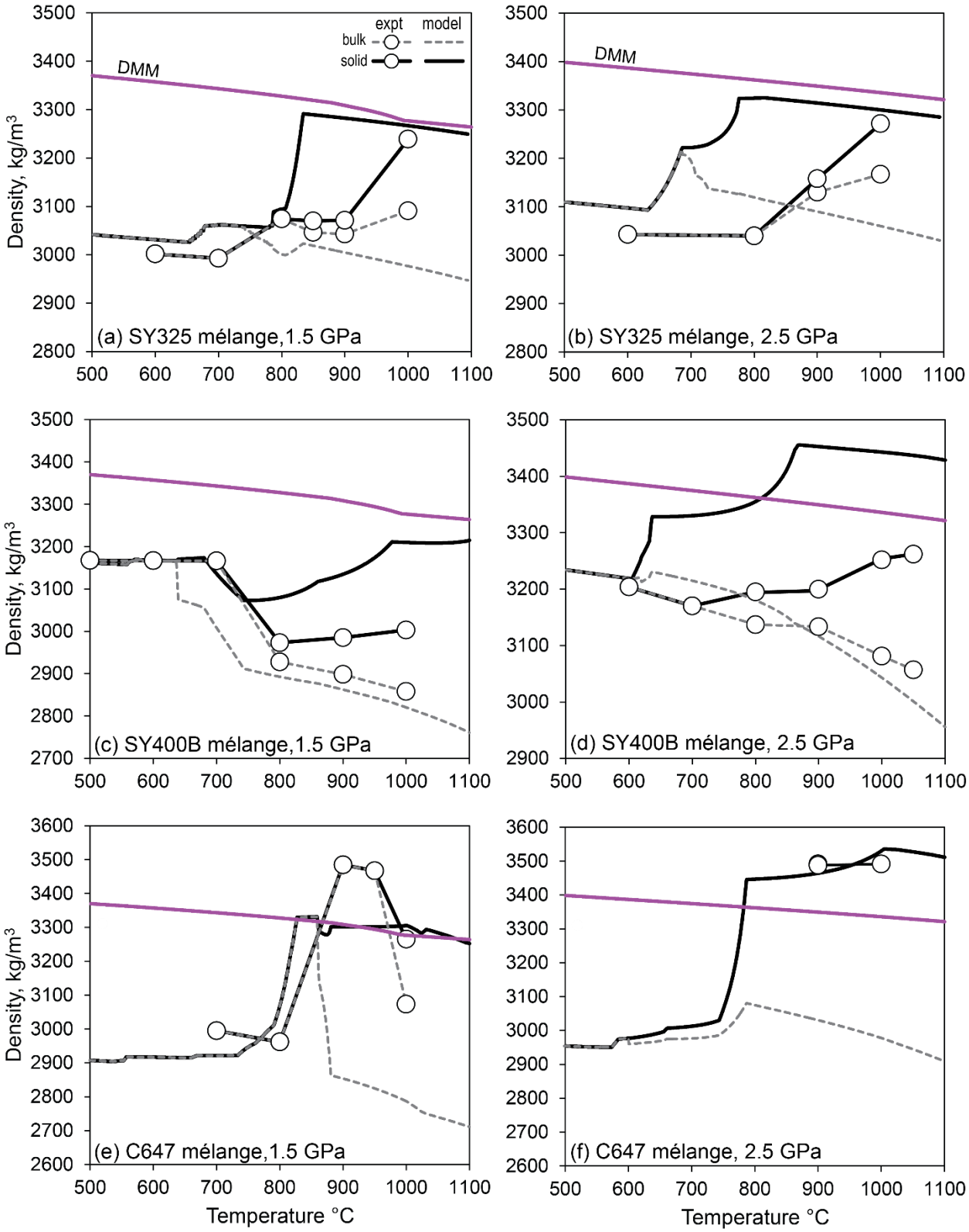

Figure 10. Comparison of the density evolution of mélange rocks constrained by mélange melting experiments (points; this study) and thermodynamic models. Solid black lines display bulk density

while the dashed gray lines display solid density assuming instantaneous melt extraction upon crossing the solid. The phase proportions are constrained by Solver. As a reference, the bulk density of depleted MORB mantle is plotted in solid purple line. Diapirism of mélange along the slab-mantle interface is promoted when the ambient mantle is denser than mélange rocks.

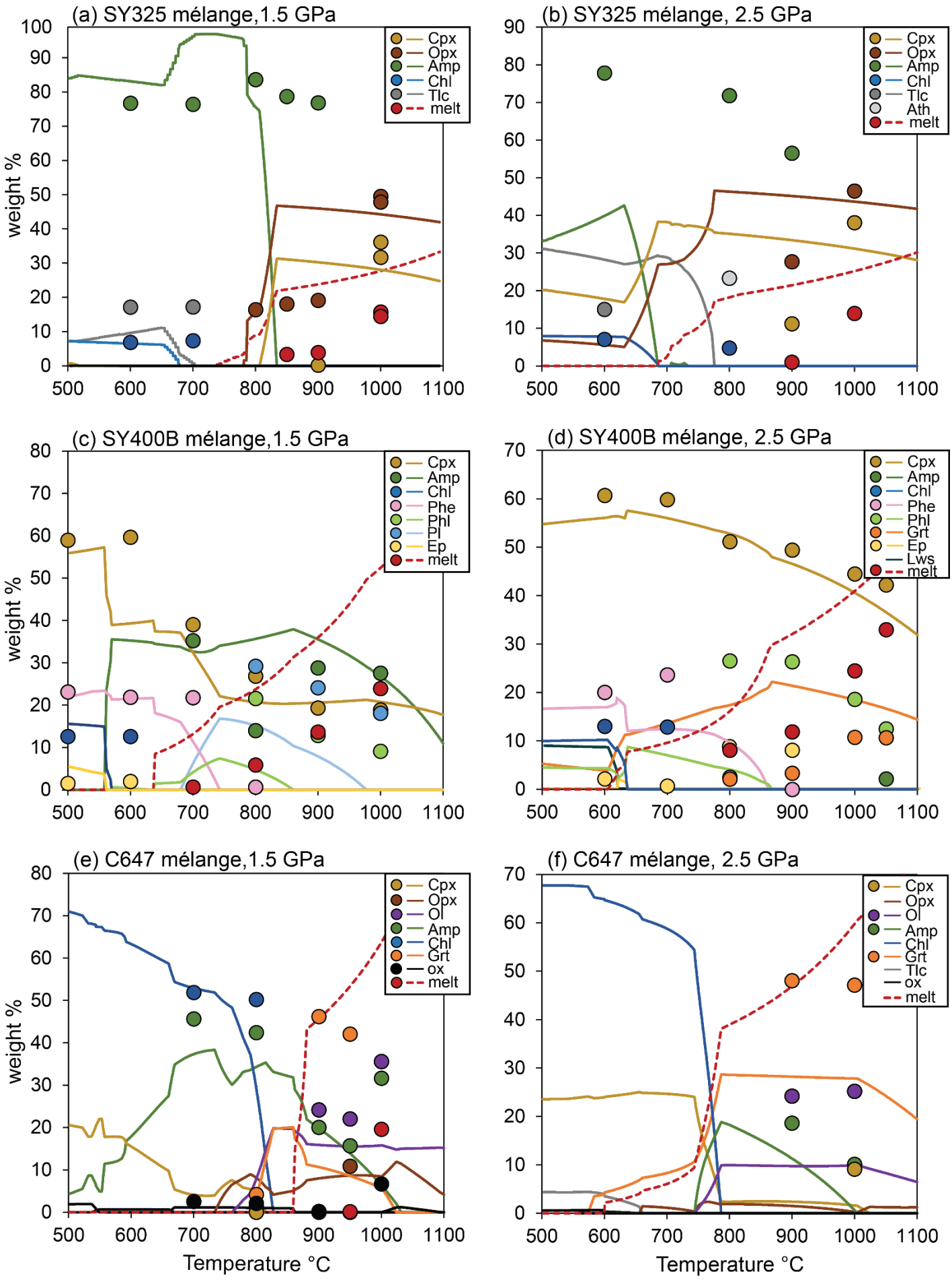
(a) SY325 mélange,1.5 GPa
Cpx
Opx
Amp
Chl
Tlc
melt
weight %
(b) SY325 mélange, 2.5 GPa
Cpx
Opx
Amp
Chl
Tlc
Ath
melt
(c) SY400B mélange,1.5 GPa
Cpx
Amp
Chl
Phe
Phl
Pl
Ep
melt
(d) SY400B mélange, 2.5 GPa
Cpx
Amp
Chl
Phe
Phl
Grt
Ep
Lws
melt
(e) C647 mélange,1.5 GPa
Cpx
Opx
Ol
Amp
Chl
Grt
ox
melt
Temperature °C
(f) C647 mélange, 2.5 GPa
Cpx
Opx
Ol
Amp
Chl
Grt
Tlc
ox
melt
Temperature °C

Figure 11. Comparison of the mineralogy and phase proportions constrained by mélange melting experiments (colored points; this study) and thermodynamic models. The phase proportions are constrained by Solver. Mineral phases such as quartz, kyanite, lawsonite, and mica that are predicted by models in trace quantities (< 3 wt. %) but are not observed in the experiments are not displayed in this figure. Mineral abbreviations are from Whitney and Evans (2010).

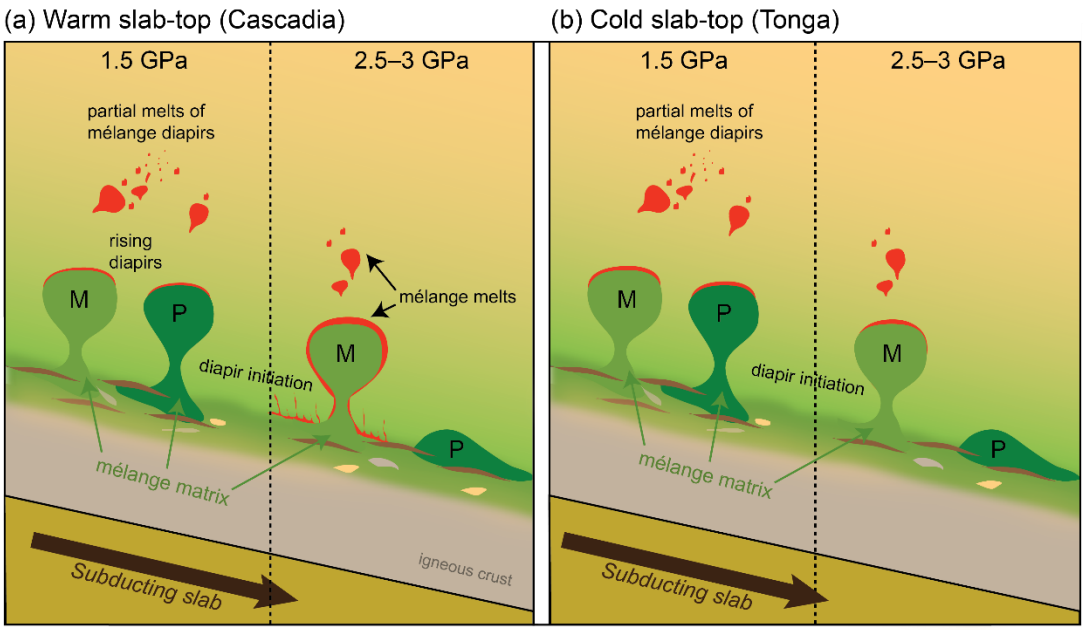

Figure 12. Schematic cartoon that portrays the possible fates of mélange rocks along the slab-mantle interface in warm (Cascadia) and cold (Tonga) subduction zones based on this study. Mélanges display block-in matrix facies wherein blocks of sediment (yellow), igneous crust (gray), and serpentinite (brown) are embedded within mélange matrix. (a) In a warm subduction zone (e.g., Cascadia), the density contrast between both metaluminous (M) and peraluminous (P) mélanges and mantle wedge would allow for buoyancy-driven diapirism at relatively low pressures (1.5 GPa) and melting could occur later in the hotter mantle wedge during ascent. At higher pressure (2.5–3 GPa), metaluminous mélanges may undergo melting near the slab-top and may continue to melt as they rise into the hotter mantle wedge. (b) In a cold subduction zone (e.g., Tonga), the density contrast between both metaluminous (M) and peraluminous (P) mélanges and mantle wedge would also allow for buoyancy-driven diapirism at relatively low pressures (1.5 GPa) and melting could subsequently occur in the hotter mantle wedge during ascent. At higher pressure (2.5–3 GPa), metaluminous mélanges may also be able to rise into the hotter mantle wedge and undergo melting later during their ascent. On the other hand, peraluminous mélanges densify during prograde subduction due to the formation of garnet. This implies that they are likely to remain along slab-tops and be dragged to deeper depths until they melt. In all scenarios, melt extraction leads to densification of melting residue.

References

Abers, G.A., Hacker, B.R., 2016. A MATLAB toolbox and Excel workbook for calculating the densities, seismic wave speeds, and major element composition of minerals and rocks at pressure and temperature. Geochemistry, Geophysics, Geosystems 17, 616–624. https://doi.org/10.1002/2015GC006171

Agard, P., Plunder, A., Angiboust, S., Bonnet, G., Ruh, J., 2018. The subduction plate interface: rock record and mechanical coupling (from long to short timescales). Lithos 320–321, 537–566. https://doi.org/10.1016/j.lithos.2018.09.029

Angiboust, S., Agard, P., De Hoog, J.C.M., Omrani, J., Plunder, A., 2013. Insights on deep, accretionary subduction processes from the Sistan ophiolitic "mélange" (Eastern Iran). Lithos 156–159, 139–158. https://doi.org/10.1016/j.lithos.2012.11.007

Angiboust, S., Glodny, J., Oncken, O., Chopin, C., 2014. In search of transient subduction interfaces in the Dent Blanche–Sesia Tectonic System (W. Alps). Lithos 205, 298–321. https://doi.org/10.1016/j.lithos.2014.07.001

Bebout, G., Barton, M., 2002. Tectonic and metasomatic mixing in a high-T, subduction-zone m??lange - Insights into the geochemical evolution of the slab-mantle interface. https://doi.org/10.1016/S0009-2541(02)00019-0

Bebout, G.E., 1991. Field-Based Evidence for Devolatilization in Subduction Zones: Implications for Arc Magmatism. Science 251, 413. https://doi.org/10.1126/science.251.4992.413

Bebout, G.E., Penniston-Dorland, S.C., 2016. Fluid and mass transfer at subduction interfaces—The field metamorphic record. Lithos 240–243, 228–258. https://doi.org/10.1016/j.lithos.2015.10.007

Behn, M.D., Kelemen, P.B., Hirth, G., Hacker, B.R., Massonne, H.-J., 2011. Diapirs as the source of the sediment signature in arc lavas. Nature Geoscience 4, 641.

Breeding, C.M., Ague, J.J., Bröcker, M., 2004. Fluid–metasedimentary rock interactions in subduction-zone mélange: Implications for the chemical composition of arc magmas. Geology 32, 1041–1044. https://doi.org/10.1130/G20877.1

Burov, E., Jaupart, C., Guillou-Frottier, L., 2003. Ascent and emplacement of buoyant magma bodies in brittle-ductile upper crust. Journal of Geophysical Research: Solid Earth 108. https://doi.org/10.1029/2002JB001904

Castro, A., Gerya, T., García-Casco, A., Fernández, C., Díaz-Alvarado, J., Moreno-Ventas, I., Löw, I., 2010. Melting Relations of MORB–Sediment Mélanges in Underplated Mantle Wedge Plumes; Implications for the Origin of Cordilleran-type Batholiths. Journal of Petrology 51, 1267–1295. https://doi.org/10.1093/petrology/egq019

Castro, A., Gerya, T.V., 2008. Magmatic implications of mantle wedge plumes: Experimental study. Lithos 103, 138–148. https://doi.org/10.1016/j.lithos.2007.09.012

Chatterjee, N., Jagoutz, O., 2015. Exhumation of the UHP Tso Morari eclogite as a diapir rising through the mantle wedge. Contributions to Mineralogy and Petrology 169, 3. https://doi.org/10.1007/s00410-014-1099-y

Codillo, E.A., Klein, F., Dragovic, B., Marschall, H.R., Baxter, E., Scambelluri, M., Schwarzenbach, E., 2022a. Fluid-mediated Mass Transfer between Mafic and Ultramafic rocks in Subduction Zones. Geochemistry, Geophysics, Geosystems n/a, e2021GC010206. https://doi.org/10.1029/2021GC010206

Codillo, E.A., Klein, F., Marschall, H.R., 2022b. Preferential Formation of Chlorite over Talc during Si-metasomatism of Ultramafic Rocks in Subduction Zones. Geophysical Research Letters n/a, e2022GL100218. https://doi.org/10.1029/2022GL100218

Codillo, E.A., Le Roux, V., Marschall, H.R., 2018. Arc-like magmas generated by mélange-peridotite interaction in the mantle wedge. Nature Communications 9, 2864. https://doi.org/10.1038/s41467-018-05313-2

Connolly, J., 1990. Multivariable phase diagrams: an algorithm based on generalized thermodynamics. American Journal of Science 290, 666–718. https://doi.org/10.2475/ajs.290.6.666

Connolly, J.A.D., 2009. The geodynamic equation of state: What and how. Geochemistry, Geophysics, Geosystems 10. https://doi.org/10.1029/2009GC002540

Cooper, L.B., Ruscitto, D.M., Plank, T., Wallace, P.J., Syracuse, E.M., Manning, C.E., 2012. Global variations in H2O/Ce: 1. Slab surface temperatures beneath volcanic arcs. Geochemistry, Geophysics, Geosystems 13. https://doi.org/10.1029/2011GC003902

Cruz-Uribe, A.M., Marschall, H.R., Gaetani, G.A., Le Roux, V., 2018. Generation of alkaline magmas in subduction zones by partial melting of mélange diapirs—An experimental study. Geology 46, 343–346. https://doi.org/10.1130/G39956.1

Currie, C.A., Beaumont, C., Huismans, R.S., 2007. The fate of subducted sediments: A case for backarc intrusion and underplating. Geology 35, 1111–1114. https://doi.org/10.1130/G24098A.1

Deschamps, F., Godard, M., Guillot, S., Hattori, K., 2013. Geochemistry of subduction zone serpentinites: A review. Lithos 178, 96–127. https://doi.org/10.1016/j.lithos.2013.05.019

Ducea, M.N., Currie, C.A., Balica, C., Lazar, I., Mallik, A., Petrescu, L., Vlasceanu, M., 2022. Diapirism of carbonate platforms subducted into the upper mantle. Geology 50, 929–933. https://doi.org/10.1130/G50000.1

Dvir, O., Pettke, T., Fumagalli, P., Kessel, R., 2011. Fluids in the peridotite–water system up to 6 GPa and 800°C: new experimental constrains on dehydration reactions. Contributions to Mineralogy and Petrology 161, 829–844. https://doi.org/10.1007/s00410-010-0567-2

Elliott, T., Plank, T., Zindler, A., White, W., Bourdon, B., 1997. Element transport from slab to volcanic front at the Mariana arc. Journal of Geophysical Research: Solid Earth 102, 14991–15019. https://doi.org/10.1029/97JB00788

Gale, A., Dalton, C.A., Langmuir, C.H., Su, Y., Schilling, J.-G., 2013. The mean composition of ocean ridge basalts. Geochemistry, Geophysics, Geosystems 14, 489–518. https://doi.org/10.1029/2012GC004334

Gerya, T., Stöckhert, B., 2006. Two-dimensional numerical modeling of tectonic and metamorphic histories at active continental margins. International Journal of Earth Sciences 95, 250–274. https://doi.org/10.1007/s00531-005-0035-9

Gerya, T.V., Connolly, J.A.D., Yuen, D.A., Gorczyk, W., Capel, A.M., 2006. Seismic implications of mantle wedge plumes. Physics of the Earth and Planetary Interiors 156, 59–74. https://doi.org/10.1016/j.pepi.2006.02.005

Gerya, T.V., Yuen, D.A., 2003. Rayleigh–Taylor instabilities from hydration and melting propel 'cold plumes' at subduction zones. Earth and Planetary Science Letters 212, 47–62. https://doi.org/10.1016/S0012-821X(03)00265-6

Giordano, D., Russell, J.K., Dingwell, D.B., 2008. Viscosity of magmatic liquids: A model. Earth and Planetary Science Letters 271, 123–134. https://doi.org/10.1016/j.epsl.2008.03.038

Gómez-Tuena, A., Cavazos-Tovar, J.G., Parolari, M., Straub, S.M., Espinasa-Pereña, R., 2018. Geochronological and geochemical evidence of continental crust 'relamination' in the origin of intermediate arc magmas. Lithos 322, 52–66. https://doi.org/10.1016/j.lithos.2018.10.005

Gorczyk, W., Gerya, T.V., Connolly, J.A.D., Yuen, D.A., Rudolph, M., 2006. Large-scale rigid-body rotation in the mantle wedge and its implications for seismic tomography. Geochemistry, Geophysics, Geosystems 7. https://doi.org/10.1029/2005GC001075

Gyomlai, T., Agard, P., Marschall, H.R., Jolivet, L., Gerdes, A., 2021. Metasomatism and deformation of block-in-matrix structures in Syros: The role of inheritance and fluid-rock interactions along the subduction interface. Lithos 386–387, 105996. https://doi.org/10.1016/j.lithos.2021.105996

Hack, A., Thompson, A., 2010. Density and Viscosity of Hydrous Magmas and Related Fluids and their Role in Subduction Zone Processes. Journal of Petrology 52, 1333–1362. https://doi.org/10.1093/petrology/egq048

Hacker, B.R., Kelemen, P.B., Behn, M.D., 2011. Differentiation of the continental crust by relamination. Earth and Planetary Science Letters 307, 501–516. https://doi.org/10.1016/j.epsl.2011.05.024

Harlow, G.E., Tsujimori, T., Sorensen, S.S., 2015. Jadeitites and Plate Tectonics. Annu. Rev. Earth Planet. Sci. 43, 105–138. https://doi.org/10.1146/annurev-earth-060614-105215

Hawkesworth, C.J., Gallagher, K., Hergt, J.M., McDermott, F., 1993. Mantle and Slab Contributions in Arc Magmas. Annu. Rev. Earth Planet. Sci. 21, 175–204. https://doi.org/10.1146/annurev.ea.21.050193.001135

Hawkesworth, C.J., Turner, S.P., McDermott, F., Peate, D.W., van Calsteren, P., 1997. U-Th Isotopes in Arc Magmas: Implications for Element Transfer from the Subducted Crust. Science 276, 551. https://doi.org/10.1126/science.276.5312.551

Hawthorne, F.C., Oberti, R., Harlow, G.E., Maresch, W.V., Martin, R.F., Schumacher, J.C., Welch, M.D., 2012. Nomenclature of the amphibole supergroup. American Mineralogist 97, 2031–2048. https://doi.org/10.2138/am.2012.4276

Hermann, J., Spandler, C.J., 2008. Sediment Melts at Sub-arc Depths: an Experimental Study. Journal of Petrology 49, 717–740. https://doi.org/10.1093/petrology/egm073

Hilairet, N., Reynard, B., Wang, Y., Daniel, I., Merkel, S., Nishiyama, N., Petitgirard, S., 2007. High-Pressure Creep of Serpentine, Interseismic Deformation, and Initiation of Subduction. Science 318, 1910–1913. https://doi.org/10.1126/science.1148494

Hirth, G., Kohlstedt, D., 2004. Rheology of the Upper Mantle and the Mantle Wedge: A View from the Experimentalists, in: Inside the Subduction Factory, Geophysical Monograph Series. pp. 83–105. https://doi.org/10.1029/138GM06

Holt, A.F., Condit, C.B., 2021. Slab Temperature Evolution Over the Lifetime of a Subduction Zone. Geochemistry, Geophysics, Geosystems 22, e2020GC009476. https://doi.org/10.1029/2020GC009476

Iacovino, K., Till, C., 2018. DensityX: A program for calculating the densities of hydrous magmatic liquids from 427-1,627 °C and up to 30 kbar. Volcanica 2, 1–10. https://doi.org/10.30909/vol.02.01.0110

Ji, S., Martignole, J., 1994. Ductility of garnet as an indicator of extremely high temperature deformation. Journal of Structural Geology 16, 985–996. https://doi.org/10.1016/0191-8141(94)90080-9

Jull, M., Kelemen, P.B., 2001. On the conditions for lower crustal convective instability. Journal of Geophysical Research: Solid Earth 106, 6423–6446. https://doi.org/10.1029/2000JB900357

King, R.L., Bebout, G.E., Moriguti, T., Nakamura, E., 2006. Elemental mixing systematics and Sr–Nd isotope geochemistry of mélange formation: Obstacles to identification of fluid sources to arc volcanics. Earth and Planetary Science Letters 246, 288–304. https://doi.org/10.1016/j.epsl.2006.03.053

Klein, B.Z., Behn, M.D., 2021. On the Evolution and Fate of Sediment Diapirs in Subduction Zones. Geochemistry, Geophysics, Geosystems 22, e2021GC009873. https://doi.org/10.1029/2021GC009873

Klimm, K., Blundy, J.D., Green, T.H., 2008. Trace Element Partitioning and Accessory Phase Saturation during H2O-Saturated Melting of Basalt with Implications for Subduction Zone Chemical Fluxes. Journal of Petrology 49, 523–553. https://doi.org/10.1093/petrology/egn001

Krawczynski, M., Olive, J., 2011. A new fitting algorithm for petrological mass-balance problems. AGU Fall Meeting Abstracts 2613.

Kronenberg, A.K., Kirby, S.H., Pinkston, J., 1990. Basal slip and mechanical anisotropy of biotite. Journal of Geophysical Research: Solid Earth 95, 19257–19278. https://doi.org/10.1029/JB095iB12p19257

Kusbach, V., Janoušek, V., Hasalová, P., Schulmann, K., Fanning, C.M., Erban, V., Ulrich, S., 2015. Importance of crustal relamination in origin of the orogenic mantle peridotite–high-pressure granulite association: example from the Náměšť Granulite Massif (Bohemian

Massif, Czech Republic). Journal of the Geological Society 172, 479–490. https://doi.org/10.1144/jgs2014-070

Lakey, S., Hermann, J., 2022. An Experimental Study of Chlorite Stability in Varied Subduction Zone Lithologies with Implications for Fluid Production, Melting, and Diapirism in Chlorite-Rich Mélange Rocks. Journal of Petrology 63, egac029. https://doi.org/10.1093/petrology/egac029

Lambert, I.B., Wyllie, P.J., 1970. Melting in the deep crust and upper mantle and the nature of the low velocity layer. Physics of the Earth and Planetary Interiors 3, 316–322. https://doi.org/10.1016/0031-9201(70)90068-3

Laporte, D., 1994. Wetting behavior of partial melts during crustal anatexis: the distribution of hydrous silicic melts in polycrystalline aggregates of quartz. Contributions to Mineralogy and Petrology 116, 486–499. https://doi.org/10.1007/BF00310914

Li Huijuan, Hermann Joerg, Zhang Lifei, 2022. Melting of subducted slab dictates trace element recycling in global arcs. Science Advances 8, eabh2166. https://doi.org/10.1126/sciadv.abh2166

Lin, C., Shih, M., Lai, Y., 2019. A Strong Seismic Reflector within the Mantle Wedge above the Ryukyu Subduction of Northern Taiwan. Seismological Research Letters 91, 310–316. https://doi.org/10.1785/0220190174

Lin, C.-H., Shih, M.-H., Lai, Y.-C., 2021. Mantle wedge diapirs detected by a dense seismic array in Northern Taiwan. Sci Rep 11, 1561–1561. https://doi.org/10.1038/s41598-021-81357-7

Little, T.A., Hacker, B.R., Gordon, S.M., Baldwin, S.L., Fitzgerald, P.G., Ellis, S., Korchinski, M., 2011. Diapiric exhumation of Earth's youngest (UHP) eclogites in the gneiss domes of the D'Entrecasteaux Islands, Papua New Guinea. Tectonophysics 510, 39–68. https://doi.org/10.1016/j.tecto.2011.06.006

Liu, J., Bohlen, S.R., Ernst, W.G., 1996. Stability of hydrous phases in subducting oceanic crust. Earth and Planetary Science Letters 143, 161–171. https://doi.org/10.1016/0012-821X(96)00130-6

Mann, U., Schmidt, M.W., 2015. Melting of pelitic sediments at subarc depths: 1. Flux vs. fluid-absent melting and a parameterization of melt productivity. Chemical Geology 404, 150–167. https://doi.org/10.1016/j.chemgeo.2015.02.032

Marschall, H.R., Schumacher, J.C., 2012. Arc magmas sourced from mélange diapirs in subduction zones. Nature Geosci 5, 862–867. https://doi.org/10.1038/ngeo1634

McCulloch, M.T., Gamble, J.A., 1991. Geochemical and geodynamical constraints on subduction zone magmatism. Earth and Planetary Science Letters 102, 358–374. https://doi.org/10.1016/0012-821X(91)90029-H

Miller, D.P., Marschall, H.R., Schumacher, J.C., 2009. Metasomatic formation and petrology of blueschist-facies hybrid rocks from Syros (Greece): Implications for reactions at the slab–mantle interface. Lithos 107, 53–67. https://doi.org/10.1016/j.lithos.2008.07.015

Miller, N.C., Behn, M.D., 2012. Timescales for the growth of sediment diapirs in subduction zones. Geophysical Journal International 190, 1361–1377. https://doi.org/10.1111/j.1365-246X.2012.05565.x

Mori, Y., Shigeno, M., Nishiyama, T., 2014. Fluid-metapelite interaction in an ultramafic mélange: implications for mass transfer along the slab-mantle interface in subduction zones. Earth, Planets and Space 66, 47. https://doi.org/10.1186/1880-5981-66-47

Nesbitt, H.W., Young, G.M., 1984. Prediction of some weathering trends of plutonic and volcanic rocks based on thermodynamic and kinetic considerations. Geochimica et Cosmochimica Acta 48, 1523–1534. https://doi.org/10.1016/0016-7037(84)90408-3

Nichols, G.T., Wyllie, P.J., Stern, C.R., 1994. Subduction zone melting of pelagic sediments constrained by melting experiments. Nature 371, 785–788. https://doi.org/10.1038/371785a0

Nielsen, S.G., Marschall, H.R., 2017. Geochemical evidence for mélange melting in global arcs. Sci Adv 3. https://doi.org/10.1126/sciadv.1602402

Parolari, M., Gómez-Tuena, A., Errázuriz-Henao, C., Cavazos-Tovar, J.G., 2021. Orogenic andesites and their link to the continental rock cycle. Lithos 382–383, 105958. https://doi.org/10.1016/j.lithos.2020.105958

Pawley, A., 2003. Chlorite stability in mantle peridotite: the reaction clinochlore+enstatite=forsterite+pyrope+H2O. Contributions to Mineralogy and Petrology 144, 449–456. https://doi.org/10.1007/s00410-002-0409-y

Penniston-Dorland, S.C., Gorman, J.K., Bebout, G.E., Piccoli, P.M., Walker, R.J., 2014. Reaction rind formation in the Catalina Schist: Deciphering a history of mechanical mixing and metasomatic alteration. Chemical Geology 384, 47–61. https://doi.org/10.1016/j.chemgeo.2014.06.024

Plank, T., Cooper, L.B., Manning, C.E., 2009. Emerging geothermometers for estimating slab surface temperatures. Nature Geoscience 2, 611–615. https://doi.org/10.1038/ngeo614

Plank, T., Langmuir, C.H., 1998. The chemical composition of subducting sediment and its consequences for the crust and mantle. Chemical Geology 145, 325–394. https://doi.org/10.1016/S0009-2541(97)00150-2

Plank, T., Langmuir, C.H., 1993. Tracing trace elements from sediment input to volcanic output at subduction zones. Nature 362, 739.

Pogge von Strandmann, P.A.E., Dohmen, R., Marschall, H.R., Schumacher, J.C., Elliott, T., 2015. Extreme Magnesium Isotope Fractionation at Outcrop Scale Records the Mechanism and Rate at which Reaction Fronts Advance. Journal of Petrology 56, 33–58. https://doi.org/10.1093/petrology/egu070

Proenza, J.A., González-Jiménez, J.M., Garcia-Casco, A., Belousova, E., Griffin, W.L., Talavera, C., Rojas-Agramonte, Y., Aiglsperger, T., Navarro-Ciurana, D., Pujol-Solà, N., Gervilla, F., O'Reilly, S.Y., Jacob, D.E., 2017. Cold plumes trigger contamination of oceanic mantle wedges with continental crust-derived sediments: Evidence from chromitite zircon grains

of eastern Cuban ophiolites. Geoscience Frontiers. https://doi.org/10.1016/j.gsf.2017.12.005

Schmidt, M.W., 2015. Melting of pelitic sediments at subarc depths: 2. Melt chemistry, viscosities and a parameterization of melt composition. Chemical Geology 404, 168–182. https://doi.org/10.1016/j.chemgeo.2015.02.013

Sharp, Z.D., Essene, E.J., Smyth, J.R., 1992. Ultra-high temperatures from oxygen isotope thermometry of a coesite-sanidine grospydite. Contributions to Mineralogy and Petrology 112, 358–370. https://doi.org/10.1007/BF00310466

Skora, S., Blundy, J., 2010. High-pressure Hydrous Phase Relations of Radiolarian Clay and Implications for the Involvement of Subducted Sediment in Arc Magmatism. Journal of Petrology 51, 2211–2243. https://doi.org/10.1093/petrology/egq054

Sorensen, S.S., Grossman, J.N., 1989. Enrichment of trace elements in garnet amphibolites from a paleo-subduction zone: Catalina Schist, southern California. Geochimica et Cosmochimica Acta 53, 3155–3177. https://doi.org/10.1016/0016-7037(89)90096-3

Syracuse, E.M., Keken, P.E. van, Abers, G.A., 2010a. The global range of subduction zone thermal models. Physics of the Earth and Planetary Interiors 183, 73–90. https://doi.org/10.1016/j.pepi.2010.02.004

Syracuse, E.M., van Keken, P.E., Abers, G.A., 2010b. The global range of subduction zone thermal models. Physics of the Earth and Planetary Interiors 183, 73–90. https://doi.org/10.1016/j.pepi.2010.02.004

Tera, F., Brown, L., Morris, J., Sacks, I.S., Klein, J., Middleton, R., 1986. Sediment incorporation in island-arc magmas: Inferences from 10Be. Geochimica et Cosmochimica Acta 50, 535–550. https://doi.org/10.1016/0016-7037(86)90103-1

Till, C.B., Grove, T.L., Withers, A.C., 2012. The beginnings of hydrous mantle wedge melting. Contributions to Mineralogy and Petrology 163, 669–688. https://doi.org/10.1007/s00410-011-0692-6

Tullis, J., Wenk, H.-R., 1994. Effect of muscovite on the strength and lattice preferred orientations of experimentally deformed quartz aggregates. Materials Science and Engineering: A 175, 209–220. https://doi.org/10.1016/0921-5093(94)91060-X

Turner, S., Evans, P., Hawkesworth, C., 2001. Ultrafast Source-to-Surface Movement of Melt at Island Arcs from ^{226}Ra-^{230}Th Systematics. Science 292, 1363. https://doi.org/10.1126/science.1059904

Wang, K., Cai, K., Sun, M., Wang, X., Xia, X.-P., Zhang, B., Wan, B., 2022. Diapir Melting of Subducted Mélange Generating Alkaline Arc Magmatism and Its Implications for Material Recycling at Subduction Zone Settings. Geophysical Research Letters 49, e2021GL097693. https://doi.org/10.1029/2021GL097693

Wei, C., Powell, R., 2004. Calculated Phase Relations in High-Pressure Metapelites in the System NKFMASH (Na2O–K2O–FeO–MgO–Al2O3–SiO2–H2O). Journal of Petrology 45, 183–202. https://doi.org/10.1093/petrology/egg085

Weinberg, R.F., Podladchikov, Y., 1994. Diapiric ascent of magmas through power law crust and mantle. Journal of Geophysical Research: Solid Earth 99, 9543–9559. https://doi.org/10.1029/93JB03461

Whitney, D.L., Evans, B.W., 2010. Abbreviations for names of rock-forming minerals. American Mineralogist 95, 185–187. https://doi.org/10.2138/am.2010.3371

Workman, R.K., Hart, S.R., 2005. Major and trace element composition of the depleted MORB mantle (DMM). Earth and Planetary Science Letters 231, 53–72. https://doi.org/10.1016/j.epsl.2004.12.005

Yin, A., Manning, C.E., Lovera, O., Menold, C.A., Chen, X., Gehrels, G.E., 2007. Early Paleozoic Tectonic and Thermomechanical Evolution of Ultrahigh-Pressure (UHP) Metamorphic Rocks in the Northern Tibetan Plateau, Northwest China. International Geology Review 49, 681–716. https://doi.org/10.2747/0020-6814.49.8.681

Zhang, N., Behn, M.D., Parmentier, E.M., Kincaid, C., 2020. Melt Segregation and Depletion During Ascent of Buoyant Diapirs in Subduction Zones. Journal of Geophysical Research: Solid Earth 125, e2019JB018203. https://doi.org/10.1029/2019JB018203

Zhu, G., Gerya, T.V., Yuen, D.A., Honda, S., Yoshida, T., Connolly, J.A.D., 2009. Three-dimensional dynamics of hydrous thermal-chemical plumes in oceanic subduction zones. Geochemistry, Geophysics, Geosystems 10. https://doi.org/10.1029/2009GC002625

Chapter 5

Arc-like magmas generated by mélange-peridotite interaction in the mantle wedge

This chapter was originally published as:
Codillo, E.A., Le Roux, V., Marschall, H.R., 2018. Arc-like magmas generated by mélange-peridotite interaction in the mantle wedge. Nature Communications 9, 2864. https://doi.org/10.1038/s41467-018-05313-2. Used with permission as granted in the original copyright agreement.

Abstract

In subduction zones, the mechanisms of transfer of crustal materials from the subducting slab to the overlying mantle wedge are still debated. In recent years, it has been argued that mélange rocks, which are formed from physical and metasomatic mixing of sediments, oceanic crust and ultramafic rocks along the slab-mantle interface, could migrate from the slab-top to the overlying mantle, and transfer their compositional signatures to the source region of arc magmas. However, the compositions of melts that would result from the interaction of mélange rocks with the peridotite mantle wedge remains unknown. Such information is critical to determine whether mélange rocks are viable contributors to arc magmatism worldwide. Here we present the first experimental evidence for the generation of arc-like tholeiites and calc-alkaline magmas by mélange-peridotite interaction in subduction zones. We show that melting of peridotite hybridized by limited volumes of mélange rocks produces melts that carry the major and trace element abundances, and trace element ratios observed in natural arc magmas. We propose that the differences in nature and relative contributions of mélange materials assimilated into the mantle wedge can result in the formation of compositionally diverse primary arc magmas ranging from arc tholeiites to calc-alkaline magmas. Thus, we argue that the ascent and assimilation of mélange material into the mantle wedge may play a key role in transferring material and characteristic subduction signatures from the slab to the source of arc magmas.

1 Introduction

Subduction zones are widely studied because they are a major locus of volcanic and seismic hazards. In particular, the compositions of arc magmas have been used to understand the magmatic processes operating in the deep Earth. During subduction, hydrated oceanic crust and sediments are subducted and recycled back into the Earth's interior. Although the fate of subducted sediments is uncertain, their signature is imprinted in the chemistry of most arc magmas around the world[1]. Sediments are globally enriched in many trace elements (e.g., K, Rb, Th, rare earth elements) relative to peridotite mantle[2], thus small volumes of sediments can drastically shift the trace element budget of the mantle wedge. Arc magmas are also characteristically enriched in fluid-mobile large-ion lithophile elements (LILE) such as Ba and Sr, and depleted in high field strength elements (HFSE) such as Nb, relative to mid-ocean ridge basalt (MORB)[3]. The LILE enrichment has usually been attributed to mantle wedge metasomatism by slab-derived fluids[4] produced during dehydration of the subducting slab. The HFSE depleted character, on the other hand, has been attributed to different processes such as a 'pre-subduction' mantle depletion[5,6], selective retention of HFSE by accessory phases (e.g., rutile, sphene, and perovskite) stabilized in the mantle wedge and/or in the slab[7,8], and preferred partitioning of HFSE into orthopyroxene during melt-rock reaction[9]. Although extensive geochemical studies have suggested that arc magma chemistry reflects variable contributions from a depleted MORB mantle (DMM), altered oceanic crust and sediments[10,11], experimental studies have faced challenges to simultaneously reproduce both the major and trace element characteristics of tholeiites and calc-alkaline melts, the most common types of arc magmas. In addition, the processes by which typical trace element signatures are produced and transferred to arc magmas remain a matter of debate. In particular, Nielsen and Marschall[12] recently argued that the trace element and isotope variability of global arc magmas could not be reconciled with the classic model of arc magma genesis, which invokes hybridization of the mantle wedge by discrete pulses of melted sediments and aqueous fluids from dehydrating AOC. Instead, they showed that the trace element and isotope data of global arcs can only be reconciled if physical mixing of sediments + fluids + mantle takes place early on in the subduction process before any melting occurs. This prerequisite redefines the order of events in subduction zones and supports an important role for mélange rocks in arc magmatism. However, the trace and major element chemistry of melts that would result from the interaction of natural mélange rocks with a peridotitic mantle in subduction zones has never been investigated experimentally and

remains unknown. Such information is critical to determine whether mélange rocks are viable contributors to arc magmatism worldwide.

Mélange rocks are observed in field studies worldwide[13] and are believed to form by deformation-assisted mechanical mixing, metasomatic interactions and diffusion at different *P-T* conditions along the slab-mantle interface during subduction[13–16]. Mélanges are hybrid rocks composed of cm to km-sized blocks of altered oceanic crust, metasediments, and serpentinized peridotite embedded in mafic to ultramafic matrices[14,17,18]. These matrix rocks include near-monomineralic chlorite schists, talc schists, and jadeitites with variable amounts of Ca-amphibole, omphacite, phengite, epidote and accessory minerals (e.g., titanite, rutile, zircon, apatite, monazite, sulfides), among others. Although the volumes of mélange rocks at depth are poorly constrained, several km-thick low-seismic velocity regions observed at the slab-top in subduction zones worldwide indicate the persistence of hydrated rocks – mélange zones – at the slab-mantle interface[14,15,19]. This km-scale estimate of mélange rocks from seismic observations is corroborated by numerous field studies of exhumed high-pressure terranes reporting thicknesses ranging from several hundreds of meters up to several kilometers[14,17,20–22]. Mélange rocks display significant spatial heterogeneity, but detailed field observations indicate that chemical potential gradients between juxtaposed lithologies (e.g., metasediments, eclogite and serpentinized peridotites) may be reduced to homogenous matrices through diffusion and fluid advection processes as mélanges mature[14,23]. For the purpose of this first study, we will assume that mélange matrices are broadly representative of the bulk composition of the mélange and provide a relevant first-order approximation of mélange compositional variability as they form at the expense of, and reflect chemical contributions from their protoliths[15,21]. Although more compositions will be studied in the future, the mélange matrix samples used here reflect two contrasting members in the range of mélange materials that we use to explore possible melt compositions produced by mélange-peridotite interaction.

Laboratory[24] and numerical simulations of subduction process[25–28] have shown that hydration and partial melting may induce gravitational instabilities at the slab-mantle interface, which can develop into diapiric structures composed of partially molten materials. Although these diapirs have not been unambiguously imaged in active subduction zones, we note that along-arc geophysical studies are rare, that the current resolution of seismic techniques may not be appropriate to image mixed mélange-peridotite lithologies, and that magnetotelluric approach,

sensitive to interconnected free fluids, would not easily detect the presence of mélanges, where most of the water may be crystallographically bounded. With their intrinsic buoyancy, mélange diapirs have been predicted to form at the slab-top, migrate to the overlying mantle[25,26], and transfer the compositional signatures of slab-derived rocks to the source region of arc magmas[23,29]. In particular, physical mixing and homogenization of viscous mélange diapirs and sub-solidus mantle peridotites is predicted in the hot zones of the mantle wedge[30]. Recent findings on ophiolitic zircon grains also support the idea that material can be transported in the wedge via cold plumes[31]. However, as stated previously, the major and trace element compositions of melts that would be produced by melting of a mélange-hybridized mantle wedge remains unexplored.

Here we present the first experimental study on the generation of arc-like magmas by melting of mélange-hybridized mantle sources. We performed piston-cylinder experiments at 1.5 GPa and 1150–1350 ºC and simulated a scenario where mélange materials rise as a bulk[26,32] into the hot corner of the wedge and homogenize with the peridotite mantle (Fig. 1). Using powder mixtures of DMM-like natural peridotite (LZ-1, Fig. S1; 85–95 vol. %) and natural mélange rocks from a high-pressure terrane (SY400B, SY325; 5–15 vol. %), we show that experimentally produced glasses display the major and trace element characteristics typical of arcs magmas (e.g., high Ba contents, high Sr/Y ratios and negative Nb anomaly). Our study provides evidence that the compositional signatures of sediments and fluids, initially imparted to mélange rocks during their formation at the slab-mantle interface, can be delivered to the source region of arc magmas by mixing of mélange materials with mantle wedge peridotites, and variably enhanced during melting of mélange-hybridized peridotite source. We show that depending on the types and relative contributions of mélange materials that hybridize the mantle wedge, the compositions of the melts vary from tholeiitic to calc-alkaline. We further discuss how lithological heterogeneities observed in supra-subduction ophiolites and arc- xenoliths could represent direct evidence for peridotite-mélange interactions.

2 Results

2.1 Experimental techniques

We performed piston-cylinder experiments to investigate the composition of melts produced by partial melting of a natural DMM-like peridotite hybridized by small proportions of natural mélange matrix. We used two starting mixes that consisted of homogenized 'peridotite + sediment-dominated mélange matrix' (PER-SED mix) and homogenized 'peridotite + serpentinite-dominated mélange matrix' (PER-SERP mix). Both mélange matrices are fine-grained chlorite schists from Syros (Greece) with estimated water contents between 2–3 wt. %. These two types of natural mélange matrices span a range of compositions that reflect the first-order variability of global mélange rocks in terms of mineralogy (Table S1), immobile element chemistry (Fig. 2), and trace element chemistry (Fig. S6). As mélange rocks should be volumetrically small compared to peridotite in the mantle wedge, we only added limited volumes (5–15 %) of natural mélange matrix to a natural lherzolite powder (85–95 %). We note that mélange rocks would not necessarily represent 5-15 vol. % of the sub-arc region at all times because of the 3-D nature of mélange diapirs. Certain regions of the wedge could be hybridized by different amount of mélange materials at different times. Although this experimental design is more challenging because it produces small melt pools, it simulates a more realistic scenario. Experimental melts were collected using glassy carbon spheres placed at the top of Au-Pd capsules. The natural peridotite (LZ-1; from Lherz, France) displays modal proportions and major and trace element compositions similar to DMM (Fig. S1). The PER-SED and PER-SERP starting materials were partially melted at 1.5 GPa and 1280–1350 ºC, conditions applicable to arc magmatism[33,34]. In addition, near-solidus (1230 ºC) and solidus (1150 ºC) experiments were performed to better constrain the solid phase assemblage at the beginning of and before melting, respectively. The quenched, dendrite-free glasses were analyzed for major elements using electron microprobe (EPMA) at the Massachusetts Institute of Technology. In addition, chemical maps for major elements were acquired on all experiments (Figs. 3 and S2). Trace element compositions of glass pools were analyzed using a Cameca 3F secondary ion mass spectrometer (SIMS) at the North East National Ion Microprobe Facility (Woods Hole Oceanographic Institution). Backscattered electron (BSE) images and energy dispersive spectroscopy (EDS) maps were acquired on all experiments using a Hitachi tabletop SEM-EDS TM-3000. The major and trace element compositions of starting mixes and experimental melts are summarized in Tables S1 and S2, respectively. We assessed approach to equilibrium by performing a time-series of experiments at 1.5 GPa and 1280 ºC, with run durations ranging from 3 h to 96 h. The capsules were pre-conditioned to minimize Fe loss, although we still

observed a decrease in FeO_T with increasing run duration. We observed that melt compositions performed between 72 and 96 h were indistinguishable in terms of SiO_2, Al_2O_3, MgO, Na_2O, CaO, K_2O, MnO, and TiO_2, within 1 s.d. value (Fig. S4). Thus, a 72-h run duration was chosen to closely approach equilibrium in those experiments. Mass balance calculations yielded a sum of squared residuals <0.39 (FeO excluded), attesting for a close system for all other major oxides. Phase proportions for each experiment were calculated from mass balance calculations and are reported in Table S3. Additional information is provided in the Supplementary Material.

2.2 Phase assemblages

Solidus (PER-SED 95-5 at 1150 ºC) and near-solidus (PER-SED 85-15 at 1230 ºC and PER-SERP 85-15 at 1230 ºC) experiments were performed at 1.5 GPa to determine the phase assemblages at and near the onset of melting. The solidus experiment produced an assemblage of olivine (ol) + orthopyroxene (opx) + clinopyroxene (cpx) + spinel (sp) (± isolated melt drops), while both near- solidus experiments produced silicate melt + ol + opx + cpx + minor sp which typically occurred as small inclusions (~2 μm diameter) in olivine. The compositions of these melts were not analyzed due to their limited exposure. Also, abundant dendrites have compromised their composition. These near- and solidus experiments show that although mélanges have complex mineralogies (Table S3), the hybrid peridotite assemblage is standard. At 1280 – 1315 ºC, PER-SED experiments produced the following assemblages: silicate melt + ol + opx + cpx (Table S3). Melt proportions vary from 10 to 31%. PER-SERP experiments produced an assemblage of silicate melt + ol + opx + cpx from 1280 to 1350 °C. Melt proportions vary from 3 to 25%. In all experiments, no accessory phase was observed in the chemical maps (Fig 3 and S2) and high-resolution BSE images (Fig SX). In all 72-hour experiments, an opx-rich reaction band developed along the interface of the accumulated melts and the residue (Fig. 3). The thickness of the opx-rich reaction zone is similar in all experiments, ranging from 125–370 μm. The opx-reaction zone is not present in the 3-hour experiment due to the short run duration (Fig. S2). Mineral compositions are homogeneous in individual experiment and show variability between experiments (Table S5; Supp. Mat). Modal proportions in each experiment were calculated using the mass balances (excluding FeO) and are reported in Table S3. Representative EDS maps and BSE images are presented in Fig S3.

2.3 Major element composition of the melts

The major element compositions of hybrid peridotite-mélange melts are reported in Table S2 (volatile-free basis). They range in composition from trachyandesite to basaltic trachyandesite and basaltic compositions (49.9–56.5 wt. % SiO_2, 2.2–8.8 wt. % Na_2O+K_2O) with increasing melting temperatures. The water contents of the melts range from ~ 0.6 to ~ 5 wt. % and were estimated from the difference between major element totals and 100 %. The melts also show a large range in Al_2O_3 contents (14.8–19.5 wt. %) and MgO contents (7.0–15.9 wt. %) (Fig. S5). The melt composition is homogeneous throughout the capsule and does not vary with distance to the Opx-rich reaction zone. The melt compositions from PER-SED and PER-SERP experiments show an increase in CaO, MgO and MnO, a decrease in K_2O, Na_2O, Al_2O_3, SiO_2, TiO_2 and P_2O_5, with increasing temperature. The alkali contents of melts produced from PER-SED experiments are higher than those from PER-SERP experiments at similar temperatures, due to the higher alkali contents of PER-SED starting material (Table S1 and Fig. S6). The FeO_T contents of peridotite-mélange melts are lower than global arc data due to some limited Fe loss to the capsule (Fig. S7). This does not affect the conclusions of the study. We now compare the major element compositions of experimental melts (Figs. 4 and S7) with fractionation-corrected global arc data[35] (normalized to MgO = 6 wt. %), primitive arc melts compilations[33,34], and previous experimental studies (Table S4). Experimental hydrous peridotite melt compositions[36] match well the major element compositions of global arcs, although alkali contents are expectedly lower than in most arc magmas. Experimental melts from mantle hybridized by slab melts[37] are lower in CaO, and higher in TiO_2, Na_2O, K_2O, and SiO_2 compared to arc datasets. Experimental melts from olivine hybridized by sediment melt[38] are lower in CaO, and higher in Na_2O and K_2O compared to arc datasets. Experimental mélange-type 1 and type 2 melts[27,39] are both lower in CaO and MnO and higher in K_2O and SiO_2 compared to arc datasets. Interestingly, the major element compositions of experimental mélange-type 2 melts[40], which are partial melts from the sediment-dominated mélange material used in this study (SY400B), plot in the continuity of PER-SED experiments but with higher elemental abundances. Experimental melts from mantle hybridized by sediment melts[41] are higher in K_2O compared to arc datasets. Conversely, partial melts of peridotite hybridized by mélange materials produced in this study plot within or near the compositional field defined by arc datasets for SiO_2, MgO, Na_2O, K_2O, TiO_2, P_2O_5 and CaO. In terms of alkali contents, lower degree melts (10–19 %) of PER-SED experiments are slightly higher than global

arcs but plot within the field of global arcs at higher degree of melting (25–31 %). Overall, partial melts of peridotite hybridized by mélange materials are similar to partial melts of hydrous peridotites and match well the alkali and major element compositions of typical arcs magmas.

Experimental melts from PER-SED experiments range from the boundary between tholeiitic and calc-alkaline fields to high-K calc-alkaline field (Fig. 5). On the other hand, experimental melts from PER-SERP experiments plot tightly within the tholeiitic field. Experimental mélange-type 2 melts[40] show a strong enrichment in K_2O and plot in the ultrapotassic shoshonitic field. Our results, along with the experimental data of Cruz-Uribe *et al*.[40], highlight a continuum in alkali enrichment from tholeiitic melts produced by melting of mantle hybridized by serpentinite-dominated mélange, to calc-alkaline melts produced by melting of mantle hybridized by sediment-dominated mélange materials, to ultrapotassic shoshonitic melts from melting of pure sediment-dominated mélange materials.

2.4 Trace element composition of the melts

The trace element compositions of hybrid peridotite-mélange melts are presented in N-MORB-normalized spider diagrams (Fig. 6) along with global arc data[35], with emphasis on the dominant primitive arc magma types[33] (i.e., calc-alkaline and tholeiite), and published experimental studies that provided both major and trace element contents of experimental melts (Table S4). Primitive calc-alkaline arc magmas are geochemically characterized by up to two orders of magnitude higher trace element concentrations compared to primitive arc tholeiites. Pure sediment melts[7] and melts from olivine hybridized by sediment melts[38] have higher trace element concentrations than global arc magmas and display elemental fractionations that are different from global arcs (e.g., Ba/Th, Sr/Nd). Other previous studies[37,40,42] display trace element abundances that plot in the highest range for natural arc magmas, but with major element compositions that are missing CaO or reflect ultra-potassic melts (high K_2O). Here we show that, compared to N-MORB, partial melts of hybrid peridotite-mélange materials display enrichment in LILE (e.g., Ba, Th, Sr, K), high LREE/HREE (e.g., Ce/Yb), high LILE/HFSE (e.g., high Th/Nb, Ba/Nb, K/Ti), and plot tightly within the trace element fractionation range defined by global arc data (Fig. 7). Experimental melts from PER-SED experiments record elevated trace element concentrations and show fractionations that are characteristic of primitive calc-alkaline magmas. Sr/Nd ratios still fall within the range of global arcs (Fig. 7), although within the lower range of values. Experimental

melts from PER-SERP experiments display trace element concentrations that are an order of magnitude lower than melts from PER-SED experiments, and show a slight enrichment in Sr relative to Ce and Nd. In PER-SED experiments, Zr-Hf are slightly enriched compared to Sm and Ti, whereas in PER-SERP experiments, Zr-Hf are not fractionated from Sm and Ti. Trace element concentrations in the melts generally decrease with increasing temperature, consistent with dilution at higher melting extents in the absence of accessory phases that would retain trace elements in the residue. Overall, melts produced from melting of a peridotite source hybridized by mélange rocks (this study) carry trace element signatures typical of natural arc magmas. In particular, peridotite hybridized by serpentinite-dominated and sediment-dominated mélanges produced melts that carry the trace element characteristics of arc tholeiites and calc-alkaline magmas, respectively.

3 Discussion

Geodynamic models of rising mélange diapirs have predicted an uneven distribution of mélange rocks in the mantle wedge that involves both complete and incomplete mixing of mélange rocks and peridotites[30]. Our experiments investigate a scenario where the peridotite mantle wedge and limited volumes of mélange rocks are fully mixed and form a new hybrid source that partially melts (Fig. 1). As the extent and volumetric significance of mélange rocks at the slab-mantle interface are still debated, a growing number of studies support their ubiquitous occurrence and importance at the slab-mantle interface. Petrologic modelling[43], numerical instability analysis of subduction zones[44,45], and metamorphic *P-T-t* histories of exhumed high-pressure mélange terranes[46–48] strongly support the possibility of exhumation of high-pressure rocks through diapirism within the mantle wedge. Further experiments will model how the path of mélange materials would be affected by the thermal structure of individual subduction zones but are beyond the scope of the current study. For the purpose of this study, we consider that the two end-member mélange matrices from Syros (Fig. 2) offer compositions that represent a reasonable first-order approximation of global mélange variability. Our choice of using natural chlorite schist matrix from Syros (Greece) was guided by the fact that the Syros mélange record the mechanical and metasomatic interactions at *P*–*T* conditions appropriate for slab-mantle interface at depths of about 50–60 km in subduction zones[16,21,23]. In addition, the chlorite ± talc -dominated assemblage in

global mélange matrices (including Syros mélange) is relatively insensitive to pressure[49,50], making them a reasonable proxy to the type of mélange extending down to sub-arc depths[14,15,51]. Importantly, our natural starting mélange materials record minimal late-stage modification and overprinting during their exhumation, making their mineralogy, elemental and volatile concentrations[21] closely approximate the in-situ compositions of mélange rocks at the slab-mantle interface. Thus, the present study offers a reasonable approximation of subduction dynamics where mélange rocks formed at 1.6–2.2 GPa, detach from the slab and homogenizes with peridotite in the hot zones of the mantle wedge at 1.5 GPa (~ 45 km depth).

Results from our experiments support the idea that primary melts in arcs are not only limited to MgO-rich basalt (up to 15.9 wt.%) but may also resemble trachyandesite and basaltic trachyandesite with MgO contents of around 7 wt. % (Table S2), covering the MgO range of primitive arc magmas[33]. All of our experiments display CaO, K_2O, Na_2O, TiO_2 and P_2O_5 that more accurately reproduce the chemistry of global arc magmas compared to previous studies that simulated hybridization of the wedge by discrete slab melts or discrete sediment melts. The fact that the hybrid source is largely peridotite-like (85-95%) explains why realistic, arc-like major element compositions can be produced in our experiments. Indeed, the large dominance of mantle-equilibrated arc magmas from different subduction zones should reflect the fundamental control of mantle peridotites in controlling the major element compositions of primary arc melts[34,52].

The presence of mall mélange components within the mantle wedge significantly affects the trace element budget of melts generated by melting of a mélange-hybridized mantle source. Although hydrous melting of peridotite would typically produce melts that display a MORB-like trace element pattern[53,54], the trace element compositions of peridotite-mélange melts show striking similarity with global arc magmas, with enriched LILE such as Ba, Th, and K, and depleted HFSE such as Nb and Ti. Previous experimental studies on mantle hybridization by slab melts[37] and sediment melts[42] also produce melts enriched in LILE and depleted in HFSE (Fig. 6d); however their major element compositions mostly reflect (ultra-) potassic shoshonitic melts (high K_2O) that occur lesser widely in subduction zones worldwide. Traditionally, melts with high Sr/Y signature have been interpreted as slab melts due to the presence of garnet in the melting residue[55] while the high Th/Nb signature was interpreted to record contribution from sediments melts, as Th can be mobilized more efficiently in sediment melts[56]. In addition, high Ba contents have traditionally been ascribed to addition of fluids[57]. The peridotite-mélange melts plot tightly within

the range defined by global arcs for ratios that have traditionally required discrete sedimentary, slab melt, and/or AOC fluid addition to the arc magma source[57]. In particular, the peridotite-mélange melts carry arc-like Sr/Y, Th/Nb, Ba/Th, K/Ti ratios among others (Fig. 7).

In nature, there exists a large compositional variability in primitive arc magmas, ranging from arc tholeiites to calc-alkaline and shoshonites. However, such compositional variability and their spatial distributions (or the lack thereof) have not been satisfactorily explained. Primitive arc tholeiites are usually thought to be produced by decompression style melting (similar to MORB), whereas the classically invoked model for the formation of primitive calc-alkaline magmas envisages their production by flux melting of the mantle induced by the addition hydrous slab components. These slab components are responsible for the up to two orders of magnitude higher trace element concentrations of primitive calc-alkaline magmas relative to N-MORB. For instance, the elevated Th-Zr-TiO_2 concentrations of primitive calc-alkaline magmas reflects higher slab contributions in their sources[33]. We have shown that melts produced from melting of a mantle hybridized by sediment-dominated mélanges (PER-SED) strongly resembled primitive calc-alkaline magmas whereas melts produced from melting of a mantle hybridized by serpentinite-dominated mélanges (PER-SERP) strongly resembled primitive arc tholeiites, both in terms of major (e.g., K_2O, TiO_2) and trace element abundances (e.g., Ba, Th, Zr) and in terms of fractionation characteristics (Fig. 6).

It is critical to determine whether those abundances and fractionations are simply inherited from the starting material or if they are enhanced during melting of the mélange-hybridized peridotite. We make several important observations regarding elemental abundances and fractionations in the melt compared to the starting materials. The bulk starting compositions of PER-SED 95-5 and PER-SERP 85-15 experiments (the two types of experiments that are dominated by ultramafic component – either peridotite or serpentine) fall either outside of the global arc range or within the lower range of values observed in arcs (Fig. 6a and c). It is thus clear that melting plays an important role in producing elemental abundances that are similar to values observed in global arc magmas.

The bulk composition of PER-SED 85-15 experiments (more strongly influenced by a sediment-dominated mélange) is already similar to global arcs for most elements (Fig. 6b), and less surprisingly, melting produces melts that are also similar to arcs. Yet, regardless of abundances, characteristic element ratios acquire a slightly enhanced “arc-like” signature for most

elemental ratios during melting of mélange-hybridized peridotite. Specifically, Ba/Th, Sr/Y, Zr/Hf, Zr/Sm, and K/Ti slightly increased in melts compared to the starting materials; Ba/Nb, Sr/Nd and Sm/Nd stay relatively unchanged whereas Th/Nb and Th/Zr slightly decreased compared to the starting materials.

Experimental melts produced from PER-SED experiments have higher Ba than melts produced from PER-SERP experiments because the sediment-dominated mélange matrix initially had a higher Ba content than the serpentine-dominated mélange matrix (Figs. S6 and S8). Still, melts that are produced during melting of PER-SED and PER-SERP starting materials have slightly higher Ba/Th, Sr/Y, Zr/Hf, Zr/Sm, and K/Ti and slightly lower Th/Nb and Th/Zr ratios (compared to starting materials), and thus are not simply inherited from the starting materials.

In Fig. S9, we show that primitive arc magmas mainly record Nb/Ce_N <1 (normalized to N-MORB[58]), but their Zr/Sm_N can be below or above 1 and is unrelated to the magma type. In addition to Nb depletion and low Nb/Ce ratios, depletion in Zr and Hf is seen for example in shoshonites from Sulawesi and Fiji, and in calc-alkaline basalts from Solomon and Bismarck[33]. However, Zr, Hf, and Zr/Hf are actually variable in natural primitive arc magmas. Elevated Zr-Hf and Zr/Sm_N (>1) observed in low-degree melts from PER-SED experiments are features that are observed in natural arc magmas such as calc-alkaline andesites from Japan and New Zealand, calc-alkaline basalts from Mexico, and depleted andesites from Izu-Bonin. Meanwhile, low-degree melts from PER-SERP experiments have Zr/Sm_N <1 that overlap with some HFSE-depleted arc magmas such as tholeiitic basalts and andesites from Japan, Cascades and Tonga arcs. We note that in PER-SED experiments, elevated Zr/Sm (and Hf/Sm) do not reflect inheritance from the mélange matrix (Fig. S6). Instead, the variability in Zr-Hf contents and Zr/Hf in natural mélange matrices most likely reflect some Zr-Hf mobility in the absence/destabilization of zircon[15]. Overall, the trace element characteristics of our experimental melts plot well within the range of primitive arc magmas (Fig. 7). Thus, these experiments do not only reproduce elemental abundances (major and trace) but also elemental fractionations observed in global arc magmas. In addition, we show that those arc-like abundances and fractionation signatures can be readily produced and variably enhanced during melting of a mélange-hybridized mantle source.

Using chemical maps and high-resolution BSE images, we did not observe accessory phases, unlike what had been found in pure mélange melt residues[40]. Our results indicate that elements that have similar incompatibilities during pure peridotite melting can still be slightly

fractionated during mélange-hybridized peridotite melting. Also, we did not observe HFSE- or REE- compatible accessory phases that could retain these elements in the residue. Niobium depletion was in part inherited from the starting bulk compositions (Fig. S6) but we hypothesize that it was enhanced by the preferential partitioning of Nb into orthopyroxene[9]. In particular, the presence of an opx-rich reaction zone in all 72-h experiments could have contributed to Nb depletion in the melts. The opx-rich band is likely due to reaction of hydrous melts with the peridotite assemblage, as has been observed in previous studies[59]. Natural pyroxenites, including orthopyroxenites, have been ubiquitously found in exhumed mantle sections. Previous experimental[27,59] and field-based studies[60–62] have pointed out that orthopyroxenites should form as reaction products of hydrous melts and mantle minerals. The ubiquitous occurrence of orthopyroxenites exposed in supra-subduction zone ophiolites such as in the Josephine[62], Coast range ophiolites[63], and UHP Maowu Ultramafic Complex[64], and sampled in arc-related xenoliths[65], may also potentially record the hybridization of mantle wedge by mélange materials[31]. Thus, the incorporation of mélange diapirs into the mantle wedge may also have implications for the formation of mineralogical and lithological heterogeneities in the mantle.

This study has important implications for the understanding of subduction zone magmatism. During subduction, mélange diapirs may propagate, and dynamically mix with the overlying mantle. Our study shows that depending on the nature and relative contributions of the hybridizing mélange materials in the source of arc magmas, a large variety of primary magmas with characteristic arc-like signatures can be produced. As LILE-enriched shoshonitic melts are expected to form from melting of pure sediment-dominated mélange materials[40], our study shows that both primitive arc tholeiites and primitive calc-alkaline magmas, which are the two most abundant magma types in subduction zones worldwide, can be produced by melting of mantle hybridized by serpentinite-dominated and sediment-dominated mélange materials, respectively. The rarer occurrence of ultrapotassic shoshonites as compared to tholeiites and calc-alkaline magmas likely reflects the volumetric significance of peridotites in the wedge and the dilution effect due to mixing of mélange materials with mantle wedge peridotites. The absence of systematic along- and across-arc spatial distributions of primitive tholeiitic and calc-alkaline arc magmas may reflect the complexity involved in mélange-diapir ascent paths, and their eventual distributions and mixing with peridotite in the mantle wedge.

In summary, our study provides unique constraints for the role of mélange materials in arc magmatism as invoked in previous studies. For the first time, we have shown that melting of a mélange-hybridized peridotite represents a mechanism to generate melts with major element, trace element and trace element ratios characteristic of tholeiitic and calc-alkaline arc magmas. Where mélanges can form and ascend into the wedge, variations in their compositions, thicknesses, and relative contributions in the arc magma source, will likely result in the formation of compositionally diverse primary arc melts and can result in the formation of lithological heterogeneities in the mantle. Mélange transfer from the subducting slab to the mantle wedge may be one of several mechanisms by which arc magmas are produced, but we emphasize that both major and trace element of experimental melts need to be reported to better assess how closely we can simulate arc processes. Although further experiments will help decipher the type and amount of mélange materials that could be involved in individual subduction zones, we show that hybridization of peridotite by buoyant mélange rocks is a viable process to transfer crustal signatures from the slab surface to arc magmas.

Acknowledgment/Contributions

This project was supported by the WHOI Ocean Exploration Institute (OEI) 27071178 to VLR. Previous related projects were supported by NSF EAR-1348063 and WHOI OEI to HRM. We thank Brian Monteleone and Kathryn Rose Pietro for their help with SIMS analyses. VLR thanks Glenn Gaetani for sharing his facility and advice, and Ed Stolper and Mike Baker for helpful discussions. We are also thankful for Emily Sarafian's help during preparation of the experiments. Finally, we are grateful for two anonymous reviews that significantly improved the manuscript. VLR designed the experimental study and provided peridotite rocks, EAC and VLR performed the experiments, EAC and VLR performed the chemical analyses, HRM provided mélange rocks. All authors contributed to the manuscript.

FIGURES

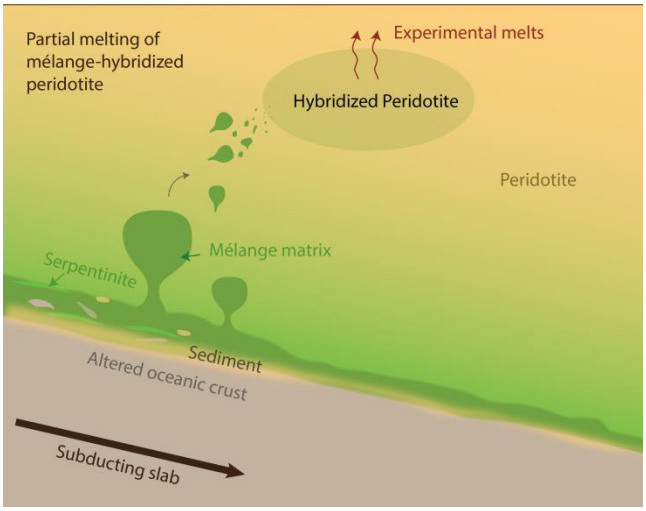

Figure 1 | Conceptual illustration of hybridization of peridotite mantle wedge with mélange material during subduction. Experiments performed in this study simulate the partial melting of a mélange-hybridized peridotite in the mantle wedge.

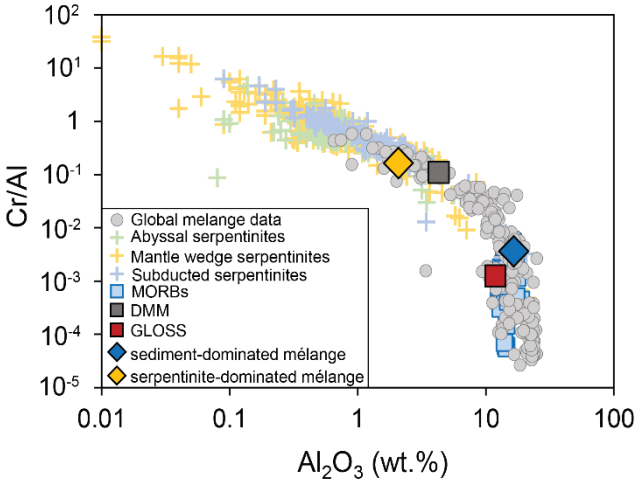

Figure 2 | Global variability of mélange rocks plotted in terms of immobile elements, Cr/Al versus Al_2O_3. The two types of mélange matrices used in this study cover a large range of the natural variability of mélanges, with one matrix that carries a serpentinite/ultramafic flavor, and one matrix that carries a sediment (GLOSS) flavor. Literature data sources: Global mélange compilation[23], abyssal, mantle wedge and subducted serpentinite compilation[66], MORB compilation[58], DMM composition[67], and GLOSS[2].

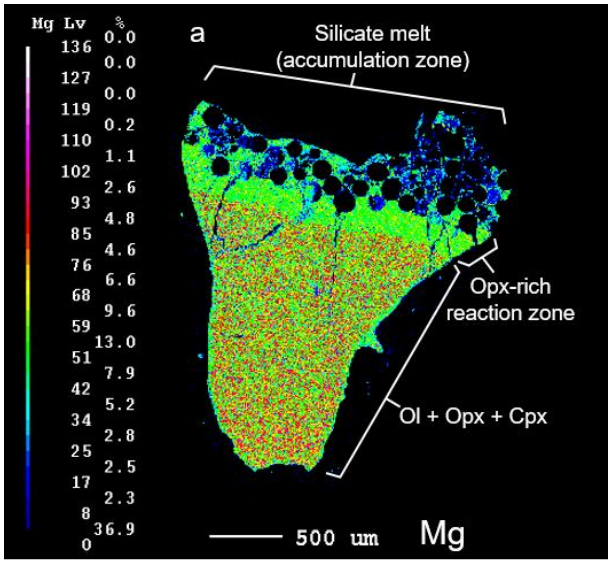

Figure 3 | Mg compositional map of a representative experiment, PER-SERP (85-15), performed at 1.5 GPa and 1315 ºC. An opx-rich reaction zone was observed along the interface between the melt pool and the residual minerals and is particularly visible in Mg maps (bright yellow green band). PER-SERP experiments produced hydrous melt + ol + opx + cpx at all temperatures investigated.

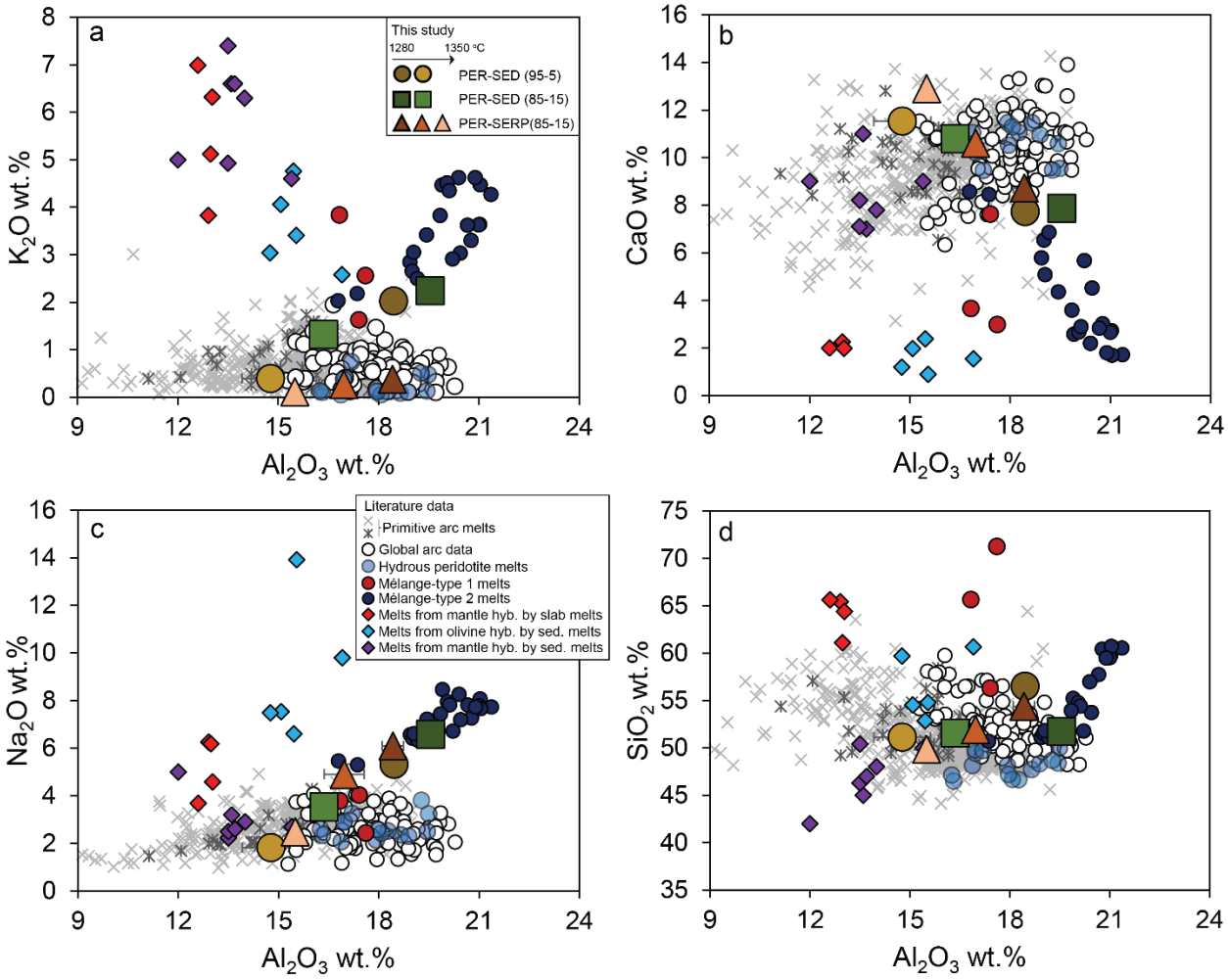

Figure 4 | Major element variations (a) K_2O, (b) CaO, (c) Na_2O, (d) SiO_2 vs Al_2O_3 of experimental peridotite-mélange melts from this study compared to global arcs[35] (normalized to MgO = 6 wt. %), two primitive arc melts compilations, and previous experimental studies[37,38,41]. The two primitive arc melts compilations are from Schmidt and Jagoutz[33] (gray asterisk) and Till *et al.*[34] (light gray cross). Hydrous peridotite melts are from Gaetani and Grove[36]. Experimental melts from mantle hybridized by slab melts and sediment melts are from Rapp *et al.*[37] and Mallik *et al.*[41], respectively. Experimental melts of olivine hybridized by sediment melts are from Pirard and Hermann[38]. Experimental mélange-type 1 melts are from Castro and Gerya[27] and Castro *et al.*[39], while the experimental mélange-type 2 melts are from Cruz-Uribe *et al.*[40] Our experiments are plotted as averages with error bars representing 1 s.d. All the data, including the literature, are plotted on volatile-free basis.

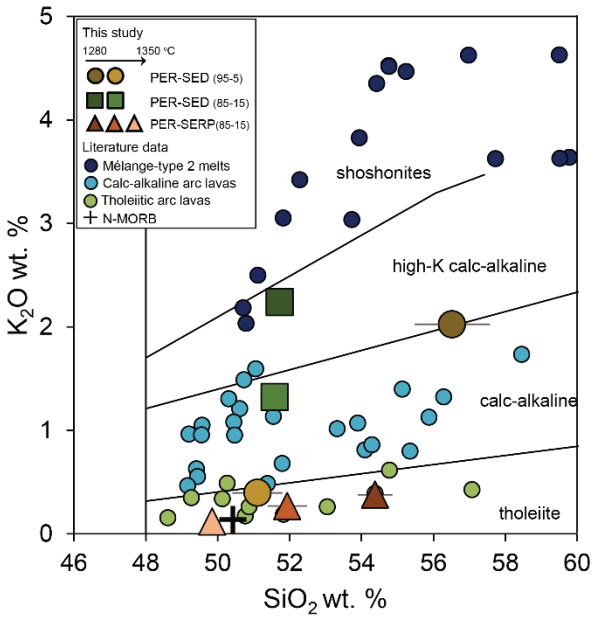

Figure 5 | SiO_2-K_2O diagram[68], modified from Schmidt and Jagoutz[33], highlighting different primitive arc magma types. The experimental peridotite-mélange melts from this study are plotted in comparison with compared to primitive calc-alkaline arc magmas (light blue circles), primitive tholeiitic arc magmas (green circles) and experimental melts of a sediment-dominated mélange material (dark blue circles) of Cruz-Uribe *et al.*[40] Our experiments are plotted as averages with error bars representing 1 s.d. All the data, including the literature, are plotted on volatile-free basis. Compilation of primitive calc-alkaline and primitive tholeiitic arc magmas are from Schmidt and Jagoutz[33]. The average N-MORB value is from Gale *et al.*[58]

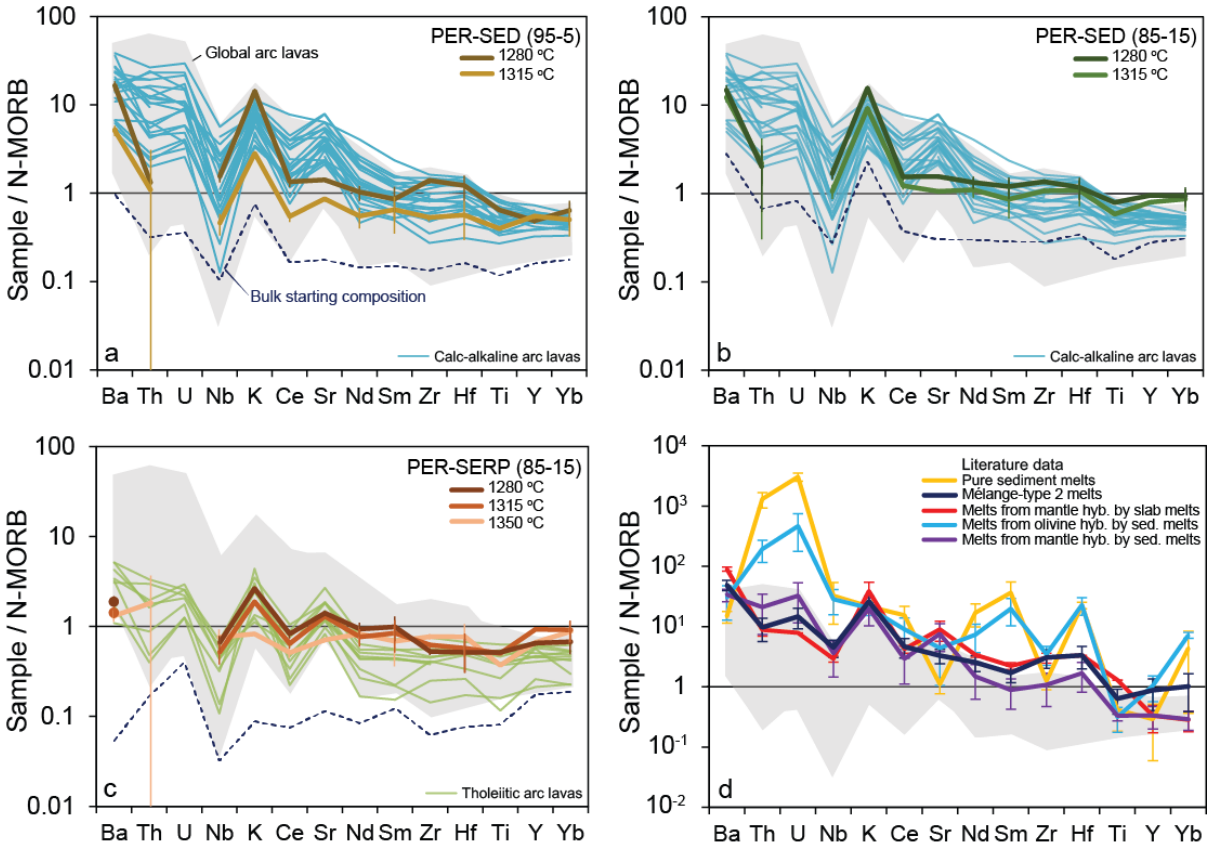

Figure 6 | Normalized trace element concentrations of experimental peridotite-mélange melts (a-c) and previously published experimental studies (d), compared to global arcs[35] (normalized to MgO = 6 wt. %; gray field) with emphasis on the primitive calc-alkaline (light blue) and arc tholeiites (green) from Schmidt and Jagoutz[33]. The average N-MORB value used in the normalization is from Gale *et al.*[58]. Data from this study are melt compositions with error bars representing 2SE total (2SE internal error propagated with 2SE from calibration curve). K and Ti were analyzed using EPMA. Bulk starting compositions of the three types of experiments are reported as a dotted blue line. Experimental melts from mantle hybridized by slab melts and sediment melts are from Rapp *et al.*[37] and Mallik *et al.*[42], respectively. Experimental melts of olivine hybridized by sediment melts are from Pirard and Hermann[38]. Experimental pure sediment melts are from Skora and Blundy[7]. Experimental melts of a sediment-dominated mélange material (mélange-type 2 melts) are from Cruz-Uribe *et al.*[40] The literature data are plotted as averages with error bars representing 1 s.d.

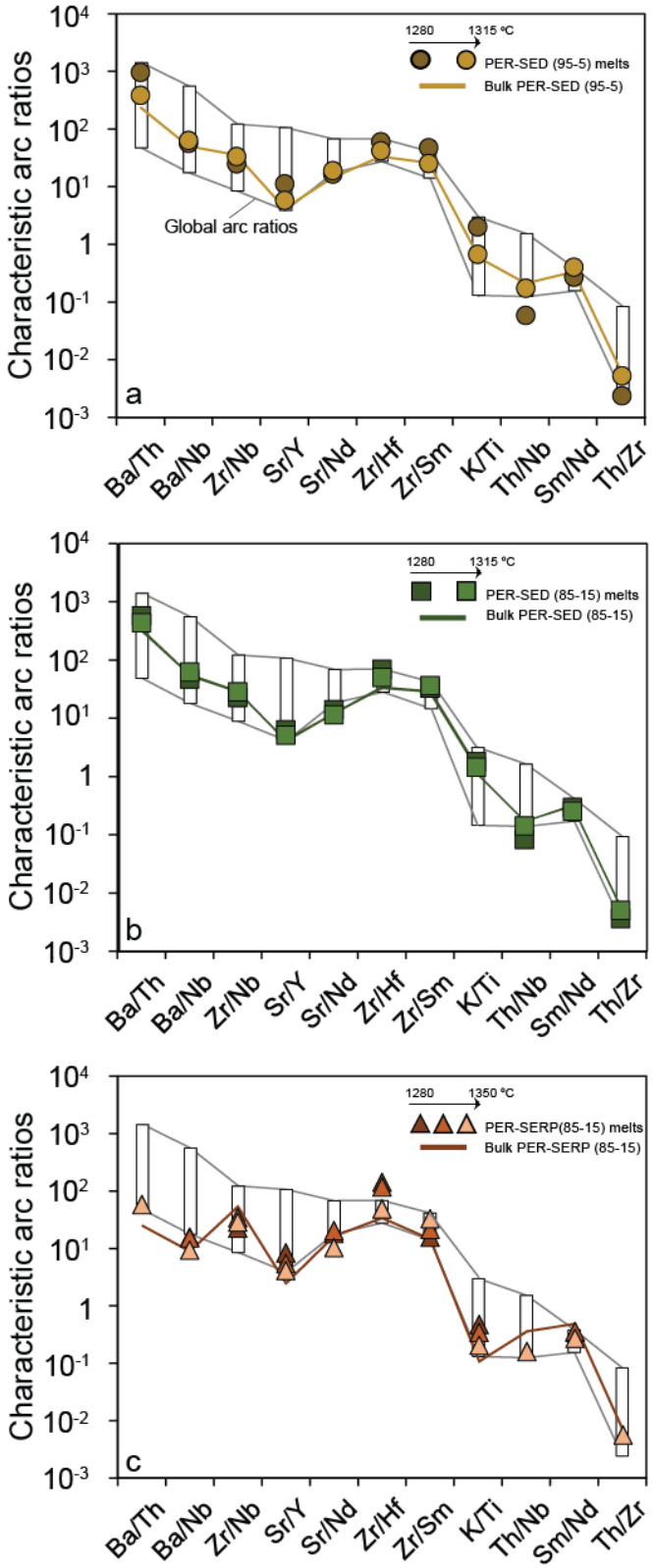
Characteristic arc ratios
10^4
10^3
10^2
10^1
1
10^-1
10^-2
10^-3
1280
1315 °C
PER-SED (95-5) melts
Bulk PER-SED (95-5)
Global arc ratios
a
Ba/Th
Ba/Nb
Zr/Nb
Sr/Y
Sr/Nd
Zr/Hf
Zr/Sm
K/Ti
Th/Nb
Sm/Nd
Th/Zr
Characteristic arc ratios
1280
1315 °C
PER-SED (85-15) melts
Bulk PER-SED (85-15)
b
Ba/Th
Ba/Nb
Zr/Nb
Sr/Y
Sr/Nd
Zr/Hf
Zr/Sm
K/Ti
Th/Nb
Sm/Nd
Th/Zr
Characteristic arc ratios
1280
1350 °C
PER-SERP(85-15) melts
Bulk PER-SERP (85-15)
c
Ba/Th
Ba/Nb
Zr/Nb
Sr/Y
Sr/Nd
Zr/Hf
Zr/Sm
K/Ti
Th/Nb
Sm/Nd
Th/Zr

Figure 7 | Trace element fractionations of experimental peridotite-mélange melts (a-c) compared to the bulk starting compositions (yellow, green and red lines) and global arc ratios defined by Turner and Langmuir database[35] (normalized to MgO = 6 wt. %; white rectangles).

References

1. Tera, F. *et al.* Sediment incorporation in island-arc magmas: Inferences from 10Be. *Geochim. Cosmochim. Acta* **50,** 535–550 (1986).
2. Plank, T. & Langmuir, C. H. The chemical composition of subducting sediment and its consequences for the crust and mantle. *Chem. Geol.* **145,** 325–394 (1998).
3. Pearce, J. Trace Element Characteristics of Lavas from Destructive Plate Boundaries. in *Andesites: Orogenic andesites and related rocks* (John Wiley and Sons, 1982).
4. Tatsumi, Y., Hamilton, D. L. & Nesbitt, R. W. Chemical characteristics of fluid phase released from a subducted lithosphere and origin of arc magmas: Evidence from high-pressure experiments and natural rocks. *J. Volcanol. Geotherm. Res.* **29,** 293–309 (1986).
5. Duncan, R. A. & Green, D. H. Role of multistage melting in the formation of oceanic crust. *Geology* **8,** 22–26 (1980).
6. McCulloch, M. T. & Gamble, J. A. Geochemical and geodynamical constraints on subduction zone magmatism. *Earth Planet. Sci. Lett.* **102,** 358–374 (1991).
7. Skora, S. & Blundy, J. High-pressure Hydrous Phase Relations of Radiolarian Clay and Implications for the Involvement of Subducted Sediment in Arc Magmatism. *J. Petrol.* **51,** 2211–2243 (2010).
8. Hermann, J. & Rubatto, D. Accessory phase control on the trace element signature of sediment melts in subduction zones. *Chem. Geol.* **265,** 512–526 (2009).
9. Kelemen, P. B., Johnson, K. T. M., Kinzler, R. J. & Irving, A. J. High-field-strength element depletions in arc basalts due to mantle–magma interaction. *Nature* **345,** 521–524 (1990).
10. Hawkesworth, C. J., Gallagher, K., Hergt, J. M. & McDermott, F. Mantle and Slab Contributions in Arc Magmas. *Annu. Rev. Earth Planet. Sci.* **21,** 175–204 (1993).
11. Elliott, T., Plank, T., Zindler, A., White, W. & Bourdon, B. Element transport from slab to volcanic front at the Mariana arc. *J. Geophys. Res. Solid Earth* **102,** 14991–15019 (1997).
12. Nielsen, S. G. & Marschall, H. R. Geochemical evidence for mélange melting in global arcs. *Sci. Adv.* **3,** (2017).
13. Bebout, G. E. & Penniston-Dorland, S. C. Fluid and mass transfer at subduction interfaces—The field metamorphic record. *Lithos* **240–243,** 228–258 (2016).

14. Bebout, G. E. & Barton, M. D. Tectonic and metasomatic mixing in a high-T, subduction-zone mélange—insights into the geochemical evolution of the slab–mantle interface. *Chem. Geol.* **187,** 79–106 (2002).
15. King, R. L., Bebout, G. E., Moriguti, T. & Nakamura, E. Elemental mixing systematics and Sr–Nd isotope geochemistry of mélange formation: Obstacles to identification of fluid sources to arc volcanics. *Earth Planet. Sci. Lett.* **246,** 288–304 (2006).
16. Ague, J. J. Models of permeability contrasts in subduction zone mélange: Implications for gradients in fluid fluxes, Syros and Tinos Islands, Greece. *Chem. Geol.* **239,** 217–227 (2007).
17. Spandler, C., Hermann, J., Faure, K., Mavrogenes, J. A. & Arculus, R. J. The importance of talc and chlorite 'hybrid' rocks for volatile recycling through subduction zones; evidence from the high-pressure subduction mélange of New Caledonia. *Contrib. Mineral. Petrol.* **155,** 181–198 (2008).
18. Sorensen, S.S & Grossman, J.N. Enrichment of trace elements in garnet amphibolites from a paleo-subduction zone: Catalina Schist, southern California. *Geochim. Cosmochim. Acta* **53,** 3155–3177 (1989).
19. Abers, G. A. Hydrated subducted crust at 100–250 km depth. *Earth Planet. Sci. Lett.* **176,** 323–330 (2000).
20. Bebout, G. E. Field-Based Evidence for Devolatilization in Subduction Zones: Implications for Arc Magmatism. *Science* **251,** 413 (1991).
21. Miller, D. P., Marschall, H. R. & Schumacher, J. C. Metasomatic formation and petrology of blueschist-facies hybrid rocks from Syros (Greece): Implications for reactions at the slab–mantle interface. *Lithos* **107,** 53–67 (2009).
22. Harlow, G. E., Flores, K. E. & Marschall, H. R. Fluid-mediated mass transfer from a paleosubduction channel to its mantle wedge: Evidence from jadeitite and related rocks from the Guatemala Suture Zone. *Lithos* **258–259,** 15–36 (2016).
23. Marschall, H. R. & Schumacher, J. C. Arc magmas sourced from mélange diapirs in subduction zones. *Nat. Geosci* **5,** 862–867 (2012).
24. Hall, P. S. & Kincaid, C. Diapiric Flow at Subduction Zones: A Recipe for Rapid Transport. *Science* **292,** 2472 (2001).

25. Gerya, T. V. & Yuen, D. A. Rayleigh–Taylor instabilities from hydration and melting propel 'cold plumes' at subduction zones. *Earth Planet. Sci. Lett.* **212,** 47–62 (2003).
26. Gerya, T. V., Connolly, J. A. D., Yuen, D. A., Gorczyk, W. & Capel, A. M. Seismic implications of mantle wedge plumes. *Phys. Earth Planet. Inter.* **156,** 59–74 (2006).
27. Castro, A. & Gerya, T. V. Magmatic implications of mantle wedge plumes: Experimental study. *Lithos* **103,** 138–148 (2008).
28. Zhu, G *et al.* Three-dimensional dynamics of hydrous thermal-chemical plumes in oceanic subduction zones. *Geochem. Geophys. Geosystems* **10,** (2009).
29. van Hinsberg, V. J., Franz, G. & Wood, B. J. Determining subduction-zone fluid composition using a tourmaline mineral probe. *Geochem. Perspect. Lett.* **3,** 160–169 (2017).
30. Gorczyk, W., Gerya, T. V., Connolly, J. A. D. & Yuen, D. A. Growth and mixing dynamics of mantle wedge plumes. *Geology* **35,** 587–590 (2007).
31. Proenza, J. A. *et al.* Cold plumes trigger contamination of oceanic mantle wedges with continental crust-derived sediments: Evidence from chromitite zircon grains of eastern Cuban ophiolites. *Geosci. Front.* (2017). doi:10.1016/j.gsf.2017.12.005
32. Vogt, K., Castro, A. & Gerya, T. Numerical modeling of geochemical variations caused by crustal relamination. *Geochem. Geophys. Geosystems* **14,** 470–487 (2013).
33. Schmidt, M. W. & Jagoutz, O. The global systematics of primitive arc melts. *Geochem. Geophys. Geosystems* **18,** 2817–2854 (2017).
34. Till, C. B. A review and update of mantle thermobarometry for primitive arc magmas. *Am. Mineral.* **102,** 931 (2017).
35. Turner, S. J. & Langmuir, C. H. The global chemical systematics of arc front stratovolcanoes: Evaluating the role of crustal processes. *Earth Planet. Sci. Lett.* **422,** 182–193 (2015).
36. Gaetani, G. A. & Grove, T. L. The influence of water on melting of mantle peridotite. *Contrib. Mineral. Petrol.* **131,** 323–346 (1998).
37. Rapp, R.P, Shimizu, N, Norman, M.D & Applegate, G.S. Reaction between slab-derived melts and peridotite in the mantle wedge: experimental constraints at 3.8 GPa. *Chem. Geol.* **160,** 335–356 (1999).

38. Pirard, C. & Hermann, J. Focused fluid transfer through the mantle above subduction zones. *Geology* **43,** 915–918 (2015).
39. Castro, A. *et al.* Melting Relations of MORB–Sediment Mélanges in Underplated Mantle Wedge Plumes; Implications for the Origin of Cordilleran-type Batholiths. *J. Petrol.* **51,** 1267–1295 (2010).
40. Cruz-Uribe, A. M., Marschall, H. R., Gaetani, G. A. & Le Roux, V. Generation of alkaline magmas in subduction zones by partial melting of mélange diapirs—An experimental study. *Geology* **46,** 343–346 (2018).
41. Mallik, A., Nelson, J. & Dasgupta, R. Partial melting of fertile peridotite fluxed by hydrous rhyolitic melt at 2–3 GPa: implications for mantle wedge hybridization by sediment melt and generation of ultrapotassic magmas in convergent margins. *Contrib. Mineral. Petrol.* **169,** 48 (2015).
42. Mallik, A., Dasgupta, R., Tsuno, K. & Nelson, J. Effects of water, depth and temperature on partial melting of mantle-wedge fluxed by hydrous sediment-melt in subduction zones. *Geochim. Cosmochim. Acta* **195,** 226–243 (2016).
43. Hacker, B. R., Gerya, T. V. & Gilotti, J. A. Formation and Exhumation of Ultrahigh-Pressure Terranes. *Elements* **9,** 289–293 (2013).
44. Currie, C. A., Beaumont, C. & Huismans, R. S. The fate of subducted sediments: A case for backarc intrusion and underplating. *Geology* **35,** 1111–1114 (2007).
45. Behn, M. D., Kelemen, P. B., Hirth, G., Hacker, B. R. & Massonne, H.-J. Diapirs as the source of the sediment signature in arc lavas. *Nat. Geosci.* **4,** 641 (2011).
46. Little, T. A. *et al.* Diapiric exhumation of Earth's youngest (UHP) eclogites in the gneiss domes of the D'Entrecasteaux Islands, Papua New Guinea. *Tectonophysics* **510,** 39–68 (2011).
47. Gerya, T. & Stöckhert, B. Two-dimensional numerical modeling of tectonic and metamorphic histories at active continental margins. *Int. J. Earth Sci.* **95,** 250–274 (2006).
48. Chatterjee, N. & Jagoutz, O. Exhumation of the UHP Tso Morari eclogite as a diapir rising through the mantle wedge. *Contrib. Mineral. Petrol.* **169,** 3 (2015).
49. Fumagalli, P., Poli, S., Fischer, J., Merlini, M. & Gemmi, M. The high-pressure stability of chlorite and other hydrates in subduction mélanges: experiments in the system Cr2O3–MgO–Al2O3–SiO2–H2O. *Contrib. Mineral. Petrol.* **167,** 979 (2014).

50. Pawley, A. Chlorite stability in mantle peridotite: the reaction clinochlore+enstatite=forsterite+pyrope+H2O. *Contrib. Mineral. Petrol.* **144,** 449–456 (2003).
51. Till, C. B., Grove, T. L. & Withers, A. C. The beginnings of hydrous mantle wedge melting. *Contrib. Mineral. Petrol.* **163,** 669–688 (2012).
52. Grove, T., Parman, S., Bowring, S., Price, R. & Baker, M. The role of an H2O-rich fluid component in the generation of primitive basaltic andesites and andesites from the Mt. Shasta region, N California. *Contrib. Mineral. Petrol.* **142,** 375–396 (2002).
53. Mcdade, P., Blundy, J. & Wood, B. *Trace element partitioning between mantle wedge peridotite and hydrous MgO-rich melt*. **88,** (2003).
54. Gaetani, G. A., Kent, A. J. R., Grove, T. L., Hutcheon, I. D. & Stolper, E. M. Mineral/melt partitioning of trace elements during hydrous peridotite partial melting. *Contrib. Mineral. Petrol.* **145,** 391–405 (2003).
55. Defant, M. J. & Drummond, M. S. Derivation of some modern arc magmas by melting of young subducted lithosphere. *Nature* **347,** 662–665 (1990).
56. Johnson, M. C. & Plank, T. Dehydration and melting experiments constrain the fate of subducted sediments. *Geochem. Geophys. Geosystems* **1,** n/a–n/a (2000).
57. Elliott, T. Tracers of the Slab. in *Inside the Subduction Factory* 23–45 (American Geophysical Union, 2013). doi:10.1029/138GM03
58. Gale, A., Dalton, C. A., Langmuir, C. H., Su, Y. & Schilling, J.-G. The mean composition of ocean ridge basalts. *Geochem. Geophys. Geosystems* **14,** 489–518 (2013).
59. Wang, C., Liang, Y., Dygert, N. & Xu, W. L. *Formation of orthopyroxenite by reaction between peridotite and hydrous basaltic melt: an experimental study*. **171,** (2016).
60. Kelemen, P. B., Dick, H. J. B. & Quick, J. E. Formation of harzburgite by pervasive melt/rock reaction in the upper mantle. *Nature* **358,** 635 (1992).
61. Kelemen, P. B., Hirth, G., Shimizu, N., Spiegelman, M. & Dick, H. J. A review of melt migration processes in the adiabatically upwelling mantle beneath oceanic spreading ridges. *Philos. Trans. R. Soc. Lond. Ser. Math. Phys. Eng. Sci.* **355,** 283 (1997).
62. Le Roux, V., Dick, H. J. B. & Shimizu, N. Tracking flux melting and melt percolation in supra-subduction peridotites (Josephine ophiolite, USA). *Contrib. Mineral. Petrol.* **168,** 1064 (2014).

63. Jean, M. M., Shervais, J. W., Choi, S.-H. & Mukasa, S. B. Melt extraction and melt refertilization in mantle peridotite of the Coast Range ophiolite: an LA–ICP–MS study. *Contrib. Mineral. Petrol.* **159,** 113 (2009).
64. Malaspina, N., Hermann, J., Scambelluri, M. & Compagnoni, R. Polyphase inclusions in garnet–orthopyroxenite (Dabie Shan, China) as monitors for metasomatism and fluid-related trace element transfer in subduction zone peridotite. *Earth Planet. Sci. Lett.* **249,** 173–187 (2006).
65. Arai, S., Shimizu, Y., Morishita, T. & Ishida, Y. A new type of orthopyroxenite xenolith from Takashima, Southwest Japan: silica enrichment of the mantle by evolved alkali basalt. *Contrib. Mineral. Petrol.* **152,** 387 (2006).
66. Deschamps, F., Godard, M., Guillot, S. & Hattori, K. Geochemistry of subduction zone serpentinites: A review. *Lithos* **178,** 96–127 (2013).
67. Workman, R. K. & Hart, S. R. Major and trace element composition of the depleted MORB mantle (DMM). *Earth Planet. Sci. Lett.* **231,** 53–72 (2005).
68. Le Maitre, R. W. *A classification of igneous rocks and glossary of terms*. (1989). doi:10.1017/CBO9780511535581.005

Chapter 6

Mélange melting predominant in cold and mature arcs

Abstract

The physical transfer of subducted slab components into the mantle wedge is recorded in the composition of arc magmas worldwide. Whether this transfer is facilitated by fluids and/or melts sourced from discrete slab components or from mixed, hybridized mélange zones along the subduction interface remains debated. Here we assess how the trace-element and isotopic ratios of volcanic rocks in Izu-Bonin arc have changed over time. Meta-analyses of published geochemical data show that transfer of hydrous melts from discrete slab components predominate during subduction initiation. After 5–10 Myr, the geochemical systematics are best reproduced by a process whereby hydrous melts originate from mélange zones. This transition is likely triggered by decreasing slab-top temperature, which extends the decoupled region of the subduction interface to greater depths over time, promoting physical mixing and mélange formation Therefore, mélange melting plays an increasingly important role in magma formation as slab-tops cool and arcs mature.

1 Introduction

The transfer of subducted components from the slab to the mantle wedge in subduction zones is central to our understanding of the long-term chemical exchange between the surface and deep Earth reservoirs, which in turn affects the Earth's climate and habitability (Canfield, 2004). Variations in the elemental and isotopic compositions of arc lavas, relative to other mantle-derived rocks (Gill, 1981), reflect the multiple slab components involved in this transfer process (Ellam and Hawkesworth, 1988; Kay, 1980). The physical mechanisms by which subducted components are transferred into the mantle wedge, however, remain debated. One line of models (model 1) invokes the transfer of slab components into the ambient mantle by either one or a combination of aqueous fluids, hydrous melts, and supercritical fluids derived from discrete subducted materials (*e.g.*, sediment, unaltered and altered oceanic crust (UOC/AOC), serpentinite) depending on the pressure (*P*) and temperature (*T*) conditions experienced by subducting slab (Elliott et al., 1997; Hawkesworth et al., 1997; Keppler, 1996; Kessel et al., 2005; Li Huijuan et al., 2022; Miller et al., 1994; Pearce, 1982; Schmidt and Jagoutz, 2017; Turner and Langmuir, 2022). Another line of models (model 2) envisions that physical mixing, metasomatism, and homogenization of subducted materials and overlying serpentinized mantle occurs along the slab-mantle interface (Bebout and Barton, 2002; Marschall and Schumacher, 2012; Nielsen and Marschall, 2017), leading to the formation of a mélange zone. This model invokes trace element fractionation through the dehydration and melting of mélange rocks either at the slab-mantle interface or during transport as buoyant diapirs into the hotter mantle wedge (Codillo et al., 2018; Cruz-Uribe et al., 2018; Gerya and Yuen, 2003; Parolari et al., 2021; Straub et al., 2020). The two lines of models result in drastically different geochemical signatures in arc magmas (Nielsen and Marschall, 2017). Additional processes and models have been proposed to contribute to the compositional variability in arc magmas such as the role of crustal filter (Hildreth and Moorbath, 1988), wedge thermal structure and extents of mantle melting (Plank and Langmuir, 1988; Turner et al., 2016), and ambient mantle heterogeneity (Turner et al., 2017). These processes operate within the overlying mantle wedge and/or overriding crust, and their influence are likely superimposed after the slab-derived components have been transferred into the overlying mantle. Despite decades of studies on understanding slab-to-mantle transfer mechanisms and arc magma formation, consensus has not been reached on the relative importance of these models and whether they could both occur over time.

Here we use a compilation of published volcanic rock compositions with reported eruption ages (Supplementary Data 1) to investigate how the isotopic and trace-element ratios of volcanic rocks have changed over time in the Izu Bonin arc, from warm subduction initiation at ~52 Ma to cold present-day mature stage (Ishizuka et al., 2006; Reagan et al., 2010; Stern et al., 2003; Stern and Bloomer, 1992). The thermal state of the slab-top presently subducting underneath the Izu-Bonin arc is among the coldest in subduction zones worldwide based on the thermal parameter, Φ [= slab age × convergence rate × sin (dip angle)] (Kirby et al., 1991; Syracuse et al., 2010). The Izu-Bonin subduction zone is ideal to perform a detailed investigation of trace-element fractionation in arc magmas through time, because the region provides a well-studied geological context of a simple intra-oceanic subduction zone (Stern et al., 2003), and with numerous rock samples that have been previously analyzed geochemically and dated either stratigraphically or radiometrically (Supplementary Fig. 5). The Izu-Bonin arc rock record is nearly complete from subduction initiation to present-day, except for the ∼7 Myr hiatus related to the opening of the Shikoku backarc basin at ∼30–15 Ma (Stern et al., 2003). Subduction of asperities (i.e. Western Pacific Seamount Province/WPSP) was previously inferred to have occurred at ~10 Ma (Straub et al., 2015). The Bonin Ridge, a massif located presently in the forearc region in between the Quaternary volcanic front and Izu-Ogasawara Trench, offers a unique rock record to investigate magmatic processes during subduction initiation that is otherwise inaccessible in most other subduction zones (Ishizuka et al., 2020, 2006) (Supplementary Fig. 5). Since subduction initiation, the Izu-Bonin arc has produced volcanic rocks with bimodal composition, from silica-rich (dacitic to rhyolitic) to mafic (basaltic to andesitic) compositions in almost constant volumetric proportions (Bryant et al., 2003; Straub, 2008, 2003; Tamura et al., 2009). The elemental and isotopic compositions of Izu-Bonin magmas have been shown to primarily reflect the contributions from the mantle and subducted materials through time, decoupled from major tectonic changes (Bryant et al., 2003; Straub et al., 2010; Taylor and Nesbitt, 1998). Magmatism during the earliest stage after subduction initiation produced boninitic and tholeiitic rocks with an arc-like trace-element signatures (Ishizuka et al., 2020, 2006; Li et al., 2019; Stern et al., 2003). Based on radiogenic isotopes and trace-element ratios, recent studies have ascribed the progression from low-Si to high-Si boninitic compositions to reflect a rapidly changing slab input from a gabbro-derived crustal melts to fluids derived from sediment and basalt dehydration within the first ~2 Myr after initiation (Li et al., 2022). This was interpreted to reflect a change in the subduction

angle and cooling of the plate interface, wherein the uppermost parts of the slab were thought to have been scraped off and accreted near the nascent trench related to early low-angle subduction during the formation of low-Si boninites. This was followed by steepening of the subduction angle allowing for a selective melting of stratigraphically higher basalt and sediment and the dehydration of stratigraphically lower gabbro layer that generated the high-Si boninites. The locus of high-Si boninite volcanism seems to have moved westward away from the trench, as indicated by the younger high-Si boninites (~48–46 Myr) in the Bonin Islands (Li et al., 2022). In the Bonin Islands, the transition from boninitic to tholeiitic magmatism occurred at ~44–45 Ma, after which the main frontal arc magmatism has been dominated by low-K tholeiitic magmas up to the present (Bryant et al., 2003; Straub et al., 2010). The temporal Pb and Sr isotopic variations in Izu-Bonin magmas since the Oligocene have been suggested to reflect a changing type and amount of subducted sediment (*e.g.*, pelagic and volcaniclastic sediment) and igneous crust, respectively. The Nd isotope composition of the ambient mantle has evolved towards more radiogenic over time due to the ingrowth of ^{143}Nd. However, the magnitude of this effect to the Nd isotope composition of arc magmas has been shown to be insignificant compared to the isotopic contributions from subducted materials to their source (Straub et al., 2010).

Along strike heterogeneity in the slab input into the ambient mantle has been suggested to explain the along-arc variations in Neogene to Quaternary magmas, most notably the northward increase in fluid-mobile elements and Pb isotope values at near constant Nd isotope ratios (Durkin et al., 2020; Hochstaedter et al., 2001; Ishizuka et al., 2007; Stern et al., 2003; Straub et al., 2010; Taylor and Nesbitt, 1998; Tollstrup et al., 2010). Frontal volcanic arcs seem to have resulted from higher degrees of melting of an ambient mantle fluxed by aqueous slab fluids whereas the rear volcanic arcs resulted from lower degrees of melting of a mantle fluxed by supercritical slab fluid (Hochstaedter et al., 2001; Tollstrup et al., 2010). In addition, the pressure-sensitive stability of phengite was previously invoked to explain the across-arc K_2O variability (Tamura et al., 2007). Importantly, variations in magma compositions have usually been interpreted to reflect the changing type and amount of slab components added to the ambient mantle. Most of the proposed models explaining the spatial and temporal variations in the Izu-Bonin arc invoked discrete additions of aqueous fluids and hydrous silicate melts (including supercritical melts) from individual subducted materials (*e.g.*, igneous crust, sediment, serpentinite) into the ambient mantle. Alternatively, it was proposed that the Pb isotope compositions of Izu volcanic rocks could

be produced by bulk mixing of a hybridized mafic–sedimentary–ultramafic mélange component and mantle (King et al., 2007), challenging previous models of how slab components and signatures are delivered to the source region of arc magmas (Bebout and Penniston-Dorland, 2016; King et al., 2006; Marschall and Schumacher, 2012). Additional discussions of the geodynamic evolution of the Izu-Bonin arc are available elsewhere (Arculus et al., 1995; Bryant et al., 2003; Ishizuka et al., 2006; Stern et al., 2003; Taylor et al., 1992).

The compiled Izu-Bonin data were filtered (SiO_2 < 63 wt. %) to minimize the effects of intra-crustal differentiation and crustal assimilation processes (Methods; Supplementary Figs. 1 and 2). The elemental and isotopic compositions of the subducting Pacific plate are well-characterized, which allows for better assessment of the contributions from individual slab components (Durkin et al., 2020; Hauff et al., 2003; Kelley et al., 2003; Plank et al., 2007) (Methods). Using petrological and thermal models relevant to the Izu-Bonin arc, we show that the temporal geochemical variations in the Izu-Bonin arc not only record a shift in the nature and amount of slab components, but importantly record a change in slab-to-mantle transfer mechanisms, whereby individual slab components are added as discrete melts during the early stages of subduction (model 1), while mélange zones develop later as the arc matures and slab-top cools (model 2). This transition corresponds to decreasing slab-top temperatures, well-characterized by recent geodynamic modelling studies, as subduction progresses. This implies that different models of slab-to-mantle transfer are not mutually exclusive but operate at different times in the subduction lifetime of an arc system as dictated primarily by the prevailing slab-top temperature.

2 Results and Discussions

2.1 Slab-to-mantle transfer mechanisms and associated trace-element fractionations

Each of the slab-to-mantle transfer models yield predictable geochemical trends in the resultant magmas. We utilized two sets of trace-element ratios that minimally fractionate during peridotite melting, as evidenced by their limited range of values in mantle peridotites (*e.g.*, lherzolite, refertilized peridotites) and in global MORB compilations (Gale et al., 2013). The first set of ratios (Fig. 2 a, c, e) are fluid-sensitive (Ba/Th, Nd/Sr, Ce/Pb) and are commonly used to track the contributions of aqueous fluids because Ba, Sr, and Pb preferentially partitions into a

fluid phase relative to Th, Nd, and Ce (Elliott et al., 1997; Hawkesworth et al., 1997; Turner et al., 1997). The second set of ratios (Fig. 2 b, d, f) are mostly fluid-insensitive and typically fractionate in the presence of mineral phases other than the main peridotite minerals (olivine and pyroxene), such as epidote and rutile (Th/Nb), and white mica, *e.g.*, phengite (Cs/Rb) (Supplementary Fig. 7). Cesium and Rb are both fluid-mobile but significant fractionation from each other occurs when phengite is present in the melting source (Schmidt et al., 2004). These ratios are minimally affected by variations in the extents of mantle melting as well as peridotite assimilation during magma transit through the mantle wedge, thereby preserving a memory of the trace-element fractionations formed in the slab-mantle interface region. In addition, these ratios are minimally affected by fractional crystallization in the crust as evidenced by the lack of correlations with SiO_2 (Supplementary Fig. 3). This implies that insignificant changes to the ratios are imparted by fractional crystallization of olivine, pyroxene, and plagioclase relative to the signatures contributed by slab and mantle components. The isotopic composition of the subarc mantle is assumed to be similar to a depleted MORB mantle (DMM) (Salters and Stracke, 2004) and represents a relatively unmodified mantle (Nielsen and Marschall, 2017; Straub et al., 2010). Mantle isotopic heterogeneity beneath the Izu-Bonin arc is likely to be insignificant, as evidenced by the depleted subarc mantle composition inferred from primitive basalts in the Shikoku basin (Straub et al., 2010) and the relatively simple tectonic history of the region (Stern et al., 2003). Slab components in the region are dominated by pelagic and volcaniclastic sediments, and unaltered and altered oceanic crust (Durkin et al., 2020; Kelley et al., 2003; Plank et al., 2007) (Methods).

Arc magmas that are minimally affected by fractional crystallization and crustal assimilation follow specific geochemical trends dictated by the topology of idealized mixing lines between ambient mantle and different subducted slab components. The quantitative models in Fig. 1 show the expected geochemical trends for sediment-melting, slab-melting, and mélange-melting models, as well as the effect of ambient mantle isotopic heterogeneity. Using appropriate partition coefficients relevant to hydrous sediment melting at near-solidus conditions (Hermann and Rubatto, 2009), we calculated the compositions of sediment partial melts and their mixtures with discrete AOC melts to generate a range of composite slab melts. Partition coefficients for Ba and Th during sediment melting were set to $D_{Ba} = 0.45$ and $D_{Th} = 2.3$, respectively, which represent the values from hydrous sediment melting experiments at 800 °C (Hermann and Rubatto, 2009). These values are comparable to the average values ($D_{Ba} = 0.65$, $D_{Th} = 1.7$) recorded in hydrous

sediment melting from 750–900 °C (Hermann and Rubatto, 2009). We also used the globally representative endmember compositions for a 'hot' and 'cold' AOC melts generated by 10% and 30% of crustal melting (Turner and Langmuir, 2022), respectively. This compositional range of crustal melts takes into account the recent experimental results on hydrous crustal melting (Carter et al., 2015; Kessel et al., 2005; Klimm et al., 2008), as well as provides a range of Ba/Th values expected for melting of UOC. Since the Nd isotope ratio of magmas is minimally affected by fluid-mediated metasomatism (McCulloch et al., 1980), the variations in Nd isotopes should primarily reflect the contributions from ambient mantle and isotopically distinct slab-derived components. In sediment-melting model (Fig. 1a), hydrous sediment melts display higher Ba/Th ratios than starting bulk. Idealized mixing curves between the ambient mantle and sediment partial melt or bulk sediment should have very different mixing topologies. Mixing lines were calculated between ambient mantle and 1% and 75% partial sediment melts. The effect of ambient mantle isotopic heterogeneity manifests as displacement of the Nd isotope composition of the mantle to lower values (in the case of less radiogenic mantle) without changing the curvature of the mixing curves (Fig. 1b). In slab-melting model (Fig. 1c), mixing of discrete melts from subducted sediment and igneous crust form a homogenized composite slab melt which then mixes with the ambient mantle. Mixing lines were calculated between ambient mantle and composite slab melts over a range of mixing proportions. The compositions of composite slab melts represent discrete mixtures of low (1%) and high-degree (75%) partial sediment melts mixed with 'hot' and 'cold' AOC melts. This model predicts many possible mixing trajectories, from horizontal to near vertical trends, due to the large number of possible mixing combinations of discrete melts of sediment and igneous crust with variable Ba/Th ratios. In mélange-melting model (Fig.1d), mixing of bulk sediment, igneous crust, and hydrated mantle rocks first occur along the slab-mantle interface forming a new, isotopically homogenous source rock (i.e. mélange; Marschall and Schumacher, 2012) where the Nd isotope ratio is set by the bulk mixing proportions (Nielsen and Marschall, 2017). Subsequent melting of mélange source is predicted to produce magmas that follow linear horizontal trends, where the melting process fractionates Ba/Th ratio without changing the Nd isotope ratio. Available melting experiments on mélange compositions provide evidence for trace element fractionation in melts during mélange melting (Castro et al., 2010; Castro and Gerya, 2008; Codillo et al., 2018; Cruz-Uribe et al., 2018). In any of the models we described above, subcritical aqueous fluid, supercritical fluids, and hydrous silicate melts, each with different solute-carrying capacities

and transport properties, can be involved as a continuum depending primarily on the *P-T* conditions relative to the second critical points (i.e. melt-vapor miscibility at the solidus) of subducted materials (Manning, 2004).

2.2 Temporal geochemical systematics in the Izu-Bonin arc

The filtered Izu-Bonin arc dataset is plotted in isotope-trace-element ratio diagrams to distinguish processes that fractionate trace elements (dehydration and melting processes) from source variability (isotopically distinct slab and mantle components) in accordance with the slab-to-mantle transfer models (Fig. 2). We identified three stages of elemental fractionation in the compiled dataset of Izu Bonin volcanic rocks, capturing compositional evolution from early Paleogene during warm subduction initiation (defined here as 52–45 Ma), to late Paleogene (defined here as 45–23 Ma), and Neogene to Quaternary (defined here as 23–0 Ma; mature cold stage).

In the early Paleogene, boninites, low-K tholeiites, and calc-alkaline andesites have low $^{143}Nd/^{144}Nd$ (< 0.5130) and high $^{87}Sr/^{86}Sr$ ratios (0.704–0.705), and Nd and Sr isotope compositions correlate with both fluid-sensitive and fluid-insensitive ratios. Relative to a depleted mantle beneath Izu-Bonin arc, their radiogenic isotopes and trace element compositions require another component with higher Ba/Th, Th/Nb, and Cs/Rb, lower Nd/Sr and Ce/Pb, as well as with radiogenic Sr and Nd isotope ratios greater than or equal to 0.706 and 0.51275, respectively. Among seafloor materials drilled outboard of Izu arc (*e.g.*, ODP Site1149 and ODP Site 801), pelagic sediments best fit these geochemical criteria. Volcaniclastic sediments, UOC, and AOC components could still have been present in the source but early Paleogene magmas were likely dominated by the more radiogenic pelagic sediment components (Ishizuka et al., 2020, 2006; Li et al., 2019). Most of the trace-element and isotopic data of early Paleogene volcanic rocks can be accounted for by 1–3 wt. % of melts derived from high degrees (≥ 75 %) of pelagic sediment melting fluxed to the ambient mantle. The spread in the data can be accounted for by mixing between mantle and composite slab melts that contain >50% (by weight) of 'cold' AOC melts mixed with high-degree (75%) pelagic sediment melt. These estimates are consistent with recent studies documenting contributions from crustal melts in Izu-Bonin based on radiogenic and B isotopes (Ishizuka et al., 2020; Li et al., 2022, 2019). Therefore, the data are best explained by slab

melting, where discrete melts from AOC and pelagic sediments mix and homogenize before mixing with mantle melts to produce the early Paleogene magmas (model 1).

During the late Paleogene, dominantly low-K tholeiites, calc-alkaline basalt, trachybasalt, and andesite display near-constant Nd and Sr isotope compositions, with higher $^{143}Nd/^{144}Nd$ ratios (0.5129–0.5131) and lower $^{87}Sr/^{86}Sr$ ratios (0.703–0.704) compared to the early Paleogene rocks, tracing a decrease in the proportion of pelagic sediment component in the magma source (Ishizuka et al., 2020) (Fig. 2). We observed differences in the isotope and trace-element systematics of these volcanic rocks relative to those formed during early Paleogene. First, the late Paleogene rocks display a larger range of Nd/Sr and Ce/Pb values at limited Ba/Th values. The geochemical decoupling among fluid-mobile elements Ba, Pb, and Sr has also been observed in the Aleutian arc (Kelemen et al., 2003). Previous studies have attributed this decoupling to either variable contributions from sediment and eclogite melts mixed into the mantle (Yogodzinski et al., 2015) or variations in slab-top temperatures (Li Huijuan et al., 2022). While increasing temperature generally increases the solubility of divalent trace elements in melts, temperature alone would not result in the decoupling among these trace elements, but requires the presence of certain mineral assemblage in the slab region. In Izu-Bonin, the fractionations in Nd/Sr, Ce/Pb, Th/Nb, but not in Ba/Th, require a mineral assemblage that selectively retains Ba but releases Sr, Pb, and Th into the hydrous melt (Figs. 2 and 3). Epidote minerals (including allanite) are generally prescribed as the main hosts of Sr, Pb and Th in a subducted slab below ~800 °C and pressure at or below 3 GPa (Zack et al., 2002) (Fig. 3). Epidote breakdown would release these trace elements into the melt (Carter et al., 2015; Klimm et al., 2008). When phengite is present, it is the main host for Ba and is stable at higher temperatures and pressures (up to 1000 °C, >3 GPa in water-undersaturated conditions) than epidote (Schmidt and Poli, 2014). Therefore, the decoupling of Ba/Th from Nd/Sr and Ce/Pb displayed by late Paleogene magmas likely reflects the early destabilization of epidote in the slab during prograde subduction, while phengite remains stable (Schmidt et al., 2004; Schmidt and Poli, 2014; Tamura et al., 2007). Previous studies have also inferred the presence of amphibole in the source (Ishizuka et al., 2020; Li et al., 2019; Taylor et al., 1994), which were taken to indicate a shallow slab melting under amphibolite to blueschist-facies during the early stages of subduction in Izu-Bonin. Additional fractionation in Th/Nb ratio could result from the presence of rutile (Nb-compatible) in the source (Ryerson and Watson, 1987). The minerals amphibole, phengite, epidote, and rutile are stable at *P-T* conditions at or above the solidi of

subducted sediments and mafic igneous crust depending on water saturation (Hermann and Rubatto, 2009; Klimm et al., 2008). The inferred breakdown of amphibole and epidote minerals in the melting region places a minimum melting temperature at ~650 °C at pressures less than ~1.5 GPa where phengite remains stable (Fig. 3). This temperature condition is hotter than the present-day slab-top geotherm (<400 °C at 1.5 GPa approximated by the cold slab-top/high-Φ condition in Fig. 3).

Another important distinction of late Paleogene relative to early Paleogene magmas is the lack of correlations between radiogenic isotopes and trace-element ratios. Late Paleogene magmas display fractionations in Ba/Th, Nd/Sr, Ce/Pb, Th/Nb, and Cs/Rb at near-constant Nd and Sr isotope ratios. Models that invoke an ambient mantle that is fluxed by either discrete sediment melts, 'cold' and 'hot' AOC melts, or a combination of both yield variable mixing trajectories primarily with high curvatures, none of which can simultaneously account for the range in Ba/Th, Nd/Sr, Ce/Pb, Th/Nb, and Cs/Rb ratios in late Paleogene magmas (Fig. 2). To produce near horizontal geochemical trends via the slab-melting model (Li Huijuan et al., 2022; Schmidt and Jagoutz, 2017; Turner and Langmuir, 2022), for example, high Ce/Pb ratio would require 8 wt.% of a composite slab melt — 50 wt.% 'hot' AOC melt and 50 wt.% of high-degree (75%) volcaniclastic sediment melt — mixed with mantle melts. Meanwhile, the low Ce/Pb ratios would require 2 wt.% of composite slab melt — 75 wt.% 'hot' AOC melt and 25 wt.% of low-degree (1%) pelagic sediment melt — mixed with mantle melts. Such a scenario would be highly coincidental given the complexity in melt transport dynamics. A process that could simultaneously explain the fractionations in Ba/Th, Nd/Sr, Ce/Pb, Th/Nb, and Cs/Rb ratios at near-constant Nd and Sr isotope compositions is by melting of mélange source (model 2) (Nielsen and Marschall, 2017).

The Neogene and Quaternary (23–0 Ma) low-K tholeiites, basaltic to andesitic rocks are characterized by highly fractionated fluid-sensitive ratios (Ba/Th, Nd/Sr, and Ce/Pb) and fluid-insensitive ratios (Th/Nb and Cs/Rb). These volcanic rocks display constant $^{143}Nd/^{144}Nd$ (0.5129–0.5132) and $^{87}Sr/^{86}Sr$ ratios (0.703–0.704). Relative to the late Paleogene, these magmas display more radiogenic Nd isotope ratios, less radiogenic Sr isotope ratios, and more variable trace-element ratios. The fractionated trace-element ratios imply that both the phengite and epidote minerals destabilize, releasing Ba, Cs, Sr, Pb, and Th into the hydrous melt. Relative to late Paleogene, the inferred destabilization of phengite suggests higher pressure conditions

experienced by the slab (Schmidt et al., 2004; Schmidt and Poli, 2014). The simultaneous destabilization of phengite, rutile, and epidote minerals during melting requires a minimum temperature of 650 °C at water-saturated condition at pressures of at least 1.5 GPa for subducted basaltic crust and sediment (Fig. 3). This means that melting at the plate interface likely occurred at deeper depths relative to the inferred melting conditions in the late Paleogene. This translates to slab-top temperature in the Neogene to Quaternary that are colder at a given depth (or pressure) than in the late Paleogene (approximated by the intermediate to cold slab-top/high-Φ conditions in Fig. 3).

Similar to the late Paleogene, the Neogene and Quaternary magmas display no correlations between Nd isotope and trace-element ratios. These geochemical trends cannot be explained by any models that invoke an ambient mantle fluxed by discrete sediment melts, AOC melts, or composite slab melts. Even though the trend in Cs/Rb ratio seemed to follow the near-horizontal mixing trajectories between the mantle and low-degree pelagic sediment melts or composite slab melts (Fig. 2d), the range in Ba/Th cannot be explained by this process considering that phengite (Ba-compatible) also influences the Ba/Th ratios of arc magmas. For instance, the formation of magmas with variable Ba/Th ratios (*e.g.*, 300–700) at constant Nd isotope ratio of 0.51308 via the slab-melting model (Li Huijuan et al., 2022; Schmidt and Jagoutz, 2017; Turner and Langmuir, 2022) would require mantle melts to be mixed with 4–10 wt.% of composite slab melts that contained up to 90 wt.% AOC melts and 10 wt. % pelagic sediment melts. In $^{87}Sr/^{86}Sr$ vs. Nd/Sr (Supplementary Fig. 4c), a significant fraction of arc compositions plot outside the possible mixing combinations involving discrete sediment melts, AOC melts, and mantle melts (Nielsen and Marschall, 2017), and seem to require another component with low Nd/Sr ratio and unradiogenic Sr. Melts from unaltered igneous crust, mixed with discrete melts from AOC, sediment, and mantle, has been proposed for the Aleutian (Kelemen et al., 2003; Yogodzinski et al., 2015) and Mariana (Klaver et al., 2020) arcs to explain such conundrum (Li Huijuan et al., 2022). In addition, the large fraction (~90 wt.%) of crustal component required to generate the composite slab melts would be consistent with recent Th isotope constraints on some of these magmas (Freymuth et al., 2016). However, as discussed above, this scenario would be highly coincidental because of the difficulty in sustaining the required variable mixing proportions of discrete AOC and UOC melts, sediment melts, and mantle melts during their transit through the mantle wedge over an extended period of time such that they coincidentally produce a horizontal geochemical trend. Accordingly,

the Neogene to Quaternary trace element and isotope data are best explained by melting of mélange source (model 2), a process that has started in the late Paleogene.

The Neogene to Quaternary Izu-Bonin magmas display positive correlations between Sr isotope and fluid-sensitive Ba/Th, Ce/Pb, and Cs/Rb ratios (Fig. 2, Supplementary Fig. 4), consistent with previous observations (Straub et al., 2010; Taylor and Nesbitt, 1998). Numerous geochemical studies in Izu-Bonin and in other subduction zones have argued for a major role of aqueous fluids in the slab-to-mantle transfer to explain such correlations (Elliott et al., 1997; Klaver et al., 2020; Li et al., 2022; Schmidt and Jagoutz, 2017; Taylor and Nesbitt, 1998; Tollstrup et al., 2010). The source of this fluid has been suggested to include the dehydration of AOC and serpentinites in the slab (Klaver et al., 2020; Miller et al., 1994). In Izu Bonin, the composition of the fluid derived from dehydration of AOC (Kessel et al., 2005) that contained 0.2–5 wt.% of water (Durkin et al., 2020; Le Voyer et al., 2019) display Th/Nb and Cs/Rb ratios that are similar to DMM values (Supplementary Fig. 4b,d). Thus, an ambient mantle fluxed by AOC-derived fluids would produce magmas with more limited Th/Nb and Cs/Rb fractionations than observed in the Izu-Bonin data. Alternatively, supercritical fluids have physicochemical properties between aqueous fluids and hydrous silicate melts, and it can contain high dissolved trace-element contents and display fractionated fluid sensitive and insensitive trace-element ratios (Kessel et al., 2005; Manning, 2004). However, experimental studies have shown that supercritical fluids exist only at conditions of high fluid-to-rock ratios (Mibe et al., 2007; Wyllie and Ryabchikov, 2000) at a given temperature and would likely convert into either aqueous fluid or hydrous silicate melt when the conditions change (Kawamoto Tatsuhiko et al., 2012). It is more likely that supercritical fluids (Tollstrup et al., 2010), if formed, will inevitably transform into hydrous silicate melts rather than aqueous fluid as implicated by the need to transport fluid-immobile trace elements and produce the fractionated fluid-insensitive ratios in the Izu-Bonin data. Therefore, the correlation between Sr isotope and fluid-sensitive Ba/Th ratios at constant Nd isotope ratios, and the lack of correlations between fluid-insensitive Th/Nb and Sr and Nd isotope ratios in Neogene-Quaternary data can be explained if hydrous silicate melts are produced by mélange melting wherein the fluid component was sourced locally within the mélange.

Although some samples come from different geographic locations along the Izu-Bonin arc, samples that overlap temporally, but not spatially (*e.g.*, Quaternary rocks along the arc), display the same geochemical trend. In addition, samples that overlap spatially (*e.g.*, Bonin ridge), but not

temporally, display different geochemical trends that are consistent with their eruption ages and associated transfer mechanisms (Supplementary Fig. 6). This implies that the distinct geochemical trends we observed in the Izu-Bonin data clearly indicate a temporal evolution, independent of geographic sample locations, as well as the along-arc geochemical variability in the subducting slab and in the overriding crust. Our results do not contradict previous conclusions regarding the effect of slab input variability on arc magma chemistry in the Izu-Bonin. However, we uncover a previously unrecognized geodynamic process whereby different models of slab-to-mantle material transport and arc magma formation have operated at different times in the subduction lifetime of the Izu-Bonin arc as dictated by the prevailing slab-top temperature (Figs. 2 and 4).

2.3 Slab-top cooling promotes mélange formation

The temporal shift in slab-to-mantle transfer mechanisms, from the additions of discrete melts from individual subducted materials in early Paleogene (model 1) to melting of mélange 5–10 Myr after subduction initiation (model 2) can be tied directly to the evolving slab-top temperature as subduction progresses. The changing slab-top temperature is indicated by the changing stable mineral assemblage responsible for characteristic trace element fractionations in the Izu-Bonin magmas over time. This is further corroborated by results from geodynamic models (Holt and Condit, 2021; Maunder et al., 2020) and thermal histories recorded by exhumed metamorphic rocks from paleo-subduction zones (Agard et al., 2020, 2018; Soret et al., 2022). Recent geodynamic models that are relevant to the Izu-Bonin subduction zone predicted a transient heating of the plate interface at a given depth during subduction initiation (t_o), attributed to upwelling of hot asthenospheric mantle (high-Φ in Fig. 3; (Holt and Condit, 2021; Maunder et al., 2020)). These models also revealed that with continued subduction, the slab-top becomes cooler at a given depth (intermediate Φ) until it reaches a cold-steady state (t_f), as represented by present-day slab-top geotherm (high-Φ in Fig. 3). Transient heating of the plate interface during subduction initiation would allow for immediate melting of discrete subducted materials in early Paleogene, consistent with previous geochemical studies (Ishizuka et al., 2020; Li et al., 2019). We argue that cooling of the plate interface 5–10 Myr after subduction initiation would promote more extensive mélange formation and subsequent melting in late Paleogene to present.

The timing of transition between the slab-to-mantle transfer mechanisms also coincides with observations from exhumed metamorphic rock records. The *P*-*T*-time paths of exhumed

metamorphic rocks in subduction zones record progressive cooling of the plate interface at 1.0 GPa from 700–900 °C to < 500 °C in the first ~5 Myr after subduction initiation (Agard et al., 2018; Soret et al., 2022). Since these rocks record slab-top peak *P-T* conditions, the rock record translates into a changing slab-top geotherms from >20 °C/km during subduction initiation to <10 °C/km at cold steady-state subduction. This change has been suggested to coincide with the predicted transition from a strong to a weakly coupled plate interface (Agard et al., 2018, 2016). Fluids released from metamorphic dehydration results in the formation of weak hydrous minerals (*e.g.*, serpentine, talc, and chlorite) and high pore-fluid pressure along the slab-mantle interface. The sharp contrast in the rheological properties of the interface and overriding mantle wedge allows for their decoupling (Agard et al., 2020; Furukawa, 1993; Wada and Wang, 2009), and we argue that this decoupled stage, in combination with intense metasomatism, is synchronous to mélange formation (Fig. 4). This is supported by extensive field observations on exhumed high-pressure mélange terranes (Bebout and Penniston-Dorland, 2016) where composite mixtures of discrete units of variably metamorphosed subducted materials (*e.g.,* metasediment, eclogite, metagabbro) are embedded within serpentinite and metasomatic chlorite-rich mélange matrices. Fast rates of fluid-mediated rock transformation are expected at high temperatures in water-rich environment such as the plate interface mélange (Bebout and Penniston-Dorland, 2016; Beinlich et al., 2020; Pogge von Strandmann et al., 2015). This would allow for an extensive metasomatism and attain isotopic homogenization of mélanges before they melt (Bebout and Barton, 2002; King et al., 2007, 2006). Field mapping campaigns have conservatively estimated thicknesses in the order of hundreds of meters in these exhumed terranes (Agard et al., 2018; Bebout and Barton, 2002; Bebout and Penniston-Dorland, 2016).

Viscous coupling of the plate interface and the overlying mantle downdip at the maximum depth of decoupling (MDD) allows for the advection of hot asthenospheric mantle which melts the newly-formed mélange rocks. At steady-state, the maximum depth of decoupling extends to a common depth of ~80 km in global subduction zones and is believed to coincide with the breakdown of serpentine (Wada and Wang, 2009) or talc (Peacock and Wang, 2021). The formation and high *P-T* stabilities of talc, chlorite, and serpentine along the slab-mantle interface allow for wider decoupled zones and therefore, more extensive mélange zones along the slab-tops of colder subduction zones. Even though more extensive dehydration is predicted in warmer slab-tops, these fluids can immediately induce melting of discrete subducted materials before extensive

mélange formation can take place. In contrast, fluids that are derived in situ or from deeper slab depths that migrate updip can favor more extensive mélange formation in colder slab-tops (Condit et al., 2020; van Keken et al., 2011).

Our results indicate that mélange melting may be more prevalent in mature arcs with cold slab-tops. To test this hypothesis, we examined subduction zones with variable ages based on subduction initiation (SI) estimates (Crameri et al., 2020) and slab-top temperature based on their present-day Φ values (Kirby et al., 1991; Syracuse et al., 2010). The compilation can be categorized into three groups, which include arc segments that are cold (high-Φ) and mature (SI > ~50 Myr ago) (*e.g.*, Kurile, Kamchatka, Marianas), warm (low-Φ) and mature (*e.g.*, Cascadia), and warm and young (SI < ~15 Myr ago) (*e.g.*, Philippines [along the Philippine Trench], Ryukyu) (Fig. 5; Supplementary Data 3). The Quaternary magmatism in Kurile, Kamchatka, Marianas arcs (cold) record mélange-style melting while Cascadia, Philippines, and Ryukyu (warm) are dominated by slab melting, similar to the first ~5 Myr of magmatism in the young and warm Izu-Bonin. In addition, the Tonga arc, which can be categorized as mature and cold, has previously been shown to follow the mélange-melting trend (Nielsen and Marschall, 2017). Age constraints for lavas from these subduction zones are not as readily available as for Izu-Bonin, but volcanics from Kurile and Mariana arcs also record the two distinct geochemical trends attesting to a transition in melting style after subduction initiation. Temporal variations in the slab dip due to subduction of asperities (*e.g.*, ridge or seamount) may cause changes in the slab-top temperature and the resulting geochemical trends of arc magmas. Albeit speculative, it is possible that the subduction of Western Pacific Seamount Province may have resulted to the cyclical trend in the Quaternary Mariana arc, where both sediment/AOC-melting and mélange-melting trends are observed (Fig. 5b). Alternatively, the thickness of the overriding crust has been suggested to control the compositional systematics of Izu-Bonin and other subduction zone magmas by modulating the amount of melting in the mantle wedge (Hochstaedter et al., 2001; Plank and Langmuir, 1988; Tollstrup et al., 2010; Turner et al., 2016; Turner and Langmuir, 2015). Estimates of present-day crustal thicknesses in Ryukyu (low-Φ) and Kamchatka (high-Φ) arcs are similar (~25 km thick). However, these arcs display distinctly different geochemical trends that are more consistent with the expectations based on their prevailing slab-top temperatures. Despite the second-order variations in the type and amount of subducting slab inputs, ambient mantle compositions, thickness of the overriding crust and degrees of mantle melting, rock types (*e.g.*,

calc-alkaline, tholeiite, boninite), and sample locations between subduction zones worldwide, fundamental trends emerge. Convergent margins with warmer slab-top temperatures generally plot on a sediment/AOC-melting trends, consistent with the first line of models (model 1) (Elliott et al., 1997; Kelemen et al., 2003; Kessel et al., 2005; Li Huijuan et al., 2022; Miller et al., 1994; Pearce, 1982; Schmidt and Jagoutz, 2017; Turner and Langmuir, 2022; Yogodzinski et al., 2015), while those arcs with colder slab-top temperatures lead to the development of a mélange-melting trend, consistent with the second line of models (model 2) (Codillo et al., 2018; Cruz-Uribe et al., 2018; Marschall and Schumacher, 2012; Nielsen and Marschall, 2017). The dichotomy between warm and cold arcs could reflect the wider decoupled zone expected in cold slabs, where mélange zones can form more extensively and contribute in the melting process more significantly (Fig. 4).

Main figures

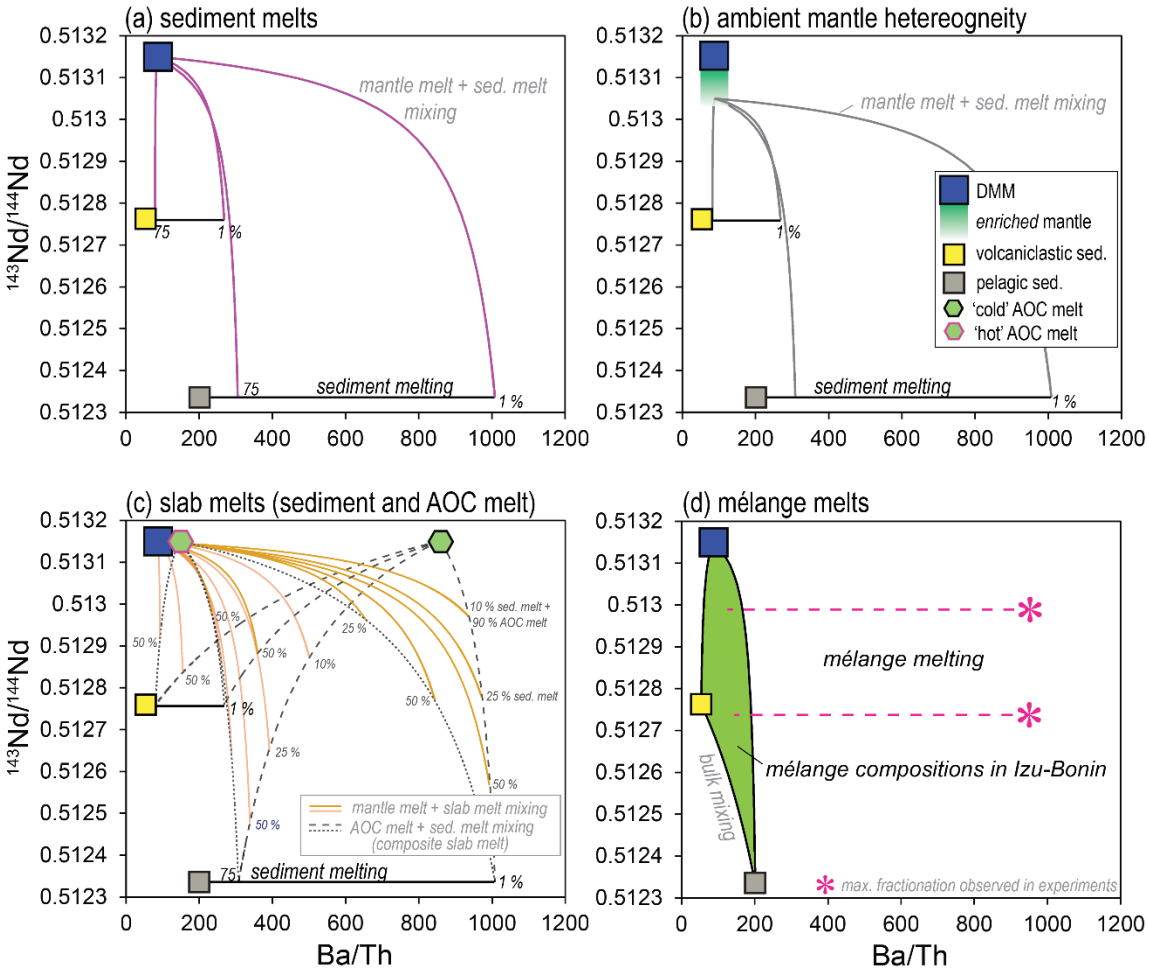

Fig. 1. Evaluation of the different models of slab-to-mantle transfer and arc magma formation based on the expected geochemical trends each of the models postulates in terms of Nd isotopes versus fluid-sensitive Ba/Th ratio space. (a) In the sediment-melting model, discrete sediment melts that are produced by variable degrees of melting in the slab mix with mantle melts in the wedge to produce arc magmas. Mixing between DMM (i.e. mantle melts, due to the lack fractionation during mantle melting) and sediment partial melts are predicted follow highly curved mixing trajectories (purple solid lines). (b) An illustration that shows that the presence isotopic heterogeneity in the ambient mantle does not change the curvature of the mixing lines. (c) In the slab-melting model, composite slab melts are first produced by mixing of partial melts from sediments and altered oceanic crust (AOC) at variable proportions. These composite slab melts

then mix with mantle melts to produce arc magmas with compositions that follow one or more of the possible mixing trajectories (yellow and peach solid lines). (d) In the mélange-melting model, bulk mixing of subducted sediment, AOC, and mantle components forms a new hybrid mélange with a set isotopic composition. Subsequent melting of mélange causes trace element fractionations without significant variations in the isotopic compositions (i.e. horizontal trends). The pink star symbol indicates the maximum fractionation observed in high *P*-*T* mélange melting experiments (Supplementary Fig. 8) which is taken as a minimum possible trace-element fractionation that can occur during mélange melting in nature. The length of the mélange melting trend points to the bulk mixing region. The starting endmember compositions of sediments, AOC, and the mantle, as well as the partition coefficients used in the melting calculations are available in the supplementary.

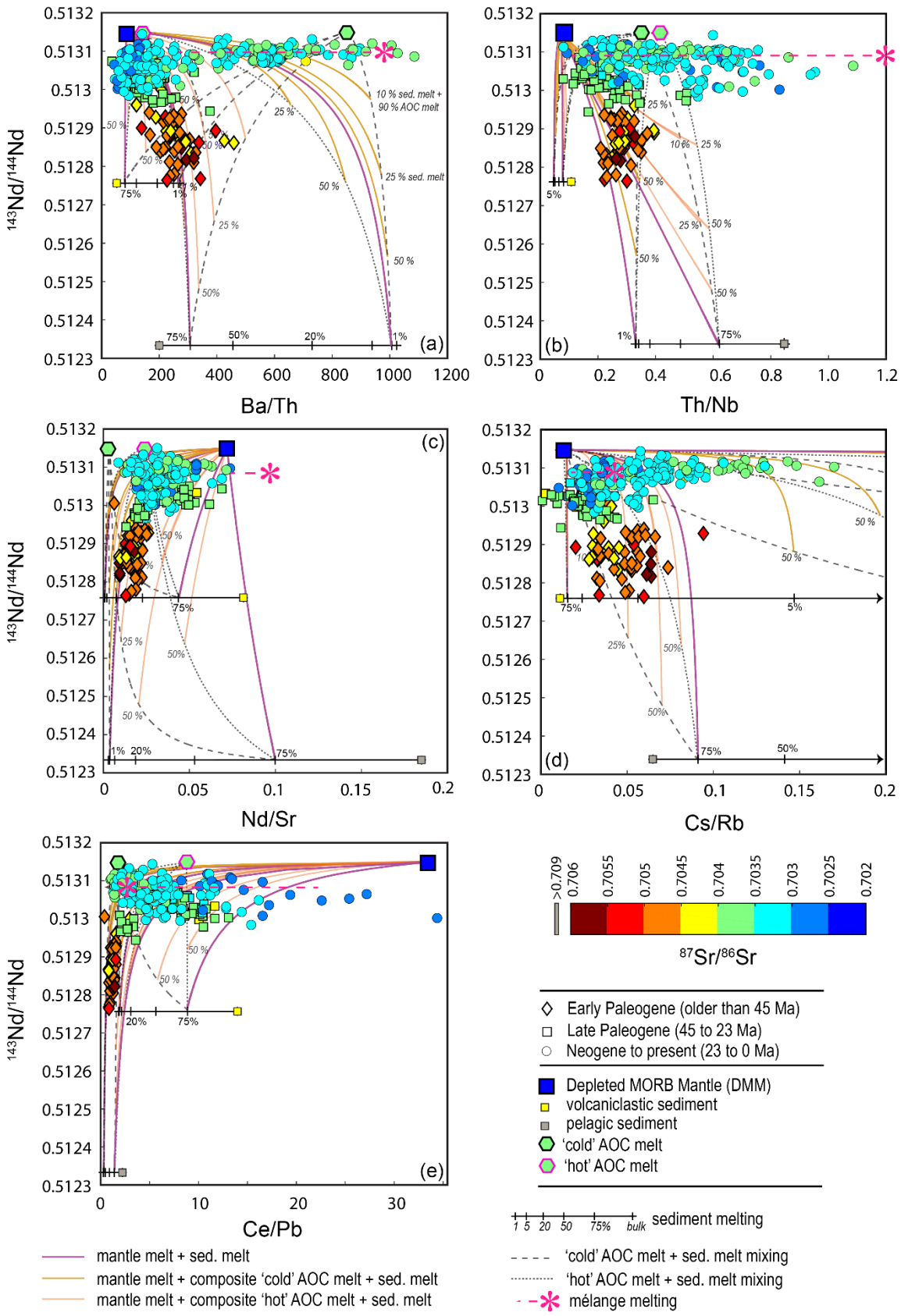
143Nd/144Nd
Ba/Th
Th/Nb
Nd/Sr
Cs/Rb
Ce/Pb
(a)
(b)
(c)
(d)
(e)
10 % sed. melt + 90 % AOC melt
25 % sed. melt
87Sr/86Sr
Early Paleogene (older than 45 Ma)
Late Paleogene (45 to 23 Ma)
Neogene to present (23 to 0 Ma)
Depleted MORB Mantle (DMM)
volcaniclastic sediment
pelagic sediment
'cold' AOC melt
'hot' AOC melt
sediment melting
mantle melt + sed. melt
mantle melt + composite 'cold' AOC melt + sed. melt
mantle melt + composite 'hot' AOC melt + sed. melt
'cold' AOC melt + sed. melt mixing
'hot' AOC melt + sed. melt mixing
mélange melting

Fig. 2. Nd isotopes versus fluid-sensitive (a, c, e) and fluid-insensitive (b, d, f) ratios in age-categorized Izu-Bonin arc volcanics (SiO_2 < 63 wt. %). The colors of arc lava symbols represent their Sr isotope compositions. Mixing lines are constructed between DMM either (i) sediment partial melts (purple bold lines) or (ii) composite slab melts (yellow and peach bold lines). The composite slab melts represent mixtures of sediment partial melts and globally representative ('cold' and 'hot') AOC melts. Mélange melting trend is shown, where the star symbol (in pink) indicates the maximum trace-element fractionation observed in high *P-T* mélange melting experiments (Supplementary Fig. 8) which is taken as a minimum possible trace-element fractionation that can occur during mélange melting in nature. The length of the mélange melting trend points to the bulk mixing region while the Nd isotope value corresponds to average value for Quaternary volcanics.

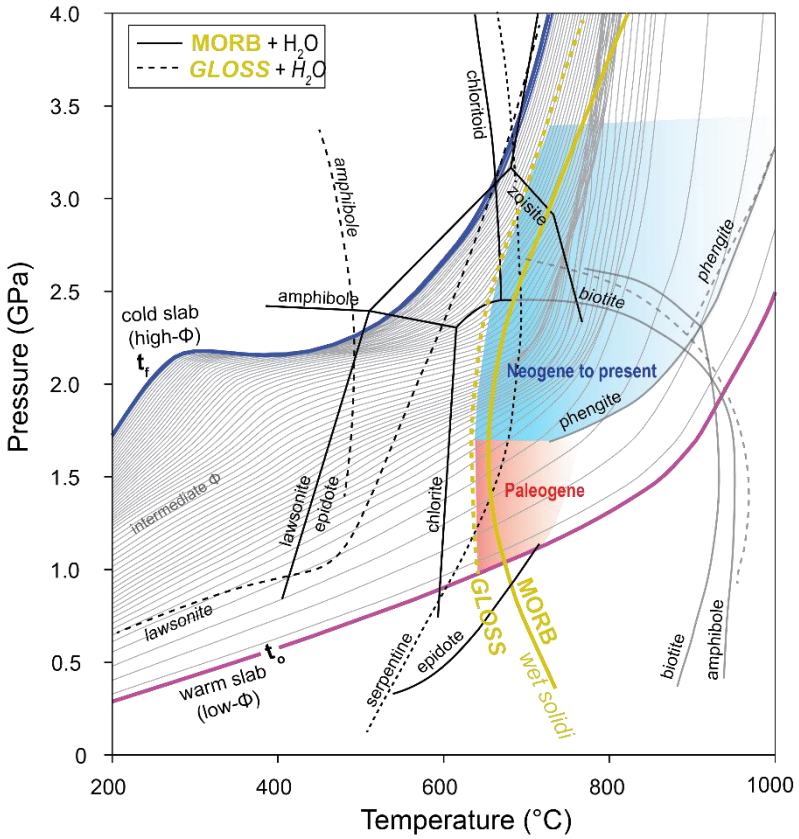

Fig. 3. Mineral-controlled trace-element fractionations indicate changing slab-top temperatures over time in the Izu-Bonin arc. (a) Published models on slab-top temperature evolution (Φ, (Holt and Condit, 2021)) , from warm subduction initiation (t_o; magenta line) to cold steady-state (t_f; blue line). The input parameters and conditions used to construct the geodynamic models are relevant to the physical conditions in the Izu-Bonin subduction zone. Superimposed are phase stabilities (Schmidt and Poli, 2014) of major silicate phases in the slab and water-saturated solidi for sediment (dashed lines) and basalt (solid lines), as well as water-undersaturated solidi corresponding to the dehydration of hydrous phases (thin pale gray lines). The shaded red and light blue colored regions indicate the likely *P-T* conditions where trace-element fractionations occurred as indicated by the mineral assemblage required to produce the fractionations.

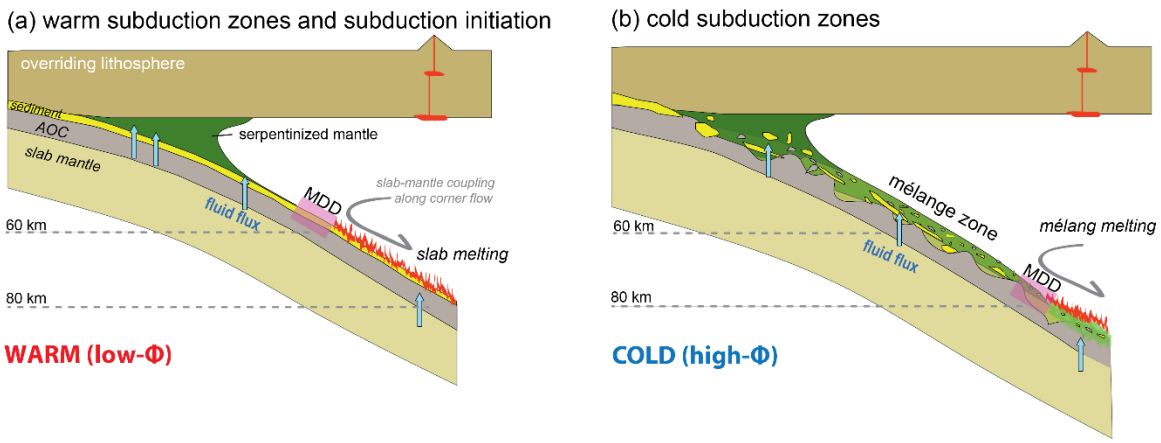

Fig. 4. Dichotomy between warm and cold subduction zones in the slab-to-mantle transfer mechanisms and primary sources. (a) After subduction initiation, hydrous melting of the hot slab-top predominates, where discrete additions of sediment and oceanic crust melts are added into the mantle wedge (model 1). (b) Progressive slab cooling, fluid-rock interactions, and deepening of the maximum decoupling depth (MDD) over time allows for a more extensive mélange zone at the slab-mantle interface. At cold steady-state, melting of slab-top mélange predominates, where mélange melts are added into the mantle wedge (model 2). Illustration not to scale.

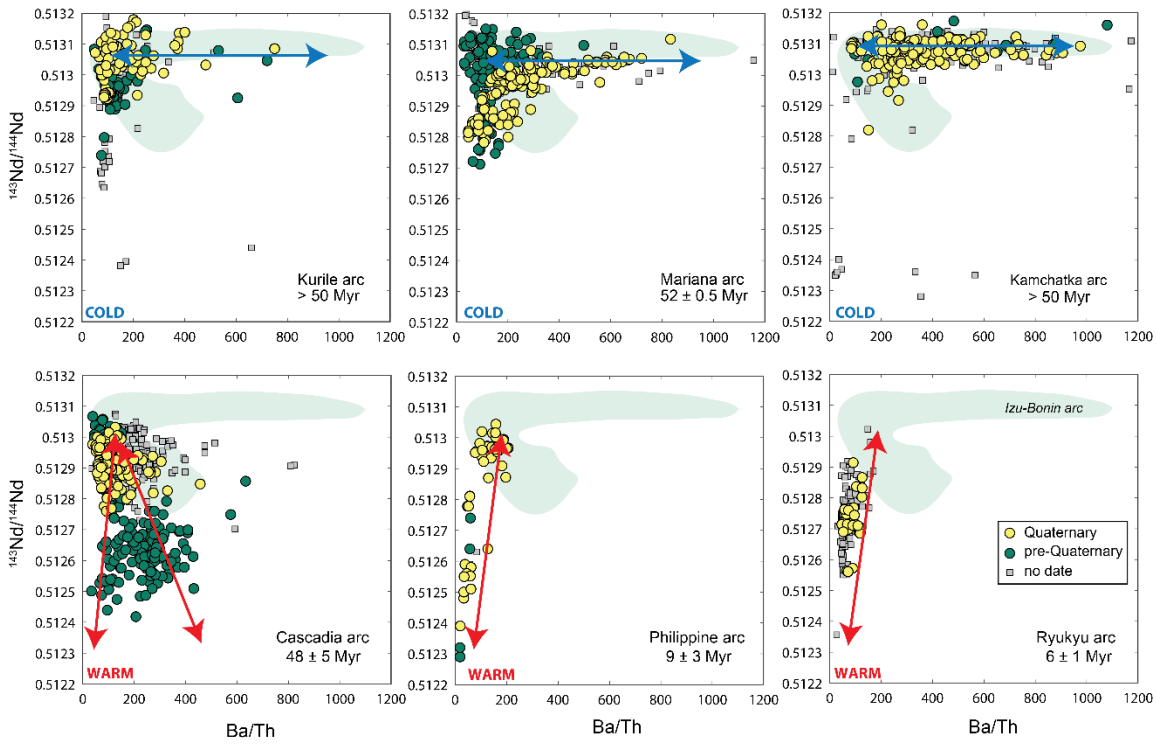

Fig. 5. Covariations in Nd isotopes and Ba/Th ratio of lavas (SiO_2 < 63 wt. %) from cold and mature (Kurile, Mariana, Kamchatka), warm and mature (Cascadia), and warm and young (Philippines [along Philippine trench], Ryukyu) arcs. For comparison, the shaded region is the Izu-Bonin arc rocks. Estimates for the timing of subduction initiation are also indicated. Blue double-arrows display mélange-melting trend (model 2) while red double-arrows display sediment/AOC-melting trend (model 1).

References

Agard, P., Plunder, A., Angiboust, S., Bonnet, G., Ruh, J., 2018. The subduction plate interface: rock record and mechanical coupling (from long to short timescales). Lithos 320–321, 537–566. https://doi.org/10.1016/j.lithos.2018.09.029

Agard, P., Prigent, C., Soret, M., Dubacq, B., Guillot, S., Deldicque, D., 2020. Slabitization: Mechanisms controlling subduction development and viscous coupling. Earth-Science Reviews 208, 103259. https://doi.org/10.1016/j.earscirev.2020.103259

Agard, P., Yamato, P., Soret, M., Prigent, C., Guillot, S., Plunder, A., Dubacq, B., Chauvet, A., Monié, P., 2016. Plate interface rheological switches during subduction infancy: Control on slab penetration and metamorphic sole formation. Earth and Planetary Science Letters 451, 208–220. https://doi.org/10.1016/j.epsl.2016.06.054

Arculus, R.J., Gill, J.B., Cambray, H., Chen, W., Stern, R.J., 1995. Geochemical Evolution of Arc Systems in the Western Pacific: The Ash and Turbidite Record Recovered by Drilling, in: Active Margins and Marginal Basins of the Western Pacific. American Geophysical Union (AGU), pp. 45–65. https://doi.org/10.1029/GM088p0045

Bebout, G.E., Barton, M.D., 2002. Tectonic and metasomatic mixing in a high-T, subduction-zone mélange—insights into the geochemical evolution of the slab–mantle interface. Chemical Geology 187, 79–106. https://doi.org/10.1016/S0009-2541 (02)00019-0

Bebout, G.E., Penniston-Dorland, S.C., 2016. Fluid and mass transfer at subduction interfaces—The field metamorphic record. Lithos 240–243, 228–258. https://doi.org/10.1016/j.lithos.2015.10.007

Beinlich, A., John, T., Vrijmoed, J.C., Tominaga, M., Magna, T., Podladchikov, Y.Y., 2020. Instantaneous rock transformations in the deep crust driven by reactive fluid flow. Nature Geoscience 13, 307–311. https://doi.org/10.1038/s41561-020-0554-9

Bryant, C.J., Arculus, R.J., Eggins, S.M., 2003. The geochemical evolution of the Izu-Bonin arc system: A perspective from tephras recovered by deep-sea drilling. Geochemistry, Geophysics, Geosystems 4. https://doi.org/10.1029/2002GC000427

Canfield, D.E., 2004. The evolution of the Earth surface sulfur reservoir. Am J Sci 304, 839. https://doi.org/10.2475/ajs.304.10.839

Carter, L.B., Skora, S., Blundy, J.D., De Hoog, J.C.M., Elliott, T., 2015. An Experimental Study of Trace Element Fluxes from Subducted Oceanic Crust. Journal of Petrology 56, 1585–1606. https://doi.org/10.1093/petrology/egv046

Castro, A., Gerya, T., García-Casco, A., Fernández, C., Díaz-Alvarado, J., Moreno-Ventas, I., Löw, I., 2010. Melting Relations of MORB–Sediment Mélanges in Underplated Mantle Wedge Plumes; Implications for the Origin of Cordilleran-type Batholiths. Journal of Petrology 51, 1267–1295. https://doi.org/10.1093/petrology/egq019

Castro, A., Gerya, T.V., 2008. Magmatic implications of mantle wedge plumes: Experimental study. Lithos 103, 138–148. https://doi.org/10.1016/j.lithos.2007.09.012

Codillo, E.A., Le Roux, V., Marschall, H.R., 2018. Arc-like magmas generated by mélange-peridotite interaction in the mantle wedge. Nature Communications 9, 2864. https://doi.org/10.1038/s41467-018-05313-2

Condit, C.B., Guevara, V.E., Delph, J.R., French, M.E., 2020. Slab dehydration in warm subduction zones at depths of episodic slip and tremor. Earth and Planetary Science Letters 552, 116601. https://doi.org/10.1016/j.epsl.2020.116601

Crameri, F., Magni, V., Domeier, M., Shephard, G.E., Chotalia, K., Cooper, G., Eakin, C.M., Grima, A.G., Gürer, D., Király, Á., Mulyukova, E., Peters, K., Robert, B., Thielmann, M., 2020. A transdisciplinary and community-driven database to unravel subduction zone initiation. Nature Communications 11, 3750. https://doi.org/10.1038/s41467-020-17522-9

Cruz-Uribe, A.M., Marschall, H.R., Gaetani, G.A., Le Roux, V., 2018. Generation of alkaline magmas in subduction zones by partial melting of mélange diapirs—An experimental study. Geology 46, 343–346. https://doi.org/10.1130/G39956.1

Durkin, K., Castillo, P.R., Straub, S.M., Abe, N., Tamura, Y., Yan, Q., 2020. An origin of the along-arc compositional variation in the Izu-Bonin arc system. Geoscience Frontiers 11, 1621–1634. https://doi.org/10.1016/j.gsf.2019.12.004

Ellam, R.M., Hawkesworth, C.J., 1988. Elemental and isotopic variations in subduction related basalts: evidence for a three component model. Contributions to Mineralogy and Petrology 98, 72–80. https://doi.org/10.1007/BF00371911

Elliott, T., Plank, T., Zindler, A., White, W., Bourdon, B., 1997. Element transport from slab to volcanic front at the Mariana arc. Journal of Geophysical Research: Solid Earth 102, 14991–15019. https://doi.org/10.1029/97JB00788

Freymuth, H., Ivko, B., Gill, J.B., Tamura, Y., Elliott, T., 2016. Thorium isotope evidence for melting of the mafic oceanic crust beneath the Izu arc. Geochimica et Cosmochimica Acta 186, 49–70. https://doi.org/10.1016/j.gca.2016.04.034

Furukawa, Y., 1993. Depth of the decoupling plate interface and thermal structure under arcs. Journal of Geophysical Research: Solid Earth 98, 20005–20013. https://doi.org/10.1029/93JB02020

Gale, A., Dalton, C.A., Langmuir, C.H., Su, Y., Schilling, J.-G., 2013. The mean composition of ocean ridge basalts. Geochemistry, Geophysics, Geosystems 14, 489–518. https://doi.org/10.1029/2012GC004334

Gerya, T.V., Yuen, D.A., 2003. Rayleigh–Taylor instabilities from hydration and melting propel 'cold plumes' at subduction zones. Earth and Planetary Science Letters 212, 47–62. https://doi.org/10.1016/S0012-821X (03)00265-6

Gill, J., 1981. Orogenic Andesites and Plate Tectonics, 1st ed. Springer Berlin, Heidelberg.

Hauff, F., Hoernle, K., Schmidt, A., 2003. Sr-Nd-Pb composition of Mesozoic Pacific oceanic crust (Site 1149 and 801, ODP Leg 185): Implications for alteration of ocean crust and the input into the Izu-Bonin-Mariana subduction system. Geochemistry, Geophysics, Geosystems 4. https://doi.org/10.1029/2002GC000421

Hawkesworth, C.J., Turner, S.P., McDermott, F., Peate, D.W., van Calsteren, P., 1997. U-Th Isotopes in Arc Magmas: Implications for Element Transfer from the Subducted Crust. Science 276, 551. https://doi.org/10.1126/science.276.5312.551

Hermann, J., Rubatto, D., 2009. Accessory phase control on the trace element signature of sediment melts in subduction zones. Chemical Geology 265, 512–526. https://doi.org/10.1016/j.chemgeo.2009.05.018

Hildreth, W., Moorbath, S., 1988. Crustal contributions to arc magmatism in the Andes of Central Chile. Contributions to Mineralogy and Petrology 98, 455–489. https://doi.org/10.1007/BF00372365

Hochstaedter, A., Gill, J., Peters, R., Broughton, P., Holden, P., Taylor, B., 2001. Across-arc geochemical trends in the Izu-Bonin arc: Contributions from the subducting slab. Geochemistry, Geophysics, Geosystems 2. https://doi.org/10.1029/2000GC000105

Holt, A.F., Condit, C.B., 2021. Slab Temperature Evolution Over the Lifetime of a Subduction Zone. Geochemistry, Geophysics, Geosystems 22, e2020GC009476. https://doi.org/10.1029/2020GC009476

Ishizuka, O., Kimura, J.-I., Li, Y.B., Stern, R.J., Reagan, M.K., Taylor, R.N., Ohara, Y., Bloomer, S.H., Ishii, T., Hargrove, U.S., Haraguchi, S., 2006. Early stages in the evolution of Izu–Bonin arc volcanism: New age, chemical, and isotopic constraints. Earth and Planetary Science Letters 250, 385–401. https://doi.org/10.1016/j.epsl.2006.08.007

Ishizuka, O., Taylor, R.N., Umino, S., Kanayama, K., 2020. Geochemical Evolution of Arc and Slab Following Subduction Initiation: a Record from the Bonin Islands, Japan. Journal of Petrology 61. https://doi.org/10.1093/petrology/egaa050

Ishizuka, O., Taylor, R.N., Yuasa, M., Milton, J.A., Nesbitt, R.W., Uto, K., Sakamoto, I., 2007. Processes controlling along-arc isotopic variation of the southern Izu-Bonin arc. Geochemistry, Geophysics, Geosystems 8. https://doi.org/10.1029/2006GC001475

Kawamoto Tatsuhiko, Kanzaki Masami, Mibe Kenji, Matsukage Kyoko N., Ono Shigeaki, 2012. Separation of supercritical slab-fluids to form aqueous fluid and melt components in subduction zone magmatism. Proceedings of the National Academy of Sciences 109, 18695–18700. https://doi.org/10.1073/pnas.1207687109

Kay, R.W., 1980. Volcanic Arc Magmas: Implications of a Melting-Mixing Model for Element Recycling in the Crust-Upper Mantle System. The Journal of Geology 88, 497–522. https://doi.org/10.1086/628541

Kelemen, P., Yogodzinski, G., Scholl, D., 2003. Along-strike variation in the Aleutian Island Arc: Genesis of high Mg# andesite and implications for continental crust. Geophysical Monograph Series 138, 223–276. https://doi.org/10.1029/138GM11

Kelley, K.A., Plank, T., Ludden, J., Staudigel, H., 2003. Composition of altered oceanic crust at ODP Sites 801 and 1149. Geochemistry, Geophysics, Geosystems 4. https://doi.org/10.1029/2002GC000435

Keppler, H., 1996. Constraints from partitioning experiments on the composition of subduction-zone fluids. Nature 380, 237–240. https://doi.org/10.1038/380237a0

Kessel, R., Schmidt, M.W., Ulmer, P., Pettke, T., 2005. Trace element signature of subduction-zone fluids, melts and supercritical liquids at 120–180 km depth. Nature 437, 724–727. https://doi.org/10.1038/nature03971

King, R.L., Bebout, G.E., Grove, M., Moriguti, T., Nakamura, E., 2007. Boron and lead isotope signatures of subduction-zone mélange formation: Hybridization and fractionation along the slab–mantle interface beneath volcanic arcs. Chemical Geology 239, 305–322. https://doi.org/10.1016/j.chemgeo.2007.01.009

King, R.L., Bebout, G.E., Moriguti, T., Nakamura, E., 2006. Elemental mixing systematics and Sr–Nd isotope geochemistry of mélange formation: Obstacles to identification of fluid sources to arc volcanics. Earth and Planetary Science Letters 246, 288–304. https://doi.org/10.1016/j.epsl.2006.03.053

Kirby, S.H., Durham, W.B., Stern, L.A., 1991. Mantle Phase Changes and Deep-Earthquake Faulting in Subducting Lithosphere. Science 252, 216–225. https://doi.org/10.1126/science.252.5003.216

Klaver, M., Lewis, J., Parkinson, I.J., Elburg, M.A., Vroon, P.Z., Kelley, K.A., Elliott, T., 2020. Sr isotopes in arcs revisited: tracking slab dehydration using δ88/86Sr and 87Sr/86Sr systematics of arc lavas. Geochimica et Cosmochimica Acta 288, 101–119. https://doi.org/10.1016/j.gca.2020.08.010

Klimm, K., Blundy, J.D., Green, T.H., 2008. Trace Element Partitioning and Accessory Phase Saturation during H2O-Saturated Melting of Basalt with Implications for Subduction Zone Chemical Fluxes. Journal of Petrology 49, 523–553. https://doi.org/10.1093/petrology/egn001

Le Voyer, M., Hauri, E.H., Cottrell, E., Kelley, K.A., Salters, V.J.M., Langmuir, C.H., Hilton, D.R., Barry, P.H., Füri, E., 2019. Carbon Fluxes and Primary Magma CO2 Contents Along the Global Mid-Ocean Ridge System. Geochemistry, Geophysics, Geosystems 20, 1387–1424. https://doi.org/10.1029/2018GC007630

Li Huijuan, Hermann Joerg, Zhang Lifei, 2022. Melting of subducted slab dictates trace element recycling in global arcs. Science Advances 8, eabh2166. https://doi.org/10.1126/sciadv.abh2166

Li, H.-Y., Li, X., Ryan, J.G., Zhang, C., Xu, Y.-G., 2022. Boron isotopes in boninites document rapid changes in slab inputs during subduction initiation. Nature Communications 13, 993. https://doi.org/10.1038/s41467-022-28637-6

Li, H.-Y., Taylor, R.N., Prytulak, J., Kirchenbaur, M., Shervais, J.W., Ryan, J.G., Godard, M., Reagan, M.K., Pearce, J.A., 2019. Radiogenic isotopes document the start of subduction in

the Western Pacific. Earth and Planetary Science Letters 518, 197–210. https://doi.org/10.1016/j.epsl.2019.04.041

Manning, C.E., 2004. The chemistry of subduction-zone fluids. Earth and Planetary Science Letters 223, 1–16. https://doi.org/10.1016/j.epsl.2004.04.030

Marschall, H.R., Schumacher, J.C., 2012. Arc magmas sourced from mélange diapirs in subduction zones. Nature Geosci 5, 862–867. https://doi.org/10.1038/ngeo1634

Maunder, B., Prytulak, J., Goes, S., Reagan, M., 2020. Rapid subduction initiation and magmatism in the Western Pacific driven by internal vertical forces. Nature Communications 11, 1874. https://doi.org/10.1038/s41467-020-15737-4

McCulloch, M.T., Gregory, R.T., Wasserburg, G.J., Taylor, H.P., 1980. A neodymium, strontium, and oxygen isotopic study of the Cretaceous Samail ophiolite and implications for the petrogenesis and seawater-hydrothermal alteration of oceanic crust. Earth and Planetary Science Letters 46, 201–211. https://doi.org/10.1016/0012-821X (80)90006-0

Mibe, K., Kanzaki, M., Kawamoto, T., Matsukage, K.N., Fei, Y., Ono, S., 2007. Second critical endpoint in the peridotite-H2O system. Journal of Geophysical Research: Solid Earth 112. https://doi.org/10.1029/2005JB004125

Miller, D.M., Goldstein, S.L., Langmuir, C.H., 1994. Cerium/lead and lead isotope ratios in arc magmas and the enrichment of lead in the continents. Nature 368, 514–520. https://doi.org/10.1038/368514a0

Nielsen, S.G., Marschall, H.R., 2017. Geochemical evidence for mélange melting in global arcs. Sci Adv 3. https://doi.org/10.1126/sciadv.1602402

Parolari, M., Gómez-Tuena, A., Errázuriz-Henao, C., Cavazos-Tovar, J.G., 2021. Orogenic andesites and their link to the continental rock cycle. Lithos 382–383, 105958. https://doi.org/10.1016/j.lithos.2020.105958

Peacock, S.M., Wang, K., 2021. On the Stability of Talc in Subduction Zones: A Possible Control on the Maximum Depth of Decoupling Between the Subducting Plate and Mantle Wedge. Geophysical Research Letters 48, e2021GL094889. https://doi.org/10.1029/2021GL094889

Pearce, J., 1982. Trace Element Characteristics of Lavas from Destructive Plate Boundaries, in: Andesites: Orogenic Andesites and Related Rocks. John Wiley and Sons.

Plank, T., Kelley, K.A., Murray, R.W., Stern, L.Q., 2007. Chemical composition of sediments subducting at the Izu-Bonin trench. Geochemistry, Geophysics, Geosystems 8. https://doi.org/10.1029/2006GC001444

Plank, T., Langmuir, C.H., 1988. An evaluation of the global variations in the major element chemistry of arc basalts. Earth and Planetary Science Letters 90, 349–370. https://doi.org/10.1016/0012-821X (88)90135-5

Pogge von Strandmann, P.A.E., Dohmen, R., Marschall, H.R., Schumacher, J.C., Elliott, T., 2015. Extreme Magnesium Isotope Fractionation at Outcrop Scale Records the Mechanism and Rate at which Reaction Fronts Advance. Journal of Petrology 56, 33–58. https://doi.org/10.1093/petrology/egu070

Reagan, M.K., Ishizuka, O., Stern, R.J., Kelley, K.A., Ohara, Y., Blichert-Toft, J., Bloomer, S.H., Cash, J., Fryer, P., Hanan, B.B., Hickey-Vargas, R., Ishii, T., Kimura, J.-I., Peate, D.W., Rowe, M.C., Woods, M., 2010. Fore-arc basalts and subduction initiation in the Izu-Bonin-Mariana system. Geochemistry, Geophysics, Geosystems 11. https://doi.org/10.1029/2009GC002871

Ryerson, F.J., Watson, E.B., 1987. Rutile saturation in magmas: implications for TiNbTa depletion in island-arc basalts. Earth and Planetary Science Letters 86, 225–239. https://doi.org/10.1016/0012-821X (87)90223-8

Salters, V.J.M., Stracke, A., 2004. Composition of the depleted mantle. Geochemistry, Geophysics, Geosystems 5. https://doi.org/10.1029/2003GC000597

Schmidt, M.W., Jagoutz, O., 2017. The global systematics of primitive arc melts. Geochemistry, Geophysics, Geosystems 18, 2817–2854. https://doi.org/10.1002/2016GC006699

Schmidt, M.W., Poli, S., 2014. 4.19 - Devolatilization During Subduction, in: Treatise on Geochemistry: Second Edition. pp. 669–701. https://doi.org/10.1016/B978-0-08-095975-7.00321-1

Schmidt, M.W., Vielzeuf, D., Auzanneau, E., 2004. Melting and dissolution of subducting crust at high pressures: the key role of white mica. Earth and Planetary Science Letters 228, 65–84. https://doi.org/10.1016/j.epsl.2004.09.020

Soret, M., Bonnet, G., Agard, P., Larson, K.P., Cottle, J.M., Dubacq, B., Kylander-Clark, A.R.C., Button, M., Rividi, N., 2022. Timescales of subduction initiation and evolution of

subduction thermal regimes. Earth and Planetary Science Letters 584, 117521. https://doi.org/10.1016/j.epsl.2022.117521

Stern, B., Fouch, M., Klemperer, S., 2003. An overview of the Izu-Bonin-Mariana subduction factory. Washington DC American Geophysical Union Geophysical Monograph Series 138, 175–222. https://doi.org/10.1029/138GM10

Stern, R., Bloomer, S., 1992. Subduction zone infancy: Examples from the Eocene Izu-Bonin-Mariana and Jurassic California arcs. GSA Bulletin 104, 1621–1636. https://doi.org/10.1130/0016-7606 (1992)104<1621:SZIEFT>2.3.CO;2

Straub, S.M., 2008. Uniform processes of melt differentiation in the central Izu Bonin volcanic arc (NW Pacific). Geological Society, London, Special Publications 304, 261. https://doi.org/10.1144/SP304.13

Straub, S.M., 2003. The evolution of the Izu Bonin - Mariana volcanic arcs (NW Pacific) in terms of major element chemistry. Geochemistry, Geophysics, Geosystems 4. https://doi.org/10.1029/2002GC000357

Straub, S.M., Goldstein, S.L., Class, C., Schmidt, A., Gomez-Tuena, A., 2010. Slab and Mantle Controls on the Sr–Nd–Pb–Hf Isotope Evolution of the Post 42 Ma Izu–Bonin Volcanic Arc. Journal of Petrology 51, 993–1026. https://doi.org/10.1093/petrology/egq009

Straub, S.M., Gómez-Tuena, A., Vannucchi, P., 2020. Subduction erosion and arc volcanism. Nature Reviews Earth & Environment 1, 574–589. https://doi.org/10.1038/s43017-020-0095-1

Straub, S.M., Woodhead, J.D., Arculus, R.J., 2015. Temporal Evolution of the Mariana Arc: Mantle Wedge and Subducted Slab Controls Revealed with a Tephra Perspective. Journal of Petrology 56, 409–439. https://doi.org/10.1093/petrology/egv005

Syracuse, E.M., van Keken, P.E., Abers, G.A., 2010. The global range of subduction zone thermal models. Physics of the Earth and Planetary Interiors 183, 73–90. https://doi.org/10.1016/j.pepi.2010.02.004

Tamura, Y., Gill, J.B., Tollstrup, D., Kawabata, H., Shukuno, H., Chang, Q., Miyazaki, T., Takahashi, T., Hirahara, Y., Kodaira, S., Ishizuka, O., Suzuki, T., Kido, Y., Fiske, R.S., Tatsumi, Y., 2009. Silicic Magmas in the Izu–Bonin Oceanic Arc and Implications for Crustal Evolution. Journal of Petrology 50, 685–723. https://doi.org/10.1093/petrology/egp017

Tamura, Y., Tani, K., Chang, Q., Shukuno, H., Kawabata, H., Ishizuka, O., Fiske, R.S., 2007. Wet and Dry Basalt Magma Evolution at Torishima Volcano, Izu–Bonin Arc, Japan: the Possible Role of Phengite in the Downgoing Slab. Journal of Petrology 48, 1999–2031. https://doi.org/10.1093/petrology/egm048

Taylor, R.N., Lapierre, H., Vidal, P., Nesbitt, R.W., Croudace, I.W., 1992. Igneous geochemistry and petrogenesis of the Izu-Bonin forearc basin.

Taylor, R.N., Nesbitt, R.W., 1998. Isotopic characteristics of subduction fluids in an intra-oceanic setting, Izu–Bonin Arc, Japan. Earth and Planetary Science Letters 164, 79–98. https://doi.org/10.1016/S0012-821X (98)00182-4

Taylor, R.N., Nesbitt, R.W., Vidal, P., Harmon, R.S., Auvray, B., Croudace, I.W., 1994. Mineralogy, Chemistry, and Genesis of the Boninite Series Volcanics, Chichijima, Bonin Islands, Japan. Journal of Petrology 35, 577–617. https://doi.org/10.1093/petrology/35.3.577

Tollstrup, D., Gill, J., Kent, A., Prinkey, D., Williams, R., Tamura, Y., Ishizuka, O., 2010. Across-arc geochemical trends in the Izu-Bonin arc: Contributions from the subducting slab, revisited. Geochemistry, Geophysics, Geosystems 11. https://doi.org/10.1029/2009GC002847

Turner, S., Hawkesworth, C., Rogers, N., Bartlett, J., Worthington, T., Hergt, J., Pearce, J., Smith, I., 1997. 238U□230Th disequilibria, magma petrogenesis, and flux rates beneath the depleted Tonga-Kermadec island arc. Geochimica et Cosmochimica Acta 61, 4855–4884. https://doi.org/10.1016/S0016-7037 (97)00281-0

Turner, S.J., Langmuir, C.H., 2022. Sediment and ocean crust both melt at subduction zones. Earth and Planetary Science Letters 584, 117424. https://doi.org/10.1016/j.epsl.2022.117424

Turner, S.J., Langmuir, C.H., 2015. The global chemical systematics of arc front stratovolcanoes: Evaluating the role of crustal processes. Earth and Planetary Science Letters 422, 182–193. https://doi.org/10.1016/j.epsl.2015.03.056

Turner, S.J., Langmuir, C.H., Dungan, M.A., Escrig, S., 2017. The importance of mantle wedge heterogeneity to subduction zone magmatism and the origin of EM1. Earth and Planetary Science Letters 472, 216–228. https://doi.org/10.1016/j.epsl.2017.04.051

Turner, S.J., Langmuir, C.H., Katz, R.F., Dungan, M.A., Escrig, S., 2016. Parental arc magma compositions dominantly controlled by mantle-wedge thermal structure. Nature Geoscience 9, 772–776. https://doi.org/10.1038/ngeo2788

van Keken, P.E., Hacker, B.R., Syracuse, E.M., Abers, G.A., 2011. Subduction factory: 4. Depth-dependent flux of H2O from subducting slabs worldwide. Journal of Geophysical Research: Solid Earth 116. https://doi.org/10.1029/2010JB007922

Wada, I., Wang, K., 2009. Common depth of slab-mantle decoupling: Reconciling diversity and uniformity of subduction zones. Geochemistry, Geophysics, Geosystems 10. https://doi.org/10.1029/2009GC002570

Wyllie, P.J., Ryabchikov, I.D., 2000. Volatile Components, Magmas, and Critical Fluids in Upwelling Mantle. Journal of Petrology 41, 1195–1206. https://doi.org/10.1093/petrology/41.7.1195

Yogodzinski, G.M., Brown, S.T., Kelemen, P.B., Vervoort, J.D., Portnyagin, M., Sims, K.W.W., Hoernle, K., Jicha, B.R., Werner, R., 2015. The Role of Subducted Basalt in the Source of Island Arc Magmas: Evidence from Seafloor Lavas of the Western Aleutians. Journal of Petrology 56, 441–492. https://doi.org/10.1093/petrology/egv006

Zack, T., Foley, S.F., Rivers, T., 2002. Equilibrium and Disequilibrium Trace Element Partitioning in Hydrous Eclogites (Trescolmen, Central Alps). Journal of Petrology 43, 1947–1974. https://doi.org/10.1093/petrology/43.10.1947

Chapter 7

Conclusions and future research directions

This thesis highlights (i) the dynamic connection between mechanical mixing of different lithologies and fluid-rock interaction processes along the slab-mantle interface in subduction zones, (ii) how these processes modify the petrophysical, geochemical, and redox properties of subducted materials, and (iii) how these processes collectively affect the mechanisms of slab-to-mantle transfer, cycling of elements and volatiles, and the formation of arc magmas. In this thesis, I have integrated constraints from petrology and experimental petrology, elemental and isotope geochemistry, mineral chemistry, and thermodynamic phase equilibrium and reaction-path models to address a diverse but interrelated set of questions. Here, I briefly summarize the main conclusions of each chapter and outline future research directions.

In Chapters 2 and 3, I investigated fluid-mediated reactions at depths relevant to subduction zones. In Chapter 2, I integrated constraints from petrology, geochemistry, and thermodynamic phase equilibrium and reaction-path models to determine when, where, and how the mass transfer occurred between juxtaposed serpentinite and eclogitic metagabbro exposed in the high-pressure Voltri Massif (Italy). I have shown that while the precursor serpentinite and oxide gabbro formed and were likely already in contact in an oceanic setting, the metasomatic reaction zones formed by diffusional Mg-metasomatism between the two rocks from prograde to peak, to retrograde metamorphic conditions in a subduction zone. The results imply that the studied serpentinite-metagabbro can be used as a natural laboratory to understand the processes that can occur when mafic and ultramafic rocks are juxtaposed in water-rich environments, such as along the slab-mantle interface. In particular, we can use the studied transect to understand the consequences of diffusional mass transfer between the two juxtaposed rock types on the mobility and fate of volatiles and fluid-mobile elements (*e.g.*, sulfur and boron) as well as on the potential to fractionate stable isotopes by kinetic processes (*e.g.*, Mg and Li isotopes).

The formation and distribution of talc affect the volatile budget, rheological properties, and the down-dip limit of the decoupling of the slab-mantle interface in subduction zones. In Chapter

3, I evaluated the conditions that control talc formation by Si-metasomatism of ultramafic rocks by slab-derived fluids using thermodynamic reaction-path models. In addition to taking the *P* and *T* conditions into account, the presented reaction path models evaluate how rock and fluid compositions can favor or limit talc formation. My model results showed that, contrary to common belief, talc is unlikely to form in high abundance in ultramafic rocks metasomatized by Si-rich slab-derived fluids. This means that talc-rich assemblages formed via Si-metasomatism along the slab-mantle interface are less likely to be playing prominent roles in processes, such as in volatile transport, in facilitating slow-slip events, and in controlling the decoupling-coupling transition of the plate interface. Rather, my models predicted the ubiquitous formation of chlorite along with other silicate minerals during Si-metasomatism due to the competing effects from other dissolved components that favor their formation over talc. However, the common co-occurrence of talc and carbonate minerals in fault zones suggest that other mechanisms such as mineral carbonation may be responsible for the formation of sizeable talc deposits in subduction zones. Future work should, therefore, evaluate talc formation by carbonation of ultramafic rocks at subduction zone conditions.

One important aspect of fluid-rock interaction is the influence of oxygen fugacity (fO_2), which is a measure of the potential for multivalent elements (*e.g.*, iron, carbon, and sulfur) to gain or lose electrons through reaction with oxygen (Evans, 2012; Gaetani, 2016). Knowledge on the fO_2 of a mineral assemblage can, for example, help constrain the speciation of redox-sensitive elements dissolved in a transient aqueous fluid that once coexisted and equilibrated with that mineral assemblage. However, the lack of thermodynamic data for solid solutions of Mg-Fe minerals at high *P*, most notably for serpentine, garnet, amphibole, and mica, prevents us from accurately predicting fO_2 variations during the metasomatism of ultramafic rocks by slab-derived fluids. Future work should involve the acquisition of new thermodynamic data from experiments to supplement the current database to improve our ability to model fO_2.

The previous chapters highlight the importance and implications of fluid-rock interactions at the slab-mantle interface and in the mantle wedge for the chemical, petrophysical, and redox characteristics of different subducted materials. In addition to *P*-*T* conditions, fluid-rock interactions determine the stable mineral assemblage that host volatiles and trace-elements at

depths. For example, the formation of metasomatic rocks by fluid-rock interactions may be associated with fractionations of certain trace-elements pairs (e.g., Th/Nb, Zr/Sm) that otherwise would behave similarly during mantle melting process. In this scenario, elemental fractionations occur by changing the effective bulk composition (under isothermal and isobaric condition) directly affecting the stability of host minerals (*e.g*., rutile, zircon). In addition, fluid-rock interactions can also fractionate trace-elements that constitute parent-daughter isotope pairs. For instance, the decrease in Sm/Nd and Rb/Sr ratios, and the increase in Lu/Hf ratio in metasomatic rocks in Voltri (Chapter 2) relative to their precursor may lead to their time-integrated evolution to less radiogenic Nd and Sr isotopes, and more radiogenic Hf isotope compositions in the mantle. These isotopically distinct reservoirs can reside in the mantle and may even be sampled and recorded in the erupted mantle-derived magmas.

As shown in Chapters 2 and 3, metasomatic rocks are compositionally unique rock-types distinct from their protoliths. Geodynamic models predict the potential for these mechanically weak, hydrous, and buoyant metasomatic rocks to be entrained from the slab-top into the overlying mantle via rising mélange diapirs. However, whether diapirs can form is tightly linked to the phase equilibria, melting, and density evolution of slab-top mélange.

In Chapter 4, I experimentally investigated the phase equilibria, melting, and density on three natural mélange rocks and showed that melting of mélange along the slab-top is unlikely at pressures below 2.5 GPa even in warm subduction zones. Under experimental conditions, the subsolidus assemblages of the mélanges are dominated by hydrous minerals such as chlorite, talc and amphibole, which are more buoyant than the overlying peridotite mantle. Because of the inverted thermal gradient of the mantle wedge, mélange melting is expected during ascent. However, the low-viscosity of hydrous mélange melts would allow for a near-instantaneous melt extraction which could densify the solid residues and arrest further ascent. Future work is needed to better understand the fates of hydrous mélange melts from the slab-top or from a rising diapir as they enter the mantle wedge. Additional work is also needed to improve our understanding of the stability of trace-element rich minor and accessory minerals on a variety of mélange compositions.

One important aspect of Chapter 4 is the comparison between the experiments and theoretical predictions based on thermodynamic models done using Perple_X. I have shown that Perple_X models generally reproduce the phase assemblage and proportions of subsolidus mélange at low-pressure conditions. However, the discrepancy between experiments and models magnify at higher pressures and at temperature conditions above the solidus. Theoretical models underpredict the solidus temperature and overpredict the melt fraction relative to the experimental data. This discrepancy is exacerbated in mélange compositions with high initial water contents. This highlights the need to perform additional experiments at higher pressures (>1.5 GPa) and on a diverse set of bulk-rock and volatile compositions, beyond the canonical basalt, pelite, or peridotite compositions, to improve the predictive power of thermodynamic models.

Aided by their buoyancy, subsolidus mélange diapirs can detach from the slab-top and migrate into the overlying mantle, and transfer their compositional signatures to the source region of arc magmas. However, the compositions of melts that would result from the interaction of mélange rocks with the peridotite mantle wedge remain unknown. In Chapter 5, I experimentally investigated the compositions of melts and mineral residues from melting of a mantle wedge hybridized with limited amounts of mélange rocks to simulate an end-member scenario where solid mélange diapirs dynamically interact with the mantle wedge. The results showed that melting of a mantle hybridized by small volume proportions of mélange can produce melts that carry the major, trace, and the fractionated trace-element characteristics of arc magmas. This finding has implications for detecting such dynamic features in the mantle wedge through geophysical techniques. For example, recent seismic studies in Taiwan have already hinted at the likelihood of rising diapirs away from the Ryukyu slab-top (Lin et al., 2019, 2021). Future work should focus on finding evidence, both geophysical and petrologically, for the existence of diapirs traversing through the mantle wedge.

In Chapter 6, I presented new interpretations on the evolution of slab-to-mantle transfer mechanisms from subduction initiation to arc maturity. Analyses of arc magma compositions reveal that mélange melting plays an increasingly important role in arc magma formation as slab-tops cool and arcs mature. This trend is attributed to the deepening of the decoupled plate interface during subduction where mélange zones can form more extensively and contribute to the melting process more significantly. However, whether melting of mélange occurs along the slab-mantle

interface or in a buoyant diapirs remains unknown. Future work should integrate geochemical results, laboratory experiments from Chapters 4 and 5, along with geodynamic models to resolve where and when mélange melting occur in subduction zones worldwide.

As much as providing new and novel insights to the current understanding of the geodynamics of subduction zones, this thesis has also forwarded new research questions to light. While this thesis investigated outstanding questions associated with a continuum of interrelated mass transfer and chemical interactions at depths relevant to the forearc and subarc regions of subduction zones, how these processes manifest beyond this depth and influence the geodynamics of the Earth's interior remain unknown. In that sense, the quest for developing new tools and approaches to continue brushing **colors** on this expansive black box continues.

Reference

Evans, K.A., 2012. The redox budget of subduction zones. Earth-Science Reviews 113, 11–32. https://doi.org/10.1016/j.earscirev.2012.03.003

Gaetani, G.A., 2016. The behavior of Fe3+/∑Fe during partial melting of spinel lherzolite. Geochimica et Cosmochimica Acta 185, 64–77. https://doi.org/10.1016/j.gca.2016.03.019

Lin, C., Shih, M., Lai, Y., 2019. A Strong Seismic Reflector within the Mantle Wedge above the Ryukyu Subduction of Northern Taiwan. Seismological Research Letters 91, 310–316. https://doi.org/10.1785/0220190174

Lin, C.-H., Shih, M.-H., Lai, Y.-C., 2021. Mantle wedge diapirs detected by a dense seismic array in Northern Taiwan. Sci Rep 11, 1561–1561. https://doi.org/10.1038/s41598-021-81357-7

Supplementary materials

Supplementary materials for Chapter 2

Methods

Mineralogy, geochemistry, and petrophysical properties

Samples were inspected in transmitted and reflected light using a Zeiss AxioImager 2 microscope, with mineral identification complemented by scanning electron microscopy, confocal Raman spectroscopy, and electron microprobe analyses (EPMA). Bulk-rock LOI translates to bulk H_2O from TG-DSC measurements (Figure S2-S3; Supplementary Table).

Analyses were performed at Woods Hole Oceanographic Institution (Woods Hole, MA) unless noted otherwise. Raman spectroscopy was carried out using a Horiba LabRam HR confocal Raman microscopy system. Analyses were conducted using a 100x objective with a numerical aperture of 0.9, a blue laser with a wavelength of 473 nm, and a 100 µm confocal hole diameter. The lateral spatial resolution was approximately 1 µm. We chose a grating with 600 grooves per mm and a slit size of 100 µm for most analyses. Raman spectra were collected between 100–2200 cm^{-1} (5 s and five accumulations for most analyses) for most silicate phases, and 3500–3800 cm^{-1} for serpentine minerals (10 s and five accumulations). The collected spectra were processed with the LabSpec 6 software for background subtraction and were compared with reference spectra (Downs, 2006; Lafuente et al., 2015; Petriglieri et al., 2015).

Compositions of minerals were determined using a JEOL JXA-8200 SuperProbe (Massachusetts Institute of Technology) and a JEOL-JXA-8530F 'HyperProbe' field-emission (Yale University) electron probe microanalyzer. Analyses were performed using a 15 kV accelerating voltage and a 10 nA beam current. The beam was fully focused for nominally-anhydrous minerals and defocused to 10 µm diameter for hydrous minerals. Data reduction was done using the CITZAF package. Counting times were 40 seconds on peak, and 20 seconds on background except for Na, which was analyzed first for 10 seconds on peak and 5 seconds on background. All the minerals (i.e. silicates, oxides, sulfides) were quantified using natural silicate and oxide standards.

To constrain mineral abundances on a thin section scale, mineral distribution maps were constructed on whole thin sections using a Zeiss Gemini Sigma 300VP Scanning Electron microscope (SEM) with a silicon drift detector (SDD) Bruker Qantax XFlash 6|60 and the mineralogic software from Zeiss at the Freie Universität Berlin. The measurements were carried out at an acceleration voltage of 20 kV, an aperture size of 120 µm and a dwell time of 0.008 s at a pixel size of 0.5 μm^2. Average counts per pixel were on the order of 5000-6000 counts and the mineral evaluation was performed after EMP analyses on the same samples.

The bulk-rock concentrations of the collected samples were analyzed using X-ray fluorescence (XRF) for major elements and inductively coupled plasma mass spectrometry (ICP-MS) technique for trace elements at GeoAnalytical Laboratory at Washington State University (Pullman, WA) following established procedures (Johnson et al., 1999). The bulk-rock Fe(III) /Fe_T (i.e. Fe_T = Fe(II) + Fe(III)) was determined by mass balance from Fe_T contents measured using XRF and acid titration of Fe(II) conducted at Activation Laboratories (Ancaster, Canada) following standard protocols (Wilson, 1955). Bulk-rock Sr isotope measurements were performed on selected samples using an IsotopX Phoenix thermal ionization mass spectrometer (TIMS) at Boston College (Boston, MA) following the protocols of Baxter and DePaolo (2002). The bulk-rock Rb concentrations were taken from the trace element measurements at WSU. An age correction of 40 Ma (Starr et al., 2020) was applied.

To determine the individual contribution of each hydrous phase to the bulk-rock volatile budget, we performed simultaneous thermogravimetric analysis (TGA) and differential scanning calorimetry (DSC) of rock powders using a TA Instruments SDT Q600 instrument. Approximately 20–40 mg of homogenous rock powder was heated in N_2 gas atmosphere at a rate of 10°C/min from 50 to 1100°C and a flow rate of 50 ml/min to determine the mass loss and heat flow, both of which reflect the formation and/or breakdown of specific minerals during heating. The skeletal density (pre-dried at 105 °C for 24 h) of samples was determined using helium-pycnometry (Micromeritics AccuPyc II). The magnetic susceptibility (K) was measured using a Bartington MS2B sensor with a Bartington MS2 magnetic susceptibility meter.

Phase equilibria and reaction-path modeling

In order to provide constraints on the pressure and temperature conditions of mass transfer and rock hybridization, equilibrium thermodynamic modeling of representative bulk compositions

was performed. *P-T* pseudosections were computed using the program Perple_X (version 6.9.0; Connolly, 2009) and the internally consistent dataset (db5.5; 2003) of Holland and Powell (1998) in the MnO-Na_2O-CaO-FeO-MgO-Al_2O_3-SiO_2-H_2O-TiO_2-O_2 (MnNCFMASHTO) chemical system. Activity-composition models were used for the following phases: feldspar (Holland and Powell, 2003), spinel (White et al., 2002) , chlorite, garnet, epidote and chloritoid (Holland and Powell, 1998), clinopyroxene (Green et al., 2007), white mica (Coggon and Holland, 2002), and amphibole (Diener and Powell, 2012) . Quartz, lawsonite, rutile and titanite were assumed to be pure (stoichiometric) phases. The fluid phase was assumed to be pure H_2O. As the whole rock water content can have a control on the mineral assemblage, T-M_{H2O} pseudosections were calculated. For all metagabbroic samples, the observed LOI content provided unrealistic mineral assemblages and *P-T* stabilities, *e.g*. garnet is calculated to be stable at unrealistically low pressure and temperatures (~300 °C and ~0.5 GPa). Additionally, for the distal Fe-Ti gabbroic lithologies, it is likely that during prograde metamorphism and isothermal decompression, some degree of dehydration occurred. As such, we assumed water to be in excess. The measured whole rock chemistries of samples B06 (Zone IV) and B10 (Zone V) were utilized for modeling the prograde to peak portion of the *P-T* evolution (i.e. the *P-T* conditions of garnet growth initiation, where appropriate). Use of the whole rock chemistry in determining the peak *P-T* conditions was deemed inappropriate, given the high abundance (up to 20% by volume) of chemically zoned garnet porphyroblasts (Lanari and Engi, 2017), and as such, the matrix chemistry was used. The matrix compositions for these samples were calculated by subtracting volumetrically-average garnet compositions (determined by EPMA traverse), at volume abundances of ~15 and 10% (inferred by SEM mineral maps), respectively, from the whole rock composition. For the matrix compositions, phase equilibria were calculated in the Na_2O-CaO-FeO-MgO-Al_2O_3-SiO_2-H_2O-TiO_2-O_2 (NCFMASHTO) chemical system, assuming all MnO was sequestered to form garnet. The Fe_2O_3 contents for the whole rock compositions were taken from the Fe titration results, and are taken to be maximum values for Fe^{3+}/Fe_{total}. The Fe_2O_3 contents used for the *P-T* pseudosection calculations were further constrained by estimation using T-M_{Fe2O3} pseudosections. Finally, representative compositions from Zones I (sample B13) and III (samples B01 and B03) were modelled, using the same parameters above (where appropriate) and coupled with petrographic observations and SEM mineral maps (where applicable), to determine the portion of the inferred *P-T* path (i.e. peak to post-peak) at which these lithologies last equilibrated.

In addition, thermodynamic reaction-path models were set up to assess the alteration history and concomitant mineralogical changes during a fluid-mediated reaction between hydrated ultramafic (serpentinites) and metamorphosed crustal rocks at subduction zone conditions. Along with *P-T* constraints from equilibrium pseudosection and garnet isopleth models, results of reaction-path models were compared with mineral assemblages from petrographic observations. Models were calculated using the EQ3/6 software package (Wolery, 1992) with the Deep Earth Water Model (DEW) database containing equilibrium constants of reactions involving minerals and aqueous species (Huang and Sverjensky, 2019; Sverjensky, 2019). We used equation of state for water of Zhang and Duan (2005), and the dielectric constant from Sverjensky et al. (2014).Thermodynamic calculations were performed over a range of *P-T* conditions (i.e. bracketing the prograde-peak-retrograde *P-T* conditions) and a range of fluid-to-rock (f/r) ratios. Activity coefficients were calculated using the B-dot equation (Helgeson, 1969). Minerals with solid-solutions such as olivine (forsterite-fayalite), garnet (pyrope-almandine-grossular), clinopyroxene (diopside-hedenbergite-jadeite), calcic amphibole (tremolite-ferrotremolite), and chlorite (clinochlore-chamosite) are included in the database. Solid solutions for some minerals present in the studied samples (*e.g.,* serpentine, Na-Ca amphibole) have not been implemented in the database yet. Similarly, ilmenite, rutile, and titanite are present in the studied samples but are not implemented in the current thermodynamic database. We suppressed periclase to account for metastable mineral equilibria. In a first modelling step, an aqueous fluid was allowed to equilibrate with a serpentinite assemblage (i.e. antigorite + diopside clinopyroxene (Cpx) + magnetite ± brucite) using EQ3. This is an iterative process where in every calculation, the predicted fluid composition is checked if it is saturated with only serpentinite assemblage only. In cases where the predicted fluid composition is saturated with other minerals other than the desired serpentinite assemblage, the pH is slightly modified until the fluid becomes saturated with only the serpentinite assemblage. Note that we do not model the serpentinization of a peridotite. Rather, we calculated the composition of an aqueous fluid buffered by serpentinite assemblage. The oxygen fugacity of the fluid (fO_2) is set to values within the redox stability of magnetite that are bound by the hematite-magnetite buffer (HM) and quartz-fayalite-magnetite buffer (QFM). Because serpentinite of Zone I does not contain clinopyroxene, we evaluated possible effects of clinopyroxene on the fluid composition over a range of temperatures. The models predict that the presence of clinopyroxene in serpentinite does not significantly affect the concentrations of dissolve Mg, Si, and Ca when

compared with clinopyroxene-free serpentinite. Since the current thermodynamic database does not allow for Fe speciation in serpentine mineral, the reducing capacity of serpentinites is diminished and hematite is favored to saturate. This renders the predicted oxygen fugacity and hydrogen concentration of equilibrium pore fluids uncertain. Since hematite is not observed in the studied rock samples, we suppressed hematite in the models. This model setup is consistent with the presence of magnetite in the studied serpentinites. Subsequently, once the fluid is saturated with only the desired serpentinite assemblage, the fluid was allowed to react with either a model oxide gabbro similar to the ones reported in Voltri Massif (Tribuzio et al., 1996) or an eclogite (representative of eclogitic metagabbro in Zone V; Figure S6). The starting compositions of the model oxide gabbro and eclogite are summarized in Table S10. For comparison, the oxide gabbro has relatively higher SiO_2, Al_2O_3, and CaO, but has lower FeO* concentrations than the eclogite. The fluid-rock interaction simulation is performed under isothermal and isobaric conditions at varying fluid-to-rock mass ratios (f/r). The gabbro-fluid model explores the possibility that fluid-mediated mass transfer occurred during prograde to peak metamorphism, modifying the bulk composition of each zone, before reaching peak eclogite-facies metamorphism and post-peak retrograde conditions. In comparison, the eclogite-fluid model explores the possibility that the fluid-mediated mass transfer only occurred at post-peak eclogite-facies and retrograde conditions. In each simulation, fluids that are equilibrated with serpentinite are titrated with 1 kg of gabbro/eclogite under isobaric and isothermal conditions. The fluid-to-rock mass ratio (f/r) decreases with increasing reaction progress (ξ). Importantly, we implemented titration models which can be used to assess heterogeneous phase equilibria in an advective system (*e.g.,* fluid percolation and reaction along a high permeability pathway such as veins or lithologic boundaries) and in a diffusive system (*e.g.,* fluid-mediated diffusive transfer at the boundary of a crustal rock and serpentinite, where the fluid composition is buffered by the rock) (Bach and Klein, 2009). Despite the simplifications and limitations in the modeling approach, the reaction-path models can simulate the evolving fluid-rock equilibria starting from the serpentinites towards the serpentinite-metagabbro contact and into the metagabbro/eclogite interior with increasing ξ (equivalent to decreasing f/r ratios).

Mass-balance calculations

To quantify chemical and mass changes associated with the formation of metasomatic reaction zones between serpentinite and metagabbro, quantitative mass balance calculations were performed (Gresens, 1967). We utilized the major element composition of the most distal eclogitic metagabbro (B10 in Zone V) as a basis to compute chemical and mass changes of subsequently more reacted rocks in Zones II to IV. We focused on the changes in the metagabbro side because of the lack of significant modal and chemical changes in the serpentine domain (Zone I). We adopted a method that utilizes an immobile element as a geochemical reference frame as it allows for the evaluation of rock mass and individual element changes (Ague and van Haren, 1996; Ague, 2017; Ague and Nicolescu, 2014; Grant, 1986; Penniston-Dorland and Ferry, 2008). Mobility of most major and trace elements during high-pressure metamorphism and metasomatism have been documented in exhumed high pressure rocks (Ague, 2017). In this study, scandium displays generally constant bulk-rock composition across the metagabbro, except for sample B12 (Figure. 6b). It is likely that the analyzed B12 sample contained very little oxide phase that likely host the bulk of Sc. However, the lack of a thin section for this sample preludes further scrutiny. The fluid immobility of Sc makes it an ideal candidate as a reference element. Uranium and Th also display fluid immobility and can be used as reference elements (Ague, 2017). We selected Sc as the geochemical reference frame over U and Th because of the larger analytical uncertainties associated with the very low abundances of U and Th in these rocks. In addition, the good agreement between the bulk-rock Sc concentrations measured by XRF and solution ICP-MS gives further confidence on the reliability of our Sc concentrations. For comparison, using Th as the reference element gave similar trends of enrichment and depletion of major elements as with Sc but the quantitative estimates of gains and losses using Th were systematically larger. We only assessed the chemical changes of major elements after illustrating that the rare-earth element (REE) concentration of the most distal samples may already have been modified during prograde subduction (see section 4.2). When mass balance calculations are performed for REE, the strong LREE depletion in distal Zone V samples would artificially lead to unrealistic chemical changes in LREE (> 1000 %) in the more reacted samples.

In our studied transect, Zone II and III experienced significant gains in Mg, LOI, Ni, losses in Ca, and variable changes in Si, Al, and Fe. Zone IV experienced significant gains in Ca without significant changes in other elements. Elemental changes in Si, Al, and Fe are variable across zones

II, III and IV (Figure S9). Accounting for thickness of each zone and rock densities, the total mass of element that was gained or lost for each zone can be calculated. The results show that for the most dominant and characteristic chemical changes, Zone II and III gained ~110 kg/m^2 MgO and ~51 kg/m^2 H_2O, and lost ~12 kg/m^2 CaO. In addition, calculations show that Zone IV gained ~104 kg/m^2 CaO and ~17 kg/m^2 MgO.

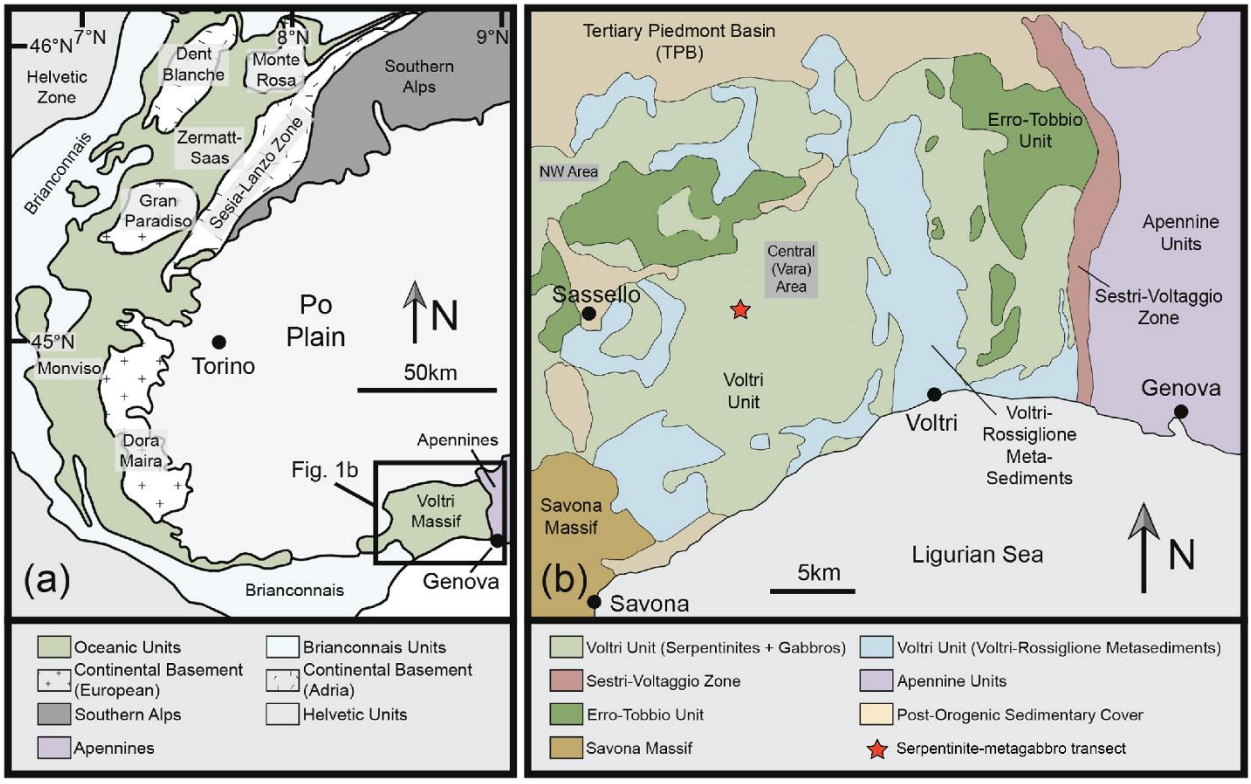

Figure S1. Geological maps of the Western Alps and the Voltri Massif modified from Starr et al. (2020). (a) Simplified geological map of the Western Alps, showing the broad distribution of oceanic rocks, continental massifs, and sedimentary units. The black box outlines the area shown in Figure. 1b. (b) Geologic map of the study area. The location of the studied serpentinite-metagabbro transect is indicated by red star.

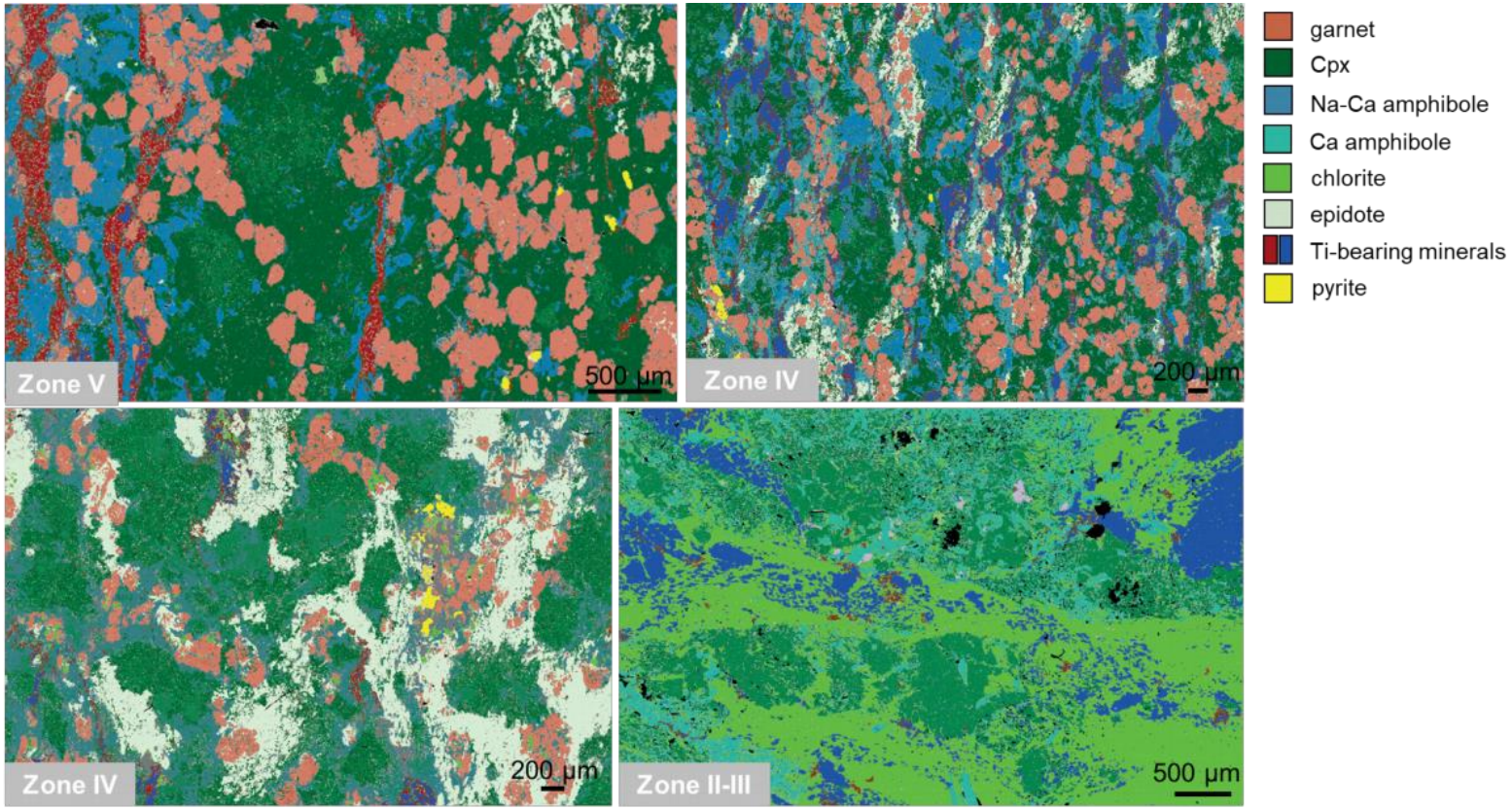

Figure S2. Representative thin-section EDS chemical maps of the different metasomatic reaction zones.

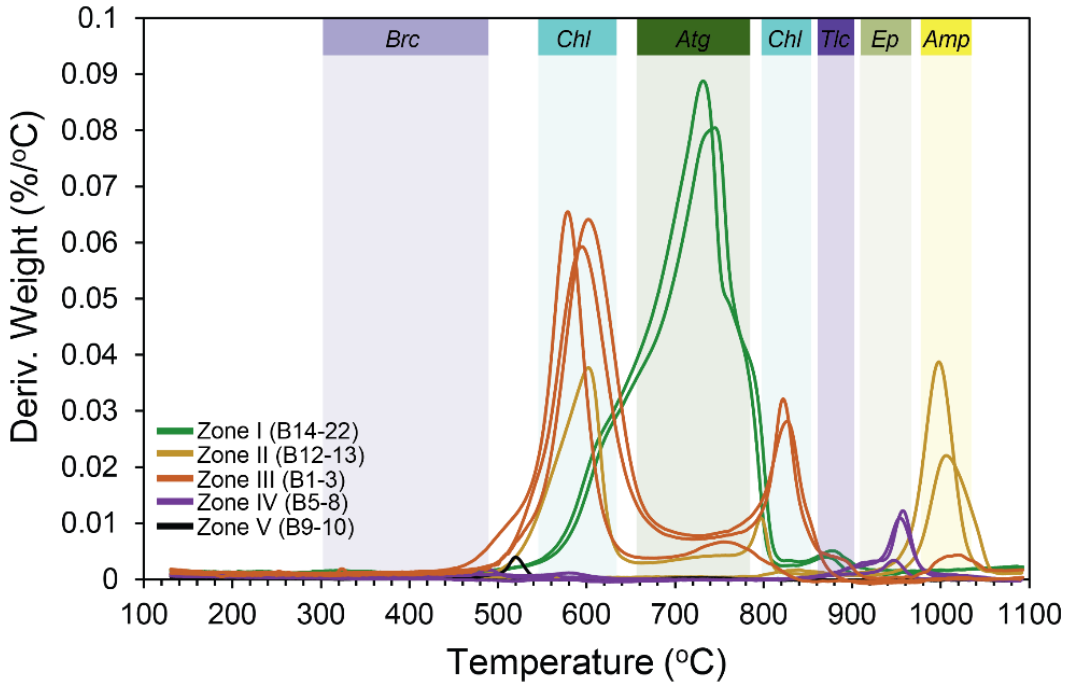

Figure S3. Thermal analysis of representative samples from each zone. First derivative (deriv.) of mass loss between ~150 and ~1100 °C. Shading indicates mass loss via dehydroxylation reaction of hydrous phases, such as brucite, chlorite, serpentine (antigorite), talc, epidote, and amphibole.

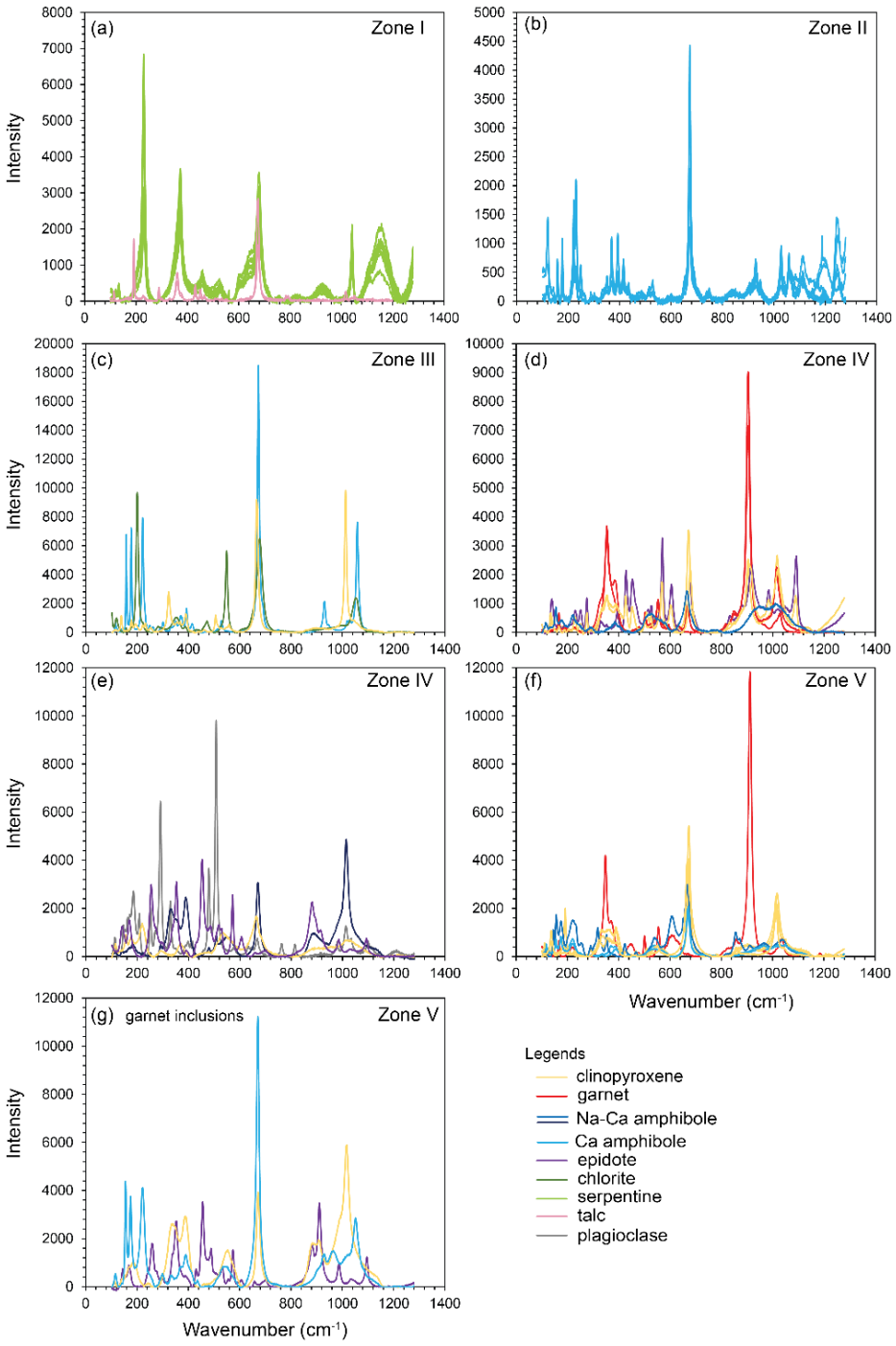

Figure S4. Representative Raman spectra of the major minerals that comprise the different metasomatic reaction zones.

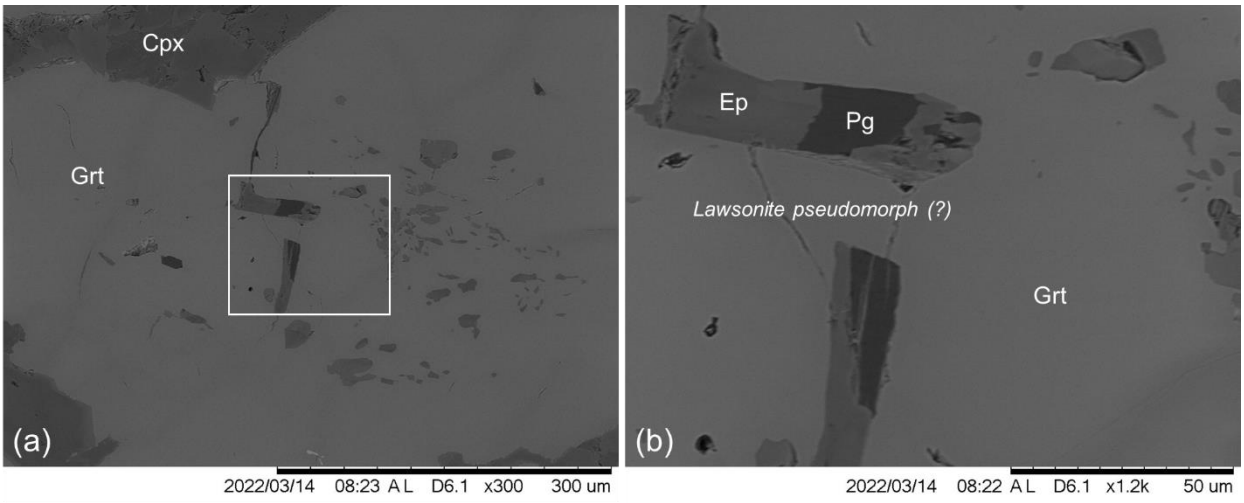

Figure S5**.** Representative thin-section back-scatter election image of garnet inclusions (epidote and paragonite) inferred to be pseudomorphic after lawsonite in sample B10 (Zone V).

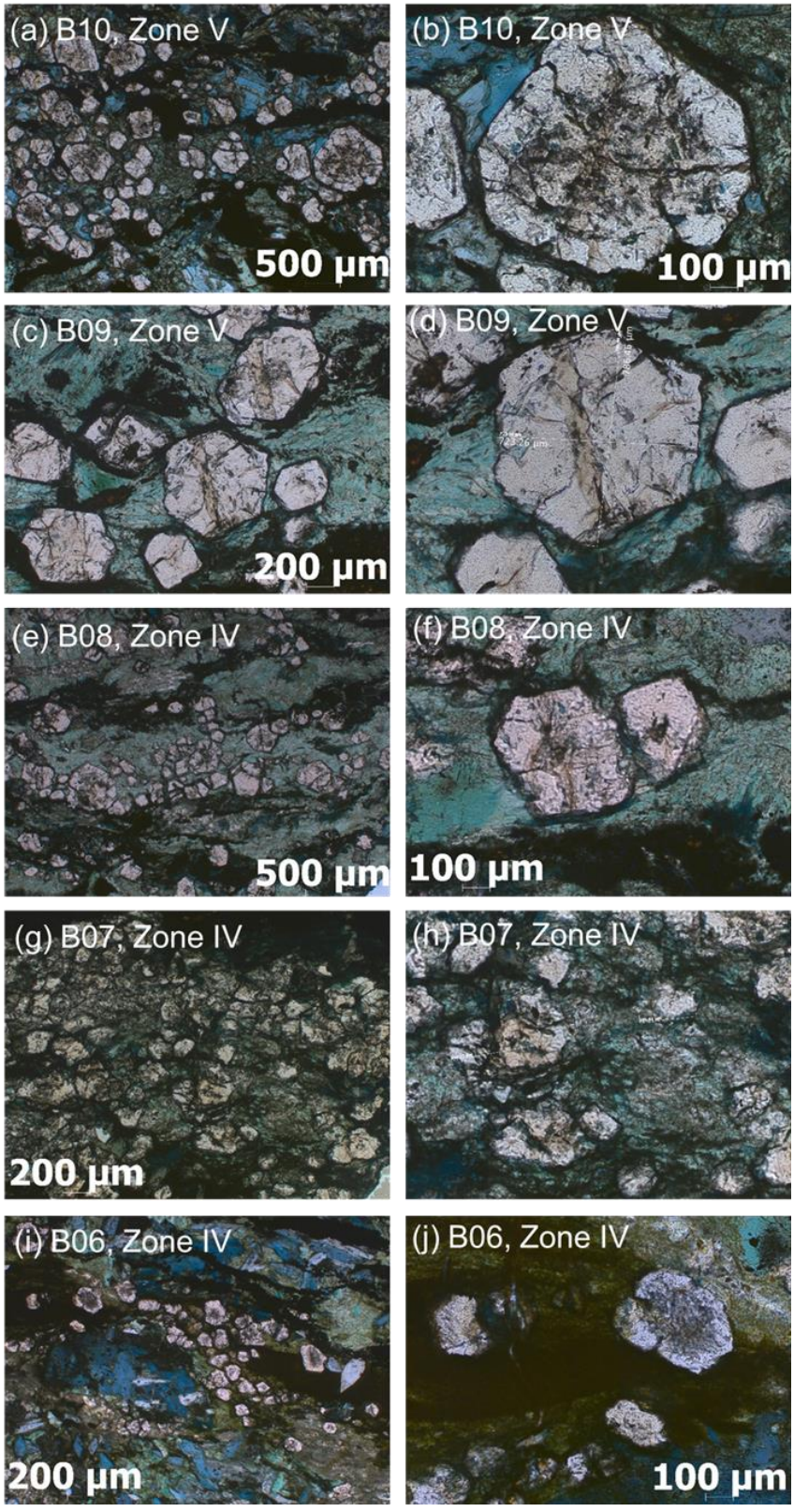

Figure S6. Thin-section photomicrographs showing representative garnets from different zones that were measured by EPMA and were used in pseudosection modeling.

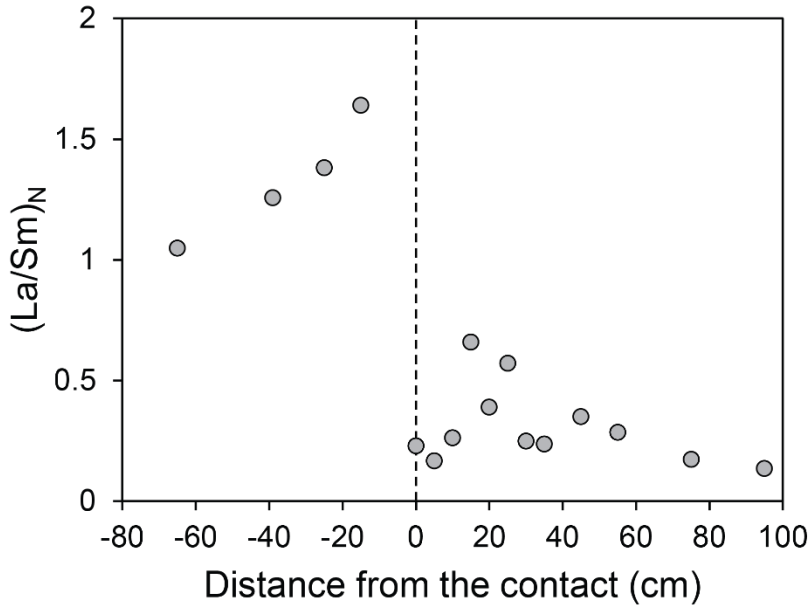

Figure S7. Primitive mantle-normalized $(La/Sm)_N$ ratio across the serpentinite-metagabbro transect. Primitive mantle is from McDonough and Sun (1995).

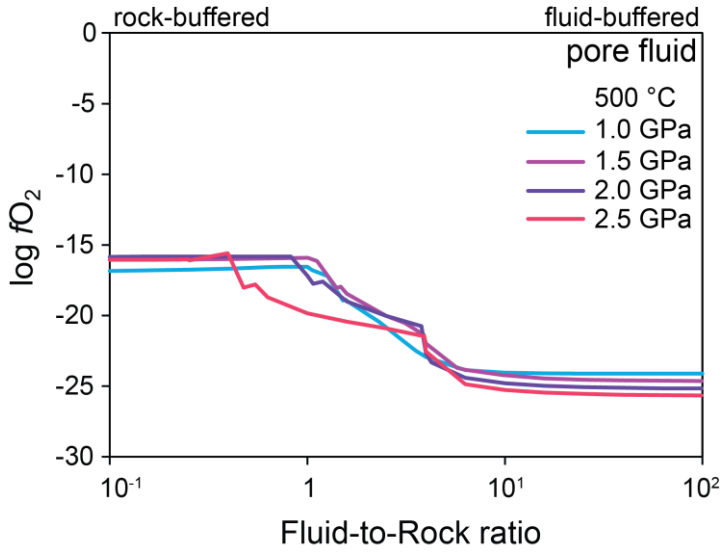

Figure S8. Predicted oxygen fugacity (fO_2) of the equilibrium fluid during high P-T metasomatism as a function of fluid-to-rock mass ratio. A fluid equilibrated with serpentinite (at f/r ~100) is subsequently allowed to react with oxide gabbro at 500 °C, 1.0–2.5 GPa. The f/r decreases as gabbro is titrated into the fluid.

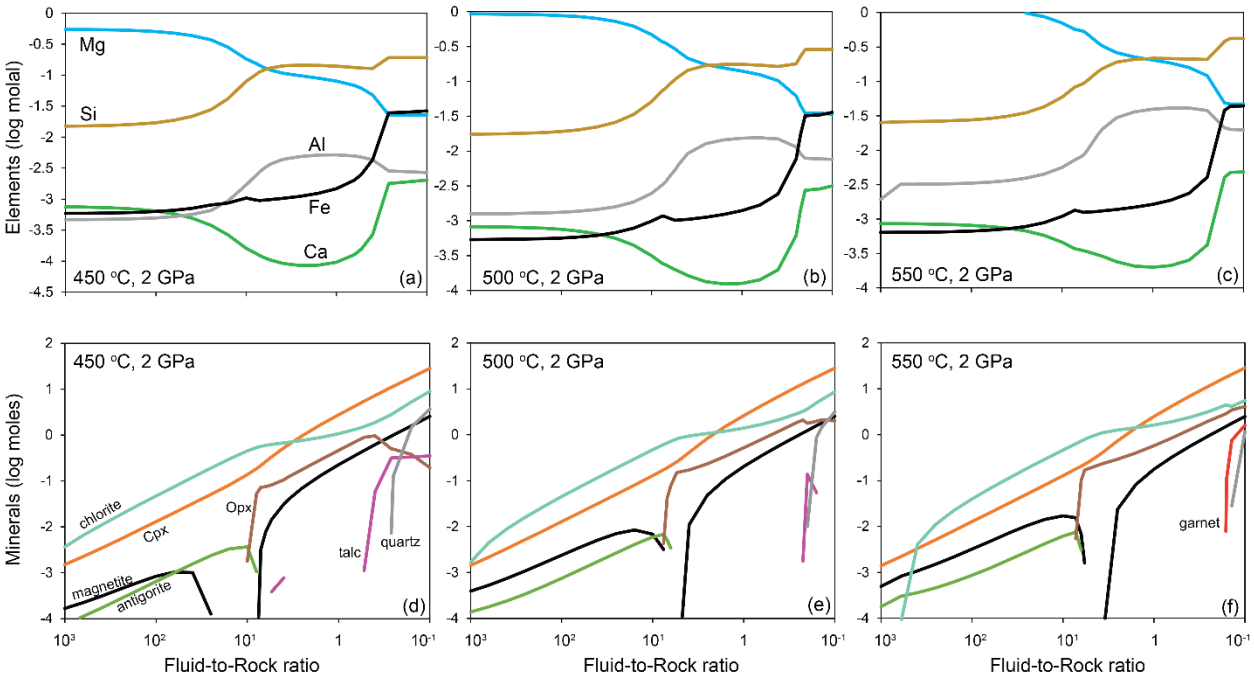

Figure S9. Predicted alteration mineralogy and fluid composition during high P-T metasomatism as a function of fluid-to-rock mass ratio. A fluid equilibrated with serpentinite (at f/r > 1000) is subsequently allowed to react with eclogitic metagabbro in Zone V at 450–550 °C, 2.0 GPa. The f/r decreases as eclogite is titrated into the fluid.

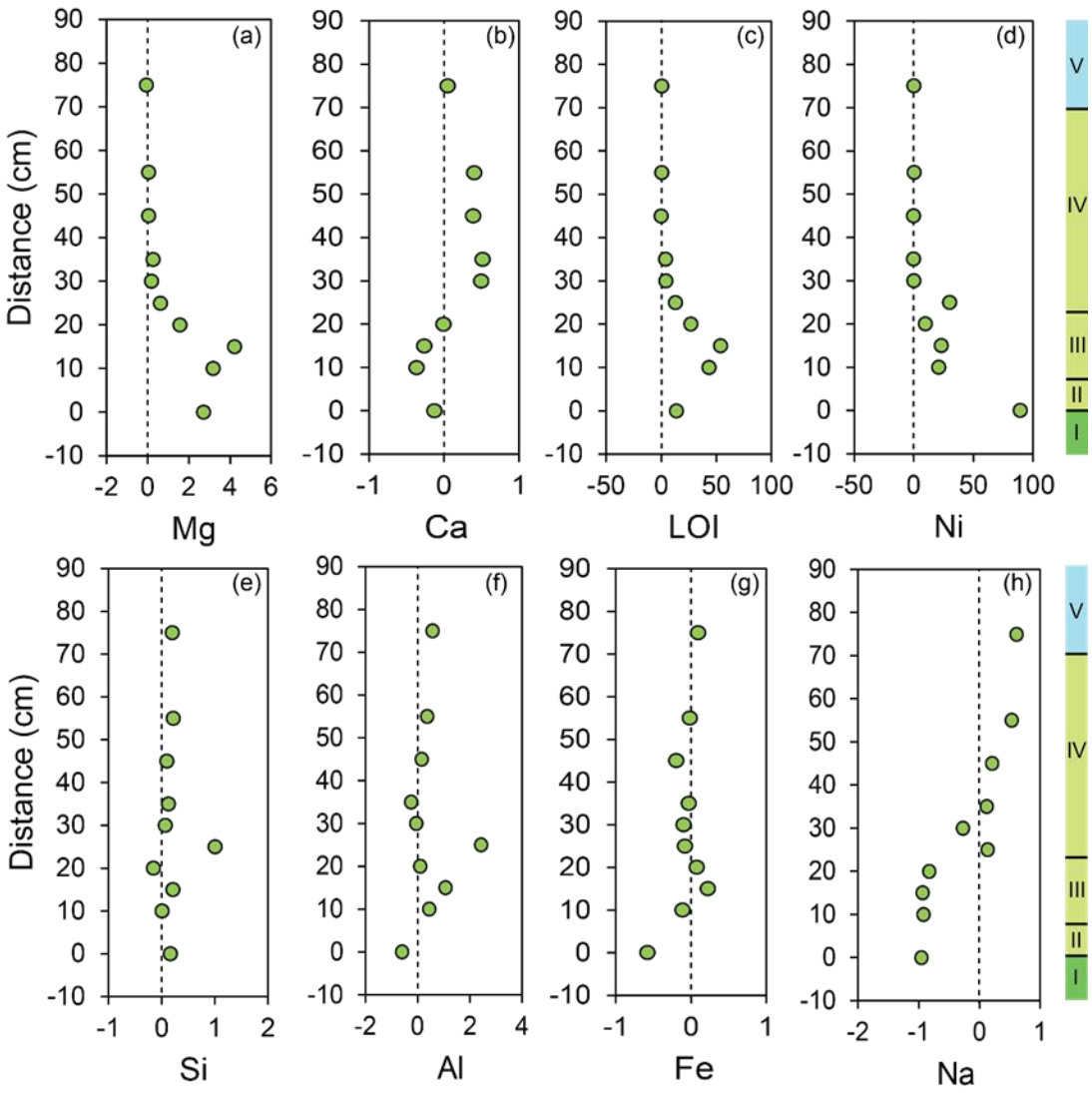

Figure S10. Mass changes for elements shown as fractions (values/100). Negative values indicate mass loss, positive values indicate gain. Details and assumptions on mass balance calculations are provided in the supplementary.

Table S1. Bulk-rock major, trace elements, and Sr isotope compositions, and petrophysical properties.

					WSU-XRF (wt. %)										
SAMPLES	Distance from the contact (cm)	Reaction zone	Magnetic susceptibility (SI x10-5)	Density (g/cm3)	SiO2	TiO2	Al2O3	FeOtot	MnO	MgO	CaO	Na2O	K2O	P2O5	LOI
V17-X808B13	0	2	14.17	3.0	49.59	4.61	3.82	9.31	0.21	23.40	8.91	0.11	0.03	0.0	3.2
V17-X808B12	5	2			58.08	0.03	0.51	5.30	0.12	25.02	10.86	0.07	0.02	0.0	3.7
V17-X808B01	10	3	238.33	3.0	36.82	5.79	11.82	16.82	0.32	22.63	5.57	0.16	0.01	0.1	6.6
V17-X808B02	15	3	375.17	3.0	34.76	6.06	13.22	18.23	0.36	22.15	5.07	0.10	0.00	0.0	6.9
V17-X808B03	20	3	246.83	3.3	32.44	11.90	9.39	21.47	0.64	14.60	9.17	0.37	0.00	0.0	4.1
V17-X808B04	25	4			45.24	0.81	17.34	10.79	0.16	5.43	18.73	1.44	0.02	0.0	1.6
V17-X808B05	30	4	15.33	3.5	43.19	5.77	8.57	18.83	0.34	7.12	14.51	1.65	0.02	0.0	0.0
V17-X808B06	35	4	32.50	3.5	42.90	7.88	6.39	19.10	0.32	7.12	13.83	2.39	0.02	0.0	0.6
V17-X808B07	45	4	42.83	3.4	44.64	5.12	10.48	16.90	0.25	6.24	13.56	2.76	0.02	0.0	0.2
V17-X808B08	55	4	35.50	3.5	43.57	6.42	10.82	18.24	0.29	5.55	12.03	3.07	0.01	0.0	0.0
V17-X808B09	75	5	33.33	3.6	41.86	8.96	12.21	19.80	0.35	4.85	8.78	3.16	0.04	0.0	0.3
V17-X808B10	95	5	25.00	3.6	41.73	8.40	9.32	21.64	0.34	6.17	10.04	2.34	0.01	0.0	0.0
V17-X808B14	-15	1	15.17	2.7	48.54	0.03	2.02	10.34	0.12	38.92	0.03	0.00	0.00	0.0	11.1
V17-X808B15	-25	1	133.50	2.7	48.54	0.13	2.08	10.23	0.11	38.89	0.01	0.00	0.00	0.0	11.0
V17-X808B16	-39	1	11.00	2.7	48.79	0.03	1.76	9.81	0.11	39.49	0.01	0.00	0.00	0.0	11.2
V17-X808B17	-65	1			48.99	0.03	1.68	9.74	0.11	39.44	0.01	0.00	0.00	0.0	11.2
V17-X808B18	-87	1			49.06	0.02	1.58	9.87	0.12	39.34	0.02	0.00	0.00	0.0	11.1
V17-X808B19	-110	1			48.29	0.02	2.02	10.64	0.13	38.87	0.02	0.00	0.00	0.0	11.3
V17-X808B20	-129	1			47.04	2.22	1.97	12.20	0.21	34.81	1.54	0.00	0.00	0.0	9.5
V17-X808B21	> 200	1	13.00	2.7	48.16	0.02	2.38	10.03	0.11	39.29	0.01	0.00	0.00	0.0	11.2
V17-X808B22	> 200	1	56.67	2.7	48.38	0.04	2.06	9.53	0.12	39.87	0.01	0.00	0.00	0.0	11.1

			WSU-XRF (ppm)						
Bulk S (wt.%)	Bulk Fe3+/Fetot		Ni	Cr	Sc	V	Ga	Cu	Zn
0.01	0.43		1035	1902	57	128	7	12	49
0.01	0.30		959	807	11	32	3	14	39
0.01	0.32		216	2	52	645	17	30	102
0.01	0.23		185	0	41	578	18	38	115
0.01	0.35		111	0	56	696	14	41	130
			189	5	31	362	27	27	60
0.02	0.49		42	0	56	737	13	49	110
0.18	0.48		12	0	53	797	12	40	130
			10	0	57	788	17	23	103
0.02	0.30		7	0	49	671	18	14	120
0.31	0.28		8	0	49	968	19	68	90
0.51	0.22		11	0	56	988	17	46	179
bdl	0.31		1753	1907	9	95	5	23	83
bdl			1654	3737	9	80	4	33	74
bdl			1635	2453	10	64	4	27	75
bdl	0.30		1644	2345	12	57	3	20	78
bdl			1668	1851	8	55	4	26	79
bdl			1621	2214	6	67	5	33	87
bdl			1428	2782	18	89	5	37	83
bdl	0.33		2173	1863	9	80	6	12	78
bdl			2008	2398	10	69	5	24	59

Cs ppm	Rb ppm	Ba ppm	Th ppm	U ppm	Nb ppm	Ta ppm	La ppm	Ce ppm	Pb ppm	Pr ppm	Sr ppm	Nd ppm	Zr ppm	Hf ppm	Sm ppm	Eu ppm	Gd ppm	Tb ppm	Dy ppm	Y ppm	Ho ppm	Er ppm	Tm ppm	Yb ppm	Lu ppm	Sc ppm
0.02	0.07	0.95	0.08	0.02	1.15	0.10	0.11	0.34	0.14	0.05	11.42	0.44	35.93	1.10	0.31	0.10	0.57	0.13	0.86	4.21	0.19	0.51	0.07	0.42	0.06	58.20
0.10	0.11	0.72	0.07	0.02	0.10	0.02	0.12	0.47	0.17	0.08	8.44	0.65	1.74	0.05	0.46	0.13	0.83	0.18	1.24	5.77	0.26	0.69	0.09	0.59	0.08	10.11
0.06	0.09	1.03	0.08	0.03	1.86	0.16	0.39	1.28	0.11	0.27	5.97	1.78	49.42	1.52	0.92	0.34	1.52	0.30	2.09	9.86	0.43	1.16	0.16	1.02	0.16	50.05
0.06	0.06	0.57	0.09	0.03	1.68	0.15	1.18	3.87	0.09	0.63	4.80	3.33	49.89	1.56	1.13	0.49	1.40	0.27	1.88	9.27	0.39	1.06	0.15	0.93	0.15	39.27
0.18	0.13	1.13	0.08	0.03	2.74	0.27	1.18	3.76	0.13	0.69	10.23	4.11	80.68	2.37	1.91	2.38	4.56	1.07	7.73	44.62	1.71	4.82	0.72	4.59	0.73	52.55
4.46	1.01	5.68	0.13	0.04	0.33	0.03	2.46	7.11	1.21	1.27	491.18	7.03	23.93	0.76	2.70	1.97	3.28	0.53	3.50	18.54	0.75	2.03	0.29	1.87	0.29	30.91
0.51	0.22	1.49	0.11	0.04	1.42	0.13	0.65	2.26	0.29	0.45	76.35	2.95	48.03	1.47	1.63	0.95	2.95	0.63	4.53	24.44	1.00	2.74	0.40	2.47	0.38	55.26
0.81	0.22	1.06	0.07	0.02	1.70	0.16	0.46	1.76	0.48	0.38	57.99	2.45	51.00	1.56	1.22	0.76	2.25	0.50	3.68	19.91	0.82	2.30	0.34	2.09	0.33	51.97
0.39	0.22	1.48	0.07	0.02	0.93	0.08	1.23	4.14	0.39	0.77	179.67	4.78	44.53	1.42	2.21	1.35	3.32	0.64	4.49	23.53	0.97	2.67	0.38	2.39	0.38	55.56
0.10	0.15	0.63	0.09	0.03	1.41	0.13	0.92	3.30	0.34	0.68	132.56	4.40	44.34	1.40	2.03	1.26	2.86	0.55	3.73	19.61	0.80	2.24	0.31	1.94	0.32	48.86
0.10	0.21	1.71	0.09	0.03	2.33	0.21	0.16	0.51	0.17	0.08	15.88	0.52	59.63	1.72	0.60	0.66	2.34	0.53	3.54	19.18	0.79	2.24	0.33	2.11	0.34	47.71
0.13	0.20	1.35	0.13	0.04	1.73	0.17	0.29	1.03	0.26	0.22	24.59	1.66	48.19	1.52	1.34	0.93	2.96	0.59	4.04	20.81	0.86	2.40	0.34	2.14	0.34	57.05
0.12	0.10	0.92	0.08	0.03	0.11	0.02	0.15	0.44	0.59	0.04	0.74	0.18	2.05	0.04	0.06	0.02	0.08	0.01	0.11	0.52	0.03	0.08	0.01	0.10	0.02	9.11
0.25	0.08	0.67	0.06	0.02	0.12	0.02	0.11	0.25	0.11	0.03	0.56	0.16	1.47	0.03	0.05	0.01	0.09	0.02	0.14	0.79	0.03	0.11	0.02	0.14	0.03	10.71
0.18	0.09	0.74	0.07	0.02	0.09	0.02	0.13	0.30	0.12	0.04	0.63	0.18	1.52	0.03	0.06	0.02	0.09	0.02	0.14	0.73	0.03	0.10	0.02	0.12	0.02	10.24
0.21	0.12	0.81	0.08	0.03	0.09	0.02	0.17	0.46	0.08	0.06	0.71	0.27	1.59	0.04	0.10	0.03	0.12	0.03	0.18	0.91	0.04	0.12	0.02	0.14	0.02	10.91
0.08	0.07	1.32	0.07	0.02	0.09	0.02	0.17	0.66	0.08	0.07	0.74	0.32	1.52	0.03	0.11	0.04	0.15	0.03	0.21	0.90	0.05	0.14	0.02	0.14	0.02	7.79
0.08	0.14	1.90	0.06	0.02	0.09	0.02	0.16	0.52	0.20	0.06	0.70	0.31	1.36	0.03	0.12	0.04	0.15	0.03	0.22	0.91	0.05	0.13	0.02	0.17	0.03	7.05
0.12	0.14	3.50	0.08	0.03	0.78	0.07	0.25	1.58	0.10	0.10	1.65	0.56	49.74	1.36	0.23	0.06	0.32	0.06	0.44	2.03	0.10	0.28	0.04	0.33	0.05	18.82
0.02	0.16	0.60	0.05	0.02	0.08	0.02	0.10	0.29	0.09	0.04	0.49	0.19	1.47	0.03	0.07	0.02	0.08	0.02	0.11	0.50	0.02	0.07	0.01	0.08	0.01	9.48
0.08	0.08	0.57	0.07	0.02	0.09	0.02	0.17	0.35	0.06	0.06	0.72	0.33	1.53	0.03	0.13	0.05	0.18	0.04	0.26	1.42	0.06	0.18	0.03	0.17	0.03	8.81

La ppm	Ce ppm	Pr ppm	Nd ppm	Sm ppm	Eu ppm	Gd ppm	Tb ppm	Dy ppm	Ho ppm	Er ppm	Tm ppm	Yb ppm	Lu ppm		87/86Sr isotope ratios	±2 S.E.
0.11	0.34	0.05	0.44	0.31	0.10	0.57	0.13	0.86	0.19	0.51	0.07	0.42	0.06		0.704	6.49E-06
0.12	0.47	0.08	0.65	0.46	0.13	0.83	0.18	1.24	0.26	0.69	0.09	0.59	0.08		0.704	4.05E-06
0.39	1.28	0.27	1.78	0.92	0.34	1.52	0.30	2.09	0.43	1.16	0.16	1.02	0.16		0.704	6.16E-06
1.18	3.87	0.63	3.33	1.13	0.49	1.40	0.27	1.88	0.39	1.06	0.15	0.93	0.15		0.704	4.48E-06
1.18	3.76	0.69	4.11	1.91	2.38	4.56	1.07	7.73	1.71	4.82	0.72	4.59	0.73		0.704	8.23E-06
2.46	7.11	1.27	7.03	2.70	1.97	3.28	0.53	3.50	0.75	2.03	0.29	1.87	0.29		0.704	4.86E-06
0.65	2.26	0.45	2.95	1.63	0.95	2.95	0.63	4.53	1.00	2.74	0.40	2.47	0.38			
0.46	1.76	0.38	2.45	1.22	0.76	2.25	0.50	3.68	0.82	2.30	0.34	2.09	0.33		0.704	4.96E-06
1.23	4.14	0.77	4.78	2.21	1.35	3.32	0.64	4.49	0.97	2.67	0.38	2.39	0.38		0.704	4.41E-06
0.92	3.30	0.68	4.40	2.03	1.26	2.86	0.55	3.73	0.80	2.24	0.31	1.94	0.32		0.704	9.79E-06
0.16	0.51	0.08	0.52	0.60	0.66	2.34	0.53	3.54	0.79	2.24	0.33	2.11	0.34		0.704	3.56E-06
0.29	1.03	0.22	1.66	1.34	0.93	2.96	0.59	4.04	0.86	2.40	0.34	2.14	0.34		0.704	6.90E-06
0.15	0.44	0.04	0.18	0.06	0.02	0.08	0.01	0.11	0.03	0.08	0.01	0.10	0.02			
0.11	0.25	0.03	0.16	0.05	0.01	0.09	0.02	0.14	0.03	0.11	0.02	0.14	0.03		0.709	1.18E-05
0.13	0.30	0.04	0.18	0.06	0.02	0.09	0.02	0.14	0.03	0.10	0.02	0.12	0.02			
0.17	0.46	0.06	0.27	0.10	0.03	0.12	0.03	0.18	0.04	0.12	0.02	0.14	0.02		0.709	6.06E-05
0.17	0.66	0.07	0.32	0.11	0.04	0.15	0.03	0.21	0.05	0.14	0.02	0.14	0.02			
0.16	0.52	0.06	0.31	0.12	0.04	0.15	0.03	0.22	0.05	0.13	0.02	0.17	0.03			
0.25	1.58	0.10	0.56	0.23	0.06	0.32	0.06	0.44	0.10	0.28	0.04	0.33	0.05			
0.10	0.29	0.04	0.19	0.07	0.02	0.08	0.02	0.11	0.02	0.07	0.01	0.08	0.01		0.708	2.04E-05
0.17	0.35	0.06	0.33	0.13	0.05	0.18	0.04	0.26	0.06	0.18	0.03	0.17	0.03			

Table S3. Representative garnet core and rim compositions in each zone measured by EPMA

	B10		B09		B08		B07		B06		B03	
Oxide (wt. %)	core	rim	core	rim	core	rim	core	rim	core	rim	highest Ca	lowest Ca
SiO2	36.74	37.36	36.53	37.16	36.79	36.82	36.85	36.89	36.84	37.22	37.80	37.70
TiO2	0.10	0.09	0.09	0.09	0.16	0.05	0.05	0.10	0.00	0.00		
Al2O3	20.85	21.64	21.41	21.74	21.52	21.65	21.41	21.58	21.55	21.44	20.70	21.20
Cr2O3	0.04	0.00	0.00	0.00	0.02	0.01	0.03	0.05	0.00	0.00		
FeO*	32.01	32.81	31.96	35.12	31.58	33.33	33.00	34.33	28.98	28.71	22.90	28.20
MnO	4.38	0.59	4.83	0.19	3.76	0.59	2.25	0.46	5.59	1.32	1.30	2.00
MgO	0.68	2.49	1.01	2.21	0.97	1.96	0.81	1.47	0.48	0.75	0.90	2.00
CaO	5.41	5.27	4.80	4.57	6.57	5.69	6.94	6.11	7.71	11.31	16.60	9.40
Total	100.21	100.25	100.63	101.08	101.37	100.10	101.34	100.99	101.16	100.76	100.20	100.50
endmember (mol%)												
almandine	72	74	71	78	69	75	72	76	64	63	49	62
pyrope	3	10	4	9	4	8	3	6	2	3	3	8
grossular	16	15	14	13	18	16	19	17	22	32	45	26
spessartine	10	1	11	0	8	1	5	1	12	3	3	4

Table S4. Representative garnet rim-to-rim compositions along a line transect and spot analses of core and rim measured by EPMA.
**Line point with no data was bad measurement*

		Elements (wt.%)										
B10 garnet	distance (micron)	SiO2	TiO2	Al2O3	FeO	MnO	MgO	CaO	Na2O	K2O	Cr2O3	Total
Grt 1_Line 1	16	37.1	0.2	21.6	33.9	0.7	1.2	6.0	0.0	0.0	0.0	101
Grt 1_Line 2	33	37.2	0.2	21.6	33.6	0.8	1.8	5.9	0.0	0.0	0.0	101
Grt 1_Line 3	49	37.0	0.1	21.8	34.8	1.0	1.5	5.1	0.0	0.0	0.0	101
Grt 1_Line 4	65	37.2	0.1	21.8	34.6	1.1	1.4	5.3	0.0	0.0	0.0	101
Grt 1_Line 5	81	37.0	0.1	21.6	33.8	1.1	1.7	5.6	0.0	0.0	0.0	101
Grt 1_Line 6	98	37.0	0.1	21.5	33.9	1.1	1.6	5.6	0.0	0.0	0.0	101
Grt 1_Line 7	114	37.2	0.1	21.8	33.8	1.0	1.7	5.6	0.0	0.0	0.0	101
Grt 1_Line 8	130	37.3	0.1	21.6	33.1	1.0	1.8	6.0	0.0	0.0	0.0	101
Grt 1_Line 9	147	37.2	0.1	21.6	33.2	1.2	1.7	6.1	0.0	0.0	0.0	101
Grt 1_Line 10	163	36.8	0.1	21.5	33.0	1.2	1.8	5.7	0.0	0.0	0.0	100
Grt 1_Line 11	179	36.9	0.1	21.7	33.5	1.2	1.5	5.5	0.1	0.0	0.0	100
Grt 1_Line 12	195	36.9	0.1	21.6	33.5	0.9	2.0	5.4	0.1	0.0	0.0	100
Grt 1_Line 13	212	37.0	0.1	21.6	33.8	1.0	1.8	5.5	0.1	0.0	0.0	101
Grt 1_Line 14	228	36.8	0.1	21.6	33.5	1.3	1.7	5.5	0.1	0.0	0.0	101
Grt 1_Line 15	244	36.9	0.1	21.7	33.3	1.2	1.8	5.5	0.1	0.0	0.0	101
Grt 1_Line 16	261	36.7	0.1	21.6	33.7	1.5	1.4	5.5	0.1	0.0	0.0	101
Grt 1_Line 17	277	36.8	0.1	21.6	34.3	1.4	1.4	5.1	0.1	0.0	0.0	101
Grt 1_Line 18	293	36.7	0.1	21.5	33.4	1.5	1.4	5.6	0.0	0.0	0.0	100
Grt 1_Line 19	309	36.7	0.1	21.6	33.3	1.4	1.5	5.7	0.0	0.0	0.0	100
Grt 1_Line 20	326	36.7	0.0	21.6	34.1	1.6	1.2	5.3	0.0	0.0	0.0	101
Grt 1_Line 21	342	37.1	0.0	21.6	33.4	1.7	1.2	6.0	0.0	0.0	0.0	101
Grt 1_Line 22	358	37.1	0.0	21.1	32.9	1.7	1.2	6.1	0.0	0.0	0.0	100
Grt 1_Line 23	375	37.1	0.0	21.6	32.5	1.9	1.8	5.9	0.0	0.0	0.0	101
Grt 1_Line 24	391	37.1	0.0	21.6	32.8	2.7	1.8	4.9	0.0	0.0	0.0	101
Grt 1_Line 25	407	37.0	0.1	21.3	31.2	3.5	0.8	7.0	0.0	0.0	0.0	101
Grt 1_Line 26	423	37.0	0.1	21.2	31.0	3.5	0.7	7.3	0.0	0.0	0.0	101
Grt 1_Line 27	440	36.9	0.1	21.2	30.7	3.5	0.8	7.3	0.0	0.0	0.0	100
Grt 1_Line 28	456	37.0	0.1	21.2	31.2	3.3	0.9	6.9	0.0	0.0	0.0	101
Grt 1_Line 29	472	37.1	0.1	21.3	31.5	3.0	1.1	6.7	0.0	0.0	0.0	101
Grt 1_Line 30	489	37.1	0.0	21.3	32.7	3.4	1.0	5.6	0.0	0.0	0.0	101
Grt 1_Line 31	505	37.1	0.1	21.2	31.5	3.4	0.8	6.3	0.0	0.0	0.0	100
Grt 1_Line 32	521	37.1	0.0	21.2	32.4	3.6	0.8	5.6	0.0	0.0	0.0	101
Grt 1_Line 33	537	37.0	0.1	21.5	31.8	3.3	0.9	6.1	0.0	0.0	0.0	101
Grt 1_Line 34	554	37.0	0.1	21.4	32.0	3.0	1.0	6.0	0.0	0.0	0.0	101
Grt 1_Line 35	570	37.0	0.0	21.5	32.6	3.2	0.9	5.3	0.0	0.0	0.0	100
Grt 1_Line 36	586	37.1	0.1	21.3	31.3	3.0	0.8	6.5	0.0	0.0	0.0	100
Grt 1_Line 37	603	37.1	0.1	21.3	31.7	2.9	0.8	6.5	0.0	0.0	0.0	100
Grt 1_Line 38	619	37.1	0.1	21.3	31.6	2.9	0.7	6.7	0.0	0.0	0.0	100
Grt 1_Line 39	635	37.1	0.1	21.3	31.6	2.8	0.8	6.6	0.0	0.0	0.0	100

Grt 1_Line 40	652	36.9	0.1	21.3	31.4	2.9	0.8	6.8	0.0	0.0	0.0	100
Grt 1_Line 41	668	36.9	0.0	21.2	32.2	2.8	0.8	6.6	0.0	0.0	0.0	101
Grt 1_Line 42	684	36.8	0.0	21.1	32.6	2.8	0.8	6.2	0.0	0.0	0.0	100
Grt 1_Line 43	700	36.8	0.1	21.3	32.6	2.7	0.9	6.1	0.0	0.0	0.0	100
Grt 1_Line 44	717	36.9	0.1	21.2	33.1	2.6	1.0	5.9	0.0	0.0	0.0	101
Grt 1_Line 45	733	37.0	0.1	21.1	32.3	2.4	0.9	6.6	0.0	0.0	0.0	100
Grt 1_Line 46	749	37.1	0.0	21.4	33.3	2.1	1.0	5.9	0.0	0.0	0.0	101
Grt 1_Line 47	766	37.0	0.0	21.5	33.7	2.0	1.0	5.8	0.0	0.0	0.0	101
Grt 1_Line 48	782	37.0	0.0	21.5	33.9	1.8	1.1	5.8	0.0	0.0	0.0	101
Grt 1_Line 49	798	37.2	0.1	21.4	33.2	1.7	1.0	6.5	0.0	0.0	0.0	101
Grt 1_Line 50	814	37.2	0.1	21.3	33.5	1.6	1.0	6.3	0.0	0.0	0.0	101
Grt 1_Line 51	831	37.0	0.0	21.6	34.2	1.5	1.0	5.8	0.1	0.0	0.0	101
Grt 1_Line 52	847	36.9	0.1	21.7	33.8	1.5	1.1	5.9	0.1	0.0	0.0	101
Grt 1_Line 53	863	36.9	0.1	21.6	34.0	1.5	1.0	5.8	0.1	0.0	0.0	101
Grt 1_Line 54	880	36.7	0.1	21.6	34.4	1.3	1.1	5.7	0.0	0.0	0.0	101
Grt 1_Line 55	896	36.9	0.1	21.8	34.7	1.1	1.3	5.3	0.0	0.0	0.0	101
Grt 1_Line 56	912	37.2	0.1	21.7	34.6	1.1	1.4	5.4	0.0	0.0	0.0	101
Grt 1_Line 57	928	36.9	0.1	21.7	34.2	0.9	1.3	6.3	0.0	0.0	0.0	101
Grt 1_Line 58	945	36.7	0.2	21.7	34.4	0.8	1.3	6.1	0.0	0.0	0.0	101
Grt 1_Line 59	961	37.1	0.1	21.8	33.8	0.6	2.0	5.6	0.0	0.0	0.0	101
Grt 1_Line 60	977	37.2	0.2	22.0	33.6	0.6	2.1	5.5	0.1	0.0	0.0	101
Grt 2_Line 1	19	37.4	0.1	21.6	32.8	0.6	2.5	5.3	0.1	0.0	0.0	100
Grt 2_Line 2	39	37.3	0.1	21.9	32.2	0.8	2.4	5.7	0.1	0.0	0.0	101
Grt 2_Line 3	58	37.3	0.1	21.7	32.5	1.2	1.9	5.6	0.1	0.0	0.0	100
Grt 2_Line 4	78	37.3	0.1	21.8	32.5	1.3	1.6	6.1	0.1	0.0	0.0	101
Grt 2_Line 5	97	37.0	0.1	21.6	33.0	1.5	1.0	6.3	0.2	0.0	0.0	101
Grt 2_Line 6	116	37.4	0.1	21.6	32.6	1.5	1.1	6.5	0.1	0.0	0.0	101
Grt 2_Line 7	136	37.1	0.1	21.6	33.3	1.6	1.1	5.6	0.1	0.0	0.0	100
Grt 2_Line 8	155	37.0	0.1	21.4	32.6	1.7	1.1	6.2	0.1	0.0	0.0	100
Grt 2_Line 9	174	37.0	0.1	21.7	31.9	1.7	1.3	6.7	0.1	0.0	0.0	100
Grt 2_Line 10	194	37.1	0.1	21.4	32.1	1.9	0.9	6.9	0.1	0.0	0.0	100
Grt 2_Line 11	213	37.0	0.0	21.4	33.0	2.0	1.0	6.3	0.1	0.0	0.0	101
Grt 2_Line 12	233	37.1	0.0	21.3	31.9	1.9	0.8	7.6	0.0	0.0	0.0	101
Grt 2_Line 13	252	36.9	0.1	21.4	33.3	2.3	0.9	6.1	0.0	0.0	0.0	101
Grt 2_Line 14	271	37.0	0.1	21.3	32.6	2.5	0.8	6.5	0.0	0.0	0.0	101
Grt 2_Line 15	291	36.8	0.0	21.5	33.7	2.7	0.9	5.0	0.1	0.0	0.0	101
Grt 2_Line 16	310	37.0	0.1	21.3	32.0	2.6	0.8	6.9	0.0	0.0	0.0	101
Grt 2_Line 17	329	36.6	0.1	21.0	32.9	2.9	0.8	6.0	0.0	0.0	0.0	100
Grt 2_Line 18	349	37.1	0.1	21.2	32.2	2.9	0.8	6.4	0.0	0.0	0.0	101
Grt 2_Line 19	368											
Grt 2_Line 20	388	37.3	0.0	21.7	32.0	3.2	0.9	6.2	0.0	0.0	0.0	101
Grt 2_Line 21	407	37.8	0.1	22.0	29.4	3.1	0.6	8.7	0.0	0.0	0.0	102
Grt 2_Line 22	426											
Grt 2_Line 23	446	36.7	0.1	20.9	32.6	3.9	0.7	5.3	0.0	0.0	0.0	100
Grt 2_Line 24	465	36.7	0.1	21.0	31.8	3.9	0.6	5.9	0.0	0.0	0.0	100
Grt 2_Line 25	485	36.7	0.1	21.0	31.0	4.1	0.6	6.7	0.0	0.0	0.0	100

Grt 2_Line 26	504	36.7	0.1	20.9	32.0	4.4	0.7	5.4	0.0	0.0	0.0	100
Grt 2_Line 27	523											
Grt 2_Line 28	543	37.0	0.1	20.8	31.4	4.0	0.6	6.9	0.0	0.0	0.0	101
Grt 2_Line 29	562	37.0	0.1	21.0	31.2	3.9	0.5	6.5	0.0	0.0	0.0	100
Grt 2_Line 30	581	36.8	0.1	20.9	32.3	3.5	1.0	5.5	0.0	0.0	0.0	100
Grt 2_Line 31	601	37.0	0.0	20.9	32.0	4.0	0.8	5.6	0.1	0.0	0.0	100
Grt 2_Line 32	620	37.0	0.1	21.0	31.2	3.5	0.8	6.9	0.0	0.0	0.1	101
Grt 2_Line 33	640	37.0	0.1	21.1	31.6	3.4	0.6	7.1	0.0	0.0	0.0	101
Grt 2_Line 34	659	36.9	0.0	21.1	31.6	3.3	0.6	7.1	0.1	0.0	0.0	101
Grt 2_Line 35	678	37.0	0.1	21.3	31.7	3.1	0.8	6.7	0.0	0.0	0.1	101
Grt 2_Line 36	698	36.9	0.0	21.3	32.5	3.1	0.8	6.1	0.1	0.0	0.0	101
Grt 2_Line 37	717											
Grt 2_Line 38	737	37.7	0.0	21.7	31.6	0.7	2.9	6.3	0.0	0.0	0.0	101
Grt 2_Line 39	756											
Grt 2_Line 40	775	37.2	0.0	21.5	34.0	0.8	1.4	6.0	0.0	0.0	0.0	101
Grt 2_Line 41	795	36.9	0.0	21.4	32.6	1.7	1.3	6.5	0.0	0.0	0.0	100
Grt 2_Line 42	814	36.8	0.0	21.6	33.5	1.8	1.2	5.8	0.0	0.0	0.0	101
Grt 2_Line 43	833	37.2	0.0	21.5	33.9	1.6	1.1	5.9	0.1	0.0	0.0	101
Grt 2_Line 44	853	37.0	0.1	21.5	33.7	1.3	1.3	5.9	0.0	0.0	0.0	101
Grt 2_Line 45	872	37.2	0.1	21.6	34.2	1.1	1.3	5.4	0.0	0.0	0.0	101
Grt 2_Line 46	892	37.0	0.1	21.5	34.6	1.1	1.2	5.6	0.1	0.0	0.0	101
Grt 2_Line 47	911	37.1	0.1	21.6	34.1	0.9	1.1	5.9	0.0	0.0	0.0	101
Grt 2_Line 48	930	37.0	0.1	21.4	34.8	0.7	1.2	5.3	0.0	0.0	0.0	101
Grt 2_Line 49	950	36.9	0.0	21.7	35.3	0.5	1.3	5.3	0.0	0.0	0.0	101
Grt 2_Line 50	969	37.1	0.1	21.6	34.9	0.4	1.4	5.6	0.0	0.0	0.0	101
Grt 3_rim		36.9	0.2	21.4	34.7	0.5	1.5	5.5	0.0	0.0	0.0	101
Grt 3_core		36.9	0.2	21.2	32.1	3.9	0.9	5.9	0.0	0.0	0.0	101
Grt 4_rim		36.8	0.2	21.3	32.1	2.7	1.0	6.6	0.0	0.0	0.0	101
Grt 4_core		36.8	0.1	21.3	34.0	0.6	1.3	6.1	0.0	0.0	0.0	100
Grt 5_rim		37.0	0.0	21.4	31.6	4.3	0.7	6.6	0.0	0.0	0.0	102
Grt 5_core		37.5	0.3	22.0	33.0	0.8	2.0	6.2	0.0	0.0	0.0	102
Grt 6_core		37.1	0.2	20.9	23.7	9.6	0.4	8.7	0.0	0.0	0.0	101

B09 garnet	distance (micron)	SiO2	TiO2	Al2O3	FeO	MnO	MgO	CaO	Na2O	K2O	Cr2O3	Total
Grt 1_Line 1	16	36.8	0.1	21.4	34.8	0.2	1.7	5.5	0.0	0.0	0.0	101
Grt 1_Line 2	31	36.4	0.1	21.4	34.6	0.3	1.6	5.4	0.0	0.0	0.0	100
Grt 1_Line 3	47	36.8	0.1	21.3	35.0	0.3	1.7	4.9	0.0	0.0	0.0	100
Grt 1_Line 4	63	36.7	0.1	21.3	34.8	0.4	1.7	5.1	0.0	0.0	0.0	100
Grt 1_Line 5	79	36.8	0.1	21.2	35.0	0.5	1.5	5.0	0.0	0.0	0.0	100
Grt 1_Line 6	94	36.7	0.2	21.1	34.7	0.6	1.4	5.4	0.0	0.0	0.0	100
Grt 1_Line 7	110	36.6	0.1	21.4	34.2	0.6	1.4	5.7	0.0	0.0	0.0	100
Grt 1_Line 8	126	37.0	0.1	21.5	34.3	0.8	1.4	5.7	0.0	0.0	0.0	101
Grt 1_Line 9	142	36.7	0.1	21.4	34.6	0.9	1.2	5.6	0.0	0.0	0.1	101

Grt 1_Line 10	157	36.8	0.1	21.4	34.3	1.1	1.2	5.7	0.0	0.0	0.0	101
Grt 1_Line 11	173	36.9	0.1	21.5	34.7	1.3	1.1	5.4	0.0	0.0	0.0	101
Grt 1_Line 12	189	36.8	0.1	21.4	35.0	1.6	1.1	5.1	0.0	0.0	0.0	101
Grt 1_Line 13	204	36.9	0.1	21.3	34.1	1.6	1.1	5.5	0.0	0.0	0.1	101
Grt 1_Line 14	220	36.9	0.1	21.5	34.2	1.9	1.0	5.5	0.0	0.0	0.0	101
Grt 1_Line 15	236	36.9	0.1	21.3	34.3	1.9	0.9	5.5	0.0	0.0	0.0	101
Grt 1_Line 16	252	36.7	0.1	21.3	34.0	2.0	1.0	5.3	0.1	0.0	0.0	101
Grt 1_Line 17	267	36.8	0.1	21.4	33.7	2.3	1.0	5.4	0.0	0.0	0.0	101
Grt 1_Line 18	283	37.0	0.1	21.3	34.1	2.4	1.2	5.4	0.0	0.0	0.0	102
Grt 1_Line 19	299											
Grt 1_Line 20	315	37.1	0.1	21.3	33.0	2.7	1.2	5.7	0.0	0.0	0.0	101
Grt 1_Line 21	330	36.8	0.1	21.5	33.3	2.6	1.3	5.4	0.0	0.0	0.0	101
Grt 1_Line 22	346	36.9	0.1	21.4	33.0	2.7	1.3	5.5	0.1	0.0	0.0	101
Grt 1_Line 23	362	36.9	0.1	21.4	32.7	2.6	1.3	5.7	0.1	0.0	0.0	101
Grt 1_Line 24	378	36.7	0.1	21.3	32.4	2.8	1.0	5.8	0.0	0.0	0.0	100
Grt 1_Line 25	393	36.9	0.1	21.3	33.2	2.9	1.1	5.5	0.0	0.0	0.0	101
Grt 1_Line 26	409	36.9	0.1	21.3	33.0	3.1	0.9	5.6	0.1	0.0	0.0	101
Grt 1_Line 27	425	36.8	0.1	21.3	33.3	2.9	1.0	5.3	0.1	0.0	0.0	101
Grt 1_Line 28	440	37.1	0.1	21.6	33.4	2.5	1.1	5.5	0.0	0.0	0.0	101
Grt 1_Line 29	456											
Grt 1_Line 30	472	36.8	0.1	21.5	32.8	2.0	1.4	5.7	0.0	0.0	0.0	100
Grt 1_Line 31	488	36.9	0.1	21.5	33.1	1.8	1.5	5.6	0.0	0.0	0.0	101
Grt 1_Line 32	503											
Grt 1_Line 33	519	36.9	0.1	21.5	33.9	1.8	1.5	5.2	0.0	0.0	0.0	101
Grt 1_Line 34	535	37.0	0.1	21.5	33.7	1.6	1.2	5.8	0.0	0.0	0.0	101
Grt 1_Line 35	551	36.6	0.1	21.3	34.1	1.4	1.2	5.5	0.0	0.0	0.0	100
Grt 1_Line 36	566	36.8	0.1	21.7	34.2	1.3	1.3	5.4	0.0	0.0	0.0	101
Grt 1_Line 37	582	36.6	0.1	21.4	34.8	1.2	1.1	5.3	0.0	0.0	0.0	101
Grt 1_Line 38	598	36.8	0.1	21.5	35.1	1.0	1.1	5.3	0.1	0.0	0.0	101
Grt 1_Line 39	613	36.8	0.1	21.2	35.1	0.8	1.2	5.0	0.0	0.0	0.0	100
Grt 1_Line 40	629	36.6	0.1	21.3	34.8	0.7	1.5	5.3	0.0	0.0	0.0	100
Grt 1_Line 41	645	36.8	0.1	21.5	34.9	0.6	1.4	5.4	0.0	0.0	0.0	101
Grt 1_Line 42	661	36.8	0.1	21.5	35.5	0.6	1.4	4.9	0.1	0.0	0.0	101
Grt 1_Line 43	676	36.8	0.1	21.4	35.2	0.5	1.5	5.2	0.0	0.0	0.0	101
Grt 1_Line 44	692	36.9	0.1	21.4	35.4	0.5	1.3	5.2	0.1	0.0	0.0	101
Grt 1_Line 45	708	37.0	0.1	21.6	35.7	0.5	1.4	5.0	0.1	0.0	0.0	101
Grt 1_Line 46	724	37.1	0.1	21.5	34.8	0.4	1.9	4.8	0.1	0.0	0.0	101
Grt 1_Line 47	739											
Grt 1_Line 48	755	37.1	0.1	21.6	35.0	0.3	2.4	4.7	0.0	0.0	0.0	101
Grt 1_Line 49	771	37.0	0.1	21.6	35.4	0.3	2.0	4.8	0.0	0.0	0.0	101
Grt 1_Line 50	786	36.8	0.1	21.6	35.6	0.2	1.8	4.8	0.0	0.0	0.0	101
Grt 2_Line 1	15	37.2	0.1	21.7	35.1	0.2	2.2	4.6	0.0	0.0	0.0	101
Grt 2_Line 2	29	37.2	0.1	21.7	35.0	0.2	2.3	4.8	0.0	0.0	0.0	101
Grt 2_Line 3	44	37.0	0.0	21.6	35.2	0.2	2.1	4.9	0.1	0.0	0.0	101
Grt 2_Line 4	58	37.0	0.1	21.5	35.8	0.2	1.8	4.6	0.0	0.0	0.0	101
Grt 2_Line 5	73	36.8	0.1	21.5	35.9	0.2	1.6	4.8	0.0	0.0	0.0	101

Grt 2_Line 6	87	36.8	0.1	21.5	35.7	0.2	1.5	5.0	0.0	0.0	0.0	101
Grt 2_Line 7	102	36.7	0.1	21.4	35.4	0.2	1.4	5.1	0.1	0.0	0.0	100
Grt 2_Line 8	116	36.7	0.1	21.4	35.2	0.2	1.4	5.3	0.0	0.0	0.0	100
Grt 2_Line 9	131	36.9	0.1	21.4	35.6	0.3	1.4	5.1	0.0	0.0	0.0	101
Grt 2_Line 10	146	36.6	0.1	21.4	36.0	0.3	1.3	4.8	0.1	0.0	0.0	101
Grt 2_Line 11	160	36.6	0.0	21.4	36.2	0.4	1.4	4.6	0.0	0.0	0.0	101
Grt 2_Line 12	175	36.7	0.1	21.3	36.0	0.4	1.4	4.7	0.0	0.0	0.0	101
Grt 2_Line 13	189	36.7	0.1	21.4	35.6	0.5	1.4	4.8	0.0	0.0	0.0	100
Grt 2_Line 14	204	36.5	0.1	21.4	35.8	0.9	1.2	4.6	0.0	0.0	0.0	101
Grt 2_Line 15	218	37.2	0.1	20.5	33.8	1.1	1.8	5.0	0.0	0.0	0.0	100
Grt 2_Line 16	233	36.7	0.1	21.4	34.8	1.4	1.0	5.2	0.0	0.0	0.0	101
Grt 2_Line 17	247	36.1	0.1	21.0	34.6	1.8	1.0	5.2	0.0	0.0	0.0	100
Grt 2_Line 18	262	36.5	0.1	21.3	33.7	2.3	0.9	5.4	0.0	0.0	0.0	100
Grt 2_Line 19	277	36.7	0.1	21.3	33.5	2.6	0.9	5.2	0.0	0.0	0.0	100
Grt 2_Line 20	291	36.5	0.1	21.4	33.4	2.7	0.9	5.3	0.0	0.0	0.0	100
Grt 2_Line 21	306	36.6	0.1	21.2	32.9	2.9	0.9	5.7	0.0	0.0	0.0	100
Grt 2_Line 22	320	36.6	0.1	21.4	33.3	3.0	0.9	5.1	0.0	0.0	0.0	100
Grt 2_Line 23	335	36.4	0.1	21.3	33.5	3.3	1.0	4.9	0.0	0.0	0.0	100
Grt 2_Line 24	349	36.5	0.1	21.2	32.2	3.3	0.8	6.3	0.0	0.0	0.0	101
Grt 2_Line 25	364	36.3	0.1	21.1	31.7	3.5	0.9	6.2	0.0	0.0	0.0	100
Grt 2_Line 26	378	36.6	0.1	21.3	31.6	3.7	1.0	5.9	0.0	0.0	0.0	100
Grt 2_Line 27	393	36.6	0.1	21.1	32.5	4.3	1.1	4.9	0.0	0.0	0.0	101
Grt 2_Line 28	408	36.4	0.1	21.0	32.4	4.5	1.0	5.0	0.0	0.0	0.0	100
Grt 2_Line 29	422	36.5	0.1	21.0	31.3	4.7	0.9	5.7	0.1	0.0	0.0	100
Grt 2_Line 30	437	36.5	0.1	21.4	32.0	4.8	1.0	4.8	0.1	0.0	0.0	101
Grt 2_Line 31	451	36.5	0.1	21.2	30.8	4.7	0.9	6.2	0.0	0.0	0.0	100
Grt 2_Line 32	466	36.4	0.1	21.3	31.3	4.8	1.0	5.4	0.1	0.0	0.0	100
Grt 2_Line 33	480	36.5	0.0	21.3	32.0	4.5	1.1	5.1	0.0	0.0	0.0	101
Grt 2_Line 34	495	36.4	0.0	21.3	32.4	3.6	1.1	5.3	0.1	0.0	0.0	100
Grt 2_Line 35	509	36.4	0.1	21.1	31.8	5.1	0.9	5.2	0.0	0.0	0.0	101
Grt 2_Line 36	524	36.5	0.2	20.9	31.0	4.6	0.9	6.0	0.0	0.0	0.0	100
Grt 2_Line 37	539	36.8	0.1	21.0	32.1	4.6	1.1	4.7	0.0	0.0	0.0	100
Grt 2_Line 38	553	36.8	0.1	21.1	31.6	3.8	1.1	5.6	0.1	0.0	0.0	100
Grt 2_Line 39	568											
Grt 2_Line 40	582	36.7	0.1	21.5	32.9	3.2	1.1	5.0	0.1	0.0	0.0	101
Grt 2_Line 41	597	36.9	0.1	21.3	32.0	2.9	1.1	6.1	0.1	0.0	0.0	101
Grt 2_Line 42	611	36.6	0.1	21.2	32.2	3.0	1.2	5.5	0.1	0.0	0.0	100
Grt 2_Line 43	626	36.5	0.1	21.3	33.1	3.0	1.1	5.1	0.1	0.0	0.0	100
Grt 2_Line 44	640	36.7	0.1	21.4	34.2	2.9	1.1	4.4	0.1	0.0	0.0	101
Grt 2_Line 45	655	36.6	0.1	21.1	33.4	2.5	1.0	5.2	0.1	0.0	0.0	100
Grt 2_Line 46	670	36.7	0.1	21.2	34.1	2.1	1.1	5.1	0.1	0.0	0.0	100
Grt 2_Line 47	684	36.7	0.1	21.2	35.0	1.8	1.1	4.9	0.0	0.0	0.0	101
Grt 2_Line 48	699	36.6	0.1	21.1	34.8	1.4	1.1	5.4	0.0	0.0	0.0	100
Grt 2_Line 49	713	36.8	0.1	21.5	35.7	1.1	1.3	4.8	0.1	0.0	0.0	101
Grt 2_Line 50	728	36.8	0.1	21.5	35.4	0.9	1.5	4.8	0.1	0.0	0.0	101
Grt 2_Line 51	742	36.8	0.1	21.3	36.1	0.8	1.4	4.6	0.0	0.0	0.0	101

Grt 2_Line 52	757	36.8	0.1	21.3	35.9	0.6	1.3	5.0	0.0	0.0	0.0	101
Grt 2_Line 53	771	36.8	0.0	21.3	36.1	0.4	1.4	4.7	0.0	0.0	0.0	101
Grt 2_Line 54	786	36.6	0.1	21.4	35.8	0.4	1.6	4.5	0.1	0.0	0.0	100
Grt 2_Line 55	801	36.8	0.1	21.2	35.7	0.3	1.6	5.0	0.1	0.0	0.0	101
Grt 2_Line 56	815	36.8	0.1	21.4	35.7	0.3	1.5	5.4	0.0	0.0	0.0	101
Grt 2_Line 57	830	36.8	0.1	21.2	35.7	0.2	1.5	5.1	0.1	0.0	0.0	101
Grt 2_Line 58	844	36.7	0.1	21.2	35.9	0.2	1.6	4.9	0.0	0.0	0.0	101
Grt 2_Line 59	859	36.7	0.0	21.4	35.4	0.2	1.8	5.1	0.0	0.0	0.0	101
Grt 2_Line 60	873	36.9	0.0	21.2	34.8	0.2	2.0	4.9	0.1	0.0	0.0	100
Grt 3_rim		37.0	0.1	21.4	33.8	0.2	2.0	6.0	0.0	0.0	0.0	101
Grt 3_core		36.8	0.1	21.1	30.9	4.9	0.8	6.2	0.1	0.0	0.0	101

B08 garnet	distance (micron)	SiO2	TiO2	Al2O3	FeO	MnO	MgO	CaO	Na2O	K2O	Cr2O3	Total
Grt 1_Line 1	11	37.2	0.0	21.3	31.8	0.7	1.9	7.3	0.1	0.0	0.0	100
Grt 1_Line 2	22	37.1	0.0	21.5	32.7	0.8	2.0	7.0	0.0	0.0	0.0	101
Grt 1_Line 3	33	37.1	0.0	21.7	33.1	0.8	2.0	6.4	0.0	0.0	0.0	101
Grt 1_Line 4	44	37.1	0.0	21.5	33.4	0.9	2.1	6.2	0.0	0.0	0.0	101
Grt 1_Line 5	55	37.2	0.0	21.6	33.8	0.5	1.8	6.4	0.0	0.0	0.0	101
Grt 1_Line 6	66	37.3	0.0	21.6	33.9	0.5	2.0	6.1	0.0	0.0	0.0	101
Grt 1_Line 7	77	37.1	0.0	21.6	34.8	0.6	1.9	5.5	0.0	0.0	0.0	102
Grt 1_Line 8	87	36.8	0.1	21.4	34.6	0.8	1.6	5.6	0.0	0.0	0.0	101
Grt 1_Line 9	98	37.0	0.1	21.4	35.1	1.0	1.4	5.4	0.0	0.0	0.0	101
Grt 1_Line 10	109	36.2	0.0	21.0	34.9	1.3	1.2	5.3	0.0	0.0	0.0	100
Grt 1_Line 11	120	36.9	0.1	21.4	34.9	1.6	1.1	5.5	0.0	0.0	0.0	101
Grt 1_Line 12	131	36.8	0.1	21.4	34.4	1.7	1.0	5.6	0.0	0.0	0.0	101
Grt 1_Line 13	142	37.0	0.1	21.6	34.4	1.9	1.0	5.6	0.0	0.0	0.0	102
Grt 1_Line 14	153	36.9	0.1	21.4	33.9	2.1	1.0	5.8	0.0	0.0	0.0	101
Grt 1_Line 15	164	37.0	0.1	21.4	33.6	2.3	1.1	5.8	0.0	0.0	0.0	101
Grt 1_Line 16	175	37.0	0.1	21.5	33.4	2.3	1.3	5.8	0.0	0.0	0.0	102
Grt 1_Line 17	186	37.1	0.1	21.6	33.1	2.3	1.9	5.2	0.0	0.0	0.0	101
Grt 1_Line 18	197	37.1	0.1	21.5	32.5	2.3	1.9	5.8	0.0	0.0	0.0	101
Grt 1_Line 19	208	37.2	0.1	21.9	32.3	2.2	1.9	5.9	0.0	0.0	0.0	102
Grt 1_Line 20	219	37.1	0.1	21.5	32.2	2.4	1.9	5.9	0.0	0.0	0.0	101
Grt 1_Line 21	230	37.1	0.1	21.8	32.7	2.7	1.7	5.4	0.0	0.0	0.0	101
Grt 1_Line 22	240	37.1	0.0	21.7	33.1	3.0	1.5	5.2	0.0	0.0	0.0	102
Grt 1_Line 23	251	36.7	0.0	21.8	33.3	3.1	1.1	5.3	0.0	0.0	0.0	101
Grt 1_Line 24	262	36.8	0.1	21.5	32.2	3.2	0.9	6.5	0.0	0.0	0.0	101
Grt 1_Line 25	273	36.9	0.1	21.5	32.3	3.4	0.8	6.3	0.0	0.0	0.0	101
Grt 1_Line 26	284	36.9	0.1	21.5	32.2	3.5	0.9	6.2	0.1	0.0	0.0	102
Grt 1_Line 27	295	36.9	0.1	21.5	31.9	3.7	0.8	6.6	0.1	0.0	0.0	102
Grt 1_Line 28	306	36.8	0.2	21.5	31.6	3.8	1.0	6.6	0.0	0.0	0.0	101
Grt 1_Line 29	317	36.8	0.1	21.5	31.7	3.3	1.4	6.2	0.0	0.0	0.0	101
Grt 1_Line 30	328	37.0	0.1	21.5	31.8	3.4	1.3	6.2	0.0	0.0	0.0	101

Grt 1_Line 31	339	36.9	0.1	21.6	31.8	3.3	1.3	6.4	0.1	0.0	0.0	101
Grt 1_Line 32	350	37.1	0.1	21.5	32.6	3.0	1.3	6.0	0.1	0.0	0.0	102
Grt 1_Line 33	361	36.9	0.1	21.5	32.9	3.0	1.1	5.9	0.0	0.0	0.0	101
Grt 1_Line 34	372	37.0	0.1	21.4	33.0	2.8	1.0	6.1	0.0	0.0	0.0	101
Grt 1_Line 35	383	36.9	0.1	21.5	33.0	2.6	1.1	6.1	0.1	0.0	0.0	101
Grt 1_Line 36	393	37.1	0.1	21.6	33.0	2.3	1.5	5.8	0.1	0.0	0.0	102
Grt 1_Line 37	404	37.2	0.1	21.7	33.5	1.9	2.0	5.4	0.1	0.0	0.0	102
Grt 1_Line 38	415	37.1	0.1	21.7	33.5	1.8	2.2	5.0	0.0	0.0	0.0	101
Grt 1_Line 39	426	37.3	0.1	21.7	33.1	1.7	2.0	5.5	0.0	0.0	0.0	101
Grt 1_Line 40	437	37.3	0.1	21.7	33.8	1.8	2.0	5.1	0.0	0.0	0.0	102
Grt 1_Line 41	448	37.1	0.1	21.7	33.5	1.6	2.0	5.3	0.0	0.0	0.0	101
Grt 1_Line 42	459	37.3	0.1	21.7	33.9	1.6	1.9	5.1	0.0	0.0	0.0	102
Grt 1_Line 43	470	36.8	0.1	21.6	34.3	1.6	1.6	4.8	0.1	0.0	0.0	101
Grt 1_Line 44	481	36.6	0.1	21.5	33.7	1.5	1.2	5.9	0.0	0.0	0.0	101
Grt 1_Line 45	492	36.7	0.1	21.4	34.3	1.4	1.2	5.6	0.0	0.0	0.0	101
Grt 1_Line 46	503	36.8	0.1	21.7	33.7	1.1	1.5	5.8	0.1	0.0	0.0	101
Grt 1_Line 47	514	36.8	0.1	21.5	33.8	1.0	1.7	5.7	0.0	0.0	0.0	101
Grt 1_Line 48	525	36.8	0.0	21.7	33.9	0.8	1.8	5.4	0.1	0.0	0.0	101
Grt 1_Line 49	536	36.9	0.1	21.7	33.5	0.7	2.0	5.7	0.0	0.0	0.0	101
Grt 1_Line 50	547	36.8	0.0	21.7	33.3	0.6	2.0	5.7	0.0	0.0	0.0	100
Grt 2_Line 1	8	36.8	0.1	21.7	33.2	0.6	2.1	5.6	0.1	0.0	0.0	100
Grt 2_Line 2	17	37.1	0.1	21.6	33.3	0.7	2.2	5.4	0.1	0.0	0.0	100
Grt 2_Line 3	25	36.9	0.1	21.6	32.6	1.5	1.7	6.3	0.0	0.0	0.0	101
Grt 2_Line 4	33	36.9	0.1	21.3	32.5	1.5	1.0	7.0	0.0	0.0	0.0	100
Grt 2_Line 5	42	37.0	0.1	21.5	32.8	1.6	0.9	6.9	0.0	0.0	0.0	101
Grt 2_Line 6	50	36.9	0.1	21.4	33.1	1.6	0.9	6.9	0.1	0.0	0.0	101
Grt 2_Line 7	58	36.8	0.1	21.4	32.6	1.7	0.8	7.1	0.0	0.0	0.0	100
Grt 2_Line 8	67	36.8	0.0	21.4	32.7	1.7	0.8	7.2	0.0	0.0	0.0	101
Grt 2_Line 9	75	36.8	0.1	21.3	32.6	1.8	0.8	7.2	0.0	0.0	0.0	101
Grt 2_Line 10	83	36.7	0.1	21.3	32.1	1.8	0.8	7.6	0.0	0.0	0.0	100
Grt 2_Line 11	91	36.7	0.1	21.2	32.5	2.1	0.8	7.3	0.0	0.0	0.0	100
Grt 2_Line 12	100	36.9	0.1	21.3	32.0	2.1	0.7	7.5	0.0	0.0	0.0	101
Grt 2_Line 13	108	36.8	0.1	21.3	32.6	2.2	0.7	7.3	0.0	0.0	0.0	101
Grt 2_Line 14	116	37.1	0.1	21.2	32.7	2.2	0.7	7.3	0.0	0.0	0.0	101
Grt 2_Line 15	125	36.8	0.1	21.3	31.8	2.4	0.8	7.4	0.0	0.0	0.0	100
Grt 2_Line 16	133	36.9	0.1	21.2	32.7	2.6	0.7	6.9	0.0	0.0	0.0	101
Grt 2_Line 17	141	37.0	0.1	21.1	32.3	2.6	0.6	7.4	0.0	0.0	0.0	101
Grt 2_Line 18	150	36.9	0.1	21.3	32.5	2.7	0.6	7.0	0.0	0.0	0.0	101
Grt 2_Line 19	158	36.8	0.1	21.2	33.0	2.7	0.7	6.8	0.0	0.0	0.0	101
Grt 2_Line 20	166	37.0	0.1	21.3	32.1	2.6	0.6	7.6	0.0	0.0	0.0	101
Grt 2_Line 21	175	36.7	0.1	21.1	32.3	2.6	0.7	7.5	0.0	0.0	0.0	101
Grt 2_Line 22	183	36.9	0.1	21.3	32.6	2.6	0.6	7.0	0.0	0.0	0.0	101
Grt 2_Line 23	191	36.8	0.0	21.3	32.7	2.6	0.6	7.0	0.0	0.0	0.0	101
Grt 2_Line 24	200	36.8	0.1	21.1	32.6	2.6	0.6	6.8	0.0	0.0	0.0	101
Grt 2_Line 25	208	36.8	0.1	21.3	32.4	2.6	0.7	6.9	0.0	0.0	0.0	101
Grt 2_Line 26	216	36.8	0.1	21.3	32.1	2.5	0.6	7.2	0.0	0.0	0.0	101

Grt 2_Line 27	224	36.8	0.0	21.2	32.6	2.6	0.7	6.9	0.0	0.0	0.0	101
Grt 2_Line 28	233	36.8	0.0	21.1	31.9	2.5	0.6	7.7	0.0	0.0	0.0	101
Grt 2_Line 29	241	36.9	0.1	21.3	32.5	2.5	0.7	7.1	0.1	0.0	0.0	101
Grt 2_Line 30	249	36.9	0.1	21.2	32.9	2.3	0.7	6.9	0.0	0.0	0.0	101
Grt 2_Line 31	258	36.9	0.0	21.4	33.5	2.3	0.7	6.5	0.0	0.0	0.0	101
Grt 2_Line 32	266	36.8	0.0	21.2	32.3	2.2	0.7	7.4	0.1	0.0	0.0	101
Grt 2_Line 33	274	36.9	0.1	21.3	33.3	2.2	0.8	6.7	0.1	0.0	0.0	101
Grt 2_Line 34	283	36.8	0.1	21.2	32.7	2.1	0.9	6.9	0.0	0.0	0.0	101
Grt 2_Line 35	291	36.8	0.1	21.2	32.7	2.0	0.7	7.2	0.1	0.0	0.0	101
Grt 2_Line 36	299	37.0	0.1	21.2	33.0	2.0	0.7	6.7	0.0	0.0	0.0	101
Grt 2_Line 37	308	36.9	0.1	21.3	32.5	1.7	0.8	7.3	0.0	0.0	0.0	101
Grt 2_Line 38	316	36.8	0.1	21.4	33.1	1.8	0.8	6.8	0.0	0.0	0.0	101
Grt 2_Line 39	324	36.9	0.1	21.3	33.6	1.7	0.8	6.7	0.1	0.0	0.0	101
Grt 2_Line 40	333	36.9	0.1	21.3	33.2	1.7	0.8	7.1	0.1	0.0	0.0	101
Grt 2_Line 41	341	36.7	0.1	21.3	33.3	1.6	0.8	7.0	0.0	0.0	0.0	101
Grt 2_Line 42	349	36.9	0.1	21.4	33.1	1.6	0.8	7.3	0.1	0.0	0.0	101
Grt 2_Line 43	358	36.7	0.0	21.5	32.9	1.5	1.0	7.2	0.0	0.0	0.0	101
Grt 2_Line 44	366	36.5	0.1	21.5	33.4	1.5	1.0	6.7	0.0	0.0	0.0	101
Grt 2_Line 45	374	36.5	0.0	21.6	34.2	1.5	1.0	6.1	0.0	0.0	0.0	101
Grt 2_Line 46	382	36.5	0.0	21.6	34.2	1.5	1.1	5.9	0.0	0.0	0.0	101
Grt 2_Line 47	391	36.5	0.0	21.6	34.7	1.4	1.1	5.7	0.0	0.0	0.0	101
Grt 2_Line 48	399	36.4	0.0	21.7	35.4	1.4	1.2	5.1	0.0	0.0	0.0	101
Grt 2_Line 49	407	36.5	0.0	21.7	35.2	1.3	1.2	5.3	0.0	0.0	0.0	101
Grt 2_Line 50	416	36.6	0.0	21.5	35.1	1.2	1.2	5.3	0.0	0.0	0.0	101
Grt 2_Line 51	424	37.5	0.0	21.3	35.3	1.2	1.7	4.8	0.0	0.0	0.0	102
Grt 2_Line 52	432	36.6	0.1	21.7	35.3	1.1	1.2	5.3	0.0	0.0	0.0	101
Grt 2_Line 53	441	36.7	0.0	21.4	35.3	1.0	1.2	5.5	0.0	0.0	0.0	101
Grt 2_Line 54	449	36.7	0.1	21.5	35.1	0.9	1.2	5.5	0.0	0.0	0.0	101
Grt 2_Line 55	457	36.8	0.1	21.5	35.1	0.7	1.2	5.7	0.0	0.0	0.0	101
Grt 2_Line 56	466	36.8	0.1	21.4	35.2	0.6	1.2	5.8	0.0	0.0	0.0	101
Grt 2_Line 57	474	36.7	0.1	21.6	35.4	0.5	1.3	5.5	0.0	0.0	0.0	101
Grt 2_Line 58	482	37.0	0.1	21.6	35.0	0.4	1.4	5.8	0.0	0.0	0.0	101
Grt 2_Line 59	491	36.9	0.1	21.7	34.7	0.3	1.5	6.0	0.0	0.0	0.0	101
Grt 2_Line 60	499	37.0	0.1	21.6	33.9	0.5	1.7	6.0	0.0	0.0	0.0	101
Grt 3_rim		37.3	0.1	21.9	32.1	1.0	2.0	6.7	0.0	0.0	0.0	101
Grt 3_core		36.7	0.1	21.2	31.6	3.5	0.5	7.3	0.1	0.0	0.0	101

B07 garnet	distance (micron)	SiO2	TiO2	Al2O3	FeO	MnO	MgO	CaO	Na2O	K2O	Cr2O3	Total
Grt 1_Line 1	9	36.9	0.1	21.6	34.3	0.5	1.5	6.1	0.0	0.0	0.0	101
Grt 1_Line 2	19	36.9	0.0	21.5	34.1	0.4	1.4	6.3	0.0	0.0	0.0	101
Grt 1_Line 3	28	36.9	0.1	21.6	33.8	0.5	1.5	6.5	0.1	0.0	0.0	101
Grt 1_Line 4	37	37.2	0.0	21.8	33.3	0.5	1.9	6.3	0.0	0.0	0.0	101
Grt 1_Line 5	46	36.9	0.0	21.7	33.9	0.5	1.8	6.0	0.0	0.0	0.0	101

Grt 1_Line 6	56	37.0	0.0	21.6	34.0	0.6	2.0	5.7	0.0	0.0	0.0	101
Grt 1_Line 7	65	37.2	0.0	21.7	34.0	0.6	2.1	5.6	0.1	0.0	0.0	101
Grt 1_Line 8	74	36.8	0.1	21.6	33.1	0.8	1.4	7.0	0.0	0.0	0.0	101
Grt 1_Line 9	83	36.9	0.1	21.4	33.1	1.0	1.2	7.2	0.1	0.0	0.0	101
Grt 1_Line 10	93	37.0	0.1	21.0	31.7	0.9	1.0	9.0	0.0	0.0	0.0	101
Grt 1_Line 11	102	37.0	0.1	21.6	33.6	1.2	1.0	7.0	0.1	0.0	0.0	102
Grt 1_Line 12	111	36.7	0.1	21.4	33.2	1.2	1.3	6.6	0.0	0.0	0.0	101
Grt 1_Line 13	120	36.7	0.1	21.1	33.4	1.4	1.0	7.1	0.0	0.0	0.0	101
Grt 1_Line 14	130	36.8	0.1	21.2	33.6	1.4	0.8	7.1	0.0	0.0	0.0	101
Grt 1_Line 15	139	36.8	0.1	21.0	32.6	1.4	0.8	7.8	0.0	0.0	0.0	101
Grt 1_Line 16	148	37.0	0.1	21.0	32.8	1.5	1.2	6.7	0.0	0.0	0.0	100
Grt 1_Line 17	157	36.8	0.1	21.3	33.2	1.7	0.8	7.0	0.0	0.0	0.0	101
Grt 1_Line 18	167	36.8	0.2	21.0	32.6	1.7	0.7	7.7	0.0	0.0	0.0	101
Grt 1_Line 19	176	36.6	0.1	21.0	32.7	1.8	1.0	7.4	0.0	0.0	0.0	101
Grt 1_Line 20	185	36.6	0.1	20.9	33.1	1.9	0.7	7.1	0.0	0.0	0.0	100
Grt 1_Line 21	195	39.2	0.2	21.3	32.3	1.9	1.8	7.1	0.0	0.0	0.0	104
Grt 1_Line 22	204	36.8	0.1	21.1	31.6	2.0	0.7	8.5	0.0	0.0	0.0	101
Grt 1_Line 23	213	36.8	0.1	21.1	32.5	2.2	0.8	7.4	0.0	0.0	0.0	101
Grt 1_Line 24	222	36.6	0.1	21.2	32.5	2.2	0.7	7.3	0.0	0.0	0.0	101
Grt 1_Line 25	232	36.9	0.0	21.4	33.0	2.3	0.8	6.9	0.0	0.0	0.0	101
Grt 1_Line 26	241	36.7	0.0	21.3	32.9	2.1	0.8	6.9	0.0	0.0	0.0	101
Grt 1_Line 27	250	36.9	0.0	21.2	32.6	1.8	0.9	7.5	0.0	0.0	0.0	101
Grt 1_Line 28	259	36.6	0.0	21.4	34.3	1.9	1.1	5.6	0.0	0.0	0.1	101
Grt 1_Line 29	269	36.6	0.0	21.4	34.6	2.0	0.9	5.5	0.1	0.0	0.0	101
Grt 1_Line 30	278	36.6	0.0	21.4	34.6	2.0	0.9	5.8	0.0	0.0	0.0	101
Grt 1_Line 31	287	36.6	0.1	21.2	34.0	1.9	0.8	6.4	0.0	0.0	0.0	101
Grt 1_Line 32	296	36.8	0.1	21.1	33.2	1.6	0.9	6.9	0.0	0.0	0.0	101
Grt 1_Line 33	306											
Grt 1_Line 34	315	37.2	0.1	21.7	33.5	1.2	1.7	6.3	0.0	0.0	0.0	102
Grt 1_Line 35	324											
Grt 1_Line 36	334	37.0	0.1	21.4	34.1	1.0	1.3	6.1	0.0	0.0	0.0	101
Grt 1_Line 37	343	37.1	0.1	21.4	33.8	1.0	1.1	6.8	0.0	0.0	0.0	101
Grt 1_Line 38	352	36.9	0.1	21.5	33.7	0.9	1.1	7.0	0.0	0.0	0.0	101
Grt 1_Line 39	361	37.0	0.1	21.3	33.8	0.7	1.2	6.7	0.0	0.0	0.0	101
Grt 1_Line 40	371	37.0	0.1	21.6	33.5	0.6	1.4	6.6	0.0	0.0	0.0	101
Grt 1_Line 41	380	37.0	0.1	21.6	33.4	0.6	1.5	6.8	0.0	0.0	0.0	101
Grt 1_Line 42	389											
Grt 1_Line 43	398	36.8	0.0	21.5	34.0	0.5	1.6	6.3	0.0	0.0	0.0	101
Grt 1_Line 44	408	36.7	0.0	21.5	34.2	0.5	1.3	6.3	0.0	0.0	0.0	101
Grt 1_Line 45	417	36.9	0.0	21.6	34.2	0.4	1.4	6.2	0.0	0.0	0.0	101
Grt 1_Line 46	426	36.7	0.0	21.6	34.5	0.4	1.5	6.0	0.0	0.0	0.0	101
Grt 1_Line 47	435	37.2	0.0	21.7	33.0	0.4	1.9	6.6	0.0	0.0	0.0	101
Grt 1_Line 48	445	37.2	0.0	21.7	31.6	0.9	2.0	7.5	0.0	0.0	0.0	101
Grt 1_Line 49	454	37.3	0.0	21.6	30.6	0.9	2.0	8.0	0.0	0.0	0.0	100
Grt 1_Line 50	463	37.4	0.0	21.7	28.6	0.6	2.3	9.8	0.0	0.0	0.0	100
Grt 2_Line 1	4	37.2	0.0	21.8	33.0	0.6	2.2	6.0	0.0	0.0	0.0	101

Grt 2_Line 2	8	36.8	0.0	21.8	33.8	0.4	2.1	5.6	0.0	0.0	0.0	100
Grt 2_Line 3	12	36.7	0.0	21.6	34.0	0.4	1.9	5.7	0.0	0.0	0.0	100
Grt 2_Line 4	16	36.8	0.0	21.7	33.8	0.3	1.8	5.8	0.0	0.0	0.0	100
Grt 2_Line 5	21	37.0	0.0	21.6	33.8	0.4	1.8	5.7	0.0	0.0	0.0	100
Grt 2_Line 6	25	37.1	0.0	21.7	33.5	0.4	1.7	6.1	0.0	0.0	0.0	100
Grt 2_Line 7	29	37.0	0.0	21.6	33.8	0.4	1.7	6.1	0.1	0.0	0.0	101
Grt 2_Line 8	33	36.9	0.0	21.6	33.7	0.4	1.7	6.0	0.0	0.0	0.0	100
Grt 2_Line 9	37	36.9	0.0	21.4	33.7	0.5	1.6	6.2	0.0	0.0	0.0	100
Grt 2_Line 10	41	36.8	0.0	21.7	33.7	0.4	1.5	6.4	0.0	0.0	0.0	101
Grt 2_Line 11	45	36.9	0.0	21.4	33.2	0.5	1.5	6.6	0.0	0.0	0.0	100
Grt 2_Line 12	49	36.8	0.0	21.4	33.5	0.5	1.3	7.0	0.0	0.0	0.0	101
Grt 2_Line 13	54	36.6	0.0	21.4	33.3	0.6	1.4	6.9	0.0	0.0	0.0	100
Grt 2_Line 14	58	36.5	0.0	21.3	33.0	0.7	1.3	7.1	0.0	0.0	0.0	100
Grt 2_Line 15	62	36.6	0.0	21.3	33.3	0.7	1.4	7.0	0.1	0.0	0.0	100
Grt 2_Line 16	66	36.8	0.0	21.3	33.5	0.7	1.3	6.7	0.0	0.0	0.0	100
Grt 2_Line 17	70	36.6	0.0	21.5	33.4	0.7	1.3	6.8	0.0	0.0	0.0	100
Grt 2_Line 18	74	36.7	0.0	21.3	33.1	0.8	1.4	7.0	0.0	0.0	0.0	100
Grt 2_Line 19	78	36.8	0.0	21.3	32.8	0.7	1.4	7.3	0.0	0.0	0.0	100
Grt 2_Line 20	82	36.6	0.0	21.5	33.0	0.8	1.2	7.2	0.0	0.0	0.0	100
Grt 2_Line 21	86	36.8	0.0	21.5	32.9	0.9	1.3	7.1	0.0	0.0	0.0	101
Grt 2_Line 22	91	36.8	0.0	21.5	32.5	1.0	1.3	7.2	0.0	0.0	0.0	100
Grt 2_Line 23	95	36.5	0.0	21.4	31.9	1.2	1.1	7.8	0.0	0.0	0.0	100
Grt 2_Line 24	99	36.8	0.0	21.1	32.1	1.2	1.5	7.2	0.0	0.0	0.0	100
Grt 2_Line 25	103	36.7	0.0	21.8	32.4	1.2	1.8	6.5	0.0	0.0	0.0	100
Grt 2_Line 26	107	36.6	0.0	21.8	32.5	1.1	1.9	6.3	0.0	0.0	0.0	100
Grt 2_Line 27	111	36.7	0.0	21.4	31.9	1.2	1.3	7.9	0.0	0.0	0.0	100
Grt 2_Line 28	115	36.5	0.0	21.3	31.7	1.2	1.2	7.8	0.1	0.0	0.0	100
Grt 2_Line 29	119											
Grt 2_Line 30	124	36.5	0.0	21.7	33.3	1.2	0.9	6.9	0.1	0.0	0.0	101
Grt 2_Line 31	128	36.6	0.0	21.3	33.1	1.2	0.9	7.0	0.1	0.0	0.0	100
Grt 2_Line 32	132	36.6	0.0	21.3	33.3	1.0	1.0	7.2	0.1	0.0	0.0	100
Grt 2_Line 33	136	36.7	0.0	21.4	32.9	0.9	1.1	7.1	0.1	0.0	0.0	100
Grt 2_Line 34	140	36.6	0.0	21.6	33.4	0.8	1.2	6.9	0.0	0.0	0.0	100
Grt 2_Line 35	144	36.7	0.0	21.6	33.6	0.8	1.3	6.7	0.1	0.0	0.0	101
Grt 2_Line 36	148	36.8	0.0	21.5	32.7	0.7	1.8	6.8	0.1	0.0	0.0	100
Grt 2_Line 37	152	36.9	0.0	21.6	31.9	0.6	2.2	7.1	0.1	0.0	0.0	101
Grt 2_Line 38	156	36.7	0.0	21.7	33.9	0.4	1.7	6.2	0.1	0.0	0.0	101
Grt 2_Line 39	161	36.8	0.0	21.6	33.8	0.4	1.5	6.6	0.0	0.0	0.0	101
Grt 2_Line 40	165	36.6	0.0	21.6	33.9	0.4	1.4	6.5	0.1	0.0	0.0	100
Grt 2_Line 41	169	36.7	0.0	21.7	34.5	0.4	1.5	6.0	0.0	0.0	0.0	101
Grt 2_Line 42	173	36.9	0.0	21.6	35.0	0.4	1.6	5.7	0.0	0.0	0.0	101
Grt 2_Line 43	177	37.0	0.0	21.7	34.6	0.4	1.8	5.4	0.0	0.0	0.0	101
Grt 2_Line 44	181	37.2	0.0	21.8	34.3	0.4	2.0	5.8	0.0	0.0	0.0	101
Grt 2_Line 45	185	37.3	0.0	21.9	33.4	0.5	2.1	6.1	0.0	0.0	0.0	101
Grt 2_Line 46	189	37.2	0.0	21.7	30.9	0.9	2.1	7.6	0.0	0.0	0.0	100
Grt 2_Line 47	194	37.4	0.0	21.8	30.1	1.0	3.1	7.2	0.0	0.0	0.0	101

Grt 2_Line 48	198	37.3	0.0	21.7	29.8	0.9	3.0	7.6	0.0	0.0	0.0	100
Grt 2_Line 49	202	37.5	0.0	21.5	28.5	0.8	2.2	9.7	0.0	0.0	0.0	100
Grt 2_Line 50	206	37.4	0.0	21.4	28.3	0.6	2.2	9.8	0.0	0.0	0.0	100

B06 garrnet	distance (micron)	SiO2	TiO2	Al2O3	FeO	MnO	MgO	CaO	Na2O	K2O	Cr2O3	Total
Grt 1_Line 1	8	37.2	0.0	21.4	28.7	1.3	0.8	11.3	0.0	0.0	0.0	101
Grt 1_Line 2	17	37.2	0.0	21.2	28.6	1.2	0.7	11.2	0.0	0.0	0.1	100
Grt 1_Line 3	25	37.1	0.0	21.3	29.3	1.3	0.8	10.4	0.0	0.0	0.0	100
Grt 1_Line 4	33	37.2	0.0	21.0	29.1	1.3	0.9	10.4	0.1	0.0	0.0	100
Grt 1_Line 5	42	37.2	0.0	21.0	29.6	1.4	0.8	10.4	0.0	0.0	0.0	100
Grt 1_Line 6	50	37.2	0.0	21.1	29.6	1.5	0.8	10.3	0.0	0.0	0.0	100
Grt 1_Line 7	59	37.2	0.0	20.8	30.2	1.8	0.7	9.8	0.0	0.0	0.0	101
Grt 1_Line 8	67	37.1	0.0	20.7	29.4	2.0	0.7	9.8	0.0	0.0	0.0	100
Grt 1_Line 9	75	37.0	0.0	20.7	29.5	2.2	0.6	10.1	0.1	0.0	0.0	100
Grt 1_Line 10	84	37.2	0.0	20.8	29.2	2.5	0.6	10.0	0.0	0.0	0.1	100
Grt 1_Line 11	92	37.0	0.0	20.8	29.1	3.0	0.6	9.5	0.0	0.0	0.0	100
Grt 1_Line 12	100											
Grt 1_Line 13	109	36.5	0.0	21.0	28.1	3.7	0.5	9.9	0.0	0.0	0.0	100
Grt 1_Line 14	117	36.4	0.1	21.1	27.6	3.9	0.5	10.4	0.0	0.0	0.0	100
Grt 1_Line 15	126	36.6	0.0	20.8	28.3	3.9	0.5	9.9	0.0	0.0	0.0	100
Grt 1_Line 16	134	36.7	0.0	21.0	28.7	3.9	0.5	9.2	0.0	0.0	0.0	100
Grt 1_Line 17	142	36.6	0.0	21.2	29.1	4.2	0.6	8.6	0.0	0.0	0.0	100
Grt 1_Line 18	151	36.5	0.0	21.0	29.2	4.4	0.6	8.7	0.1	0.0	0.0	100
Grt 1_Line 19	159	36.2	0.0	21.1	28.7	4.5	0.6	8.9	0.0	0.0	0.0	100
Grt 1_Line 20	167	36.3	0.0	21.1	28.8	5.0	0.6	8.4	0.0	0.0	0.0	100
Grt 1_Line 21	176	36.4	0.0	21.5	29.2	4.9	0.5	7.9	0.0	0.0	0.0	100
Grt 1_Line 22	184	37.1	0.0	21.5	29.0	4.5	0.6	8.2	0.0	0.0	0.0	101
Grt 1_Line 23	193											
Grt 1_Line 24	201											
Grt 1_Line 25	209											
Grt 1_Line 26	218											
Grt 1_Line 27	226	36.8	0.0	21.3	28.2	5.5	0.5	8.5	0.0	0.0	0.0	101
Grt 1_Line 28	234	37.0	0.0	21.6	28.4	5.1	0.5	8.6	0.0	0.0	0.0	101
Grt 1_Line 29	243	36.8	0.0	21.6	29.0	5.6	0.5	7.7	0.0	0.0	0.0	101
Grt 1_Line 30	251	36.8	0.0	21.5	29.2	5.4	0.5	7.6	0.0	0.0	0.0	101
Grt 1_Line 31	260	36.8	0.0	21.0	28.4	5.2	0.6	8.6	0.0	0.0	0.0	101
Grt 1_Line 32	268	36.9	0.0	21.0	28.2	5.0	0.7	8.8	0.0	0.0	0.0	101
Grt 1_Line 33	276	37.0	0.0	21.0	28.7	4.7	0.9	8.1	0.2	0.0	0.0	101
Grt 1_Line 34	285	36.9	0.0	21.0	28.6	4.7	0.6	8.7	0.0	0.0	0.0	101
Grt 1_Line 35	293	36.9	0.0	21.0	29.1	4.6	0.6	8.0	0.0	0.0	0.0	100
Grt 1_Line 36	301											
Grt 1_Line 37	310	36.7	0.0	20.9	27.6	4.4	0.5	9.5	0.0	0.0	0.0	100
Grt 1_Line 38	318											

Grt 1_Line 39	327	37.1	0.0	20.9	28.6	3.9	0.7	9.1	0.0	0.0	0.0	100
Grt 1_Line 40	335	37.1	0.0	21.0	29.0	3.9	0.7	8.7	0.0	0.0	0.0	100
Grt 1_Line 41	343	37.1	0.0	20.9	27.9	3.6	0.5	9.9	0.0	0.0	0.0	100
Grt 1_Line 42	352	37.0	0.0	21.0	27.7	3.7	0.5	10.3	0.0	0.0	0.0	100
Grt 1_Line 43	360	37.0	0.0	21.1	28.5	3.4	0.5	10.0	0.0	0.0	0.0	100
Grt 1_Line 44	368	37.2	0.0	21.3	28.9	2.6	0.7	10.0	0.0	0.0	0.0	101
Grt 1_Line 45	377	37.1	0.0	21.2	29.9	1.8	1.0	9.5	0.0	0.0	0.0	100
Grt 1_Line 46	385	37.2	0.0	21.5	29.5	1.5	0.8	10.3	0.0	0.0	0.0	101
Grt 1_Line 47	394	37.1	0.0	21.3	28.7	1.4	0.7	11.1	0.0	0.0	0.0	100
Grt 1_Line 48	402	37.2	0.0	21.2	28.0	1.4	0.7	11.5	0.0	0.0	0.0	100
Grt 1_Line 49	410	37.2	0.0	21.5	27.0	1.4	0.7	12.3	0.0	0.0	0.0	100
Grt 1_Line 50	419	37.4	0.0	21.4	27.9	1.5	2.0	10.1	0.0	0.0	0.0	100
Grt 2_rim		37.0	0.0	21.3	28.7	1.3	0.8	10.7	0.0	0.0	0.0	100
Grt 2_core		36.9	0.0	21.1	28.8	2.3	0.7	10.0	0.0	0.0	0.0	100
Grt 3_rim		37.1	0.0	21.1	28.6	1.3	0.7	11.0	0.0	0.0	0.0	100
Grt 3_core		37.0	0.0	20.8	29.1	1.5	0.8	10.4	0.0	0.0	0.0	100

B03 garnet	distance (micron)	SiO2	TiO2	Al2O3	FeO	MnO	MgO	CaO	Na2O	K2O	Cr2O3	Total
position not determined		37.9		21.0	25.0	1.3	1.5	13.6	0.0			100
position not determined		38.0		20.9	23.5	1.3	1.0	15.8	0.0			100
position not determined		37.8		20.7	22.9	1.3	0.9	16.6	0.0			100
position not determined		37.9		20.8	23.5	1.2	1.0	16.2	0.0			101
position not determined		37.7		21.2	28.2	2.0	2.0	9.4	0.0			101
position not determined		38.1		20.9	23.1	1.3	0.9	16.5	0.0			101
position not determined		38.0		20.9	24.1	1.0	1.0	15.3	0.0			100
position not determined		37.8		21.3	28.6	1.5	2.1	9.6	0.0			101
position not determined		37.8		21.3	28.3	1.4	1.9	9.9	0.0			101
position not determined		37.9		21.0	25.6	1.0	1.5	13.1	0.0			100
position not determined		37.9		21.0	24.1	1.0	1.1	15.1	0.0			100
position not determined		38.1		21.0	23.0	1.3	0.9	16.4	0.0			101
position not determined		37.9		20.9	23.1	1.3	0.9	16.2	0.0			100
position not determined		37.9		20.7	23.6	1.2	0.9	15.9	0.0			100
position not determined		38.0		20.7	24.1	1.1	1.2	15.3	0.0			100
position not determined		37.8		21.3	25.9	1.1	1.4	13.2	0.0			101
position not determined		37.7		21.1	26.1	1.0	1.5	12.8	0.0			100
position not determined		37.8		21.2	28.3	1.5	1.8	9.8	0.0			100
position not determined		37.4		21.2	28.6	1.4	1.8	9.6				100

position not determined	37.9		21.0	24.9	1.0	1.3	14.0	0.0	100
anhedral garnet included within Ca-amphibole	37.8		20.9	23.6	1.7	1.0	15.2	0.0	100
anhedral garnet included within epidote	38.0	0.1	20.9	22.9	1.9	0.9	15.7	0.0	100

Table S5. Composition of amphiboles determined by EPMA.

Sample	Distance (cm)	Oxides (wt.%)										1 SD								
		SiO2	TiO2	Al2O3	FeO*	MnO	MgO	CaO	Na2O	K2O	Total	SiO2	TiO2	Al2O3	FeO*	MnO	MgO	CaO	Na2O	K2O
B13	0	57.8		0.1	3.6	0.1	22.0	12.9	0.3	0.1	96.8	0.1		0.0	0.2	0.1	0.2	0.1	0.1	0.0
B01	10	55.8		1.4	7.3	0.1	19.8	12.7	0.6	0.0	97.7	1.8		1.2	1.5	0.1	1.2	0.3	0.4	0.0
B02	15	55.7	0.1	1.4	8.4	0.2	18.7	12.4	0.7	0.0	97.6	1.1		0.7	1.1	0.0	0.8	0.2	0.2	0.0
B03	20	40.9	0.2	12.9	20.7	0.5	8.8	11.2	3.2	0.1	98.4	0.6	0.1	0.4	0.6	0.1	0.6	0.2	0.1	0.0
B04	25	49.4	0.1	7.0	16.0	0.2	11.7	9.4	2.9	0.2	96.8									
B05	30	48.7		6.0	17.5	0.1	11.6	10.3	2.3	0.1	96.5	4.0		2.8	3.5		2.7	0.3	0.7	0.1
B06	35	50.9	0.0	6.0	16.5	0.1	12.6	9.6	2.8	0.1	98.5	2.5	0.0	1.9	1.2	0.1	1.0	0.6	0.5	0.0
B07	45	53.0	0.0	5.2	13.6	0.1	14.0	8.9	3.0	0.1	98.1	1.8	0.1	1.9	1.5	0.0	1.8	1.8	1.2	0.0
B08	55	53.3	0.0	4.8	15.7	0.0	13.1	8.8	3.0	0.1	98.9	0.6	0.0	0.5	0.4	0.0	0.6	0.5	0.3	0.0
B09	75	48.3	0.0	10.0	17.7	0.1	10.2	8.3	4.2	0.2	99.3	3.5	0.0	2.7	2.1	0.1	1.9	1.7	1.1	0.1
B10	95	55.6	0.0	2.4	12.0	0.0	16.7	9.7	2.0	0.1	98.6	0.2	0.0	0.3	0.4	0.0	0.4	0.5	0.3	0.0

Table S6. Composition of clinopyroxene determined by EPMA.

Sample	Distance (cm)	Oxide (wt. %)									1 SD							
		SiO2	TiO2	Al2O3	FeO*	MnO	MgO	CaO	Na2O	Total	SiO2	TiO2	Al2O3	FeO*	MnO	MgO	CaO	Na2O
B01	10	52.1	0.2	1.2	8.4	0.3	12.7	22.0	0.8	97.7	2.1	0.1	0.6	2.3	0.1	1.4	1.1	0.2
B02	15	52.9	0.2	1.3	9.4	0.3	13.2	21.7	1.0	99.9	1.9		0.4	3.7	0.2	1.1	1.4	0.6
B03	20	53.3	0.2	1.5	9.5	0.3	12.8	21.5	1.1	100.1	1.6	0.1	0.4	3.2	0.2	0.7	1.2	0.6
B04	25	52.6	0.1	1.8	9.6	0.3	12.0	21.7	1.4	99.5	1.3		1.0	2.6	0.1	1.1	1.6	1.1
B05	30	52.1	0.2	2.3	10.6	0.4	11.7	19.9	2.0	99.1	2.3		0.8	3.5		0.4	0.4	2.0
B06	35	53.2	0.0	2.2	11.4	0.2	11.3	19.3	2.6	100.2	0.7	0.0	0.5	1.1	0.1	1.1	1.1	1.0
B07	45	52.8	0.1	2.0	11.3	0.2	12.1	20.4	1.8	100.6	0.8	0.0	0.2	1.2	0.1	0.2	0.2	0.6
B08	55	53.8	0.0	3.8	10.7	0.1	10.5	17.7	4.1	100.8	1.9	0.0	1.7	2.1	0.2	1.3	2.2	2.1
B09	75	55.3	0.0	6.3	11.1	0.1	7.5	13.6	6.8	100.6	0.4	0.0	0.4	1.8	0.1	1.0	0.8	0.4
B10	95	53.7	0.0	3.5	10.6	0.2	10.9	18.2	3.4	100.4	1.2	0.0	1.7	1.5	0.2	1.3	2.2	2.0

Table S7. Composition of chlorite determined by EPMA.

Sample	Distance (cm)	Oxide (wt.%)							Total
		SiO2	Al2O3	FeO*	MnO	MgO	CaO	Na2O	
B13	0	31.7	14.1	8.2		30.4			85.5
B01	10	30.6	16.7	11.8	0.1	27.6	0.0	0.1	87.0
B02	15	29.3	17.4	15.5	0.2	24.6	0.1	0.1	87.0
B03	20	27.7	18.3	22.0	0.4	19.3	0.1	0.1	87.8
B04	25	28.3	19.6	12.0	0.3	24.9	0.1		85.2

1 SD						
SiO2	Al2O3	FeO	MnO	MgO	CaO	Na2O
0.2	0.1	0.2	0.0	0.2		0.0
0.4	0.3	0.8	0.0	0.8	0.0	0.0
0.3	0.2	0.6	0.1	0.5	0.1	
0.5	0.8	1.6	0.1	1.3	0.0	0.0

Table S8. Composition of epidote determined by EPMA.

		Oxide (wt.%)								1 SD						
Sample	Distance (cm)	SiO2	TiO2	Al2O3	FeO	MnO	MgO	CaO	Total	SiO2	TiO2	Al2O3	FeO	MnO	MgO	CaO
B03	20	37.4		23.9	13.0	0.3	0.0	23.3	97.9	0.1		0.6	0.6	0.1	0.0	0.1
B04	25	37.3	0.2	26.4	10.2	0.2	0.1	23.4	97.7	0.3	0.1	1.4	1.7	0.1	0.0	0.1
B05	30	36.7	0.1	24.8	12.1	0.3	0.0	23.3	97.3			0.6	0.6	0.1	0.0	
B07	45	38.3	0.0	25.7	9.9	0.0	0.0	23.4	97.4	0.1	0.0	0.6	0.7	0.0	0.0	0.2
B08	55	38.9	0.0	27.1	8.6	0.0	0.1	22.8	97.5	0.3	0.0	1.7	2.1	0.0	0.1	0.5
B09	75	39.2		28.7	6.7	0.0	0.1	23.8	98.5	0.6		2.4	2.9	0.0	0.0	0.5

Table S9. Compositions of serpentine and talc determined by EPMA.

			Oxide (wt.%)								1 SD						
Serpentine	Sample	Distance (cm)	SiO2	Al2O3	FeO	MnO	MgO	Cr2O3	NiO	Total	SiO2	Al2O3	FeO	MnO	MgO	Cr2O3	NiO
	B14	-15	41.4	2.0	8.6	0.1	34.2	0.4	0.2	87.0	0.4	0.2	0.3		0.2	0.1	
	B15	-25	41.5	1.9	8.8	0.1	34.1	0.6	0.2	87.3	0.4	0.2	0.6	0.1	0.2	0.3	0.1

Talc	Sample	Distance (cm)	SiO2	Al2O3	FeO	MnO	MgO	Cr2O3	NiO		SiO2	Al2O3	FeO	MnO	MgO	Cr2O3	NiO
	B14	-15	62.0		2.5		28.8		0.3	93.6	0.0		0.2		0.0		0.1
	B15	-25	61.8		2.7		28.8		0.3	93.6	0.3		0.1		0.6		0.1

Table S10. Compositions of ilmenite and titanite determined by EPMA.

			Oxide (wt.%)				
Ilmenite	Sample	Distance (cm)	TiO2	FeO	MnO	MgO	Total
	B13	0	51.0	43.9	1.3	1.7	97.9
	B01	10	49.0	47.5	1.7	0.8	99
	B02	15	49.0	45.9	2.0	0.7	97.62
	B03	20	51.0	41.5	4.0	0.4	96.91
	B04	25	50.0	44.3	3.5	0.4	98.19

			Oxide (wt.%)						
Titanite	Sample	Distance (cm)	SiO2	TiO2	Al2O3	FeO	MgO	CaO	Total
	B01	10	30.3	39.0	0.4	0.7	0.0	28.5	98.98
	B01	10	30.7	38.0	0.5	0.8	0.0	28.6	98.58
	B02	15	30.6	38.0	0.7	1.0	0.0	28.9	99.18
	B02	15	30.7	38.0	0.6	0.8	0.0	28.6	98.67
	B03	20	30.7	38.0	1.0	0.9		28.4	99.01
	B03	20	30.5	37.0	1.3	0.6		28.9	98.3

Table S11. Modal mineralogy of representative simple rock-types used in the reaction-path modelling.

Mineral	modal %	composition/type*
oxide gabbro		
plagioclase	45	An-0.4, Ab-0.6
clinopyroxene	45	Di-0.80,Hed-0.20
amphibole	5	tremolite/Ca2Mg5Si8O22(OH)2
oxide	5	magnetite/Fe3O4
eclogititic metagabbro		
garnet	29	Alm-0.765, Grs-0.21, Pyp-0.025
clinopyroxene	49	Di-0.3,Hed-0.2, Jd-0.5
amphibole	16	glaucophane/Na2Mg3Al2Si8O22(OH)2
oxide	6	magnetite/Fe3O4
serpentinite		
serpentine	90	antigorite/Mg24Si17073.5H31
clinopyroxene	8	Di-100
oxide	2	magnetite/Fe3O4

*mineral composition consistent with the Deep Earth Water (DEW) database

References

Ague, J., van Haren, J., 1996. Assessing metasomatic mass and volume changes using the bootstrap, with application to deep crustal hydrothermal alteration of marble. Economic Geology 91, 1169–1182. https://doi.org/10.2113/gsecongeo.91.7.1169

Ague, J.J., 2017. Element mobility during regional metamorphism in crustal and subduction zone environments with a focus on the rare earth elements (REE). American Mineralogist 102, 1796–1821. https://doi.org/10.2138/am-2017-6130

Ague, J.J., Nicolescu, S., 2014. Carbon dioxide released from subduction zones by fluid-mediated reactions. Nature Geoscience 7, 355.

Bach, W., Klein, F., 2009. The petrology of seafloor rodingites: Insights from geochemical reaction path modeling. Lithos 112, 103–117. https://doi.org/10.1016/j.lithos.2008.10.022

Baxter, E.F., DePaolo, D.J., 2002. Field measurement of high temperature bulk reaction rates II: Interpretation of results from a field site near Simplon Pass, Switzerland. American Journal of Science 302, 465–516. https://doi.org/10.2475/ajs.302.6.465

Coggon, R., Holland, T.J.B., 2002. Mixing properties of phengitic micas and revised garnet-phengite thermobarometers. Journal of Metamorphic Geology 20, 683–696. https://doi.org/10.1046/j.1525-1314.2002.00395.x

Connolly, J.A.D., 2009. The geodynamic equation of state: What and how. Geochemistry, Geophysics, Geosystems 10. https://doi.org/10.1029/2009GC002540

Diener, J.F.A., Powell, R., 2012. Revised activity–composition models for clinopyroxene and amphibole. Journal of Metamorphic Geology 30, 131–142. https://doi.org/10.1111/j.1525-1314.2011.00959.x

Downs, R.T., 2006. The RRUFF Project: an integrated study of the chemistry, crystallography, Raman and infrared spectroscopy of minerals. Program and Abstracts of the 19th General Meeting of the International Mineralogical Association in Kobe, Japan. https://doi.org/O03-13

Grant, J.A., 1986. The isocon diagram; a simple solution to Gresens' equation for metasomatic alteration. Economic Geology 81, 1976–1982. https://doi.org/10.2113/gsecongeo.81.8.1976

Green, E., Holland, T., Powell, R., 2007. An order-disorder model for omphacitic pyroxenes in the system jadeite-diopside-hedenbergite-acmite, with applications to eclogitic rocks. American Mineralogist 92, 1181–1189. https://doi.org/10.2138/am.2007.2401

Gresens, R.L., 1967. Composition-volume relationships of metasomatism. Chemical Geology 2, 47–65. https://doi.org/10.1016/0009-2541(67)90004-6

Helgeson, H.C., 1969. Thermodynamics of hydrothermal systems at elevated temperatures and pressures. Am J Sci 267, 729. https://doi.org/10.2475/ajs.267.7.729

Holland, T., Powell, R., 2003. Activity–composition relations for phases in petrological calculations: an asymmetric multicomponent formulation. Contributions to Mineralogy and Petrology 145, 492–501. https://doi.org/10.1007/s00410-003-0464-z

Holland, T.J.B., Powell, R., 1998. An internally consistent thermodynamic data set for phases of petrological interest. Journal of Metamorphic Geology 16, 309–343. https://doi.org/10.1111/j.1525-1314.1998.00140.x

Huang, F., Sverjensky, D.A., 2019. Extended Deep Earth Water Model for predicting major element mantle metasomatism. Geochimica et Cosmochimica Acta 254, 192–230. https://doi.org/10.1016/j.gca.2019.03.027

Lafuente, B., Downs, R.T., Yang, H., Stone, N., 2015. Highlights in Mineralogical Crystallography, in: Armbruster, T., Danisi, R.M. (Eds.), . De Gruyter (O), pp. 1–30. https://doi.org/10.1515/9783110417104-003

Lanari, P., Engi, M., 2017. Local Bulk Composition Effects on Metamorphic Mineral Assemblages. Reviews in Mineralogy and Geochemistry 83, 55–102. https://doi.org/10.2138/rmg.2017.83.3

McDonough, W.F., Sun, S. -s., 1995. The composition of the Earth. Chemical Geology 120, 223–253. https://doi.org/10.1016/0009-2541(94)00140-4

Penniston-Dorland, S.C., Ferry, J.M., 2008. Element mobility and scale of mass transport in the formation of quartz veins during regional metamorphism of the Waits River Formation, east-central Vermont. American Mineralogist 93, 7–21. https://doi.org/10.2138/am.2008.2461

Petriglieri, J.R., Salvioli-Mariani, E., Mantovani, L., Tribaudino, M., Lottici, P.P., Laporte-Magoni, C., Bersani, D., 2015. Micro-Raman mapping of the polymorphs of serpentine. Journal of Raman Spectroscopy 46, 953–958. https://doi.org/10.1002/jrs.4695

Starr, P.G., Broadwell, K.S., Dragovic, B., Scambelluri, M., Haws, A.A., Caddick, M.J., Smye, A.J., Baxter, E.F., 2020. The subduction and exhumation history of the Voltri Ophiolite, Italy: Evaluating exhumation mechanisms for high-pressure metamorphic massifs. Lithos 376–377, 105767. https://doi.org/10.1016/j.lithos.2020.105767

Sverjensky, D.A., 2019. Thermodynamic modelling of fluids from surficial to mantle conditions. Journal of the Geological Society 176, 348. https://doi.org/10.1144/jgs2018-105

Sverjensky, D.A., Harrison, B., Azzolini, D., 2014. Water in the deep Earth: The dielectric constant and the solubilities of quartz and corundum to 60kb and 1200°C. Geochimica et Cosmochimica Acta 129, 125–145. https://doi.org/10.1016/j.gca.2013.12.019

Tribuzio, R., Messiga, B., Vannucci, R., Bottazzi, P., 1996. Rare earth element redistribution during high-pressure–low-temperature metamorphism in ophiolitic Fe-gabbros (Liguria, northwestern Italy): Implications for light REE mobility in subduction zones. Geology 24, 711–714. https://doi.org/10.1130/0091-7613(1996)024<0711:REERDH>2.3.CO;2

White, R.W., Powell, R., Clarke, G.L., 2002. The interpretation of reaction textures in Fe-rich metapelitic granulites of the Musgrave Block, central Australia: constraints from mineral equilibria calculations in the system K2O–FeO–MgO–Al2O3–SiO2–H2O–TiO2–Fe2O3. Journal of Metamorphic Geology 20, 41–55. https://doi.org/10.1046/j.0263-4929.2001.00349.x

Wolery, T.J., 1992. EQ3/6, a software package for geochemical modeling of aqueous systems: Package overview and installation guide (Version 7.0). United States. https://doi.org/10.2172/138894

Zhang, Z., Duan, Z., 2005. Prediction of the PVT properties of water over wide range of temperatures and pressures from molecular dynamics simulation. Physics of the Earth and Planetary Interiors 149, 335–354. https://doi.org/10.1016/j.pepi.2004.11.003

Supplementary materials of Chapter 3

Methods

Thermodynamic reaction path models were set up to assess changes in mineralogy and fluid composition during Si-metasomatism of distinct ultramafic rocks at subduction zone conditions.

First, to simulate Si-enrichment of aqueous fluids, the fluids were equilibrated with metamorphosed mid-ocean ridge basalt (MORB, metabasalt) or a metapelite. The choice of starting mineral assemblages was guided by the predicted closed–system phase equilibria of precursor metabasalt and metapelite compositions at water-saturation constrained by pseudosection models (Hacker et al., 2003; Wei and Powell, 2004). The assumption of water-saturation is substantiated by geologic evidence for the former presence of free aqueous fluid within exhumed subduction interface rocks (Bebout and Penniston-Dorland, 2016; Condit and French, 2022). The composition of the metapelite is characterized by having excess molar Al_2O_3 relative to the sum of alkalis (molar Na_2O + K_2O + CaO). In contrast, the metabasalt has higher CaO content than metapelite and displays a metaluminous composition, i.e. having a deficit in its molar Al_2O_3 relative to the sum of alkalis.

In the second modeling step, we evaluate the effects of ultramafic protolith compositions on talc formation during Si-metasomatism at subduction zone conditions using monomineralic antigorite [$Mg_{48}Si_{34}O_{85}(OH)_{62}$], lherzolite (depleted MORB mantle, DMM), harzburgite (HR1), and a more refractory harzburgite (HR2). The range in peridotite compositions reflects various extents of melt depletion expected for subduction zone environments and is presented in the Supplementary Table (Le Roux et al., 2007; Workman and Hart, 2005). Models were calculated using the EQ3/6 software package version 6 (Wolery, 1992) with the DEW database containing equilibrium constants of reactions involving minerals and aqueous species (Huang and Sverjensky, 2019; Sverjensky et al., 2014). We used the equation of state for water of Zhang and Duan (2005), and the dielectric constants from Sverjensky et al. (2014). Thermodynamic calculations were performed over a range of *P-T* conditions relevant to the global range of slab-top geotherms (1–2.5 GPa, 300–600 °C), and a range of fluid-to-rock (f/r) mass ratios, defined as the mass of fluid present divided by the mass of rock reacted. Activity coefficients for aqueous species were calculated using the B-dot equation (Helgeson, 1969).

The oxygen fugacity of the fluid (fO_2) was set to values close to the quartz-fayalite-magnetite buffer (QFM, within the redox stability of magnetite). This assumption is supported by the common occurrence of magnetite in high-pressure serpentinite (Deschamps et al., 2013). However, the lack of solid solutions of key Mg-Fe minerals in the current thermodynamic database including serpentine, brucite, and talc, prevents us from capturing the complexity of Fe-distribution and H_2 formation in natural serpentinization systems.

We modeled the isobaric and isothermal metasomatism of ultramafic rocks by allowing them to react with a fluid that was previously in equilibrium with metabasalt or metapelite over a range of fluid-to-rock ratios. The concentrations of dissolved Ca and Fe in equilibrium with metapelite are initially set to 10 mmol/kg to prevent the saturation of Ca-rich (e.g., Cpx, lawsonite) and Fe-rich oxide phases before reacting with ultramafic rock. We found that 10 mmol/kg of dissolved Ca or Fe (in the absence of buffering Ca or Fe-rich phase) can closely reproduce the reported equilibrium mineral assemblage of a metapelite or a metabasalt (Hacker et al., 2003; Wei and Powell, 2004). This assumption is also supported by experimental data on fluid/rock partitioning conducted at temperatures higher than our modeled conditions. For instance, an aqueous fluid in equilibrium with Cpx and garnet (Ca and Fe-rich eclogitic assemblage) contains approximately 10^{-1} molal Ca and $10^{-1.5}$ molal Fe (Kessel et al., 2005). This implies that the dissolved Ca and Fe concentrations in equilibrium with metapelite at lower temperatures (300–600 °C) modeled in this study are expected to be lower than those reported for an aqueous fluid in equilibrium with an eclogitic assemblage at 700 °C. To simulate Si-metasomatism, the ultramafic rock was titrated in small mass increments into the fluid. The reaction-path portrays a system that is initially fluid-dominated, such as in a fracture or vein, but that becomes increasingly rock-dominated as more ultramafic rock is added, such as in the rock matrix adjacent to a fracture or vein. We explored a range of f/r ratios (i.e. $f/r >> 1$) to simulate conditions likely relevant to high permeability zones, such as along lithologic contacts and shear zones. We limit our model predictions to $f/r >> 1$ as key minerals (e.g., serpentine, brucite, clinopyroxene, amphibole, garnet, spinel) and their solid solutions anticipated to form at lower f/r (< 1) are presently not included in the DEW database.

To provide a frame of reference, we also calculated a series of reaction-path models for the same *P-T* conditions to investigate the fluid-mediated metasomatism of ultramafic rocks by fluids buffered by quartz only (i.e. the compositions of other dissolved elements are set to trace

concentrations). This highlights the importance of the concentrations of other dissolved elements in the reactant fluid in determining the alteration mineralogy during the metasomatism of ultramafic rocks by slab-derived fluids. All the model results that support the findings of this study are freely available at https://doi.org/10.5281/zenodo.6760195. Companion spreadsheets (see Supplementary Tables S4–S15) that were used to tabulate and plot the model results are also included in the Supplementary Information.

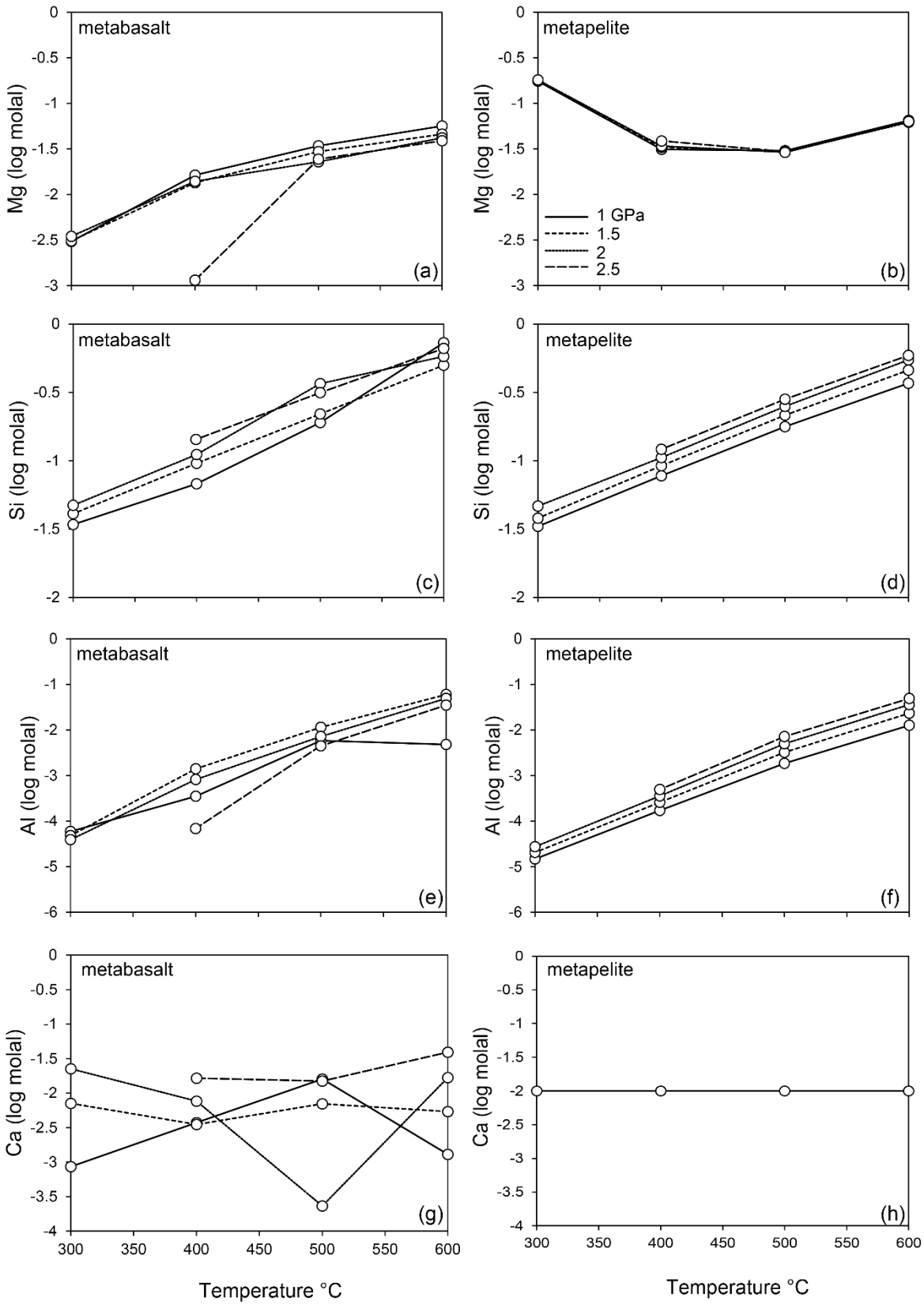

Fig. S1**.** The predicted composition of fluids in equilibrium with a metabasalt (a,c,e) and a metapelite (b,d,f) from 300–600 °C, 1–2.5 GPa.

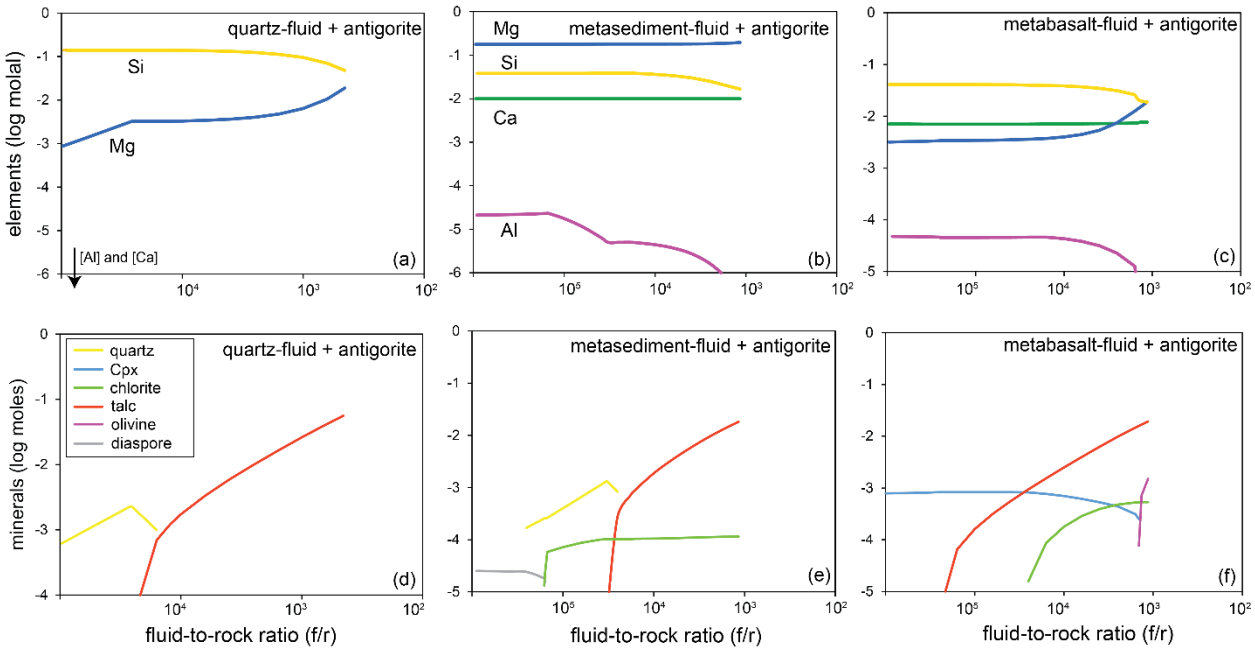

Fig. S2. Predicted mineral assemblages and pore fluid compositions of reaction-path models that simulated metasomatism of antigorite at 300°C and 1.5 GPa as a function of fluid-to-rock ratio. A fluid equilibrated with quartz (a,d), metasediment (b,e), or metabasalt (c,f) is subsequently allowed to react with ultramafic compositions (DMM, HZ1, and HZ2). The f/r decreases as ultramafic rock is titrated into the fluid. Mineral abbreviations are from Whitney and Evans (2010).

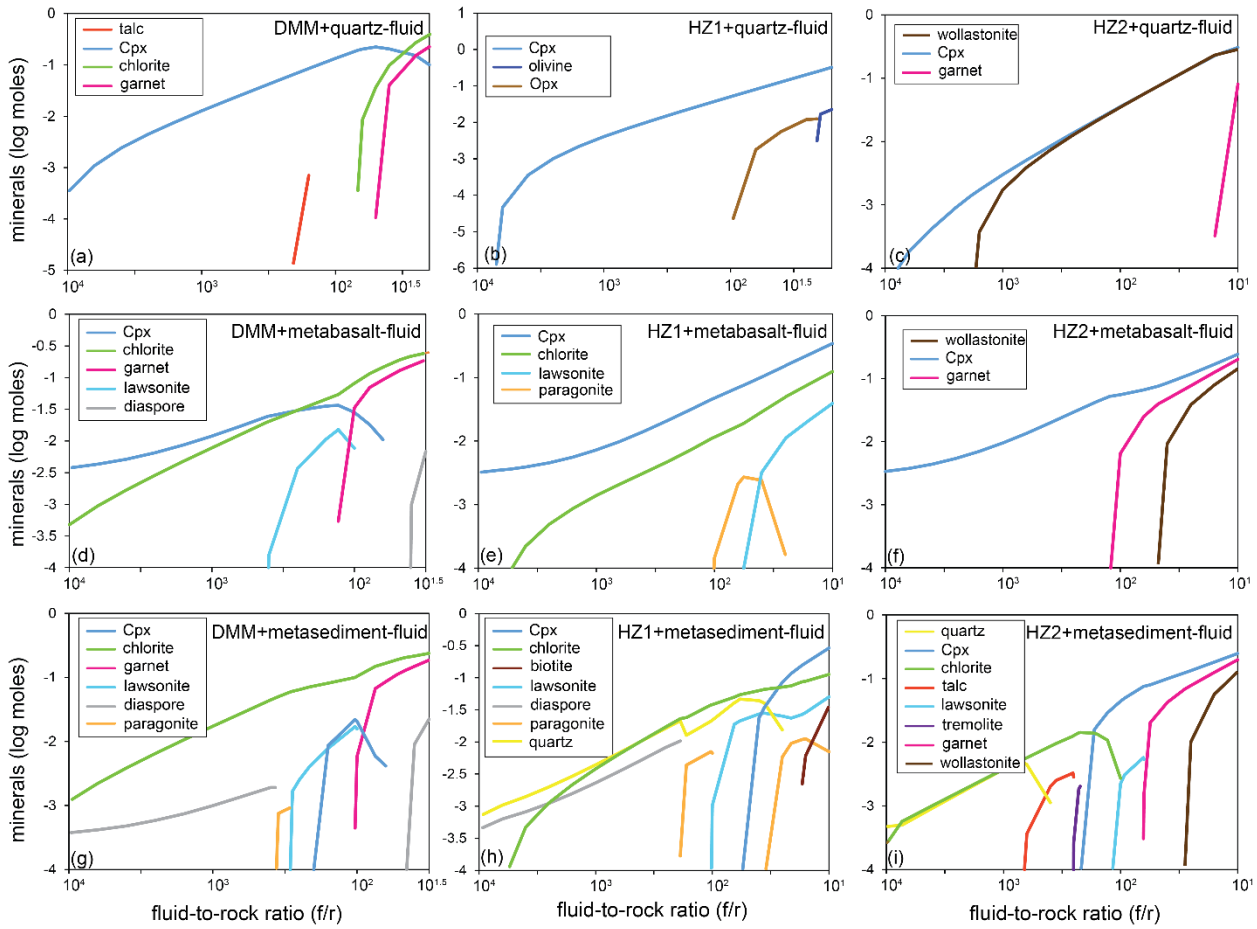

Fig. S3. Predicted mineral assemblages of reaction-path models that simulated metasomatism at 400°C and 1.5 GPa as a function of fluid-to-rock ratio. A fluid equilibrated with quartz (a-c), metabasalt (d-f), or metasediments (g-i) is subsequently allowed to react with ultramafic compositions (DMM, HZ1, and HZ2). The f/r decreases as ultramafic rock is titrated into the fluid. Please see the Supporting Information for additional model predictions including fluid compositions over a wider range of pressures and temperatures. Mineral abbreviations are from Whitney and Evans (2010).

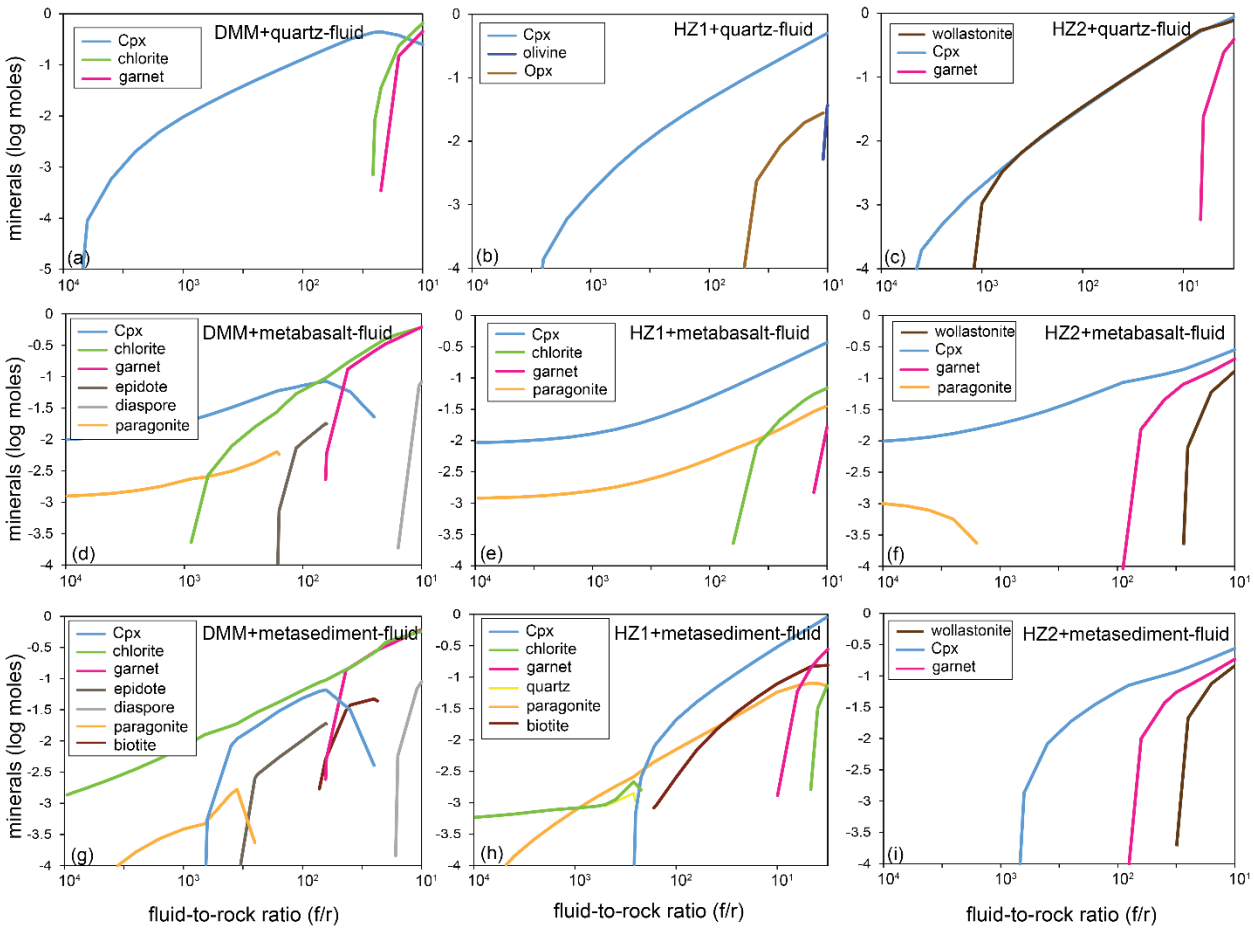

Fig. S4. Predicted mineral assemblages of reaction-path models that simulated metasomatism at 500°C and 1.5 GPa) as a function of fluid-to-rock ratio. A fluid equilibrated with quartz (a-c), metabasalt (d-f), or metasediments (g-i) is subsequently allowed to react with ultramafic compositions (DMM, HZ1, and HZ2). The f/r decreases as ultramafic rock is titrated into the fluid. Please see the Supporting Information for additional model predictions including fluid compositions over a wider range of pressures and temperatures. Mineral abbreviations are from Whitney and Evans (2010).

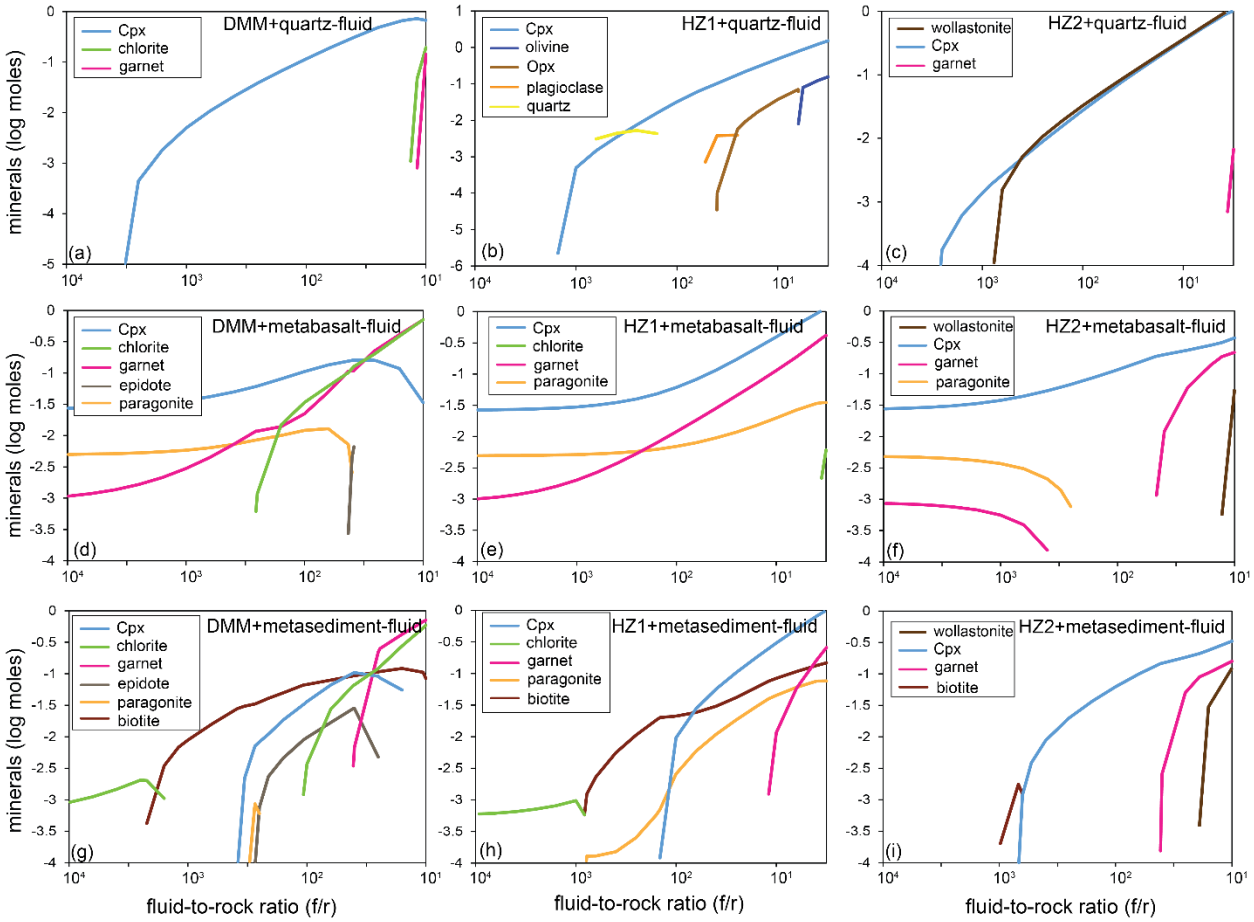

Fig. S5. Predicted mineral assemblages of reaction-path models that simulated metasomatism at 600°C and 1.5 GPa as a function of fluid-to-rock ratio. A fluid equilibrated with quartz (a-c), metabasalt (d-f), or metasediments (g-i) is subsequently allowed to react with ultramafic compositions (DMM, HZ1, and HZ2). The f/r decreases as ultramafic rock is titrated into the fluid. Please see the Supporting Information for additional model predictions including fluid compositions over a wider range of pressures and temperatures. Mineral abbreviations are from Whitney and Evans (2010).

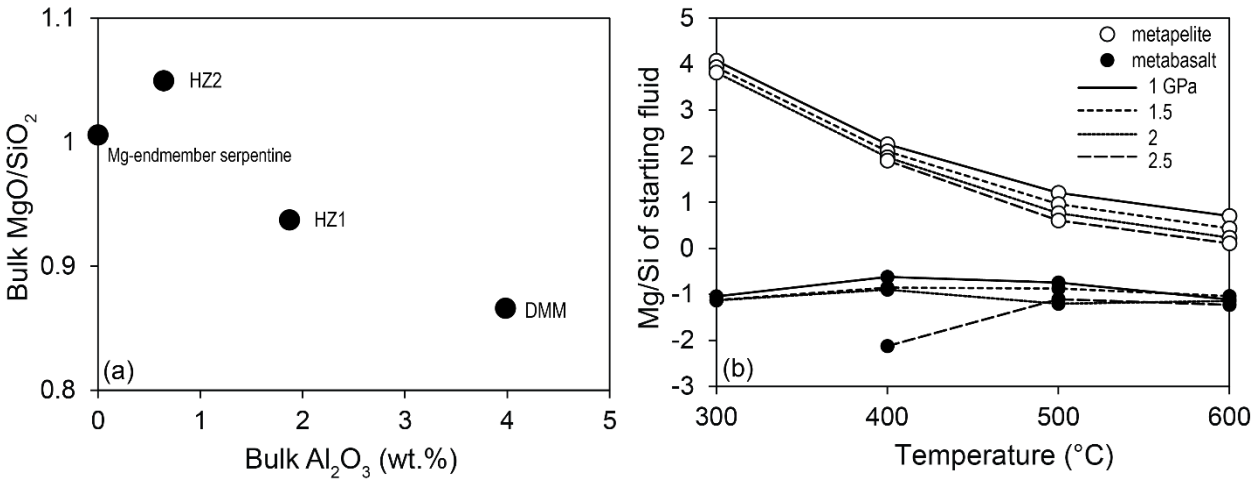

Fig. S6. (a) MgO/SiO_2 vs. Al_2O_3 plot of the starting ultramafic compositions. (b) Predicted Mg/Si of fluids in equilibrium with a metabasalt and a metapelite from 300–600 °C, 1–2.5 GPa.

Table S1. Bulk compositions of mantle peridotites used in this study.

	DMM	HZ1	HZ2
wt. %	lherzolite (Workman and Hart, 2005)	harzburgite (05LA2, Le Roux et al. 2007)	harzburgite (05LA16, Le Roux et al. 2007)
SiO2	44.71	44.7	42.3
Al2O3	3.98	1.87	0.64
FeO*	8.18	7.31	7.94
MgO	38.73	41.9	44.4
CaO	3.17	0.73	0.32
Na2O	0.13	0.09	0.08

*total Fe as FeO

References

Le Roux, V., Bodinier, J.-L., Tommasi, A., Alard, O., Dautria, J., Vauchez, A., Riches, A., 2007. The Lherz spinel lherzolite: Refertilized rather than pristine mantle. Earth and Planetary Science Letters 259. https://doi.org/10.1016/j.epsl.2007.05.026

Workman, R.K., Hart, S.R., 2005. Major and trace element composition of the depleted MORB mantle (DMM). Earth and Planetary Science Letters 231, 53–72. https://doi.org/10.1016/j.epsl.2004.12.005

Table S2. Predicted composition of fluids in equilibrium with a metabasalt and a metapelite from 300–600 °C, 1–2.5 GPa.

metabasalt-equilibrated

Pressure (GPa)	Temperature (°C)	Starting mineral assemblage*	logfO_2	Ca (log molal)	Mg (log molal)	Al (log molal)	Si (log molal)	Fe (log molal)
1	300	glaucophane, lawsonite, pumpellyite, quartz, clinochlore	-37.2	-3.06	-2.51	-4.23	-1.47	-2.06
1	400	glaucophane, clinozoisite, clinochlore, quartz, albite	-29.8	-2.43	-1.79	-3.45	-1.17	-2.22
1	500	albite, clinozoisite, tremolite, quartz, clinochlore	-24.1	-1.80	-1.47	-2.23	-0.72	-2.00
1	600	anortite, magnetite, tremolite, quartz, albite	-19.7	-2.89	-1.25	-2.32	-0.14	-0.41
1.5	300	jadeite, tremolite, clinochlore, quartz, lawsonite	-37.9	-2.15	-2.51	-4.32	-1.39	-2.01
1.5	400	jadeite, tremolite, clinochlore, quartz, lawsonite	-30.4	-2.45	-1.87	-2.85	-1.02	-2.02
1.5	500	jadeite, tremolite, clinochlore, quartz, clinozoisite	-24.6	-2.16	-1.53	-1.94	-0.66	-2.02
1.5	600	jadeite, tremolite, almadine, diopside, quartz, clinozoisite	-20.2	-2.27	-1.34	-1.22	-0.30	-1.49

2	300	jadeite, tremolite, clinochlore, quartz, lawsonite	-37.9	-1.65	-2.46	-4.41	-1.33	-2.00
2	400	jadeite, tremolite, clinochlore, quartz, lawsonite	-31.0	-2.12	-1.85	-3.09	-0.95	-2.01
2	500	jadeite, tremolite, almadine, diopside, quartz	-25.2	-3.63	-1.64	-2.14	-0.44	-2.29
2	600	jadeite, tremolite, almadine, diopside, quartz, clinozoisite	-20.6	-1.77	-1.38	-1.30	-0.24	-1.45
2.5	400	jadeite, lawsonite, almandine, diopside, quartz	-31.6	-1.78	-2.96	-4.17	-0.84	-1.78
2.5	500	jadeite, tremolite, almandine, diopside, quartz	-25.7	-1.82	-1.61	-2.35	-0.50	-1.43
2.5	600	jadeite, tremolite, almandine, diopside, quartz, clinozoisite	-21.1	-1.41	-1.41	-1.46	-0.18	-1.42

*mineral assemblages at different P-T conditions are guided by the pseudosection models of Hacker et al. (2003) for basalt

metapelite-equilibrated

Pressure (GPa)	Temperature (°C)	Starting mineral assemblage**	logfO_2	Ca (log molal)	Mg (log molal)	Al (log molal)	Si (log molal)	K (log molal)	Fe (log molal)
1	300	paragonite, clinochlore, quartz, kyanite, muscovite	-37.2	-2.00	-0.76	-4.83	-1.48	-1.80	-2.00

1	400	paragonite, clinochlore, quartz, kyanite, muscovite	-29.8	-2.00	-1.50	-3.77	-1.11	-1.20	-2.00
1	500	paragonite, clinochlore, quartz, kyanite, muscovite	-24.1	-2.00	-1.52	-2.73	-0.75	-1.14	-2.00
1	600	paragonite, clinochlore, quartz, kyanite, muscovite	-19.7	-2.00	-1.19	-1.89	-0.43	-1.15	-2.00
1.5	300	paragonite, clinochlore, quartz, kyanite, muscovite	-37.9	-2.00	-0.75	-4.68	-1.42	-1.79	-2.00
1.5	400	paragonite, clinochlore, quartz, kyanite, muscovite	-30.4	-2.00	-1.48	-3.59	-1.04	-1.18	-2.00
1.5	500	paragonite, clinochlore, quartz, kyanite, muscovite	-24.6	-2.00	-1.53	-2.49	-0.67	-1.13	-2.00
1.5	600	paragonite, clinochlore, quartz, kyanite, muscovite	-20.2	-2.00	-1.20	-1.63	-0.34	-1.13	-2.00
2	300	paragonite, clinochlore, quartz, kyanite, muscovite	-37.9	-2.00	-0.74	-4.56	-1.33	-1.75	-2.00
2	400	paragonite, clinochlore, quartz, kyanite, muscovite	-31.0	-2.00	-1.47	-3.45	-0.98	-1.15	-2.00
2	500	paragonite, clinochlore, quartz, kyanite, muscovite	-25.2	-2.00	-1.54	-2.30	-0.60	-1.10	-2.00

2	600	paragonite, clinochlore, quartz, kyanite, muscovite	-20.6	-2.00	-1.21	-1.44	-0.26	-1.10	-2.00
2.5	400	paragonite, clinochlore, quartz, kyanite, muscovite	-31.6	-2.00	-1.42	-3.32	-0.92	-1.12	-2.00
2.5	500	paragonite, clinochlore, quartz, kyanite, muscovite	-25.7	-2.00	-1.54	-2.14	-0.55	-1.07	-2.00
2.5	600	paragonite, glaucophane, quartz, kyanite, muscovite	-21.1	-2.00	-1.20	-1.31	-0.23	-1.06	-2.01

**mineral assemblages at different P-T conditions are guided by the pseudosection models of Wei and Powell (2004) for pelite

Reference
s

Hacker, B.R., Abers, G.A., Peacock, S.M., 2003. Subduction factory 1. Theoretical mineralogy, densities, seismic wave speeds, and H2O contents. Journal of Geophysical Research: Solid Earth 108. https://doi.org/10.1029/2001JB001127

Wei, C., Powell, R., 2004. Calculated Phase Relations in High-Pressure Metapelites in the System NKFMASH (Na2O–K2O–FeO–MgO–Al2O3–SiO2–H2O). Journal of Petrology 45, 183–202. https://doi.org/10.1093/petrology/egg085

Table S3. Summary of modelled conditions that facilitate talc formation by metasomatism of ultramafic compositions

Reaction with quartz-saturated fluid

	1 GPa				1.5 GPa				2 GPa				2.5 GPa			
	Atg	DMM	HZ1	HZ2	Atg	DMM	HZ1	HZ2	Atg	DMM	HZ1	HZ2	Atg	DMM	HZ1	HZ2
300 °C	y	n	n	n	y	y	y	n	y	y	y	n	-	-	-	-
400 °C	y	n	n	n	y	y	n	n	y	y	y	n	y	y	n	n
500 °C	y	n	n	n	y	n	n	n	y	y	n	n	y	y	n	n
600 °C	y	n	n	n	y	n	n	n	y	y	n	n	y	y	n	n

Reaction with MORB-buffered fluid

	1 GPa				1.5 GPa				2 GPa				2.5 GPa			
	Atg	DMM	HZ1	HZ2	Atg	DMM	HZ1	HZ2	Atg	DMM	HZ1	HZ2	Atg	DMM	HZ1	HZ2
300 °C	y	n	n	n	y	n	n	n	y	y	y	y	-	-	-	-
400 °C	y	n	n	n	y	n	n	n	y	y	y	y	y	n	n	n
500 °C	y	n	n	n	y	n	n	n	y	n	n	n	y	n	n	n
600 °C	y	n	n	n	y	n	n	n	y	n	n	n	y	n	n	n

Reaction with metapelite-buffered fluid

	1 GPa				1.5 GPa				2 GPa				2.5 GPa			
	Atg	DMM	HZ1	HZ2	Atg	DMM	HZ1	HZ2	Atg	DMM	HZ1	HZ2	Atg	DMM	HZ1	HZ2
300 °C	y	n	n	y	y	n	n	y	y	n	y	y	-	-	-	-

400 °C	y	n	n	y	y	n	n	y	y	n	-	y	y	n	n	n
500 °C	y	n	n	n	y	n	n	n	y	n	n	n	y	n	n	n
600 °C	y	n	n	n	y	n	n	n	y	n	n	n	y	y	y	y

Note:
y = talc was predicted to form
n = talc was not predicted to form

References

Bebout, G.E., Penniston-Dorland, S.C., 2016. Fluid and mass transfer at subduction interfaces—The field metamorphic record. Lithos 240–243, 228–258. https://doi.org/10.1016/j.lithos.2015.10.007

Condit, C.B., French, M.E., 2022. Geologic Evidence of Lithostatic Pore Fluid Pressures the Base of the Subduction Seismogenic Zone. Geophysical Research Letters 49, e2022GL098862. https://doi.org/10.1029/2022GL098862

Deschamps, F., Godard, M., Guillot, S., Hattori, K., 2013. Geochemistry of subduction zone serpentinites: A review. Lithos 178, 96–127. https://doi.org/10.1016/j.lithos.2013.05.019

Hacker, B.R., Abers, G.A., Peacock, S.M., 2003. Subduction factory 1. Theoretical mineralogy, densities, seismic wave speeds, and H2O contents. Journal of Geophysical Research: Solid Earth 108. https://doi.org/10.1029/2001JB001127

Helgeson, H.C., 1969. Thermodynamics of hydrothermal systems at elevated temperatures and pressures. Am J Sci 267, 729. https://doi.org/10.2475/ajs.267.7.729

Huang, F., Sverjensky, D.A., 2019. Extended Deep Earth Water Model for predicting major element mantle metasomatism. Geochimica et Cosmochimica Acta 254, 192–230. https://doi.org/10.1016/j.gca.2019.03.027

Kessel, R., Schmidt, M.W., Ulmer, P., Pettke, T., 2005. Trace element signature of subduction-zone fluids, melts and supercritical liquids at 120–180 km depth. Nature 437, 724–727. https://doi.org/10.1038/nature03971

Le Roux, V., Bodinier, J.-L., Tommasi, A., Alard, O., Dautria, J., Vauchez, A., Riches, A., 2007. The Lherz spinel lherzolite: Refertilized rather than pristine mantle. Earth and Planetary Science Letters 259. https://doi.org/10.1016/j.epsl.2007.05.026

Sverjensky, D.A., Harrison, B., Azzolini, D., 2014. Water in the deep Earth: The dielectric constant and the solubilities of quartz and corundum to 60kb and 1200°C. Geochimica et Cosmochimica Acta 129, 125–145. https://doi.org/10.1016/j.gca.2013.12.019

Wei, C., Powell, R., 2004. Calculated Phase Relations in High-Pressure Metapelites in the System NKFMASH (Na2O–K2O–FeO–MgO–Al2O3–SiO2–H2O). Journal of Petrology 45, 183–202. https://doi.org/10.1093/petrology/egg085

Whitney, D.L., Evans, B.W., 2010. Abbreviations for names of rock-forming minerals. American Mineralogist 95, 185–187. https://doi.org/10.2138/am.2010.3371

Wolery, T.J., 1992. EQ3/6, a software package for geochemical modeling of aqueous systems: Package overview and installation guide (Version 7.0). United States. https://doi.org/10.2172/138894

Workman, R.K., Hart, S.R., 2005. Major and trace element composition of the depleted MORB mantle (DMM). Earth and Planetary Science Letters 231, 53–72. https://doi.org/10.1016/j.epsl.2004.12.005

Zhang, Z., Duan, Z., 2005. Prediction of the PVT properties of water over wide range of temperatures and pressures from molecular dynamics simulation. Physics of the Earth and Planetary Interiors 149, 335–354. https://doi.org/10.1016/j.pepi.2004.11.003

Supplementary materials for Chapter 4

Supplementary Figures

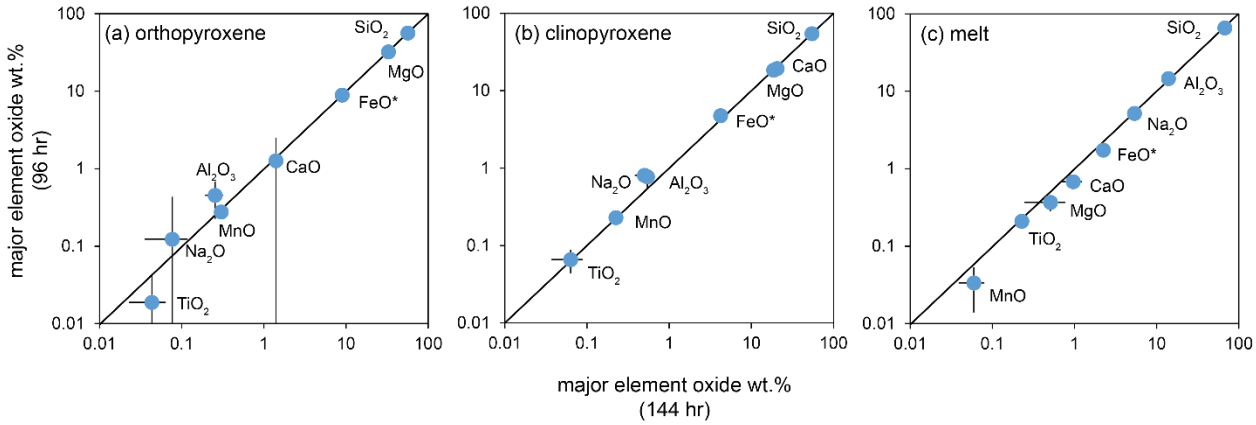

Figure S1. Concentration (log)-concentration (log) plot of all the major elements measured in experimental melts and residual minerals. No significant difference in the major element compositions of (a) orthopyroxene, (b) clinopyroxene, and (c) melt between 96 h and 144 h experimental run durations performed on SY325 mélange. Our experiments are plotted as averages (on volatile-free basis) with error bars representing 1 σ.

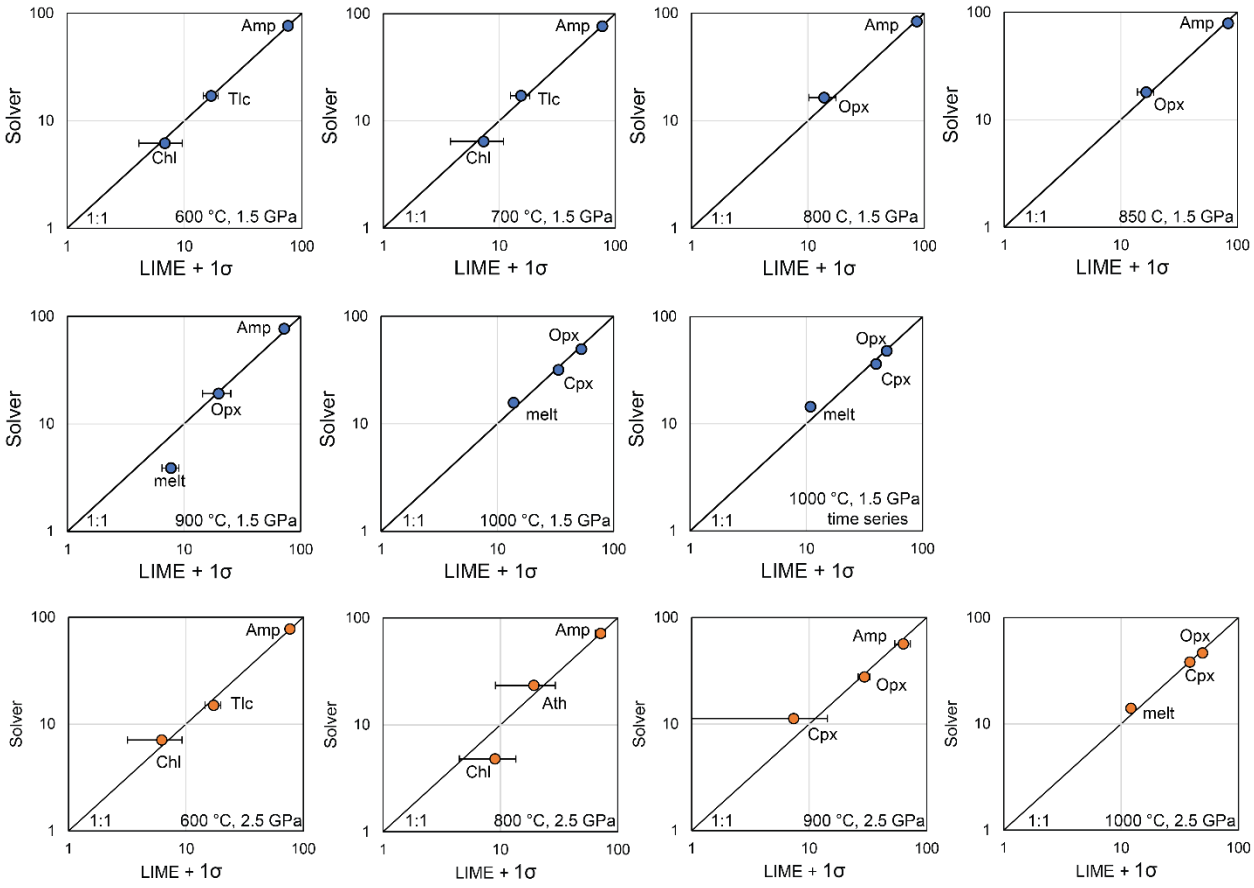

Figure S2. Comparison between the phase proportions (in wt. %) in SY325 experiments calculated using Solver and LIME. The LIME data are plotted as averages with error bars representing 1 σ.

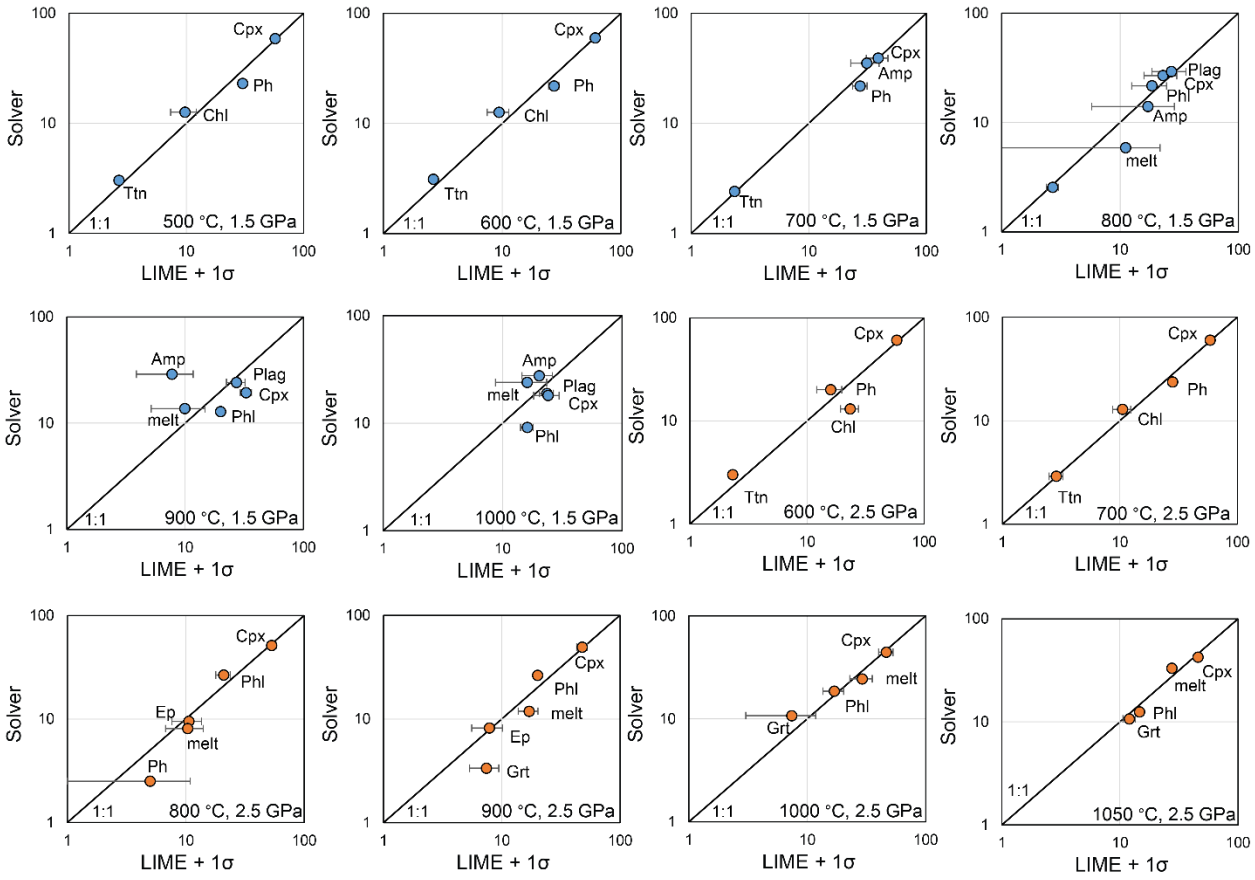

Figure S3. Comparison between the phase proportions (in wt. %) in SY400B experiments calculated using Solver and LIME. The LIME data are plotted as averages with error bars representing 1 σ.

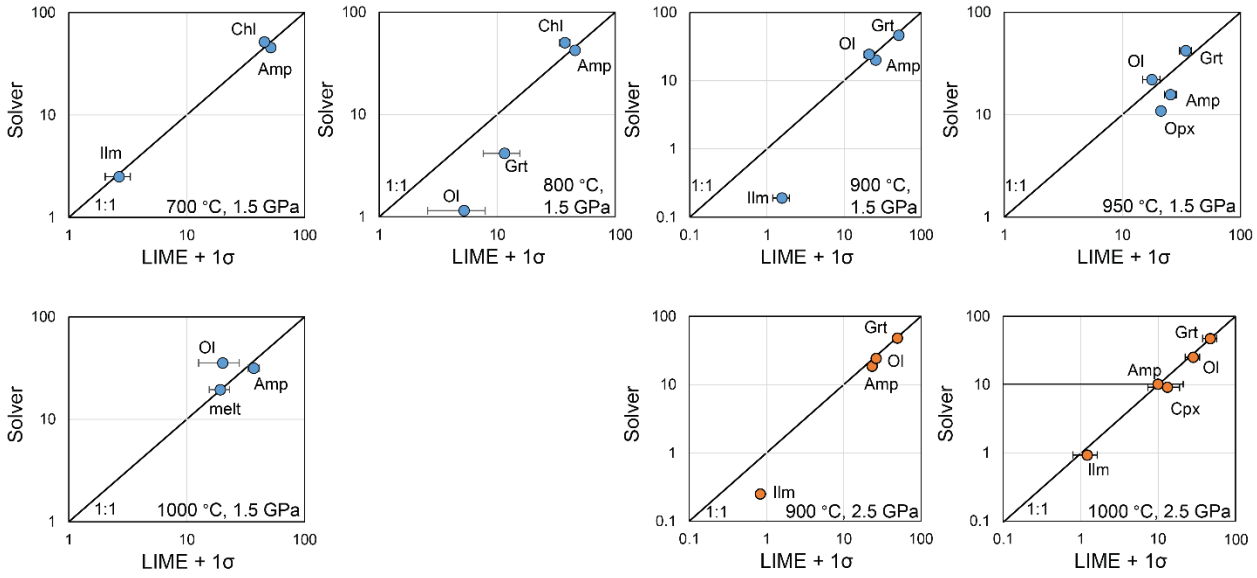

Figure S4. Comparison between the phase proportions (in wt. %) in C647 experiments calculated using Solver and LIME. The LIME data are plotted as averages with error bars representing 1 σ.

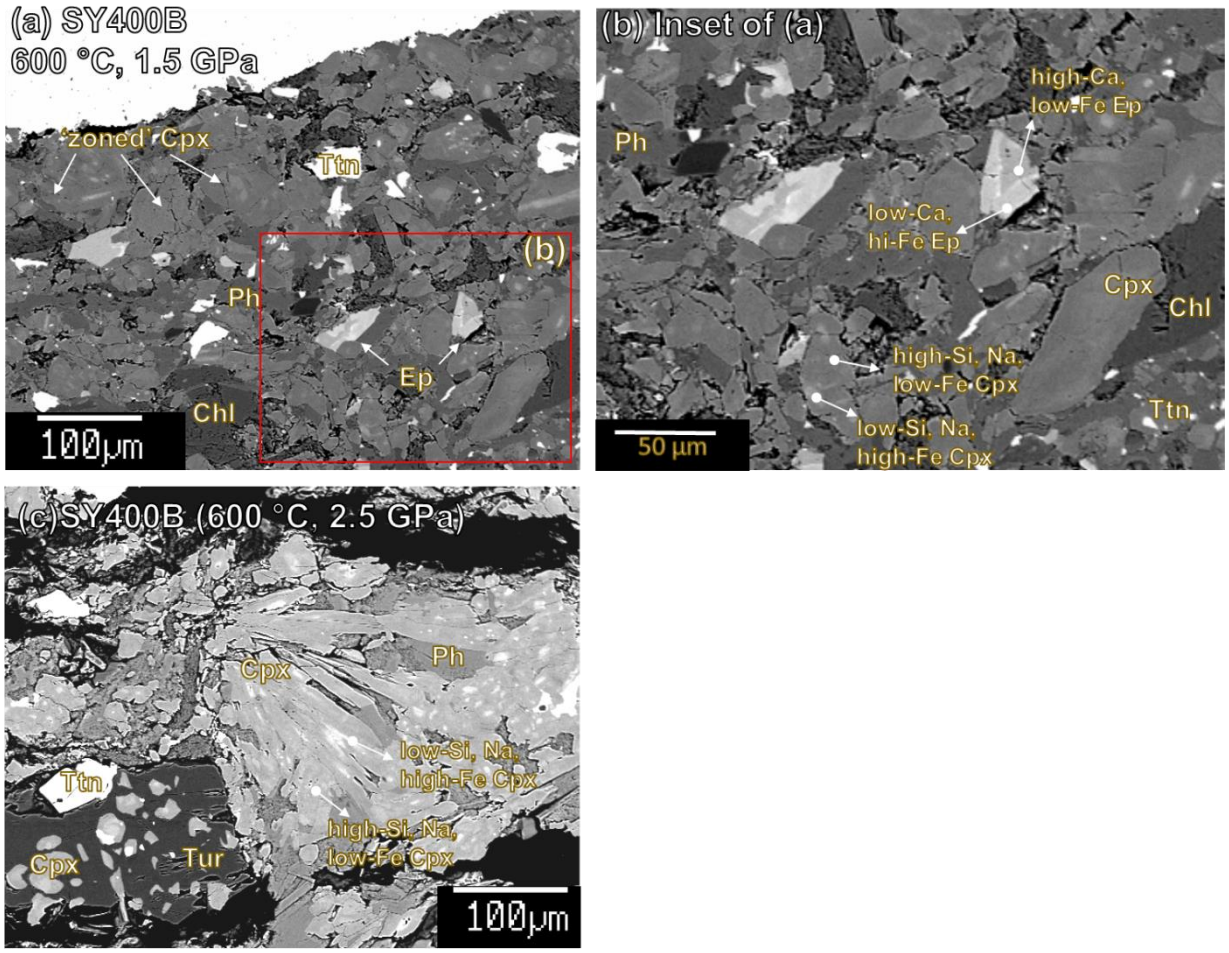

Figure S5. Additional electron backscatter (BSE) images of low-temperature subsolidus SY400B experiments. In the experiments conducted at 600 °C and 1.5 GPa (a) and 2.5 GPa (c), omphacitic clinopyroxene displays patchy chemical zoning while epidote displays sector zoning. (b) Magnified inset of (a) outlined in red rectangle. The compositions of relatively minor 'light' patchy cores of clinopyroxene contain lower SiO_2 and Na_2O contents but higher FeO contents than the more dominant 'dark' patchy mantle and rims of clinopyroxene. The light' sectors in epidote display lower CaO and higher FeO contents than the 'dark' sectors.

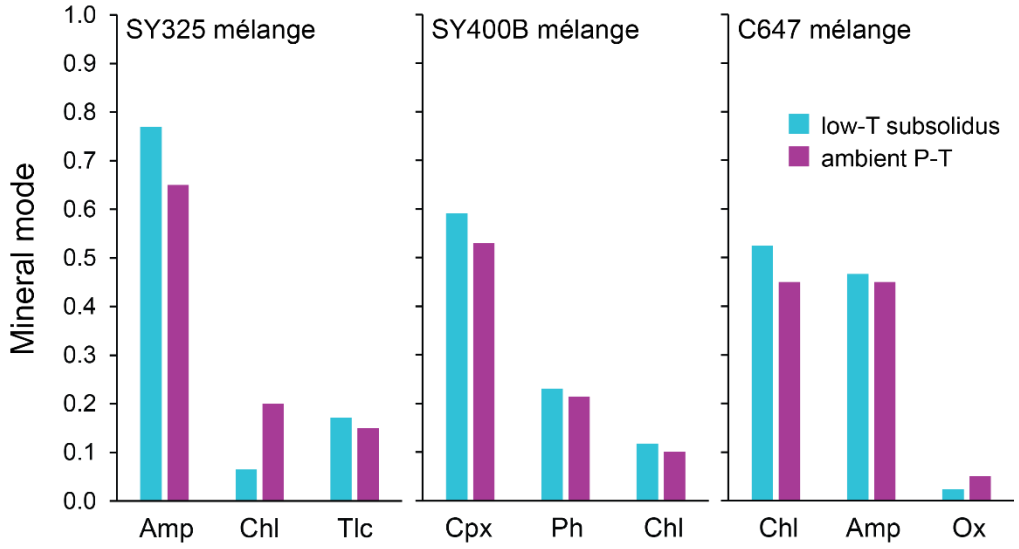

Figure S6. Comparison of mineral modes (by weight) calculated for low-temperature subsolidus experiments in this study and reported mineral modes at ambient *P-T* conditions reported in previous studies. Literature sources for mineral modes are based from thin section estimate and/or mean modal proportions inverted from bulk rock and mineral analyses. Literature-reported modal estimates are from Marschall et al. (2006) for SY325 and SY400B mélanges and King et al. (2006) for C647 mélange.

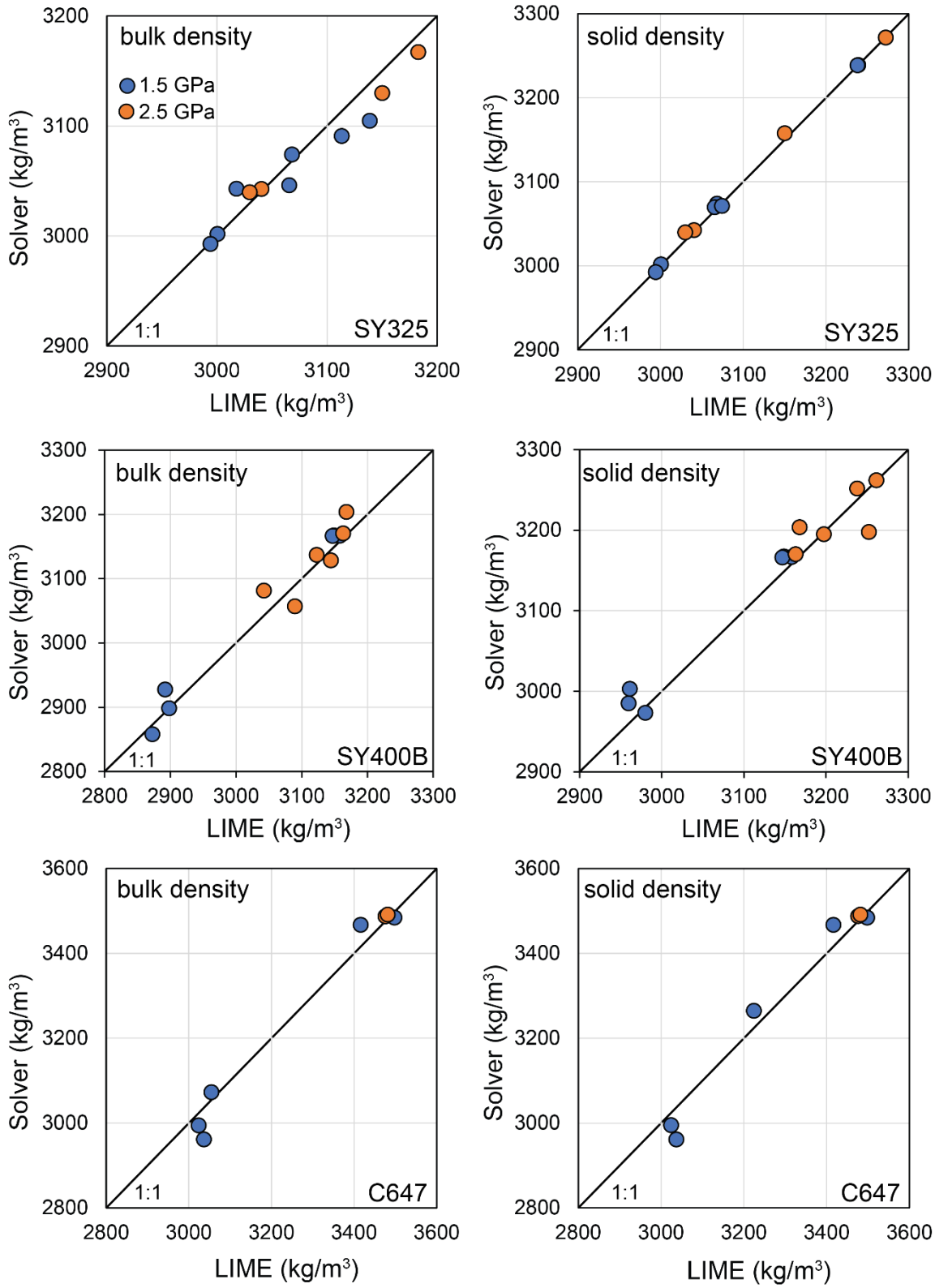

Figure S7. Comparison between the bulk (mineral + melt) and solid (mineral-only) densities calculated using the phase proportions constrained by Solver and LIME. Each data point represents an experiment at specific P-T condition.

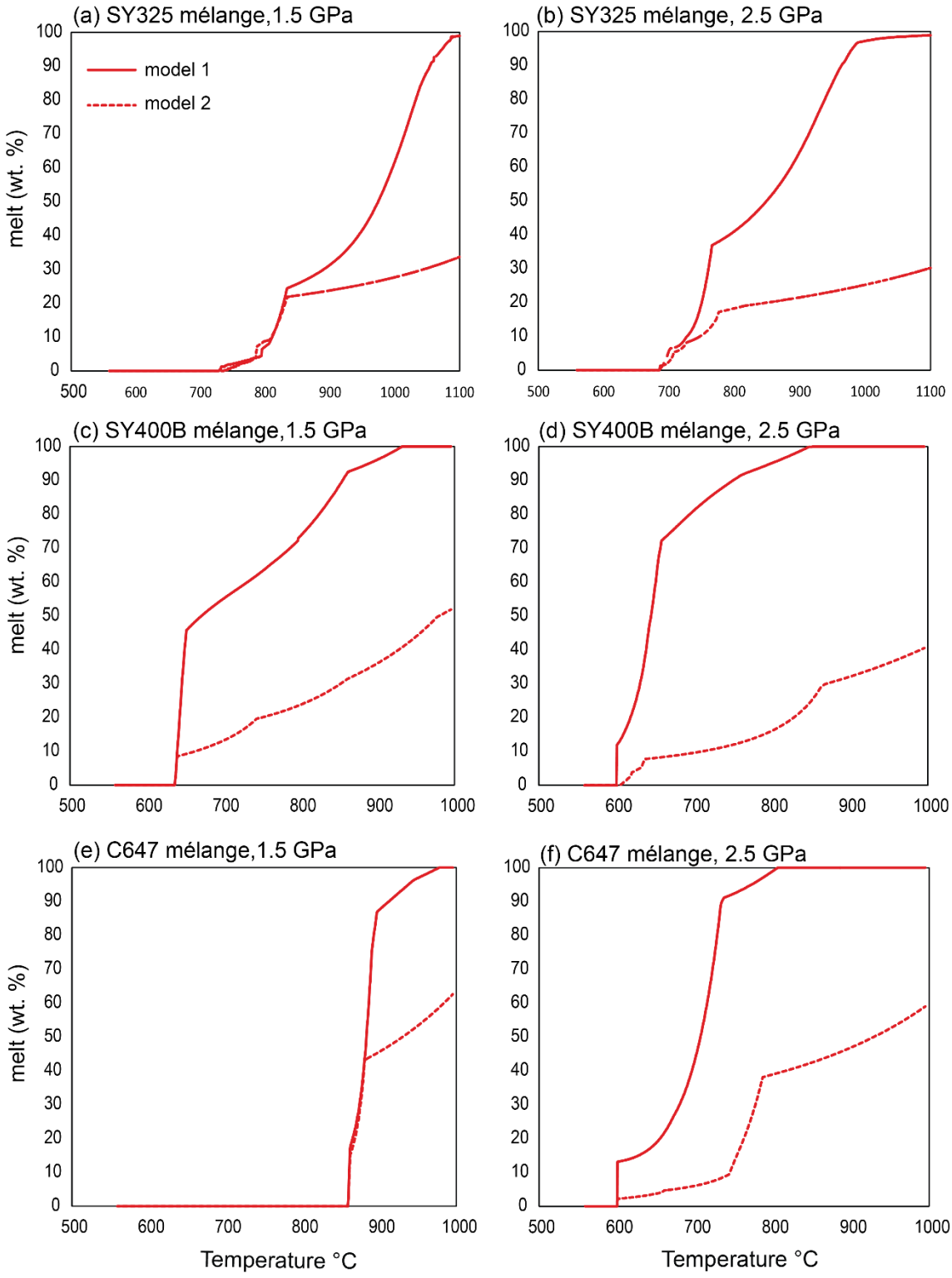

Figure S8. Comparison between the predicted solidus temperatures and melt proportions (in wt. %) constrained by model 1 and model 2 of Perple_X. Model 1 simulates a water-saturated condition wherein a free fluid phase is always present at all *P-T* conditions. Model 2 simulates a scenario wherein the H_2O content is fixed at a value similar to the bulk starting composition.

Thermodynamic phase equilibrium modeling

Thermodynamic phase equilibria models of mélange melting were constructed with the Gibbs free energy minimization software Perple_X (Connolly, 2009; version 6.9.1, downloaded May 24, 2021). All calculations were conducted in the system SiO_2-TiO_2-Al_2O_3-FeO-MgO-CaO-Na_2O-K_2O-H_2O-O_2 using each of the experimental bulk compositions and including O_2 sufficient to yield bulk Fe3/FeT ratios of 0.1. H_2O was added to each calculation based on the assumption that the deficit from 100% in the original whole rock analyses of the natural samples reflects the H_2O present in the samples. In all cases this resulted in fluid-saturation at sub-solidus conditions. Models were calculated along 1D isobaric profiles at 1.5 GPa and 2.5 GPa from 450 °C to 1100 °C, and included solution models for melt, clinopyroxene, orthopyroxene, olivine, garnet and spinel from Holland et al., (2018), clinoamphibole from Green et al., (2016), chlorite, white mica and FeTi oxides from White et al., (2014), epidote from Holland Powell (2011), ternary feldspars from Holland and Powell (2003), antigorite from Padrón-Navarta et al., (2013), and lastly an ideal mixing model for talc. Additional models for the 1.5 and 2.5 GPa phase equilibria of anhydrous depleted MORB mantle (Workman and Hart, 2005) were also calculated using the same approach and including all anhydrous solutions models listed above.

References

Connolly, J.A.D. (2009) The geodynamic equation of state: What and how. *Geochemistry, Geophysics, Geosystems* 10, n/a-n/a.

Green, E.C.R., White, R.W., Diener, J.F.A., Powell, R., Holland, T.J.B., Palin, R.M. (2016) Activity-composition relations for the calculation of partial melting equilibria in metabasic rocks. *Journal of Metamorphic Geology* 34, 845–869.

Holland, T., Powell, R. (2003) Activity–composition relations for phases in petrological calculations: an asymmetric multicomponent formulation. *Contributions to Mineralogy and Petrology* 145, 492–501.

Holland, T.J.B., Green, E.C.R., Powell, R. (2018) Melting of Peridotites through to Granites: A Simple Thermodynamic Model in the System KNCFMASHTOCr. *Journal of Petrology* 59, 881–900.

Holland, T.J.B., Powell, R. (2011) An improved and extended internally consistent thermodynamic dataset for phases of petrological interest, involving a new equation of state for solids. *Journal of Metamorphic Geology* 29, 333–383.

Padrón-Navarta, J.A., Sánchez-Vizcaíno, V.L., Hermann, J., Connolly, J.A.D., Garrido, C.J., Gómez-Pugnaire, M.T., Marchesi, C. (2013) Tschermak's substitution in antigorite and consequences for phase relations and water liberation in high-grade serpentinites. *Lithos* 178, 186–196.

White, R.W., Powell, R., Holland, T.J.B., Johnson, T.E., Green, E.C.R. (2014) New mineral activity–composition relations for thermodynamic calculations in metapelitic systems. *Journal of Metamorphic Geology* 32, 261–286.

Workman, R.K., Hart, S.R. (2005) Major and trace element composition of the depleted MORB mantle (DMM). *Earth and Planetary Science Letters* 231, 53–72.

Table S1. Major and trace element compositions of starting materials

Samples	Description	Modal mineralogy (wt. %)	metamorphic P-T condition	SiO2	TiO2	Al2O3	FeO*	MnO	MgO	CaO	Na2O	K2O	P2O5	Cr2O3	NiO	Total	LOI (=100-total)
SY400B*	chlorite-omphacite schist (sediment-dominated melange)	Ep-10, Phe- 21.4, Chl-10, Rt-0.83, Ttn-0.50, Ap-0.22, Tur-3.4, Omph-53	0.6–1.3 GPa (Breeding et al., 2004; Marschall et al., 2006)	49.9	1.1	16.7	5.6	0.1	8.2	8.1	5.0	2.2	0.1	0.0	0.0	97.1	2.9
SY325*	talc-chlorite-actinolite schist (serpentine-dominated melange)	Ca-amph-65, Chl-20, Tlc-15, minor Rt	0.6–1.3 GPa (Breeding et al., 2004; Marschall et al., 2006)	55.8	0.1	2.3	7.2	0.2	22.0	7.4	1.5	0.1	0.0	0.3	0.2	97.0	3.0
Catalina 6-4-7**	High trace element concentration amphibolite facies Catalina	A tremolite-chlorite (both ~45%) schist with minor anthophyllite-cummingtonite (~5%) and Fe-rich opaques (~5%).	600-700 C, 0.9-1.3 GPa (King et al. 2007)	38.6	1.1	12.4	9.1	0.1	23.5	5.9	0.8	0.1	0.0	0.2	0.1	91.5	8.5

* major and trace element compositions are reported in Codillo et al. (2018)
** major and trace element compositions are reported in King et al. (2006)

Sc (ppm)	Cs (ppm)	Rb (ppm)	Ba (ppm)	Th (ppm)	U (ppm)	B (ppm)	Nb (ppm)	Ta (ppm)	La (ppm)	Ce (ppm)	Pb (ppm)	Pr (ppm)	Sr (ppm)	Nd (ppm)	Zr (ppm)	Hf (ppm)	Sm (ppm)	Eu (ppm)	Gd (ppm)	Tb (ppm)	Dy (ppm)	Ho (ppm)	Er (ppm)	Tm (ppm)	Yb (ppm)	Y (ppm)	Li (ppm)	Lu (ppm)
27.2	0.7	48.1	374.9	0.9	0.4		6.5	0.4	9.9	9.9	2.3	4.0	181.0	17.7	162.7	4.8	5.2	1.3	6.0	1.2	7.7	1.7	4.8	0.7	4.9	43.9		0.8
6.1	0.0	0.2	2.2	0.1	0.2		0.4	0.0	0.8	0.8	1.5	0.3	16.3	2.0	8.5	0.2	1.3	0.5	2.6	0.6	4.0	0.8	2.3	0.3	2.2	20.8		0.3
	0.0	0.4	5.2	4.1	0.3	3.8	20.8	1.7	16.2	34.1	0.7	4.0	64.4	15.7	9.0	0.4	3.2	0.8	3.0	0.5	2.9	0.6	1.6	0.2	1.5	16.3	8.7	0.2

Table S2. Summary of experimental set-up and conditions

Experiment	Starting material	Temperature (°C)	Pressure (GPa)	Run duration (hr)
ECSY400B-6b	SY400B	500	1.5	96
ECSY400B-2	SY400B	600	1.5	97.6
ECSY400B-3	SY400B	700	1.5	97.6
ECSY400B-9	SY400B	800	1.5	96
ECSY400B-10	SY400B	900	1.5	96
ECSY400B-8	SY400B	1000	1.5	96
ECSY400B-7	SY400B	600	2.5	96
ECSY400B-4	SY400B	700	2.5	96
ECSY400B-5	SY400B	800	2.5	96
ECSY400B-11	SY400B	900	2.5	96
ECSY400B-12	SY400B	1000	2.5	96
ECSY400B-13	SY400B	1050	2.5	96
ECSY325-4	SY325	600	1.5	168
ECSY325-3	SY325	700	1.5	96
ECSY325-2	SY325	800	1.5	96
ECSY325-9	SY325	850	1.5	96
ECSY325-1	SY325	900	1.5	96
ECSY325-6	SY325	1000	1.5	96
ECSY325-10	SY325	1000	1.5	144
ECSY325-5	SY325	600	2.5	120
ECSY325-11	SY325	800	2.5	96
ECSY325-8	SY325	900	2.5	96
ECSY325-7	SY325	1000	2.5	96
EC647-4	C647	700	1.5	96
EC647-3	C647	800	1.5	96
EC647-2	C647	900	1.5	96
EC647-6	C647	950	1.5	96
EC647-1	C647	1000	1.5	96
EC647-7	C647	900	2.5	96
EC647-5	C647	1000	2.5	96

Table S3. Summary of major phase proportions in SY400B experiments constrained using Solver and their respective bulk and solid densities.

Experiment	T (°C)	P (GPa)	Phases (wt. %)									Bulk density, kg/m^3	Solid density, kg/m^3	$\sum r^2$
			Cpx	Ph	Chl	Ep	Ttn	Plag	Amp	Phl	melt			
ECSY400B-6b	1.5	500	58.9	23.1	12.6	1.5	3.0					3167	3167	0.96
ECSY400B-2	1.5	600	59.7	21.9	12.6	2.0	3.1					3167	3167	1.36
ECSY400B-3	1.5	700	39.0	21.8			2.4		35.2			3166	3166	0.73
ECSY400B-9	1.5	800	26.8				2.5	29.2	14.0	21.6	5.9	2927	2973	0.39
ECSY400B-10	1.5	900	19.3					24.1	28.8	12.8	13.7	2898	2985	0.69
ECSY400B-8	1.5	1000	18.9					18.1	27.5	9.1	23.9	2858	3003	2.99

			Cpx	Ph	Chl	Ep	Tnt	Amp	Phl	Grt	melt	Bulk density, kg/m^3	Solid density, kg/m^3	$\sum r^2$
ECSY400B-7	2.5	600	60.7	20.0	13.0	2.7	3.0					3204	3204	1.26
ECSY400B-4	2.5	700	59.9	23.6	12.9	0.3	2.9					3170	3170	0.62
ECSY400B-5	2.5	800	51.2	2.5		9.5			26.6	2.1	8.1	3137	3195	0.69
ECSY400B-11	2.5	900	49.4			8.2			26.4	3.4	11.9	3112	3186	0.26
ECSY400B-12	2.5	1000	44.5						18.6	10.8	24.5	3081	3252	1.9
ECSY400B-13	2.5	1050	42.3					2.2	12.5	10.7	33.0	3057	3262	0.82

Table S4. Summary of major phase proportions in SY325 experiments constrained using Solver and their respective bulk and solid densities.

			Phases (wt. %)								
Experiment	T (°C)	P (GPa)	Amp	Chl	Tlc/Ath	Opx	Cpx	melt	Bulk density, kg/m^3	Solid density, kg/m^3	$\sum r^2$
ECSY325-4	1.5	600	76.7	6.2	17.1				3002	3002	0.53
ECSY325-3	1.5	700	76.4	6.4	17.2				2993	2993	0.78
ECSY325-2	1.5	800	83.6			16.4			3074	3074	1.26
ECSY325-9	1.5	850	78.7			18.0		3.3	3046	3070	0.68
ECSY325-1	1.5	900	76.8			19.1	0.1	3.9	3043	3071	0.93
ECSY325-6	1.5	1000				49.5	31.7	15.7	3091	3239	1.35
ECSY325-10	1.5	1000				47.8	36.1	14.4	3105	3239	1.82
ECSY325-5	2.5	600	77.8	7.1	15.0				3043	3043	0.49
ECSY325-11	2.5	800	71.8	4.8	23.4				3040	3040	0.19
ECSY325-8	2.5	900	56.6			27.7	11.2	4.5	3130	3158	0.71
ECSY325-7	2.5	1000	0.0			46.5	38.1	14.0	3167	3272	1.33

Table S5. Summary of major phase proportions in C647 experiments constrained using Solver and their respective bulk and solid densities.

Experiment	T (°C)	P (GPa)	Phases (wt. %)								Bulk density, kg/m^3	Solid density, kg/m^3	$\sum r^2$
			oxide	Amp	Chl	Grt	Ol	Opx	Cpx	melt			
EC647-4	1.5	700	2.5	45.6	51.9						2994.9	2994.9	0.45
EC647-3	1.5	800	2.1	42.4	50.2	4.2	1.2				2961.7	2961.7	0.34
EC647-2	1.5	900	0.2	20.0		46.2	24.1				3484.6	3484.6	2.86
EC647-6	1.5	950		15.7		42.1	22.0	10.9			3467.2	3467.2	3.81
EC647-1*	1.5	1000	6.7	31.6			35.6	*minor*		19.5	3073.1	3265.0	1.11
EC647-7	2.5	900	0.2	18.6		48.1	24.2				3487.8	3487.8	0.95
EC647-5	2.5	1000	0.9	10.1		47.2	25.2		9.1		3491.5	3491.5	0.36

*difference in the proportions of olivine and orthopyroxene constrained by LIME estimates. However, the calculated densities display good agreement between the two methods.

Table S6. Major element composition of minerals and melt in SY400B experiments

Experiment	T (°C)	P (GPa)	Phase	*n*	Average (wt.%) *+ 1 σ*												Comments
					SiO2	TiO2	Al2O3	FeO	MnO	MgO	CaO	Na2O	K2O	P2O5	Cr2O3	NiO	
ECSY400B-6b	500	1.5	Cpx	8	56.36	0.09	11.55	5.52	0.13	7.08	10.71	8.74					
					0.35	*0.05*	*1.02*	*0.49*	*0.03*	*0.78*	*1.23*	*0.77*					
			Ph	8	50.38	0.22	30.48	2.38		3.10	0.01	0.52	6.03				
					0.66	*0.03*	*0.73*	*0.19*		*0.22*	*0.02*	*0.11*	*0.15*				
			Chl	8	28.15		21.27	11.60	0.20	26.10						0.11	
					0.17		*0.22*	*0.29*	*0.02*	*0.37*						*0.03*	
			Ep	10	38.35	0.10	27.19	7.25	0.14		22.92	0.04		0.04	0.09	0.08	
					0.41	*0.03*	*0.48*	*0.50*	*0.06*		*0.68*	*0.02*		*0.02*	*0.08*	*0.02*	
			Plag	3	67.51		19.23	0.21			0.06	12.04	0.03				
					0.41		*0.06*	*0.04*			*0.02*	*0.06*	*0.01*				
			Ttn	7	30.59	38.64	1.02	0.34	0.05	0.02	28.64	0.08	0.02	0.06		0.05	
					0.25	*0.44*	*0.28*	*0.13*	*0.01*	*0.02*	*0.20*	*0.03*	*0.01*	*0.04*		*0.03*	
			Ap	1	0.22	0.06	0.02	0.23	0.03	0.01	58.90		0.02	41.43			Accessory
			Tur	5	36.89	0.40	31.38	3.85	0.02	9.87	0.24	2.93	0.02			0.05	Accessory
					0.40	*0.09*	*0.14*	*0.27*	*0.01*	*0.22*	*0.08*	*0.08*	*0.01*			*0.03*	
ECSY400B-2	600	1.5	Cpx	7	56.11	0.11	11.86	5.52	0.13	6.82	10.25	9.00					
					0.53	*0.03*	*0.69*	*0.21*	*0.01*	*0.43*	*0.61*	*0.45*					

			Ph	8	50.61	0.24	30.50	2.32		3.17		0.58	6.01		0.06		
					0.44	*0.04*	*0.73*	*0.10*		*0.19*		*0.11*	*0.15*		*0.05*		
			Chl	10	28.24		21.33	11.83	0.20	26.04						0.11	
					0.20		*0.16*	*0.19*	*0.02*	*0.29*						*0.04*	
			Ep	8	38.65	0.16	27.34	7.31	0.15	0.10	23.22		0.03		0.16	0.06	
					0.23	*0.07*	*0.55*	*0.68*	*0.05*	*0.05*	*0.67*		*0.01*		*0.03*	*0.03*	
			Plag	7	68.71		19.58	0.18			0.07	11.99	0.02				
					0.79		*0.28*	*0.06*			*0.06*	*0.13*	*0.01*				
			Ttn	7	30.98	38.14	1.27	0.41	0.03		28.64	0.08		0.02		0.03	
					0.17	*0.48*	*0.24*	*0.05*	*0.01*		*0.21*	*0.03*		*0.01*		*0.01*	
			Tur	4	37.28	0.35	31.17	4.52		9.49	0.18	2.84					Accessory
					0.22	*0.06*	*0.33*	*0.08*		*0.12*	*0.02*	*0.05*					
ECSY400B-3	700	1.5	Cpx	8	56.65	0.08	11.63	5.56	0.12	6.97	10.71	8.76					
					0.28	*0.03*	*0.45*	*0.49*	*0.02*	*0.38*	*0.46*	*0.27*					
			Amp	7	46.02	0.56	15.91	9.08	0.25	12.89	8.94	3.79	0.26		0.05		
					0.81	*0.20*	*0.78*	*0.79*	*0.07*	*0.73*	*0.35*	*0.37*	*0.05*		*0.04*		
			Ph	10	50.18	0.18	30.55	2.35		2.97	0.02	0.52	6.44		0.07		
					0.83	*0.05*	*0.74*	*0.17*		*0.32*	*0.05*	*0.12*	*0.77*		*0.04*		
			Ep	6	38.47	0.06	27.06	7.72	0.19		23.02	0.04		0.05		0.08	
					0.32	*0.04*	*0.71*	*0.96*	*0.04*		*0.65*	*0.03*		*0.03*		*0.01*	

			Plag	2	65.00		21.47	0.42	0.01	0.46	2.51	10.07	0.33	0.02		0.02	
					0.09		*0.20*	*0.08*	*0.00*	*0.10*	*0.40*	*0.30*	*0.18*	*0.01*		*0.01*	
			Ttn	6	30.89	38.18	1.40	0.40	0.04		28.65	0.05		0.02			
					0.11	*0.38*	*0.10*	*0.06*	*0.01*		*0.19*	*0.03*		*0.01*			
			Tur	3	37.86	0.31	31.37	4.34	0.02	9.46	0.20	2.90	0.27		0.05	0.05	Accessory
					1.16	*0.16*	*0.71*	*0.31*	*0.01*	*0.69*	*0.05*	*0.14*	*0.42*		*0.04*	*0.04*	
			Ap	1	0.09	0.00	0.00	0.19	0.03	0.03	57.57	0.11	0.03	41.10	0.00	0.01	Accessory
			melt														with visible melt surrounding residual phases; the size is too small to obtain good analysis.
ECSY400B-9	800	1.5	Cpx	4	51.83	0.19	7.71	8.13	0.18	9.53	17.27	4.37	0.02	0.02	0.07	0.02	
					0.29	*0.08*	*0.99*	*0.62*	*0.02*	*0.44*	*0.52*	*0.46*	*0.01*	*0.01*	*0.02*	*0.01*	
			Amp	12	41.69	0.66	16.69	9.22	0.20	12.78	9.72	4.29	0.99			0.04	
					0.26	*0.23*	*0.61*	*0.50*	*0.02*	*0.24*	*0.19*	*0.26*	*0.21*			*0.02*	
			Phlog	9	38.02	0.36	20.04	8.06	0.11	17.86	0.05	0.94	7.59		0.05	0.09	
					0.68	*0.26*	*0.73*	*0.30*	*0.02*	*0.88*	*0.02*	*0.18*	*0.65*		*0.03*	*0.03*	
			Ph	3	49.67	0.17	31.51	2.28		2.83		0.78	6.35		0.07		
					0.52	*0.04*	*0.58*	*0.22*		*0.31*		*0.11*	*0.10*		*0.02*		
			Ep	9	38.25	0.10	27.16	7.51	0.12	0.07	23.33		0.03	0.02	0.15		
					0.35	*0.03*	*1.50*	*1.49*	*0.06*	*0.06*	*0.64*		*0.01*	*0.01*	*0.06*		
			Ttn	10	30.63	32.16	1.28	0.40	0.05		28.90	0.08	0.04	0.02	0.03		

					0.17	*0.72*	*0.24*	*0.09*	*0.02*		*0.23*	*0.02*	*0.03*	*0.01*	*0.01*			
			Plag	7	60.67		24.32	0.38			5.31	8.15	0.65					
					1.14		*0.83*	*0.12*			*0.74*	*0.40*	*0.27*					
			melt	9	59.37	0.07	18.36	0.60		0.17	0.99	2.85	1.23					
					0.91	*0.03*	*0.90*	*0.07*		*0.21*	*0.15*	*0.41*	*0.16*					
ECSY400B-10	900	1.5	Cpx	12	51.00	0.30	7.37	7.91	0.23	10.99	18.66	3.00			0.10			
					0.91	*0.10*	*0.66*	*0.58*	*0.02*	*0.44*	*0.78*	*0.57*			*0.05*			
			Amp	10	42.80	1.34	14.84	9.25	0.16	13.55	9.89	4.11	1.06	0.03		0.03		
					0.48	*0.51*	*0.47*	*0.19*	*0.01*	*0.31*	*0.21*	*0.20*	*0.10*	*0.02*		*0.01*		
			Phl	10	36.86	0.34	20.31	8.11	0.09	18.89	0.06	0.96	8.60		0.04	0.08		
					0.57	*0.27*	*0.67*	*0.21*	*0.01*	*0.26*	*0.03*	*0.11*	*0.15*		*0.02*	*0.03*		
			Ttn	10	30.83	37.05	1.28	0.39	0.03	0.01	28.56							
					0.15	*0.47*	*0.23*	*0.09*	*0.01*	*0.01*	*0.21*							
			Ep	9	38.61	0.09	27.37	7.17	0.14	0.05	23.26							
					0.13	*0.02*	*0.70*	*0.82*	*0.04*	*0.05*	*0.65*							
			Plag	10	60.84		24.52	0.29			5.49	8.20	0.62					
					1.81		*1.57*	*0.05*			*1.17*	*0.65*	*0.13*					
			Rt	3	0.28	96.88	0.37	2.40		0.04	0.70				0.09			Accessory
					0.29	*0.87*	*0.03*	*0.18*		*0.02*	*0.54*				*0.03*			
			melt	10	62.12	0.18	20.36	0.90	0.03	0.26	1.09	4.29	1.57	0.03				

					0.29	*0.08*	*0.11*	*0.03*	*0.01*	*0.02*	*0.04*	*0.18*	*0.04*	*0.02*			
ECSY400B-8	1000	1.5	Cpx	10	52.20	0.26	6.76	6.20	0.20	13.13	19.36	2.13	0.03		0.12	0.03	
					0.60	*0.18*	*1.50*	*0.73*	*0.02*	*0.95*	*0.59*	*0.54*	*0.01*		*0.06*	*0.02*	
			Amp	14	41.69	1.73	16.71	8.27	0.14	14.21	10.25	3.51	1.11				
					0.62	*1.45*	*1.14*	*0.39*	*0.02*	*0.70*	*0.35*	*0.19*	*0.17*				
			Plag	4	60.30	0.02	24.67	0.14	0.03		6.19	7.45	0.68				
					0.75	*0.01*	*0.36*	*0.01*	*0.02*		*0.42*	*0.36*	*0.03*				
			Phl	8	37.13	0.14	20.54	7.06	0.06	20.95	0.05	1.32	8.05		0.02	0.11	
					0.28	*0.12*	*0.59*	*0.47*	*0.01*	*0.63*	*0.02*	*0.11*	*0.11*		*0.01*	*0.04*	
			Ep	3	38.04	0.10	27.02	6.98	0.17	0.20	22.01	0.05					
					0.28	*0.03*	*0.39*	*0.25*	*0.03*	*0.05*	*0.72*	*0.03*					
			Ttn	5	*30.57*	*38.74*	*1.04*	*0.41*	*0.05*		*28.54*	*0.02*	*0.04*	*0.05*		*0.05*	
					0.26	*0.32*	*0.24*	*0.11*	*0.02*		*0.13*	*0.01*	*0.02*	*0.02*		*0.03*	
			Apatite	3	0.14	0.02		0.26	0.05	0.02	57.37	0.04	0.07	41.76		0.05	Accessory
					0.10	*0.01*		*0.04*	*0.01*	*0.01*	*0.29*	*0.03*	*0.03*	*0.18*		*0.01*	
			melt	11	60.91	0.24	21.47	1.81	0.06	0.80	1.76	4.16	1.58	0.19			
					0.24	0.05	0.13	0.07	0.02	0.02	0.07	0.17	0.02	0.04			
ECSY400B-7	600	2.5	Cpx	7	56.16	0.12	12.33	5.14	0.09	6.78	10.04	9.02	0.14				
					0.66	*0.04*	*0.75*	*0.28*	*0.04*	*0.74*	*0.88*	*0.87*	*0.12*				

			Ph	4	49.94	0.22	29.86	2.39		2.63	0.10	0.57	6.91	0.04	0.15	0.02	
					3.97	*0.07*	*1.35*	*0.12*		*0.28*	*0.07*	*0.33*	*0.63*	*0.03*	*0.09*	*0.01*	
			Chl	1	26.54	0.08	18.29	11.49	0.16	25.83	0.13	0.54	0.03		0.11	0.09	
			Ep	4	38.80	0.05	27.15	7.64	0.12	0.07	22.89	0.02		0.03	0.10		
					0.08	*0.04*	*0.54*	*0.72*	*0.06*	*0.04*	*0.95*	*0.00*		*0.02*	*0.05*		
			Ttn	7	31.02	38.51	1.14	0.35	0.06	0.03	28.65	0.06	0.04	0.08	0.12	0.05	
					0.12	*0.62*	*0.26*	*0.05*	*0.01*	*0.01*	*0.10*	*0.02*	*0.02*	*0.03*	*0.01*	*0.02*	
			Tur	3	36.45	0.41	31.04	3.45	0.01	9.63	0.28	2.82			0.02		
					0.13	*0.09*	*0.09*	*0.16*	*0.00*	*0.28*	*0.06*	*0.03*					
			Rt														
ECSY400B-4	700	2.5	Cpx	7	56.14	0.09	11.10	5.15	0.09	7.31	11.67	8.16			0.10		
					0.31	0.02	0.88	0.44	0.02	0.60	1.06	0.46			0.02		
			Ph	9	49.66	0.20	31.39	2.37	0.03	2.58	0.05	0.60	6.68			0.03	
					0.47	*0.04*	*0.63*	*0.11*	*0.01*	*0.23*	*0.02*	*0.15*	*0.17*			*0.02*	
			Ep	10	38.11	0.08	26.91	7.94	0.11	0.08	23.07			0.02	0.06		
					0.24	*0.02*	*0.70*	*0.93*	*0.04*	*0.05*	*0.61*			*0.01*	*0.04*		
			Ttn	4	31.27	37.94	1.37	0.49	0.03		28.06			0.06	0.02		
					0.37	*0.62*	*0.27*	*0.07*	*0.02*		*0.52*			*0.04*	*0.01*		
			Ap	3		0.05		0.11	0.05	0.04	57.24		0.03	42.03			Accessory
						0.01		*0.07*	*0.00*	*0.01*	*0.35*		*0.02*	*0.18*			
			Chl														no measurement

			rutile														Accessory
ECSY400B-5	800	2.5	Cpx	9	56.43	0.07	11.42	5.30	0.12	7.23	11.06	8.55					
					0.26	*0.04*	*0.48*	*0.50*	*0.02*	*0.48*	*0.76*	*0.46*					
			Ph	8	50.34	0.20	31.48	2.35		2.96		0.58	6.42				
					0.44	*0.04*	*0.79*	*0.20*		*0.27*		*0.09*	*0.58*				
			Grt	3	39.51	0.21	23.67	17.83	1.22	13.22	5.21		0.05	0.22	0.08	0.04	
					0.79	*0.15*	*1.44*	*0.70*	*0.26*	*0.68*	*0.58*		*0.02*	*0.04*	*0.02*	*0.01*	
			Ep	6	38.55	0.13	26.80	7.30	0.09	0.04	23.53		0.03	0.04	0.13		
					0.14	*0.09*	*0.51*	*0.67*	*0.04*	*0.01*	*0.61*		*0.02*	*0.01*	*0.05*		
			Tur	5	37.11	0.31	30.06	4.39		9.55	0.17	2.99					Accessory
					0.18	*0.22*	*0.21*	*0.49*		*0.25*	*0.07*	*0.02*					
			Ap	2				0.26	0.08	0.04	57.04		0.04	41.56	0.06	0.06	Accessory
								0.02	*0.01*	*0.02*	*0.14*		*0.01*	*0.04*	*0.03*	*0.02*	
			melt	9	62.31	0.36	15.95	0.53	0.02	0.19	1.58	2.38	0.86	0.17			
					1.76	*0.40*	*1.24*	*0.07*	*0.01*	*0.07*	*0.08*	*0.74*	*0.15*	*0.03*			
ECSY400B-11	900	2.5	Cpx	8	56.28	0.10	11.47	5.25	0.11	7.33	11.75	8.24			0.05		
					0.44	*0.05*	*1.17*	*0.60*	*0.02*	*0.76*	*1.19*	*0.68*			*0.04*		
			Phl	10	39.13	1.25	21.32	7.09	0.02	15.42	0.07	0.83	8.69			0.06	
					1.16	*0.88*	*0.86*	*0.34*	*0.01*	*2.55*	*0.08*	*0.17*	*0.32*			*0.02*	

			Ph	7	48.76	0.20	30.57	2.29	0.01	2.77	0.05	0.62	9.13			0.02	
					0.74	*0.04*	*0.96*	*0.12*	*0.01*	*0.25*	*0.02*	*0.16*	*0.90*			*0.01*	
			Ep	8	38.48	0.10	27.70	7.26	0.12	0.07	23.37			0.02	0.07		
					0.15	*0.04*	*0.60*	*0.70*	*0.05*	*0.05*	*0.59*			*0.01*	*0.04*		
			Grt	10	39.80	0.57	22.73	17.71	1.14	10.18	8.52	0.17	0.03		0.04		
					0.27	*0.06*	*0.21*	*0.35*	*0.24*	*0.37*	*0.42*	*0.03*	*0.01*		*0.02*		
			Ky	3	36.96	0.19	63.07	1.00	0.01	0.22	0.03	0.01	0.01	0.03			accessory
					0.18	*0.10*	*0.12*	*0.16*	*0.00*	*0.07*	*0.01*	*0.02*	*0.00*	*0.00*			
			melt	10	62.00	0.18	18.73	0.85	0.02	0.42	1.69	4.34	2.40	0.12			
					0.19	*0.02*	*0.08*	*0.04*	*0.01*	*0.04*	*0.04*	*0.24*	*0.06*	*0.02*			
			corundum														accessory
ECSY400B-12	1000	2.5	Cpx	10	54.26	0.20	11.27	5.54	0.13	8.32	13.27	6.71			0.03		
					1.92	*0.16*	*2.14*	*0.52*	*0.04*	*0.62*	*1.03*	*0.94*			*0.02*		
			Amp	9	41.79	0.80	18.33	7.92	0.11	13.24	9.30	3.91	1.57			0.03	
					0.48	*0.12*	*0.77*	*0.11*	*0.02*	*0.26*	*0.35*	*0.18*	*0.07*			*0.02*	
			Phl	8	37.65	2.96	19.31	8.12	0.03	16.25	0.05	0.82	8.73			0.07	
					0.35	*1.45*	*0.99*	*0.10*	*0.01*	*0.43*	*0.02*	*0.05*	*0.10*			*0.01*	
			Grt	9	40.01	0.57	22.72	15.11	0.69	13.53	7.31	0.15	0.02		0.04		
					0.41	0.06	0.08	0.14	0.08	0.38	0.47	0.03	0.01		0.02		

			melt	10	60.44	0.34	20.29	1.41	0.03	0.70	1.37	3.86	1.51	0.19			
					0.35	*0.02*	*0.05*	*0.06*	*0.01*	*0.05*	*0.06*	*0.23*	*0.06*	*0.07*			
			Ap	3	0.34			0.13			54.27		0.04	41.58			accessory
					0.44			*0.01*			*0.84*		*0.03*	*0.96*			
			Rt	1	0.37	98.26	1.08	1.27	0.00	0.19	0.06						accessory
			Tnt	1	44.41	14.88	6.76	3.16	0.05	4.59	19.57	4.32	0.01				accessory
ECSY400B-13	1050	2.5	Cpx	9	51.84	0.72	12.25	4.21	0.09	10.13	15.80	4.61			0.09		
					0.73	*0.16*	*0.64*	*0.36*	*0.03*	*0.41*	*0.65*	*0.41*			*0.03*		
			Amp	2	41.13	1.20	19.45	7.24	0.11	12.42	9.41	4.18	1.49		0.07	0.02	
					0.13	*0.58*	*0.91*	*0.04*	*0.00*	*0.10*	*0.02*	*0.44*	*0.58*		*0.04*	*0.01*	
			Phl	11	37.46	2.45	19.04	8.04	0.05	17.24	0.05	0.87	8.62		0.06	0.05	
					0.48	*0.80*	*1.19*	*0.23*	*0.01*	*0.32*	*0.02*	*0.07*	*0.13*		*0.04*	*0.04*	
			Grt	10	40.11	0.68	22.85	14.96	0.48	12.95	8.41	0.12			0.10		
					0.22	*0.17*	*0.25*	*0.87*	*0.09*	*0.81*	*0.89*	*0.05*			*0.04*		
			Rt	2		98.26	1.08	1.27		0.19	0.06				0.04		
						1.39	*0.15*	*0.05*		*0.17*	*0.03*				*0.02*		
			melt	9	56.36	0.49	20.68	1.97	0.03	1.06	1.61	6.55	3.08	0.11			
					0.12	*0.02*	*0.08*	*0.05*	*0.01*	*0.07*	*0.05*	*0.20*	*0.03*	*0.02*			

Table S7. Major element composition of minerals and melt in SY325 experiments

Experiment	T (°C)	P (GPa)	Phase	*n*	Average (wt.%) *+ 1 σ* SiO2	TiO2	Al2O3	FeO	MnO	MgO	CaO	Na2O	K2O	P2O5	Cr2O3	NiO	Comments
ECSY325-4	600	1.5	Amp	15	56.12		1.08	7.26	0.29	19.93	9.56	2.22	0.11		0.26	0.13	
					0.35		*0.29*	*0.46*	*0.04*	*0.53*	*0.59*	*0.39*	*0.04*		*0.17*	*0.05*	
			Chl	7	30.84		15.78	10.42	0.12	28.58	0.02					0.29	
					0.61		*0.33*	*0.13*	*0.02*	*0.66*	*0.01*					*0.06*	
			Tlc	7	61.27		0.04	3.94	0.03	28.70		0.03				0.24	
					0.53		*0.03*	*0.36*	*0.02*	*0.58*		*0.01*				*0.08*	
ECSY325-3	700		Amp	13	56.11		0.89	7.34	0.27	19.89	9.38	2.15	0.13		0.17	0.14	
					0.57		*0.31*	*0.66*	*0.05*	*0.43*	*0.80*	*0.53*	*0.03*		*0.13*	*0.05*	
			Chl	7	30.20		15.78	10.47	0.13	28.08	0.04				1.10	0.31	
					0.39		*0.59*	*0.14*	*0.01*	*0.40*	*0.03*				*0.94*	*0.05*	
			Tlc	8	61.56		0.06	3.45	0.02	27.85	0.05				0.02	0.23	
					0.59		*0.03*	*0.58*	*0.01*	*0.96*	*0.03*				*0.07*	*0.07*	
ECSY325-2	800		Amp	20	55.84	0.03	1.21	7.16	0.27	20.37	9.53	1.73	0.11		0.20	0.13	
					0.48	*0.02*	*0.40*	*0.54*	*0.04*	*1.02*	*0.59*	*0.42*	*0.03*		*0.15*	*0.03*	
			Opx	8	55.14	0.03	3.12	7.72	0.12	33.39	0.26	0.06				0.20	
					0.24	*0.02*	*0.22*	*0.33*	*0.02*	*0.38*	*0.03*	*0.02*				*0.03*	

ECSY325-9	850		Amp	16	55.94	0.03	1.31	7.06	0.28	20.27	9.47	1.82	0.12		0.26	0.14	
					0.49	*0.02*	*0.72*	*0.64*	*0.04*	*0.46*	*0.60*	*0.30*	*0.02*		*0.17*	*0.05*	
			Opx	12	56.43	0.06	2.74	6.10	0.09	33.95	0.31	0.12				0.30	
					0.83	*0.03*	*0.70*	*1.46*	*0.05*	*1.57*	*0.06*	*0.06*				*0.07*	
			melt														with visible melt surrounding residual phases; the size is too small to obtain good analysis.
ECSY325-1	900		Amp	8	56.03		1.00	7.17	0.31	20.31	9.63	1.74	0.12		0.28	0.13	
					0.18		*0.20*	*0.29*	*0.05*	*0.65*	*0.35*	*0.33*	*0.02*		*0.21*	*0.07*	
			Opx	8	55.65	0.03	2.17	7.41	0.16	33.69	0.43	0.07			0.08	0.28	
					0.71	*0.01*	*1.06*	*2.69*	*0.11*	*1.83*	*0.13*	*0.03*			*0.09*	*0.09*	
			Cpx	2	54.93	0.05	0.43	7.55	0.55	17.17	18.62	0.61		0.03	0.33	0.12	
					1.47	*0.02*	*0.09*	*1.21*	*0.08*	*0.98*	*1.31*	*0.06*		*0.01*	*0.07*	*0.01*	
			melt	3	69.86	0.06	14.83	0.84	0.03	1.43	1.04	2.91	0.43	0.13			
					2.61	*0.01*	*1.09*	*0.12*	*0.01*	*1.27*	*0.26*	*0.65*	*0.16*	*0.03*			
ECSY325-6	1000	1.5	Opx	14	56.46	0.04	0.26	8.96	0.30	32.77	1.40	0.08			0.18	0.20	
					0.43	*0.02*	*0.07*	*0.64*	*0.02*	*0.86*	*0.26*	*0.04*			*0.05*	*0.09*	
			Cpx	13	54.56	0.06	0.54	4.21	0.22	18.65	20.56	0.50		0.03	0.57	0.13	
					0.43	*0.03*	*0.13*	*0.58*	*0.02*	*0.89*	*0.88*	*0.12*		*0.02*	*0.12*	*0.12*	

			melt	16	67.23	0.23	13.85	2.24	0.06	0.51	0.96	5.36	0.95	0.04		
					1.12	*0.01*	*0.61*	*0.26*	*0.02*	*0.26*	*0.27*	*0.34*	*0.07*	*0.02*		
ECSY325-10	1000	1.5	Cpx	12	54.61	0.07	0.78	4.75	0.23	18.39	19.30	0.81			0.92	0.10
*time-series					*0.28*	*0.02*	*0.23*	*0.59*	*0.02*	*0.78*	*1.26*	*0.31*			*0.67*	*0.04*
			Opx	11	56.69		0.45	8.90	0.28	32.32	1.26	0.12			0.34	0.20
					0.66		*0.22*	*0.50*	*0.03*	*0.74*	*0.19*	*0.06*			*0.23*	*0.10*
			melt	13	66.04	0.21	14.66	1.74	0.03	0.37	0.68	5.18	1.00	0.04		
					1.07	*0.03*	*0.30*	*0.17*	*0.02*	*0.08*	*0.14*	*0.62*	*0.10*	*0.01*		
ECSY325-5	600	2.5	Amp	9	56.54		0.93	7.41	0.27	19.97	9.51	2.26	0.14		0.21	0.14
					0.51		*0.37*	*0.46*	*0.04*	*0.51*	*0.55*	*0.43*	*0.02*		*0.15*	*0.07*
			Chl	7	31.10		14.93	10.32	0.11	28.65	0.06	0.03			0.73	0.33
					0.27		*0.25*	*0.04*	*0.01*	*1.28*	*0.02*	*0.02*			*0.95*	*0.09*
			Tlc	9	61.44			3.64		29.93	0.03					0.17
					0.56			*0.76*		*0.41*	*0.01*					*0.03*
ECSY325-11	800	2.5	Amp	10	56.69	0.03	1.09	7.19	0.29	19.03	9.94	1.98	0.12		0.28	0.12
					0.55	*0.02*	*0.41*	*0.51*	*0.05*	*0.41*	*0.50*	*0.27*	*0.03*		*0.23*	*0.03*
			Chl/Saponite ?	4	41.72	0.18	8.49	3.55	0.04	19.41	0.42	0.74	0.03		0.93	0.58
					2.18	*0.02*	*0.58*	*0.17*	*0.01*	*3.30*	*0.43*	*0.41*	*0.02*		*0.34*	*0.04*

			Ant	13	56.21	0.04	4.06	6.62	0.09	31.12	0.32	0.15			0.04		
					0.62	*0.02*	*0.96*	*0.31*	*0.02*	*0.49*	*0.07*	*0.03*			*0.03*		
			oxide (chromite)	3	1.53	0.80	5.24	33.75	0.83	4.93	0.19				43.09	0.23	fine aggregates
					1.20	0.56	3.57	6.08	0.03	1.50	0.09				1.43	0.12	
ECSY325-8	900	2.5	Amp	9	55.99	0.03	0.97	7.26	0.27	20.13	9.47	2.37	0.13		0.28	0.14	
					0.52	*0.01*	*0.31*	*0.33*	*0.04*	*0.27*	*0.38*	*0.29*	*0.03*		*0.22*	*0.03*	
			Cpx	11	54.40	0.14	3.49	3.98	0.20	15.75	18.57	2.31			0.74	0.14	
					0.23	*0.05*	*0.58*	*0.39*	*0.03*	*0.69*	*0.70*	*0.40*			*0.63*	*0.04*	
			Opx	12	56.07	0.03	2.00	8.38	0.17	32.75	0.59	0.11			0.18	0.27	
					1.01	*0.02*	*1.21*	*2.53*	*0.11*	*1.63*	*0.15*	*0.05*			*0.24*	*0.12*	
			melt														with visible melt surrounding residual phases; the size is too small to obtain good analysis.
ECSY325-7	1000	2.5	Cpx	12	54.22	0.07	1.17	5.18	0.25	18.27	18.61	1.01			0.56	0.13	
					0.37	*0.02*	*0.42*	*0.82*	*0.05*	*0.95*	*1.25*	*0.22*			*0.24*	*0.03*	
			Opx	12	56.58		0.45	8.97	0.26	32.76	1.20	0.13			0.09	0.19	
					0.52		*0.32*	*1.84*	*0.10*	*1.36*	*0.39*	*0.03*			*0.08*	*0.13*	
			melt	10	65.79	0.18	14.36	0.82		0.24	0.36	7.72	1.00	0.02			
					1.09	*0.02*	*0.56*	*0.35*		*0.43*	*0.08*	*1.33*	*0.07*	*0.01*			

Table S8. Major element composition of minerals and melt in C647 experiments

Experiment	T (°C)	P (GPa)	Phase	*n*	Average (wt.%) *+ 1 σ* SiO2	TiO2	Al2O3	FeO	MnO	MgO	CaO	Na2O	K2O	P2O5	Cr2O3	NiO	Comments
EC647-4	700	1.5	Amp	8	48.74	0.19	7.82	7.60	0.14	18.99	11.80	1.68	0.23		0.03	0.08	
					0.88	*0.03*	*0.47*	*0.14*	*0.02*	*0.98*	*0.71*	*0.11*	*0.03*		*0.03*	*0.03*	
			Chl	3	32.27	0.03	17.45	8.85	0.05	28.47	0.21		0.01		0.05	0.10	
					1.64	*0.01*	*0.88*	*0.22*	*0.00*	*0.32*	*0.30*		*0.00*		*0.03*	*0.02*	
			Ilm	2	0.13	51.44	0.02	43.43	0.98	2.90			0.16		0.26		
					0.14	*0.06*	*0.01*	*0.44*	*0.04*	*0.23*			*0.14*		*0.35*		
EC647-3	800	1.5	Amp	3	51.16	0.20	5.72	6.88	0.13	18.72	12.15	1.37	0.21		0.10	0.07	
					0.88	*0.02*	*0.62*	*0.10*	*0.03*	*0.35*	*0.26*	*0.13*	*0.03*		*0.03*	*0.03*	
			Chl	9	29.72	0.04	17.80	8.67	0.04	28.41						0.10	
					1.38	*0.02*	*0.70*	*0.69*	*0.02*	*1.21*						*0.02*	
			Ol	9	40.03	0.04	0.37	20.39	0.25	40.33	0.21				0.02	0.22	
					1.05	*0.02*	*0.07*	*0.18*	*0.05*	*0.43*	*0.06*				*0.01*	*0.01*	
			Grt	15	40.46	0.45	22.80	16.39	0.88	13.23	5.19				0.13		
					0.71	*0.11*	*0.61*	*0.62*	*0.12*	*1.25*	*0.59*				*0.07*		
			Ilm	5	0.28	53.22	0.44	36.38	0.43	8.07	0.21		0.26	0.29	0.41		
					0.29	*0.49*	*0.37*	*0.43*	*0.05*	*0.26*	*0.02*		*0.05*	*0.02*	*0.03*		
			high Al-phase (spinel?)														fine grains are too small to obtain good analysis.

EC647-2	900	1.5	Amp	6	50.56	0.29	6.84	7.26	0.16	19.01	12.13	1.65	0.26		0.10	0.05
					0.90	*0.04*	*0.83*	*0.39*	*0.02*	*0.55*	*0.17*	*0.10*	*0.06*		*0.09*	*0.02*
			Ol	10	40.03	0.12	0.12	14.44	0.13	45.28	0.07				0.08	0.22
					1.27	*0.08*	*0.06*	*0.14*	*0.03*	*1.26*	*0.01*				*0.05*	*0.04*
			Grt	6	40.90	0.64	22.72	11.63	0.42	16.77	6.93	0.11		0.06	0.11	
					1.69	*0.10*	*1.64*	*0.42*	*0.04*	*1.19*	*0.56*	*0.10*		*0.01*	*0.05*	
			Ilm	1	0.02	56.64	0.31	29.99	0.32	11.78	0.12		0.21	0.30	0.34	
EC647-6	950	1.5	Amp	9	48.25	0.29	7.18	7.41	0.16	18.59	11.97	1.73	0.27			0.06
					1.00	*0.04*	*0.73*	*0.30*	*0.01*	*0.37*	*0.22*	*0.15*	*0.05*			*0.03*
			Opx	10	51.78	0.49	8.18	9.58	0.14	28.68	0.73					
					0.92	*0.13*	*1.35*	*0.26*	*0.03*	*0.67*	*0.08*					
			Ol	10	39.23	0.10	0.15	15.06	0.07	45.42	0.10					0.19
					0.28	*0.04*	*0.11*	*0.17*	*0.09*	*0.34*	*0.02*					*0.04*
			Grt	10	40.15	0.86	23.12	11.97	0.48	15.10	8.58				0.07	
					0.31	*0.10*	*0.17*	*0.14*	*0.02*	*0.19*	*0.29*				*0.02*	
			Ilm	9	0.02	55.74	0.43	31.07	0.00	11.45	0.15					0.10
					0.02	*0.61*	*0.02*	*0.22*	*0.00*	*0.28*	*0.06*					*0.02*

			melt													with visible melt surrounding residual phases; the size is too small to obtain good analysis.
EC647-1	1000	1.5	Amp	7	42.33	2.16	15.39	5.63	0.09	17.61	11.58	1.77	0.26		0.07	0.04	
					0.52	*0.14*	*0.56*	*0.31*	*0.02*	*0.21*	*0.16*	*0.11*	*0.01*		*0.06*	*0.02*	
			Ol	10	39.29	0.09	0.28	14.53	0.16	45.66	0.21				0.03	0.13	
					0.36	*0.05*	*0.15*	*0.27*	*0.02*	*0.07*	*0.03*				*0.02*	*0.02*	
			Opx	16	52.57	0.42	6.30	9.49	0.19	29.42	0.96	0.03			0.05		
					0.49	*0.06*	*0.79*	*0.37*	*0.02*	*0.38*	*0.13*	*0.02*			*0.03*		
			Cpx	9	50.44	1.05	5.98	4.58	0.12	16.50	21.45	0.17			0.06	0.05	
					2.10	*0.62*	*2.35*	*0.41*	*0.04*	*1.21*	*0.70*	*0.05*			*0.03*	*0.01*	
			melt	7	51.69	0.83	21.56	2.36	0.08	1.32	10.13	0.54	0.21	0.15			
					1.99	*0.11*	*0.38*	*0.68*	*0.02*	*0.51*	*0.43*	*0.06*	*0.19*	*0.01*			
			high Al-phase (spinel?)														fine grains are too small to obtain good analysis.
EC647-7	900	2.5	Amp	10	49.85	0.23	6.63	7.26	0.14	18.25	12.04	1.68	0.23			0.08	
					0.50	*0.02*	*0.51*	*0.24*	*0.02*	*0.35*	*0.15*	*0.14*	*0.04*			*0.02*	
			Ol	9	39.59	0.07		12.65		47.48	0.09					0.25	
					0.39	*0.04*		*0.63*		*0.57*	*0.03*					*0.04*	

			Grt	10	41.11	1.22	22.63	10.95	0.23	16.45	7.12				0.10	
					0.55	0.08	0.71	0.49	0.04	0.60	0.43				0.04	
			Ilm	9	0.03	56.62	0.27	29.83		12.71	0.11				0.04	0.08
					0.02	*0.24*	*0.01*	*0.21*		*0.14*	*0.04*				*0.03*	*0.02*
EC647-5	1000	2.5	Amp	7	43.87	1.50	12.59	4.27	0.02	19.51	11.14	3.02	0.52		0.15	
					0.51	*0.04*	*0.49*	*0.03*	*0.01*	*0.38*	*0.20*	*0.07*	*0.02*		*0.05*	
			Ol	14	39.40	0.13	0.23	12.66	0.08	47.48	0.22					0.21
					0.22	*0.04*	*0.25*	*0.33*	*0.04*	*0.62*	*0.15*					*0.05*
			Cpx	5	53.30	0.44	2.53	3.94	0.07	18.22	21.21	0.53			0.08	
					0.61	*0.12*	*0.55*	*0.68*	*0.03*	*0.57*	*0.84*	*0.11*			*0.05*	
			Grt	6	40.83	1.03	23.23	9.56	0.20	16.10	6.13	0.03			0.15	
					0.47	*0.57*	*0.47*	*0.56*	*0.06*	*0.58*	*0.55*	*0.02*			*0.05*	
			Ilm	4	0.12	56.47	0.40	27.84	0.16	14.48			0.02	0.02		
					0.09	*0.97*	*0.03*	*0.33*	*0.00*	*0.74*			*0.01*	*0.01*		

Table S9. Viscosities of experimental melange melts calculated using the parametrization of Giordano et al. 2008.

Experiment	T (°C)	P (GPa)	log n (Pa s)
SY400B-9	800	1.5	1.8
SY400B-10	900	1.5	2.4
SY400B-8	1000	1.5	2.1
SY400B-5	800	2.5	2.1
SY400B-11	900	2.5	2.3
SY400B-12	1000	2.5	1.6
SY400B-13	1050	2.5	1.3
SY325-1	900	1.5	3.1
SY325-6	1000	1.5	2.1
SY325-7	1000	2.5	1.6
Cat647-1	1000	1.5	1.1

Table 10. Summary of major phase proportions in SY400B experiments constrained using LIME and their respective bulk and solid densities.

			Phases (wt. %)									1 σ										
Experiment	T (°C)	P (GPa)	Cpx	Ph	Chl	Ep	Ttn	Plag	Amp	Phl	melt	Cpx	Ph	Chl	Ep	Ttn	Plag	Amp	Phl	melt	Bulk density, kg/m^3	Solid density, kg/m^3
ECSY400B-6b	1.5	500	57.3	30.3	9.7		2.7					3.2	2.4	2.4		0.2					3149	3149
ECSY400B-2	1.5	600	60.6	27.3	9.4		2.6					2.6	2.7	1.9		0.1					3158	3158
ECSY400B-3	1.5	700	39.0	27.5			2.3		31.2			8.2	3.8			0.2		8.5			3147	3147
ECSY400B-9	1.5	800	23.0				2.7	27.2	17.3	18.6	11.2	7.1				0.3	8.7	11.5	6.0	10.6	2892	2980
ECSY400B-10	1.5	900	32.8					27.2	7.8	20.0	9.9	3.5				0.2	4.8	3.9	1.0	4.8	2898	2960
ECSY400B-8	1.5	1000	23.5					24.0	20.3	16.1	16.1	3.1					5.8	5.8	2.0	7.3	2873	2961

			Cpx	Ph	Chl	Ep	Tnt	Amp	Phl	Grt	melt	Cpx	Ph	Chl	Ep	Tnt	Amp	Phl	Grt	melt	Bulk density, kg/m^3	Solid density, kg/m^3
ECSY400B-7	2.5	600	58.4	15.9	23.4		2.3					4.0	3.9	4.1		0.2					3168	3168
ECSY400B-4	2.5	700	58.6	28.0	10.5		2.9					2.7	2.2	1.8		0.4					3163	3163
ECSY400B-5	2.5	800	53.1	5.0		10.6	0.0		20.9	0.0	10.4	4.6	5.9		3.0			2.9		3.6	3123	3197
ECSY400B-11	2.5	900	47.7			7.8	0.0		20.1	7.4	17.0	4.7			2.3			1.4	2.0	3.2	3144	3252
ECSY400B-12	2.5	1000	46.5				0.0		16.9	7.4	29.2	6.6						3.4	4.4	6.3	3042	3238
ECSY400B-13	2.5	1050	45.9						14.6	12.0	27.5	1.7						0.7	1.4	1.3	3090	3261

Table S11. Summary of major phase proportions in SY325 experiments constrained using LIME and their respective bulk and solid densities.

			Phases (wt. %)						1 σ							
Experiment	T (°C)	P (GPa)	Amp	Chl	Tlc/Ath	Opx	Cpx	melt	Amp	Chl	Tlc/Ath	Opx	Cpx	melt	Bulk density, kg/m^3	Solid density, kg/m^3
ECSY325-4	1.5	600	76.3	6.8	16.9				1.3	2.7254	2.4				3000	3000
ECSY325-3	1.5	700	77.3	7.3	15.4				2.1	3.5	2.9				2994	2994
ECSY325-2	1.5	800	86.2			13.8			3.6			3.6			3068	3068
ECSY325-9	1.5	850	83.5			16.5			2.6			2.6			3066	3066
ECSY325-1	1.5	900	72.4			19.8		7.7	5.1			5.4		1.3	3018	3074
ECSY325-6	1.5	1000				52.8	33.5	13.8				1.4	1.5	0.6	3113	3239
ECSY325-10	1.5	1000				49.2	39.9	10.9				2.5	2.3	0.8		3238
ECSY325-5	2.5	600	76.6	6.2	17.2				1.4	3.0	2.7				3040	3040
ECSY325-11	2.5	800	71.7	9.0	19.3				7.2	4.5	10.2				3030	3030
ECSY325-8	2.5	900	63.1			29.5	7.4		9.5			3.4	6.9		3150	3150
ECSY325-7	2.5	1000				49.3	38.5	12.1				3.1	2.9	0.8	3183	3272

Table S12. Summary of major phase proportions in C647 experiments constrained using LIME and their respective bulk and solid densities.

Experiment	T (°C)	P (GPa)	Phases (wt. %)								1 σ									
			oxide	Amp	Chl	Grt	Ol	Opx	Cpx	melt	oxide	Amp	Chl	Grt	Ol	Opx	Cpx	melt	Bulk density, kg/m^3	Solid density, kg/m^3
EC647-4	1.5	700	2.7	51.7	45.6						0.6	3.5	3.6						3024	3024
EC647-3	1.5	800		45.7	37.5	11.6	5.2					2.0	3.8	4.0	2.7				3037	3037
EC647-2	1.5	900	1.6	25.8		51.4	21.2				0.4	3.0		3.9	2.9				3498	3498
EC647-6	1.5	950	1.0	25.6		34.4	17.8	21.2			0.1	1.7		2.4	1.4	2.3			3416	3416
EC647-1*	1.5	1000		37.2			20.3	21.0	2.2	19.3		4.0			7.6	10.0	3.4	3.8	3055	3224
EC647-7	2.5	900	0.8	23.3		49.6	26.2				0.1	1.6		1.7	1.0				3476	3476
EC647-5	2.5	1000	1.2	9.9		47.2	28.4		13.2		0.4	11.2		9.7	6.1		5.8		3482	3482

*difference in the proportions of olivine and orthopyroxene constrained by Solver estimates. However, the calculated densities display good agreement between the two methods.

Supplementary materials for Chapter 5

Experimental Methods

Starting material preparation

Alteration-free, natural peridotite (LZ-1; type-locality in Lherz, France) was grinded to a fine powder using agate ball mill. The bulk composition of LZ-1 is similar to Depleted MORB Mantle[1] (DMM) in major and trace element compositions (Fig. S1) and is here considered to be representative of peridotite mantle wedge. Following grinding, the LZ-1 powder was loaded into a nickel bucket and preconditioned in a 1-atm vertical gas-mixing furnace at 1100 °C with fO_2 maintained at the FMQ buffer (Fayalite-Magnetite-Quartz buffer) for 96 h. This fO_2 was adjusted by changing the partial pressures of CO and CO_2 gases in the furnace, and is within the range of estimated fO_2 for sub-arc mantle[2,3]. Two chlorite schist matrices from Syros (Greece) were selected to represent two end-member compositions of global mélange rocks: the sediment-dominated mélange matrix (SY400B) and the serpentinite-dominated mélange matrix (SY325). Both natural mélange matrices contain water contents of ~ 2-3 wt. %. We acknowledge that there exists a wide range in chemical and mineralogical compositions of exhumed mélange rocks worldwide and that there is no single rock material that can represent such wide variability. In order to account for this and capture its first-order variability, we selected two mélange matrix rocks from Syros (Greece) based on mineralogical assemblages (Table S1), immobile element chemistry (Fig. 1 | Cr vs Cr/Al plot), and trace element chemistry (Fig. S5). In Table S1, the mineralogical assemblages of SY400B and SY325 are consistent with being derived from a sediment-like and ultramafic/serpentinite-like protoliths, respectively. Using immobile element systematics, Fig. 1 shows a mixing trend between serpentinites and sediment/upper crustal rocks to account for the range in global mélange variability where mélange material SY400B plotted close to GLOSS composition while SY325 plotted close of DMM composition. In Fig. S5, the trace element composition of SY400B closely resemble the GLOSS composition while SY325 broadly resemble the DMM-like peridotite, with exception for some highly fluid-mobile elements (e.g., U, K). SY400B and SY325 from Syros record minimal late-stage modification and overprinting during their exhumation, making their mineralogy, elemental and volatile concentrations[4] closely approximate the *in-situ* compositions of mélange rocks at the slab-mantle interface. Taken

together, the mineralogy, immobile element (Cr vs Cr/Al) and trace element chemistry strongly support for the representability of mélange materials SY400B and SY325 to cover for the first-order variability in global mélange composition. Since Syros mélange is one of the most studied and well-constrained exhumed high-pressure mélange terranes in terms of its metamorphic *P-T-t* condition[5,6] and mélange formation[4,7,8], we have more control on the conditions at which our starting materials have been subjected to and the processes that led to their formation.

These natural mélange materials were grinded to fine powders using agate ball mill. PER-SED 95-5 starting material was prepared using 95 vol. % of LZ-1 and 5 vol. % of SY400B, PER-SED 85-15 was prepared using 85 vol. % of LZ-1 and 15 vol. % of SY400B, and PER-SERP 85-15 was prepared using 85 vol. % of LZ-1 and 15 vol. % of SY325. The peridotite and mélange components were completely homogenized through a thorough process of mixing under ethanol in an agate mortar for 6 cycles, where each cycle is 1 h of grinding. The resulting powder mixes were stored in a dry box until use. Whole-rock compositions (major and trace elements) of LZ-1, SY325, SY400B as well as PER-SED 95-5, 85-15 and PER-SERP 85-15 are summarized in Table S1.

Experimental technique

Partial melting experiments were performed in 0.5" end-loaded solid medium piston cylinder device[9] at the Woods Hole Oceanographic Institution (USA). The starting mixes were packed in $Au_{80}Pd_{20}$ capsules conditioned (Fe-saturated) to minimize Fe loss[10]. The $Au_{80}Pd_{20}$ capsules were conditioned by packing MORB-like basalt powder (AII92 29-1) in the capsules and firing them at 1250 °C in a 1-atm vertical gas-mixing furnace with fO_2 maintained at 1 log unit below FMQ buffer for 48 h. Ideally, we would have used actual starting materials to condition the capsules, but due to limited quantities of starting materials we considered that a MORB-like basalt would provide enough Fe to saturate the capsules. The silicate glass was removed from the $Au_{80}Pd_{20}$ capsules using warm HF-HNO_3 bath.

When loading the starting material into the conditioned $Au_{80}Pd_{20}$ capsules, approximately 35–45 mg of the starting mix was first packed in the capsule and then topped with 3.5-4 mg of vitreous carbon spheres (80-200 µm in diameter) to act as melt entrapments. The capsule was triple-crimped and welded shut. All the experiments were performed in a CaF_2 pressure assembly with pre-dried crushable MgO spacers, straight-walled graphite furnace and alumina sleeves. The sealed capsule was strategically positioned in the assembly such that the top portion of the capsule is the side that contains the vitreous carbons spheres to facilitate easy

migration of melt during the experiment. Silica powder was placed in between the sealed capsule and alumina sleeve to fill up the space and maintain the capsule's position. Lubricated Pb foils were used to contain the friable CaF_2 assembly and to provide lubrication between the assembly and the bore of the pressure vessel.

The experiments were performed at 1280–1350 °C and 1.5 GPa, relevant to arc magma generation[11,12]. Run duration was set at 72 h after verifying approach to equilibrium from a 3h to 96-h time-series (see paragraph below). Pressure was applied using the cold piston-in technique[13] where the experiments were first raised to the desired pressure before heating them at desired temperature at the rate of 60 °C/min. The friction correction was determined from the Ca-Tschermakite breakdown reaction to the assemblage anorthite, gehlenite, and corundum[14] at 12 to 14 kbar and 1300 °C (Hays, 1966) and is within the pressure uncertainty (± 50 MPa). Thus, no correction was applied on the pressure in this study. Temperature was monitored and controlled in the experiments using $W_{97}Re_3/W_{75}Re_{25}$ thermocouple with no correction for the effect of pressure on thermocouple electromotive force (EMF). Temperatures are estimated to be accurate to ±10 °C and pressures to ±500 bars, and the thermal gradient over the capsule was <5 °C. The experiments were quenched by terminating power supply and the run products were recovered. The capsules were longitudinally cut in half before mounting in epoxy. All the mounted capsules were polished successively on 240- to 1000-grit SiC paper before the final polishing on nylon/velvet microcloth with polycrystalline diamond suspensions (3–0.25 µm) and 0.02 µm colloidal silica. Vacuum re-impregnation of capsules with epoxy was performed to reduce plucking-out of the vitreous spheres during polishing.

Approach to equilibrium and Fe loss

Approach to equilibrium was evaluated by performing a time-series of experiments using PER-SED (95-5) starting material at 1.5 GPa and 1280 °C at varying run durations of 3 h, 24 h, 48 h, 72 h and 96 h. We performed the time-series experiments at the lowest temperature used in this study (1280 °C) such that it provided the maximum amount of time necessary to approach equilibrium. We observed that the melt compositions obtained after 72 h to 96 h were indistinguishable within 1 s.d. values in terms of SiO_2, Al_2O_3, MgO, Na_2O, CaO, K_2O, MnO, TiO_2 and P_2O_5 (Fig. S4). It has been shown experimentally that hydrous melting of peridotite produces melts with lower FeO* (~ 6 wt. %) contents than anhydrous equivalents (~8 wt. %)[10] but we also observed a decrease in FeO_T with increasing run duration, which suggests Fe loss. We speculate that this Fe loss/depletion reflects one or a combination of the following causes: (1) Fe diffusion to the $Au_{80}Pd_{20}$ capsule due to incomplete Fe saturation

during conditioning; (2) formation of orthopyroxenite reaction zone, which could have further contributed to Fe depletion. Other observation that indicates a close approach to equilibrium in our experiments is the homogenous distribution of minerals in the matrix away from the reaction zone, and homogeneous major element compositions within single capsule.

Another way of assessing equilibrium between the melt and minerals, and check whether the experiment behaved as a closed system, is based on the quality of mass balance calculations performed for all the major elements. Using the MS-Excel optimization tool Solver, we obtained low values for the sum of squared residuals (<0.39), for all the major elements, except for Fe, attesting for a close approach to equilibrium for all other major oxides in our experiments, and confirming a small amount of Fe loss in the capsule walls. Phase proportions for each experiment estimated from the mass balance calculations were verified visually in every experiment.

Analytical techniques

Electron microprobe analysis

Major element compositions of the quenched melts and coexisting silicate minerals from all experimental run products were analyzed using JEOL JXA-8200 Superprobe electron probe micro-analyzer at Massachusetts Institute of Technology. Analyses were performed using a 15 kV accelerating potential and a 10 nA beam current. The beam diameter varied depending on the target point. For quenched melt pools, beam diameters varied between 3 μm to 10 μm (mostly 5 μm) depending on the size of the melt pools. For silicate minerals, a focused beam (1 μm) was used. Data reduction was done using CITZAF package (Armstrong, 1995). Counting times for most elements were 40 s on peak, and 20 s on background. In order to prevent alkali diffusion in glass, Na was analyzed first for 10 s on peak and 5 s on background. All phases (melt and coexisting minerals) were quantified using silicate and oxide standards. The compositional maps for different major elements were performed at similar instrumental setup using a focused beam. Major element compositions of melts and minerals are reported in Table S2 and S5, respectively.

Secondary ion mass spectrometry

Concentrations of selected trace elements in melt pools (usually < 30 μm diameter) were obtained using a Cameca IMS 3f ion microprobe at the Northeast National Ion Microprobe Facility (NENIMF) at the Woods Hole Oceanographic Institution (WHOI). Analyses were done using $^{16}O^-$ primary ion beam with 8.4 keV voltage, 500 pA to 1 nA current and ~10 μm beam diameter. No raster was used in the beam. Positive secondary ions are accelerated to a nominal energy of 4.5 keV. The energy window of the mass spectrometer was set to 30 eV. ^{30}Si was set as the reference isotope and ATHO-G, T1-G, StHs6/80-G glasses were used as standards[15]. Analyses were carried out in low mass resolution (m/δm= 330) with an energy offset of -85 V. Secondary ions were counted by an electron multiplier. A 1800 μm diameter field aperture size was used for most of the measurements. We did not use the field aperture to block any of the ion image from the sample since the spot was already very small. Each measurement consists of four minutes of pre-sputtering, then five cycles with an integration of 10 s/cycle for ^{30}Si and 10 s/cycle for elements ^{88}Sr, ^{89}Y, ^{90}Zr, ^{93}Nb, ^{138}Ba, and 30 s/cycle for ^{140}Ce, ^{143}Nd, ^{147}Sm, ^{174}Yb, ^{180}Hf, ^{232}Th and ^{238}U. Th concentrations are reported if 1SE error is above detection limit. 1SE error for U is below detection limit for all measurements so U is not reported. In total, each analysis spot requires a total analysis time of approximately 60 min. Reduced trace element concentrations of melts obtained by SIMS are reported in Table S2. Internal errors from analyses (2 SE) and error from calibration curves (2SE) have been propagated and are incorporated in the total 2SE error reported in the figures and Tables.

X-ray Fluorescence technique (XRF)

Whole-rock elemental concentrations of LZ-1, SY400B and SY325 were analyzed using X-ray fluorescence technique for major elements and inductively coupled mass spectrometer technique for trace elements at GeoAnalytical Laboratory at Washington State University. As stated before, whole-rock compositions (major and trace elements) of LZ-1, SY325, SY400B as well as PER-SED 95-5, 85-15 and PER-SERP 85-15 are summarized in Table S1.

Major element variability of residual phases

Major element compositions of residual minerals are homogeneous through the capsule in individual experiments, and vary between experiments due to differences in temperature and

starting compositions (Fig S10). They are within the range of values observed in peridotites worldwide, although Fe loss probably artificially increased Mg# of minerals (93–96 in olivine; 91–95 in clinopyroxene; 92–95 in orthopyroxene). Temperature (1280-1350ºC) has variable effect on mineral compositions. For example, with increasing temperature, olivines display a slight decrease in Al_2O_3, a constant CaO, and a slight increase in MgO. D_{MgO} ol/melt decreases with increasing temperature. Orthopyroxenes display a slight decrease in TiO_2 and Al_2O_3 with increasing temperature, whereas SiO_2 and MgO increase, and CaO is constant. As predicted experimentally, D_{Al2O3} opx/melt decreases with increasing temperature and D_{Na2O} opx/melt increases with increasing temperature[16]. Clinopyroxenes show limited major element variability between all experiments. The mineral compositions are reported in Table S5.

Supplementary figures

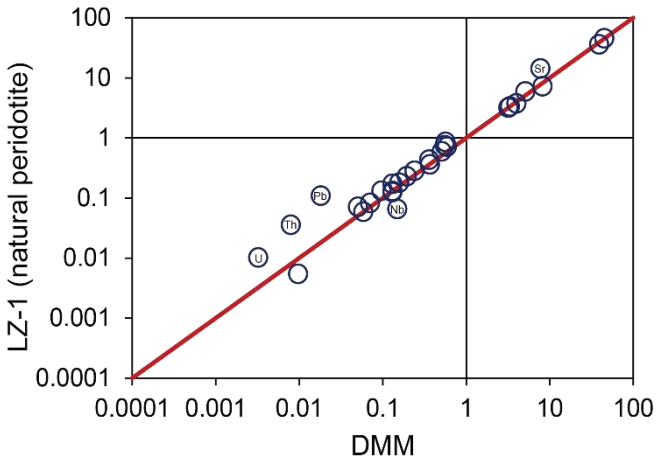

Figure S1 | DMM composition[1] plotted against the natural peridotite starting material (LZ-1). The plot demonstrates a close compositional similarity between LZ-1 and DMM compositions. The red line is the 1:1 ratio line.

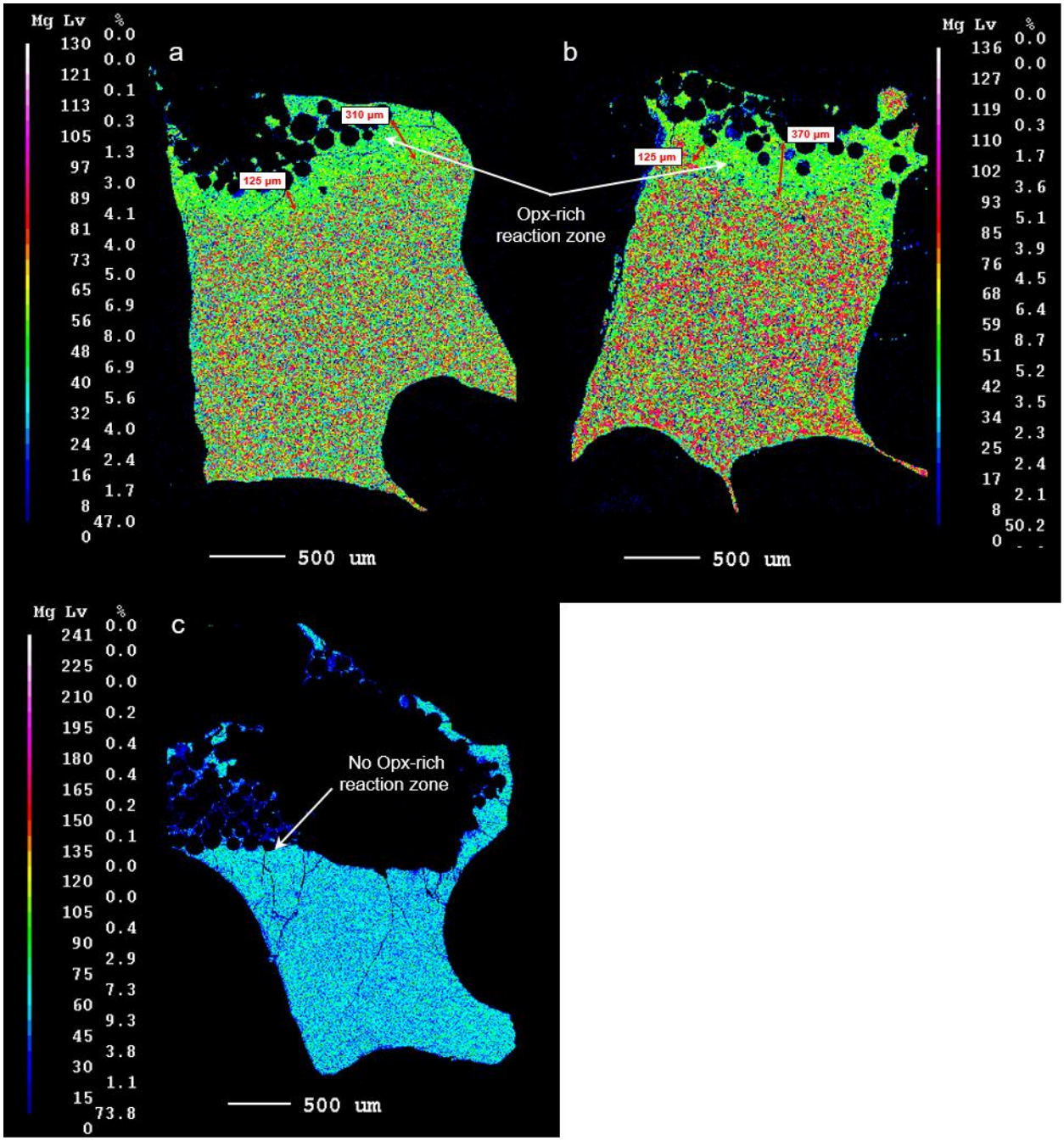

Figure S2 | Mg compositional maps of 72-h experiments performed at 1.5 GPa. (a) PER-SED (85-15) at 1280 ºC and (b) PER-SED (85-15) at 1315 ºC, showing a systematic thickening of the Opx-rich reaction zone (bright yellow green areas) with increasing temperatures. (c) No opx-rich reaction zone was observed in the 3-h experiment PER-SED (95-5) at 1.5 GPa and 1280 ºC.

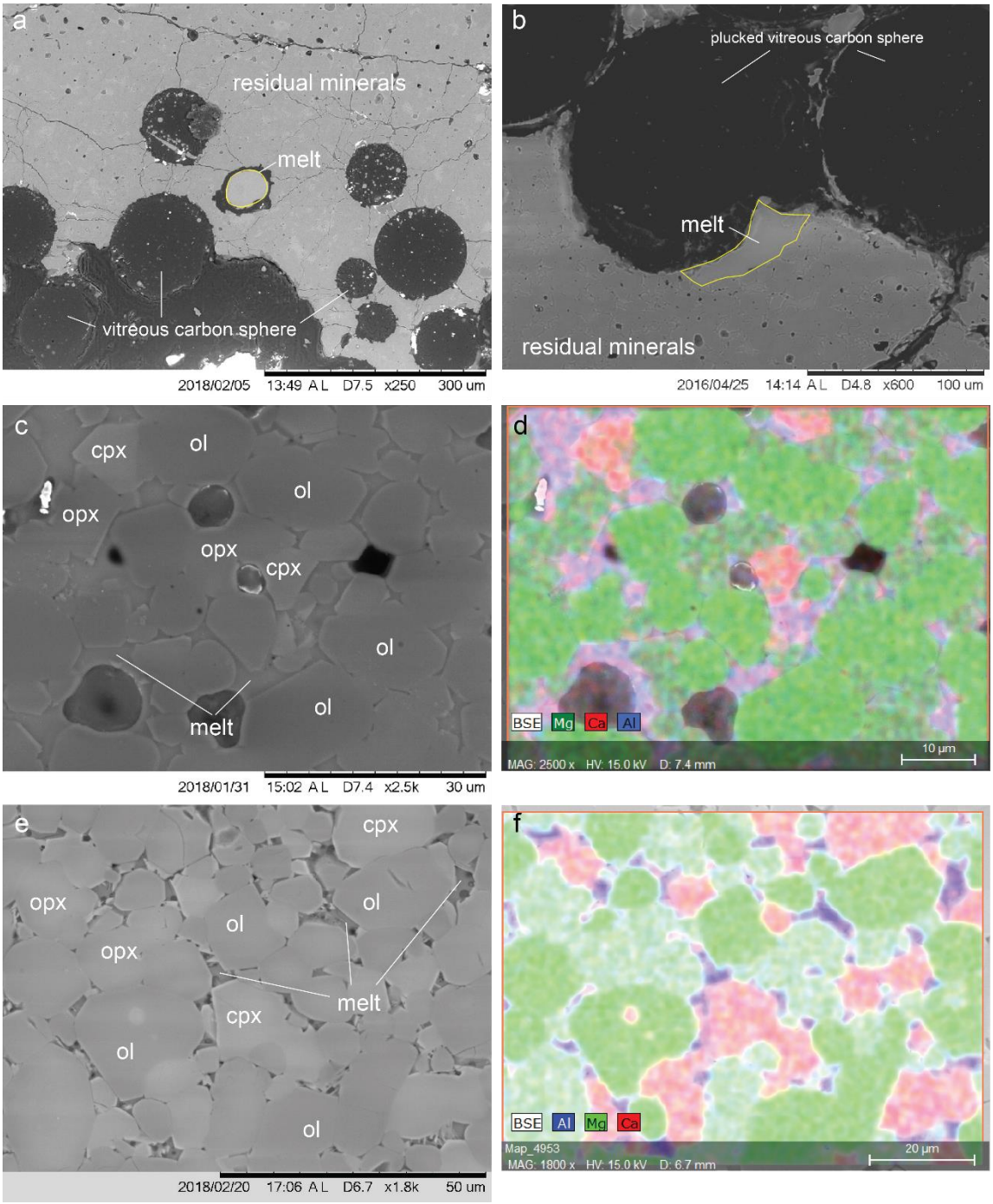

Figure S3 | Representative backscattered electron (BSE) images and chemical maps of experimental run products at 1.5 GPa. Olivine (ol), Orthopyroxene (opx), Clinopyroxene (cpx) and melt are identified. Dark zones are holes/voids left by plucked out minerals during polishing. Dark round circles are polished (and sometimes plucked) vitreous carbon spheres. (a) A rare, well-exposed circular melt pool occupying the outline of a carbon sphere in PER-SED 85-15 at 1315 ºC, and (b) melt pool around a plucked carbon sphere in PER-SED 85-15 at 1280 ºC. (c) BSE image and (d) Mg-Ca-Al chemical map of PER-SED 85-15 at 1280 ºC

highlighting the assemblage of ol + opx + cpx + melt. (e) BSE image and (f) Mg-Ca-Al chemical map of the near-solidus experiment PER-SERP 85-15 at 1230 ºC highlighting the assemblage of ol + opx + cpx + melt. Melt compositions from near-solidus experiments were not used in this study as abundant dendrites were noticed.

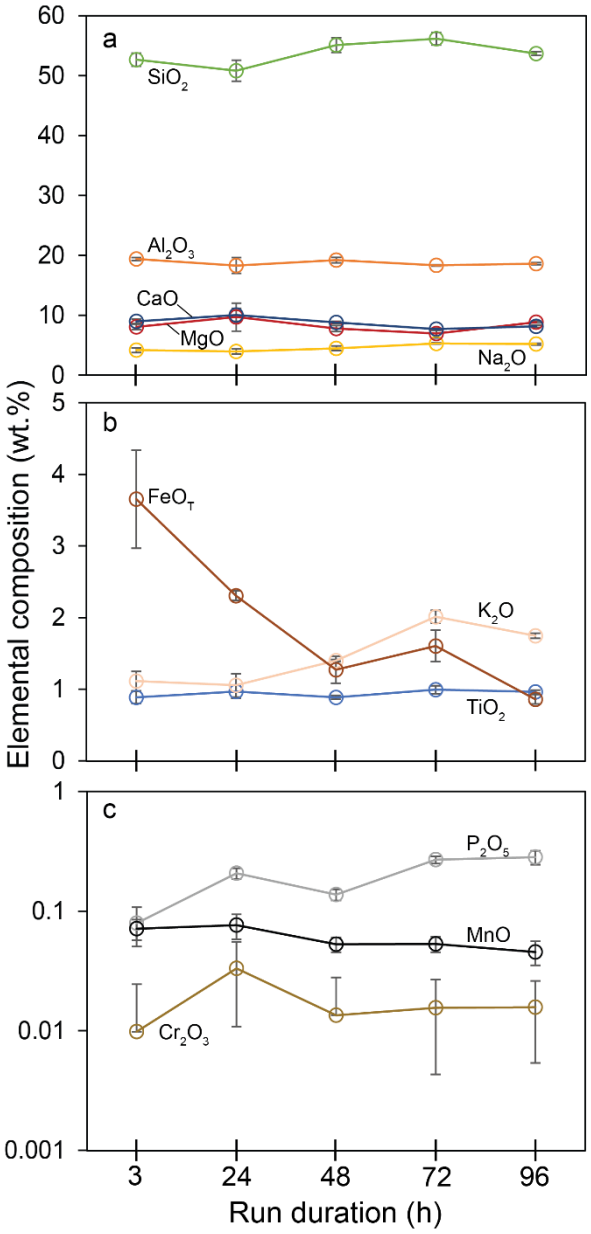

Figure S4 | Element compositional variations, (a) SiO_2, Al_2O_3, CaO, MgO, Na_2O, (b) FeO_T, K_2O, TiO_2, (c) P_2O_5, MnO, Cr_2O_3, in a time series experiments at 1.5 GPa and 1280 ºC (PER-SED 95-5; Table S2), with run duration ranging from 3-h to 96-h. We chose a run duration of 72-h to ensure close approach to equilibrium. The data are plotted as averages with error bars representing 1 s.d.

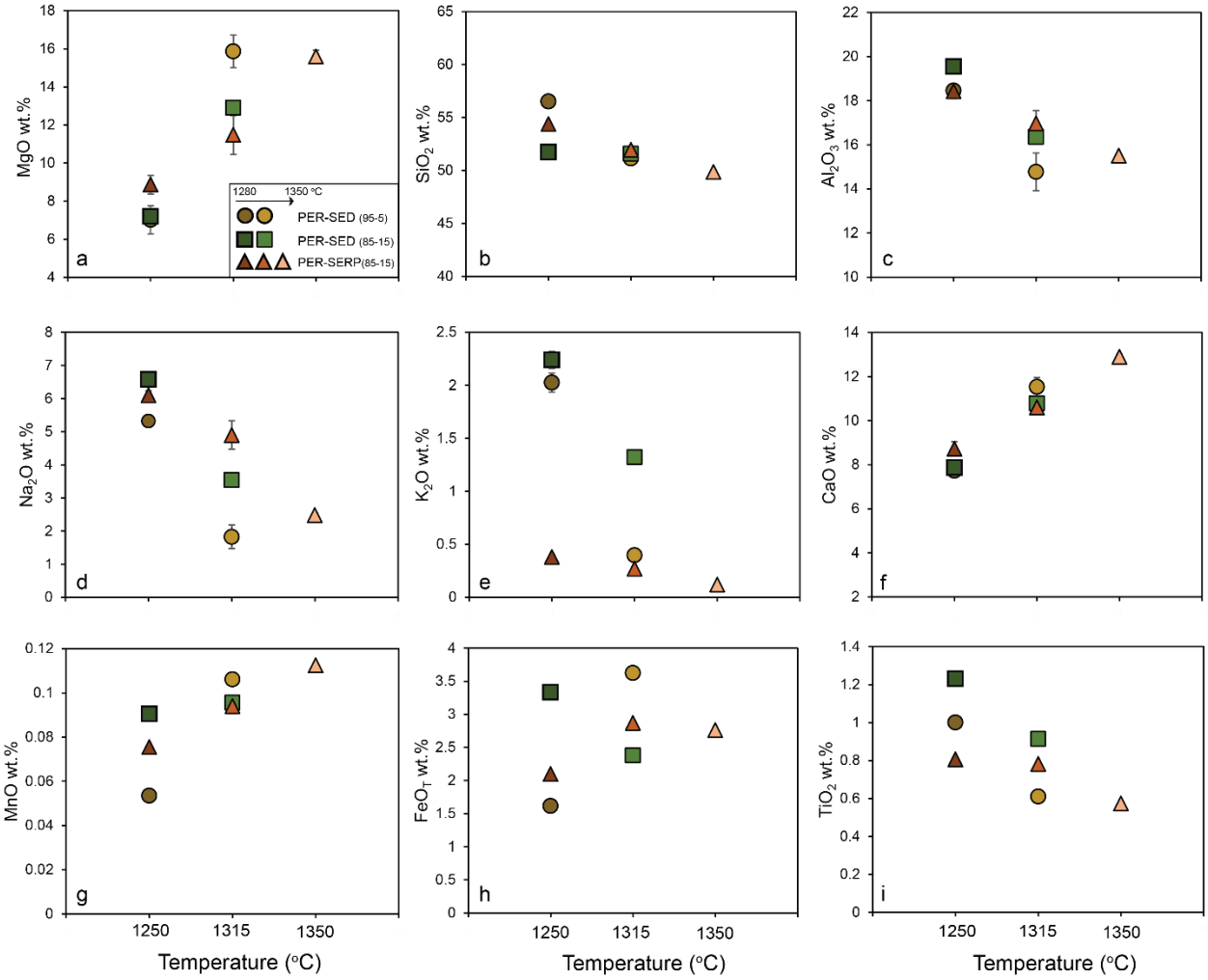

Figure S5 | Major element variations of experimental peridotite-mélange melts with temperature. (a) MgO, (b) SiO_2, (c) Al_2O_3, (d) Na_2O, (e) K_2O, (f) CaO, (g) MnO, (h) FeO_T, (i) TiO_2 variations vs temperature (^oC). The data are plotted as averages with error bars representing 1 s.d. (Table S2).

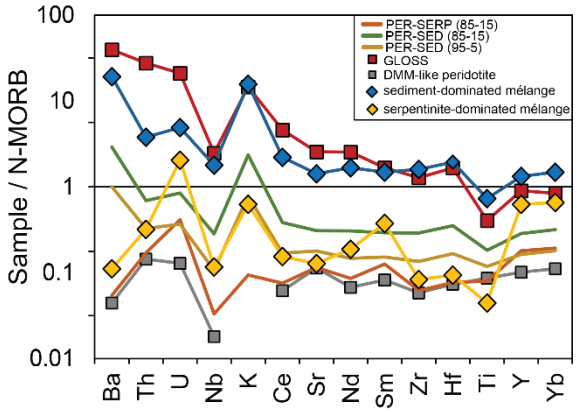

Figure S6 | Trace element compositions of starting materials and their components (Table S1). GLOSS composition is from Plank and Langmuir[17]. The average N-MORB value used in the normalization is from Gale *et al.*[18]

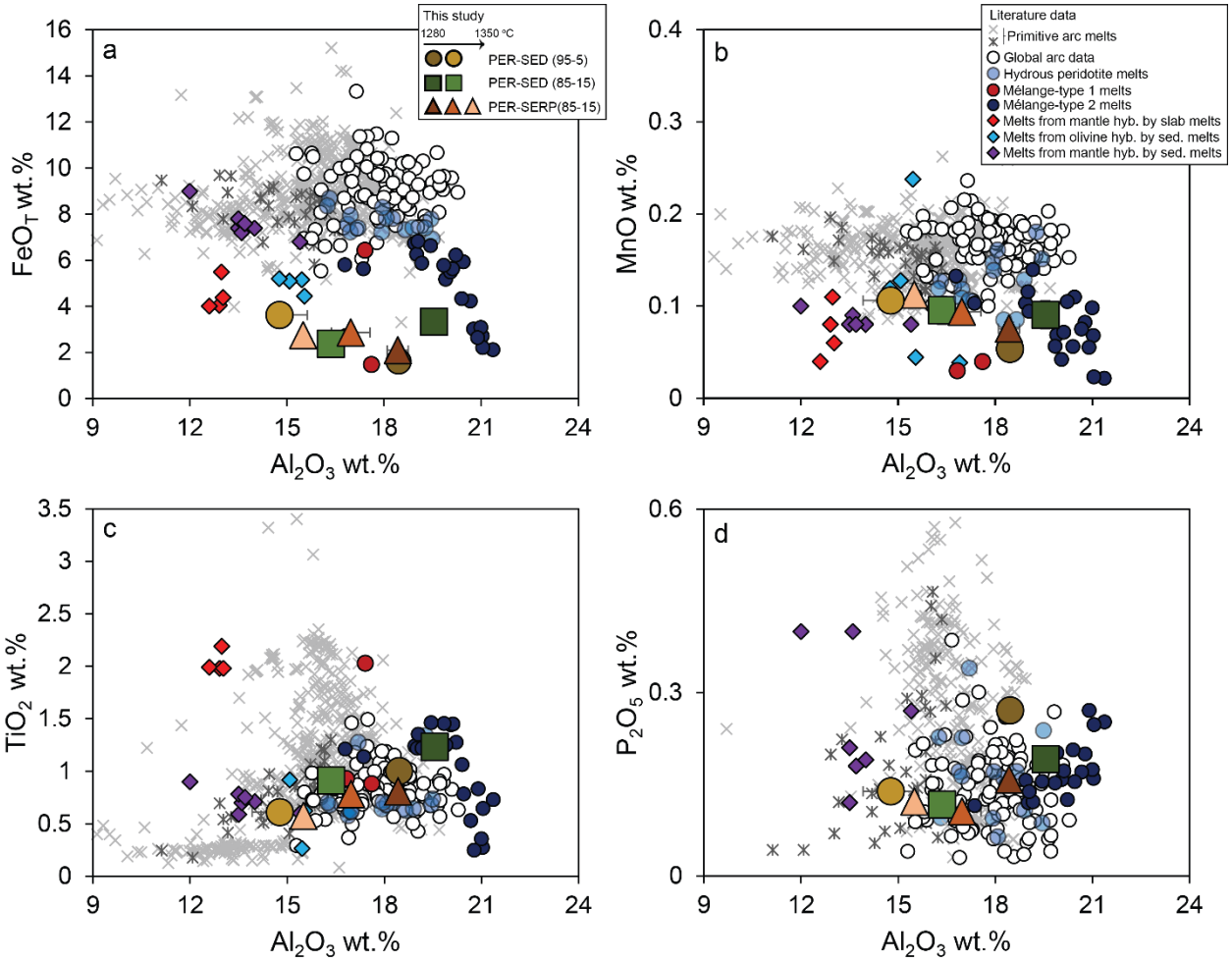

Figure S7 | Major element variations (a) FeO_T, (b) MnO, (c) TiO_2, (d) P_2O_5 vs Al_2O_3 of experimental peridotite-mélange melts from this study compared to global arcs[19] (normalized to MgO = 6 wt. %), two primitive arc melts compilations, and previous experimental studies[20–22]. The two primitive arc melts compilations are from Schmidt and Jagoutz[23] (gray asterisk) and Till *et al.*[24] (light gray cross). Hydrous peridotite melts are from Gaetani and Grove[10]. Experimental melts from mantle hybridized by slab melts and sediment melts are from Rapp *et al.*[20] and Mallik *et al.*[22], respectively. Experimental melts of olivine hybridized by sediment melts are from Pirard and Hermann[21]. Experimental mélange-type 1 melts are from Castro and Gerya[25] and Castro *et al.*[26], while the experimental mélange-type 2 melts are from Cruz-Uribe *et al.*[27] Our experiments are plotted as averages with error bars representing 1 s.d. All the data, including the literature, are plotted on volatile-free basis.

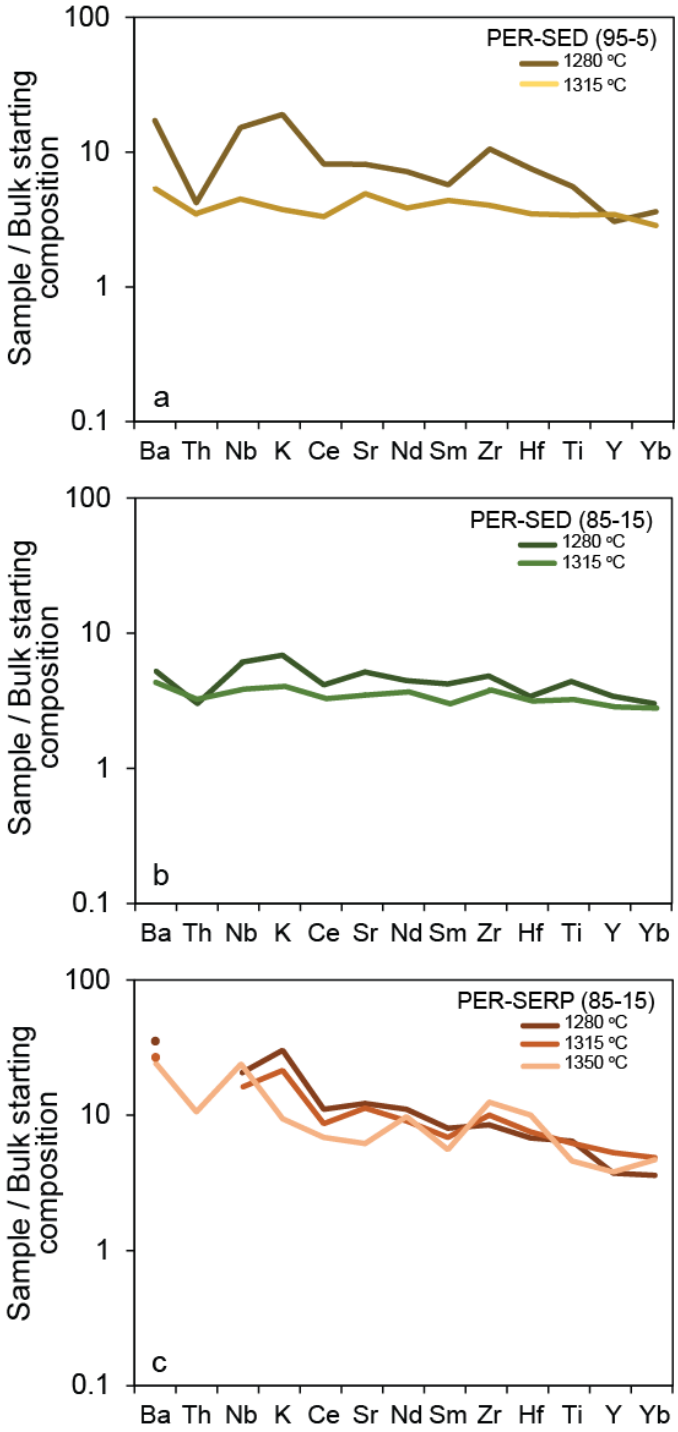

Figure S8 | Trace element concentrations of experimental peridotite-mélange melts, (a) PER-SED (95-5), (b) PER-SED (85-15) and (c) PER-SERP (85-15), normalized to bulk starting compositions. The bulk starting compositions are summarized in Table S1 and experimental melts compositions are reported in Table S2.

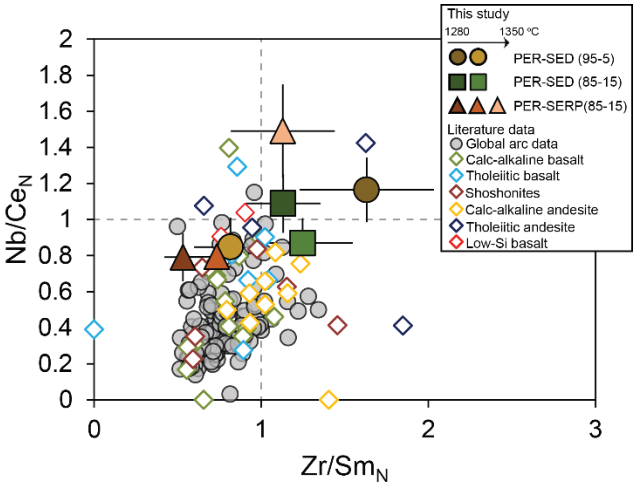

Figure S9 | N-MORB normalized Nb/Ce_N versus Zr/Sm_N plot of experimental peridotite-mélange melts compared to different arc databases. Literature databases include the global arc data[19] (circle symbol; normalized to MgO = 6 wt. %) and compiled primitive arc lavas[23] (diamond symbols). N-MORB value used in normalization is from Gale *et al.*[18]

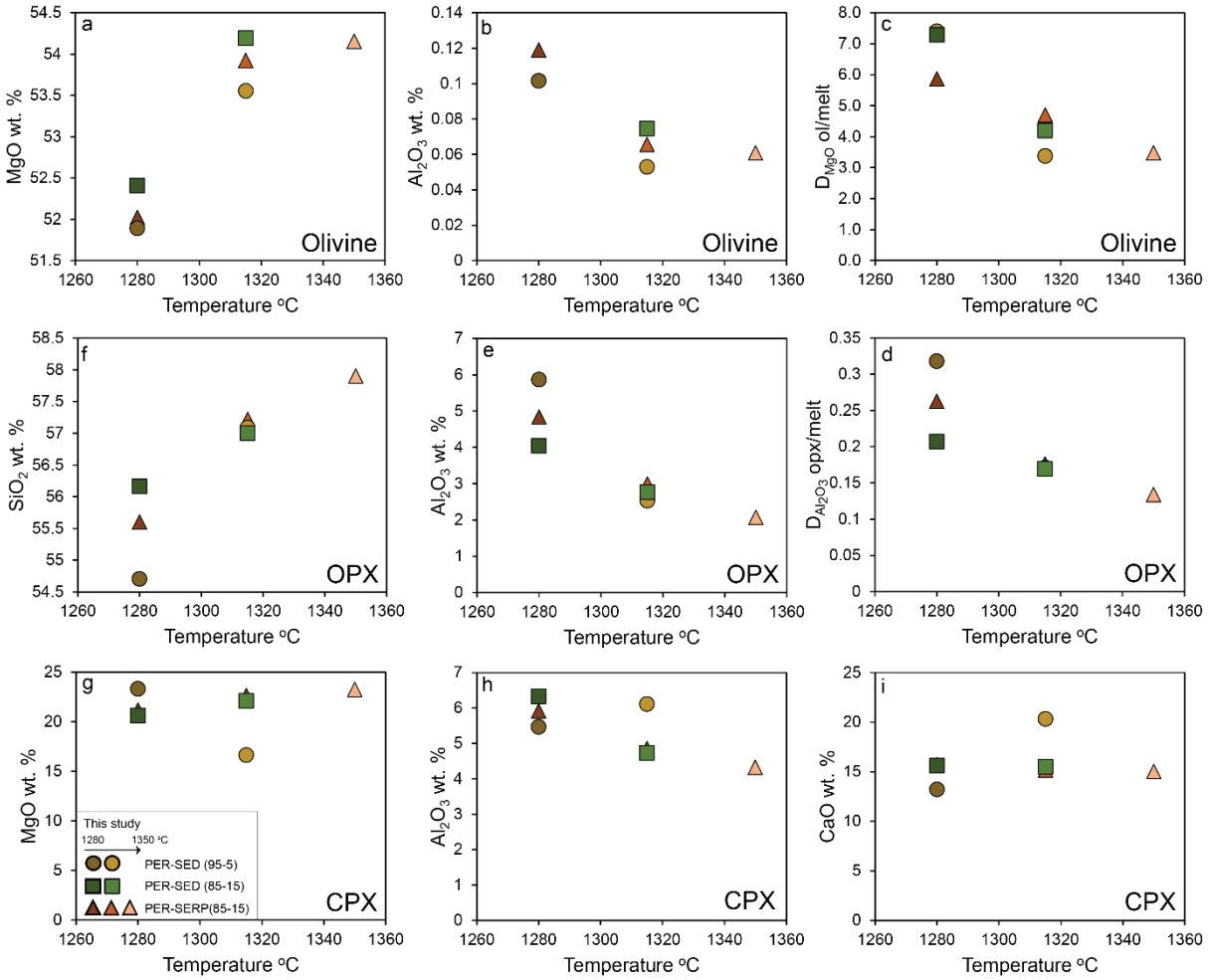

Figure S10 | Variations in (a) MgO_{ol}, (b) Al_2O_{3ol}, (c) D_{MgO} ol/melt, (d) SiO_{2opx}, (e) Al_2O_{3opx}, (f) D_{Al2O3} opx/melt, (g) MgO_{cpx}, (h) Al_2O_{3cpx}, and (i) CaO_{cpx}, with temperature. Mineral chemistry data for olivine (ol), orthopyroxene (opx) and clinopyroxene (cpx) are summarized in Table S5. The data are plotted as averages.

Table S1. Major and trace element compositions of starting materials

Major elements (wt. %) normalized to 100

Sample	Description	Modal mineralogy (wt. %)	SiO_2	TiO_2	Al_2O_3	FeO_T	MnO	MgO	CaO	Na_2O	K_2O	P_2O_5	LOI %	Density
LZ-1	Lherzolitic section of LN12-18 (Le Roux et al., 2016)	Ol-60, Opx-25, Cpx-12.5, Sp-2.5	47.2	0.136	3.90	7.52	0.130	37.6	3.32	0.178	0.001	0.001		3.3000
SY400B	Chlorite-omphacite schist (sediment-dominated melange)	Ep-10, Phe-21.4, Chl-10, Rt-0.83, Ttn-0.50, Ap-0.22, Tur-3.4, Omph-53	51.5	1.15	17.2	5.75	0.118	8.47	8.39	5.11	2.26	0.090	2.37	3.169
SY325	Talc-chlorite-actinolite schist (serpentine-dominated melange)	Ca-amph-65, Chl-20, Tlc-15, minor Rt	57.7	0.070	2.42	7.42	0.245	22.8	7.71	1.53	0.091	0.002	2.13	3.0470
PER-SED (95-5)	95 vol. % LZ-1 + 5 vol. % SY400B		47.4	0.185	4.54	7.44	0.129	36.2	3.56	0.416	0.110	0.005	0.114	3.29
PER-SED (85-15)	85 vol. % LZ-1 + 15 vol. % SY400B		47.8	0.283	5.83	7.27	0.128	33.4	4.06	0.893	0.329	0.014	0.344	3.28
PER-SERP (85-15)	85 vol. % LZ-1 + 15 vol. % SY325		48.7	0.127	3.69	7.51	0.146	35.6	3.93	0.367	0.014	0.001	0.299	3.26

Trace elements (ppm)

Sample	Rb	Sr	Y	Zr	Nb	Cs	Ba	La	Ce	Pr	Nd	Sm	Eu	Gd	Tb	Dy	Ho	Er	Tm	Yb	Lu	Hf	Ta	Pb	Th	U
LZ-1	0.072	14.50	3.37	5.96	0.07	0.00	0.87	0.23	0.77	0.14	0.72	0.29	0.13	0.44	0.08	0.60	0.13	0.38	0.06	0.36	0.06	0.18	0.01	0.11	0.04	0.01
SY400B	48.10	181.0	43.00	163.00	6.48	0.68	375.00	9.88	27.40	4.03	17.70	5.16	1.32	6.03	1.16	7.65	1.66	4.85	0.74	4.86	0.75	4.76	0.42	2.34	0.95	0.39
SY325	0.22	16.30	20.80	8.47	0.42	0.03	2.17	0.77	1.91	0.33	2.00	1.31	0.50	2.61	0.59	4.03	0.82	2.28	0.35	2.15	0.32	0.23	0.03	1.50	0.08	0.16
PER-SED (95-5)	2.39	22.50	5.32	13.50	0.38	0.03	18.90	0.70	2.05	0.33	1.54	0.52	0.19	0.71	0.14	0.94	0.21	0.59	0.09	0.58	0.09	0.40	0.03	0.22	0.08	0.03
PER-SED (85-15)	7.05	38.60	9.25	28.70	1.00	0.10	55.20	1.63	4.63	0.70	3.18	0.99	0.31	1.25	0.24	1.62	0.35	1.02	0.16	1.02	0.16	0.85	0.07	0.43	0.17	0.07
PER-SERP (85-15)	0.09	14.70	5.81	6.31	0.12	0.01	1.05	0.31	0.93	0.16	0.90	0.43	0.18	0.74	0.15	1.08	0.23	0.64	0.10	0.62	0.10	0.19	0.01	0.31	0.04	0.03

Table S2. Major and trace element compositions of experimental peridotite-mélange melts

Major elements (wt. %) normalized to 100

		EPMA (± 1 s.d)									
Experiment	n*	**SiO_2**	**TiO_2**	**Al_2O_3**	**FeO_T**	**MnO**	**MgO**	**CaO**	**Na_2O**	**K_2O**	**P_2O_5**
PER-SED 95-5_1280_3	12	53.1	0.895	19.6	4.22	0.072	8.16	9.07	3.69	1.13	0.080
		1.1	*0.084*	*0.3*	*0.40*	*0.014*	*0.46*	*0.36*	*0.68*	*0.14*	*0.029*
PER-SED 95-5_1280_24	5	52.1	0.992	18.8	4.06	0.078	9.97	10.3	2.37	1.08	0.212
		1.8	*0.091*	*1.3*	*0.41*	*0.018*	*2.33*	*1.1*	*0.07*	*0.17*	*0.021*
PER-SED 95-5_1280_48	7	55.6	0.896	19.4	4.53	0.053	7.85	8.89	1.28	1.41	0.139
		1.3	*0.028*	*0.4*	*0.38*	*0.007*	*0.50*	*0.20*	*0.19*	*0.02*	*0.014*
PER-SED 95-5_1280_72	4	56.5	1.00	18.5	1.61	0.054	7.01	7.73	5.32	2.02	0.271
		1.0	*0.05*	*0.1*	*0.22*	*0.008*	*0.74*	*0.16*	*0.09*	*0.09*	*0.019*
PER-SED 95-5_1280_96	6	54.5	0.983	18.9	5.27	0.046	9.01	8.30	0.88	1.78	0.287
		0.3	*0.020*	*0.2*	*0.15*	*0.010*	*0.17*	*0.17*	*0.07*	*0.03*	*0.038*
PER-SED 95-5_1315_72	12	51.1	0.611	14.8	3.63	0.106	15.9	11.5	1.83	0.397	0.139
		0.7	*0.037*	*0.9*	*0.19*	*0.013*	*0.8*	*0.4*	*0.35*	*0.066*	*0.113*
PER-SED 85-15_1280_72	9	51.7	1.23	19.5	3.33	0.091	7.19	7.87	6.58	2.24	0.191
		0.3	*0.04*	*0.2*	*0.48*	*0.015*	*0.30*	*0.31*	*0.23*	*0.08*	*0.040*
PER-SED 85-15_1315_72	13	51.6	0.913	16.4	2.38	0.096	12.9	10.8	3.54	1.32	0.117
		0.3	*0.028*	*0.2*	*0.22*	*0.015*	*0.2*	*0.1*	*0.13*	*0.05*	*0.021*
PER-SERP 85-15_1280_72	7	54.4	0.806	18.4	2.10	0.075	8.87	8.72	6.10	0.379	0.158
		0.5	*0.038*	*0.3*	*0.18*	*0.007*	*0.50*	*0.32*	*0.14*	*0.011*	*0.024*
PER-SERP 85-15_1315_72	10	51.9	0.781	17.0	2.87	0.094	11.5	10.6	4.90	0.269	0.105
		0.5	*0.022*	*0.6*	*0.16*	*0.009*	*1.0*	*0.3*	*0.43*	*0.015*	*0.032*
PER-SERP 85-15_1350_72	7	49.9	0.573	15.5	2.76	0.113	15.6	12.9	2.48	0.118	0.122
		0.2	*0.023*	*0.1*	*0.04*	*0.012*	*0.3*	*0.1*	*0.05*	*0.004*	*0.011*

*n indicates number of individual analysis. Most melt pools are too small to perform multiple analyses

numbers in italics are errors (± 1 s.d for EPMA, ±2 s.e. for SIMS)

** Total 2 SE reported here include 2SE internal error from analyses (n = 5 cycles) propagated with 2SE error from calibration curves

*** value is reported if 1SE error is above detection limit. Like for other elements, 2SE are reported in italics

Trace elements (ppm)

		SIMS (± *2 s.e.***)										
Experiment	n*	**Sr ppm**	**Y ppm**	**Zr ppm**	**Nb ppm**	**Ba ppm**	**Ce ppm**	**Nd ppm**	**Sm ppm**	**Yb ppm**	**Hf ppm**	**Th*** ppm**
PER-SED 95-5_1280_3												
PER-SED 95-5_1280_24												
PER-SED 95-5_1280_48												
PER-SED 95-5_1280_72	1	182	16.3	142	5.68	324	16.7	11.0	2.98	2.10	3.01	0.33
		8	*0.9*	*6*	*0.71*	*13*	*1.4*	*2.0*	*1.19*	*0.65*	*0.95*	*0.47*
PER-SED 95-5_1280_96												
PER-SED 95-5_1315_72	3	110	18.3	54	1.68	102	6.78	5.89	2.27	1.65	1.39	0.28
		5	*1.0*	*3*	*0.42*	*5*	*0.69*	*1.52*	*1.01*	*0.56*	*0.65*	*0.32*
PER-SED 85-15_1280_72	1	199	31.6	138	6.09	290	19.2	14.2	4.18	3.07	2.87	0.51
		8	*1.3*	*6*	*0.64*	*11*	*1.6*	*2.0*	*1.11*	*0.71*	*0.77*	*0.34*
PER-SED 85-15_1315_72	1	135	26.4	109	3.86	239	15.2	11.7	2.99	2.83	2.67	0.55
		6	*1.1*	*5*	*0.55*	*10*	*1.3*	*2.0*	*1.14*	*0.74*	*0.84*	*0.46*
PER-SERP 85-15_1280_72	1	180	21.6	53.5	2.37	37.1	10.3	9.9	3.44	2.21	1.27	-
		7	*1.0*	*2.8*	*0.42*	*2.3*	*0.9*	*1.7*	*1.04*	*0.58*	*0.50*	-
PER-SERP 85-15_1315_72	1	166	30.7	63.2	1.85	28.2	8.01	8.16	2.93	3.00	1.41	-
		7	*1.3*	*3.3*	*0.43*	*2.0*	*0.77*	*1.73*	*1.12*	*0.80*	*0.64*	-
PER-SERP 85-15_1350_72	1	91	22.2	78.8	2.76	25.7	6.35	8.78	2.38	2.88	1.88	0.44
		4	*1.1*	*4.0*	*0.53*	*2.0*	*0.66*	*1.86*	*1.11*	*0.82*	*0.74*	*0.47*

*n indicates number of individual analysis. Most melt pools are too small to perform multiple analyses

numbers in italics are errors (± 1 s.d for EPMA, ±2 s.e. for SIMS)

** Total 2 SE reported here include 2SE internal error from analyses (n = 5 cycles) propagated with 2SE error from calibration curves

*** value is reported if 1SE error is above detection limit. Like for other elements, 2SE are reported in italics

Table S3. Summary of experimental set-up

Experiments	Goal of the experiment	Temperature (°C)	Pressure (GPa)	Run duration (h)	Starting mix	Phases*
PER-SED 95-5_1150_96	solidus assemblage	1150	1.5	96	PER-SED (95-5)	olivine + orthopyroxene + clinopyroxene + spinel (± isolated melt drops)
PER-SED 95-5_1280_3	time-series	1280	1.5	3	PER-SED (95-5)	melt + olivine + orthopyroxene + clinopyroxene
PER-SED 95-5_1280_24	time-series	1280	1.5	24	PER-SED (95-5)	melt (0.13) + olivine (0.42) + orthopyroxene (0.35) + clinopyroxene (0.1)
PER-SED 95-5_1280_48	time-series	1280	1.5	48	PER-SED (95-5)	melt (0.09) + olivine (0.42) + orthopyroxene (0.35) + clinopyroxene (0.14)
PER-SED 95-5_1280_72	time-series / melt composition	1280	1.5	72	PER-SED (95-5)	melt (0.1) + olivine (0.44) + orthopyroxene (0.29) + clinopyroxene (0.17)
PER-SED 95-5_1280_96	time-series	1280	1.5	96	PER-SED (95-5)	melt (0.1) + olivine (0.42) + orthopyroxene (0.35) + clinopyroxene (0.13)
PER-SED 95-5_1315_72	melt composition	1315	1.5	72	PER-SED (95-5)	melt (0.25) + olivine (0.4) + orthopyroxene (0.34) + clinopyroxene (0.01)
PER-SED 85-15_1230_96	near-solidus assemblage	1230	1.5	96	PER-SED (85-15)	melt + olivine + orthopyroxene + clinopyroxene + minor spinel
PER-SED 85-15_1280_72	melt composition	1280	1.5	72	PER-SED (85-15)	melt (0.19) + olivine (0.4) + orthopyroxene (0.27) + clinopyroxene (0.14)
PER-SED 85-15_1315_72	melt composition	1315	1.5	72	PER-SED (85-15)	melt (0.31) + olivine (0.36) + orthopyroxene (0.31) + clinopyroxene (0.02)
PER-SERP 85-15_1230_96	near-solidus assemblage	1230	1.5	96	PER-SERP (85-15)	melt + olivine + orthopyroxene + clinopyroxene + minor spinel
PER-SERP 85-15_1280_72	melt composition	1280	1.5	72	PER-SERP (85-15)	melt (0.03) + olivine (0.33) + orthopyroxene (0.46) + clinopyroxene (0.18)
PER-SERP 85-15_1315_72	melt composition	1315	1.5	72	PER-SERP (85-15)	melt (0.11) + olivine (0.34) + orthopyroxene (0.41) + clinopyroxene (0.14)
PER-SERP 85-15_1350_72	melt composition	1350	1.5	72	PER-SERP (85-15)	melt (0.25) + olivine (0.4) + orthopyroxene (0.34) + clinopyroxene (0.01)

* values in the parentheses are calculated phase fraction from the mass balance

Table S4. Compiled major and trace element compositions of experimental melts from other studies on mantle wedge hybridization

			Major elements (wt. %) normalized to 100											*Trace elements (ppm)*										
Literature		**Experiments**	**SiO_2**	**TiO_2**	**Al_2O_3**	**FeO_T**	**MnO**	**MgO**	**CaO**	**Na_2O**	**K_2O**	**P_2O_5**	**Cr_2O_3**	**Sr**	**Y**	**Zr**	**Nb**	**Ba**	**Ce**	**Nd**	**Sm**	**Yb**	**Hf**	**Th**	**U**
Pirard and Hermann (2015)	melts produced from olivine hybridized by sediment melts	D1078 Low K P-H	60.6	0.606	16.9	2.58	0.039	5.29	1.55	9.81	2.58			333	26.0	279	68.0	384	71.0	50.0	47.0	24.0	47.0	33.0	21.0
		D1064 Low K P-H	54.8	0.622	15.5	4.44	0.044	6.37	0.888	13.9	3.40			444	31.0	421	115	176	120	77.0	63.0	27.0	64.0	59.0	38.0
		D1077 Low K P-H	52.9	0.264	15.5	5.15	0.238	12.3	2.38	6.61	4.76			258	22.0	193	53.0	518	59.0	41.0	37.0	21.0	32.0	27.0	18.0
		D891 High K P-H	54.5	0.916	15.1	5.10	0.128	10.7	1.97	7.54	4.06			1317	32.0	514	170	886	211	140	122	21.0	80.0	74.0	75.0
		D979 High K P-H	59.7	0.586	14.8	5.21	0.119	7.92	1.19	7.49	3.04			470	62.0	370	108	981	99.0	82.0	76.0	25.0	57.0	48.0	33.0
Rapp et al. (1999)	melts produced from mantle hybridized by slab melts	AB-1+10 AVX-51	65.8	1.99	13.0	4.07	0.080	2.77	2.16	6.29	3.85			1471	11.0	-	9.70	1670	57.7	35.0	7.71	0.840	-	2.52	-
		AB-1+16 AVX-51	61.5	2.20	13.1	5.53	0.111	3.96	2.26	6.22	5.15			815	5.80	246			48.8	39.5	9.20	1.30			
		AB-1+12 KLB-1	66.1	2.00	12.7	4.05	0.040	2.38	2.01	3.72	7.04			1560	9.00	358	11.4	1861	60.0	37.3	7.33	0.500	8.20	1.87	0.630
		AB-1+15 KLB-1	64.7	1.99	13.1	4.41	0.060	2.77	1.99	4.60	6.35			769	18.2	325			44.0	32.7	6.90	1.10			
Mallik et al. (2015)	melts produced from mantle hybridized by sediment melts	B256	50.2	0.603	15.5	6.83	0.080	10.0	0.080	9.04	2.71	4.62	0.271												
		G301	48.3	0.714	14.1	7.44	0.080	12.1	0.080	7.84	2.92	6.33	0.191												
		G303	50.4	0.590	13.5	7.40	0.080	13.6	0.080	7.10	2.23	4.93	0.120												
		G354	42.2	0.905	12.1	9.05	0.101	16.1	0.101	9.05	5.03	5.03	0.402												
		G298	44.6	0.694	13.5	7.14	0.089	12.9	0.089	10.9	3.17	6.54	0.397												
		G298	46.3	0.780	13.5	7.80	0.080	13.2	0.080	8.20	2.50	7.40	0.210												
		G300	47.2	0.753	13.8	7.63	0.080	14.1	0.080	7.03	2.61	6.63	0.181												
Castro and Gerya (2008)	melts produced from pure melange	Run2mixed Castro and Gerya, 2008	69.5	0.858	17.2	1.45	0.039	0.702	2.92	2.38	2.50	2.50													
Castro et al. (2013)		AC8120a-mixed Castro et al., 2013	55.4	2.00	17.1	6.34	-	4.46	7.50	3.96	1.60	1.60													
		AC8120b-mixed Castro et al., 2013	63.2	0.895	16.2	2.60	0.029	2.49	3.52	3.65	3.70	3.70													
Skora and Blundy (2010)	melts produced from pure sediments	c10												200	2.30	75.0	22.0	276	66.0	65.0	54.0	1.80	43.0	179	285
		c9												166	1.50	106	71.0	384	181	142	65.0	1.50	57.0	349	268
		c7												131	10.7	138	100	299	268	231	130	14.7	59.0	438	258
		c8												107	14.6	158	199	246	231	235	190	21.3	60.0	347	214
		c12												98.0	19.0	158	193	224	215	224	192	32.0	58.0	315	195
Mallik et al. (2016)	melts produced from mantle hybridized by sediment melts	B256												1373	16.2	157	18.5	650	51.8	22.7	4.48	1.36	5.91	7.46	3.69
		G301												1067	12.4	117	13.9	981	38.1	16.8	3.33	1.07	4.43	5.49	2.72
		G303												828	10.0	91.6	10.8	763	29.6	13.0	2.61	0.886	3.49	4.26	2.11

		G297											2865	28.9	375	46.8	530	135	54.6	9.77	2.23	12.8	20.4	10.0
		G296											1502	14.3	169	20.3	690	56.8	24.8	4.81	1.06	6.37	8.19	4.05
		G298											1300	12.5	145	17.4	714	48.2	21.1	4.12	0.941	5.47	6.95	3.44
		G300											1234	13.9	135	16.1	1133	44.1	19.4	3.83	1.19	5.07	6.36	3.15
		B307											938	11.5	106	12.4	566	34.5	15.2	3.02	1.00	4.03	4.96	2.45
		B307											1172	13.9	133	15.6	657	43.4	19.1	3.77	1.18	5.00	6.26	3.09
		B309											764	9.30	84.6	9.94	704	27.3	12.0	2.41	0.828	3.23	3.93	1.94
		B309											798	9.64	88.2	10.4	734	28.5	12.6	2.51	0.855	3.36	4.10	2.03
		G358											559	7.00	62.2	7.26	515	20.0	8.80	1.77	0.635	2.38	2.87	1.42
		G376											1100	13.8	130	15.1	422	42.6	18.7	3.71	1.18	4.91	6.13	3.03
		G376											1170	14.0	133	15.7	612	43.6	19.1	3.80	1.19	5.03	6.29	3.11
		G377											847	10.1	93.4	11.0	779	30.3	13.3	2.66	0.886	3.55	4.36	2.16
		G377											845	10.1	93.1	11.0	777	30.2	13.3	2.65	0.883	3.54	4.34	2.15
		G379											632	7.89	70.3	8.22	583	22.6	9.96	2.00	0.713	2.69	3.25	1.61
		G379											656	8.13	72.9	8.53	604	23.4	10.3	2.07	0.731	2.79	3.37	1.67
		G380											511	6.45	57.0	6.64	471	18.3	8.06	1.62	0.588	2.19	2.62	1.30
		G380											483	6.07	53.8	6.27	445	17.2	7.60	1.53	0.553	2.06	2.48	1.23
		G381											1185	14.2	135	15.9	608	44.3	19.4	3.85	1.22	5.11	6.38	3.15
		G378											775	9.41	85.8	10.1	714	27.7	12.2	2.44	0.837	3.27	3.98	1.97
		G378											774	9.32	85.5	10.1	712	27.6	12.2	2.43	0.825	3.26	3.98	1.97
		G374											682	8.38	75.7	8.87	628	24.4	10.7	2.15	0.750	2.89	3.51	1.73
		G374											784	9.42	86.6	10.2	722	28.0	12.3	2.46	0.833	3.30	4.03	1.99
		G375											549	6.81	60.9	7.13	505	19.6	8.64	1.73	0.614	2.33	2.82	1.39
		G375											646	7.91	71.6	8.40	595	23.1	10.2	2.04	0.707	2.73	3.32	1.64
Cruz-Uribe et al. (2018)	Melts produced from melting of sediment-dominated melange material (SY400B)	SY400-AC-1	59.8	0.273	21.0	2.72	0.068	1.53	2.73	8.08	3.64	0.160	338	22.1	231	9.35	837	38.3	15.4	3.32	3.55	5.47	1.79	1.01
		SY400-AC-2	60.4	0.248	20.8	3.02	0.083	1.66	3.02	7.27	3.30	0.200	344	24.4	368	10.9	1124	58.1	20.7	3.87	3.98	9.77	2.64	1.34
		SY400-AC-12	59.5	0.356	21.0	3.09	0.098	1.71	2.66	7.77	3.63	0.174	356	23.5	242	11.0	948	35.4	16.5	3.40	3.20	5.32	1.70	0.949
		SY400-AC-4	57.7	0.531	20.7	4.24	0.075	2.32	2.84	7.81	3.62	0.170	360	28.8	266	14.4	992	47.0	19.7	4.43	3.66	5.68	1.75	0.908
		SY400-AC-5	53.7	0.783	20.5	5.94	0.110	4.08	4.51	7.20	3.04	0.155	352	45.3	266	15.6	833	56.8	28.5	6.51	5.94	6.57	2.19	0.936
		Sy400B-2	51.1	1.24	18.9	6.74	0.103	6.48	5.79	6.57	2.85	0.156												
		SY400B-3	51.8	1.28	20.2	6.24	0.105	4.91	5.67	6.72	2.91	0.125												
		Sy400B-1	51.6	1.22	19.0	6.26	0.116	6.10	6.53	6.42	2.66	0.120												
		MEL3	51.1	1.22	19.2	5.88	0.140	6.67	6.85	6.34	2.50	0.122	320	50.5	210	11.2	927	29.7	20.8	5.87	5.94	5.20	0.984	0.570
		MEL4	50.7	1.14	17.4	5.63	0.103	9.00	8.46	5.30	2.18	0.115	270	53.5	218	9.62	655	29.0	21.7	6.37	6.97	6.33	1.15	0.620

MEL5	50.8	1.21	16.8	5.81	0.133	9.11	8.57	5.46	2.03	0.099	241	47.6	156	8.63	550	23.6	17.7	5.46	6.08	4.18	0.796	0.393
SY400-AC-13	60.5	0.729	21.4	2.12	0.022	1.24	1.72	7.74	4.27	0.252	692	10.3	458	21.1	726	77.7	32.9	4.78	0.854	13.5	3.68	2.00
SY400-AC-10	60.7	0.646	21.0	2.22	0.023	1.27	1.70	7.66	4.47	0.248	560	14.4	290	18.9	1009	85.1	29.1	5.36	1.57	6.54	2.96	1.60
SY400-AC-6	59.5	0.832	20.9	2.65	0.055	1.65	1.80	7.73	4.63	0.271	479	17.2	611	19.3	1078	69.2	26.0	4.72	1.77	17.2	3.21	1.97
SY400-AC-7	57.0	1.06	20.4	4.34	0.056	1.87	2.20	8.26	4.62	0.206	535	12.7	376	24.6	1076	79.0	31.7	5.56	0.916	8.68	3.42	1.52
SY400-AC-8	55.2	1.25	19.9	5.18	0.069	2.66	2.57	8.46	4.47	0.202	496	15.1	254	21.6	1223	64.1	29.4	5.68	1.06	6.42	2.47	1.07
SY400-AC-9	54.8	1.44	20.1	5.49	0.042	2.91	2.67	7.95	4.52	0.158	477	17.4	276	23.2	1219	58.2	30.1	7.39	1.54	7.25	2.36	1.24
SY400-AC-14	54.4	1.45	20.1	5.63	0.072	3.07	2.89	7.82	4.35	0.172	474	20.8	397	22.7	1150	73.6	35.8	7.31	1.59	11.0	2.64	1.43
SY400-AC-15	53.9	1.45	19.8	5.79	0.057	3.91	3.58	7.45	3.82	0.152	465	26.1	357	19.0	1060	56.4	32.0	7.78	2.21	10.7	2.14	1.26
SY400-AC-16	52.3	1.46	19.4	6.64	0.087	4.93	4.36	7.22	3.42	0.155	418	34.8	298	16.6	917	68.9	36.5	8.30	3.15	8.48	2.92	1.08
SY400-AC-17	51.8	1.35	19.0	6.82	0.095	5.97	5.08	6.62	3.05	0.138	418	61.5	345	15.9	914	91.8	45.4	10.4	6.05	9.33	4.87	1.21

Table S5. Major element composition of mineral phases analyzed by EPMA

Major elements (wt. %) normalized to 100

		Olivine							
	n*	SiO_2	TiO_2	Al_2O_3	FeO_T	MnO	MgO	CaO	NiO
PER-SED 95-5_1150_96	10	40.7	-	0.048	7.29	0.105	51.5	0.140	0.207
		0.4	-	*0.026*	*0.28*	*0.022*	*0.4*	*0.018*	*0.078*
PER-SED 95-5_1280_24	9	41.3	-	0.070	5.30	0.094	52.8	0.234	0.135
		0.1	-	*0.015*	*0.14*	*0.016*	*0.3*	*0.015*	*0.017*
PER-SED 95-5_1280_48	8	41.6	0.030	-	4.61	0.072	53.0	0.353	0.018
		0.4	*0.021*	-	*0.70*	*0.017*	*1.3*	*0.264*	*0.015*
PER-SED 95-5_1280_72	8	40.8	-	0.102	6.62	0.095	51.9	0.249	0.204
		0.2	-	*0.045*	*0.46*	*0.013*	*0.4*	*0.046*	*0.181*
PER-SED 95-5_1280_96	6	41.2	-	0.075	5.43	0.115	52.8	0.218	0.138
		0.1	-	*0.011*	*0.61*	*0.007*	*0.6*	*0.011*	*0.026*
PER-SED 95-5_1315_72	10	41.8	0.018	0.053	4.29	0.088	53.6	0.208	0.029
		0.2	*0.008*	*0.028*	*0.13*	*0.018*	*0.5*	*0.025*	*0.011*
PER-SED 85-15_1230_96	13	40.5	-	0.020	9.18	0.131	49.9	0.165	0.091
		0.1	-	*0.014*	*0.07*	*0.022*	*0.1*	*0.018*	*0.031*
PER-SED 85-15_1280_72	5	41.9	-	-	5.02	0.123	52.4	0.274	0.091
		0.6	-	-	*0.05*	*0.020*	*0.8*	*0.075*	*0.039*
PER-SED 85-15_1315_72	10	41.8	-	0.075	3.55	0.088	54.2	0.253	0.034
		0.2	-	*0.007*	*0.05*	*0.020*	*0.2*	*0.016*	*0.033*
PER-SERP 85-15_1230_96	13	39.6	-	0.035	11.01	0.163	48.8	0.200	0.176
		0.1	-	*0.009*	*0.25*	*0.023*	*0.3*	*0.017*	*0.016*
PER-SERP 85-15_1280_72	10	41.2	-	0.119	6.01	0.114	52.0	0.263	0.276
		0.4	-	*0.109*	*0.94*	*0.023*	*1.1*	*0.039*	*0.057*
PER-SERP 85-15_1315_72	6	41.7	-	0.066	3.92	0.103	53.9	0.248	0.065
		0.1	-	*0.011*	*0.61*	*0.024*	*0.7*	*0.008*	*0.031*
PER-SERP 85-15_1350_72	6	41.6	-	0.061	3.71	0.119	54.2	0.277	0.077
		0.1	-	*0.011*	*0.08*	*0.026*	*0.2*	*0.019*	*0.032*

*n indicates number of individual analysis
numbers in italics are ± 1 s.d

		Clinopyroxene									
	n*	SiO_2	TiO_2	Al_2O_3	FeO_T	MnO	MgO	CaO	Na_2O	K_2O	Cr_2O_3
PER-SED 95-5_1150_96	6	49.0	0.816	10.48	3.45	0.134	18.5	16.8	0.458	-	0.262
		1.5	*0.171*	*1.83*	*0.32*	*0.021*	*2.4*	*1.6*	*0.071*	-	*0.130*
PER-SED 95-5_1280_24	6	53.1	0.223	5.83	2.67	0.098	21.0	16.1	0.604	-	0.312
		0.6	*0.034*	*0.89*	*0.37*	*0.029*	*0.8*	*1.0*	*0.037*	-	*0.068*
PER-SED 95-5_1280_48	4	52.2	0.376	7.56	2.36	0.110	20.5	15.7	0.746	-	0.490
		0.7	*0.106*	*0.87*	*0.28*	*0.002*	*0.5*	*0.6*	*0.187*	-	*0.261*
PER-SED 95-5_1280_72	1	53.0	0.244	5.46	3.53	0.113	23.3	13.2	0.664	-	0.465
		-	-	-	-	-	-	-	-	-	-
PER-SED 95-5_1280_96	6	52.4	0.328	6.83	2.58	0.092	20.0	16.7	0.874	-	0.234
		0.4	*0.060*	*0.73*	*0.33*	*0.017*	*0.5*	*0.8*	*0.094*	-	*0.034*
PER-SED 95-5_1315_72	10	51.7	0.429	6.11	2.85	0.089	16.6	20.3	1.113	-	0.756
		0.7	*0.102*	*1.03*	*0.36*	*0.015*	*1.2*	*0.5*	*0.515*	-	*0.170*
PER-SED 85-15_1230_96	10	47.8	1.137	10.01	6.41	0.139	15.2	18.4	0.611	-	0.258
		2.0	*0.248*	*1.87*	*0.99*	*0.022*	*2.7*	*2.0*	*0.204*	-	*0.090*
PER-SED 85-15_1280_72	6	53.1	0.314	6.33	2.83	0.110	20.6	15.6	0.807	0.008	0.265
		0.3	*0.048*	*0.81*	*0.42*	*0.010*	*0.9*	*0.9*	*0.091*	*0.004*	*0.100*
PER-SED 85-15_1315_72	4	54.2	0.187	4.73	1.97	0.110	22.1	15.5	0.687	-	0.435
		0.5	*0.024*	*0.48*	*0.11*	*0.010*	*0.4*	*1.1*	*0.014*	-	*0.420*
PER-SERP 85-15_1230_96	12	52.1	0.162	3.95	4.30	0.123	19.1	18.7	0.646	-	0.907
		0.3	*0.095*	*0.47*	*0.24*	*0.013*	*0.7*	*0.5*	*0.169*	-	*0.098*
PER-SERP 85-15_1280_72	6	53.0	0.226	5.91	2.82	0.132	21.2	15.7	0.768	-	0.244
		0.6	*0.070*	*0.86*	*0.85*	*0.022*	*1.0*	*1.0*	*0.090*	-	*0.051*
PER-SERP 85-15_1315_72	6	54.1	0.150	4.85	2.07	0.104	22.7	15.2	0.618	-	0.245
		0.5	*0.029*	*0.52*	*0.41*	*0.012*	*0.8*	*0.9*	*0.045*	-	*0.059*
PER-SERP 85-15_1350_72	6	54.3	0.103	4.32	2.06	0.121	23.3	15.0	0.526	-	0.253
		0.5	*0.018*	*0.57*	*0.17*	*0.013*	*0.9*	*0.9*	*0.032*	-	*0.046*

		Orthopyroxene									
	n*	SiO_2	TiO_2	Al_2O_3	FeO_T	MnO	MgO	CaO	Na_2O	K_2O	Cr_2O_3
PER-SED 95-5_1150_96	10	54.8	0.163	4.80	5.45	0.126	32.9	1.27	0.065	-	0.442
		1.2	*0.062*	*1.53*	*0.34*	*0.019*	*1.6*	*0.52*	*0.053*	-	*0.193*
PER-SED 95-5_1280_24	6	55.8	0.112	4.79	3.57	0.095	33.1	2.03	0.117	-	0.376
		0.8	*0.063*	*1.45*	*0.42*	*0.005*	*0.3*	*0.11*	*0.004*	-	*0.205*
PER-SED 95-5_1280_48	4	55.6	0.136	5.33	3.72	0.115	33.0	1.78	0.118	-	0.188
		1.0	*0.069*	*1.77*	*0.61*	*0.010*	*0.9*	*0.43*	*0.028*	-	*0.148*
PER-SED 95-5_1280_72	1	54.7	0.166	5.86	4.70	0.136	32.0	1.79	0.264	-	0.362
		0.8	*0.062*	*1.45*	*0.16*	*0.007*	*0.4*	*0.07*	*0.238*	-	*0.045*
PER-SED 95-5_1280_96	6	55.2	0.150	5.52	3.94	0.126	32.6	2.07	0.167	-	0.290
		0.7	*0.038*	*1.24*	*0.70*	*0.018*	*0.3*	*0.09*	*0.017*	-	*0.082*
PER-SED 95-5_1315_72	10	57.1	-	2.53	3.12	0.108	34.8	1.50	0.055	-	0.787
		0.3	-	*0.40*	*0.25*	*0.024*	*0.3*	*0.08*	*0.022*	-	*0.118*
PER-SED 85-15_1230_96	15	55.6	0.076	2.59	5.74	0.134	33.3	1.62	0.054	-	0.847
		0.2	*0.017*	*0.19*	*0.11*	*0.014*	*0.2*	*0.12*	*0.031*	-	*0.138*
PER-SED 85-15_1280_72	6	56.2	0.127	4.04	4.41	0.123	33.2	1.56	0.114	-	0.277
		0.8	*0.033*	*0.93*	*0.68*	*0.017*	*1.0*	*0.75*	*0.027*	-	*0.206*
PER-SED 85-15_1315_72	4	57.0	0.085	2.77	3.52	0.109	34.3	1.79	0.099	-	0.349
		0.6	*0.042*	*1.38*	*0.43*	*0.016*	*1.2*	*0.48*	*0.016*	-	*0.159*
PER-SERP 85-15_1230_96	15	54.4	0.074	3.28	7.01	0.154	32.8	1.68	0.078	-	0.588
		0.3	*0.017*	*0.19*	*0.25*	*0.013*	*0.4*	*0.27*	*0.029*	-	*0.154*
PER-SERP 85-15_1280_72	6	55.6	0.123	4.84	4.27	0.132	32.6	2.06	0.161	-	0.200
		0.4	*0.010*	*0.42*	*0.43*	*0.012*	*0.4*	*0.16*	*0.016*	-	*0.084*
PER-SERP 85-15_1315_72	6	57.2	0.075	2.99	2.96	0.113	34.4	1.97	0.145	-	0.162
		0.6	*0.023*	*1.17*	*0.46*	*0.027*	*0.7*	*0.54*	*0.030*	-	*0.087*
PER-SERP 85-15_1350_72	6	57.9	0.045	2.07	2.79	0.116	34.7	2.13	0.107	-	0.170
		0.6	*0.016*	*0.49*	*0.07*	*0.019*	*0.2*	*0.32*	*0.026*	-	*0.054*

References

1. Workman, R. K. & Hart, S. R. Major and trace element composition of the depleted MORB mantle (DMM). *Earth Planet. Sci. Lett.* **231,** 53–72 (2005).
2. Mallmann, G. & O'Neill, H. S. C. The Crystal/Melt Partitioning of V during Mantle Melting as a Function of Oxygen Fugacity Compared with some other Elements (Al, P, Ca, Sc, Ti, Cr, Fe, Ga, Y, Zr and Nb). *J. Petrol.* **50,** 1765–1794 (2009).
3. Lee, C.-T. A. *et al.* The redox state of arc mantle using Zn/Fe systematics. *Nature* **468,** 681 (2010).
4. Miller, D. P., Marschall, H. R. & Schumacher, J. C. Metasomatic formation and petrology of blueschist-facies hybrid rocks from Syros (Greece): Implications for reactions at the slab–mantle interface. *Lithos* **107,** 53–67 (2009).
5. Trotet, F., Jolivet, L. & Vidal, O. Tectono-metamorphic evolution of Syros and Sifnos islands (Cyclades, Greece). *Tectonophysics* **338,** 179–206 (2001).
6. Trotet, F., Vidal, O. & Jolivet, L. Exhumation of Syros and Sifnos metamorphic rocks (Cyclades, Greece). New constraints on the P-T paths. *Eur. J. Mineral.* **13,** 901–902 (2001).
7. Breeding, C. M., Ague, J. J. & Bröcker, M. Fluid–metasedimentary rock interactions in subduction-zone mélange: Implications for the chemical composition of arc magmas. *Geology* **32,** 1041–1044 (2004).
8. Pogge von Strandmann, P. A. E., Dohmen, R., Marschall, H. R., Schumacher, J. C. & Elliott, T. Extreme Magnesium Isotope Fractionation at Outcrop Scale Records the Mechanism and Rate at which Reaction Fronts Advance. *J. Petrol.* **56,** 33–58 (2015).
9. Boyd, F. R. & England, J. L. Apparatus for phase-equilibrium measurements at pressures up to 50 kilobars and temperatures up to 1750°C. *J. Geophys. Res.* **65,** 741–748 (1960).
10. Gaetani, G. A. & Grove, T. L. The influence of water on melting of mantle peridotite. *Contrib. Mineral. Petrol.* **131,** 323–346 (1998).
11. Syracuse, E. M., Keken, P. E. van & Abers, G. A. The global range of subduction zone thermal models. *Phys. Earth Planet. Inter.* **183,** 73–90 (2010).
12. England, P. C. & Katz, R. F. Melting above the anhydrous solidus controls the location of volcanic arcs. *Nature* **467,** 700–703 (2010).

13. Johannes, W. *et al.* An interlaboratory comparison of piston-cylinder pressure calibration using the albite-breakdown reaction. *Contrib. Mineral. Petrol.* **32,** 24–38 (1971).
14. Hays, J. F. Lime-alumina-silica. *Carnegie Inst. Wash. Yearb.* **65,** 234–239 (1966).
15. Jochum Klaus Peter *et al.* MPI-DING reference glasses for in situ microanalysis: New reference values for element concentrations and isotope ratios. *Geochem. Geophys. Geosystems* **7,** (2006).
16. Wasylenki, L. E., Baker, M. B., Kent, A. J. R. & Stolper, E. M. Near-solidus Melting of the Shallow Upper Mantle: Partial Melting Experiments on Depleted Peridotite. *J. Petrol.* **44,** 1163–1191 (2003).
17. Plank, T. & Langmuir, C. H. The chemical composition of subducting sediment and its consequences for the crust and mantle. *Chem. Geol.* **145,** 325–394 (1998).
18. Gale, A., Dalton, C. A., Langmuir, C. H., Su, Y. & Schilling, J.-G. The mean composition of ocean ridge basalts. *Geochem. Geophys. Geosystems* **14,** 489–518 (2013).
19. Turner, S. J. & Langmuir, C. H. The global chemical systematics of arc front stratovolcanoes: Evaluating the role of crustal processes. *Earth Planet. Sci. Lett.* **422,** 182–193 (2015).
20. Rapp, R.P, Shimizu, N, Norman, M.D & Applegate, G.S. Reaction between slab-derived melts and peridotite in the mantle wedge: experimental constraints at 3.8 GPa. *Chem. Geol.* **160,** 335–356 (1999).
21. Pirard, C. & Hermann, J. Focused fluid transfer through the mantle above subduction zones. *Geology* **43,** 915–918 (2015).
22. Mallik, A., Nelson, J. & Dasgupta, R. Partial melting of fertile peridotite fluxed by hydrous rhyolitic melt at 2–3 GPa: implications for mantle wedge hybridization by sediment melt and generation of ultrapotassic magmas in convergent margins. *Contrib. Mineral. Petrol.* **169,** 48 (2015).
23. Schmidt, M. W. & Jagoutz, O. The global systematics of primitive arc melts. *Geochem. Geophys. Geosystems* **18,** 2817–2854 (2017).
24. Till, C. B. A review and update of mantle thermobarometry for primitive arc magmas. *Am. Mineral.* **102,** 931 (2017).
25. Castro, A. & Gerya, T. V. Magmatic implications of mantle wedge plumes: Experimental study. *Lithos* **103,** 138–148 (2008).

26. Castro, A. *et al.* Melting Relations of MORB–Sediment Mélanges in Underplated Mantle Wedge Plumes; Implications for the Origin of Cordilleran-type Batholiths. *J. Petrol.* **51,** 1267–1295 (2010).

27. Cruz-Uribe, A. M., Marschall, H. R., Gaetani, G. A. & Le Roux, V. Generation of alkaline magmas in subduction zones by partial melting of mélange diapirs—An experimental study. *Geology* **46,** 343–346 (2018).

Supplementary materials for Chapter 6

Methods

Data filtering

The compiled data used in this study are from the GEOROC database (http://georoc.mpch-mainz.gwdg.de), additional data on Quaternary volcanic arc lavas are from EarthChem (https://doi.org/10.1594/IEDA/100664), as well as from individual studies (Ishizuka et al., 2020; Li et al., 2019). The geochemical data in this compilation were obtained using X-ray fluorescence (XRF) for major element oxides (e.g., MgO, SiO_2), either Inductively Coupled Plasma Mass Spectrometry (ICPMS) or Inductively Coupled Plasma Atomic Emission Spectroscopy (ICPAES) for trace elements (e.g,, Ba, Sr, Th, Pb), and either Thermal Ionization Mass Spectrometry (TIMS) or Multicollector-Inductively Coupled Plasma Mass Spectrometry (MC-ICPMS) for radiogenic isotopes (e.g., Sr and Nd isotope ratios). We selected whole rock compositions where the sum of major element oxides is ~96–100 wt. %, applicable for these hydrous arc magmas. Most of the data have totals of 98–100 wt. %. The published datasets on volcanic rock composition were filtered (SiO_2 < 63 wt. %) to minimize the minor effects of intra-crustal differentiation and crustal contamination based on (i) correlations (or the lack thereof) between radiogenic Sr-Nd-Pb isotopes and SiO_2 or Eu/Eu* [=Eu/$(Sm_N \times Gd_N)^{1/2}$, where N is chondrite-normalized (McDonough and Sun, 1995)] (Supplementary Fig. 1), and (ii) using P-Zr- SiO_2 systematics (Lee and Bachmann, 2014) (Supplementary Fig. 2). The SiO_2 content of these magmas do not follow the liquid lines of descent expected for fractional crystallization-controlled compositions based on P-Zr-SiO_2 systematics (Supplementary Fig. 2). In addition, the lack of strong correlations between radiogenic Sr-Nd-Pb isotope ratios and SiO_2 and Eu/Eu* > 0.9 [=Eu/$(Sm_N \times Gd_N)^{1/2}$, where N is chondrite-normalized; i.e. proxy for plagioclase fractionation (Weill Daniel F. and Drake Michael J., 1973) or assimilation of evolved plagioclase-rich crustal rocks (Turner and Langmuir, 2015)], all indicate that Izu-Bonin rocks are minimally affected by crustal assimilation during magma transit through a thin overriding crust (16–22 km) (Stern et al., 2003). These geochemical observations and the uniformly thin overriding crust indicate that the compositions of Izu Bonin magmas primarily reflect the contributions from ambient mantle and subducted slab components (Straub, 2003; Straub et al., 2010). We note that using an unfiltered geochemical dataset of Izu-Bonin rocks, the

same geochemical systematics are observed. For all other subduction zones, we filtered and plotted volcanic rock compositions with SiO_2 less than 63 wt. % to minimize the effects of magmatic differentiation and crustal assimilation, similar to the Izu-Bonin volcanic rocks (Supplementary Data 1 and 3).

Compositions of mantle and subducted materials

The isotopic compositions of the subarc mantle in Izu-Bonin were previously inferred from the isotopic composition of basalts from PSP and Shikoku Basin (SB), corrected for radiogenic ingrowth (Supplementary Data 2). The Sr isotope composition of the mantle is assumed to be 0.7026. This value corresponds to the Sr isotope composition of fresh pillow basalt glass drilled in the Shikoku back-arc basin (Straub et al., 2010) and is very similar to the MORB-like samples from the Mariana Trough (Gribble et al., 1996). Previous estimates on the Nd isotope composition range from less radiogenic (0.51305) to more radiogenic, DMM-like values (0.51315) (Straub et al., 2010; Tollstrup et al., 2010). To this end, this study used the composition of DMM(Salters and Stracke, 2004) to represent a mantle relatively unaffected by previous melt metasomatism. Importantly, using a different Nd isotope composition for subarc mantle, *e.g.*, $^{143}Nd/^{144}Nd = 0.3105$ (Straub et al., 2010), would only slightly change the relative mixing proportions between subducted slab and mantle components but would not change the curvature of mixing trajectories and would not impact any of our conclusions.

The Sr isotope composition of igneous crust altered by seawater in oceanic settings displays more radiogenic Sr isotope composition, close to seawater. The Nd isotope composition of igneous crust is relatively insensitive to seawater alteration, and should therefore reflect the source composition. The Sr and Nd isotope composition of altered igneous crust is constrained by the composition of ODP Site1149 (outboard of the Izu arc) from Hauff et al. (2003). The lack of isotopic fractionation between slab (oceanic igneous crust) and fluid during slab dehydration at high *P-T* conditions during subduction suggests that the Sr and Nd isotope compositions of fluid produced from the dehydration of altered oceanic crust is the same as the source. The elemental composition of altered oceanic crust is reported by Kelley *et al*. (2003).

The elemental and Sr and Nd isotope compositions of subducted sediments are summarized by Ishizuka *et al*. (2020), which were constrained from the compositions of sediments outboard of

Izu arc reported from ODP Site 1149 by Plank *et al*. (2007) and from ODP Site 801 by Plank and Langmuir (1998).

Trace-element fractionations during hydrous sediment and mélange melting

The extent of fractionations during hydrous melting of sediment (Hermann and Rubatto, 2009), mélange (Castro et al., 2010; Cruz-Uribe et al., 2018), and mantle-hybridized by small volume proportion of mélange components (5–15 vol. % mélange; Codillo et al., 2018) are shown (Supplementary Fig. 8). Extensive fractionations in trace-element ratios are observed during sediment melting. This is because the partition coefficients used for these calculations contain hydrous melt coexisting with phases such as phengite, epidote, and rutile which produce the fractionations. The melting and mixing models presented in Figs. 1 and 2 demonstrate that residual phases such as phengite, epidote, and rutile are necessary to produce the range in trace-element ratios we observed in Izu-Bonin magmas. Available mélange melting experiments also show trace-element fractionations, but experiments are still limited and do not currently cover the full range of natural mélange compositions. Therefore, we combine results from mélange experiments and sediment melting experiments to identify the residual phases that can fractionate the selected trace-element ratios. A limited number of melting experiments on a natural chlorite-rich mélange rock have reported residual pyroxenes ± olivine ± amphibole ± phlogopite ± garnet ± plagioclase ± rutile ± ilmenite coexisting with hydrous melt (Cruz-Uribe et al., 2018). Melting of mélange-hybridized mantle also produced limited fractionations in absence of phases such as phengite, epidote, and rutile. To provide a minimum possible trace-element fractionation during melting of mélange rocks and mélange-hybridized mantle in nature, we plotted the maximum observed fractionations (pink star) from available mélange melting experimental data (Supplementary Fig. 8) in Figs. 1 and 2. The pink dashed line connects the pink star to a presumed mélange composition that can be formed by bulk mixing of different slab and mantle components. Importantly, exhumed high-pressure mélange rocks, such as from Western Alps (Europe), Catalina and Franciscan Complex (USA), Sistan (Iran), and Rio San Juan Complex (Dominican Republic) contain variable proportions of chlorite, talc, amphibole, pyroxene, garnet, zircon, rutile, phengite, phlogopite, epidote, monazite, and sulfides, among others (Bebout and Penniston-Dorland, 2016; Marschall and Schumacher, 2012). Therefore, if phases such as phengite, epidote, and rutile are present in the residue during melting of mélange rocks, the resulting melts will display significant trace-

element fractionations, similar to the trends displayed by hydrous sediment melting models (Supplementary Fig. 7).

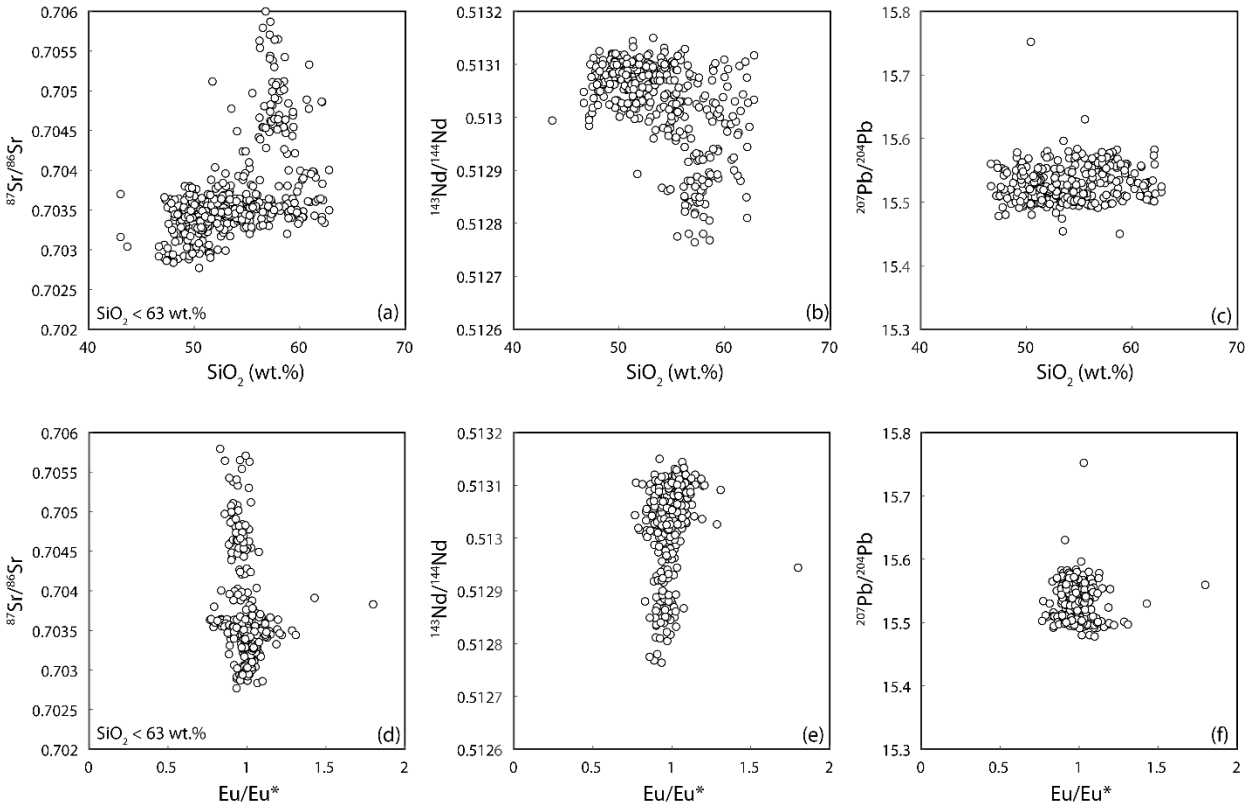

Supplementary Fig. 1. Plots of Sr-Nd-Pb isotopes against SiO_2 and Eu/Eu* for volcanic rocks (SiO_2 < 63 wt. %) in the Izu-Bonin investigated in this study. The SiO_2 content is taken as proxy for fractionation crystallization while Eu/Eu* is a proxy for plagioclase fractionation or assimilation of plagioclase-rich evolved crustal rocks during magma transit through the overriding crust.

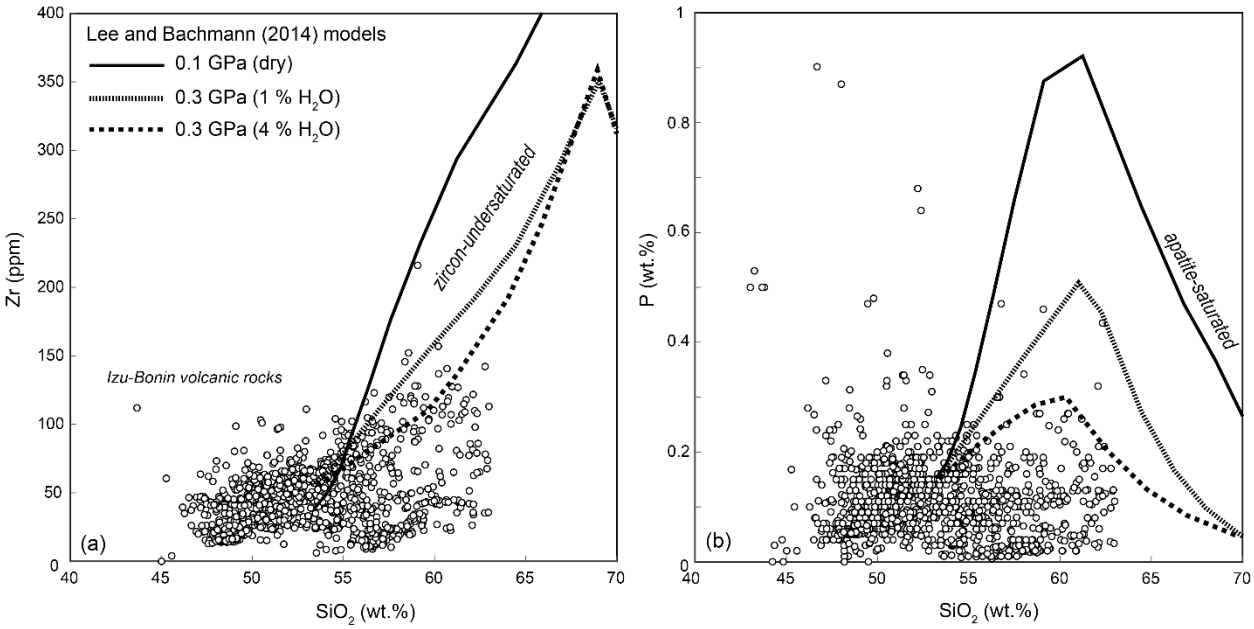

Supplementary Fig. 2. Plots of P_2O_5 (wt. %) and Zr (ppm) versus SiO_2 (wt. %) for Izu-Bonin volcanics filtered for SiO_2 < 63 wt. %. Modeled residual liquids formed by equilibrium crystallization of dry and hydrous parental basalts calculated by Lee and Bachmann (2014) using Rhyolite-Melts (Gualda et al., 2012).

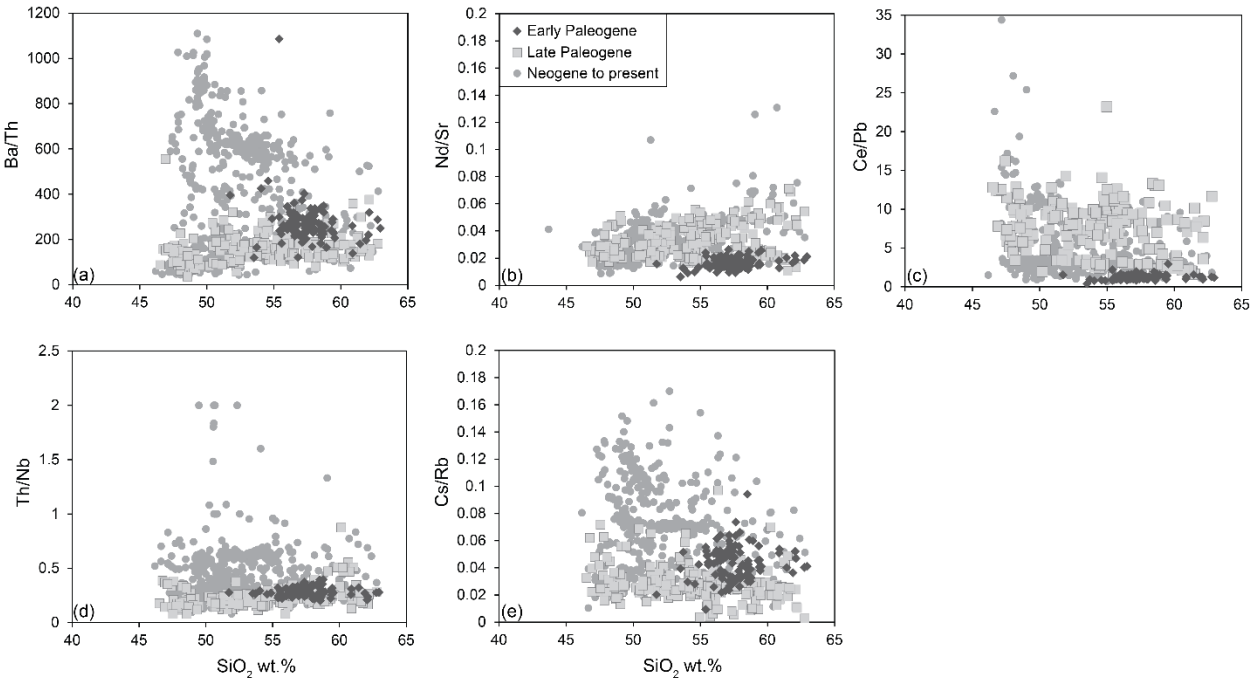

Supplementary Fig. 3. Correlations between trace-element ratios used in this study versus SiO_2. The SiO_2 contents is taken as an index for fractional crystallization. The lack of correlations suggest that these trace-element ratios are not significantly affected by magmatic differentiation processes.

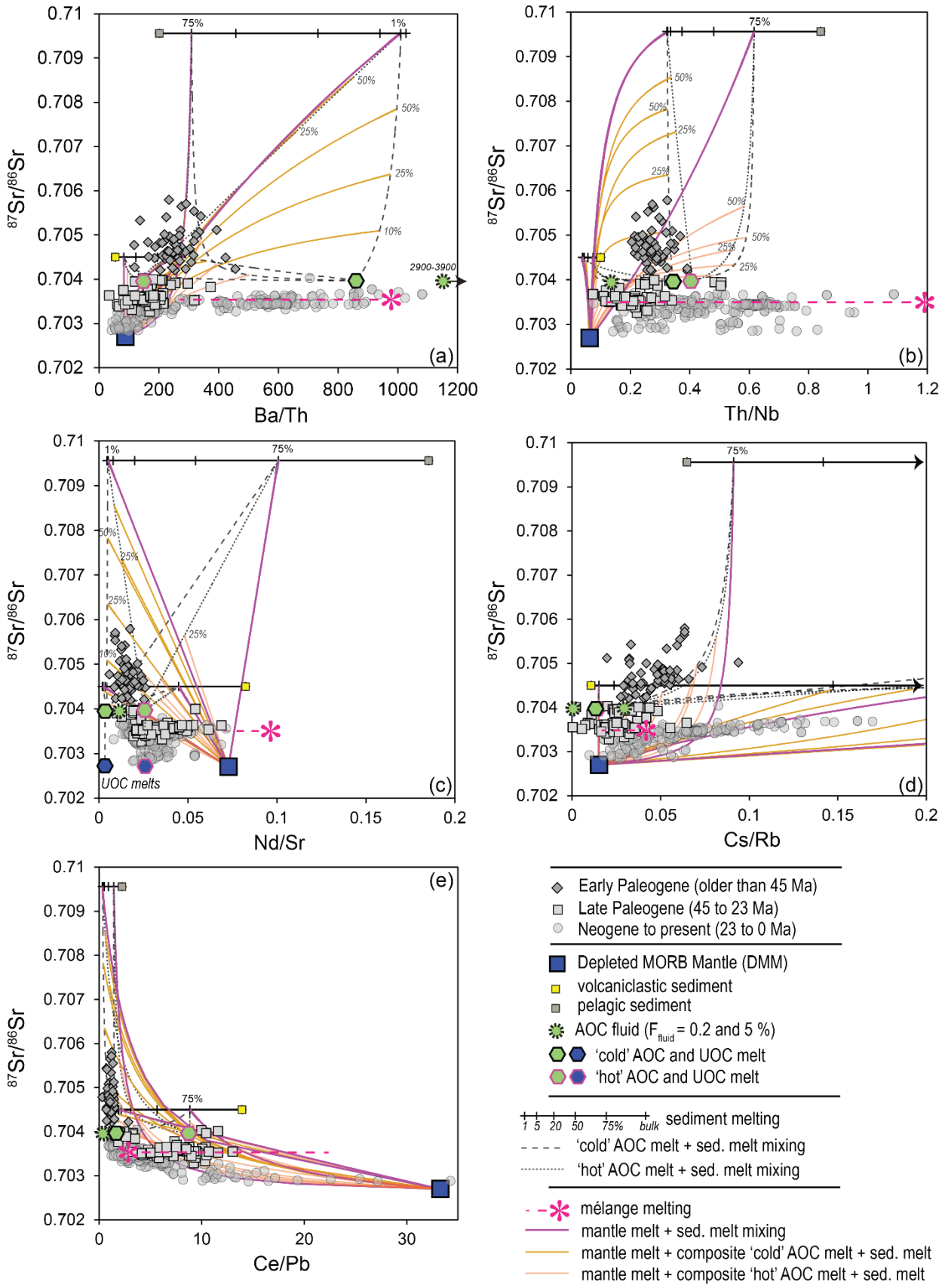
87Sr/86Sr
Ba/Th
Th/Nb
Nd/Sr
Cs/Rb
Ce/Pb
(a)
(b)
(c)
(d)
(e)
UOC melts
2900-3900
Early Paleogene (older than 45 Ma)
Late Paleogene (45 to 23 Ma)
Neogene to present (23 to 0 Ma)
Depleted MORB Mantle (DMM)
volcaniclastic sediment
pelagic sediment
AOC fluid (F fluid = 0.2 and 5 %)
'cold' AOC and UOC melt
'hot' AOC and UOC melt
1 5 20 50 75% bulk sediment melting
'cold' AOC melt + sed. melt mixing
'hot' AOC melt + sed. melt mixing
mélange melting
mantle melt + sed. melt mixing
mantle melt + composite 'cold' AOC melt + sed. melt
mantle melt + composite 'hot' AOC melt + sed. melt

Supplementary Fig. 4. Discrimination of the different models of slab-to-mantle transfer based on Sr isotope and trace element ratios. Sr isotopes versus fluid-sensitive (a, c, e) and fluid-insensitive (b, d, f) ratios in age-categorized Izu-Bonin arc volcanics (SiO_2 < 63 wt. %). Mixing lines are constructed between DMM either (i) sediment partial melts (purple bold lines) or (ii) composite slab melts (yellow and peach bold lines). The composite slab melts represent mixtures of sediment partial melts and globally representative ('cold' and 'hot') AOC melts. The Nd/Sr values of UOC melts are assumed to be similar that of AOC melts but with Sr isotope composition similar to DMM. Composition of fluids derived from dehydration of AOC that contained 0.2–5 wt. % of water were calculated using Rayleigh distillation equation. Mélange melting trend is shown, where the star symbol (in pink) indicates the maximum trace-element fractionation observed in high *P-T* mélange melting experiments which is taken as a minimum possible trace-element fractionation that can occur in nature. The length of the mélange melting trend points to the bulk mixing region while the Sr isotope value corresponds to average value for Quaternary volcanics. Notably, quantitative constraints on the melting and mixing processes for all the different models of slab-to-mantle transfer are consistent with constraints obtained in Fig.1 (Nd isotopes versus trace-element ratios).

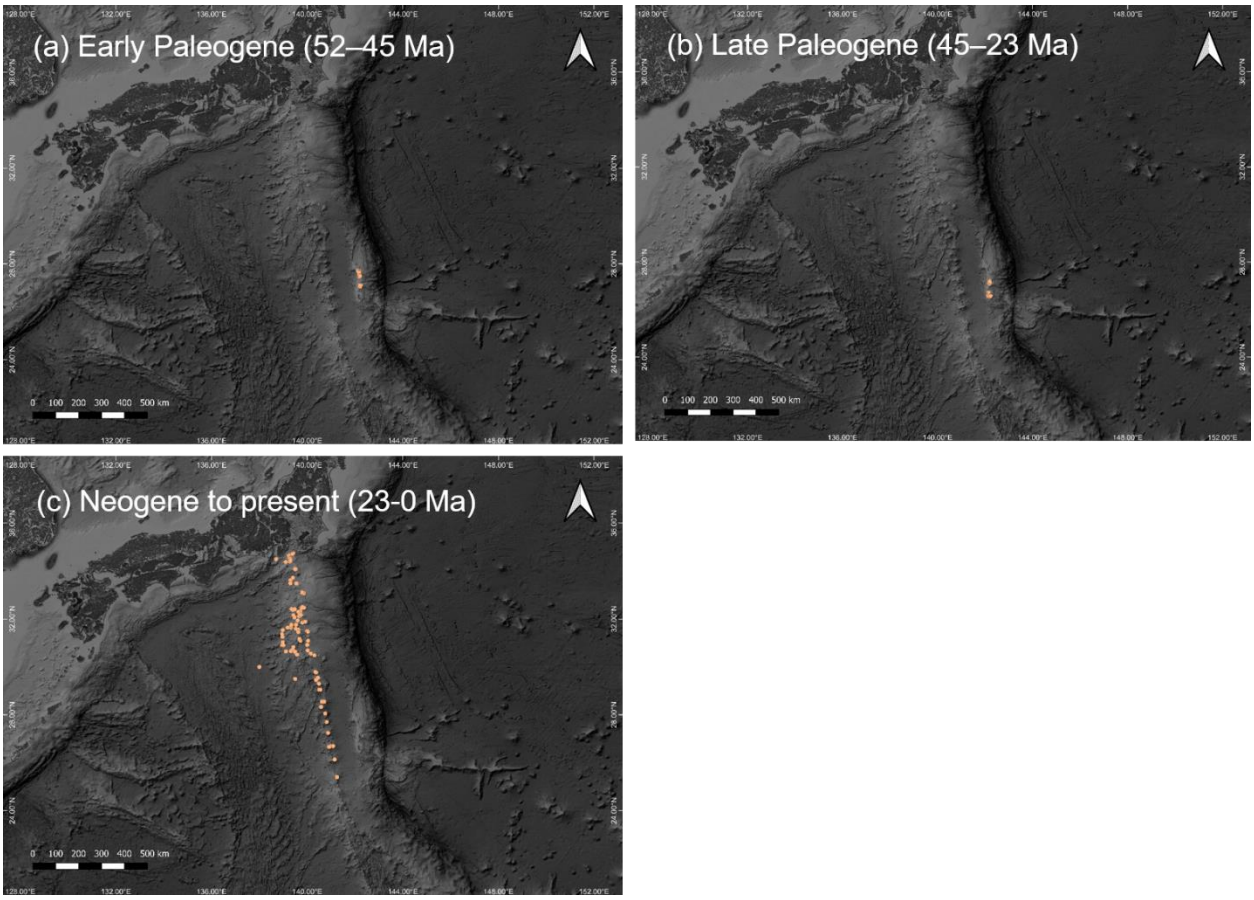

Supplementary Fig. 5. Sample location maps of the volcanic rock dataset (filtered for SiO_2 < 63 wt. %) used in this study. Location maps categorized according to their eruption ages for (a) Early Paleogene, (b) Late Paleogene, and (c) Neogene to present. Note that the number of points on the map does not equate to the number of geochemical data points plotted in Fig. 2 as multiple samples and measurements were taken from a single location.

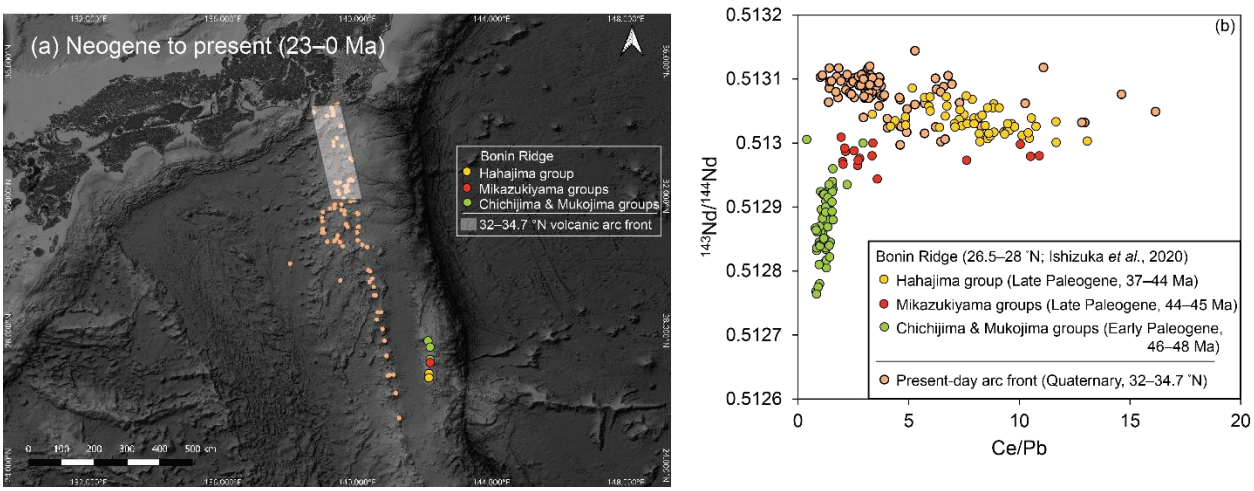

Supplementary Fig. 6. Location vs. time geochemical variability. Geochemical variations in well-dated rocks from the geographically restricted Bonin Islands (~26–28 °N) and select Quaternary rocks from the northern segment of the present-day volcanic arc front (32–34.7 °N). (a) Sample location map. (b) Ce/Pb vs. $^{143}Nd/^{144}Nd$ isotope ratios. The Bonin Islands capture the geochemical transition from melting of discrete subducted materials (model 1) as recoded by Chichijima and Mukojima groups to mélange-melting model (model 2) as recorded by Mikazukiyama and Hahajima groups. This shows that samples that overlap spatially (i.e. samples restricted in the Bonin Ridge), but not temporally (i.e. transition from Early Paleogene to Late Paleogene), still display distinctly different geochemical trends. In comparison, the compositions of the select Quaternary rocks that are geographically distant from the Bonin Islands record geochemical trends similar to, and overlapping with the Hahajima group. These strongly suggest that the transition in the models of slab-to-mantle transfer (from model 1 to 2) that we documented in Izu-Bonin is a temporal trend related to the evolving slab-top temperature and is not due to the changing location of magmatic activity and slab input over time.

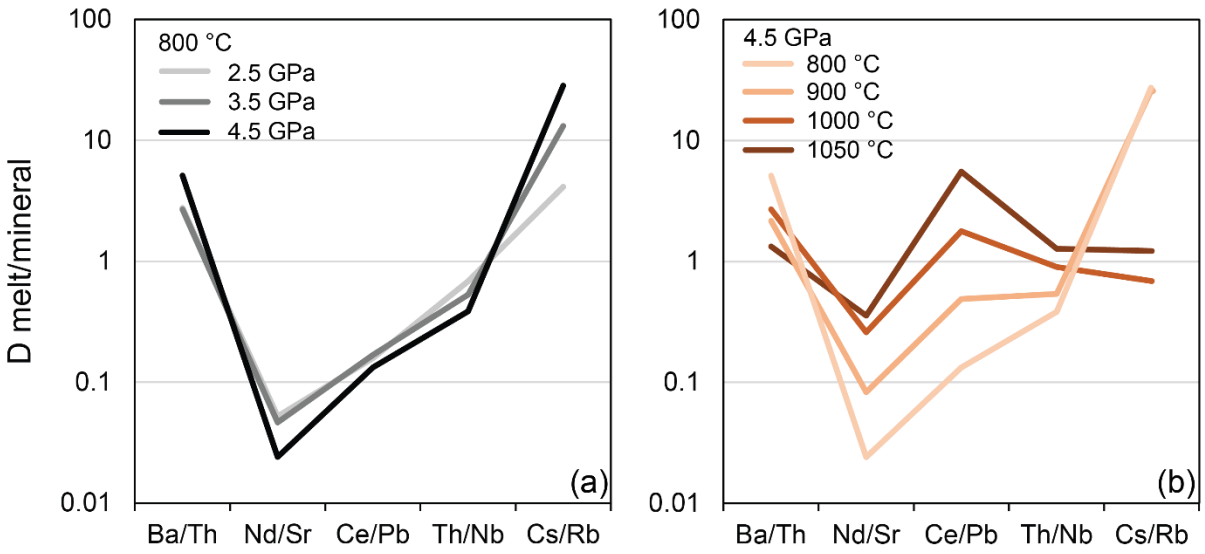

Supplementary Fig. 7. Behavior of trace-element ratios used in this study during hydrous sediment melting as a function of (a) pressure and (b) temperature (Hermann and Rubatto, 2009). These experimental data show higher sensitivity of the measured partition of coefficients to temperature than to pressure.

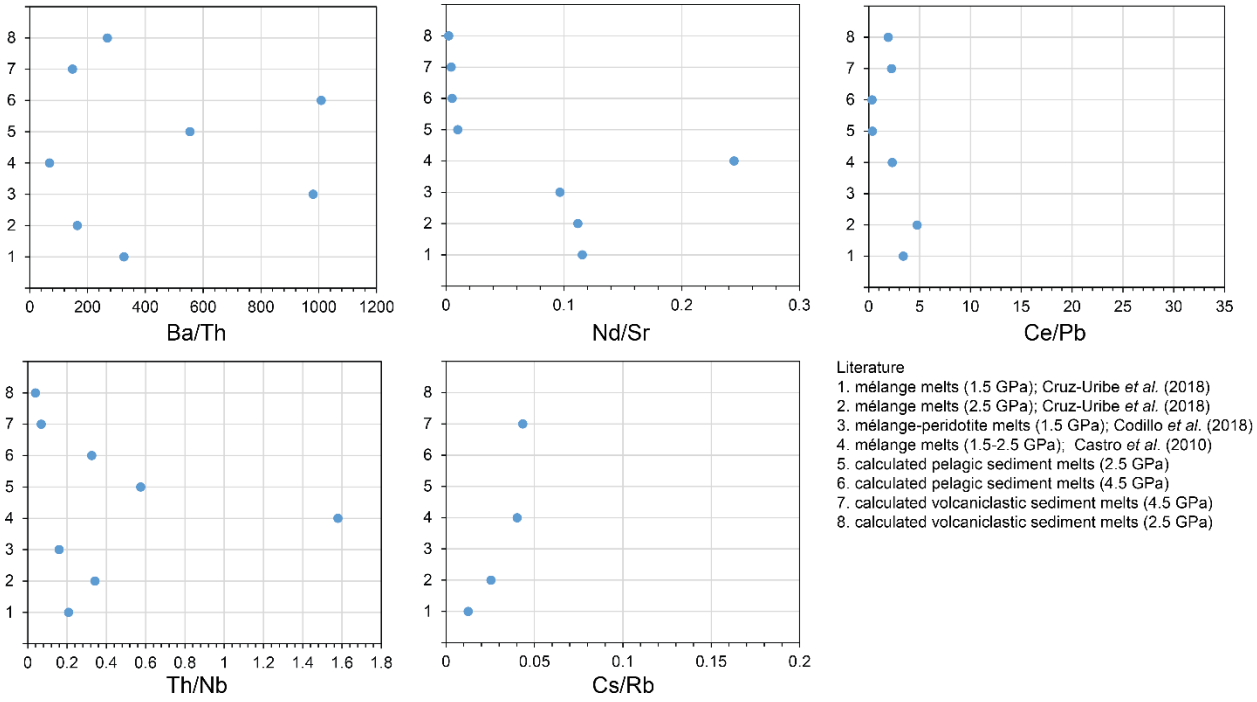

Supplementary Fig. 8. Extent of trace-element fractionations in (a) Ba/Th, (b) Nd/Sr, (c) Ce/Pb, (d) Th/Nb, and (e) Cs/Rb, produced during hydrous melting of sediment (Hermann and Rubatto, 2009), during mélange melting (Castro et al., 2010; Cruz-Uribe et al., 2018), and during melting of mélange-hybridized mantle (Codillo et al., 2018). The fractionations are expected to be more extensive in nature as experiments do not cover the full range of mélange/sediment compositions and degrees of melting.

Table 1. Compilation of geochemical data from the Izu-Bonin arc (This online dataset can be downloaded here: https://doi.org/10.5281/zenodo.7199013)

Table 3. Compilation of geochemical data from the Philippine, Ryukyu, Cascadia, Kurile, Kamchatka, and Mariana arcs. (This online dataset can be downloaded here: https://doi.org/10.5281/zenodo.7199013)

Table 2. Summary of elemental and isotopic compositions of subducted materials and ambient mantle, and relevant partition coefficients used in melting and dehydration models.

Bulk partition coefficents used for melting and dehydration models				**Compositions of subducted sediments, MORB, and mantle**			
	D solid/melt		**D eclogite/aqueous fluid**	**Marianas Volcaniclastic sediment**	**Izu pelagic sediment**	**N-MORB**	**Depleted MORB Mantle (DMM)**
conditions	800 ^{o}C. 4.5 GPa		700 ^{o}C, 4 GPa				
sources	Hermann and Rubatto (2009)		Kessel et al. (2005)	Plank and Langmuir (1998)	Plank et al. (2007)	Gale et al. (2013)	Salters and Stracke (2004)
				ppm	ppm	ppm	ppm
Rb	1.3		0.0	26.0	46.3	1.8	0.1
Sr	0.1		2.9	267.0	136.0	128.0	9.8
Nb	0.9		18.0	25.0	5.2	3.6	0.2
Cs	0.0		0.0	0.3	3.0	0.0	0.0
Ba	0.4		0.2	134.0	884.0	19.6	1.2
Ce	2.2		8.2	39.0	34.3	12.4	0.8
Nd	2.6		18.3	22.0	25.2	10.7	0.7
Th	2.3		8.4	2.5	4.4	0.3	0.0
Pb	0.3		0.3	2.8	15.4	0.5	0.0

Compositions of 'cold' and 'hot' crustal melts	
F = 10%	F = 30%
Turner and Langmuir (2022)	
ppm	ppm
16.2	6.1
834.0	415.0
0.6	1.1
0.2	0.1
172.0	65.0
4.5	13.5
3.8	10.6
0.2	0.4
2.6	1.5

	igneous crust[1]	**pelagic sediment[2]**	**volcaniclastics[3]**	**depleted mantle[4]**
	Site 1149 average	Site 1149 (Izu)	Site 801	
$^{87}Sr/^{86}Sr$	0.70397	0.7096	0.7045	0.7027
$^{143}Nd/^{144}Nd$	0.513149	0.512336	0.51276	0.51315

*The isotopic composition of subducted sediments, igneous crust, and mantle endmembers were adapted from Ishizuka et al. (2020) and references therein.

[1] Isotopic compositions of igneous crust at ODP Site1149 (outboard of the Izu arc) from Hauff et al. (2003).

[2] Isotopic compositions of pelagic sediment outboard of Izu arc from ODP Site 1149 by Plank et al. (2007).

[3] Isotopic compositions of volcaniclastic sediment from ODP Site 801 by Plank and Langmuir (1998).

[4] Isotopic compositions of depleted mantle adapted from Nielsen and Marschall (2017) and Straub et al. (2010).

References

Bebout, G.E., Penniston-Dorland, S.C., 2016. Fluid and mass transfer at subduction interfaces—The field metamorphic record. Lithos 240–243, 228–258. https://doi.org/10.1016/j.lithos.2015.10.007

Castro, A., Gerya, T., García-Casco, A., Fernández, C., Díaz-Alvarado, J., Moreno-Ventas, I., Löw, I., 2010. Melting Relations of MORB–Sediment Mélanges in Underplated Mantle Wedge Plumes; Implications for the Origin of Cordilleran-type Batholiths. Journal of Petrology 51, 1267–1295. https://doi.org/10.1093/petrology/egq019

Codillo, E.A., Le Roux, V., Marschall, H.R., 2018. Arc-like magmas generated by mélange-peridotite interaction in the mantle wedge. Nature Communications 9, 2864. https://doi.org/10.1038/s41467-018-05313-2

Cruz-Uribe, A.M., Marschall, H.R., Gaetani, G.A., Le Roux, V., 2018. Generation of alkaline magmas in subduction zones by partial melting of mélange diapirs—An experimental study. Geology 46, 343–346. https://doi.org/10.1130/G39956.1

Gribble, R.F., Stern, R.J., Bloomer, S.H., Stüben, D., O'Hearn, T., Newman, S., 1996. MORB mantle and subduction components interact to generate basalts in the southern Mariana Trough back-arc basin. Geochimica et Cosmochimica Acta 60, 2153–2166. https://doi.org/10.1016/0016-7037(96)00078-6

Gualda, G.A.R., Ghiorso, M.S., Lemons, R.V., Carley, T.L., 2012. Rhyolite-MELTS: a Modified Calibration of MELTS Optimized for Silica-rich, Fluid-bearing Magmatic Systems. Journal of Petrology 53, 875–890. https://doi.org/10.1093/petrology/egr080

Hauff, F., Hoernle, K., Schmidt, A., 2003. Sr-Nd-Pb composition of Mesozoic Pacific oceanic crust (Site 1149 and 801, ODP Leg 185): Implications for alteration of ocean crust and the input into the Izu-Bonin-Mariana subduction system. Geochemistry, Geophysics, Geosystems 4. https://doi.org/10.1029/2002GC000421

Hermann, J., Rubatto, D., 2009. Accessory phase control on the trace element signature of sediment melts in subduction zones. Chemical Geology 265, 512–526. https://doi.org/10.1016/j.chemgeo.2009.05.018

Ishizuka, O., Taylor, R.N., Umino, S., Kanayama, K., 2020. Geochemical Evolution of Arc and Slab Following Subduction Initiation: a Record from the Bonin Islands, Japan. Journal of Petrology 61. https://doi.org/10.1093/petrology/egaa050

Kelley, K.A., Plank, T., Ludden, J., Staudigel, H., 2003. Composition of altered oceanic crust at ODP Sites 801 and 1149. Geochemistry, Geophysics, Geosystems 4. https://doi.org/10.1029/2002GC000435

Lee, C.-T.A., Bachmann, O., 2014. How important is the role of crystal fractionation in making intermediate magmas? Insights from Zr and P systematics. Earth and Planetary Science Letters 393, 266–274. https://doi.org/10.1016/j.epsl.2014.02.044

Li, H.-Y., Taylor, R.N., Prytulak, J., Kirchenbaur, M., Shervais, J.W., Ryan, J.G., Godard, M., Reagan, M.K., Pearce, J.A., 2019. Radiogenic isotopes document the start of subduction in the Western Pacific. Earth and Planetary Science Letters 518, 197–210. https://doi.org/10.1016/j.epsl.2019.04.041

Marschall, H.R., Schumacher, J.C., 2012. Arc magmas sourced from mélange diapirs in subduction zones. Nature Geosci 5, 862–867. https://doi.org/10.1038/ngeo1634

McDonough, W.F., Sun, S. -s., 1995. The composition of the Earth. Chemical Geology 120, 223–253. https://doi.org/10.1016/0009-2541(94)00140-4

Plank, T., Kelley, K., Murray, R., Stern, L., 2007. Chemical composition of sediments subducting at the Izu-Bonin trench. Geochem. Geophys. Geosyst 3060, 4–16. https://doi.org/10.1029/2006GC001444

Plank, T., Langmuir, C.H., 1998. The chemical composition of subducting sediment and its consequences for the crust and mantle. Chemical Geology 145, 325–394. https://doi.org/10.1016/S0009-2541(97)00150-2

Salters, V.J.M., Stracke, A., 2004. Composition of the depleted mantle. Geochemistry, Geophysics, Geosystems 5. https://doi.org/10.1029/2003GC000597

Stern, B., Fouch, M., Klemperer, S., 2003. An overview of the Izu-Bonin-Mariana subduction factory. Washington DC American Geophysical Union Geophysical Monograph Series 138, 175–222. https://doi.org/10.1029/138GM10

Straub, S.M., 2003. The evolution of the Izu Bonin - Mariana volcanic arcs (NW Pacific) in terms of major element chemistry. Geochemistry, Geophysics, Geosystems 4. https://doi.org/10.1029/2002GC000357

Straub, S.M., Goldstein, S.L., Class, C., Schmidt, A., Gomez-Tuena, A., 2010. Slab and Mantle Controls on the Sr–Nd–Pb–Hf Isotope Evolution of the Post 42 Ma Izu–Bonin Volcanic Arc. Journal of Petrology 51, 993–1026. https://doi.org/10.1093/petrology/egq009

Tollstrup, D., Gill, J., Kent, A., Prinkey, D., Williams, R., Tamura, Y., Ishizuka, O., 2010. Across-arc geochemical trends in the Izu-Bonin arc: Contributions from the subducting slab, revisited. Geochemistry, Geophysics, Geosystems 11. https://doi.org/10.1029/2009GC002847

Turner, S.J., Langmuir, C.H., 2015. The global chemical systematics of arc front stratovolcanoes: Evaluating the role of crustal processes. Earth and Planetary Science Letters 422, 182–193. https://doi.org/10.1016/j.epsl.2015.03.056

Weill Daniel F., Drake Michael J., 1973. Europium Anomaly in Plagioclase Feldspar: Experimental Results and Semiquantitative Model. Science 180, 1059–1060. https://doi.org/10.1126/science.180.4090.1059